

**ROCKET PROPULSION AND
SPACEFLIGHT DYNAMICS**

SCHÖYER
WAKKER
CORNELISSE

ROCKET PROPULSION AND SPACEFLIGHT DYNAMICS



J W CORNELISSE H F R SCHÖYER K F WAKKER



PITMAN

Rocket Propulsion and Spaceflight Dynamics is designed to be a complete and integrated text on the basis of spaceflight, incorporating rocket propulsion, trajectory analysis, orbital mechanics and interplanetary flights. It is introduced by a general discussion on astronautics, on the basic concepts in astronomy and geophysics, and on the mechanics of particles, bodies and fluids.

Derived from the authors' experience in presenting a series of postgraduate courses at the Department of Aerospace Engineering of Delft University of Technology, this text is unique in co-ordinating established data from diverse sources and in providing a thorough working knowledge of astronautics. It is ideally suited both as a handbook for those working in the field, and as a textbook for self-study and for graduate courses.

The authors, although aiming at uniform notation and presentation, have not only provided a text with sufficient flexibility to enable it to be used with other texts and source material, but which will also assist the reader in gaining an overall understanding of the field, whilst clarifying the frequently confused nomenclature.

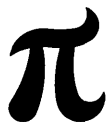
This text will prove invaluable to institutions in aerospace research, development and operations, to all concerned with contributory components and systems, and as a textbook for senior undergraduate and graduate level courses.

Rocket Propulsion and Spaceflight Dynamics

J. W. Cornelisse ESTEC, Noordwijk

H. F. R. Schöyer Delft University of Technology

K. F. Wakker Delft University of Technology



Pitman

LONDON · SAN FRANCISCO · MELBOURNE

ACCESSION No.		155472	
CLASS No.		629.411 COR	
		9 AUG 1979	
G/S	N		NORMAL

B119

PITMAN PUBLISHING LIMITED
39 Parker Street, London WC2B 5PB

FEARON-PITMAN PUBLISHERS INC.
6 Davis Drive, Belmont, California 94002, USA

Associated Companies

Copp Clark Ltd, Toronto
Pitman Publishing New Zealand Ltd, Wellington
Pitman Publishing Pty Ltd, Melbourne

First published 1979

British Library Cataloguing in Publication Data

Cornelisse, J. W.

Rocket propulsion and spaceflight dynamics.

1. Astrodynamics 2. Space vehicles—Propulsion systems

1. Title II. Schoyer, H F R III. Wakker, K F

629.411 TL1050 78-40059

ISBN 0-273-01141-3

© J. W. Cornelisse, H. F. R. Schoyer and K. F. Wakker, 1979

All rights reserved. No part of this publication may be reproduced, stored in a retrieval system, or transmitted in any form or by any means, electronic, mechanical, photocopying, recording and/or otherwise without the prior written permission of the publishers.

Printed in Northern Ireland at the Universities Press (Belfast) Ltd.

Contents

Preface	xii
Symbols	xvi
1 The Range of Astronautics	1
1.1 Some historical remarks	1
1.2 The rocket motor	3
1.3 Rocket trajectories and performance	3
1.4 Satellite orbits and interplanetary trajectories	4
2 Basic Concepts in Astronomy and Geophysics	6
2.1 The universe	6
2.2 The solar system	6
2.2.1 The Sun	7
2.2.2 The planets	7
2.2.3 Asteroids, comets and meteoroids	8
2.3 Reference frames and coordinate systems	9
2.3.1 Position on the Earth's surface	9
2.3.2 The celestial sphere	10
2.3.3 The ecliptic	11
2.3.4 Geocentric reference frames	12
2.3.5 Heliocentric reference frames	13
2.3.6 Motion of the vernal equinox	13
2.3.7 The velocity vector	14
2.4 Time and calendar	15
2.4.1 Sidereal time	15
2.4.2 Solar time	16
2.4.3 Mean solar time	17
2.4.4 Standard time	17
2.4.5 Ephemeris time and atomic time	18
2.4.6 The year	18
2.4.7 The Julian date	19
2.5 The Earth	19
2.5.1 The shape of the Earth	19
2.6 The Earth's atmosphere	21
2.6.1 The troposphere, stratosphere and mesosphere	22
2.6.2 The ionosphere, thermosphere and exosphere	23

3 Mechanics of Particles, Bodies and Fluids	25
3.1 Newton's first law	25
3.2 Newton's second law	27
3.3 Non-inertial frames	28
3.3.1 Rotation	28
3.3.2 Newton's laws	30
3.4 Dynamics of particle systems	32
3.4.1 Systems of discrete particles	33
3.4.2 Bodies	36
3.4.3 Rigid bodies	37
3.4.4 Solidification principle	40
3.5 Gravitation	41
3.6 Motion of a particle in an inverse-square field	44
3.6.1 Constants of motion	45
3.6.2 Trajectory geometry	47
3.6.3 Classification and characteristics of conic sections	50
3.7 Mechanics of fluids	54
3.7.1 Conservation of mass	54
3.7.2 Conservation of linear momentum	56
3.7.3 Conservation of energy	58
3.7.4 Conservation of angular momentum	61
References	62
4 The Equations of Motion of Rigid Rockets	63
4.1 Reference frames	64
4.1.1 The relative orientation of the various reference frames	65
4.2 The dynamical equations	69
4.2.1 The apparent forces	70
4.2.2 The apparent moments	72
4.2.3 The inertial moment	74
4.2.4 The external forces	74
4.2.5 The external moments	76
4.2.6 The equations of motion	77
4.3 The kinematical equations	79
4.3.1 The position of the rocket	81
4.3.2 The orientation of the rocket	82
4.3.3 The velocity components in the vehicle-centered horizontal reference frame	83
5 The Chemical Rocket Motor	85
5.1 The ideal rocket motor	86
5.1.1 The exhaust velocity	87
5.1.2 Nozzle geometry	90
5.1.3 Mass flow and exit pressure	93
5.1.4 The exit surface	96

5.1.5 Maximum thrust	98
5.2 Real rocket motors	99
5.2.1 The effect of ambient pressure on the nozzle flow	102
5.2.2 Other nozzle designs	106
5.2.3 Thrust misalignment	107
5.2.4 Thrust vector control	108
5.2.5 Thrust magnitude control	110
References	111
6 Characteristic Coefficients and Parameters of the Rocket Motor	113
6.1 Some notes on rocket testing	113
6.2 Total and specific impulse	114
6.3 The volumetric specific impulse	115
6.4 The thrust coefficient	116
6.5 The characteristic velocity	118
6.6 The effective exhaust velocity	120
6.7 Characteristic length and residence time	120
References	122
7 Thermochemistry of the Rocket Motor	123
7.1 Concepts of chemical thermodynamics	123
7.1.1 General definitions	123
7.1.2 Chemical equilibrium	130
7.2 Combustion in the rocket motor	136
7.2.1 The composition in the combustion chamber and the adiabatic flame temperature	137
7.3 Expansion through the nozzle	138
7.3.1 Constant properties flow	139
7.3.2 Frozen flow	140
7.3.3 Equilibrium flow	144
7.3.4 The modified Bray approximation	145
References	148
8 Heat Transfer in Rocket Motors	151
8.1 The energy equation	151
8.2 Heat transfer processes	152
8.2.1 Conductive heat transfer	152
8.2.2 Radiative heat transfer	152
8.2.3 Radiating gases	155
8.2.4 Convective heat transfer	156
8.3 Heat transfer in the rocket motor	160
8.3.1 Gas-side heat transfer	160
8.3.2 Heat transfer in the wall	162
8.3.3 Coolant-side heat transfer	164
8.3.4 Radiation cooling	166
References	168

9 The Solid-Propellant Rocket Motor	169
9.1 Solid propellants	170
9.1.1 Double-Base propellants	170
9.1.2 Composite propellants	171
9.1.3 The burning rate	174
9.1.4 Combustion models	177
9.2 Internal ballistics	180
9.2.1 Equilibrium chamber pressure	180
9.2.2 The flow in a cylindrical grain	185
9.2.3 The flow between the grain end and the nozzle	191
9.3 Propellant grains	194
9.3.1 Definitions	196
9.3.2 Cylindrical grains	197
9.3.3 Three-dimensional grains	202
9.4 Burning rate augmentation	203
9.4.1 Erosive burning	203
9.4.2 Pressure-induced burning rate changes	204
9.4.3 Acceleration-induced burning rate augmentation	205
References	206
10 The Liquid-Propellant Rocket Motor	208
10.1 Liquid propellants	209
10.2 Propellant tanks	211
10.3 The propellant feed system	213
10.3.1 Pumps	213
10.3.2 Turbines	221
10.3.3 The injector	224
10.4 The thrust chamber	226
10.4.1 Aspects of oscillatory combustion	227
10.4.2 The shape of the combustion chamber	227
10.4.3 The chamber volume	227
10.5 Cooling of liquid engines	228
10.5.1 Active cooling systems	229
10.5.2 Passive cooling systems	231
References	232
11 Two-Dimensional Rocket Motion in Vacuum	234
11.1 The equations of motion	234
11.2 Rocket motion in free space	237
11.2.1 Tsiolkovsky's equation	238
11.2.2 Rocket parameters	239
11.2.3 The burnout range	242
11.3 Rocket motion in a homogeneous gravitational field	246
11.3.1 Vertical flight	247

11.3.2 Constant pitch angle	250
11.3.3 Gravity turns	255
References	261
12 The Multi-Stage Rocket	262
12.1 Nomenclature of the multi-stage rocket	262
12.2 The ideal velocity of the multi-stage rocket	265
12.3 Vertical ascent in a homogeneous gravitational field and in vacuum	272
12.3.1 The burnout velocity	273
12.3.2 The culmination altitude	274
12.3.3 Vertical ascent of a two-stage rocket	276
12.4 Parallel staging	280
References	281
13 Ballistic Missile Trajectories	282
13.1 The boost phase	283
13.2 The ballistic phase	286
13.2.1 The orientation of the trajectory plane	287
13.2.2 Trajectory geometry	288
13.2.3 A graphical technique	293
13.2.4 Optimal flights	295
13.2.5 Time of flight	298
13.3 The re-entry phase	304
13.4 The position of the impact point	306
13.4.1 Spherical Earth	306
13.4.2 Oblate Earth	308
13.4.3 Influence coefficients	310
References	315
14 Rocket Motion in the Atmosphere	317
14.1 The equations of motion	317
14.1.1 Aerodynamic forces, moments and coefficients	318
14.2 The magnitude of the aerodynamic coefficients	321
14.2.1 The normal force and pitching moment coefficients	321
14.2.2 The drag coefficient	323
14.3 Some aspects of aerodynamic stability	325
14.3.1 Static longitudinal stability	325
14.3.2 Dynamic longitudinal stability	326
14.3.3 Some aspects of non-linear instability	329
14.4 Other atmospheric effects	331
References	334
15 The Many-Body Problem	336
15.1 The general N -body problem	336
15.1.1 Integrals of motion	337

x Contents

15.1.2	The Virial theorem	340
15.2	The circular restricted three-body problem	342
15.2.1	Jacobi's integral	344
15.2.2	Surfaces of zero velocity	346
15.2.3	Stability of motion near the libration points	350
15.2.4	Applications to spaceflight	353
15.3	Relative motion in the N -body problem	354
15.3.1	Satellite orbit perturbations by a third body	357
15.3.2	Sphere of influence	358
References		360
16	The Two-Body Problem	362
16.1	Equations of motion	362
16.2	General characteristics of motion	363
16.2.1	The circular orbit	366
16.2.2	The elliptic orbit	368
16.2.3	The parabolic orbit	369
16.2.4	The hyperbolic orbit	369
16.3	Relations between position and time	370
16.3.1	The elliptic orbit	371
16.3.2	The parabolic orbit	373
16.3.3	The hyperbolic orbit	373
16.4	Expansions in elliptic motion	375
16.5	Orbital elements	377
16.6	Relations between orbital elements and position and velocity	379
16.6.1	Rectangular coordinates from orbital elements	380
16.6.2	Orbital elements from rectangular coordinates	381
16.6.3	Orbital elements from spherical coordinates	382
16.7	f and g series	383
16.8	Relativistic effects	385
References		387
17	The Launching of a Satellite	389
17.1	Launch vehicle ascent trajectories	389
17.2	The injection of a satellite	390
17.2.1	General aspects of satellite injection	391
17.2.2	Dependence of orbital parameters on in-plane injection parameters	392
17.3	Launch vehicle performances	395
17.4	Orbit deviations due to injection errors	401
17.4.1	Small injection errors	402
References		405
18	Perturbed Satellite Orbits	407
18.1	Special and general perturbations	409

18.2 Cowell's method	410
18.3 Encke's method	411
18.4 Method of variation of orbital elements	413
18.4.1 Lagrange's planetary equations	414
18.4.2 Modification of the sixth Lagrange equation	420
18.4.3 Other forms of the planetary equations	422
18.5 A simple general perturbations approach	425
18.6 First-order effects of the asphericity of the Earth	427
References	434
19 Interplanetary Missions	436
19.1 Basic concepts	437
19.2 Two-dimensional interplanetary trajectories	439
19.2.1 Hohmann trajectories	440
19.2.2 Launch opportunities	444
19.2.3 Fast interplanetary trajectories	446
19.3 Three-dimensional interplanetary trajectories	449
19.4 The launch of interplanetary spacecraft	453
19.5 Trajectory about the target planet	455
References	460
20 Low-Thrust Trajectories	462
20.1 Equations of motion	463
20.2 Constant radial thrust acceleration	465
20.3 Constant tangential thrust	468
20.3.1 Characteristics of the motion	469
20.3.2 Linearization of the equations of motion	472
20.3.3 Performance analysis	474
References	479
Tables	480
T.1 Physical constants	480
T.2 Selected astronomical constants	480
T.3 Planetary orbital elements	482
T.4 Planetary orbits and physical elements	483
T.5 Satellite orbits and physical elements	484
Appendices	485
Appendix 1 Gauss' Theorem	485
Appendix 2 Reynolds' Transport Theorem	486
Appendix 3 The First Law of Thermodynamics	489
Index	491

Preface

In scarcely two decades astronautics has outgrown its infancy and has become increasingly important in daily life. Many countries have their own space programs, cooperate in international projects, and are members of international space organizations. Many thousands of people make their living in the fields of space technology, space research and space applications; most of them are required to have a thorough knowledge of the physical and mathematical backgrounds to astronautics. The aim of this book is to meet the demand for this knowledge in three basic, and highly related areas of astronautics: rocket propulsion, rocket trajectory analysis and flight mechanics of satellites and interplanetary spacecraft.

Up to now, it is the chemical rocket motor that has provided the thrust for large launch vehicles that carry Earth satellites, interplanetary spacecraft or other payloads. This chemical rocket motor, which derives its power from chemical reactions, is the only well developed, reliable and extensively flight-proven motor that can provide the large thrust necessary to lift the heavy vehicles from the Earth's surface. Therefore, a basic understanding of its principles and limitations is mandatory for anyone working in astronautics.

As the main purpose of the launch vehicle is delivering a payload at a prescribed position with a specified velocity, the success of the mission is highly dependent on the ability to predict accurately the vehicle's trajectory, which is determined by the thrust and Earth's gravitation and is influenced by the atmosphere. On successful completion of the launch vehicle's flight, the main mission will start and a satellite is injected into an Earth orbit, or a space vehicle will set course to one or various bodies of our solar system.

Earth satellites are launched with a variety of objectives: pure scientific satellites, which help to unravel the enigma of the universe, or will give a better understanding of the geometrical, climatological or electromagnetic picture of the Earth, but also commercial communications satellites, which provide relatively cheap high-capacity space links for maritime, aeronautical and public use.

Interplanetary spacecraft have greatly extended our horizons. They have mapped the towering mountains and battered plains of Mars and the spinning clouds of Venus; they have opened the possibility for exciting discoveries on Mercury, Jupiter and beyond. All this will eventually lead to a better insight into the history, nature and destiny of our solar system in general, and our own planet, the Earth, in particular. It will be clear that for all these

missions, careful trajectory selection is crucial as small errors may seriously degrade the value of the mission.

This book introduces the reader to all these astronautical topics and illustrates their intense interrelationship. The text is based on a series of postgraduate courses given by the authors at the Department of Aerospace Engineering of Delft University of Technology (DUT). Until now, there was, to the authors' knowledge, no single text available which combined these highly related topics in astronautics; so someone with a knowledge of one part of astronautics had to refer to several sources to familiarize himself with other areas. Books on orbital mechanics mostly seem to forget that the satellite has to be injected by a launch vehicle. Texts on rocket propulsion sometimes seem to consider rocket propulsion as a goal in itself, and not as a tool for launching satellites or for reaching 'heavenly bodies', as Walter Hohmann wrote in 1925. The trajectory of the launch vehicle often seems to be a step-child, either of rocket propulsion or of orbital mechanics. A student in rocket trajectory analysis had to refer to various articles or to texts on military exterior ballistics or to flight handbooks to grasp the subject. Moreover, the nomenclature in the various sources is not uniform, and equations describing the same phenomenon are often presented in slightly different forms, hampering a clear understanding and correct use. In the present text, the authors have aimed at a uniform notation and presentation, though they have not pursued this to extremes. For example, in mechanics it is customary to denote the angular momentum by the symbol B , while the symbol H is used in celestial mechanics. To facilitate communication with other texts, these conventions are adopted here too; such rare cases are, however, clearly stated in the text. The mathematical derivations are given with many intermediate steps, to make them clear and readily understandable. Clarity of derivation and formulation is favored above the addition of more subjects, and as far as possible the physical nature of what is happening is emphasized, since an expression or formula is merely a shorthand for a physical phenomenon.

Throughout the book, SI units (*Système International*) are used. This system of units has for a long time been accepted by the scientific world, and its consistency and ease of use also promoted its rapid adoption in technology during the last decade. Both NASA and ESA already use the SI units in their publications, but to the authors' knowledge this is the first comprehensive text on space technology to use solely SI units in a rigorous manner, which enhances its value as a teaching text.

The book is written for those engineers and scientists who, for various reasons, have more than a passing interest in astronautics and/or related areas, and for students in the aerospace sciences. The experienced worker in the field will find an easily accessible corridor to related areas, while the student is introduced to a field of related topics in a logical and rigorous way. We hope that this book may also be of much value to ballisticians and to those who use rockets and missiles, such as military people and

experimenters using sounding rockets or satellites for their investigations. Often, this last category of people needs to know the limitations dictated by the rocket, the trajectory or the orbit, and this book may elucidate these restrictions.

The book, which contains twenty chapters, consists of four major parts. The first three chapters introduce the reader to astronautics, astronomy and geophysics, and cover the basic concepts of the mechanics and physics needed for an understanding of the remainder. Readers who are familiar with these notions may forego these chapters and turn to the following parts; the first three chapters then merely serve as a reference source.

In Chapter 4 a rigorous derivation of the equations of motion of a rocket vehicle is given.

Chapters 5 to 10 deal with rocket propulsion. The basic theory of the ideal (chemical) rocket motor is given, and linked with the real rocket motor. The combustion process in the rocket motor is discussed on the basis of chemical (equilibrium) reactions. As, in general, very high temperatures will occur in some parts of the rocket motor, relevant aspects of heat transfer are also covered, while finally the solid and liquid propellant motors are discussed extensively.

Chapters 11 to 14 deal with the trajectory and performances of the rocket vehicle. These chapters comprise rocket motion in a vacuum, the theory of multi-stage rockets, trajectories of intercontinental ballistic missiles and the influence of the atmosphere on the trajectory of a rocket vehicle.

In the concluding six chapters, satellite orbits and interplanetary flights are treated. These chapters start with some topics of classical celestial mechanics. Then, the theory of Keplerian orbits is presented, and the problems of the launching and injection of satellites are discussed and explained with the help of performance diagrams for expendable launch vehicles and the Space Shuttle. Methods for computing perturbed satellite orbits are treated in some detail, and the analysis of interplanetary trajectories is discussed. The last chapter deals with low-thrust trajectories of spacecraft with, for example, an electric rocket motor or a solar sail.

Tables are included, giving physical and astronomical constants and data on our solar system. Much care has been taken to make this set of data consistent. The book concludes with an Appendix on some often used concepts, such as Gauss' theorem, Reynolds' transport theorem and the first law of thermodynamics, thus facilitating the reader to check on these topics.

The authors have done everything to keep errors to a minimum, but of course, it is possible that some errors still occur; we will appreciate being informed of these.

The authors are indebted to many people who have contributed in various ways; not least by giving advice and providing necessary data and information. Though it is not possible to name them all, a few should be mentioned

here. The authors wish to express their sincere thanks to Prof. H. Wittenberg, Dean of the Department of Aerospace Engineering of DUT and to Prof. J. A. van Ghesel Grothe, Managing Director of the same department, for their encouragement to write the present work and their permission to the authors to devote part of their time to its preparation. Professor H. Wolff of Technion, Israel Institute of Technology, Haifa, read the complete first version of the manuscript and gave many highly useful comments, based on his vast industrial and teaching experience. Mr. R. S. de Boer of the National Defense Organization (T.N.O.), Dr. F. P. Israel of Leiden University and Mr. B. A. C. Ambrosius of DUT gave comments which proved highly valuable. Mr. D. M. van Paassen of DUT prepared all the artwork, and certainly should be mentioned here for his excellent contribution. The manuscript was typed by Mrs. C. G. van Niel-Wilderink and Miss M. M. Derwort, who succeeded in patiently transforming the handwritten version with all its changes into a readable and printable manuscript. The authors are also much indebted to Dr. Th. van Holten of DUT, who betted that the text would never be completed and who lost! This wager and his sarcasm were at least a great stimulus. Finally, we wish to thank our families, who accepted that so much time had to be sacrificed for the preparation of this book. If it proves to be valuable to the reader, and contributes to the enthusiasm for astronautics, this time was not spent in vain.

J. W. Cornelisse
H. F. R. Schöyer
K. F. Wakker

Delft, The Netherlands
August 1978

Symbols

The symbol index is arranged alphabetically, giving English and then Greek symbols. Script and astrological symbols appear immediately following the Greek alphabet. The final portion of the index consists of the most commonly used subscripts and superscripts. For subscripted and superscripted symbols that do not appear in the main body of the symbol index, the meaning may be determined by looking up the symbol and subscript or superscript in the separate portions of the index.

A	rotation matrix	C _{d_c}	cross-flow drag coefficient
<i>A</i>	surface; area	C _F	thrust coefficient
<i>A_e</i>	surface bounded by nozzle exit contour; exit surface	C _{F^o}	characteristic thrust coefficient
<i>A_p</i>	product	C _{F_a} , C _{m_a} , etc.	stability derivatives
<i>A_r</i>	reactant	C _b , C _n , etc.	aerodynamic moment coefficients
<i>a</i>	acceleration	C _p	heat capacity at constant pressure
<i>a</i>	velocity of sound	C _v	heat capacity at constant volume
<i>a</i>	activity	<i>c</i>	velocity of light in vacuum
<i>a</i>	semi-major axis	<i>c</i>	specific heat capacity
<i>a_{cm}</i>	acceleration of center of mass relative to rocket structure	<i>c</i>	effective exhaust velocity
B	angular momentum	<i>c</i>	chord
B	impact parameter	c _d	discharge coefficient
<i>b</i>	width of impeller	c _p	specific heat capacity at constant pressure
<i>b</i>	wing span	<i>c_s</i>	specific consumption
<i>b</i>	semi-minor axis	<i>c_v</i>	specific heat capacity at constant volume
C	structure factor	cm	center of mass
C	circumferential perturbing acceleration	cp	center of pressure
<i>C</i>	Jacobian constant		
<i>C_D</i>	mass flow factor		
<i>C_D, C_L, etc.</i>	aerodynamic force coefficients		

c^*	characteristic exhaust velocity	H	enthalpy
D	drag	ΔH	heat change at con- stant pressure; heat of reaction
D	diameter; outer diameter	H	hour angle
D	distance	H.T.A.	Hohmann transfer
D.A.	direct ascent		ascent
D_b	ballistic linear range	H_e	pumphead
d	rocket base diameter	ΔH_f°	standard heat of formation
E	matrix of unit vectors	H_{G_0}	Greenwich hour angle at 0 ^h U.T.
E	internal energy	h	specific enthalpy
ΔE	heat change at constant volume	h	Planck's constant
E	eccentric anomaly	h	altitude
e	unit vector	h_c	convective heat
e	specific internal energy	I	transfer coefficient
e	(numerical) eccen- tricity	I	inertia tensor
F	force; thrust	I_{sp}	total impulse
F	Gibbs free energy	I_δ	specific impulse
F	augmented function	I	volumetric specific impulse
F	focus		polar moment of inertia
F	hyperbolic anomaly	I_{xx}, I_{yy}, I_{zz}	moments of inertia
F_s	total external force applied to system	I_{xy}, I_{yz} , etc.	products of inertia
	S	i	inclination
F_0	rocket motor vacuum thrust	J	linear momentum
f	fugacity	J	throat to port area ratio
G	universal gravita- tional constant		coefficient of zonal harmonics, tes- seral harmonics and sectorial har- monics
g	force per unit mass; (gravitational) field strength	K	klemmung
g_0	standard surface gravity	K	drag parameter
g_0	reference gravita- tional acceleration	K_n	equilibrium constant (on basis of number of mols)
H	angular momentum of system of point masses	K_p	equilibrium constant (on basis of partial pressure)
H	angular momentum per unit mass	K_{pf}	equilibrium constant of formation

k	Boltzmann's constant	N	normal force
k	thermal conductivity	N	pump's number of revolutions per second; rotational speed
k_i	injection velocity parameter		
k_λ	spectral absorption coefficient of a gas	N	perturbing acceleration normal to velocity vector
L	lift	N	number of revolutions
L	length	$NPSE$	net positive suction energy
L	gas layer thickness		
L	mean longitude		
L	Lagrange libration point	Nu	Nusselt number
L_{eq}	equivalent beam length	N_A	Avogadro's number
L^*	rocket motor characteristic length	N_s	pump specific speed
L', M', N'	aerodynamic moments	N_{ss}	suction specific speed
l_b	perimeter of cross-section of performance in propellant grain	N'	yawing moment
M	moment of a force	\mathbf{n}	unit normal
M	total mass of a system (of particles); mass of a body; mass of a satellite or spacecraft	n	concentration or number of mols
M	mean anomaly	n	dimensionless acceleration
M_a	Mach number	n	(mean) angular motion
M_c	structural mass	np	dimensionless radius
M_e	empty (final) rocket mass	O	of planet orbit
M_F	moment due to thrust (misalignment)	P	neutral point
M_p	(useful) propellant mass	Pr	origin of reference frame
M_u	payload mass	P_i	power
M'	pitching moment	P_u	Prandtl number
m	mass of particles or point mass	p	power delivered to pump
m	mass flow; flux of matter	p	useful power
		p, q, r	pressure
		p_a	semi-latus rectum
		p_i	angular velocity components
		p_0	(undisturbed) atmospheric pressure
			partial pressure of species i
			front-end stagnation pressure

Q	heat		propellant; burning rate
Q	volumetric flow rate		
q	energy flux; heat flux	r_e	position vector for center of mass
q	dimensionless semi-latus rectum	r_e	flow
\hat{q}	dynamic pressure	\hat{r}	erosive burning rate
\mathbf{R}	position vector; radius vector	S	dimensionless distance
R	Earth radius; planet radius; local radius of Standard Ellipsoid	S	mass-system inertial reference frame
R	gas constant	S	entropy
R	perturbing or disturbing potential	S	(closed) surface
Re	Reynolds number	S	reference area; rocket cross-sectional base area
\tilde{R}	disturbing function	S	radial perturbing acceleration
R_c	ballistic cross-range influence coefficient	St	Stanton number
ΔR_c	cross-range error	S_R	outer wall of the rocket
R_{cap}	capture radius	S_r	reference area
R_D	ballistic down-range influence coefficient	S_w	projected wing area
ΔR_D	down-range error: down-range correction	s	structure ratio
R_e	mean equatorial Earth radius	s	distance
R_p	Earth polar radius	Δs	distance covered by rocket
$R_{s.i.}$	radius of sphere of influence or activity sphere	T	torque
R_0	universal gas constant	T	tangential force
R_o	mean Earth radius	T	tangential perturbing acceleration
\mathbf{r}	radius vector; position vector (relative to center of mass of rocket)	T_b	temperature
r	recovery factor	T_f	time of flight
r	velocity of burning surface with respect to solid	T_r	orbital period
		T_{syn}	bulk temperature
		T_∞	fluid film temperature
		T'	flame temperature
		t	recovery temperature

xx Symbols

t_b	burning-time	W	normal perturbing acceleration
t_c	coast-time	w	propellant grain web thickness
t_f	time of flight	X_a, Y_a, Z_a	aerodynamic forces
\hat{t}	dimensionless time	x, y, z	axes of a reference frame
\mathbf{U}	identity matrix		
U	potential function;		
	potential; potential energy per unit mass		
u	ideal velocity ratio	α	absorptance
u	argument of latitude	α	angle of attack; angle of incidence
u, v, w	linear velocity components	α	nozzle divergence angle
u_{cm}	velocity of center of mass relative to rocket structure	α	turbine nozzle angle
\mathbf{V}	velocity vector	α	right ascension
ΔV	velocity increment of a rocket	α	general orbital element
V_c	local circular velocity	α	asymptotic deflection angle
V_{char}	launch vehicle characteristic velocity	α	correction factor
V_{char}^*	mission characteristic velocity	$\bar{\alpha}_\lambda$	monochromatic absorptivity of a gas layer
ΔV_{char}^*	launch site and launch azimuth velocity penalty	β	specific thrust
V_e	exhaust velocity	β	blade angle
\bar{V}_e	mean exhaust velocity	β	sideslip angle
V_{esc}	local escape velocity	Γ	Vandenkerckhove function
V_i	propellant injection velocity	Γ	velocity factor
V_{id}	ideal velocity of N -stage rocket	Γ'	time factor
ΔV_{id}	ideal velocity increment)	γ	ratio of specific heats
V_L	limiting value of V_e	γ	flight path angle
V_l	volumetric loading fraction	γ	dimensionless distance
V_∞	hyperbolic excess velocity	δ	declination
W	gravitational force	δ	thickness
W	work	δ	thrust (misalignment) angle
		δ_0	kick angle
		ε	structural efficiency (hemispherical)
		ε	emittance
		ε	obliquity of the ecliptic
		ε	flattening of the

ε	Earth	ρ	reflectance
ε_{tot}	downwash angle	ρ	mass density; air density
$\bar{\varepsilon}_\lambda$	total structural efficiency	ρ_i	ratio of injection
	monochromatic emissivity of a gas layer	ρ_p	radius and re-entry radius
η	efficiency	Σ	average propellant density
θ	angular coordinate	Σ	dimensionless burning surface
θ	angular displacement	σ	ballistic angular range
θ	pitch angle	τ	Stefan-Boltzmann constant
θ	true anomaly	τ	transmittance
$\Delta\theta$	heliocentric transfer angle	τ	Thoma parameter
κ	thermal diffusivity	τ^*	time of (last) peri-center passage
Λ	mass ratio	Φ	residence time
Λ	geographic longitude	Φ'	geocentric latitude
λ	payload ratio	φ	geodetic or geographic latitude
λ	wavelength	φ	propellant ratio
λ	nozzle reduction factor	φ	bank angle
λ	celestial longitude	φ	angular coordinate
μ	attraction parameter; gravitation parameter	φ_{tot}	celestial latitude
μ	dynamic viscosity	ψ	total propellant ratio
μ	dimensionless mass	ψ	angular coordinate
μ	mass flow parameter	ψ	flight path azimuth; down-range heading
ν	stoichiometric coefficient	ψ	yaw angle
ν	Lagrange multiplier	ψ	pressure parameter
ξ	extent of reaction	ψ_0	thrust-to-weight ratio
ξ	quality factor	Ω	angular or rotational velocity
ξ, η, ζ	coordinate axes	Ω	right ascension of ascending node
π	sensitivity coefficient for burning propellant	ω	longitude of ascending node
\mathbf{p}	position vector (with respect to center of mass)	ω	angular velocity
\mathbf{p}	position vector for (unperturbed) reference orbit	ω_e	argument of peri-center
			angular velocity of

	the Earth about its axis	<i>f</i>	fluid film
$\bar{\omega}$	longitude of peri-center	<i>f</i>	friction
\mathcal{E}	total energy (per unit mass)	<i>f</i>	flame
\mathcal{E}_k	kinetic energy	<i>f</i>	impact
\mathcal{E}_p	potential energy	<i>G</i>	Greenwich
M	(mean) molecular weight	<i>g</i>	rotating geocentric reference frame
\mathcal{V}	(material) volume	<i>g</i>	gas
\mathcal{V}_p	volume available to store propellants	<i>g</i>	propellant grain-end
Υ	vernal equinox; first point of Aries	<i>H</i>	Hohmann
$\underline{\Omega}$	autumnal equinox; Libra	<i>i</i>	interference
		<i>i</i>	body <i>i</i>
		<i>i</i>	sub-rocket
		<i>i</i>	injection
		<i>i</i>	impact
		<i>in</i>	inertial
		<i>l</i>	launch (site)
		<i>max</i>	maximum
		<i>o</i>	point of application of a force
<i>a</i>	aerodynamic	<i>p</i>	pressure
<i>a</i>	apocenter	<i>p</i>	product
<i>abs</i>	absolute	<i>p</i>	propellant
<i>as</i>	outgoing asymptote	<i>p</i>	propellant port area
<i>B</i>	body	<i>p</i>	pericenter
<i>b</i>	burnout	<i>p</i>	planet
<i>c</i>	(rocket) chamber	<i>par</i>	parking orbit
<i>c</i>	condensed phase	<i>r</i>	reactant
<i>c</i>	Coriolis	<i>r</i>	radiative
<i>c</i>	circular (orbit)	<i>r</i>	vehicle reference frame
<i>c</i>	critical	<i>rel</i>	relative
<i>c</i>	culmination	<i>s</i>	constant entropy
<i>c</i>	spacecraft	<i>s</i>	stagnation
<i>cm</i>	center of mass	<i>s</i>	Sun
<i>cr</i>	critical	<i>s</i>	satellite
<i>D</i>	drag	<i>t</i>	throat; sonic
<i>d</i>	directional	<i>t</i>	target planet
<i>d</i>	disturbing body	<i>th</i>	theoretical
<i>dr</i>	dragging	<i>tot</i>	total
<i>e</i>	exit of nozzle	<i>v</i>	vehicle-centered horizontal reference frame
<i>e</i>	after the reaction	<i>W</i>	fin
<i>e</i>	re-entry	<i>w</i>	wall
<i>e</i>	Earth	<i>x, y, z</i>	component in <i>x</i> -, <i>y</i> -, and <i>z</i> -direction
<i>esc</i>	escape		
<i>exp</i>	experimental		

0	initial		bolic trajectory about the target planet
0	reference temperature		
0	before the reaction	4	at leaving the sphere of influence of swingby planet
0	propellant grain front-end		
0	in the parking orbit about	λ	at a wavelength
	the Earth		
1	at the start of the inter-		
	planetary heliocentric leg		
2	on arrival at the target		
	planet in the interplane-		
	tary heliocentric leg		
3	at pericenter of the hyper-		

Superscripts

'	small perturbation
\circ	at standard reference state
-	mean value; average

1 The Range of Astronautics

More than a thousand satellites have been launched since 1957, and many of these still encircle the Earth. They comprise communications, navigation, and Earth survey satellites, satellites for scientific and technical purposes, military satellites, etc. All were put into a more or less elliptical orbit by large rockets. To modern man, astronautics is an accepted part of human society. A manned flight to the Moon is not regarded as anything peculiar anymore, and an unmanned flight to Jupiter hardly affects 'the man in the street'. On the other hand, one notices the great interest in the findings and achievements of astronautics, completely in agreement with the historical development of our society and the inquisitive nature of mankind.

1.1 Some historical remarks

Astronautics belongs to the youngest endeavors of men. Like the desire to master the art of flying, the need to visit and survey the planets seems deeply rooted in our minds. For long there have existed tales about humans flying to the Moon, Sun or stars. The large market for science-fiction novels illustrates the natural human interest in space travel.

In ancient times, astronomical events, especially the solar and lunar eclipses, puzzled and frightened people as they were not understood. One tried to explain the lunar eclipse for instance, by imagining that an evil black wolf swallowed the Moon. Fortunately, there was always a hunter who killed the wolf, opened its stomach, and the Moon came out, not hurt at all. This in fact, may be the origin of the well-known tale of Little Red Ridinghood.

In the ancient, agricultural world, a calendar was of utmost importance, and astronomy, which had to provide this instrument of time-keeping started to develop in Mesopotamia as is assumed by archeologists. The first primitive calendars usually were based on the phases of the Moon. Soon, the astronomers could predict the eclipses and they got some insight into the motion of Moon, Sun and stars.

When people started sailing the seas, their only means of navigation at night were the stars and this again promoted the interest in astronomy. Around the middle of the seventeenth century the first science-fiction novels about travels to the Moon appeared, but certainly Jules Verne's *De la Terre à la Lune* (From the Earth to the Moon) from 1865 belongs to the most inspiring ones.

The rocket, as a small weapon, was well developed at this time. We are

2 Rocket Propulsion & Spaceflight Dynamics

told of Asian armies, armed with rocket-weapons when Europeans still used the bow. However, the theory of rocket flight was still lacking. It was the Russian teacher Tsiolkovsky, who in 1903 published in the Moscow Technical Review an article with the title *Study of Space by Jet-Propelled Devices*, in which he derived the equation, relating the velocity of a rocket to its exhaust velocity and mass ratio, and which presently is known as Tsiolkovsky's equation. His work, however, did not become generally known, and in 1923, Oberth, in his Ph.D. thesis, independently arrived at a similar result.

Especially in Germany, in Russia where Tsiolkovsky continued his studies, and in the United States, there were at that time people trying to promote space flight. These people, like Oberth, Hohmann, Goddard and others, foresaw that space travel might soon become a reality, and they devoted much time, energy and money, to what most other people regarded as a foolish and dangerous hobby. Much work of those days has become the classical foundation of modern astronautics.

The German rearmament after 1933 gave a strong impetus to the development of the rocket-weapon, and the final outcome was the notorious V-2. After World War II, the large scale development of rockets continued, especially in the United States and Russia, which culminated in the successful launch of the first 'artificial moon', the Sputnik, on October 4, 1957 by Russia. The United States accomplished their first successful launch of a satellite on January 31, 1958 with Explorer 1. On May 25, 1961, President Kennedy told the American congress that '*this nation should commit itself to achieving the goal, before the decade is out, of landing a man on the Moon and returning him safely to Earth*'. This was the official start of the famous Apollo project, which reached a climax in Neil Armstrong and Edwin Aldrin setting foot on the Moon on July 20, 1969.

Meanwhile, many applications for civil and military use of space were found, and many satellites had been launched. Both Russia and the United States had orbited animals and men, and spacecraft were sent out to explore our solar system, and to survey and map the planets. Nowadays, scientific and technical research is carried out in space laboratories and the day when the manufacturing of special products in space will be a normal procedure, may not be far off.

In the foreseeable future, reusable rocket vehicles, like the Space Shuttle, will provide an efficient means of manned space flight both for civil and military purposes.

The missile has become a very sophisticated weapon. Large warheads can be targeted with extremely high precision at intercontinental distances. If one compares this with the V-2, which carried a warhead of about 1000 kg at a range of about 300 km, this development is both frightening and dramatic. The highly increased reliability and accuracy of the rocket vehicle are mainly due to the improvements in rocket engine technology and the miniaturization of the electronic guidance and control systems.

Now that more and more countries have their own space program, and companies operate their own telecommunications satellites, one may say that space technology has grown mature.

1.2 The rocket motor

The basic principle of the rocket is simple: matter, the propellant, is accelerated, resulting in a reaction force, the thrust. As the rocket contains all the propellant itself, it is independent of its environment and, hence, can operate in empty space.

If chemical energy, contained within the propellants is used to produce gases of a high temperature and pressure, one speaks of a chemical rocket motor.

If the high pressure and temperature of the propulsive gas are caused by a nuclear reactor, one speaks of a nuclear rocket engine. Electric rocket motors may electrically heat a propulsive gas, but the electric energy can also be used to create a strong electromagnetic field to accelerate electrically charged particles. The energy may stem for instance from a nuclear power source or from the Sun.

The chemical rocket motors can be subdivided into liquid, solid and hybrid motors. The liquid motor uses liquid propellants, usually a fuel and an oxidizer stored in separate tanks. The solid motor uses a solid propellant which combines fuel and oxidizer. The reaction and gasification take place at the propellant's surface. The hybrid motor combines a solid and a liquid propellant; the solid usually is the fuel. At the present time, liquid and solid rockets are the most used types. Both can deliver high thrusts during a relatively short period. The nuclear rocket is still in its experimental stage. Applications are especially seen for deep space missions. There are various types of electric engines, but all have in common that they deliver a low thrust and have long operation times. Therefore, the electric rocket motor is especially suited for low-thrust trajectories in interplanetary space, for stationkeeping of satellites, etc. Some electric motors have flown already.

Table 1.1 lists the various types of rocket motors mentioned, and their characteristics. In this book, we will devote our attention to the solid and liquid rocket motors. Of course, much of the general theory of the chemical rocket motor can be applied to the nuclear motor, some types of electric engines and the cold gas jets.

1.3 Rocket trajectories and performance

Tsiolkovsky's equation shows that the velocity increment of a single-stage rocket, which is an important performance parameter, depends on the exhaust velocity and the mass ratio, i.e. the ratio of take-off mass and burnout mass. Both have to be as high as possible. At the present time, for Earth-based launch vehicles, only chemical rockets can be used, and of

4 Rocket Propulsion & Spaceflight Dynamics

Table 1.1 The various types of rocket motor

Type	Order of magnitude of thrust (N)	Order of magnitude of operation time	Typical applications	Development status
Various types of electric propulsion	10^{-6} to 10^2	up to years	Satellite stationkeeping, stabilization and control, interplanetary flights, satellite orbit transfer	Some types have already flown. Experimental and development stage
Nuclear reactor	up to 10^5	minutes to hours	Interplanetary, and Earth-Moon flights	Experimental. Development stopped in 1973
Chemical (Liquid)	up to 10^7	seconds to minutes	Launch vehicles, missiles, stabilization and control, Earth-Moon and interplanetary missions	Well developed
Chemical (Solid)	up to 10^7	seconds to minutes	Launch vehicles, missiles, various small rocket weapons, sounding rockets, interplanetary missions, boosters	Well developed
Chemical (Hybrid)	up to 10^5	seconds to minutes	Sounding rockets, small rocket weapons, final stages of launch vehicles	Experimental. Some models have flown

those the liquid rockets yield the highest exhaust velocity. For a variety of reasons such as storage, handling characteristics and costs, solid motors prove to be very useful too. The solid motor has many applications, especially for missiles, boost motors and small sounding rockets.

To obtain a high effective mass ratio, high-performance rocket vehicles use the multi-stage concept. After burnout of a stage, it is discarded, thus effectively increasing the mass ratio of the remaining vehicle. For ballistic missiles, the stages are usually ignited directly after the burnout of the previous one. Shut-down of the final stage takes place at the moment that the resulting ballistic trajectory yields an impact point as near to the target as possible. The ballistic trajectories of rockets are, at a first approximation, Keplerian orbits.

If the vehicle is used to launch a satellite, the powered flight usually is followed by a ballistic flight to the apogee. Near apogee, there is another firing of a rocket motor to place the satellite in its required orbit. An interplanetary spacecraft is usually first placed into a parking orbit about the Earth, from which it is injected into its required interplanetary trajectory.

1.4 Satellite orbits and interplanetary trajectories

Just like the ballistic rocket trajectories the orbits of satellites about the Earth can be approximated by Keplerian orbits. The existence of disturbing

forces means that this approximation does not hold if one considers the orbit for a longer period of time. It turns out that the major perturbations are due to the non-central force field of the Earth, the atmosphere, the attraction by Moon and Sun, and the solar radiation pressure. Which of the perturbing forces dominates, depends on the altitude of the orbit and the mass and dimensions of the satellite.

In many cases, the orbit perturbations observed can be used to obtain quantitative information about the specific perturbing forces. For instance, one can in this way obtain information on the atmospheric density at high altitudes, and determine the shape of the Earth, etc. One can also deliberately use these perturbations to obtain certain desired orbital changes.

The trajectories of interplanetary spacecraft can be approximated by heliocentric and planetocentric Keplerian orbits.

The position and velocity of interplanetary spacecraft during their flight are measured, and corrective midcourse manoeuvres can be executed if necessary. As it may take a long time for the spacecraft to reach its target (for a Jovian journey a year or more, and for a journey to Saturn a few years), the reliability of the complete spacecraft is of utmost importance, as a premature breakdown of one component may wreck the whole mission.

Especially on these long-duration flights, electric propulsion, with its long operation times, can considerably reduce the time of flight, or facilitate flights which are beyond the capability of the launch vehicle.

Another technique that enables flights to regions for which the present launch vehicles have insufficient power, is the swingby technique. Here, the gravitational field of a planet accelerates the spacecraft and deflects its trajectory into the required direction for the encounter with a target planet.

2 Basic Concepts in Astronomy and Geophysics

2.1 The universe

According to our present view, 10 to 20 billion years ago there was nothing but an exploding, enormously hot and dense *Primeval Fireball* that contained all the matter and energy of the present universe. In this rapidly expanding and cooling gas of elementary particles, such as protons, neutrons and electrons, particles gradually combined and nearly all matter took the form of hydrogen atoms. In later stages clumps of gas were formed.

Looking at the universe now, we get a picture of a nearly complete emptiness; the mean mass density is extremely low, corresponding to that of a few hydrogen atoms per ten cubic meters. We observe that matter in the universe is mainly concentrated in objects with extremely large dimensions and of complex structure: the *galaxies*. Billions of these galaxies are assumed to be present in the universe. The mean distance between them is of the order of 10^{18} to 10^{20} km. To express those large distances we usually take the *light year* as the unit of length. The light year is defined as the distance traversed by light in vacuum during one year, which corresponds to about 9.46×10^{12} km.

Our Sun belongs to one of those galaxies, named the *Milky Way*. This Milky Way, which comprises about 100 billion stars, has the appearance of a large, relatively flat structure with spiral arms and a diameter of about 100,000 light years. Our Sun is located at a distance of about 30,000 light years from the center of this galaxy and is moving with a velocity of roughly 250 km/s about this center, completing one revolution in about 250 million years. The galaxy nearest to the Milky Way is the *Great Magellanic Cloud* at a distance of about 160,000 light years from the Sun. Light emitted by stars in this galaxy takes 160,000 years to reach us. Consequently, all our observations of those distant objects are related to conditions in those galaxies of many thousands or even millions of years ago.

In the neighborhood of our Sun there is about one star per thousand cubic light years, and a quantity of interstellar gas and dust with a mass density equal to that of 2 to 3 hydrogen atoms per cubic centimeter.

2.2 The solar system

The volume of space very close to the Sun, up to a distance of about 1 light year, is called the *solar system*. It is in this tiny part of the universe that our

space travel will take place in the foreseeable future. In this solar system the planets and a great many other bodies move in orbits about the Sun.

2.2.1 The Sun

The Sun comprises 99.86% of all matter in the solar system. Its energy flux equals roughly 4×10^{26} W. At Earth-distance from the Sun, the solar power density is still about 1400 W/m^2 . The energy emitted by the Sun is generated by nuclear reactions which take place in the interior of the Sun. There, at a temperature of about 10^7 K and a pressure of about 10^{10} MPa, hydrogen is converted into helium whereby large amounts of energy are released. The visible light of the Sun is emitted from the *photosphere*, a relatively thin layer with a temperature of about 6000 K. This photosphere forms the visible surface or *disk* of the Sun. Its radius is about 7×10^5 km. The outermost region of the Sun is called the *corona*. This corona, which is visible from Earth during solar eclipses, extends up to many photospheric radii. The corona continuously emits matter, mainly in the form of protons and electrons. At crossing the Earth's orbit, this *solar wind* has a velocity of 300–500 km/s and contains about 10 protons per cubic centimeter.

Some temporary phenomena on the Sun, like *sunspots* and *solar flares*, are associated with an 11-year solar activity cycle. As a result of large solar flares occurring at a solar activity maximum, high-energy solar particles and a strongly enhanced UV- and X-ray radiation are emitted. When this radiation interacts with the Earth's atmosphere, it may cause auroral effects, disturbances of the geomagnetic field and radio-interference. The solar activity thus is strongly related to many physical conditions on Earth.

2.2.2 The planets

The main bodies orbiting about the Sun are the nine *planets*: Mercury, Venus, Earth, Mars, Jupiter, Saturn, Uranus, Neptune and Pluto, in order of increasing distance from the Sun. Unlike the Sun, these bodies hardly emit radiation in the visible part of the spectrum; the only reason that they are visible is because of their reflection of solar light. The first six planets mentioned were already known in ancient times. Uranus was discovered accidentally in 1781 by Herschel who was making a routine telescopic survey of the sky. From irregularities in the orbit of Uranus, it soon became clear that still another planet had to be present. Using the perturbation theory of celestial mechanics (Chapter 18), Adams and Leverrier, independently of each other, predicted the mass and position of this eighth planet. From the data of Leverrier, Neptune was discovered in 1846 by Galle. Following the discovery of Neptune, it was observed that small discrepancies still existed between the predicted and observed position of Uranus and Neptune. Again the probable position of a ninth planet was calculated, in

8 Rocket Propulsion & Spaceflight Dynamics

this case by Lowell. In 1930 Tombaugh identified Pluto on a photographic plate made from the region of the sky where Pluto was predicted.

In Table T.4, some relevant data on the planets are given. We note that the planets Mercury, Venus, Earth, Mars and Pluto are relatively small as compared to the giant planets Jupiter, Saturn and, to a lesser extent, also as compared to Uranus and Neptune. Compared to the Sun, even the largest planet is small: the Jovian diameter is about one tenth of the solar disk diameter. All planets, except Mercury and probably Pluto, are surrounded by an appreciable gaseous atmosphere. Mercury and Venus are closer to the Sun than the Earth and are named the *inner planets*. Their surface temperatures are higher. The lighted side of Mercury is assumed to have a surface temperature of about 620 K. The planet Uranus, on the other hand, receives very little solar energy so that its surface temperature may be as low as 80 K and substances like methane, ammonia and carbon dioxide could be present as liquid or solid. The low mean density of Saturn is remarkable; this density is less than that of water. This may indicate the presence of a large abundance of hydrogen and helium.

All planets move in nearly circular orbits about the Sun. The orbits of Mercury and Pluto are the most elliptic; the minimum distance of Pluto from the Sun is even less than the distance between Neptune and the Sun. The orbital planes of the planets are nearly coincident. Again Mercury and Pluto are exceptions; their orbital planes are inclined about 7° and 17° , respectively, to the orbital plane of the Earth. All planets orbit in the same direction about the Sun: counter-clockwise as viewed from the north. Their mean distance from the Sun ranges from about 58×10^6 km for Mercury to about 59×10^8 km for Pluto; the period needed to complete one revolution thereby varies from 88 days for Mercury to about 246 years for Pluto. To express the distances in the solar system we commonly use the *Astronomical Unit* (AU) which is about the mean distance of the Earth from the Sun (Table T.2).

Each planet, except Mercury, Venus and perhaps Pluto, is accompanied by one or more natural satellites or *moons*. The Earth has one natural satellite, the Moon. Mars has two, and Jupiter even fourteen known satellites (Table T.5). Six of the 34 known satellites are about as large as, or larger than our Moon. One of the Jovian satellites, Ganymede, is even larger than the planet Mercury. It is known that some of the larger moons of Jupiter and Saturn possess atmospheres. Saturn is the only planet which has a ring-system consisting of billions of pieces of matter orbiting around the planet.

2.2.3 Asteroids, comets and meteoroids

Between the orbits of Mars and Jupiter there exists a belt in which millions of smaller bodies, called *asteroids*, orbit about the Sun. The largest asteroid, Ceres, which was discovered in 1801, measures about 750 km in diameter.

Thousands have been identified and only a few hundred are over 25 km across; most of the asteroids are very small. Besides the asteroids in the belt, there are asteroids which periodically pass the Earth quite closely.

Comets are mostly rather small objects, composed of frozen gases and solid particles, coming from the outerpart of the solar system where they are assumed to have been produced as a by-product in the formation of the solar system. Owing to the attraction of the nearest stars, some comets are directed into the inner part of the solar system. When a comet moves in closer to the Sun, it warms up and the *nucleus* releases gases and dust particles forming a large cloud around the nucleus: the *coma*. Some of the constituents are expelled more or less radially from the Sun by the solar wind and the radiation pressure of solar light to form the characteristic *cometary tail*. These tails can become as long as 10^8 km.

Meteoroids are too small to be observed in their orbit about the Sun. Their presence becomes known only when they enter the Earth's atmosphere, where they are heated by friction until they melt or vaporize. The luminous phenomenon created this way is called a *meteor*. Rarely does such a meteoroid survive its entry into the atmosphere and impact on the Earth's surface. The material left is called a *meteorite*. Though the vast majority of meteoroids are no larger than gravel, occasionally very large meteorites have struck the Earth, producing *meteor craters*. The largest known meteorites have masses of about 50 tons. Sometimes, a great number of meteoroids are found to have the same orbit, they constitute a *meteoroid stream*. It is thought that such streams of meteoroids are the debris remaining from the breakup of a cometary nucleus. When the Earth is passing through a meteoroid stream a large number of meteors are seen for some days: a *meteor shower*.

2.3 Reference frames and coordinate systems

A large part of this book deals with the computation of the trajectories of rockets, satellites and interplanetary spacecraft. We describe the motion of these vehicles in terms of a time-varying position vector and its time derivatives. This requires, of course, a reference frame with respect to which position, velocity and acceleration are measured.

2.3.1 Position on the Earth's surface

To denote a position relative to the Earth, one usually takes a reference frame which is based on the Earth's axis of rotation. The points where this axis crosses the Earth's surface are called the *north pole* and the *south pole*. For simplicity, we will assume temporarily that the shape of the Earth is exactly spherical. Then, the great circle on the Earth's surface halfway between the poles is the Earth's *equator*. The great circles passing through the poles are called *meridians*; they intersect the equator at right angles. By

10 Rocket Propulsion & Spaceflight Dynamics

convention we take a meridian to be bisected by the Earth's rotation axis into an upper and lower branch; the upper branch containing the observer. Henceforth, with a meridian we will always mean its upper branch. Through any point P (Fig. 2.1) on the Earth's surface, the poles excepted, we can imagine just one meridian. The *geographic longitude*, Λ , of that point is defined as the arc length in degrees measured along the equator from the meridian passing through the Royal Observatory at Greenwich, England, indicated in Fig. 2.1 by G , to the meridian passing through point P . Longitudes are measured either to the east or west of the Greenwich meridian from 0° to 180° , indicated E or W. It is more convenient, however, to measure a longitude positive to the east of Greenwich and negative to the west; in this case the indication W or E can be dropped. The *geocentric latitude*, Φ , of P is given by the geocentric angle in degrees measured along its meridian, from the equator to P . Latitudes are measured either to the north or to the south of the equator from 0° to 90° ; positive north and negative south of the equator.

2.3.2 The celestial sphere

In denoting angular positions of celestial objects, it is convenient to make use of the concept of a fictitious *celestial sphere*. This is a sphere with an infinitely large radius, centered at an observer on Earth or at the mass center of the Earth. The remote stars appear to be set on the inner surface of this sphere. It will be clear that only for nearby objects, like spacecraft, different angular positions will be measured on the observer-centered celestial sphere and the Earth-centered celestial sphere. For astrodynamical

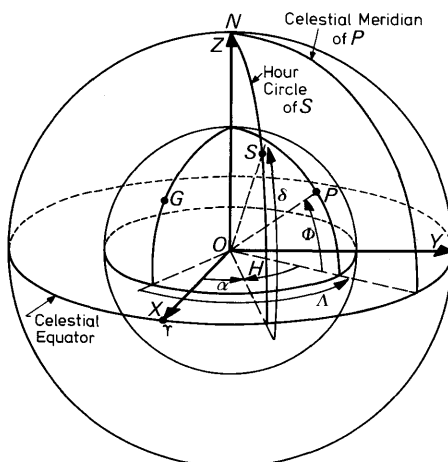


Fig. 2.1 The various concepts used to describe positions on Earth and on the celestial sphere

purposes we will use the latter type. The *celestial poles* are defined as the points where the Earth's rotation axis intersects the celestial sphere; the north celestial pole corresponds to the Earth's north pole. This celestial north pole presently lies very near to a moderately bright star, α Ursae Minoris, called the *pole star* or *Polaris*. The intersection of the Earth's equatorial plane with the celestial sphere is the *celestial equator*. Great circles passing through the celestial poles are called *hour circles*. Again, we consider an hour circle to be limited to its upper branch.

When the meridian of an observer on Earth is projected onto the celestial sphere, we speak of the observer's *celestial meridian*. This celestial meridian, of course, passes through the celestial poles and through a point directly above the observer: his *zenith*. Owing to the Earth's rotation, the observer's celestial meridian continuously sweeps around the celestial sphere. To put it another way, the observer watches the celestial sphere rotating about the Earth's spin axis in a westward direction; celestial objects thereby passing the observer's stationary celestial meridian. This is the so-called *diurnal motion*.

2.3.3 The ecliptic

If the Sun is observed from the Earth, it is found to possess a second motion in addition to the diurnal motion. The Sun moves eastward among the stars at a rate of about 1° per day, returning to its original position on the celestial sphere in one year. The path of the Sun over the celestial sphere is called the *ecliptic*. It is important to realize that seen from the Sun, the ecliptic is nothing but the intersection of the plane of the Earth's orbit about the Sun with the celestial sphere. The ecliptic plane is inclined to the equatorial plane at an angle ε referred to as the *obliquity of the ecliptic*. At the present time $\varepsilon = 23^\circ 27'$. The *axis of the ecliptic*, being the line through the center of the celestial sphere perpendicular to the ecliptic, intersects the celestial sphere in the *ecliptic poles*. The angular distance between the celestial north pole and the ecliptic north pole equals the angle ε . Great circles through the ecliptic poles are called *circles of celestial longitude*. As we did with meridians and hour circles, we will only consider the upper branch of these great circles. The intersecting line of the equatorial plane and the ecliptic plane plays a fundamental role in the definition of reference frames. This line is called the *equinox line* because when, for an observer on Earth, the Sun crosses this line, day and night have equal length. This is the case at 21 March and 23 September each year. These crossing points are called the *vernal equinox* and the *autumnal equinox*, respectively. They are also referred to as *First Point of Aries* γ and *Libra* Ω , respectively. Their position is known relative to the stars. It should be recognized that the designation vernal and autumnal equinox is somewhat misleading, since for an observer in the southern hemisphere autumn starts when the Sun crosses the vernal equinox.

2.3.4 Geocentric reference frames

For describing the motion of small rockets with respect to the Earth's surface, usually a *geocentric rotating reference frame* is used. In this frame, the Z -axis is directed along the Earth's spin axis towards the north pole and the X -axis is in the Earth's equatorial plane, crossing the upper branch of the Greenwich meridian. The Y -axis lies in the equatorial plane oriented such as to make the reference frame right-handed. In spherical coordinates, position can be expressed by the length of the geocentric radius vector, r , and the geocentric latitude, Φ , and geographic longitude, Λ .

For the trajectories of intercontinental ballistic missiles (ICBM), launch vehicles and Earth satellites, usually a non-rotating reference frame with origin at the Earth's center of mass is chosen. Its positive Z -axis coincides with the rotation axis of the Earth and points at the north pole; the positive X -axis lies in the equatorial plane and points towards the vernal equinox. The Y -axis completes a right-handed Cartesian frame of reference. This frame is called the *geocentric non-rotating equatorial reference frame* (Fig. 2.1). As this reference frame is not rotating with respect to the celestial sphere, the position of stars in this frame will remain fixed rather than changing rapidly as in the geocentric rotating frame mentioned before. The geocentric angle in degrees measured along the hour circle through a celestial object, indicated by S in Fig. 2.1, from the celestial equator to that object is called the *declination*, δ , of that object. It is measured from 0° to 90° ; positive when north of the equator, negative when south of it. Declination in this reference frame is analogous to geocentric latitude on the surface of the Earth. The geocentric angle in degrees measured along the celestial equator, from the point Υ to the foot of the hour circle through S is called the *right ascension*, α , of the object. Right ascension is measured from 0° to 360° from the point Υ eastward. The declination, right ascension and distance from the Earth's center describe the position of a vehicle in spherical coordinates.

For a discussion of planetary motion and other phenomena in the solar system, it is often more convenient to use the ecliptic plane as the fundamental plane for a reference frame. Then, we speak of a *geocentric non-rotating ecliptic reference frame* (Fig. 2.2), in which the XY -plane coincides with the ecliptic plane. The X -axis points to the vernal equinox. The Z -axis is along the axis of the ecliptic and points to the ecliptic north pole. The Y -axis is normal to the X - and Z -axis such that the frame is right-handed. The angular position of the celestial object S in Fig. 2.2, can be specified by two quantities, the *celestial longitude*, λ , and the *celestial latitude*, φ . The celestial latitude is defined as the geocentric angular distance in degrees measured along the circle of celestial longitude passing through the object from the ecliptic to that object. It is taken positive for objects north and negative for objects south of the ecliptic. The celestial longitude is defined as the angular distance in degrees measured along the ecliptic from the point

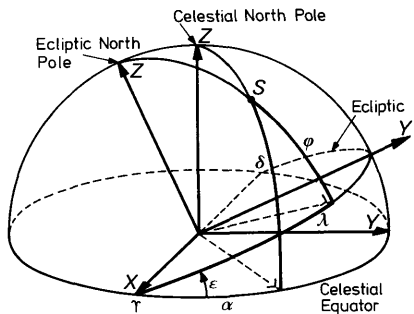


Fig. 2.2 The geocentric equatorial and ecliptic systems of coordinates

Υ to the foot of the circle of celestial longitude through that object. This angle is measured from 0° to 360° eastward along the ecliptic.

2.3.5 Heliocentric reference frames

For describing planetary positions, or the motion of interplanetary space-craft, the Sun is more convenient as origin of a reference frame. In most cases the ecliptic plane is taken as the XY -plane in a heliocentric reference frame. Since the celestial sphere was considered to have an infinite radius, every point in the solar system can be regarded as being the center of this celestial sphere. Consequently, parallel lines through the Sun and through the Earth will intersect the celestial sphere at a common point. Thus, the point Υ can serve as the directional reference for the X -axis in a heliocentric reference frame too. In the *heliocentric non-rotating ecliptic frame*, a position can be described by a *heliocentric radius*, r , and by the *heliocentric longitude* and *latitude*, defined analogously to celestial longitude and latitude in the geocentric ecliptic frame.

Besides the reference frames mentioned, in astrodynamics still other reference frames are in use. Discussions on these other frames, used for specific applications, are beyond the scope of this introductory chapter.

2.3.6 Motion of the vernal equinox

Up to now, we have tacitly assumed that the point Υ , being fundamental to the non-rotating reference frames, is fixed between the stars on the celestial sphere. In fact, however, this is not the case. Firstly, the mass distribution of the Earth is not spherically symmetrical. As a consequence, the gravitational attraction of Sun and Moon causes precession and nutation of the Earth's rotation axis; i.e. the orientation of the equatorial plane varies. Secondly, the mutual attractions between the Earth and the other planets result in variations in the orientation of the ecliptic plane. Finally, the stars are only at a finite distance, showing some of their own motion on the celestial sphere. Because of these effects, the point Υ moves on the celestial sphere at a rate of about $0.8'$ a year, while the obliquity decreases with about $0.5''$ a

14 Rocket Propulsion & Spaceflight Dynamics

year. The First Point of Aries, as its name suggests, was some 2000 years ago located in the constellation of Aries, the Ram. More recently, it has been in Pisces, the Fish, and presently it is moving into the constellation of Aquarius, the Water Carrier. In order to avoid inaccuracies in calculations, we have to specify which orientations of the equatorial plane and the ecliptic plane, and so the location of the point Υ , are taken for the reference frame. Usually, the mean vernal equinox and equator (or ecliptic) of a reference epoch are selected, whereby mean refers to the fact that the relatively short-period nutation motion is filtered out. In astrodynamics, two choices for the reference epoch are commonly used: the beginning of the year 1950 and the date for which the computations are performed. We then speak of the *mean equinox of 1950 reference frame* and the *mean equinox of date reference frame*.

2.3.7 The velocity vector

The velocity vector of a rocket, satellite or spacecraft can be described by the magnitude of the velocity and by two angles determining the direction of this velocity vector. To this end, we first define a *local horizontal coordinate system*. The *local horizontal plane* can be defined as the plane normal to the radius vector, r (Fig. 2.3). In the geocentric equatorial reference frame, the north-south direction is defined by the intersection of the plane through the local hour circle with the local horizontal plane. The *flight path angle*, γ , is the angle between the velocity vector, V , and the horizontal plane. This angle varies between -90° and $+90^\circ$; $+90^\circ$ corresponding with a radially outward directed velocity. The angle between the local north direction and the projection of the velocity vector on the horizontal plane is called the *flight path azimuth*, ψ . This azimuth is measured from the north in a clockwise direction from 0° to 360° .

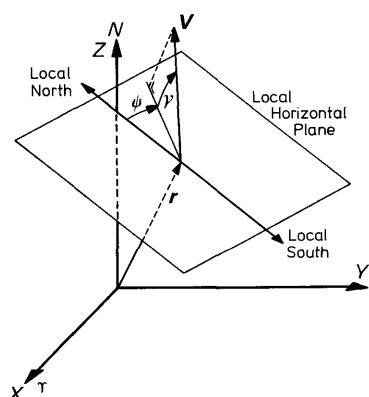


Fig. 2.3 The local horizontal plane and the angles γ and ψ

2.4 Time and calendar

Man has long held a belief that there is a ‘uniform time’. This concept of uniformity, however, turns out to lack meaning. We have no master standard of which we are sure that it runs uniformly. All we really need is that our chronometric variable, if inserted into our physical laws, furnishes reproducible predictions that are in agreement with our observations. In effect, we take a suitable repetitive physical phenomenon and define successive periods of repetition to be equal in length. Nowadays, it is felt that the time provided by a cesium clock should correlate to the highest accuracy with our physical laws, and we take by definition that this time progresses uniformly. We call this *Atomic Time* (A.T.). Though in this way we can define a unit of time, for the fitting of time in our conventional scale we are committed to astronomical observations, which historically form the basis for time reckoning systems.

In astronomy, the measurement of time intervals is based on the rotation of the Earth. The observer’s time is defined as the angular distance covered by a reference object on the celestial sphere after its last crossing of the upper branch of the observer’s celestial meridian. The time interval between two successive crossings is called a *day*. Though the actual length of a day will, in general, depend on the reference object chosen, each type of day is divided into 24 equal parts, called *hours*. These hours again are subdivided into 60 *minutes* and each minute into 60 *seconds*.

The *hour angle*, H , of an object is defined as the angular distance in degrees measured along the celestial equator from the observer’s meridian to the foot of the object’s hour circle. Because for an observer on Earth, the apparent motion of celestial objects on the celestial sphere is in a westward direction, the hour angle is measured positive to the west so that the hour angle increases with time. For a celestial object S , this hour angle is indicated in Fig. 2.1. As an increment in the hour angle of 360° corresponds to a time increment of exactly one day, time can be defined as the hour angle of the reference object. As reference object a particular star can be selected, e.g. Antares. When Antares crosses the observer’s meridian we can speak of $0^{\text{h}}0^{\text{m}}0^{\text{s}}$ Antares-time. Instead of selecting a particular star, it turns out to be more convenient to use the vernal equinox or the Sun as reference object, resulting in *sidereal time* or *solar time*, respectively. As the hour angle of a given point on the celestial sphere differs at a certain epoch for observers with a different geographical longitude, both types of time are local and we speak of local sidereal time and local solar time.

2.4.1 Sidereal time

The sidereal day is defined as the interval between two successive passages of the vernal equinox across the observer’s meridian. From the definitions of

16 Rocket Propulsion & Spaceflight Dynamics

hour angle and right ascension, it will be clear that a celestial object always transits the observer's meridian at a local sidereal time equal to the right ascension of that object. The sidereal time at Greenwich is called the *Greenwich sidereal time*. From our definitions, we conclude that the Greenwich sidereal time is obtained by adding the west-longitude of an observer to his local sidereal time. As the point γ is moving slowly at a non-uniform rate on the celestial sphere, the sidereal day will not have a constant length when compared to an atomic clock, but will vary slightly. The sidereal day, however, is to within one hundredth of a second equal to the true period of rotation of the Earth with respect to a fixed point on the celestial sphere.

2.4.2 Solar time

Sidereal time is very useful to astronomy; our lives and working days, however, are to a large extent regulated by the Sun. Therefore, it is often desirable to use solar time. A *solar day* is defined as the period of the Earth's rotation with respect to the Sun. As the Sun moves, for an observer on Earth, at about 1° per day along the ecliptic in an eastward direction, it will be clear from inspection of Fig. 2.4 that a solar day is longer than a sidereal day. After one revolution of the Earth relative to the point γ , an observer P has still to cover the angle PP' before his solar time is increased by 24 hours. As it takes the Earth about 4 minutes to rotate through an angle of 1° , the solar day is about 4 minutes longer than the sidereal day. *Apparent solar time* is related to the hour angle of the Sun. At midday apparent solar time, the Sun passes the upper branch of the observer's meridian. It is convenient not to start a solar day at the Sun's crossing of the upper branch of the observer's meridian (noon), but at the crossing of the lower branch (midnight). Consequently, the elapsed apparent solar time since the beginning of a solar day is the hour angle of the Sun plus 12 hours.

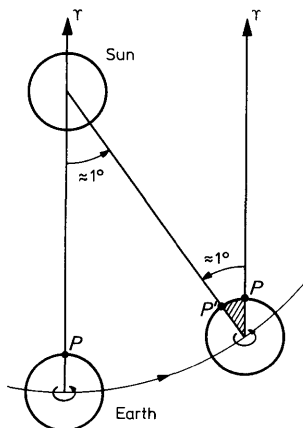


Fig. 2.4 Difference between a sidereal day and a solar day

On September 23, the Sun passes through the autumnal equinox. The vernal equinox then passes the meridian of an observer for whom it is midnight. At that moment, local apparent solar time and local sidereal time are equal for the observer mentioned. With each succeeding day from then, sidereal time gains some minutes on solar time, until just one year later the difference between them is 24 hours.

2.4.3 Mean solar time

Owing to the ellipticity of the Earth's orbit about the Sun, and the fact that the equatorial plane and the ecliptic plane do not coincide, the apparent motion of the Sun on the celestial sphere is not 'uniform'. For that reason the solar day has not a constant length. Therefore, the concept of a fictitious *mean Sun* has been introduced, which is assumed to move at a uniform rate eastward along the celestial equator, with a sidereal motion equal to the mean sidereal motion of the true Sun at January 0.5 (i.e. December 31, 12 hours E.T.*), 1900. This period is the so-called *tropical year* of January 0.5, 1900, to be discussed in Section 2.4.6. A *mean solar day*, or *civil day*, is the interval between two successive crossings of the mean Sun through the observer's meridian, and *mean solar time* is defined as the hour angle of the mean Sun plus 12 hours. The maximum difference between both kinds of solar time can be as much as 17 minutes. In astrodynamics, we often use a standardized mean solar time: the *Greenwich mean solar time* or *Universal Time* (U.T.).

2.4.4 Standard time

For civil life, in 1884 an international agreement was reached to establish a system of 25 time zones around the world. All but two cover a longitude interval of 15° . The Greenwich zone, Zone 0, has bounding meridians 7.5°W and 7.5°E . All other zones are numbered from the Greenwich zone; positively to the west. The *Standard Time* or *Zone Time* (Z.T.) of any place on Earth is given by the mean solar time of the meridian through the center of the Zone of that place. The convention is made that the Zone from 172.5°W to 180°W is Zone 12, while the zone from 172.5°E to 180°E is Zone -12. The meridian separating these two zones is the *International Date Line*. Going eastward from Greenwich one finds the time at the Date Line to be 12 hours later than the time at Greenwich; going westward one finds a time 12 hours earlier than at Greenwich. Consequently, a crossing of the Date Line results in a discontinuity of 24 hours. We therefore omit one day from our calendar when crossing the Date Line in a westward direction and count a day twice when crossing it in the opposite direction. For geographical and political reasons, the actual Date Line and the zone boundaries deviate from the strict classification given above.

* See Section 2.4.5

2.4.5 Ephemeris time and atomic time

Because of irregularities in the Earth's rotation rate, even the mean solar day varies slightly as compared to A.T. over the years. For very precise determinations of time therefore a new kind of time was introduced in 1950: *Ephemeris Time* (E.T.). This is the time which is consistent with the laws of dynamics, and causes the position of celestial bodies, as predicted from the dynamical equations of motion, to agree with observation. The fundamental unit of E.T. is the *ephemeris second* which is $1/31,556,925.9747$ tropical year of 1900, January 0 at Greenwich mean noon, and is chosen such that it equals the length of a mean solar second at that epoch. In 1975 U.T. and E.T. differed by about 45 seconds owing to changes in the Earth's rotation rate since January 0, 1900.

We have seen that, formally, two definitions of uniform time are in use. In astronomy, E.T. was devised from the laws of dynamics; in physics, A.T. was introduced. The big advantage of A.T. is that it can be measured in a laboratory environment, in contrast to E.T. The epoch at which A.T. starts is usually set at 1958, January 1, 0 hours U.T. The atomic second is now defined so that the frequency corresponding to a certain resonance of the cesium atom is 9, 192, 631, 770 cycles per second. This numerical value is such that the A.T. second is equal to the observationally determined value of the E.T. second over the period 1956 to 1965. At 1958, January 1, A.T. and E.T. differed by about 32 seconds and assuming that A.T. and E.T. run at an equal rate, presently the difference is still about 32 seconds.

In January 1972, the atomic second was adopted for all timing, replacing the ephemeris second.

2.4.6 The year

In addition to the day as a unit of time, we are accustomed in civil life to other natural units: the year, the month and the week. Here we will discuss only the year. The year is defined as the orbital period of the Earth in its motion about the Sun. Various types of years can be distinguished. The most important are the *tropical year*, the *Julian year* and the *civil calendar year*.

The tropical year is defined as the time interval between two successive passages of the Sun through the vernal equinox. It equals about 365.2422 mean solar days.

In the Julian calendar, every year counts 365 mean solar days, except those years divisible by four: the leap years, which have 366 mean solar days. So, the average length of the Julian year is 365.25 mean solar days.

To approximate the tropical year more closely, the Gregorian calendar was introduced. The difference between the both calendars being that in the Gregorian calendar those century years not divisible by 400 are ordinary years. Today, the Gregorian calendar is the civil calendar in use over most of the globe. The average length of a Gregorian year is 365.2425 mean solar

days, which is so close to the tropical year that the error in using the Gregorian calendar is only three days in 10,000 years.

2.4.7 The Julian date

Finally, the concept of *Julian Date* (J.D.) has to be mentioned. This is a system of Julian day numbers which involves a continuing count of mean solar days rather than years, and so provides a simpler way of determining the interval of time between two dates than use of the conventional calendar. The epoch at which the Julian Date was exactly zero was set at 4713 B.C., January 1, Greenwich noon, on the Julian calendar. This epoch is close to the one that in medieval times was believed to have marked the creation of the Earth. As an example: the Julian Date for 1975 August 1, 18 hours U.T. is 2, 442, 626.25. In order to avoid those large numbers for indicating dates in our times, it is convenient to express epochs in *Modified Julian Dates* (M.J.D.), which are related to Julian Dates by:

$$\text{M.J.D.} = \text{J.D.} - 2,400,000.5.$$

It should be recognized that while a Julian Date starts at Greenwich mean noon, a Modified Julian Date starts at Greenwich midnight.

2.5 The Earth

Our planet Earth can, in a first approximation, be considered a sphere with a radius of 6371 km. As its mass equals about 5.98×10^{24} kg, its mean density amounts to 5520 kg/m^3 . Because the mean density of the material near the Earth's surface is about 2700 kg/m^3 , the interior of the Earth must be much denser. The outermost layer of the Earth, the *crust*, extends to a depth of about 35 km beneath the continents, but only to about 5 km under the ocean floors. Beneath the crust there is the *mantle* which extends down to a depth of about 3000 km. From a depth of 3000 km to about 5000 km, we speak of the *outer-core*, consisting of liquid material. The innermost part of the Earth, the *inner-core*, is probably solid and extremely hot.

The Earth rotates about its polar axis at a rate of about $0.25'/\text{s}$. The force acting on a body on the Earth's surface, the *gravity force*, is the resultant of the gravitational force (Section 3.5) and the centrifugal force caused by the Earth's rotation. We can regard this resultant force as being derived from the so-called *geopotential*. The gravity force per unit of mass varies from 9.78 m/s^2 at the Earth's equator to 9.83 m/s^2 at the poles.

2.5.1 The shape of the Earth

If the Earth had no rigidity at all, its surface should be an equipotential surface with a constant value of the geopotential. But the Earth has a certain amount of rigidity, and its surface shows an irregular shape. The oceans,

20 Rocket Propulsion & Spaceflight Dynamics

however, making up more than 70% of the Earth's surface, can, in the absence of tidal and meteorological effects, be considered to have a surface on which the geopotential is constant. As a convenient mathematical model for the Earth's shape we therefore take a fictitious equipotential surface coinciding with mean ocean level and its continuation under the continents. This equipotential level is called the *geophysical geoid*. Though this geoid is a much smoother surface than the Earth's actual profile, its mathematical description is still quite complex.

The geoid can be approximated by an ellipsoid of revolution; i.e. an ellipse rotated about its minor axis, which coincides with the Earth's rotation axis. The best approximation then is obtained by selecting the minor and major axes of this ellipse such that deviations from the geoid are minimized. The one adopted in astrodynamics is a *Standard Ellipsoid* with a semi-major axis (Earth's equatorial radius) of 6378.140 km and a semi-minor axis (Earth's polar radius) of 6356.755 km. The deviation of this ellipsoid from a pure sphere has a severe consequence for the determination of the latitude of a place on Earth. The local vertical on the ellipsoid (Fig. 2.5) will, in general, not pass through the mass center of the Earth. It strikes the equatorial plane at an angle called the *geodetic* or *geographic latitude*, Φ' . This geodetic latitude can differ up to an amount of about 11' from the geocentric latitude of that place. Similar difficulties arise in the measurement of the altitude h . Since altitude is always measured perpendicular to the surface, the altitude above a point on the ellipsoid is, in general, not measured along the geocentric radius vector to that point, as it is for a spherical Earth.

Though the deviations of the geoid from the ellipsoid are only very small, they can be determined by observations of the gravitational perturbations of satellite orbits (Chapter 18). After the launching of the first Vanguard satellite in 1958, an accurate study of its orbit showed that the geoid's radius to the north pole is somewhat longer than the radius to the south pole, which sometimes is described as the Earth's *pear shape*. Also the geoid's equator is not circular but shows slight deviations. These deviations can be measured by studying the orbital behavior of geostationary satellites (Sec-

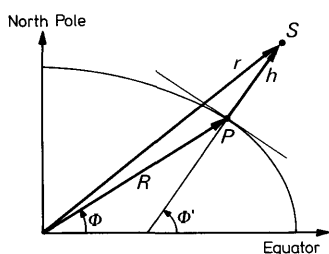


Fig. 2.5 Geocentric and geodetic latitudes

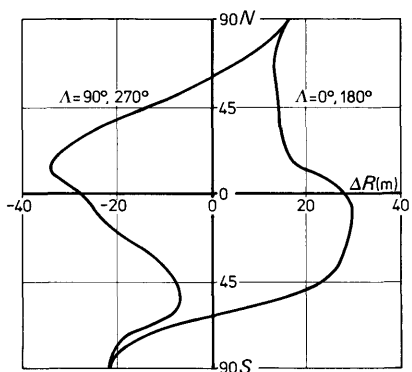


Fig. 2.6 The deviation of the geoid relative to the Standard Ellipsoid

tion 16.2.1). The orbits of those satellites are particularly sensitive to longitudinal variations in the gravitational field since these satellites always keep the same position relative to the Earth's surface.

To a better approximation we can therefore visualize the shape of the geoid as an ellipsoid, with small corrections superimposed on it such that a pear shape in north-south direction and a slightly elliptic equator results. The north polar radius is about 38 m longer than the south polar radius. The major axis of the equatorial ellipse intersects the geoid's surface at longitudes of about 18°W and 162°E, and is about 138 m longer than the minor axis. Figure 2.6 shows the deviations of this geoid model relative to the Standard Ellipsoid for cross-sections along two meridians.

2.6 The Earth's atmosphere

Though the total mass of the Earth's atmosphere is only about one millionth of the mass of the Earth, the atmosphere has a major effect on trajectories of rockets and low Earth satellites, because any motion with respect to this atmosphere generates aerodynamic forces.

The structure of the atmosphere is primarily determined by the radiation input from the Sun and from the Earth's surface. It absorbs most of the solar radiation; only radiation from the near-ultraviolet region to the near-infrared region and radio-waves between 1 cm and about 20–40 m can reach the Earth's surface. The atmosphere shows an immense variability. Temperature, density, pressure and composition strongly depend on altitude, latitude, time of day, season of the year, degree of solar activity and even the phases of the Moon.

For a discussion of the general conditions in the atmosphere, it is convenient to divide the atmosphere into regions differentiated by their temperature distribution. Other subdivisions, based for example on the amount of ionized particles, are also in use. Figure 2.7 presents a scheme of nomenclature for the atmospheric regions.

22 Rocket Propulsion & Spaceflight Dynamics

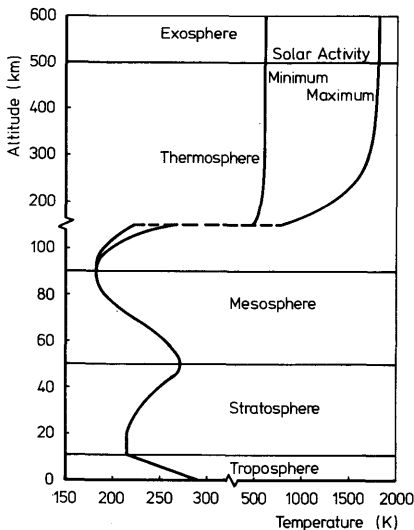


Fig. 2.7 Classification of atmospheric regions

2.6.1 The troposphere, stratosphere and mesosphere

The lowest region of the atmosphere is called the *troposphere*. This region contains about 80% of the total atmospheric mass. On the equator, the troposphere extends to an altitude of about 18 km, over the poles to about 8 km. It is a region of atmospheric turbulence and mixing, of clouds and ever-shifting weather. Expressed in volume percentages, tropospheric dry air consists of 78.1% N₂, 20.9% O₂, 0.9% Ar and 0.03% CO₂. All other constituents together occupy less than 0.07%. Water vapor and carbon dioxide in the troposphere play a key role in maintaining the Earth's climate, as these constituents absorb solar infrared radiation and infrared radiation emitted by the Sun-heated Earth. Thereby they tend to hold in the heat of the lower atmosphere.

The temperature in the troposphere decreases with increasing distance from the Sun-warmed Earth's surface. Density and pressure also decrease with increasing altitude, until in the upper part of the troposphere their values are roughly 30% and 22% of their respective values at the Earth's surface.

The atmospheric region from about 11 km to about 50 km is called the *stratosphere*. Like the troposphere, the chemical composition in the stratosphere is essentially uniform. An exception, however, is the ozone concentration. Though the total amount of ozone is extremely small, the presence of this ozone is very important to life on Earth because it absorbs the solar ultraviolet radiation from 0.2 μm to 0.3 μm, which is not absorbed in the

higher atmosphere. Decomposition of ozone under the influence of this radiation causes heating of the stratosphere. Though the maximum ozone concentration occurs at about 25–30 km, the amount of ozone at greater altitudes so effectively absorbs this part of the ultraviolet radiation that the maximum heating takes place at an altitude of about 50 km. Density and pressure in the stratosphere further decrease until at 50 km altitude they reach values of 0.08% of their respective values at the Earth's surface.

In the *mesosphere*, reaching from an altitude of about 50 km to about 90 km, the temperature decreases because of the diminishing ozone concentration and because no other heat generating reactions of major importance take place.

2.6.2 The ionosphere, thermosphere and exosphere

The *ionosphere* reaches from an altitude of about 50 km upwards to hundreds of kilometers above the Earth's surface. Its major characteristic is the relatively large concentration of free electrons, though neutral particles still dominate strongly. The electron concentration reaches its maximum value at an altitude of about 300 km, where the ratio between the electron concentration and the neutral particles concentration is about 10^{-3} . The charged particles are produced mainly by the absorption of solar radiation. Because of the very low particle density in this region, the free electrons and the positive ions do not recombine quickly and the ionosphere continues to exist even at night when the ionizing solar radiation is no longer present.

The region between about 90 km and 500 km above the Earth's surface is called the *thermosphere*. In the lower thermosphere, the temperature increases rapidly with increasing altitude until at about 300–500 km the so-called *exospheric temperature* (T_∞) is reached. From this altitude upwards the (kinetic) temperature remains constant. The heating of this atmospheric region is mainly due to solar radiation up to 0.2 μm . While below about 90 km the mean molecular weight is nearly constant, above 120 km there is a gradual decrease of molecular weight with increasing altitude. The conditions in the thermosphere are strongly influenced by the solar activity. During periods of solar disturbances the increased solar ultraviolet and corpuscular radiation cause additional heating of the Earth's upper atmosphere. The increased heating produces an outward expansion of the atmosphere resulting in an increase of density. At an altitude of 600 km, for instance, the ratio of densities at high and low solar activity can be as large as 200.

The region of the atmosphere above about 500 km is called the *exosphere*. Some of the lighter atoms are so fast, and the density is here so low, that these atoms can escape into outer space. Ionized species and electrons, however, cannot escape because their motion is restricted by the Earth's magnetic field. This region up to the transition of the geomagnetic field to the interplanetary magnetic field is therefore also called the *magnetosphere*. Figure 2.8 gives an indication of the dependence of pressure, density and

24 Rocket Propulsion & Spaceflight Dynamics

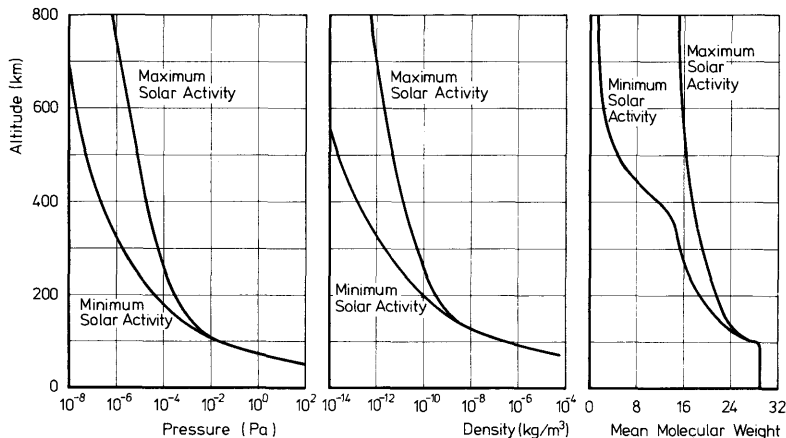


Fig. 2.8 Variation of pressure, density and mean molecular weight in the CIRA 1972 Reference Atmosphere

mean molecular weight on altitude in the upper atmosphere. At an altitude of more than 1000 km, the density is less than $10^{-13} \text{ kg}/\text{m}^3$. Because of this low density, aerodynamic forces on space vehicles can mostly be neglected at altitudes above 1000 km. Therefore, we will omit a discussion of the outermost region of the atmosphere.

For rocket vehicles, the atmosphere ceases to have any measurable effect at much lower altitudes.

3 Mechanics of Particles, Bodies and Fluids

Up to the present the velocities encountered in astronautics are relatively small as compared to the velocity of light, and so classical or Newtonian mechanics will suffice our purpose. Newtonian mechanics is based on the *three laws of Newton*, *Galileo's principle of relativity* and the *three classical conservation laws*: conservation of mass, linear momentum and energy. Moreover, the assumption is made that forces behave as vectors and can be represented mathematically as such. We will now state Newton's laws for particles, where a particle is defined as a constant mass concentrated at a point.

1. Every particle continues in its state of uniform motion in a straight line (or rest), unless compelled to change that state by forces acting upon it.
2. The time rate of change of linear momentum of a particle is proportional to the force acting upon that particle and is collinear with and in the direction of that force.
3. The mutual forces of two particles acting upon each other are equal in magnitude and opposite in direction (action = reaction).

3.1 Newton's first law

In analyzing the first law, we must realize that it is a statement about motion, which is a relative concept. If we speak about motion of an object, we have to specify a frame of reference relative to which the object is moving.

In the first law no reference frame is specified. We know from experience that we cannot just choose any reference frame, i.e. there are special reference frames wherein the first law is valid. We can in fact turn the first law around and make the following statement:

There exist certain reference frames with respect to which the motion of a particle, free of all external forces, is uniform (motion in a straight line with constant speed, including zero).

Those frames are called *inertial frames*. The first law then becomes in fact the definition of an inertial frame of reference.

It is a direct consequence of this definition that if such a frame exists, a whole class of inertial frames can be found. To show this, let us suppose that the frame S is an inertial frame. If another frame S' translates uniformly,

26 Rocket Propulsion & Spaceflight Dynamics

with velocity \mathbf{V} , (i.e. \mathbf{V} is constant), with respect to S and if the time in S' differs by only a constant from the time in S , then S' is an inertial frame too. We will now proceed to prove this statement, known as *Galileo's principle of relativity*.

The transformation of space and time coordinates from S to S' is given by the following relations:

$$\begin{aligned}\mathbf{r}' &= \mathbf{r} - \mathbf{V}t - \mathbf{R}, \\ t' &= t + T.\end{aligned}\tag{3.1-1}$$

This transformation of coordinates is called the *Galilean transformation*. Herein, \mathbf{r} and \mathbf{r}' are the position vectors of a particle P with respect to the origins of S and S' , respectively. \mathbf{R} is a constant vector defining the position of S' relative to S at time $t=0$; t and t' are respectively the times in S and S' , while T , finally, is the constant time difference between S and S' . If no forces are acting on the particle P , then according to the first law the velocity of the particle relative to S is a constant

$$\mathbf{V}_r = \frac{d\mathbf{r}}{dt}.$$

The velocity of the particle relative to S' is defined as

$$\mathbf{V}'_r = \frac{d\mathbf{r}'}{dt'}.$$

Using Eqs. (3.1-1) we find

$$\mathbf{V}'_r = \frac{d\mathbf{r}'}{dt} \frac{dt}{dt'} = \frac{d\mathbf{r}'}{dt} = \frac{d\mathbf{r}}{dt} - \mathbf{V} = \mathbf{V}_r - \mathbf{V}.$$

Since both \mathbf{V}_r and \mathbf{V} are constant, we conclude that \mathbf{V}'_r is a constant too. According to the definition of inertial frames, S' and thus any frame which translates uniformly with respect to S is an inertial frame.

As we will see later on, this is not true for reference frames which rotate, whether or not uniformly, relative to an inertial frame. Any such rotational motion will produce apparent accelerations. We therefore have to conclude that Newtonian mechanics requires an absolute reference for rotational motion. Translational motion on the other hand is relative in that an arbitrary uniform translation may be superimposed. Experience has proved that for all motions we can find a frame that behaves as an inertial one, at least within our measuring accuracy. To describe the motion of the planets in our solar system, the heliocentric frame that is not rotating relative to the fixed stars can be considered as an inertial frame. Likewise, as for experiments within a laboratory on Earth a frame fixed to the laboratory can be viewed as an inertial one. We therefore define an inertial frame to be one in which, experimentally, the first law holds within our desired accuracy.

3.2 Newton's second law

The second law, like the first law, deals with motion and again from experience it is found that the second law holds only with respect to inertial frames. The second law can be expressed as

$$\mathbf{F} = \frac{d}{dt} (m \mathbf{V}). \quad (3.2-1)$$

Here $m \mathbf{V}$ is the linear momentum of a particle with mass m and velocity \mathbf{V} .

The mass in this law is the so-called *inertial mass*, in contrast with the *gravitational mass* which will appear in Newton's law of gravitation later on. Newton, however, tacitly assumed the equivalence of inertial and gravitational mass. Experiments by Eötvös *et al.* [1] in the beginning of this century, and more recently by Roll *et al.* [2] and Braginsky and Panov [3] have established the constancy of the ratio of inertial to gravitational mass within 1 part in 10^{11} or better. In Einstein's general theory of relativity the equivalence between inertial and gravitational mass is a consequence of the principle of equivalence [4, 5].

We have seen that from the Galilean principle of relativity and from the first law it followed that systems translating uniformly relative to an inertial system are inertial systems themselves. We can only use this statement if the second law is invariant under the Galilean transformation. This invariance exists indeed if mass and force are invariant and if, moreover, the mass of the particle is a constant, as will be shown. Consider therefore again the systems S and S' as described before. If \mathbf{F} is the force on the particle P in S , and \mathbf{F}' is the force on P in S' , then since the force is invariant, $\mathbf{F} = \mathbf{F}'$. It follows from Eqs. (3.1-1) that the time rate of change of linear momentum of the particle in the two reference systems is related by

$$\frac{d}{dt} \left(m \frac{d\mathbf{r}}{dt} \right) = \frac{d}{dt'} \left[m' \left(\frac{d\mathbf{r}'}{dt'} + \mathbf{V} \right) \right] = \frac{d}{dt'} \left(m' \frac{d\mathbf{r}'}{dt'} \right) + \mathbf{V} \frac{dm'}{dt'}.$$

Applying Newton's second law in both systems, we obtain:

$$\text{In system } S : \mathbf{F} = \frac{d}{dt} \left(m \frac{d\mathbf{r}}{dt} \right),$$

$$\text{In system } S' : \mathbf{F}' = \frac{d}{dt'} \left(m' \frac{d\mathbf{r}'}{dt'} \right) + \mathbf{V} \frac{dm'}{dt'}.$$

We see that the second law is invariant only if the mass of the particle is a constant.

It was for that reason that we stated the laws of motion for particles with constant mass.

The third law, finally, is clear in itself. However, we have to add the requirement that the action and reaction forces are *collinear*. This collinearity is essential for the conservation of mechanical angular momentum of an

isolated system. It is true for all Newtonian gravitational and mechanical interaction forces but does not apply to certain forces between moving electrically charged particles. This, however, will not concern us in this book.

3.3 Non-inertial frames

We have seen that the first and second of Newton's laws are valid only in inertial frames. This does not mean that studying the motion of an object in a non-inertial frame prohibits us from using Newton's laws. We will have to modify these laws in such a way that they are applicable in non-inertial frames too. In this section we will derive the laws for the said modification.

Suppose S is an inertial frame and S' is a non-inertial one. We know by now that if S' is non-inertial it is moving with respect to S with a velocity which is not uniformly translational. According to *Chasles' theorem* [6], the most general motion of S' with respect to S consists of a translational motion and a rotational motion. By a translational motion of S' is meant that in the infinitesimal time interval Δt every point fixed with respect to S' undergoes a displacement $\Delta \mathbf{r}$ relative to S , where $\Delta \mathbf{r}$ is the same for all points of S' . The translational velocity is defined as

$$\mathbf{V}_{S'} = \lim_{\Delta t \rightarrow 0} \frac{\Delta \mathbf{r}}{\Delta t}. \quad (3.3-1)$$

The system S' is in pure rotational motion relative to S if every point fixed with respect to S' undergoes an angular displacement $\Delta\theta$ in the time interval Δt , where $\Delta\theta$ is measured about a line fixed in S : the *axis of rotation*. We now define a vector $\Delta\boldsymbol{\Theta}$ with magnitude $\Delta\theta$ and directed along this axis of rotation with a sense according to the right-hand rule. The angular velocity $\boldsymbol{\Omega}$ of S' is then defined as

$$\boldsymbol{\Omega} = \lim_{\Delta t \rightarrow 0} \frac{\Delta\boldsymbol{\Theta}}{\Delta t}. \quad (3.3-2)$$

3.3.1 Rotation

In order to concentrate a moment on rotation, suppose the origin of system S' coincides with the origin of S . Suppose S' is in pure rotational motion relative to S about an axis through the origins of both systems. If P is a point fixed in S' , with position vector \mathbf{r} with respect to the origin of S' , then the point P describes in the time interval Δt part of a circle (Fig. 3.1) with radius $r \sin \varphi$ and lying in a plane perpendicular to the axis of rotation. Here φ is the angle between the vector \mathbf{r} and the axis of rotation. Neglecting second order terms, the point P undergoes a displacement $\Delta \mathbf{r}$ perpendicular to \mathbf{r} and the axis of rotation and with magnitude $\Delta r = r \sin \varphi \Delta\theta$. So $\Delta \mathbf{r}$ is

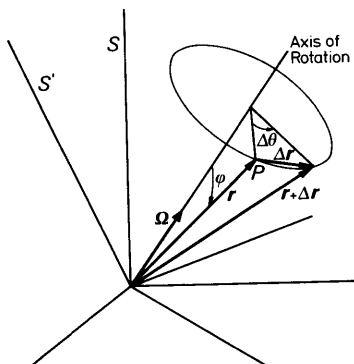


Fig. 3.1 Rotation of vector \mathbf{r} fixed with respect to S' relative to reference frame S

proportional to the vector $\mathbf{r} \times \boldsymbol{\Omega}$ and we can write

$$\Delta \mathbf{r} = \frac{\mathbf{r} \times \boldsymbol{\Omega}}{|\mathbf{r} \times \boldsymbol{\Omega}|} r \sin \varphi \Delta \theta.$$

Now

$$\Delta \theta = \boldsymbol{\Omega} \Delta t \quad \text{and} \quad |\mathbf{r} \boldsymbol{\Omega}| = r \boldsymbol{\Omega} \sin \varphi.$$

It thus follows

$$\Delta \mathbf{r} = \mathbf{r} \times \boldsymbol{\Omega} \Delta t.$$

We finally get the velocity of P by dividing $\Delta \mathbf{r}$ by Δt and taking the limit for $\Delta t \rightarrow 0$. So the velocity of P due to the rotation of S' relative to S is

$$\mathbf{V}_P = \boldsymbol{\Omega} \times \mathbf{r}. \quad (3.3-3)$$

With this result we can derive a formula which relates the time derivative of a vector in a rotating frame to the time derivative of that vector in a non-rotating frame. Again, let S' rotate with angular velocity $\boldsymbol{\Omega}$ relative to S . If \mathbf{e}_x , \mathbf{e}_y and \mathbf{e}_z form a Cartesian unit-vector triad in S' , then any vector \mathbf{A} can be expressed as

$$\mathbf{A} = A_x \mathbf{e}_x + A_y \mathbf{e}_y + A_z \mathbf{e}_z.$$

By differentiating \mathbf{A} we get

$$\frac{d\mathbf{A}}{dt} = \frac{dA_x}{dt} \mathbf{e}_x + \frac{dA_y}{dt} \mathbf{e}_y + \frac{dA_z}{dt} \mathbf{e}_z + A_x \frac{d\mathbf{e}_x}{dt} + A_y \frac{d\mathbf{e}_y}{dt} + A_z \frac{d\mathbf{e}_z}{dt}.$$

Now define

$$\frac{\delta \mathbf{A}}{\delta t} = \frac{dA_x}{dt} \mathbf{e}_x + \frac{dA_y}{dt} \mathbf{e}_y + \frac{dA_z}{dt} \mathbf{e}_z,$$

then $\frac{\delta \mathbf{A}}{\delta t}$ is the time rate of change of the vector \mathbf{A} as viewed by an observer in the rotating system S' . For, only the components of \mathbf{A} can change for such an observer since the unit vectors \mathbf{e}_x , \mathbf{e}_y and \mathbf{e}_z are fixed for him. For an observer in the inertial system S , $\frac{d\mathbf{e}_x}{dt}$ is the velocity of the point with position vector \mathbf{e}_x due to the rotation $\boldsymbol{\Omega}$. According to Eq. (3.3-3) this velocity is $\boldsymbol{\Omega} \times \mathbf{e}_x$. Likewise:

$$\frac{d\mathbf{e}_y}{dt} = \boldsymbol{\Omega} \times \mathbf{e}_y \quad \text{and} \quad \frac{d\mathbf{e}_z}{dt} = \boldsymbol{\Omega} \times \mathbf{e}_z.$$

So the rate of change of \mathbf{A} for an observer in the inertial system is

$$\frac{d\mathbf{A}}{dt} = \frac{\delta \mathbf{A}}{\delta t} + \boldsymbol{\Omega} \times \mathbf{A}. \quad (3.3-4)$$

Though we have assumed that S is an inertial frame, it is important to note that nowhere have we actually used this fact. Therefore Eq. (3.3-4) generally holds for two systems rotating relative to each other. If, for example, a system S' is rotating with respect to a system S'' with angular velocity $\boldsymbol{\Omega}_{S''}$ as viewed from S'' , then for any vector \mathbf{A}

$$\left(\frac{\delta \mathbf{A}}{\delta t} \right)_{S''} = \left(\frac{\delta \mathbf{A}}{\delta t} \right)_{S'} + \boldsymbol{\Omega}_{S''} \times \mathbf{A}. \quad (3.3-5)$$

Likewise

$$\left(\frac{\delta \mathbf{A}}{\delta t} \right)_{S'} = \left(\frac{\delta \mathbf{A}}{\delta t} \right)_{S''} + \boldsymbol{\Omega}_{S'} \times \mathbf{A}, \quad (3.3-6)$$

where $\boldsymbol{\Omega}_{S''}$ is the rotation rate of S'' as viewed by an observer in S' . As $\boldsymbol{\Omega}_{S''} = -\boldsymbol{\Omega}_{S'}$, both expressions are alike.

3.3.2 Newton's laws

We will now turn to the problem how to modify Newton's laws such that they are valid in non-inertial frames. Let S' be a system which translates and rotates relative to S (Fig. 3.2). If \mathbf{R} is the position vector of the origin of S' with respect to the origin of S and \mathbf{r} and \mathbf{p} the position vectors of a particle P with mass m relative to the origins of S and S' , respectively, then

$$\mathbf{r} = \mathbf{R} + \mathbf{p}. \quad (3.3-7)$$

By differentiating Eq. (3.3-7) we obtain the *absolute velocity* of P

$$\mathbf{V}_{abs} = \frac{d\mathbf{r}}{dt} = \frac{d\mathbf{R}}{dt} + \frac{d\mathbf{p}}{dt}. \quad (3.3-8)$$

All derivatives in Eq. (3.3-8) are rates of change as viewed from the inertial

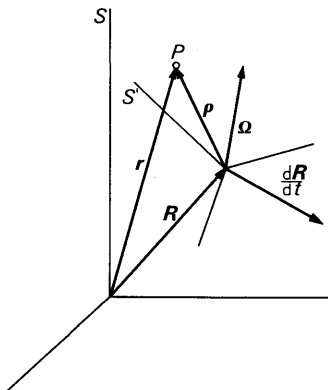


Fig. 3.2 The position vectors of a particle, P , with respect to a fixed frame, S , and a moving frame, S'

frame. Applying Eq. (3.3-4) for the vector ρ we can rewrite Eq. (3.3-8) as

$$\mathbf{V}_{abs} = \frac{d\mathbf{R}}{dt} + \boldsymbol{\Omega} \times \mathbf{\rho} + \frac{\delta \mathbf{\rho}}{\delta t}. \quad (3.3-9)$$

In order to explain the different terms in Eq. (3.3-9), let P' be a point fixed in S' coinciding with P at the instant t . Then $\frac{d\mathbf{R}}{dt} + \boldsymbol{\Omega} \times \mathbf{\rho}$ is the velocity of P' relative to S due to the translation and rotation of S' . The term $\frac{\delta \mathbf{\rho}}{\delta t}$ is the velocity of P relative to P' for an observer in S' as well as for an observer in S . This velocity is called the *relative velocity* of P , \mathbf{V}_{rel} .

If no force is applied to P then, according to Newton's first law, \mathbf{V}_{abs} has to be a constant. The velocity of P in S' is given by

$$\mathbf{V}_{rel} = \mathbf{V}_{abs} - \frac{d\mathbf{R}}{dt} - \boldsymbol{\Omega} \times \mathbf{\rho}.$$

This velocity can only be a constant for any point P in S if and only if $\boldsymbol{\Omega} = 0$ and $\frac{d\mathbf{R}}{dt} = \text{constant}$. Indeed we see that only those systems translating uniformly with respect to S are inertial systems.

By differentiating Eq. (3.3-9) we get the *absolute acceleration* of P

$$\mathbf{a}_{abs} = \frac{d^2\mathbf{R}}{dt^2} + \frac{d\boldsymbol{\Omega}}{dt} \times \mathbf{\rho} + \boldsymbol{\Omega} \times \frac{d\mathbf{\rho}}{dt} + \frac{d}{dt} \left(\frac{\delta \mathbf{\rho}}{\delta t} \right).$$

Again using Eq. (3.3-4), we obtain

$$\mathbf{a}_{abs} = \frac{d^2\mathbf{R}}{dt^2} + \frac{d\boldsymbol{\Omega}}{dt} \times \mathbf{\rho} + \boldsymbol{\Omega} \times (\boldsymbol{\Omega} \times \mathbf{\rho}) + 2\boldsymbol{\Omega} \times \frac{\delta \mathbf{\rho}}{\delta t} + \frac{\delta^2 \mathbf{\rho}}{\delta t^2}. \quad (3.3-10)$$

32 Rocket Propulsion & Spaceflight Dynamics

The sum of the first three terms of the right-hand side of Eq. (3.3-10) represents the acceleration of the fixed point P' for an observer in S . This is called the *dragging acceleration*, \mathbf{a}_{dr} . The term $\frac{d^2\mathbf{R}}{dt^2}$ is the absolute acceleration of the origin of S' . The term $\boldsymbol{\Omega} \times (\boldsymbol{\Omega} \times \mathbf{p})$ is due to the rotation of S' and represents a *centripetal acceleration*. The term $\frac{d\boldsymbol{\Omega}}{dt} \times \mathbf{p}$, often called the *tangential acceleration* is due to the rate of change of rotational velocity. The sum of the last two terms in Eq. (3.3-10) is the acceleration of P relative to P' for an observer in S . The term $2\boldsymbol{\Omega} \times \frac{\delta\mathbf{p}}{\delta t}$ is called the *Coriolis acceleration*, \mathbf{a}_c . The term $\frac{\delta^2\mathbf{p}}{\delta t^2}$, finally, is the acceleration of P as viewed by an observer in S' and is called the *relative acceleration*, \mathbf{a}_{rel} .

So, in general, we can write

$$\mathbf{a}_{abs} = \mathbf{a}_{dr} + \mathbf{a}_c + \mathbf{a}_{rel}.$$

If \mathbf{F} is the actual force applied to the particle P , then according to Newton's second law

$$\mathbf{F} = m\mathbf{a}_{abs} = m\mathbf{a}_{dr} + m\mathbf{a}_c + m\mathbf{a}_{rel}.$$

We now define two apparent forces: a *dragging force*

$$\mathbf{F}_{dr} = -m\mathbf{a}_{dr}, \quad (3.3-11)$$

and a *Coriolis force*

$$\mathbf{F}_c = -m\mathbf{a}_c. \quad (3.3-12)$$

Thus we can write the second law in the form

$$\mathbf{F}_{tot} = \mathbf{F} + \mathbf{F}_{dr} + \mathbf{F}_c = m\mathbf{a}_{rel}. \quad (3.3-13)$$

According to Eq. (3.3-13), we can apply Newton's second law in non-inertial frames if for the total force acting on the particle we take the sum of the external force and the two apparent forces.

3.4 Dynamics of particle systems

With the laws and formulae stated and derived in the previous sections, the motion of a single particle under influence of a known force can be calculated in a fairly straightforward way. By applying Newton's second law, a second-order vector differential equation is obtained. This vector equation can be split into 3 scalar second-order differential equations for motion in physical space. These differential equations, together with appropriate initial conditions, have to be solved, either analytically or numerically. In this way one gets velocity and position as a function of time. In Section 3.6 we will consider the motion of a particle in a gravitational force field, as this analysis

will be very useful in the treatment of satellite orbits and ballistic trajectories.

First, we will consider the dynamics of a group of interacting particles, where we are interested only in the over-all aspects of the motion and not in the motion of each individual particle. The formulae as derived in this section are particularly useful for the analysis of the motion of continuous particle systems, i.e. bodies, whether rigid or not. Although fluids can be treated as particle systems too, it is customary to treat fluids using a different approach (Section 3.7).

3.4.1 Systems of discrete particles

Consider a mass-system S consisting of N particles P_i , each with a constant mass m_i and position vector \mathbf{r}_i with respect to the origin O of an inertial frame XYZ , as shown in Fig. 3.3. In the most general case the system will have a variable mass which is expressed by N being a function of time.

The forces as applied to P_i consist of an *external force*, \mathbf{F}_i , arising from sources external to the system S , and *internal forces* due to interactions among the particles. If \mathbf{F}_{ik} is the internal force acting on P_i due to the particle P_k , we know from Newton's third law

$$\mathbf{F}_{ik} = -\mathbf{F}_{ki}. \quad (3.4-1)$$

We have already pointed out that we will suppose \mathbf{F}_{ik} and \mathbf{F}_{ki} to be collinear, i.e. they act along the straight line connecting the particles. In agreement with Eq. (3.4-1), $\mathbf{F}_{ii} = 0$, which means that particle P_i cannot exert a force on itself.

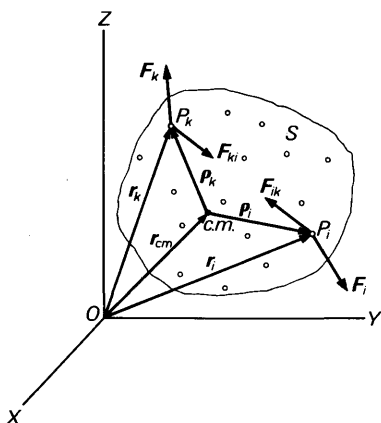


Fig. 3.3 The particle system, S , with position vectors of, and forces on the particles P_i and P_k

34 Rocket Propulsion & Spaceflight Dynamics

The linear momentum of P_i relative to XYZ is

$$\mathbf{J}_i = m_i \frac{d\mathbf{r}_i}{dt}. \quad (3.4-2)$$

Applying Newton's second law on P_i , we get

$$\mathbf{F}_i + \sum_{k=1}^N \mathbf{F}_{ik} = \frac{d\mathbf{J}_i}{dt}. \quad (3.4-3)$$

Now summing Eq. (3.4-3) over all N particles which form the system S at time t , we obtain

$$\sum_{i=1}^N \mathbf{F}_i + \sum_{i=1}^N \sum_{k=1}^N \mathbf{F}_{ik} = \sum_{i=1}^N \frac{d\mathbf{J}_i}{dt}. \quad (3.4-4)$$

Now let $\sum_{i=1}^N \mathbf{F}_i = \mathbf{F}_S$: the total external force applied to the system S at time t .

From Eq. (3.4-1) we see that

$$\sum_{i=1}^N \sum_{k=1}^N \mathbf{F}_{ik} = 0.$$

So Eq. (3.4-4) can be written in the form

$$\mathbf{F}_S = \sum_{i=1}^N \frac{d\mathbf{J}_i}{dt} = \sum_{i=1}^N m_i \frac{d^2\mathbf{r}_i}{dt^2}. \quad (3.4-5)$$

This equation is known as the *translational equation* of system S .

For an invariable system, i.e. a system where no particles enter or leave the system, the translational equation can be written in a simpler and more familiar form. In that case, summation and differentiation can be interchanged, leading to

$$\sum_{i=1}^N m_i \frac{d^2\mathbf{r}_i}{dt^2} = \frac{d^2}{dt^2} \left(\sum_{i=1}^N m_i \mathbf{r}_i \right) = \frac{d^2}{dt^2} (M\mathbf{r}_{cm}) = M \frac{d^2\mathbf{r}_{cm}}{dt^2},$$

where M is the total (constant) mass of the system, given by $M = \sum_{i=1}^N m_i$, and \mathbf{r}_{cm} is the position vector of the center of mass of the system, defined as

$$\mathbf{r}_{cm} = \frac{1}{M} \sum_{i=1}^N m_i \mathbf{r}_i. \quad (3.4-6)$$

The translational equation can be written as

$$\mathbf{F}_S = M \frac{d^2\mathbf{r}_{cm}}{dt^2}. \quad (3.4-7)$$

This equation states that the motion of the center of mass of the system is the same as if the entire mass of the system were concentrated at the center

of mass and were driven by an external force equal to the forces external to the system.

The *equation of rotational motion* of the system S can be obtained by vectorial multiplication of Eq. (3.4-3) with \mathbf{r}_i :

$$\mathbf{r}_i \times \mathbf{F}_i + \sum_{k=1}^N \mathbf{r}_i \times \mathbf{F}_{ik} = \mathbf{r}_i \times \frac{d\mathbf{J}_i}{dt}. \quad (3.4-8)$$

Now, the moment of \mathbf{F}_i with respect to O is defined as

$$\mathbf{M}_i = \mathbf{r}_i \times \mathbf{F}_i,$$

and the angular momentum of P_i is

$$\mathbf{B}_i = \mathbf{r}_i \times \mathbf{J}_i = m_i \mathbf{r}_i \times \frac{d\mathbf{r}_i}{dt}. \quad (3.4-9)$$

Then, the right-hand side of Eq. (3.4-8) can be written as

$$\mathbf{r}_i \times \frac{d\mathbf{J}_i}{dt} = \frac{d}{dt} (\mathbf{r}_i \times \mathbf{J}_i) = \frac{d\mathbf{B}_i}{dt}.$$

Equation (3.4-8) can thus be written as

$$\mathbf{M}_i + \sum_{k=1}^N \mathbf{r}_i \times \mathbf{F}_{ik} = \frac{d\mathbf{B}_i}{dt}. \quad (3.4-10)$$

By summing Eq. (3.4-10) over all particles N , we obtain

$$\sum_{i=1}^N \mathbf{M}_i + \sum_{i=1}^N \sum_{k=1}^N \mathbf{r}_i \times \mathbf{F}_{ik} = \sum_{i=1}^N \frac{d\mathbf{B}_i}{dt}. \quad (3.4-11)$$

Now $\sum_{i=1}^N \mathbf{M}_i = \mathbf{M}_S$: the total moment about O due to the external forces on the system S . Because of Eq. (3.4-1) and the collinearity of the internal forces

$$\sum_{i=1}^N \sum_{k=1}^N \mathbf{r}_i \times \mathbf{F}_{ik} = 0,$$

as can be seen by taking the terms in pairs together

$$\mathbf{r}_i \times \mathbf{F}_{ik} + \mathbf{r}_k \times \mathbf{F}_{ki} = (\mathbf{r}_i - \mathbf{r}_k) \times \mathbf{F}_{ik} = \mathbf{r}_{ik} \times \mathbf{F}_{ik} = 0.$$

Finally, the rotational equation for the system is found to be

$$\mathbf{M}_S = \sum_{i=1}^N \frac{d\mathbf{B}_i}{dt} = \sum_{i=1}^N m_i \mathbf{r}_i \times \frac{d^2 \mathbf{r}_i}{dt^2}. \quad (3.4-12)$$

Again, for an invariable system this equation can be written in a more familiar form by defining the total angular momentum relative to O as

$$\mathbf{B} = \sum_{i=1}^N m_i \mathbf{r}_i \times \frac{d\mathbf{r}_i}{dt},$$

36 Rocket Propulsion & Spaceflight Dynamics

and as summation and differentiation can be interchanged, we get for such a system

$$\mathbf{M}_s = \frac{d\mathbf{B}}{dt}. \quad (3.4-13)$$

3.4.2 Bodies

After having derived the equations of motion for mass systems consisting of a finite number of discrete particles we now can quite easily give the equations for continuous mass systems, i.e. for bodies. They can be thought of as consisting of an infinite number of particles with an infinitesimal mass. In that case the summation signs in Eqs. (3.4-5) and (3.4-12) must be replaced by integration signs, thus leading to:

$$\mathbf{F}_s = \int_M \frac{d^2\mathbf{r}}{dt^2} dM, \quad (3.4-14)$$

$$\mathbf{M}_s = \int_M \mathbf{r} \times \frac{d^2\mathbf{r}}{dt^2} dM. \quad (3.4-15)$$

Although there appears only one integral sign in Eqs. (3.4-14) and (3.4-15), one has to note that the integrals are in fact triple integrals for a three-dimensional system. For dM can be written as ρdV where ρ is the mass density and dV a volume element. This volume integral will be indicated by \int_M .

The Equations (3.4-14) and (3.4-15) can be written in a form more suited for our applications. If \mathbf{r}_{cm} is the location of the center of mass of the system defined by

$$\mathbf{r}_{cm} \int_M dM = \int_M \mathbf{r} dM, \quad (3.4-16)$$

and \mathbf{p} is the position vector of a point P of the system with respect to the center of mass, then

$$\mathbf{r} = \mathbf{r}_{cm} + \mathbf{p}. \quad (3.4-17)$$

For the absolute acceleration of P , we obtain by using Eq. (3.3-10)

$$\frac{d^2\mathbf{r}}{dt^2} = \frac{d^2\mathbf{r}_{cm}}{dt^2} + \frac{d\Omega}{dt} \times \mathbf{p} + \Omega \times (\Omega \times \mathbf{p}) + 2\Omega \times \frac{\delta \mathbf{p}}{\delta t} + \frac{\delta^2 \mathbf{p}}{\delta t^2}, \quad (3.4-18)$$

where Ω is the rotational velocity of the system relative to XYZ. Substitution of this expression for $\frac{d^2\mathbf{r}}{dt^2}$ into the translational equation, Eq. (3.4-14), and taking into account that $\int_M \mathbf{p} dM = 0$, leads to

$$\mathbf{F}_s = M \frac{d^2\mathbf{r}_{cm}}{dt^2} + 2\Omega \times \int_M \frac{\delta \mathbf{p}}{\delta t} dM + \int_M \frac{\delta^2 \mathbf{p}}{\delta t^2} dM. \quad (3.4-19)$$

This equation is the general translational equation for an arbitrary body with variable mass.

The rotational equation as given in Eq. (3.4-15) can be simplified by taking the center of mass of the system, instead of a fixed point in inertial space, as reference point for calculating the external moment and angular momentum. If \mathbf{r}_0 and \mathbf{p}_0 are the location vectors of the point of application of the total external force with respect to O and the center of mass, respectively, then

$$\mathbf{M}_S = \mathbf{r}_0 \times \mathbf{F}_S = (\mathbf{r}_{cm} + \mathbf{p}_0) \times \mathbf{F}_S.$$

The total moment due to the external force relative to the center of mass is

$$\mathbf{M}_{cm} = \mathbf{p}_0 \times \mathbf{F}_S = \mathbf{M}_S - \mathbf{r}_{cm} \times \mathbf{F}_S.$$

By substituting the expressions for \mathbf{M}_S and \mathbf{F}_S into the above equation and using Eq. (3.4-17) we obtain, as \mathbf{r}_{cm} is independent of the three dummy variables of the integration,

$$\mathbf{M}_{cm} = \int_M \mathbf{p} \times \frac{d^2 \mathbf{r}}{dt^2} dM. \quad (3.4-20)$$

Thus with Eq. (3.4-18) the rotational equation finally becomes:

$$\begin{aligned} \mathbf{M}_{cm} = & \int_M \mathbf{p} \times \left(\frac{d\Omega}{dt} \times \mathbf{p} \right) dM + \int_M \mathbf{p} \times \{ \boldsymbol{\Omega} \times (\boldsymbol{\Omega} \times \mathbf{p}) \} dM + \\ & + 2 \int_M \mathbf{p} \times \left(\boldsymbol{\Omega} \times \frac{\delta \mathbf{p}}{\delta t} \right) dM + \int_M \mathbf{p} \times \frac{\delta^2 \mathbf{p}}{\delta t^2} dM. \end{aligned} \quad (3.4-21)$$

This is the general equation of rotational motion for an arbitrary flexible body with variable mass.

3.4.3 Rigid bodies

For a rigid body: $\frac{\delta \mathbf{p}}{\delta t} = \frac{\delta^2 \mathbf{p}}{\delta t^2} = 0$ and the translational equation takes the familiar form

$$\mathbf{F}_S = M \frac{d^2 \mathbf{r}_{cm}}{dt^2}. \quad (3.4-22)$$

For a rigid body the total angular momentum of the body relative to the center of mass is, according to Eq. (3.3-9)

$$\mathbf{B}_{cm} = \int_M \mathbf{p} \times (\boldsymbol{\Omega} \times \mathbf{p}) dM. \quad (3.4-23)$$

We then find

$$\mathbf{M}_{cm} = \frac{d\mathbf{B}_{cm}}{dt} = \int_M \mathbf{p} \times \left(\frac{d\boldsymbol{\Omega}}{dt} \times \mathbf{p} \right) dM + \int_M \mathbf{p} \times \{ \boldsymbol{\Omega} \times (\boldsymbol{\Omega} \times \mathbf{p}) \} dM. \quad (3.4-24)$$

38 Rocket Propulsion & Spaceflight Dynamics

Evaluating the quadruple vector product of the second integral on the right-hand side of Eq. (3.4-24) and using Eq. (3.4-23), we obtain

$$\mathbf{M}_{cm} = \int_M \boldsymbol{\rho} \times \left(\frac{d\boldsymbol{\Omega}}{dt} \times \boldsymbol{\rho} \right) dM + \boldsymbol{\Omega} \times \mathbf{B}_{cm}. \quad (3.4-25)$$

Let us now take a reference system xyz , fixed to the body and with origin O coinciding with the center of mass of that body. If the unit vectors in this reference frame are \mathbf{e}_x , \mathbf{e}_y and \mathbf{e}_z , and if x , y , z are the coordinates of point P in this frame, then

$$\boldsymbol{\rho} = x\mathbf{e}_x + y\mathbf{e}_y + z\mathbf{e}_z, \quad (3.4-26a)$$

and

$$\boldsymbol{\Omega} = p\mathbf{e}_x + q\mathbf{e}_y + r\mathbf{e}_z, \quad (3.4-26b)$$

where p , q , r are the components of $\boldsymbol{\Omega}$ in this frame.

We now can evaluate Eq. (3.4-23) as

$$\begin{aligned} \mathbf{B}_{cm} = \int_M & [\mathbf{e}_x \{(y^2 + z^2)p - xyq - xzr\} + \\ & + \mathbf{e}_y \{-yxp + (x^2 + z^2)q - yzr\} + \\ & + \mathbf{e}_z \{-zxp - zyq + (x^2 + y^2)r\}] dM. \end{aligned} \quad (3.4-27)$$

We now define:

$$I_{xx} = \int_M (y^2 + z^2) dM, \quad I_{yy} = \int_M (x^2 + z^2) dM,$$

$$I_{zz} = \int_M (x^2 + y^2) dM, \quad I_{xy} = I_{yx} = \int_M -xy dM, \quad (3.4-28)$$

$$I_{yz} = I_{zy} = \int_M -yz dM, \quad I_{xz} = I_{zx} = \int_M -xz dM.$$

These are the nine components of the *inertia tensor* \mathbf{I} ; I_{xx} , I_{yy} and I_{zz} are called the *moments of inertia*, and I_{xy} , I_{yz} , I_{xz} , etc., are called the *products of inertia*. Hence, we may write

$$\mathbf{B}_{cm} = \mathbf{e}_x B_x + \mathbf{e}_y B_y + \mathbf{e}_z B_z, \quad (3.4-29)$$

where

$$B_x = I_{xx}p + I_{xy}q + I_{xz}r,$$

$$B_y = I_{xy}p + I_{yy}q + I_{yz}r, \quad (3.4-30)$$

$$B_z = I_{xz}p + I_{yz}q + I_{zz}r.$$

Thus, Eq. (3.4-23) can also be written as

$$\mathbf{B}_{cm} = \int_M \mathbf{\rho} \times (\mathbf{\Omega} \times \mathbf{\rho}) dM = \mathbf{I} \cdot \mathbf{\Omega}. \quad (3.4-31)$$

This last equation is nothing but a formalization of Eq. (3.4-30) and it shows us that the dot product of the tensor \mathbf{I} with the vector $\mathbf{\Omega}$ again is a vector. Generalizing this result, and replacing $\mathbf{\Omega}$ by $\frac{d\mathbf{\Omega}}{dt}$, we can evaluate the first integral of Eq. (3.4-24), and obtain

$$\mathbf{M}_{cm} = \mathbf{I} \cdot \frac{d\mathbf{\Omega}}{dt} + \mathbf{\Omega} \times \mathbf{B}_{cm}. \quad (3.4-32)$$

If one resolves \mathbf{M}_{cm} in Eq. (3.4-32) into its components M_x, M_y, M_z , one can write the vector equation for rotational motion as three scalar equations:

$$\begin{aligned} M_x &= I_{xx} \frac{dp}{dt} + I_{xy} \frac{dq}{dt} + I_{xz} \frac{dr}{dt} + qB_z - rB_y, \\ M_y &= I_{yx} \frac{dp}{dt} + I_{yy} \frac{dq}{dt} + I_{yz} \frac{dr}{dt} + rB_x - pB_z, \\ M_z &= I_{zx} \frac{dp}{dt} + I_{zy} \frac{dq}{dt} + I_{zz} \frac{dr}{dt} + pB_y - qB_x. \end{aligned} \quad (3.4-33)$$

It can be proved that it is always possible to find a coordinate system with its origin coinciding with the center of mass of the body such that the products of inertia are zero simultaneously [7]. The three coordinate axes for this case are known as the *principal axes* and the corresponding moments of inertia are called the *principal moments of inertia*. In that case the Eqs. (3.4-33) reduce to

$$\begin{aligned} M_x &= I_{xx} \frac{dp}{dt} + (I_{zz} - I_{yy})qr, \\ M_y &= I_{yy} \frac{dq}{dt} + (I_{xx} - I_{zz})pr, \\ M_z &= I_{zz} \frac{dr}{dt} + (I_{yy} - I_{xx})pq. \end{aligned} \quad (3.4-34)$$

40 Rocket Propulsion & Spaceflight Dynamics

These equations are known as *Euler's equations of motion*. They are widely used in solving for the rotational motion of a rigid body.

We have seen that by writing the rotational equations in terms of the components along the body axes, the equations simplify considerably. It is sometimes convenient to do the same with the equation for translational motion, especially when the forces are most easily specified in the body axis system. This very often is the case for a thrusting space vehicle flying through the atmosphere. If \mathbf{V} is the velocity of the center of mass relative to the inertial system, the translational equation for a rigid body can be written as

$$\mathbf{F}_s = M \frac{d\mathbf{V}}{dt} = M \left(\frac{\delta \mathbf{V}}{\delta t} + \boldsymbol{\Omega} \times \mathbf{V} \right). \quad (3.4-35)$$

If F_x , F_y and F_z are the body-axis components of \mathbf{F}_s , and u , v and w are the components of the vector \mathbf{V} along the body axes, then according to Eq. (3.4-35)

$$\begin{aligned} F_x &= M \left(\frac{du}{dt} + wq - vr \right), \\ F_y &= M \left(\frac{dv}{dt} + ur - wp \right), \\ F_z &= M \left(\frac{dw}{dt} + vp - uq \right). \end{aligned} \quad (3.4-36)$$

Note, that if we solve the complete equations of motion for p , q , r and u , v and w , a transformation of these components to a fixed coordinate system is required in order to find position and orientation of the body.

3.4.4 Solidification principle

We now return to the general equations of motion for an arbitrary body with variable mass as given in Eqs. (3.4-19) and (3.4-21). Defining the following apparent forces and moments

Coriolis force

$$\mathbf{F}_c = -2\boldsymbol{\Omega} \times \int_M \frac{\delta \mathbf{p}}{\delta t} dM, \quad (3.4-37)$$

Relative force

$$\mathbf{F}_{rel} = - \int_M \frac{\delta^2 \mathbf{p}}{\delta t^2} dM, \quad (3.4-38)$$

Coriolis moment

$$\mathbf{M}_c = -2 \int_M \mathbf{p} \times \left(\boldsymbol{\Omega} \times \frac{\delta \mathbf{p}}{\delta t} \right) dM, \quad (3.4-39)$$

Relative moment

$$\mathbf{M}_{rel} = - \int_M \boldsymbol{\rho} \times \frac{\delta^2 \boldsymbol{\rho}}{\delta t^2} dM. \quad (3.4-40)$$

the equations of motion can be written as

$$\mathbf{F}'_S = \mathbf{F}_S + \mathbf{F}_c + \mathbf{F}_{rel} = M \frac{d^2 \mathbf{r}_{cm}}{dt^2}, \quad (3.4-41)$$

$$\begin{aligned} \mathbf{M}'_{cm} = \mathbf{M}_{cm} + \mathbf{M}_c + \mathbf{M}_{rel} &= \int_M \boldsymbol{\rho} \times \left(\frac{d\boldsymbol{\Omega}}{dt} \times \boldsymbol{\rho} \right) dM + \\ &+ \int_M \boldsymbol{\rho} \times \{ \boldsymbol{\Omega} \times (\boldsymbol{\Omega} \times \boldsymbol{\rho}) \} dM. \end{aligned} \quad (3.4-42)$$

These equations have the same form as the equations for a rigid body. We now will end this section by stating the following important principle known as the *Principle of Solidification*:

In general, equations of translational and rotational motion of an arbitrary variable mass system at time t can be written as the translational and rotational equations for a rigid body with mass M equal to the mass of the system at time t , while in addition to the true external forces and moments, two apparent forces and two apparent moments are applied: the Coriolis and relative forces and moments, respectively.

3.5 Gravitation

Since gravitational forces belong to the most important forces in the dynamics of space vehicles, we will devote a separate section to this subject.

In the case of gravitational forces, in classical mechanics we again use one of the greatest discoveries of Newton: his *law of gravitation*. Briefly the story of his discovery amounts to the following: for many years the Danish astronomer Tycho Brahe (1546–1601) had collected accurate records of the planetary motions. In 1600 Johannes Kepler (1571–1630) joined him as an assistant and began to study the data of Mars from which he derived his three laws:

1. The orbit of each planet lies in a fixed plane containing the Sun and is an ellipse with the Sun at one focus.
2. The line joining the Sun and the planet sweeps out equal areas in equal times.
3. The squares of the planetary periods are proportional to the cubes of the semi-major axes of their respective orbits.

Since the distances of the planets to the Sun are very large compared to the dimensions of the planets and the Sun, Newton considered these celestial bodies as particles and formulated his law of gravitation as:

42 Rocket Propulsion & Spaceflight Dynamics

Any two particles attract each other with a force which is proportional to the product of their masses and inversely proportional to the square of the distance between them and acts along the line joining the particles.

Or, in a formula

$$\mathbf{F}_{12} = G \frac{m_1 m_2}{r_{12}^3} \mathbf{r}_{12}. \quad (3.5-1)$$

In this equation \mathbf{F}_{12} is the force that particle 2 with mass m_2 exerts on particle 1 with mass m_1 . The vector \mathbf{r}_{12} , with magnitude r_{12} , is the position vector of particle 2 with respect to particle 1. G , finally, is a proportionality factor and is known as the *universal gravitational constant*. (Tables T.1 and T.2).

Compared to the dimensions of the solar system, the planets may be regarded as particles; but is this still allowed in calculating the force that a planet exerts on an object near that planet, for example on the planet's surface? Since the planets can be approximated by spheres, one could answer this question by calculating the force that a sphere exerts on a particle with mass m_1 outside that sphere. This can be accomplished in the following way: consider the sphere as a collection of an infinite number of particles with mass dm and position vector \mathbf{r} relative to the particle. The force between the particle and an infinitesimal particle of the sphere is

$$d\mathbf{F} = G \frac{m_1 dm}{r^3} \mathbf{r}.$$

The total force between particle and sphere could be obtained by integration of the equation for $d\mathbf{F}$ over the sphere. We will follow a different method, but we first have to explain the important notions of *conservative fields* and *potentials*.

If we have a particle P with mass m then the force, \mathbf{g} , exerted by P on a particle with unit mass is given by

$$\mathbf{g} = -\frac{m}{r^3} \mathbf{r}, \quad (3.5-2)$$

where \mathbf{r} is the position vector of the unit mass relative to P . We can conceive this force as a force that is exerted remotely by P on the unit mass. We can also follow another way of thought. By putting the particle P in the space, the space around P is changed. Where before no force on the unit mass was observed, now a definite force is measured. We say around P there exists a *gravitational field* which manifests itself by the fact that on a unit mass in the space around P a force is observed. The *field strength* of the field is defined as the force on the unit mass and thus equals \mathbf{g} . So the gravitational field is a vector field.

A force field is said to be *conservative* if, and only if, the line integral $\int_A^B \mathbf{g} \cdot d\mathbf{r}$ is a function of the end points only, which implies that $\oint \mathbf{g} \cdot d\mathbf{r} = 0$.

The line integral represents the work done by the field as the unit mass moves from A to B . Since the work is only a function of the endpoints, the integrand must be an exact differential. Thus

$$\mathbf{g} \cdot d\mathbf{r} = -dU. \quad (3.5-3)$$

It is convenient to choose the minus sign. The scalar quantity U is called the *potential energy per unit mass*, or briefly *potential*. From Eq. (3.5-3), we see that the work done by the field is $W = U_A - U_B$, or the decrease in potential energy is equal to the work done on the particle by the force field. Since the potential U , defined in Eq. (3.5-3), except for a constant, is a function of position only, we can write in Cartesian coordinates

$$dU = \frac{\partial U}{\partial x} dx + \frac{\partial U}{\partial y} dy + \frac{\partial U}{\partial z} dz. \quad (3.5-4)$$

If x , y and z and g_x , g_y and g_z are the components of \mathbf{r} and \mathbf{g} , respectively, then

$$\mathbf{g} \cdot d\mathbf{r} = g_x dx + g_y dy + g_z dz. \quad (3.5-5)$$

Combining Eqs. (3.5-3) to (3.5-5) leads to

$$g_x = -\frac{\partial U}{\partial x}, \quad g_y = -\frac{\partial U}{\partial y}, \quad g_z = -\frac{\partial U}{\partial z},$$

or briefly

$$\mathbf{g} = -\nabla U. \quad (3.5-6)$$

Or in words: For a conservative force field there exists a scalar function U , the potential, such that the field strength, \mathbf{g} , equals minus the gradient of U . The converse is not always true especially in case of a time-varying field.

Now returning to the gravitational field

$$\int_A^B \mathbf{g} \cdot d\mathbf{r} = - \int_A^B \frac{Gm}{r^3} \mathbf{r} \cdot d\mathbf{r} = - \int_A^B \frac{Gm}{r^2} dr = Gm \left(\frac{1}{r_B} - \frac{1}{r_A} \right) \quad (3.5-7)$$

This shows the line integral to be a function of the endpoints only and thus the gravitational field is a conservative one. From Eqs. (3.5-3) and (3.5-7) it follows:

$$U = -\frac{Gm}{r} + C. \quad (3.5-8)$$

It is common use to choose $C = 0$. The potential energy is then always negative and approaches zero as r approaches infinity.

We will now return to the original problem of finding the gravitational force between a sphere and a particle. Suppose that a closed surface S

44 Rocket Propulsion & Spaceflight Dynamics

encloses a volume \mathcal{V} containing a particle of mass m . Then by Gauss' Theorem (Appendix 1),

$$\int_{\mathcal{V}} \nabla \cdot \mathbf{g} d\mathcal{V} = \int_S \mathbf{g} \cdot \mathbf{n} dS. \quad (3.5-9)$$

In spherical coordinates, the divergence of a vector \mathbf{A} is given by [8]:

$$\nabla \cdot \mathbf{A} = \frac{1}{r^2} \frac{\partial}{\partial r} (r^2 A_r) + \frac{1}{r \sin \theta} \frac{\partial}{\partial \theta} (A_\theta \sin \theta) + \frac{1}{r \sin \theta} \frac{\partial A_\Phi}{\partial \Phi}.$$

According to Eq. (3.5-2), $g_r = -\frac{Gm}{r^2}$, $g_\theta = g_\Phi = 0$, and thus

$$\nabla \cdot \mathbf{g} = -\frac{G \partial m}{r^2 \partial r}.$$

For the volume element $d\mathcal{V}$ we can write $d\mathcal{V} = r^2 dr d\Omega$, where $d\Omega$ is the element of solid angle, Equation (3.5-9) then becomes

$$\int_S \mathbf{g} \cdot \mathbf{n} dS = - \int_{\mathcal{V}} G \frac{\partial m}{\partial r} dr d\Omega = -4\pi Gm.$$

If we have a number of particles within S with a total mass M then

$$\int_S \mathbf{g} \cdot \mathbf{n} dS = -4\pi GM, \quad (3.5-10)$$

where \mathbf{g} is the field strength due to all particles within S . Now suppose there is a sphere with mass M inside S , then Eq. (3.5-10) will still hold. Now let S be a spherical surface concentric with the sphere and with a radius r . If the density of the sphere is a function of the distance to the center only then by symmetry \mathbf{g} is everywhere directed normal (inward) to S and has the same magnitude everywhere on S . The surface integral in Eq. (3.5-10) takes the value $-4\pi r^2 g$. From Eq. (3.5-10) it then follows that $g = \frac{GM}{r^2}$ and

$$\mathbf{g} = -\frac{GM}{r^3} \mathbf{r}. \quad (3.5-11)$$

We conclude that the gravitational field of a sphere, with the above mentioned symmetry of mass distribution, is outside that sphere the same as if all mass were concentrated at the sphere's center.

3.6 Motion of a particle in an inverse-square field

We will now consider the motion of a particle in an inverse-square gravitational field, such as that due to another particle or a sphere of mass M . We will suppose that the field is inertial, i.e. a reference frame fixed with respect to the field is an inertial frame.

The field strength is given by

$$\mathbf{g} = -\frac{\mu}{r^2} \mathbf{e}_r \quad (3.6-1)$$

where $\mu = GM$ and is called the *attraction or gravitation parameter* of the mass M and \mathbf{e}_r is the unit vector in radial direction from the center of M . The equation of motion of a particle with mass m then is given by Newton's second law:

$$m \frac{d^2 \mathbf{r}}{dt^2} = m \mathbf{g},$$

or

$$\frac{d^2 \mathbf{r}}{dt^2} = -\frac{\mu}{r^3} \mathbf{r}. \quad (3.6-2)$$

It will be shown in Section 16.1 that this so-called *one-body problem* is a good approximation for the motion of rockets and satellites.

3.6.1 Constants of motion

First, we will derive two constants of motion for this case. By multiplying Eq. (3.6-2) vectorially with \mathbf{r} , we obtain

$$\mathbf{r} \times \frac{d^2 \mathbf{r}}{dt^2} = 0, \quad \text{or} \quad \frac{d}{dt} \left(\mathbf{r} \times \frac{d\mathbf{r}}{dt} \right) = 0,$$

So,

$$\mathbf{r} \times \frac{d\mathbf{r}}{dt} = \mathbf{r} \times \mathbf{V} = \mathbf{H} = \text{constant}. \quad (3.6-3)$$

We see that \mathbf{H} is the angular momentum per unit mass of the particle. As is customary in celestial mechanics, we will use the symbol \mathbf{H} here to denote angular momentum, instead of \mathbf{B} we used before. Since the instantaneous plane of motion is defined as the plane through \mathbf{r} and \mathbf{V} , we also conclude from Eq. (3.6-3) that the trajectory of the particle lies in a plane defined by \mathbf{r} and \mathbf{V} at the initial time, t_0 . Introducing in this plane the polar coordinates r and φ , the tangential velocity is given by

$$V_\varphi = r \frac{d\varphi}{dt}. \quad (3.6-4)$$

If γ is the flight path angle defined in Section 2.3.7 then also

$$V_\varphi = V \cos \gamma. \quad (3.6-5)$$

The magnitude of \mathbf{H} is

$$H = rV \cos \gamma = rV_\varphi = r^2 \frac{d\varphi}{dt}. \quad (3.6-6)$$

46 Rocket Propulsion & Spaceflight Dynamics

In the case that $H = 0$ and $r \neq 0$, the motion is rectilinear. We will omit these kinds of degenerate trajectories from our discussion. According to Fig. 3.4, the area that is swept out by the radius vector \mathbf{r} during the time interval Δt is

$$\Delta A = \frac{1}{2} r^2 \Delta\varphi + 0(r \Delta\varphi \Delta r).$$

Dividing by Δt and taking the limit for $\Delta t \rightarrow 0$ we obtain the so-called *areal velocity*:

$$\frac{dA}{dt} = \frac{1}{2} r^2 \frac{d\varphi}{dt} = \frac{H}{2}, \quad (3.6-7)$$

and we conclude that $\frac{dA}{dt}$ is a constant. So, the radius vector sweeps out equal areas in equal times, which verifies Kepler's second law. A second constant of motion can be obtained by scalar multiplication of Eq. (3.6-2) with $\frac{dr}{dt}$:

$$\frac{d\mathbf{r}}{dt} \cdot \frac{d^2\mathbf{r}}{dt^2} = -\frac{\mu}{r^3} \mathbf{r} \cdot \frac{d\mathbf{r}}{dt},$$

or,

$$\frac{1}{2} \frac{d}{dt} \left(\frac{d\mathbf{r}}{dt} \cdot \frac{d\mathbf{r}}{dt} \right) = -\frac{\mu}{r^3} \frac{1}{2} \frac{d}{dt} (\mathbf{r} \cdot \mathbf{r}) = \frac{d}{dt} \left(\frac{\mu}{r} \right).$$

So after integration, we obtain

$$\frac{1}{2} V^2 - \frac{\mu}{r} = \mathcal{E} = \text{constant}. \quad (3.6-8)$$

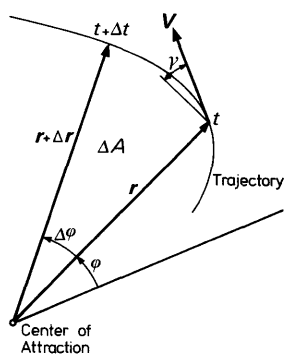


Fig. 3.4 The position of a particle moving in an inverse-square force field at times t and $t + \Delta t$

Equation (3.6-8) is the law of conservation of energy, since $\frac{V^2}{2}$ is the kinetic energy per unit mass and, as derived in the foregoing section, $-\frac{\mu}{r}$ is the potential energy per unit mass.

3.6.2 Trajectory geometry

As the motion takes place in a plane, the vector equation (3.6-2) can be written as two scalar second-order differential equations. We therefore use a reference system with the origin in the attraction center and with three mutually perpendicular axes: the r , φ and z -axis. The r -axis joins the particle with the attraction center, the φ -axis lies in the plane of motion, positive in the direction of the tangential velocity. The z -axis, finally, is normal to the plane of motion and is positive in the direction of the angular momentum. Owing to the tangential velocity of the particle this reference system is rotating with angular velocity

$$\boldsymbol{\Omega} = \frac{d\varphi}{dt} \mathbf{e}_z.$$

We can write

$$\mathbf{r} = r \mathbf{e}_r, \quad (3.6-9)$$

By differentiating Eq. (3.6-9) and using Eq. (3.3-4), we obtain

$$\frac{d\mathbf{r}}{dt} = \frac{dr}{dt} \mathbf{e}_r + r \boldsymbol{\Omega} \times \mathbf{e}_r = \frac{dr}{dt} \mathbf{e}_r + r \frac{d\varphi}{dt} \mathbf{e}_\varphi.$$

By differentiating again

$$\frac{d^2\mathbf{r}}{dt^2} = \frac{d^2r}{dt^2} \mathbf{e}_r + \left(\frac{dr}{dt} \frac{d\varphi}{dt} + r \frac{d^2\varphi}{dt^2} \right) \mathbf{e}_\varphi + \frac{dr}{dt} \boldsymbol{\Omega} \times \mathbf{e}_r + r \frac{d\varphi}{dt} \boldsymbol{\Omega} \times \mathbf{e}_\varphi,$$

or

$$\frac{d^2\mathbf{r}}{dt^2} = \left[\frac{d^2r}{dt^2} - r \left(\frac{d\varphi}{dt} \right)^2 \right] \mathbf{e}_r + \left[r \frac{d^2\varphi}{dt^2} + 2 \frac{dr}{dt} \frac{d\varphi}{dt} \right] \mathbf{e}_\varphi. \quad (3.6-10)$$

Substitution of Eqs. (3.6-9) and (3.6-10) into Eq. (3.6-2) leads to

$$\frac{d^2r}{dt^2} - r \left(\frac{d\varphi}{dt} \right)^2 = -\frac{\mu}{r^2}, \quad (3.6-11)$$

$$r \frac{d^2\varphi}{dt^2} + 2 \frac{dr}{dt} \frac{d\varphi}{dt} = 0. \quad (3.6-12)$$

Equation (3.6-12) can be integrated directly after multiplication by r . The result is then $r^2 \frac{d\varphi}{dt} = \text{constant}$. This was already found, since according to

48 Rocket Propulsion & Spaceflight Dynamics

Eq. (3.6-6), $r^2 \frac{d\varphi}{dt}$ is the absolute value of the angular momentum, which is a constant of motion.

Equation (3.6-11) can be used to determine the shape of the trajectory, i.e. r as a function of φ . In order to solve Eq. (3.6-11) for r as a function of φ we replace t by φ using the relation

$$\frac{d}{dt} = \frac{d\varphi}{dt} \frac{d}{d\varphi}. \quad (3.6-13)$$

With the use of Eq. (3.6-6) we can write

$$\frac{d}{dt} = \frac{H}{r^2} \frac{d}{d\varphi}. \quad (3.6-14)$$

In order to avoid mathematical difficulties it is useful to substitute

$$r = \frac{1}{u}, \quad (3.6-15)$$

Then

$$V_r = \frac{dr}{dt} = Hu^2 \frac{d}{d\varphi} \left(\frac{1}{u} \right) = -H \frac{du}{d\varphi}, \quad (3.6-16)$$

and

$$\frac{d^2r}{dt^2} = -H^2 u^2 \frac{d^2u}{d\varphi^2}. \quad (3.6-17)$$

Substitution of these relations into Eq. (3.6-11) and dividing the resulting equation by $H^2 u^2$ leads to the second-order linear differential equation

$$\frac{d^2u}{d\varphi^2} + u = \frac{\mu}{H^2}. \quad (3.6-18)$$

The general solution of this equation is

$$u = \frac{\mu}{H^2} + C \cos(\varphi - \omega), \quad (3.6-19)$$

where C and ω are integration constants which have to be determined from the initial conditions. Let the initial conditions at $t = t_0$ be given by:

$$V(t_0) = V_0, \quad \gamma(t_0) = \gamma_0, \quad r(t_0) = r_0 \quad \text{and} \quad \varphi(t_0) = \varphi_0.$$

Since the energy \mathcal{E} is a constant of motion we can write

$$\mathcal{E} = \frac{V_0^2}{2} - \frac{\mu}{r_0} = \frac{V^2}{2} - \frac{\mu}{r}.$$

By using Eq. (3.6-16) and Eq. (3.6-6) we find

$$V^2 = V_r^2 + V_\varphi^2 = H^2 \left(\frac{du}{d\varphi} \right)^2 + H^2 u^2,$$

and the energy equation can be written as

$$\frac{H^2}{2} \left[\left(\frac{du}{d\varphi} \right)^2 + u^2 \right] - \mu u = \mathcal{E}.$$

Substitution of Eq. (3.6-19) in this expression results in

$$\frac{H^2}{2} \left[C^2 - \frac{\mu^2}{H^4} \right] = \mathcal{E},$$

from which equation we obtain C as

$$C = \sqrt{\frac{2\mathcal{E}}{H^2} + \frac{\mu^2}{H^4}}. \quad (3.6-20)$$

We have chosen the positive root for C since any possible sign change can be handled by the choice of ω . Substitution of Eq. (3.6-20) into Eq. (3.6-19) gives

$$u = \frac{\mu}{H^2} \left[1 + \left(\sqrt{\frac{2\mathcal{E}H^2}{\mu^2} + 1} \right) \cos(\varphi - \omega) \right].$$

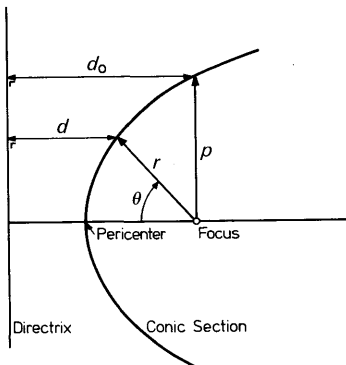
The constant ω can be determined from the above equation together with Eq. (3.6-16) at $t = t_0$. However, since the reference line from where φ is measured can be chosen arbitrarily we make the substitution $\theta = \varphi - \omega$. The orbit equation then becomes

$$r = \frac{H^2/\mu}{1 + \left(\sqrt{\frac{2\mathcal{E}H^2}{\mu^2} + 1} \right) \cos \theta}. \quad (3.6-21)$$

We see that r is minimal when $\theta = 0$, so θ is measured from a line drawn from the center of attraction to the closest point of the trajectory, the *pericenter*. The point farthest away is called the *apocenter*. Also the terms *periapsis* and *apoapsis* are used.

The angle θ is called *true anomaly*, while the angle ω , determining the polar angle of the pericenter, is known as the *argument of pericenter*. The equation of the orbit is the representation in polar coordinates of a so-called *conic section* as we will prove now. In general, a conic section is the locus of

points with a constant ratio $\frac{r}{d}$ (Fig. 3.5), where r is the distance to a given point F , the *focus*, and d is the distance to a given line l , the *directrix*. The constant ratio is called the (numerical) *eccentricity* of the conic and is denoted by e . From Fig. 3.5 we see that $d_0 = d + r \cos \theta$ and since

**Fig. 3.5** The general conic section

$\frac{p}{d_0} = \frac{r}{d} = e$, we can also write $\frac{p}{e} = \frac{r}{e} + r \cos \theta$, and by solving for r we obtain

$$r = \frac{p}{1 + e \cos \theta}. \quad (3.6-22)$$

This is the general equation for a conic section. The radius at $\theta = 90^\circ$ is called the *semi-latus rectum* and is denoted by p . Comparing Eqs. (3.6-21) and (3.6-22), we see that they are the same and we conclude that the trajectory of a particle in an inverse-square force field is a conic section with eccentricity and semi-latus rectum given by

$$e = \sqrt{\frac{2\mathcal{E}H^2}{\mu^2} + 1}, \quad (3.6-23)$$

$$p = \frac{H^2}{\mu}. \quad (3.6-24)$$

This statement is Kepler's first law.

3.6.3 Classification and characteristics of conic sections

From the general theory of conic sections, we know that conics are classified depending upon the value of the eccentricity. If $0 \leq e < 1$ the conic is an *ellipse*, with $e = 0$ as a special case, the *circle*. If $e = 1$ we have a *parabola* and for $e > 1$ the conic is a *hyperbola*. We will now briefly discuss those characteristics of the various conic sections, which will be needed in the subsequent chapters.

Ellipse. (Fig. 3.6). Although defined here as the locus of points with a

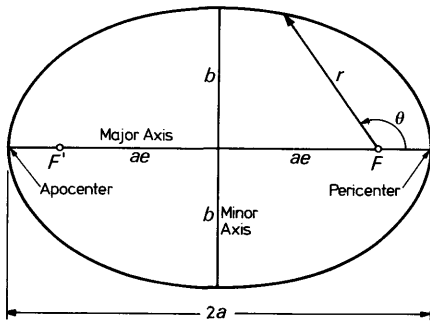


Fig. 3.6 The ellipse

constant ratio $\frac{r}{d}$, the ellipse can also be defined as the locus of points such that the sum of the distances from the two foci F and F' is a constant. This constant is equal to the length of the line that connects the two vertices, the *major axis*, which is denoted by $2a$.

The minimum value of r , known as the *pericenter distance* is

$$r_p = \frac{p}{1+e}, \quad (3.6-25)$$

while the maximum value of r , the *apocenter distance*, is given by

$$r_a = \frac{p}{1-e}. \quad (3.6-26)$$

The *semi-major axis*, a , and the *eccentricity*, e , follow from

$$a = \frac{1}{2}(r_p + r_a) = \frac{p}{1-e^2}, \quad e = \frac{r_a - r_p}{r_a + r_p}. \quad (3.6-27)$$

The distance between the two foci F and F' is

$$2f = 2a - 2r_p = \frac{2pe}{1-e^2} = 2ae. \quad (3.6-28)$$

The *semi-minor axis*, b , then follows from

$$b = \sqrt{a^2 - f^2} = a\sqrt{1 - e^2}. \quad (3.6-29)$$

Parabola. For a given value of p we see from Eq. (3.6-27) that if e approaches unity the semi-major axis approaches infinity. In the limit, if $e = 1$, the conic is not a finite closed curve anymore and has become a parabola. This also follows from Eq. (3.6-22), for, if $e = 1$, r approaches infinity for $\theta \rightarrow 180^\circ$.

52 Rocket Propulsion & Spaceflight Dynamics

The pericenter distance is related to the semi-latus rectum by Eq. (3.6-25), which for $e = 1$ yields

$$r_p = \frac{1}{2}p. \quad (3.6-30)$$

So, we can write the equation for a parabola as

$$r = \frac{2r_p}{1 + \cos \theta}. \quad (3.6-31)$$

Hyperbola. If $e > 1$, the denominator on the right-hand side of Eq. (3.6-22) changes sign for $\cos \theta = -\frac{1}{e}$. The result of this is that the hyperbola has two branches with asymptotes making an angle $\theta_a = \text{arcos} \left(\frac{1}{e} \right)$ with the line joining the two vertices. This line is the major axis. In order to use the same equations for all conics, the value of the semi-major axis is taken negative for a hyperbola. So, the Eqs. (3.6-25) to (3.6-27) remain valid for a hyperbola, while the distance between the two foci is given by

$$2f = -2a + 2r_p = -\frac{2pe}{1 - e^2} = -2ae. \quad (3.6-32)$$

The semi-minor axis is imaginary for a hyperbola.

Returning to the orbit of the particle we can calculate the semi-major axis of the trajectory with Eqs. (3.6-23), (3.6-24) and (3.6-27) resulting in

$$a = -\frac{\mu}{2\mathcal{E}}. \quad (3.6-33)$$

The semi-major axis thus is only dependent on the total energy per unit mass of the particle, i.e. only a function of V_0 and r_0 . The energy equation (3.6-8) can now be written in the following form:

$$V^2 = \mu \left(\frac{2}{r} - \frac{1}{a} \right) \quad (3.6-34)$$

This is known as the *vis-viva integral*.

We can conclude directly from Eq. (3.6-33) that the trajectory is an ellipse if $\mathcal{E} < 0$, a parabola if $\mathcal{E} = 0$ and a hyperbola if $\mathcal{E} > 0$, which of course follows from Eq. (3.6-23) too. Expressed in the initial conditions V_0 and r_0 this means that if

$$V_0 < \sqrt{\frac{2\mu}{r_0}} \quad \text{the trajectory is an ellipse,}$$

if

$$V_0 = \sqrt{\frac{2\mu}{r_0}} \quad \text{the trajectory is a parabola,}$$

and if

$$V_0 > \sqrt{\frac{2\mu}{r_0}} \quad \text{the trajectory is a hyperbola.}$$

So, increasing the speed will gradually change a closed conic into an open one. The minimum speed that is required to escape permanently from the gravitational field is called the *escape velocity* and is

$$V_{esc} = \sqrt{\frac{2\mu}{r_0}}. \quad (3.6-35)$$

A special case of an elliptic orbit occurs for $e = 0$. For such a circular orbit we find from Eq. (3.6-23)

$$\frac{2\mathcal{E}H^2}{\mu^2} + 1 = 0,$$

Expressing \mathcal{E} and H in r_0 , V_0 and γ_0 we obtain

$$\frac{2}{\mu^2} \left(\frac{V_0^2}{2} - \frac{\mu}{r_0} \right) (r_0 V_0 \cos \gamma_0)^2 + 1 = 0.$$

This equation can also be written as

$$\sin^2 \gamma_0 + \cos^2 \gamma_0 \left(1 - \frac{r_0 V_0^2}{\mu} \right)^2 = 0.$$

As both terms in this equation are pure squares, a requirement for a circular orbit is $\gamma_0 = 0$ and $V_0 = \sqrt{\frac{\mu}{r_0}}$. For the so-called *circular velocity* we obtain

$$V_c = \sqrt{\frac{\mu}{r_0}}. \quad (3.6-36)$$

From Eqs. (3.6-35) and (3.6-36) follows the relation between circular and escape velocity

$$V_{esc} = \sqrt{2} V_c. \quad (3.6-37)$$

Finally, we will derive Kepler's third law for elliptic orbits. The period, T , of the orbit is found by dividing the area of the ellipse by the areal velocity

$$T = \frac{\pi ab}{\frac{dA}{dt}} = \frac{2\pi a^2 \sqrt{1-e^2}}{H}.$$

From Eqs. (3.6-24) and (3.6-27) we see that

$$H = \sqrt{\mu p} = \sqrt{\mu a(1-e^2)},$$

and we find for the period

$$T = 2\pi \sqrt{\frac{a^3}{\mu}}, \quad (3.6-38)$$

which verifies Kepler's third law.

A more extensive discussion of motion in a gravitational field will be given in Chapter 16 where the two-body problem is treated.

3.7 Mechanics of fluids

The same laws of Newton as applied to particles and bodies in the previous sections, govern the mechanics of fluids. Our treatment will ignore gravity, friction and electromagnetic forces, as their effects are of minor importance, or completely absent in our applications. Friction comes, among others, into play in heat transfer problems (Chapter 8), and will be dealt with there.

There are two ways of looking at a fluid. The first one is concerned with what happens to the fluid particles in the course of time, what paths they describe, what velocities they possess, etc. This is called the *Lagrangian description*. The second one, is the *Eulerian description*. It attempts to find out what happens in a given point in the fluid field. We will apply both methods here.

3.7.1 Conservation of mass

Consider an undefeatable volume, \mathcal{V} , fixed with respect to an inertial system and bounded by a permeable surface, S , Fig. 3.7. The unit vector normal to S , directed outward, is called the *unit normal*, n . The fluid is assumed to have a mass density, ρ , and a velocity, \mathbf{V} , both of which are a function of position and time.

In general, the mass contained by \mathcal{V} will change due to the flow of matter through S . The influx of matter through a surface element dS is given by:

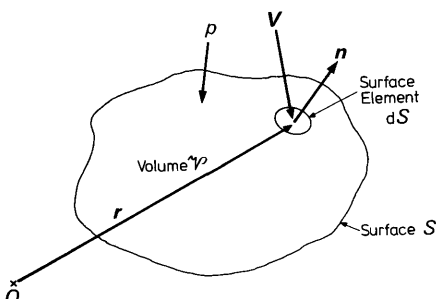


Fig. 3.7 The control volume, \mathcal{V}

$-\rho \mathbf{V} \cdot \mathbf{n} dS$. The minus sign occurs because \mathbf{n} is positive in the outward direction. By integration over the entire surface we find the total flux of matter, m , through S :

$$m = - \int_S \rho \mathbf{V} \cdot \mathbf{n} dS,$$

which must equal the time rate of change of the mass contained by \mathcal{V} , i.e.

$$\frac{\partial}{\partial t} \int_{\mathcal{V}} \rho d\mathcal{V} = - \int_S \rho \mathbf{V} \cdot \mathbf{n} dS. \quad (3.7-1)$$

Equation (3.7-1) is called the *conservation of mass equation* and states that the time rate of change of mass contained by a volume of fixed shape is equal to the flux of matter through the boundaries of that volume as long as no mass is created spontaneously.

It is practical to derive some other forms of Eq. (3.7-1). According to Gauss' Theorem as given in Appendix 1, the right-hand side of Eq. (3.7-1) can be transformed into a volume integral

$$\int_S \rho \mathbf{V} \cdot \mathbf{n} dS = \int_{\mathcal{V}} (\nabla \cdot \rho \mathbf{V}) d\mathcal{V}.$$

As \mathcal{V} is assumed constant, the order of differentiation and integration can be interchanged. So Eq. (3.7-1) can be written as

$$\int_{\mathcal{V}} \frac{\partial \rho}{\partial t} d\mathcal{V} = - \int_{\mathcal{V}} (\nabla \cdot \rho \mathbf{V}) d\mathcal{V},$$

or

$$\int_{\mathcal{V}} \left[\frac{\partial \rho}{\partial t} + \nabla \cdot (\rho \mathbf{V}) \right] d\mathcal{V} = 0. \quad (3.7-2)$$

As Eq. (3.7-2) must hold for any volume, the integrand must be zero,

$$\frac{\partial \rho}{\partial t} + \nabla \cdot (\rho \mathbf{V}) = 0. \quad (3.7-3)$$

Equation (3.7-3) is known as the *law of conservation of mass*, or the *equation of continuity*.

The reader himself can derive the special forms of Eq. (3.7-3) such as for *steady-state flow*, $\left(\frac{\partial \rho}{\partial t} = 0\right)$, or for *incompressible media* ($\rho = \text{constant}$).

A pure one-dimensional form of Eq. (3.7-3) is

$$\frac{\partial \rho}{\partial t} + \frac{\partial \rho V}{\partial x} = 0. \quad (3.7-4)$$

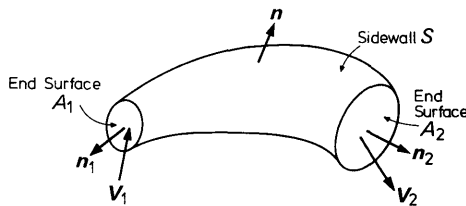


Fig. 3.8 The streamtube

This form applies only to strictly one-dimensional flows. In many applications, however, we have small deviations from one-dimensionality. In these cases a quasi one-dimensional form of Eq. (3.7-1) for steady-state flow, which takes into account the variation of the cross-sectional area is very useful. Consider a streamtube of variable cross-sectional area as given in Fig. 3.8. According to the concept of the streamtube there is no mass transport through the sidewall, \$S\$, but only through the surfaces, \$A_1\$ and \$A_2\$, at both ends of the tube. These surfaces, \$A_1\$ and \$A_2\$, are arbitrarily chosen, and are not necessarily planar. As there is no mass-transport through \$S\$, only the surfaces, \$A_1\$ and \$A_2\$, contribute to the surface integral of Eq. (3.7-1), and this equation can be written as

$$\int_V \frac{\partial \rho}{\partial t} dV = - \int_{A_1} \rho \mathbf{V} \cdot \mathbf{n} dA_1 - \int_{A_2} \rho \mathbf{V} \cdot \mathbf{n} dA_2, \quad (3.7-5)$$

and in case of a steady-state flow through the tube,

$$\int_{A_1} \rho \mathbf{V} \cdot \mathbf{n} dA_1 = - \int_{A_2} \rho \mathbf{V} \cdot \mathbf{n} dA_2. \quad (3.7-6)$$

Often \$A_1\$ and \$A_2\$ are assumed to be planar surfaces over which both the density, \$\rho\$, and the normal velocity component, \$V_n\$, are constant. In that case, Eq. (3.7-6) yields the well-known expression,

$$\rho_1 V_{1n} A_1 = \rho_2 V_{2n} A_2. \quad (3.7-7)$$

This equation is often referred to as the *one-dimensional steady-state equation of continuity*. It should be emphasized, however, that this is only a quasi one-dimensional form as the foregoing will have made clear.

3.7.2 Conservation of linear momentum

Because Newton's second law holds only for invariable mass systems, we consider a material volume, \$V\$, bounded by a *fluid surface*, \$S\$. The material volume is defined such that it is always composed of the same fluid particles and so its mass is constant with time. The surface, \$S\$, however, may change in time, due to the displacement of particles. According to Eq. (3.4-5) we

have

$$\mathbf{F} = \frac{d}{dt} \sum_{i=1}^N m_i \mathbf{V}_i \quad (3.7-8)$$

In passing from a system of discrete particles to a fluid, considered as a continuum, the sum in Eq. (3.7-8) changes into the integral

$$\mathbf{I} = \int_M \mathbf{V} dM.$$

Since we neglect gravity, viscosity and electromagnetic effects, the external force, \mathbf{F} , in Eq. (3.7-8) consists only of pressure forces on the fluid surface, S ,

$$\mathbf{F} = - \int_S p \mathbf{n} dS.$$

The minus sign occurs, because the pressure force is opposite to the unit normal on S . Application of Newton's second law to the *material volume*, \mathcal{V} , containing fluid of density ρ gives

$$\frac{d}{dt} \int_{\mathcal{V}} \rho \mathbf{V} d\mathcal{V} = - \int_S p \mathbf{n} dS. \quad (3.7-9)$$

The total derivative in this equation is, as we will show, dependent on the path. Therefore, consider a scalar or vector quantity in the fluid field, which is a function of position and time, in general. Using Cartesian coordinates, $A = A(t, x, y, z)$, and the total derivative is given by

$$\frac{dA}{dt} = \frac{\partial A}{\partial t} + \frac{\partial A}{\partial x} \frac{dx}{dt} + \frac{\partial A}{\partial y} \frac{dy}{dt} + \frac{\partial A}{\partial z} \frac{dz}{dt}.$$

It is clear that this derivative is dependent on the path, given by

$$x = x(t), \quad y = y(t), \quad z = z(t).$$

As we follow the particles with the material volume, \mathcal{V} , we take a special path such that

$$\frac{dx}{dt} = u, \quad \frac{dy}{dt} = v, \quad \frac{dz}{dt} = w,$$

where u , v and w are the components of the fluid velocity, \mathbf{V} . This special total derivative is called the *material time derivative* or *substantial derivative*. It is denoted by

$$\frac{D}{Dt} = \frac{\partial}{\partial t} + u \frac{\partial}{\partial x} + v \frac{\partial}{\partial y} + w \frac{\partial}{\partial z}, \quad (3.7-10)$$

and it is easily seen that this is equivalent to

$$\frac{D}{Dt} = \frac{\partial}{\partial t} + \mathbf{V} \cdot \nabla. \quad (3.7-11)$$

58 Rocket Propulsion & Spaceflight Dynamics

Returning now to Eq. (3.7-9), we note that we consider a material volume, \mathcal{V} , and so for the total derivative, the substantial derivative has to be taken. With the help of the *Reynolds' transport theorem*, (Appendix 2), Eq. (3.7-9) can be written as

$$\int_{\mathcal{V}} \left(\frac{\partial \rho \mathbf{V}}{\partial t} + \rho \mathbf{V}(\nabla \cdot \mathbf{V}) + (\mathbf{V} \cdot \nabla)(\rho \mathbf{V}) \right) d\mathcal{V} = - \int_S p \mathbf{n} \cdot d\mathbf{S}.$$

Using Gauss' theorem we can transform the surface integral into a volume integral and obtain

$$\int_{\mathcal{V}} \left\{ \frac{\partial}{\partial t} (\rho \mathbf{V}) + \rho \mathbf{V}(\nabla \cdot \mathbf{V}) + (\mathbf{V} \cdot \nabla)(\rho \mathbf{V}) + \nabla p \right\} d\mathcal{V} = 0.$$

As this must hold for any volume, \mathcal{V} , it follows that

$$\frac{\partial}{\partial t} (\rho \mathbf{V}) + \rho \mathbf{V}(\nabla \cdot \mathbf{V}) + (\mathbf{V} \cdot \nabla)(\rho \mathbf{V}) + \nabla p = 0. \quad (3.7-12)$$

Multiplication of the continuity equation, Eq. (3.7-3), by \mathbf{V} and subtracting this form from Eq. (3.7-12) leads to the *Euler equation*, or the *equation of conservation of linear momentum*,

$$\frac{\partial \mathbf{V}}{\partial t} + (\mathbf{V} \cdot \nabla) \mathbf{V} + \frac{1}{\rho} \nabla p = 0. \quad (3.7-13)$$

3.7.3 Conservation of energy

The third relation to be derived, is the energy balance for a flowing fluid. For an adiabatic system, the first law of thermodynamics (Appendix 3) states: $\delta E + \delta W = 0$. The δ indicates that we deal with small increments, during a time interval, δt . The work, δW , done by the material volume, \mathcal{V} , Fig. 3.7, neglecting terms of order δ^2 and higher, equals: $\delta W = p \delta \mathcal{V}$, where $\delta \mathcal{V}$ is the change in the volume, \mathcal{V} , during the time interval, δt . For the material volume, \mathcal{V} , moving along with the fluid, the change in an elementary volume element, $d\mathcal{V}$, bounded by a surface element, dS' , equals

$$\delta d\mathcal{V} = dS' \mathbf{n} \cdot \mathbf{V} \delta t,$$

and as $\mathbf{n} \cdot \mathbf{V}$ on neighboring elements cancel, the total amount of work, δW , amounts to

$$\delta W = \int_S p \mathbf{n} \cdot \mathbf{V} dS \delta t, \quad (3.7-14a)$$

where S is the outer surface of the control volume, \mathcal{V} .

In the first law of thermodynamics, E stands for the total internal energy of a system. A flowing fluid not only possesses a *specific internal energy*, e ,

but also a *specific kinetic energy*, $\frac{1}{2}\mathbf{V} \cdot \mathbf{V}$. Thus the energy contained by \mathcal{V} is

$$E = \int_{\mathcal{V}} \rho(e + \frac{1}{2}\mathbf{V} \cdot \mathbf{V}) d\mathcal{V},$$

and the change in the energy content during the time interval, δt , is

$$\delta E = \frac{D}{Dt} \int_{\mathcal{V}} \rho(e + \frac{1}{2}\mathbf{V} \cdot \mathbf{V}) d\mathcal{V} \delta t. \quad (3.7-14b)$$

Combining the Eqs. (3.7-14a) and (3.7-14b) yields:

$$\frac{D}{Dt} \int_{\mathcal{V}} \rho(e + \frac{1}{2}\mathbf{V} \cdot \mathbf{V}) d\mathcal{V} + \int_S p\mathbf{n} \cdot \mathbf{V} dS = 0.$$

With the help of Gauss' theorem and Reynolds' transport theorem, this equation is easily transformed into

$$\int_{\mathcal{V}} \left\{ \frac{\partial}{\partial t} \left\{ \rho(e + \frac{1}{2}\mathbf{V} \cdot \mathbf{V}) \right\} + \nabla \cdot \left\{ (\rho\mathbf{V})(e + \frac{1}{2}\mathbf{V} \cdot \mathbf{V}) + p\mathbf{V} \right\} \right\} d\mathcal{V} = 0,$$

or, with the same reasoning as before

$$\frac{\partial}{\partial t} \left\{ \rho(e + \frac{1}{2}\mathbf{V} \cdot \mathbf{V}) \right\} + \nabla \cdot \left\{ (e + \frac{1}{2}\mathbf{V} \cdot \mathbf{V})(\rho\mathbf{V}) \right\} + \nabla \cdot (p\mathbf{V}) = 0. \quad (3.7-15)$$

This is the expression for the conservation of energy. However, simpler expressions can be obtained. Multiplying the continuity equation, Eq. (3.7-3) by $e + \frac{1}{2}\mathbf{V} \cdot \mathbf{V}$ and subtracting the result from Eq. (3.7-15) gives

$$\rho \frac{\partial}{\partial t} (e + \frac{1}{2}\mathbf{V} \cdot \mathbf{V}) + (\rho\mathbf{V} \cdot \nabla)(e + \frac{1}{2}\mathbf{V} \cdot \mathbf{V}) + \nabla \cdot (p\mathbf{V}) = 0. \quad (3.7-16)$$

Now

$$\nabla \cdot (p\mathbf{V}) = \frac{p}{\rho} \nabla \cdot (\rho\mathbf{V}) + \rho(\mathbf{V} \cdot \nabla) \left(\frac{p}{\rho} \right).$$

By using the equation of conservation of mass, Eq. (3.7-3), we find

$$\nabla \cdot (p\mathbf{V}) = -\frac{p}{\rho} \frac{\partial \rho}{\partial t} + \rho(\mathbf{V} \cdot \nabla) \left(\frac{p}{\rho} \right),$$

and the *energy equation* becomes

$$\frac{\partial}{\partial t} \left(e + \frac{p}{\rho} + \frac{1}{2}\mathbf{V} \cdot \mathbf{V} \right) + \mathbf{V} \cdot \nabla \left(e + \frac{p}{\rho} + \frac{1}{2}\mathbf{V} \cdot \mathbf{V} \right) - \frac{1}{\rho} \frac{\partial p}{\partial t} = 0. \quad (3.7-17)$$

With the concept of enthalpy, h , defined as (Appendix 3),

$$h = e + \frac{p}{\rho}, \quad (3.7-18)$$

60 Rocket Propulsion & Spaceflight Dynamics

Eq. (3.7-17) can be written as

$$\frac{\partial}{\partial t} (h + \frac{1}{2}\mathbf{V} \cdot \mathbf{V}) + \mathbf{V} \cdot \nabla (h + \frac{1}{2}\mathbf{V} \cdot \mathbf{V}) - \frac{1}{\rho} \frac{\partial p}{\partial t} = 0. \quad (3.7-19)$$

For ideal gases Eq. (3.7-19) can be simplified. Scalar multiplication of Eq. (3.7-13) by \mathbf{V} leads to

$$\frac{\partial}{\partial t} (\frac{1}{2}\mathbf{V} \cdot \mathbf{V}) + \mathbf{V} \cdot \nabla (\frac{1}{2}\mathbf{V} \cdot \mathbf{V}) + \frac{1}{\rho} \mathbf{V} \cdot \nabla p = 0.$$

Subtracting this equation from Eq. (3.7-19) and substituting the *perfect gas law*

$$p = \rho RT,$$

and

$$h = h_0 + c_p T,$$

gives

$$\frac{1}{RT} \left\{ \frac{\partial}{\partial t} (c_p T) + \mathbf{V} \cdot \nabla (c_p T) \right\} - \frac{1}{p} \left\{ \frac{\partial p}{\partial t} + \mathbf{V} \cdot \nabla p \right\} = 0.$$

As

$$c_p/R = \frac{\gamma}{\gamma-1},$$

we find

$$\frac{\partial}{\partial t} \left\{ \ln \left(\frac{T^{\gamma/(\gamma-1)}}{p} \right) \right\} + \mathbf{V} \cdot \nabla \left\{ \ln \left(\frac{T^{\gamma/(\gamma-1)}}{p} \right) \right\} = 0,$$

which, after integration yields

$$T = c_1 p^{(\gamma-1)/\gamma} \quad (3.7-20a)$$

Or, using the perfect gas law,

$$p = c_2 \rho^\gamma, \quad (3.7-20b)$$

$$T = c_3 \rho^{\gamma-1}, \quad (3.7-20c)$$

where c_1 , c_2 and c_3 are constants. These famous results, known as the *Poisson relations*, are usually derived for a static system in thermodynamics. From the derivation given here, it follows that this law also holds for moving gases.

It should be kept in mind that the simple forms Eq. (3.7-20) of the energy equation hold only if

1. There is no dissipation of energy and no heat is added to or withdrawn from the system. Therefore the process must be isentropic.

2. The gases must satisfy the perfect gas law, and c_p must be independent of the temperature.

Even in cases where these assumptions are questionable, we will often use the relations Eq. (3.7-20) instead of the more complicated form of Eq. (3.7-19), because in practice the differences may be very small.

3.7.4 Conservation of angular momentum

Although not an independent equation, we will derive the equation for conservation of angular momentum, because it will be used in Chapter 10. From Section 3.4, we know that for an invariable system of particles the rate of change of angular momentum with respect to an inertially fixed reference point, O , is equal to the moment due to the external forces. The angular momentum, \mathbf{B} , of the fluid contained by the material volume, \mathcal{V} , with respect to O is, Fig. (3.7),

$$\mathbf{B} = \int_{\mathcal{V}} \mathbf{r} \times \mathbf{V} \rho \, d\mathcal{V}, \quad (3.7-21)$$

where \mathbf{r} is the position vector of an element, $d\mathcal{V}$, with respect to O . The moment, \mathbf{M}_S , due to external forces on the material volume, \mathcal{V} , follows from

$$\mathbf{M}_S = - \int_S \mathbf{r} \times \mathbf{n} p \, dS, \quad (3.7-22)$$

and, according to Eq. (3.4-13),

$$\frac{D}{Dt} \int_{\mathcal{V}} \mathbf{r} \times \mathbf{V} \rho \, d\mathcal{V} = - \int_S \mathbf{r} \times \mathbf{n} p \, dS. \quad (3.7-23)$$

By using the Reynolds' transport theorem, (Appendix 2), Eq. (3.7-23) can be transformed into

$$\begin{aligned} \int_{\mathcal{V}} \frac{\partial}{\partial t} (\mathbf{r} \times \rho \mathbf{V}) \, d\mathcal{V} + \int_{\mathcal{V}} \{(\mathbf{r} \times \rho \mathbf{V})(\nabla \cdot \mathbf{V}) + (\mathbf{V} \cdot \nabla)(\mathbf{r} \times \rho \mathbf{V})\} \, d\mathcal{V} \\ = - \int_S \mathbf{r} \times \mathbf{n} p \, dS. \end{aligned} \quad (3.7-24)$$

Transformation of the second volume integral into a surface integral, with the help of Gauss' theorem, leads to

$$\int_{\mathcal{V}} \frac{\partial}{\partial t} (\mathbf{r} \times \rho \mathbf{V}) \, d\mathcal{V} + \int_S \{(\rho \mathbf{V} \cdot \mathbf{n})(\mathbf{r} \times \mathbf{V}) + \mathbf{r} \times \mathbf{n} p\} \, dS = 0. \quad (3.7-25)$$

For many applications, such as turbines and pumps, Eq. (3.7-25) proves to be very useful.

Application of Gauss' theorem to the surface integral in Eq. (3.7-24) leads to the partial differential equation for the *conservation of angular*

momentum

$$\frac{\partial}{\partial t} (\mathbf{r} \times \rho \mathbf{V}) + (\mathbf{r} \times \mathbf{V})(\nabla \cdot \rho \mathbf{V}) + (\rho \mathbf{V} \cdot \nabla)(\mathbf{r} \times \mathbf{V}) - \nabla \times \mathbf{r} \rho = 0. \quad (3.7-26)$$

We have discussed those aspects of dynamics needed in the following chapters. Many interesting aspects of dynamics that we will not encounter have purposely been omitted.

References

- 1 Eötvos, R. V., Pekar, D. and Fekete, E. (1922), Beitrage zum Gesetze der Proportionalität von Tragheit und Gravität, *Ann. d. Physik*, **68**, 11–66.
- 2 Roll, P. G., Krotkov, R. and Dicke, R. H. (1964), The equivalence of inertial and passive gravitational mass, *Ann. Phys.*, **26**, 442–517.
- 3 Braginsky, V. B. and Panov, V. I. (1971), Verification of the equivalence of inertial and gravitational mass, *Zh. Eksp. Teor. Fiz.*, **61**, 873–879 (in Russian).
- 4 Einstein, A. and Grossmann, M. (1913), Entwerf einer verallgemeinerten Relativitätstheorie und einer Theorie der Gravitation, *Zeit. Math. Phys.*, **62**, 225–261.
- 5 Møller, C. (1952), *The Theory of Relativity*, Clarendon Press, Oxford, p. 220.
- 6 Corben, H. C. and Stehle, P. (1965), *Classical Mechanics*, John Wiley, New York, p. 139.
- 7 Slater, J. C. and Frank, N. H. (1933), *Introduction to Theoretical Physics*, McGraw-Hill, New York, p. 96.
- 8 Chambers, L. G. (1969), *A Course in Vector Analysis*, Chapman and Hall, London, p. 100.

4 The Equations of Motion of Rigid Rockets

In Chapter 3 the equations of motion for a non-rigid, variable mass system were derived (Eqs. (3.4-41) and (3.4-42)). As a rocket is such a mass system we can apply these equations. In order to evaluate the various terms in these equations as a function of various rocket parameters, we will first have to specify exactly which mass system we call rocket and which assumptions are made.

We define the rocket as the mass system bounded by a closed surface S formed by the outer wall S_R of the vehicle and any surface A_e bounded by the nozzle exit contour (Fig. 4.1). The following assumptions are made:

1. Except for the burned propellant, all mass bounded by the surface S forms an undeformable body. This is the reason why we call this hypothetical rocket rigid. In reality there are no *rigid rockets*. For liquid propellant rockets there is fluid motion through pipes and inside tanks, and there is rotating equipment such as turbines and pumps. In general, and especially for large rockets, the rocket structure is not rigid and will deflect. We have to note, however, that a rigid rocket defined this way is not a rigid body in the common mechanical sense. For, not all particles of the rocket are at rest relative to each other, nor will the mass of the rocket be a constant.
2. The outer wall S_R of the vehicle, except perhaps the part of S_R which is formed by the outer wall of the nozzle, has an axis of symmetry: the *longitudinal axis* of the rocket.
3. The center of mass of the rocket lies on this axis.
4. The longitudinal axis is a principal axis of inertia.

The rocket motion as computed with these simplifying assumptions will, in general, approximate the real motion of the rocket very well.

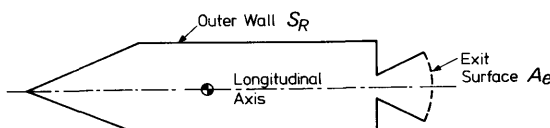


Fig. 4.1 The rocket and the boundary surfaces S_R and A_e

64 Rocket Propulsion & Spaceflight Dynamics

Despite these assumptions, the equations of motion remain rather complicated. This is due to a number of terms which cannot be determined without again making a lot of assumptions. These terms, however, are very small relative to the other terms, and have no or hardly any influence on the motion. When we encounter such small terms we will mention it and neglect them further without an attempt to rigorously prove that this is permissible. In most cases, such a proof is impossible, but it is experience that tells us what terms can be neglected.

4.1 Reference frames

In order to derive the equations of motion of a rocket and to describe position and orientation of the rocket, we will need various reference frames. The choice of some of these reference frames depends on the mission of the rocket. As most rocket vehicles move in the neighborhood of the Earth, we will use reference frames which are Earth-bound in some way. To simplify the mathematical treatment, matrices will be used. As we will have to transform from one coordinate frame to another one, which we will do by means of matrices, the matrix consisting of the unit vectors along the axes of the reference frame is given for each reference frame.

Inertial reference frame (XYZ). In Section 3.4, the equations of motion for an arbitrary mass system are given relative to an inertial frame. In order to apply these equations to a rocket vehicle, we will have to specify an inertial frame. For rocket motion in the neighborhood of the Earth, the non-rotating geocentric equatorial reference frame as described in Section 2.3.4 can be used as an inertial frame. If e_x , e_y and e_z are the unit vectors along the axes of this frame, we define a 3×1 matrix with these unit vectors as elements

$$\mathbf{E} = \begin{bmatrix} e_x \\ e_y \\ e_z \end{bmatrix}. \quad (4.1-1)$$

Rotating geocentric reference frame ($X_g Y_g Z_g$). This reference frame, which is also described in Section 2.3.4, is a convenient reference frame to specify the position of the rocket relative to the Earth's surface. For short-duration, high-thrust rocket motion, the acceleration due to the rotation of this reference frame can often be neglected, and the reference frame can then be regarded as an inertial frame. We define the matrix \mathbf{E}_g as

$$\mathbf{E}_g = \begin{bmatrix} e_{X_g} \\ e_{Y_g} \\ e_{Z_g} \end{bmatrix}, \quad (4.1-2)$$

where again the elements are the unit vectors along the axes.

Vehicle-centered horizontal reference frame ($X_vY_vZ_v$). This reference frame is used to describe the orientation of the rocket and its velocity vector relative to the Earth's surface. At any moment, the origin of this reference system coincides with the center of mass of the vehicle. The orientation of the reference frame is such that it constitutes a local horizontal system as described in Section 2.3.7. The X_vY_v -plane is taken to be the local horizontal plane. The X_v -axis is along the north-south direction, positive to the north. The Y_v -axis is along the east-west direction, positive to the east. The Z_v -axis is along the radius vector from the center of the Earth and is positive downwards. With e_{X_v} , e_{Y_v} and e_{Z_v} being the unit vectors along the axes, the matrix \mathbf{E}_v is defined as

$$\mathbf{E}_v = \begin{bmatrix} e_{X_v} \\ e_{Y_v} \\ e_{Z_v} \end{bmatrix}. \quad (4.1-3)$$

Vehicle reference frame (xyz). The center of mass of the vehicle is the origin of this frame. The x -axis lies along the longitudinal axis of the rocket and is positive forwards. The y - and z -axis lie along the other two principal axes of inertia of the vehicle such that the frame is right-handed. If e_x , e_y and e_z are the unit vectors along the axes of the vehicle reference frame, the matrix \mathbf{E}_r , is defined as

$$\mathbf{E}_r = \begin{bmatrix} e_x \\ e_y \\ e_z \end{bmatrix}. \quad (4.1-4)$$

The vehicle reference frame is particularly useful to denote the aerodynamic forces and moments, and the apparent forces and moments.

4.1.1 The relative orientation of the various reference frames

Non-rotating geocentric equatorial frame/Rotating geocentric frame (Fig. 4.2). The rotating geocentric frame which is fixed to the Earth rotates with angular velocity ω_e about the Z -axis of the non-rotating geocentric equatorial reference frame. Thus, the relative orientation of these reference frames is determined by the angle between the X - and the X_g -axis. According to Section 2.4, this is the Greenwich hour angle of the vernal equinox: H_G . If at $t = t_0$ both reference frames coincide (zero Greenwich sidereal time), the angle H_G at any time is given by

$$H_G = \omega_e(t - t_0). \quad (4.1-5)$$

The following relation between the unit vectors in both systems holds:

$$\mathbf{E}_g = \mathbf{A}_g \mathbf{E}, \quad (4.1-6)$$

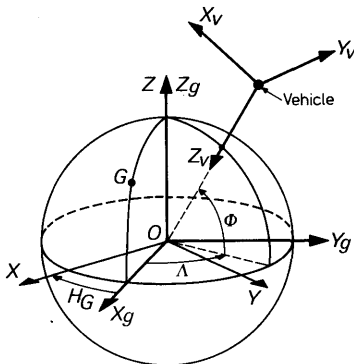


Fig. 4.2 The non-rotating geocentric equatorial frame, the rotating geocentric frame and the vehicle-centered horizontal frame

where the rotation matrix \mathbf{A}_g is given by

$$\mathbf{A}_g = \begin{bmatrix} \cos H_G & \sin H_G & 0 \\ -\sin H_G & \cos H_G & 0 \\ 0 & 0 & 1 \end{bmatrix}. \quad (4.1-7)$$

Rotating geocentric frame/Vehicle-centered horizontal frame (Fig. 4.2). The vehicle-centered horizontal frame is obtained from the rotating geocentric frame by two successive rotations and a translation. We first rotate the $X_g Y_g Z_g$ -frame about the Z_g -axis over an angle Λ . The thus obtained frame is then rotated about its Y -axis over an angle $-(\pi/2 + \Phi)$. Now a reference frame is obtained which has the same orientation as the vehicle-centered horizontal frame. Finally, a translation of this reference frame from the center of the Earth to the center of mass of the vehicle is required to obtain the vehicle-centered horizontal frame. According to Section 2.3.4, Λ is the geographic longitude and Φ the geocentric latitude of the vehicle. The relation between the unit vectors in both systems is

$$\mathbf{E}_v = \mathbf{A}_{vg} \mathbf{E}_g, \quad (4.1-8)$$

where

$$\mathbf{A}_{vg} = \begin{bmatrix} -\sin \Phi \cos \Lambda & -\sin \Phi \sin \Lambda & \cos \Phi \\ -\sin \Lambda & \cos \Lambda & 0 \\ -\cos \Phi \cos \Lambda & -\cos \Phi \sin \Lambda & -\sin \Phi \end{bmatrix}. \quad (4.1-9)$$

Vehicle-centered horizontal frame/Vehicle frame (Fig. 4.3). The relative orientation of these two reference frames is determined by three angles: the so-called *Euler angles*.

The original vehicle-centered horizontal reference frame is first rotated

about the Z_v -axis over an angle ψ , which results in the $X'_v Y'_v Z'_v$ -frame (Fig. 4.3a). Then, the $X'_v Y'_v Z'_v$ -frame is rotated about the Y'_v -axis over an angle θ , resulting in the $X''_v Y''_v Z''_v$ -frame (Fig. 4.3b). This last frame, finally, is rotated about the X''_v -axis over an angle φ , from which the vehicle reference frame xyz is obtained (Fig. 4.3c). As follows from Fig. 4.3, ψ is the angle between the vertical plane through the longitudinal axis of the rocket and the X_v -axis: the *yaw angle*; θ is the angle between the longitudinal axis and the local horizontal plane, the *pitch angle*; and φ is the angle between the z -axis and the vertical plane through the longitudinal axis, the *bank angle*. The unit vectors in both systems are related by the equation

$$\mathbf{E}_r = \mathbf{A}_{rv} \mathbf{E}_v, \quad (4.1-10)$$

where the rotation matrix \mathbf{A}_{rv} is

$$\mathbf{A}_{rv} = \begin{bmatrix} C\theta C\psi & C\theta S\psi & -S\theta \\ -C\varphi S\psi + S\varphi S\theta C\psi & C\varphi C\psi + S\varphi S\theta S\psi & S\varphi C\theta \\ S\varphi S\psi + C\varphi S\theta C\psi & -S\varphi C\psi + C\varphi S\theta S\psi & C\varphi C\theta \end{bmatrix}. \quad (4.1-11)$$

where $C\theta = \cos \theta$, $S\theta = \sin \theta$, etc. This method of fixing the relative orientation of two reference systems by Euler angles has one drawback: if one specific angle, in our case the pitch angle, equals $\pm 90^\circ$, the other two angles are undetermined. This is immediately evident by substitution of $\theta = \pm 90^\circ$ into Eq. (4.1-11). Then \mathbf{A}_{rv} is only a function of $(\varphi \mp \psi)$ and not anymore of φ and ψ separately. So, for vertical flight, yaw angle and bank angle are not uniquely determined.

Non-rotating geocentric equatorial frame/Vehicle frame. In order to fix the orientation of the xyz -frame relative to the XYZ -frame, the method of Euler angles could be used. However, the orientation of the rocket relative to the inertial frame is determined by the kinematical equations which will be derived in Section 4.3. If use were made of Euler angles, the kinematical equations would be differential equations in the Euler angles, and would have singular points if a specific angle becomes $\pm 90^\circ$, which causes difficulties for the numerical integration of the kinematical equations. To avoid these difficulties we will use a different method to fix the orientation of the xyz -frame relative to the inertial frame: the so-called *method of direction cosines*.

Let \mathbf{A}_r be the transformation matrix which transforms the unit vectors of the XYZ -frame into the unit vectors of the xyz -frame:

$$\mathbf{E}_r = \mathbf{A}_r \mathbf{E}. \quad (4.1-12)$$

Multiplying this equation by \mathbf{E}^T , i.e. the transpose of \mathbf{E} , and noting that $\mathbf{E} \cdot \mathbf{E}^T = \mathbf{U}$, where \mathbf{U} is the identity matrix, we obtain

$$\mathbf{A}_r = \mathbf{E}_r \cdot \mathbf{E}^T = \begin{bmatrix} e_x \cdot e_X & e_x \cdot e_Y & e_x \cdot e_Z \\ e_y \cdot e_X & e_y \cdot e_Y & e_y \cdot e_Z \\ e_z \cdot e_X & e_z \cdot e_Y & e_z \cdot e_Z \end{bmatrix}. \quad (4.1-13)$$

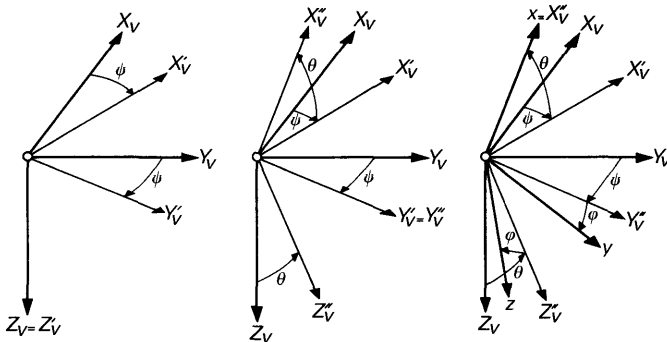


Fig. 4.3 The vehicle-centered horizontal reference frame, the vehicle reference frame and the yaw, pitch and bank angles

The elements of \mathbf{A}_r are the cosines of the angles between the axes of both systems. Defining

$$\begin{aligned} a_{11} &= \cos(x, X) = \mathbf{e}_x \cdot \mathbf{e}_X, \\ a_{12} &= \cos(x, Y) = \mathbf{e}_x \cdot \mathbf{e}_Y, \quad \text{etc.}, \end{aligned} \quad (4.1-14)$$

we can write

$$\mathbf{A}_r = [a_{ij}] \quad i, j = 1, 2, 3. \quad (4.1-15)$$

A disadvantage of this method of direction cosines is that there are nine variables instead of three as in the case that Euler angles are used. Consequently, there are six more kinematical differential equations. However, the nine elements of \mathbf{A}_r are not independent. Multiplying Eq. (4.1-12) with \mathbf{E}_r^T , we obtain

$$\mathbf{E}_r \cdot \mathbf{E}_r^T = \mathbf{A}_r \mathbf{E} \cdot \mathbf{E}_r^T. \quad (4.1-16)$$

As

$$\mathbf{E}_r \cdot \mathbf{E}_r^T = \mathbf{U},$$

and according to Eq. (4.1-13),

$$\mathbf{E} \cdot \mathbf{E}_r^T = (\mathbf{E}_r \cdot \mathbf{E}^T)^T = \mathbf{A}_r^T,$$

it follows from Eq. (4.1-16) that

$$\mathbf{A}_r \mathbf{A}_r^T = \mathbf{U}. \quad (4.1-17)$$

As $\mathbf{A}_r \mathbf{A}_r^T$ is a symmetric matrix, Eq. (4.1-17) leads to six non-linear equations in the elements a_{ij} . Thus, generally, only three of the nine direction cosines will be independent. Because of the non-linearity of Eq. (4.1-17) it is in general not possible to eliminate all six dependent direction cosines. The Eq. (4.1-17) can be used to check the accuracy of the numerical integration method that is used to integrate the nine differential equations for the direction cosines.

From Eq. (4.1-17) it follows that the transpose of the matrix \mathbf{A}_r is also its inverse. So the matrix is *orthogonal*. As all rotation matrices in rectangular Cartesian coordinate systems have direction cosines as elements, all rotation matrices derived in this section are orthogonal.

The transformation \mathbf{A}_r can, of course, also be obtained by successively applying the transformations \mathbf{A}_g , \mathbf{A}_{vg} and \mathbf{A}_{rv} ,

$$\mathbf{A}_r = \mathbf{A}_{rv} \mathbf{A}_{vg} \mathbf{A}_g. \quad (4.1-18)$$

It is important to note that in all cases where the transformation matrix is derived by applying successive rotations to the reference frame, the order of the rotations is not to be changed. This is a consequence of the fact that matrix multiplication is not commutative.

4.2 The dynamical equations

If \mathbf{V}_{cm} is the velocity of the center of mass of the rocket relative to the inertial frame, and $\boldsymbol{\Omega}$ is the angular velocity of the rocket relative to the inertial frame, then, according to Section 3.4.4, the equations of motion for a rocket can be written as

$$M \frac{d\mathbf{V}_{cm}}{dt} = \mathbf{F}_S + \mathbf{F}_c + \mathbf{F}_{rel}, \quad (4.2-1)$$

$$\int_M \mathbf{r} \times \left(\frac{d\boldsymbol{\Omega}}{dt} \times \mathbf{r} \right) dM + \int_M \mathbf{r} \times \{ \boldsymbol{\Omega} \times (\boldsymbol{\Omega} \times \mathbf{r}) \} dM = \mathbf{M}_{cm} + \mathbf{M}_c + \mathbf{M}_{rel}, \quad (4.2-2)$$

where \mathbf{r} is the position vector of a mass element dM relative to the center of mass of the rocket. The terms at the right-hand side of these equations are *external* and *apparent* forces, and moments, respectively. According to Section 3.4.4, the apparent forces and moments can be expressed as volume integrals over the total mass system:

$$\mathbf{F}_c = -2\boldsymbol{\Omega} \times \int_M \frac{\delta \mathbf{r}}{\delta t} dM, \quad (4.2-3a)$$

$$\mathbf{F}_{rel} = - \int_M \frac{\delta^2 \mathbf{r}}{\delta t^2} dM, \quad (4.2-3b)$$

$$\mathbf{M}_c = -2 \int_M \mathbf{r} \times \left(\boldsymbol{\Omega} \times \frac{\delta \mathbf{r}}{\delta t} \right) dM, \quad (4.2-3c)$$

$$\mathbf{M}_{rel} = - \int_M \mathbf{r} \times \frac{\delta^2 \mathbf{r}}{\delta t^2} dM. \quad (4.2-3d)$$

The factors $\delta \mathbf{r}/\delta t$ and $\delta^2 \mathbf{r}/\delta t^2$ in these relations represent relative velocity and acceleration of combustion products with respect to the center of mass of the rocket. If \mathbf{V} and \mathbf{a} are velocity and acceleration of the combustion

70 Rocket Propulsion & Spaceflight Dynamics

products relative to the rigid rocket structure, the following relations hold:

$$\frac{\delta \mathbf{r}}{\delta t} = \mathbf{V} - \mathbf{u}_{cm}, \quad (4.2-4a)$$

$$\frac{\delta^2 \mathbf{r}}{\delta t^2} = \mathbf{a} - \mathbf{a}_{cm}, \quad (4.2-4b)$$

where \mathbf{u}_{cm} and \mathbf{a}_{cm} are velocity and acceleration of the center of mass relative to the rocket structure. As we deal here with flowing gases i.e. combustion products, we note that the derivative $\delta/\delta t$ is the material derivative D/Dt used in fluid mechanics (Section 3.7.2). We will, however, continue using $\delta/\delta t$ to make it evident that it is a derivative in a rotating system. We can now use Eq. (A2-7) of Appendix 2 relating the derivative of the integrand to the derivative of the integral. This equation can be written as

$$\int_M \frac{\delta \mathbf{P}}{\delta t} dM = \frac{\delta}{\delta t} \int_M \mathbf{P} dM + \int_{A_e} \mathbf{P} (\rho \mathbf{V} \cdot \mathbf{n}) dA_e, \quad (4.2-5)$$

for any vector \mathbf{P} . Here ρ is the density of the fluid and \mathbf{n} is the outward unit normal on A_e . Instead of the integral over the total control surface S of our system. We can now use Eq. (A2-7) of Appendix 2 relating the derivative is only a mass transport through this part of the control surface.

4.2.1 The apparent forces

The Coriolis force. Using Eq. (4.2-5) this force can be written as

$$\mathbf{F}_c = -2\Omega \times \left[\frac{\delta}{\delta t} \int_M \mathbf{r} dM + \int_{A_e} \mathbf{r} (\rho \mathbf{V} \cdot \mathbf{n}) dA_e \right]. \quad (4.2-6)$$

From the definition of the center of mass

$$\int_M \mathbf{r} dM = 0. \quad (4.2-7)$$

Introducing the mass flow, m , defined as

$$m = -\frac{dM}{dt}, \quad (4.2-8)$$

it follows from the principle of conservation of mass that m is the total mass flow through the surface A_e ,

$$m = \int_{A_e} (\rho \mathbf{V} \cdot \mathbf{n}) dA_e. \quad (4.2-9)$$

We now define a *center of mass flow* by its position vector \mathbf{r}_e

$$\mathbf{r}_e = \frac{1}{m} \int_{A_e} \mathbf{r} (\rho \mathbf{V} \cdot \mathbf{n}) dA_e. \quad (4.2-10)$$

By using Eqs. (4.2-7) and (4.2-10), the expression for the Coriolis force simplifies to

$$\mathbf{F}_c = -2m\boldsymbol{\Omega} \times \mathbf{r}_e. \quad (4.2-11)$$

The relative force. Again using Eq. (4.2-5), the relative force can be written as

$$\mathbf{F}_{rel} = -\frac{\delta}{\delta t} \int_M \frac{\delta \mathbf{r}}{\delta t} dM - \int_{A_e} \frac{\delta \mathbf{r}}{\delta t} (\rho \mathbf{V} \cdot \mathbf{n}) dA_e. \quad (4.2-12)$$

The first integral on the right-hand side of this equation also appears in the expression for the Coriolis force. Comparing Eq. (4.2-3a) with Eq. (4.2-11) leads to

$$\int_M \frac{\delta \mathbf{r}}{\delta t} dM = m \mathbf{r}_e. \quad (4.2-13)$$

Substituting Eq. (4.2-4a) into the second integral of Eq. (4.2-12), and using the expression for the mass flow, Eq. (4.2-9), leads to

$$\int_{A_e} \frac{\delta \mathbf{r}}{\delta t} (\rho \mathbf{V} \cdot \mathbf{n}) dA_e = \int_{A_e} \mathbf{V} (\rho \mathbf{V} \cdot \mathbf{n}) dA_e - m \mathbf{u}_{cm}. \quad (4.2-14)$$

The integral on the right-hand side of this expression is the flux of linear momentum through the surface A_e . This flux can be written as the product of the mass flow, m , and a mean exhaust velocity, $\bar{\mathbf{V}}_e$, defined by

$$\bar{\mathbf{V}}_e = \frac{1}{m} \int_{A_e} \mathbf{V} (\rho \mathbf{V} \cdot \mathbf{n}) dA_e. \quad (4.2-15)$$

Substitution of Eqs. (4.2-13) to (4.2-15) into Eq. (4.2-12) leads to

$$\mathbf{F}_{rel} = -\frac{\delta}{\delta t} (m \mathbf{r}_e) - m (\bar{\mathbf{V}}_e - \mathbf{u}_{cm}). \quad (4.2-16)$$

In general, the relative velocity of the center of mass and of the center of mass flow will be very small compared to the mean exhaust velocity, which for most chemical rockets lies between 2000 m/s and 5000 m/s. In addition, the time rate of change of mass flow will be so small that also the term $\mathbf{r}_e dm/dt$ is negligible compared to $m\bar{\mathbf{V}}_e$. We then may write as a good approximation

$$\mathbf{F}_{rel} = -m \bar{\mathbf{V}}_e, \quad (4.2-17)$$

and we conclude that the relative force has the same magnitude, but is in the opposite direction to the flux of linear momentum through the exit surface A_e .

4.2.2 The apparent moments

The Coriolis moment. We may write

$$\frac{\delta}{\delta t} \{ \mathbf{r} \times (\boldsymbol{\Omega} \times \mathbf{r}) \} = 2\mathbf{r} \times \left(\boldsymbol{\Omega} \times \frac{\delta \mathbf{r}}{\delta t} \right) + \mathbf{r} \times \left(\frac{\delta \boldsymbol{\Omega}}{\delta t} \times \mathbf{r} \right) + \boldsymbol{\Omega} \times \left(\frac{\delta \mathbf{r}}{\delta t} \times \mathbf{r} \right). \quad (4.2-18)$$

Substituting this result into Eq. (4.2-3c), we obtain for the Coriolis moment

$$\mathbf{M}_c = - \int_M \left[\frac{\delta}{\delta t} \{ \mathbf{r} \times (\boldsymbol{\Omega} \times \mathbf{r}) \} - \mathbf{r} \times \left(\frac{\delta \boldsymbol{\Omega}}{\delta t} \times \mathbf{r} \right) - \boldsymbol{\Omega} \times \left(\frac{\delta \mathbf{r}}{\delta t} \times \mathbf{r} \right) \right] dM. \quad (4.2-19)$$

By the use of Eq. (4.2-5), which relates the integral of the time rate of change to the time rate of change of that integral, one finds:

$$\begin{aligned} \mathbf{M}_c = & - \frac{\delta}{\delta t} \int_M \mathbf{r} \times (\boldsymbol{\Omega} \times \mathbf{r}) dM + \int_M \mathbf{r} \times \left(\frac{\delta \boldsymbol{\Omega}}{\delta t} \times \mathbf{r} \right) dM \\ & - \int_{A_e} \{ \mathbf{r} \times (\boldsymbol{\Omega} \times \mathbf{r}) \} (\rho \mathbf{V} \cdot \mathbf{n}) dA_e - \boldsymbol{\Omega} \times \int_M \mathbf{r} \times \frac{\delta \mathbf{r}}{\delta t} dM. \end{aligned} \quad (4.2-20)$$

With Eq. (3.4-31), we find

$$\begin{aligned} \mathbf{M}_c = & - \frac{\delta}{\delta t} (\mathbf{I} \cdot \boldsymbol{\Omega}) + \mathbf{I} \cdot \frac{\delta \boldsymbol{\Omega}}{\delta t} - \int_{A_e} \{ \mathbf{r} \times (\boldsymbol{\Omega} \times \mathbf{r}) \} (\rho \mathbf{V} \cdot \mathbf{n}) dA_e \\ & - \boldsymbol{\Omega} \times \int_M \mathbf{r} \times \frac{\delta \mathbf{r}}{\delta t} dM. \end{aligned} \quad (4.2-21)$$

For a point on the surface A_e , we can write

$$\mathbf{r} = \mathbf{r}_e + \mathbf{v}. \quad (4.2-22)$$

Then, according to Eq. (4.2-10),

$$\int_{A_e} \mathbf{v} (\rho \mathbf{V} \cdot \mathbf{n}) dA_e = 0 \quad (4.2-23)$$

Substitution of the Eqs. (4.2-9), (4.2-22) and (4.2-23) into Eq. (4.2-21) leads to

$$\begin{aligned} \mathbf{M}_c = & - \frac{\delta \mathbf{I}}{\delta t} \cdot \boldsymbol{\Omega} - m \mathbf{r}_e \times (\boldsymbol{\Omega} \times \mathbf{r}_e) - \int_{A_e} \mathbf{v} \times (\boldsymbol{\Omega} \times \mathbf{v}) (\rho \mathbf{V} \cdot \mathbf{n}) dA_e \\ & - \boldsymbol{\Omega} \times \int_M \mathbf{r} \times \frac{\delta \mathbf{r}}{\delta t} dM. \end{aligned} \quad (4.2-24)$$

This is the complete expression for the Coriolis moment. However, as the dimensions of the nozzle exit are small as compared to the longitudinal dimensions of the rocket, i.e. $|\mathbf{v}| \ll |\mathbf{r}_e|$, the integral over A_e in Eq. (4.2-24) can be neglected. The volume integral in Eq. (4.2-24) represents the angular momentum of the rocket due to relative motion with respect to the center of mass. It is easily seen that only the moving gases contribute to this angular

momentum. As the total mass of combustion products within the rocket is very small, while by good approximation the mean gas flow in the rocket is parallel to the longitudinal axis, this angular momentum is negligible. We then, finally, find for the Coriolis moment

$$\mathbf{M}_c = -\frac{\delta \mathbf{I}}{\delta t} \cdot \boldsymbol{\Omega} - m \mathbf{r}_e \times (\boldsymbol{\Omega} \times \mathbf{r}_e). \quad (4.2-25)$$

Relative moment. Using Eq. (4.2-5), the relative moment can be written as

$$\mathbf{M}_{rel} = -\frac{\delta}{\delta t} \int_M \mathbf{r} \times \frac{\delta \mathbf{r}}{\delta t} dM - \int_{A_e} \mathbf{r} \times \frac{\delta \mathbf{r}}{\delta t} (\rho \mathbf{V} \cdot \mathbf{n}) dA_e. \quad (4.2-26)$$

Substitution of Eq. (4.2-4a) into Eq. (4.2-26) and using the definition of \mathbf{r}_e (Eq. (4.2-10)) leads to

$$\mathbf{M}_{rel} = -\frac{\delta}{\delta t} \int_M \mathbf{r} \times \frac{\delta \mathbf{r}}{\delta t} dM - \int_{A_e} \mathbf{r} \times \mathbf{V} (\rho \mathbf{V} \cdot \mathbf{n}) dA_e + m \mathbf{r}_e \times \mathbf{u}_{cm}. \quad (4.2-27)$$

On the surface A_e the velocity, \mathbf{V} , can be written as

$$\mathbf{V} = \bar{\mathbf{V}}_e + \boldsymbol{\eta}. \quad (4.2-28)$$

Then according to Eqs. (4.2-9) and (4.2-15),

$$\int_{A_e} \boldsymbol{\eta} (\rho \mathbf{V} \cdot \mathbf{n}) dA_e = 0. \quad (4.2-29)$$

By substitution of Eq. (4.2-22) and Eq. (4.2-28) into Eq. (4.2-27) and using Eqs. (4.2-9), (4.2-23) and (4.2-29), we obtain

$$\mathbf{M}_{rel} = -\frac{\delta}{\delta t} \int_M \mathbf{r} \times \frac{\delta \mathbf{r}}{\delta t} dM - \int_{A_e} (\boldsymbol{\nu} \times \boldsymbol{\eta}) (\rho \mathbf{V} \cdot \mathbf{n}) dA_e - m \mathbf{r}_e \times (\bar{\mathbf{V}}_e - \mathbf{u}_{cm}).$$

By the same reasoning as before, we neglect the term containing the volume integral in this expression. Furthermore $|\boldsymbol{\nu}| \ll |\mathbf{r}_e|$, while also $\boldsymbol{\eta}$ as well as the relative velocity, \mathbf{u}_{cm} , of the center of mass will be small relative to the mean exhaust velocity. Therefore, the relative moment can very well be approximated by

$$\mathbf{M}_{rel} = -m \mathbf{r}_e \times \bar{\mathbf{V}}_e. \quad (4.2-30)$$

Now, we have derived expressions for the apparent forces and moments in terms of the rocket parameters m , $\bar{\mathbf{V}}_e$, \mathbf{r}_e and \mathbf{I} and the angular velocity of the rocket $\boldsymbol{\Omega}$. Mass flow, mean exhaust velocity and center of mass flow are determined by the internal ballistics of the rocket motor (Chapter 5). The position of the center of mass and the components of the inertia tensor can be determined if the mass distribution is known at anytime. The angular velocity $\boldsymbol{\Omega}$, finally, is an independent variable in the equations of motion.

4.2.3 The inertial moment

The terms on the left-hand side of the equations of motion (Eqs. (4.2-1) and (4.2-2)) are *inertial terms*. The inertial force in Eq. (4.2-1) needs no further explanation; the inertial moment, however, requires some elaboration.

Using Eq. (3.3-4), we can write for the inertial moment

$$\mathbf{M}_{in} = \int_M \left[\frac{d}{dt} \{ \mathbf{r} \times (\boldsymbol{\Omega} \times \mathbf{r}) \} - \frac{\delta}{\delta t} \{ \mathbf{r} \times (\boldsymbol{\Omega} \times \mathbf{r}) \} + \mathbf{r} \times \left(\frac{\delta \boldsymbol{\Omega}}{\delta t} \times \mathbf{r} \right) \right] dM. \quad (4.2-31)$$

By use of Eq. (4.2-5), we get

$$\begin{aligned} \mathbf{M}_{in} = & \frac{d}{dt} \int_M \mathbf{r} \times (\boldsymbol{\Omega} \times \mathbf{r}) dM + \int_{A_e} \{ \mathbf{r} \times (\boldsymbol{\Omega} \times \mathbf{r}) \} (\rho \mathbf{V} \cdot \mathbf{n}) dA_e \\ & - \frac{\delta}{\delta t} \int_M \mathbf{r} \times (\boldsymbol{\Omega} \times \mathbf{r}) dM - \int_{A_e} \{ \mathbf{r} \times (\boldsymbol{\Omega} \times \mathbf{r}) \} (\rho \mathbf{V} \cdot \mathbf{n}) dA_e \\ & + \int_M \mathbf{r} \times \left(\frac{\delta \boldsymbol{\Omega}}{\delta t} \times \mathbf{r} \right) dM. \end{aligned} \quad (4.2-32)$$

In the same way as for Eq. (3.4-31), one finally finds

$$\mathbf{M}_{in} = \frac{d}{dt} (\mathbf{I} \cdot \boldsymbol{\Omega}) - \frac{\delta}{\delta t} (\mathbf{I} \cdot \boldsymbol{\Omega}) + \mathbf{I} \cdot \frac{\delta \boldsymbol{\Omega}}{\delta t}, \quad (4.2-33)$$

or

$$\mathbf{M}_{in} = \frac{d}{dt} (\mathbf{I} \cdot \boldsymbol{\Omega}) - \frac{\delta \mathbf{I}}{\delta t} \cdot \boldsymbol{\Omega}. \quad (4.2-34)$$

4.2.4 The external forces

The most important external forces acting on a rocket in free flight can be divided into *gravitational forces*, *pressure forces* and *frictional forces*. If the rocket is not in free flight, i.e. during launch or during staging, there are also other external forces. In general, these phases of the flight are relatively short. They will not be discussed here.

Gravitational forces. These forces are due to the presence of celestial bodies which yield a gravitational field of strength \mathbf{g} at the location of the rocket. The gravitational force acting on the rocket is

$$\mathbf{W} = M\mathbf{g}. \quad (4.2-35)$$

As rockets are used in the close vicinity of the Earth, the contribution of other celestial bodies to the total field strength \mathbf{g} can be neglected. In most cases, it will also be possible to consider the gravitational field of the Earth as a central field following the inverse-square law (Section 18.6). Then, the field strength is only a function of the position vector \mathbf{R}_{cm} of the center of

mass of the vehicle relative to the center of the Earth

$$\mathbf{g} = -\frac{\mu}{R_{cm}^3} \mathbf{R}_{cm}, \quad (4.2-36)$$

where μ is the gravitation parameter of the Earth.

Pressure forces. If dS is an element of the control surface S , and p is the external pressure at dS , then the external pressure force on dS is

$$d\mathbf{F}_p = -p\mathbf{n} dS,$$

where \mathbf{n} is the outward unit normal on dS . The total external pressure force on the rocket then is

$$\mathbf{F}_p = - \int_S p\mathbf{n} dS. \quad (4.2-37)$$

For every closed surface S , we have

$$\int_S \mathbf{n} dS = 0,$$

and the pressure force can be written too as

$$\mathbf{F}_p = - \int_S (p - p_a)\mathbf{n} dS, \quad (4.2-38)$$

where p_a is any constant pressure. It will be convenient to take for p_a the undisturbed atmospheric pressure at the position of the rocket. The surface S consists of the surface S_R and the exit surface A_e . So, the integral in Eq. (4.2-38) can be split into two integrals

$$\mathbf{F}_p = - \int_{S_R} (p - p_a)\mathbf{n} dS - \int_{A_e} (p - p_a)\mathbf{n} dA_e. \quad (4.2-39)$$

If the rocket is not moving with respect to the surrounding atmosphere, the pressure everywhere on S_R will equal p_a and the first integral of Eq. (4.2-39) will vanish. So the first term of the pressure force is exclusively due to the motion of the rocket relative to the surrounding atmosphere. It is called the *aerodynamic pressure force*. If the rocket is thrusting, the pressure p on A_e will generally differ from the atmospheric pressure. Thus, the second term of the pressure force is due to motor operation and is called the *pressure thrust*.

Frictional forces. The resultant friction force \mathbf{F}_f is also only due to motion of the rocket relative to the surrounding air and the frictional force is an aerodynamic force too.

The *total aerodynamic force*, \mathbf{F}_a is the sum of the aerodynamic pressure force and the frictional force,

$$\mathbf{F}_a = - \int_{S_R} (p - p_a)\mathbf{n} dS + \mathbf{F}_f. \quad (4.2-40)$$

76 Rocket Propulsion & Spaceflight Dynamics

A more extensive discussion on aerodynamic forces and moments is given in Chapter 14.

The total external force, finally, is the sum of the aerodynamic force, the gravitational force and the pressure thrust:

$$\mathbf{F}_s = \mathbf{F}_a + \mathbf{W} - \int_{A_e} (p - p_a) \mathbf{n} dA_e. \quad (4.2-41)$$

4.2.5 The external moments

Just like the total external force, the total external moment is due to gravitation, pressure and friction.

Gravitational moment. Because of the dependence of the gravitational field strength on position, the center of gravity does, in general, not coincide with the center of mass of the rocket. Therefore, gravitational forces will cause a moment about the center of mass of the rocket. However, the dimensions of rockets are very small compared to the distance from the attraction center and consequently the distance between the center of mass and the center of gravity will be negligible. Consequently, the moment due to gravitational forces is small compared to the other moments and can be neglected.

Pressure moment. The moment of the pressure force on the surface element dS is

$$d\mathbf{M}_p = \mathbf{r} \times d\mathbf{F}_p,$$

and the total moment due to pressure forces is

$$\mathbf{M}_p = - \int_S pr \times \mathbf{n} dS. \quad (4.2-42)$$

For any closed surface S , we have

$$\int_S \mathbf{r} \times \mathbf{n} dS = 0,$$

and the total moment due to pressure can be written as

$$\mathbf{M}_p = - \int_S (p - p_a) \mathbf{r} \times \mathbf{n} dS, \quad (4.2-43)$$

or, again splitting the integral into two parts,

$$\mathbf{M}_p = - \int_{S_R} (p - p_a) \mathbf{r} \times \mathbf{n} dS - \int_{A_e} (p - p_a) \mathbf{r} \times \mathbf{n} dA_e. \quad (4.2-44)$$

The first term is due to the motion of the rocket relative to the surrounding air and we call it the *aerodynamic pressure moment*. The second integral is

due to the pressure thrust.

The *total aerodynamic moment* is

$$\mathbf{M}_a = \mathbf{M}_f - \int_{S_R} (p - p_a) \mathbf{r} \times \mathbf{n} \, dS, \quad (4.2-45)$$

where \mathbf{M}_f is the *frictional moment*.

The total external moment, finally, is given by

$$\mathbf{M}_{cm} = \mathbf{M}_a - \int_{A_e} (p - p_a) \mathbf{r} \times \mathbf{n} \, dA_e \quad (4.2-46)$$

4.2.6 The equations of motion

We have derived expressions for the apparent and external forces and moments, as well as for the inertial moment. Substituting these expressions into Eqs. (4.2-1) and (4.2-2) leads to

$$M \frac{d\mathbf{V}_{cm}}{dt} = -2m\boldsymbol{\Omega} \times \mathbf{r}_e - m\bar{\mathbf{V}}_e - \int_{A_e} (p - p_a) \mathbf{n} \, dA_e + \mathbf{W} + \mathbf{F}_a, \quad (4.2-47)$$

$$\frac{d}{dt} (\mathbf{I} \cdot \boldsymbol{\Omega}) = -m\mathbf{r}_e \times (\boldsymbol{\Omega} \times \mathbf{r}_e) - m\mathbf{r}_e \times \bar{\mathbf{V}}_e - \int_{A_e} (p - p_a) \mathbf{r} \times \mathbf{n} \, dA_e + \mathbf{M}_a \quad (4.2-48)$$

We now define

$$\mathbf{F} = -m\bar{\mathbf{V}}_e - \int_{A_e} (p - p_a) \mathbf{n} \, dA_e. \quad (4.2-49)$$

The force \mathbf{F} is exclusively due to the motor operation of the rocket. During a static test, where the aerodynamic force and Coriolis force are absent, it is, apart from the weight \mathbf{W} and the reaction forces of the test stand, the only 'force acting on the rocket'. It is therefore called the *thrust*. The first term, due to transport of linear momentum through A_e , is called the *impulse thrust*. The second term represents the already defined *pressure thrust*.

If the thrust is not acting along a line through the center of mass, a moment will result

$$\mathbf{M}_F = -m\mathbf{r}_e \times \bar{\mathbf{V}}_e - \int_{A_e} (p - p_a) \mathbf{r} \times \mathbf{n} \, dA_e. \quad (4.2-50)$$

If this moment is generated deliberately, e.g. for changing the orientation of the rocket, we speak of *thrust vector control* (Section 5.2.4.). For rockets that do not use thrust vector control, it is endeavoured to let the thrust act along a line through the center of mass. Owing to construction inaccuracies, however, this cannot be realized exactly. In that case, we speak of *thrust misalignment* and the resulting moment is the *thrust misalignment moment*. As the impulse thrust is much larger than the pressure thrust, the moment

78 Rocket Propulsion & Spaceflight Dynamics

due to the thrust can be approximated very well by

$$\mathbf{M}_F = \mathbf{r}_e \times \mathbf{F}. \quad (4.2-51)$$

As the velocity of the center of mass flow due to the rotation of the rocket is very small as compared to the mean exhaust velocity, i.e. $|\boldsymbol{\Omega} \times \mathbf{r}_e| \ll \bar{V}_e$, the Coriolis force can be neglected with respect to the thrust. The Coriolis moment, however, will in general be of the same order of magnitude as the aerodynamic moment and the thrust misalignment moment. Therefore, the Coriolis moment cannot be neglected. Note that the Coriolis moment consists of two terms. The term $-mr_e \times (\boldsymbol{\Omega} \times \mathbf{r}_e)$ is due to the exhaust jet and, as we will see in Chapter 14, is a damping moment. It is therefore often called the *jet damping moment*. Most authors only take this jet damping moment into account neglecting the term $-\boldsymbol{\Omega} \cdot \delta \mathbf{I} / \delta t$ of the Coriolis moment. This is certainly not permissible since the term can decrease the damping by some 30%.

Finally, we can write the equations of motion as

$$M \frac{d\mathbf{V}_{cm}}{dt} = \mathbf{F} + \mathbf{W} + \mathbf{F}_a, \quad (4.2-52)$$

$$\frac{d}{dt} (\mathbf{I} \cdot \boldsymbol{\Omega}) = -mr_e \times (\boldsymbol{\Omega} \times \mathbf{r}_e) + \mathbf{r}_e \times \mathbf{F} + \mathbf{M}_a, \quad (4.2-53)$$

where, according to Eq. (4.2-49) and Eq. (4.2-15), the thrust \mathbf{F} is given by

$$\mathbf{F} = - \int_{A_e} \{ \mathbf{V}(\rho \mathbf{V} \cdot \mathbf{n}) + (p - p_a) \mathbf{n} \} dA_e. \quad (4.2-54)$$

In Chapter 5 the thrust will be determined explicitly in terms of rocket motor parameters.

Now, we will dissolve the two vector equations of motion into six scalar equations. As the thrust, the aerodynamic forces and moments, the inertia tensor and the vector \mathbf{r}_e are most easily expressed in the vehicle reference frame, the vector equations are usually resolved along the axes of this frame. As this frame is rotating with angular velocity $\boldsymbol{\Omega}$ relative to the inertial frame, we have

$$\frac{d\mathbf{V}_{cm}}{dt} = \frac{\delta \mathbf{V}_{cm}}{\delta t} + \boldsymbol{\Omega} \times \mathbf{V}_{cm}, \quad (4.2-55)$$

and

$$\frac{d}{dt} (\mathbf{I} \cdot \boldsymbol{\Omega}) = \frac{\delta \mathbf{I}}{\delta t} \cdot \boldsymbol{\Omega} + \mathbf{I} \cdot \frac{d\boldsymbol{\Omega}}{dt} + \boldsymbol{\Omega} \times (\mathbf{I} \cdot \boldsymbol{\Omega}). \quad (4.2-56)$$

We resolve the vectors occurring in Eqs. (4.2-52) and (4.2-53) in the following way:

$$\mathbf{V}_{cm} = [u, v, w]\mathbf{E}_r \quad (4.2-57a)$$

$$\boldsymbol{\Omega} = [p, q, r]\mathbf{E}_r \quad (4.2-57b)$$

$$\mathbf{F} = [F_x, F_y, F_z]\mathbf{E}_r \quad (4.2-57c)$$

$$\mathbf{F}_a = [X_a, Y_a, Z_a]\mathbf{E}_r \quad (4.2-57d)$$

$$\mathbf{M}_a = [L', M', N']\mathbf{E}_r \quad (4.2-57e)$$

$$\mathbf{r}_e = [x_e, y_e, z_e]\mathbf{E}_r \quad (4.2-57f)$$

$$\mathbf{g} = [g_x, g_y, g_z]\mathbf{E}_r \quad (4.2-57g)$$

We have to note that F_y and F_z are small compared to F_x , and that y_e and z_e are small compared to x_e , because these terms are a consequence of asymmetry, which will be restricted to a minimum. We will therefore neglect terms of second-order in these quantities.

Substitution of Eqs. (4.2-55) to (4.2-57) into Eqs. (4.2-52) and (4.2-53) leads to

$$M \frac{du}{dt} = M(vr - wq) + F_x + Mg_x + X_a, \quad (4.2-58a)$$

$$M \frac{dv}{dt} = M(wp - ur) + F_y + Mg_y + Y_a, \quad (4.2-58b)$$

$$M \frac{dw}{dt} = M(uq - vp) + F_z + Mg_z + Z_a, \quad (4.2-58c)$$

$$I_{xx} \frac{dp}{dt} = -p \frac{dI_{xx}}{dt} + rq(I_{yy} - I_{zz}) + mx_e(y_e q + z_e r) + L', \quad (4.2-58d)$$

$$I_{yy} \frac{dq}{dt} = -q \frac{dI_{yy}}{dt} + pr(I_{zz} - I_{xx}) - mqx_e^2 - x_e F_z + z_e F_x + M', \quad (4.2-58e)$$

$$I_{zz} \frac{dr}{dt} = -r \frac{dI_{zz}}{dt} + pq(I_{xx} - I_{yy}) - mrx_e^2 + x_e F_y - y_e F_x + N'. \quad (4.2-58f)$$

These are the *dynamical equations of motion*.

4.3 The kinematical equations

In the dynamical equations, the thrust, the gravitational field strength and the aerodynamic forces and moments are dependent on the position and orientation of the rocket. We will therefore need equations which relate position and orientation of the rocket to the translational and rotational velocity. These are the *kinematical equations*.

80 Rocket Propulsion & Spaceflight Dynamics

According to Eq. (4.1-12), the orientation of the rocket is determined completely by the rotation matrix \mathbf{A}_r . Differentiating Eq. (4.1-12) gives

$$\frac{d\mathbf{E}_r}{dt} = \frac{d\mathbf{A}_r}{dt} \mathbf{E} + \mathbf{A}_r \frac{d\mathbf{E}}{dt}. \quad (4.3-1)$$

As the matrix \mathbf{E} has the unit vectors along the axes of the inertial system as elements

$$\frac{d\mathbf{E}}{dt} = 0.$$

The vehicle reference system is rotating with velocity $\boldsymbol{\Omega}$ relative to the inertial system, so

$$\frac{d\mathbf{E}_r}{dt} = \frac{d\mathbf{E}_r}{dt} + \boldsymbol{\Omega} \times \mathbf{E}_r.$$

The elements of \mathbf{E}_r , which are the unit vectors in the vehicle reference frame, are constants in the vehicle reference frame. This implies that

$$\frac{d\mathbf{E}_r}{dt} = 0.$$

Using these relations, Eq. (4.3-1) simplifies to

$$\boldsymbol{\Omega} \times \mathbf{E}_r = \frac{d\mathbf{A}_r}{dt} \mathbf{E},$$

which, after scalar multiplication with \mathbf{E}^T , yields

$$\frac{d\mathbf{A}_r}{dt} = (\boldsymbol{\Omega} \times \mathbf{E}_r) \cdot \mathbf{E}^T. \quad (4.3-2)$$

According to Eq. (4.1-12),

$$\mathbf{E}^T = \mathbf{E}_r^T \mathbf{A}_r. \quad (4.3-3)$$

Substitution of Eq. (4.3-3) into Eq. (4.3-2) leads to

$$\frac{d\mathbf{A}_r}{dt} = (\boldsymbol{\Omega} \times \mathbf{E}_r) \cdot \mathbf{E}_r^T \mathbf{A}_r. \quad (4.3-4)$$

By using Eq. (4.2-57b), we obtain

$$\boldsymbol{\Omega} \times \mathbf{E}_r = (pe_x + qe_y + re_z) \times \begin{bmatrix} e_x \\ e_y \\ e_z \end{bmatrix} = \begin{bmatrix} re_y - qe_z \\ pe_z - re_x \\ qe_x - pe_y \end{bmatrix},$$

and

$$(\boldsymbol{\Omega} \times \mathbf{E}_r) \cdot \mathbf{E}_r^T = \begin{bmatrix} re_y - qe_z \\ pe_z - re_x \\ qe_x - pe_y \end{bmatrix} \cdot [e_x \ e_y \ e_z] = \begin{bmatrix} 0 & r & -q \\ -r & 0 & p \\ q & -p & 0 \end{bmatrix}. \quad (4.3-5)$$

Substitution of Eq. (4.3-5) into Eq. (4.3-4) finally yields

$$\frac{d\mathbf{A}_r}{dt} = \begin{bmatrix} 0 & r & -q \\ -r & 0 & p \\ q & -p & 0 \end{bmatrix} \mathbf{A}_r. \quad (4.3-6)$$

Writing out this matrix equation gives nine first-order differential equations in the elements of \mathbf{A}_r , which are the direction cosines between the vehicle reference system and the inertial reference system.

Finally, we will have to derive the differential equations for the position of the rocket. If X , Y and Z are the coordinates of the center of mass of the rocket in the inertial system, we can write

$$\mathbf{R}_{cm} = [X, Y, Z]\mathbf{E} \quad (4.3-7)$$

By differentiating Eq. (4.3-7) and using Eq. (4.2-57a), we obtain

$$\frac{d\mathbf{R}_{cm}}{dt} = \mathbf{V}_{cm} = \frac{d}{dt} [X, Y, Z]\mathbf{E} = [u, v, w]\mathbf{E}_r. \quad (4.3-8)$$

Substitution of Eq. (4.1-12) into Eq. (4.3-8) leads to

$$\frac{d}{dt} [X, Y, Z] = [u, v, w]\mathbf{A}_r. \quad (4.3-9)$$

These differential equations relate the position of the rocket to its velocity components u , v and w and the direction cosines a_{ij} .

So far, we have derived a set of 18 differential equations: the dynamical equations, Eqs. (4.2-58), and the kinematical equations, Eqs. (4.3-6) and Eq. (4.3-9). Together with appropriate initial conditions, these equations can be integrated simultaneously yielding the velocity components u , v and w , the angular velocity components p , q and r , the direction cosines a_{ij} and the coordinates X , Y and Z . The accuracy of the integration method used may be checked with the help of Eq. (4.1-17).

4.3.1 The position of the rocket

When the coordinates of the center of mass of the rocket in the inertial frame are known, the position of the rocket relative to the rotating geocentric frame can be determined. If X_g , Y_g and Z_g are the coordinates of the center of mass in the rotating geocentric frame, we can write

$$[X_g, Y_g, Z_g]\mathbf{E}_g = [X, Y, Z]\mathbf{E}. \quad (4.3-10)$$

By using Eq. (4.1-6), it follows that

$$[X_g, Y_g, Z_g] = [X, Y, Z]\mathbf{A}_g^T. \quad (4.3-11)$$

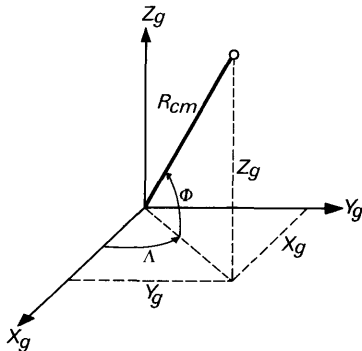


Fig. 4.4 The cartesian and polar coordinates in the rotating geocentric frame

Usually, the position relative to the rotating geocentric frame is given in the polar coordinates R_{cm} , Φ and Λ , where R_{cm} is the distance between the rocket and the center of the Earth, and Φ and Λ are geocentric latitude and geographic longitude, respectively. These coordinates follow from the relations (Fig. 4.4)

$$R_{cm} = \sqrt{X_g^2 + Y_g^2 + Z_g^2}, \quad (4.3-12)$$

$$\sin \Phi = \frac{Z_g}{R_{cm}}, \quad -90^\circ \leq \Phi \leq 90^\circ \quad (4.3-13)$$

$$\sin \Lambda = \frac{Y_g}{\sqrt{X_g^2 + Y_g^2}}, \quad -180^\circ < \Lambda \leq 180^\circ \quad (4.3-14)$$

$$\cos \Lambda = \frac{X_g}{\sqrt{X_g^2 + Y_g^2}}.$$

Conversely, if the initial position of the rocket is given in the polar coordinates R_{cm} , Φ and Λ , the initial values of X , Y and Z follow from

$$[X, Y, Z] = R_{cm} [\cos \Phi \cos \Lambda, \cos \Phi \sin \Lambda, \sin \Phi] \mathbf{A}_g. \quad (4.3-15)$$

4.3.2 The orientation of the rocket

Solution of the equations of motion also yields the orientation of the rocket relative to the inertial system. If geographic longitude and geocentric latitude of the rocket are known the orientation of the rocket relative to the vehicle-centered horizontal frame, expressed in pitch angle θ , yaw angle ψ and bank angle φ , can be determined.

From Eq. (4.1-18) follows

$$\mathbf{A}_{rv} = \mathbf{A}_r \mathbf{A}_g^T \mathbf{A}_{vg}^T. \quad (4.3-16)$$

Solution of the equations of motion yields \mathbf{A}_r , and the coordinates X , Y and Z , from which, with Eqs. (4.3-10), (4.3-13), (4.3-14) and (4.1-9), the matrix \mathbf{A}_{vg} can be determined. According to Eqs. (4.1-5) and (4.1-7), the matrix \mathbf{A}_g is only a function of the time t . The right-hand side of Eq. (4.3-16) then is completely known.

Let c_{ij} be the elements of the matrix \mathbf{A}_{rv} . Then, from Eq. (4.1-11) we find for the pitch angle

$$\sin \theta = -c_{13}, \quad -90^\circ \leq \theta \leq 90^\circ \quad (4.3-17)$$

and, if $|c_{13}| \neq 1$, for the yaw and bank angle

$$\sin \psi = \frac{c_{12}}{\cos \theta}, \quad \cos \psi = \frac{c_{11}}{\cos \theta}, \quad (4.3-18)$$

$$\sin \varphi = \frac{c_{23}}{\cos \theta}, \quad \cos \varphi = \frac{c_{33}}{\cos \theta}. \quad (4.3-19)$$

If $|c_{13}| = 1$, which is the case in vertical flight, the yaw and bank angle are undetermined, which we mentioned already in Section 4.1.

Conversely, the initial value of the matrix \mathbf{A}_r can be determined from the initial values of pitch, yaw and bank angle and geographic longitude and geocentric latitude with Eq. (4.1-17).

4.3.3 The velocity components in the vehicle-centered horizontal reference frame

Sometimes, it may be convenient to describe the translational velocity of the rocket by its magnitude V_{cm} , the *flight path angle*, γ , and the *flight path azimuth*, ψ (Section 2.3.7). The velocity \mathbf{V}_{cm} can then be written as

$$\mathbf{V}_{cm} = V_{cm} [\cos \gamma \cos \psi, \cos \gamma \sin \psi, -\sin \gamma] \mathbf{E}_v. \quad (4.3-20)$$

According to Eqs. (4.2-57a) and (4.1-10), we may also write

$$\mathbf{V}_{cm} = [u, v, w] \mathbf{A}_{rv} \mathbf{E}_v. \quad (4.3-21)$$

Thus the magnitude of the velocity, flight path angle and flight path azimuth can be determined from

$$\mathbf{V}_{cm} [\cos \gamma \cos \psi, \cos \gamma \sin \psi, -\sin \gamma] = [u, v, w] \mathbf{A}_{rv} \quad (4.3-22)$$

where the matrix \mathbf{A}_{rv} is determined by Eq. (4.3-16). Equation (4.3-22) may also be used to compute the initial values of u , v and w if the initial values of V_{cm} , γ and ψ are known.

The angular velocity of the rocket, finally, may be expressed in terms of *pitch rate*, *yaw rate* and *bank rate*, being the time rates of change of the corresponding angles. These rates can be determined by differentiating Eq. (4.3-16), resulting in

$$\frac{d\mathbf{A}_{rv}}{dt} = \frac{d\mathbf{A}_r}{dt} \mathbf{A}_g^T \mathbf{A}_{vg}^T + \mathbf{A}_r \frac{d\mathbf{A}_g^T}{dt} \mathbf{A}_{vg}^T + \mathbf{A}_r \mathbf{A}_g^T \frac{d\mathbf{A}_{vg}^T}{dt}. \quad (4.3-23)$$

84 Rocket Propulsion & Spaceflight Dynamics

From this equation, expressions for $d\theta/dt$, $d\psi/dt$ and $d\varphi/dt$ may be derived. These expressions, however, will be quite complex. This is a consequence of the fact that the rates mentioned are not components of the angular velocity $\boldsymbol{\Omega}$. We have to note that $\boldsymbol{\Omega}$ is the angular velocity relative to the inertial system, while pitch, yaw and bank rate are measured relative to the vehicle-centered horizontal reference frame, which is rotating itself. The last two terms on the right-hand side of Eq. (4.3-23) are due to this rotation. The first of these is due to the rotation of the rotating geocentric frame relative to the inertial frame, while the last one is a result of the rotation of the vehicle-centered horizontal reference frame relative to the rotating geocentric reference frame. The sum of these last two terms therefore is of the order $V_{cm} \cos \gamma / R_{cm}$. If $|\boldsymbol{\Omega}| \gg V_{cm} \cos \gamma / R_{cm}$, the last two terms of Eq. (4.3-23) may be neglected. This is the case for flight in the atmosphere where the angular velocity is mainly due to small oscillations of the rocket about the center of mass, or to a certain steering program. In that case Eq. (4.3-23) can be written as

$$\frac{d\mathbf{A}_{rv}}{dt} = \begin{bmatrix} 0 & r & -q \\ -r & 0 & p \\ q & -p & 0 \end{bmatrix} \mathbf{A}_{rv}, \quad (4.3-24)$$

where use has been made of Eqs. (4.3-6) and (4.3-16). Solving these equations for the rates of pitch, yaw and bank angle yields

$$\frac{d\theta}{dt} = q \cos \varphi - r \sin \varphi, \quad (4.3-25)$$

$$\frac{d\psi}{dt} = q \frac{\sin \varphi}{\cos \theta} + r \frac{\cos \varphi}{\cos \theta}, \quad (4.3-26)$$

$$\frac{d\varphi}{dt} = p + q \sin \varphi \tan \theta + r \cos \varphi \tan \theta. \quad (4.3-27)$$

We have derived the complete equations of motion for a rocket vehicle in free flight. In general, these equations cannot be solved analytically. Only in some very special cases (vacuum, homogeneous gravitational field) an analytical solution can be obtained. These cases will be treated in Chapter 11.

5 The Chemical Rocket Motor

The rocket motor is used to propel vehicles under conditions where other types of propulsion systems cannot operate, are inadequate or inefficient. All rocket motors are based on the same principle: mass is accelerated and expelled. The forces necessary to accomplish this, create, according to Newton's third law, reaction forces which thrust the rocket vehicle. While this is also true for the jet engine, the main difference between the rocket motor and the jet engine is that the first takes along its *propellants*, while the second only takes along *fuel*, but consumes oxygen from the surrounding atmosphere. Note that *fuel* and *oxidizer* together are called *propellants*.

In the *combustion chamber* of the chemical rocket a reaction takes place between fuel and oxidizer (*combustion*). The main combustion products are gases which are heated by the *chemical energy* released. As these hot gases are contained in a relatively small volume (*the combustion chamber*), the thermal expansion of the gases results in a high pressure. These pressurized gases are expanded and accelerated by a *nozzle*, resulting in a reaction force on the rocket vehicle. In a *nuclear* rocket motor, a gas may be heated by a nuclear reactor instead of by a combustion process. For this type of motor the same theory applies as for the chemical motor as far as the flow through the nozzle is concerned. This type of rocket motor is still experimental.

For the chemical rocket motor, the gas temperature in the combustion chamber lies somewhere between 2000 and 3500 K. As this temperature is higher than the melting point of most metals, care must be taken to prevent failure. Measures may be: cooling, insulation, heat sinks or the use of special materials, such as graphite or ceramics for certain parts. The operation time of the chemical rocket motor is very short as compared to other propulsive systems: a few milliseconds up to a few hundred seconds.

In principle, every combination of chemicals which gives gases of high temperature as reaction products is suitable for rocket propulsion. However, if the combustion products are very aggressive, such as e.g. hydrogen-fluoride, they may pose serious problems.

Also the propellants themselves may cause such serious problems, so that their use is not practicable (O_3).

Depending on the state of aggregation of the stored propellants, one distinguishes: *liquid propellants*, *solid propellants* and *hybrid propellants*, and one speaks of liquid-, solid-, or hybrid-propellant rockets.

In the liquid-propellant rocket, the propellants are stored in separate fuel and oxidizer tanks. In some cases *monopropellants* such as hydrogen

86 Rocket Propulsion & Spaceflight Dynamics

peroxide or hydrazine are used. Such propellants can break up in high-temperature gases. Turbine-driven pumps feed the propellants into the combustion chamber. Some of the energy of the gases in the combustion chamber may be used to drive the turbines, but also systems employing a separate *gas-generator* to drive the turbines are used. In the modern, high-pressure rocket motors (pressures up to 40 MPa) a pre-combustion may take place. Here all fuel is injected into a pre-combustion chamber to react with part of the oxidizer. The high-pressure pre-combustion products drive the turbines and then enter the main combustion chamber, where the main combustion takes place with the remaining oxidizer. For simple liquid-propellant rockets, pumps and turbines may be avoided by *pressurizing* the propellant tanks.

In the solid-propellant rocket, all propellant is stored in the combustion chamber itself. The propellant burns at its surface. Much attention is to be paid to the shape of the *propellant grain*, as this shape determines the *thrust history* of the solid-propellant rocket. The solid propellant may either be a propellant which combines fuel and oxidizer in one molecule (*double-base*), or a mixture of fuel and oxidizer (*composite*).

In the hybrid rocket engine, one of the propellants (fuel in general), is a solid, while the other is a liquid (oxidizer). In general, the oxidizer is stored in a pressure vessel and pressure fed into the combustion chamber. At the fuel surface a reaction with the oxidizer takes place, producing high-temperature and -pressure combustion products.

5.1 The ideal rocket motor

To apply the simple theory of fluid mechanics, as given in Section 3.7, to the rocket motor, we will make the following assumptions:

1. The combustion and flow are steady; i.e. there are no variations in time.
2. Details of the combustion process are ignored. For our purpose we will assume here that the combustion fully takes place in a (small) region of the chamber, the *combustion zone*.
3. At the entrance of the nozzle we assume uniform chamber conditions; i.e. pressure, density and temperature are constant.
4. The velocity at the *nozzle entrance* is negligible. In a certain way this defines the nozzle entrance.
5. Except for shocks, the flow is isentropic; i.e. friction and heat transfer are not taken into account.
6. The combustion products are ideal gases with constant specific heats.
7. On surfaces normal to the streamlines the flow variables are assumed constant. These surfaces will be called *surfaces of constant properties*.

The most important parameter for rocket performances is the thrust, \mathbf{F} , which, according to Eq. (4.2-54), equals

$$\mathbf{F} = - \int_{A_e} \{(\rho \mathbf{V} \cdot \mathbf{n}) \mathbf{V} + (p - p_a) \mathbf{n}\} dA_e. \quad (5.1-1)$$

The density, ρ , the velocity, \mathbf{V} , and the pressure, p , have to be known on the exit surface, A_e , to evaluate the integral in Eq. (5.1-1). The ambient pressure is indicated by p_a . The outward unit normal on A_e is \mathbf{n} . According to Eq. (4.2-9), the mass flow through the exit surface is

$$m = \int_{A_e} \rho \mathbf{V} \cdot \mathbf{n} dA_e. \quad (5.1-2)$$

Until now, the exit surface, A_e , has not been specified. We will assume A_e to be a surface of constant properties. Then density and velocity are constant on A_e , and the flow velocity is normal to A_e , and Eq. (5.1-2) becomes

$$m = \rho_e V_e A_e, \quad (5.1-3)$$

and the thrust, \mathbf{F} , can be written as

$$\mathbf{F} = - \left[m \frac{V_e}{A_e} + (p_e - p_a) \right] \int_{A_e} \mathbf{n} dA_e. \quad (5.1-4)$$

The integral at the right-hand side of Eq. (5.1-4) can be calculated if the shape of the exit surface is known.

In the following sections, we will discuss the various terms contributing to the thrust, such as exit or exhaust velocity, V_e , mass flow through the nozzle, m , and exit pressure, p_e .

5.1.1 The exhaust velocity

As the flow is assumed steady and isentropic, we may apply the energy equation, Eq. (3.7-19), to the flow of the gases after combustion has taken place:

$$\mathbf{V} \cdot \nabla(h + \frac{1}{2} \mathbf{V} \cdot \mathbf{V}) = 0. \quad (5.1-5)$$

Integration along a streamline leads to

$$h + \frac{1}{2} \mathbf{V} \cdot \mathbf{V} = \text{constant}. \quad (5.1-6)$$

As we assumed uniform chamber conditions, and since all streamlines originate in the chamber, this means that Eq. (5.1-6) holds for the whole flow field. Using the fact that

$$h = c_p T, \quad (5.1-7)$$

we can write Eq. (5.1-6) as

$$c_p T + \frac{1}{2} \mathbf{V} \cdot \mathbf{V} = c_p T_c + \frac{1}{2} \mathbf{V}_c \cdot \mathbf{V}_c = c_p T_{tot} = h_{tot}. \quad (5.1-8)$$

The chamber conditions are indicated with the index c , while h_{tot} and T_{tot} denote the total enthalpy and total temperature, respectively. The index tot ,

88 Rocket Propulsion & Spaceflight Dynamics

in general, refers to the *total* or *stagnation conditions*, i.e. the conditions that result if the flow were brought to rest ($\mathbf{V} = 0$) by an isentropic process. The total, or stagnation temperature, T_{tot} , follows from Eq. (5.1-8), while the total pressure, p_{tot} , and the total density, ρ_{tot} , are related to T_{tot} by the Poisson relations, Eqs. (3.7-20).

In the chamber we assumed a negligible velocity, and we may write approximately,

$$T_c = T_{tot}. \quad (5.1-9)$$

In that case Eq. (5.1-8) simplifies to

$$c_p T + \frac{1}{2} \mathbf{V} \cdot \mathbf{V} = c_p T_c. \quad (5.1-10)$$

In those cases where the chamber velocity, V_c , is not negligible one still could apply the following results: instead of using the chamber conditions one would have to use the total or stagnation conditions. With

$$c_p = \frac{\gamma}{\gamma - 1} R, \quad (5.1-11)$$

we find for the velocity, V ,

$$V = \sqrt{\frac{2\gamma}{\gamma - 1} RT_c [1 - T/T_c]}. \quad (5.1-12)$$

We now have a relation between the gas velocity, V , the temperature, T , and the combustion chamber temperature, T_c .

As we assumed an isentropic flow, we may use the Poisson relations, Eqs. (3.7-20),

$$T/T_c = \left(\frac{p}{p_c}\right)^{(\gamma-1)/\gamma}, \quad (5.1-13)$$

and find

$$V = \sqrt{\frac{2\gamma}{\gamma - 1} RT_c [1 - (p/p_c)^{(\gamma-1)/\gamma}]}. \quad (5.1-14)$$

The exhaust velocity, V_e , is obtained by substituting the exit pressure, p_e , for p in Eq. (5.1-14)

$$V_e = \sqrt{\frac{2\gamma}{\gamma - 1} RT_c \left[1 - \left(\frac{p_e}{p_c}\right)^{(\gamma-1)/\gamma} \right]}. \quad (5.1-15)$$

It will be shown in the Chapters 11 and 12 that the rocket performances are strongly dependent on V_e . For high rocket performance, high values of the exhaust velocity, V_e , are needed. From Eq. (5.1-15) it is clear that V_e increases with decreasing pressure ratio p_e/p_c . Figure 5.1 shows the dependence of the dimensionless exhaust velocity, $V_e/\sqrt{RT_c}$, on the *pressure ratio*,

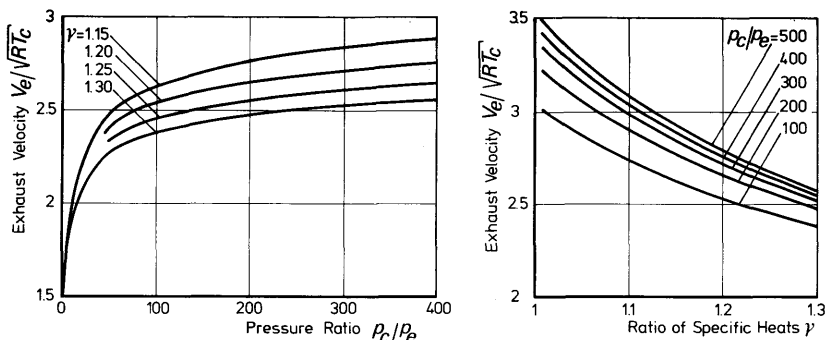


Fig. 5.1 The dimensionless exhaust velocity as a function of the ratio of specific heats and the pressure ratio

p_c/p_e , and the ratio of specific heats, γ . It is easily shown that for $\gamma \rightarrow 1$,

$$V_e \rightarrow \sqrt{2RT_c \ln\left(\frac{p_c}{p_e}\right)}. \quad (5.1-16)$$

But $\gamma = 1$ implies $R = 0$ and $c_p = c_v$ which is a physical impossibility. For an exit pressure $p_e = 0$ (*expansion to vacuum*) the exhaust velocity reaches its maximum, or *limiting value*, V_L ,

$$V_L = \sqrt{\frac{2\gamma}{\gamma-1} RT_c}. \quad (5.1-17)$$

Figure 5.2 shows the dependence of the velocity ratio, V_e/V_L , on the pressure ratio p_c/p_e . It turns out that for large pressure ratios and increase in pressure ratio has only little effect on the velocity ratio.

As the gas constant, R , is given by

$$R = \frac{R_0}{M}, \quad (5.1-18)$$

where M is the mean molecular weight of the gases and R_0 is the universal gas constant, a small value of M will result in a relatively large exhaust

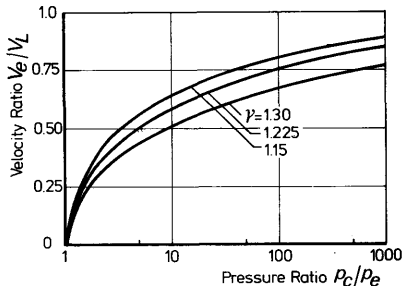


Fig. 5.2 The velocity ratio versus the pressure ratio

90 Rocket Propulsion & Spaceflight Dynamics

velocity. This is one of the reasons for the use of hydrogen as a rocket propellant. From Eq. (5.1-15) it is clear that a large value of the combustion chamber temperature, T_c , and a high pressure ratio, p_c/p_e , also lead to high exhaust velocities. The exit pressure, p_e , depends strongly on the nozzle geometry, which will be discussed in the next section.

5.1.2 Nozzle geometry

As we will need the concept of *Mach number* and the *velocity of sound*, we will make some brief remarks on these important quantities. The velocity of sound is defined as the propagation speed of a small pressure disturbance in the fluid. It can be shown [1] that for isentropic changes of state the velocity of sound, a , is equal to

$$a = \sqrt{\left(\frac{dp}{d\rho}\right)_s}, \quad (5.1-19)$$

where the index s indicates at constant entropy. For a perfect gas this means

$$a = \sqrt{\gamma RT} = \sqrt{\gamma \frac{p}{\rho}}. \quad (5.1-20)$$

The Mach number, M_a , is defined as the ratio of flow speed, V , and velocity of sound, a ,

$$M_a = V/a. \quad (5.1-21)$$

A Mach number unity means that the velocity of the flow equals the velocity of sound (*sonic flow*). A Mach number larger than one (*supersonic flow*) means that the fluid velocity is larger than the speed at which a small pressure disturbance propagates in the fluid. In that case, effects downstream cannot propagate upstream. Therefore, a disturbance in the supersonic part of the nozzle flow will not influence the chamber conditions. The chamber conditions therefore are independent of the conditions at the nozzle exit and, consequently, independent of the atmosphere.

In Section 5.1.1 we argued that the kinetic energy in the combustion chamber was negligible as compared to the enthalpy, and therefore the total temperature, T_{tot} , could be set equal to the combustion chamber temperature, T_c . By using the Poisson relations, Eqs. (3.7-20), the definitions of the speed of sound and the Mach number, Eq. (5.1-20) and Eq. (5.1-21), we can write the steady-state energy equation, Eq. (5.1-10), as

$$\frac{p_c}{p} = \left(1 + \frac{\gamma - 1}{2} M_a^2\right)^{\gamma/(\gamma-1)}, \quad (5.1-22)$$

$$\frac{\rho_c}{\rho} = \left(1 + \frac{\gamma - 1}{2} M_a^2\right)^{1/(\gamma-1)}, \quad (5.1-23)$$

$$\frac{T_c}{T} = \left(1 + \frac{\gamma - 1}{2} M_a^2\right), \quad (5.1-24)$$

$$\frac{a_c}{a} = \left(1 + \frac{\gamma - 1}{2} M_a^2\right)^{1/2}. \quad (5.1-25)$$

Most rocket motors use nozzles of the *De Laval* type, i.e. a nozzle which first *converges* (decreasing cross-sectional area) and later *diverges* (Fig. 5.3). The narrowest part of the nozzle is called the *throat*. The convergent and divergent sections may be conical, but also other geometries, such as contour or bell-shaped nozzles, are used (Section 5.2.2).

The convergent and divergent sections are generally joined by toroidal sections. In general, the radius of curvature at the throat is between two and three times the throat radius. To understand why the nozzle consists of a convergent and a divergent section, consider the quasi one-dimensional steady-state continuity equation, Eq. (3.7-6):

$$-\int_{A_1} \rho \mathbf{V} \cdot \mathbf{n} dA_1 = \int_{A_2} \rho \mathbf{V} \cdot \mathbf{n} dA_2, \quad (5.1-26)$$

or with the assumptions made,

$$\rho V A = \text{constant}, \quad (5.1-27)$$

Taking the logarithmic differential of Eq. (5.1-27) gives

$$\frac{d\rho}{\rho} + \frac{dV}{V} + \frac{dA}{A} = 0. \quad (5.1-28)$$

According to the Poisson relations, Eqs. (3.7-20), ρ can be expressed as a function of p only and hence we find

$$d\rho = \frac{dp}{dp} dp = 1/a^2 dp, \quad (5.1-29)$$

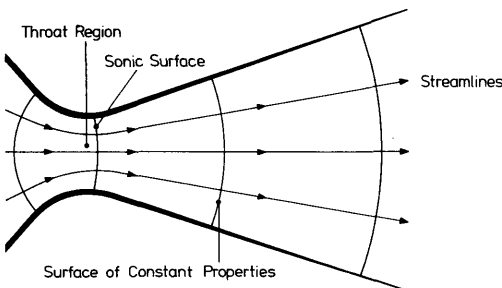


Fig. 5.3 The De Laval nozzle and the concept of streamlines and surfaces of constant properties

where use is made of Eq. (5.1-19), as the Poisson relations hold for an isentropic change of state.

Substitution of Eq. (5.1-29) into Eq. (5.1-28) yields

$$\frac{1}{a^2} \frac{dp}{\rho} + \frac{dV}{V} = - \frac{dA}{A}. \quad (5.1-30)$$

The steady-state energy equation, Eq. (5.1-10), can also be written as

$$\frac{\gamma}{\gamma-1} \frac{p}{\rho} + \frac{1}{2} V^2 = \text{constant}. \quad (5.1-31)$$

Taking the differentials and rewriting the result with the help of the Poisson relations, Eqs. (3.7-20), yields

$$\frac{dp}{\rho} + V dV = 0. \quad (5.1-32)$$

Substituting Eq. (5.1-32) into Eq. (5.1-30) and using the definition of the Mach number, we finally get

$$(1 - M_a^2) \frac{dV}{V} = - \frac{dA}{A}. \quad (5.1-33)$$

This is a relation between the velocity increment of the fluid, the local Mach number, M_a , and the change of the area of a surface of constant properties. For subsonic flow ($M_a < 1$) we see that an increase in fluid velocity requires a decreasing surface area. For supersonic flow ($M_a > 1$) the opposite is the case. For sonic flow, i.e. $M_a = 1$ we find that $dA = 0$ must hold as we must require dV , the velocity increment, to remain finite. So we see that, to accelerate the fluid, the surface area, A , has to decrease in the subsonic section, and A has to increase in the supersonic part of the nozzle. Sonic conditions are reached when A is a minimum. On the other hand, it will be clear that $dA = 0$ does not imply that we have sonic flow. If $M_a \neq 1$, this only means that $dV = 0$. The sonic surface, i.e. the surface of constant properties where $M_a = 1$, lies in the neighborhood of the throat.

From Eq. (5.1-22) it follows that the Mach number increases with increasing pressure ratios, p_c/p . Hence, if the pressure ratio exceeds a certain *critical ratio*, the flow becomes sonic. This pressure ratio is called the *critical pressure ratio*. Accordingly, one also has the critical density ratio and the critical temperature ratio. They are indicated by the subscript *cr*. Inserting $M_a = 1$ in the Eqs. (5.1-22) through (5.1-24) yields

$$(p_c/p)_{cr} = \left(\frac{\gamma+1}{2} \right)^{\gamma/(\gamma-1)}, \quad (5.1-34a)$$

$$(\rho_c/\rho)_{cr} = \left(\frac{\gamma+1}{2} \right)^{1/(\gamma-1)}, \quad (5.1-34b)$$

$$(T_c/T)_{cr} = \left(\frac{\gamma+1}{2} \right). \quad (5.1-34c)$$

As it is the pressure ratio that determines whether or not the critical conditions are reached, this is the most important relationship.

5.1.3 Mass flow and exit pressure

In Section 5.1 we have made some brief remarks about the mass flow. We will now consider the steady-state mass flow through the nozzle in more detail. According to Eq. (5.1-27), we have

$$m = \rho V A = \text{constant.} \quad (5.1-35)$$

Substituting of Eq. (5.1-14) into Eq. (5.1-35), and using the Poisson relations, Eqs. (3.7-20), in the form

$$\rho = \rho_c \left(\frac{p}{p_c} \right)^{1/\gamma}, \quad (5.1-36)$$

gives

$$\frac{m}{A} = p_c \sqrt{\frac{2\gamma}{\gamma-1} \frac{1}{RT_c} \left(\frac{p}{p_c} \right)^{2/\gamma} \left[1 - \left(\frac{p}{p_c} \right)^{(\gamma-1)/\gamma} \right]}. \quad (5.1-37)$$

This equation is often referred to as *De Saint Venant's Equation*. It relates the mass flow per unit area to the chamber conditions and the pressure ratio p/p_c . Figure 5.4 shows the dimensionless mass flow per unit area as a function of the pressure ratio. In general, the pressure ratio will have a value somewhere between zero and unity. It is easily seen from Eq. (5.1-37) that for a pressure ratio equal to one, the mass flow per unit area is zero. This is clear, because if there is no pressure difference between the chamber and a point downstream, there cannot be a steady flow and thus $m = 0$. The second zero of Eq. (5.1-37) occurs for $p/p_c = 0$.

In this case we have expanded to vacuum. As the mass flow itself is a constant for steady flow, this means that the surface area has to be infinitely large. On the sonic surface, where A attains its minimum value, we find the maximum mass flow per unit area. The pressure ratio at which this occurs is found by differentiation of Eq. (5.1-37) with respect to (p/p_c) and setting the result equal to zero:

$$\frac{p}{p_c} = \left(\frac{2}{\gamma+1} \right)^{\gamma/(\gamma-1)}. \quad (5.1-38)$$

This agrees with the critical pressure ratio for which the flow becomes sonic, Eq. (5.1-34a). We knew this already to occur on the sonic surface.

An explicit relation between the mass flow, m , and the area of the sonic surface, A_s , can be found by substitution of Eq. (5.1-38) into Eq. (5.1-37) and setting $A = A_s$. We then find

$$m = \Gamma \frac{p_c}{\sqrt{RT_c}} A_s \quad (5.1-39)$$

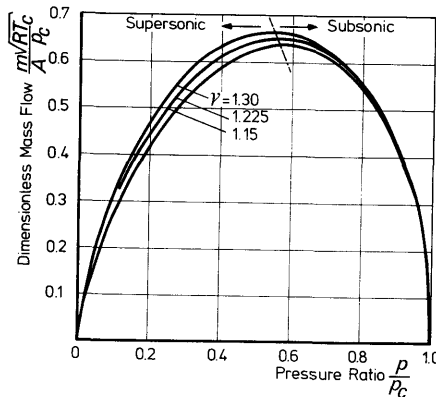


Fig. 5.4 The dimensionless mass flow per unit area versus the pressure ratio for a converging-diverging nozzle

where Γ is the *Vandenbergkernhove function* defined as

$$\Gamma = \sqrt{\gamma} \left(\frac{2}{\gamma + 1} \right)^{(\gamma+1)/(2(\gamma-1))} \quad (5.1-40)$$

We see that the mass flow through the nozzle is proportional to the chamber pressure, p_c , and the area of the sonic surface, A_t , and inversely proportional to the square root of the chamber temperature, T_c . Substitution of Eq. (5.1-39) into Eq. (5.1-37) yields

$$\frac{A}{A_t} = \frac{\Gamma}{\sqrt{\frac{2\gamma}{\gamma-1}} \left(\frac{p}{p_c} \right)^{2/\gamma} \left[1 - \left(\frac{p}{p_c} \right)^{(\gamma-1)/\gamma} \right]}. \quad (5.1-41)$$

This is a direct relationship between the local pressure ratio, p/p_c , and the *expansion ratio* A/A_t . Figure 5.5 gives the pressure ratio as a function of the expansion ratio and γ , for the supersonic part of the nozzle. Equation (5.1-41) allows the direct calculation of the expansion ratio, A/A_t , for given pressure ratio, p/p_c . However, for a given expansion ratio iterative methods have to be used to find the pressure ratio. One should always be aware that there are two real solutions of Eq. (5.1-41) for a given expansion ratio: the subsonic and the supersonic solution.

The relation between exit pressure and exit surface is found by setting $A = A_e$ and $p = p_e$ in Eq. (5.1-41),

$$\frac{A_e}{A_t} = \frac{\Gamma}{\sqrt{\frac{2\gamma}{\gamma-1}} \left(\frac{p_e}{p_c} \right)^{2/\gamma} \left[1 - \left(\frac{p_e}{p_c} \right)^{(\gamma-1)/\gamma} \right]}. \quad (5.1-42)$$

With the theory as developed in this section, we can compute the flow

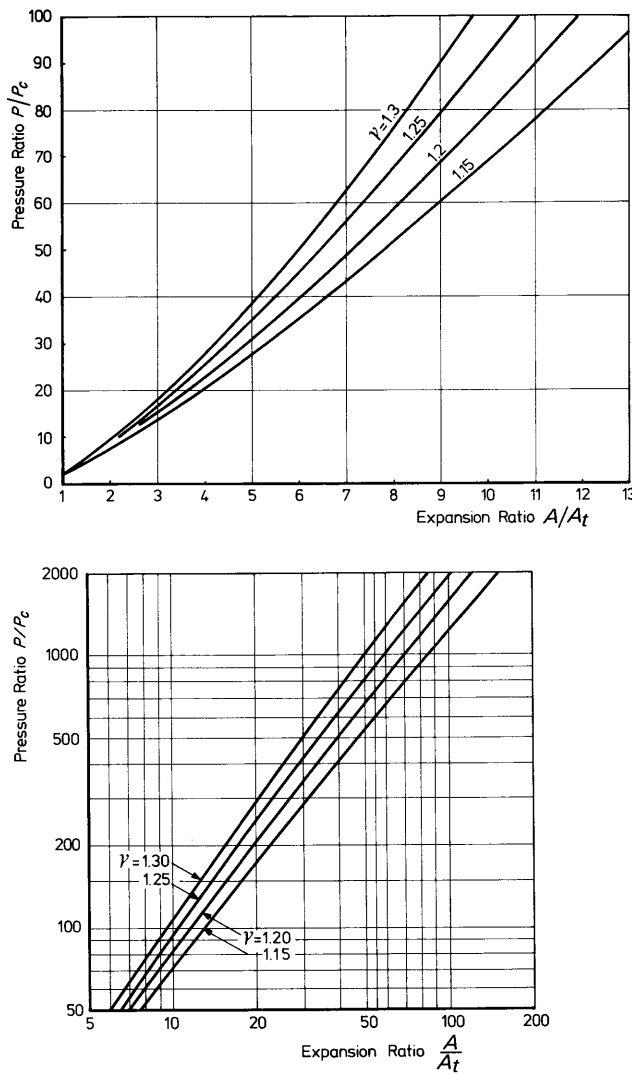


Fig. 5.5 The pressure ratio versus the expansion ratio for the supersonic part of a converging-diverging nozzle

variables as a function of the local expansion ratio, A/A_t . As soon as we make specific assumptions about the surfaces of constant properties we can compute A/A_t as a function of the location in the nozzle. In general, the Mach number and velocity will increase with the distance travelled downstream, while pressure, temperature, density and the local speed of sound will decrease. This is depicted in Fig. 5.6.

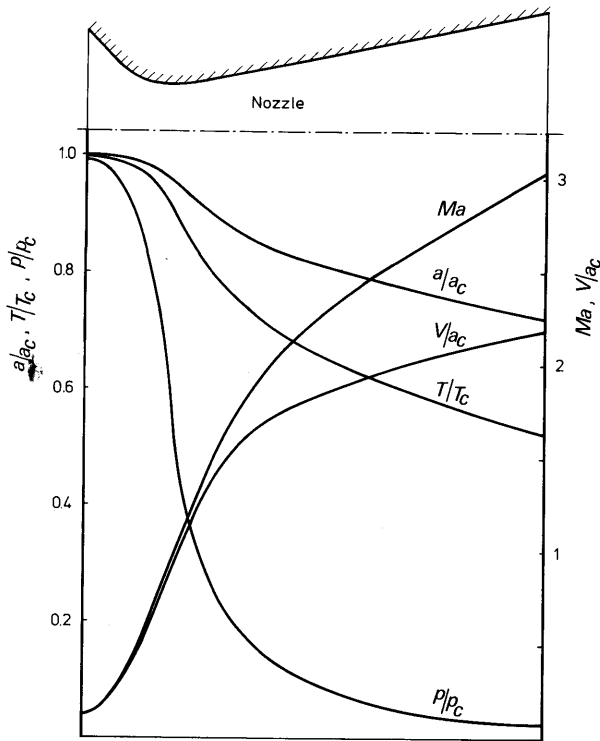


Fig. 5.6 Pressure, temperature, velocity of sound, fluid velocity and Mach number versus nozzle length

5.1.4 The exit surface

We still did not specify the shape of the exit surface. For a given exhaust pressure ratio, p_e/p_c , the exit surface area, A_e , follows from Eq. (5.1-42). This, however, does not allow us to calculate the integral in the expression for the thrust, Eq. (5.1-4). To compute this integral, we will have to make some assumptions about the exit surface. The most simple assumption we could make is to consider the exit surface planar and normal to the symmetry axis of the nozzle. In that case the flow is considered one-dimensional; Eq. (5.1-4) then becomes

$$\mathbf{F} = -\mathbf{n}_e [m V_e + (p_e - p_a) A_e]. \quad (5.1-43)$$

Usually, the second term at the right-hand side of Eq. (5.1-43) is much smaller than the first one. As the unit normal, \mathbf{n}_e , is directed backwards, it follows from Eq. (5.1-43) that \mathbf{F} is directed forwards. In the following we will use the index e to denote properties on the planar exit surface. On special exit surfaces we will use another index.

As many nozzles in use are conical, the simple assumption of an exhaust velocity parallel to the rocket axis is often not correct. A correction for the thrust of a conical nozzle was first given by Malina [2]. We will more or less follow his reasoning. Consider a conical nozzle, Fig. 5.7. All streamlines are assumed to originate in the apex, T , of the diverging cone, so that surfaces of constant properties become sections of spheres with their center in T . The exit surface of constant properties is indicated by A_s . Introducing a Cartesian coordinate system, Fig. 5.8, we can express \mathbf{n}_s , the unit normal vector to A_s , in the unit vectors \mathbf{e}_{x_s} , \mathbf{e}_{y_s} , \mathbf{e}_{z_s} and the angles θ and φ ,

$$\mathbf{n}_s = \mathbf{e}_{x_s} \sin \theta \cos \varphi + \mathbf{e}_{y_s} \sin \theta \sin \varphi + \mathbf{e}_{z_s} \cos \theta, \quad (5.1-44)$$

with

$$dA_s = r^2 \sin \theta d\theta d\varphi. \quad (5.1-45)$$

These expressions for \mathbf{n}_s and dA_s enable us to compute the integral on the right-hand side of Eq. (5.1-4)

$$\begin{aligned} \int_{A_s} \mathbf{n}_s dA_s &= r^2 \int_{\theta=0}^{\alpha} d\theta \int_{\varphi=0}^{2\pi} \sin \theta (\mathbf{e}_{x_s} \sin \theta \cos \varphi + \mathbf{e}_{y_s} \sin \theta \sin \varphi + \mathbf{e}_{z_s} \cos \theta) d\varphi \\ &= \pi r^2 (1 - \cos^2 \alpha) \mathbf{e}_{z_s}. \end{aligned} \quad (5.1-46)$$

Integration of Eq. (5.1-45) yields

$$A_s = 2\pi r^2 (1 - \cos \alpha). \quad (5.1-47)$$

Substitution of Eq. (5.1-46) and (5.1-47) into Eq. (5.1-4) and using

$$A_e = \pi r^2 \sin^2 \alpha, \quad (5.1-48)$$

yields

$$\mathbf{F} = - \left[m V_s \frac{1 + \cos \alpha}{2} + (p_s - p_a) A_e \right] \mathbf{e}_{z_s}. \quad (5.1-49)$$

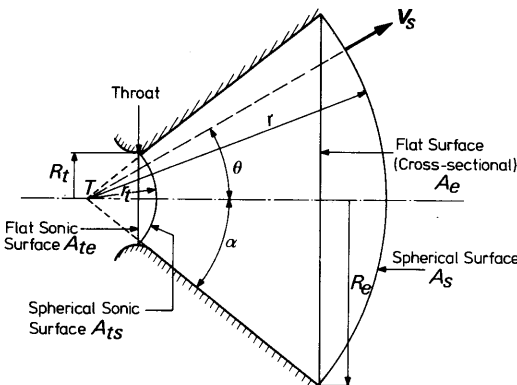


Fig. 5.7 Conical nozzle flow

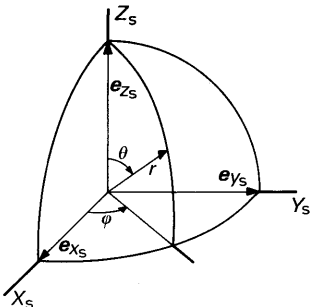


Fig. 5.8 The nozzle coordinate system $X_s Y_s Z_s$ and the spherical coordinates r, φ and θ

We know from Eq. (5.1-15) that the exhaust velocity depends on the exhaust pressure ratio, p_e/p_c . On the other hand, we also know from Eq. (5.1-42), that the exhaust pressure ratio is a direct function of the expansion ratio, A_e/A_r . Therefore, the exhaust velocity and the exit pressure are direct functions of the expansion ratio. Now define

$$\lambda = \frac{1 + \cos \alpha}{2}. \quad (5.1-50)$$

Then, from Eq. (5.1-49) one finds

$$\mathbf{F} = -[\lambda m V_s + (p_s - p_a) A_e] \mathbf{e}_z. \quad (5.1-51)$$

Now the velocity, V_s , and the pressure, p_s , on the spherical exit surface, A_s , will be very near to the values of velocity and pressure on the flat surface, A_e , and we see that λ is a reduction factor accounting for the fact that there is a sideward velocity component that does not contribute to the thrust. In Eq. (5.1-51) one now can approximate V_s by V_e and p_s by p_e , i.e. the exhaust velocity and pressure, respectively, as follow from the one-dimensional computation (i.e. flat surfaces of constant properties). The loss in thrust due to sideward components of the exhaust velocity is called the *divergence loss*. In general, it amounts to a few percent only. For exit cones of 17° and a spherical exit surface it is only 2.2% of the impulse thrust. This loss can be reduced by the use of *contoured nozzles* which are also advantageous in other respects. These contoured nozzles diverge rapidly after the throat but the divergence diminishes with increasing distance from the throat, to vanish towards the nozzle exit. Then the exhaust velocity is parallel or nearly parallel to the axis of symmetry and λ is very near to unity for such a nozzle.

5.1.5 Maximum thrust

The thrust, \mathbf{F} , is the sum of the impulse thrust and the pressure thrust. Both depend on the exit pressure, p_e . With decreasing exit pressure the impulse

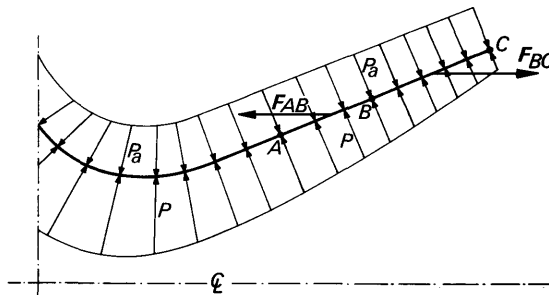


Fig. 5.9 The pressure on a rocket nozzle

thrust will increase, due to the increase in exhaust velocity, while the pressure thrust will decrease. It follows from physical reasoning that the maximum thrust is obtained when there is no pressure thrust. Therefore, consider Fig. 5.9, which shows a part of the nozzle. The ambient pressure, p_a , acts on the outside of the nozzle wall, while the pressure of the combustion products acts at the inside of the wall. This pressure decreases continuously towards the exit. The thrust actually is due to the pressure forces acting on the nozzle and chamber walls. At point B the pressure at the inside of the nozzle wall is supposed to equal the ambient pressure. A nozzle with its exit area located at point A would gain an extra thrust F_{AB} by lengthening it to B, due to the fact that over interval AB the pressure at the inside of the nozzle wall is larger than the ambient pressure at the outside. If one would lengthen the nozzle from B to C then the fluid pressure, p , is smaller than the ambient pressure. Over the interval BC the resultant force is directed backwards, and therefore diminishes the thrust. These arguments hold for all types of converging-diverging nozzles which therefore should expand to ambient pressure to achieve a maximum thrust.

In actual flight, the ambient pressure depends on altitude and it is not possible to expand to ambient pressure during the whole powered flight. One may design the nozzle in such a way that the exit pressure is a weighted average of the ambient pressure during the powered flight. If the rocket motor is to operate in vacuum, the compromise between weight, thrust, costs, size and strength will determine the actual dimensions of the nozzle.

5.2 Real rocket motors

To analyse the rocket motor in a simple way, we had to make a good many assumptions in Section 5.1.

Transient phenomena. We have ignored the non-stationary phenomena. This means that starting and shut-down effects are completely ignored. Moreover, the chamber pressure and temperature often show fluctuations.

In many cases, these fluctuations are small and do not influence the overall rocket performances. If this is not the case, special analysis of oscillatory combustion is necessary [3, 4]. In some cases a coupling between the unsteady combustion process, the vehicle structure and the propellant feed lines may take place. This effect is known as *POGO instability* [5]. It is especially known to occur in liquid-propellant rocket motors. In solid-propellant test motors, pressure fluctuations up to 30% of the mean chamber pressure have been measured [6]. Non-stationary effects therefore, can be very important. However, one mostly aims at a smooth thrust-time history, even if the thrust varies with time. Then, the non-stationary effects are so small that they can be ignored.

Uniform, localized combustion. The combustion was assumed to take place in the combustion zone. This, however, is not fully the case. Chemical reactions and recombinations take place in the nozzle itself. We will deal partly with these effects in Chapter 7. In general, however, the approximation that all combustion takes place in a small region, turns out to give results with an error of less than 5%.

At the nozzle entrance uniform chamber conditions were assumed. In general, this is not the case. Analysis of the effects of non-uniform chamber conditions shows that the thrust may change a little (in the order of a few percent) depending on the shape of the throat [7] as compared to idealized theory.

Isentropic flow. The assumption that the flow is isentropic, is clearly an idealization. Heat transfer is a serious problem in the design of rocket motors. However, except for small motors, it is more a problem of cooling than a problem of performance loss. Apart from this we have boundary layer effects. Both heat transfer and boundary layers are strongly dependent on the nozzle shape and size. These losses usually are of the order of 2% to 3% of the thrust.

Ideal gas combustion products. The assumption that the combustion products are ideal gases and have constant specific heats is certainly an oversimplification. In many cases, solid particles are present in the flow (*two-phase flow*). Because of their drag, these particles are exhausted too, but usually, there is a velocity difference between the particles and the gas. The particles may impinge on the nozzle walls, leading to erosion of, or the formation of a deposit on, the nozzle wall. To improve the rocket performances, one should try to avoid impingement as much as possible. This would result in nozzles with a very long throat and flaring out towards the exit. This, however, leads to higher divergence losses and heat transfer creates more problems too [8]. The presence of solid particles in the combustion products may be due to incomplete combustion, but in many cases they are due to metal additives. In solid-propellant rockets and in high-performance liquid-propellant rockets, metal additives are used to

increase the combustion temperature. The presence of solid particles in the exhaust flow will also increase the molecular weight of the combustion products, hence, the performance gain will be a little less than one might expect from the raised combustion temperature alone.

Other effects. The specific heats not being constant may change the rocket performances, as compared to idealized theory. We will deal with this in Chapter 7.

Even if we forego viscous effects, such as boundary layers, surfaces of constant properties, as defined in Section 5.1, can only exist in very special cases (e.g. purely one-dimensional flow, rotationally-symmetrical flow). The concept, however, is useful to account for three-dimensional effects. More accurate analyses of the nozzle flow will account for heat transfer and *viscous effects* [9] and *chemical reactions* [10]. Often, however, approximate methods [11] or the method of characteristics [1] are used for the computation of the nozzle flow.

Quality factors. To compare the actual performances with the ideal performances, the following quality factors are often used

$$\xi_F = \frac{F_{\text{exp}}}{F_{\text{th}}}, \quad (5.2-1)$$

which is the ratio of actual thrust, or the thrust as determined by an experiment, to the theoretical thrust. In general, ξ_F has values between 0.92 and 0.96. The ratio of actual exhaust velocity to theoretical exhaust velocity,

$$\xi_V = \frac{V_{e_{\text{exp}}}}{V_{e_{\text{th}}}}. \quad (5.2-2)$$

In general, ξ_V has values somewhere between 0.85 and 0.98, but much lower values are possible. The ratio of the actual mass flow, as determined by an experiment, and the theoretical mass flow.

$$\xi_m = \frac{m_{\text{exp}}}{m_{\text{th}}}. \quad (5.2-3)$$

Values for ξ_m range between 0.98 and 1.15. That the correction factor for the propellant mass flow can become larger than unity is a result of:

1. Recombination, as a result of which the molecular weight of the gases can increase during expansion.
2. Heat transfer to the nozzle walls; as the temperature is lowered owing to heat transfer, the density is increased.
3. Other influences such as incomplete combustion, solid particles in the exhaust products and the change of the specific heats as a result of temperature drop and recombination.

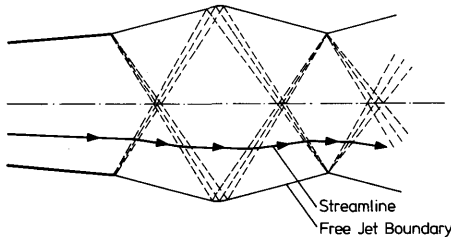


Fig. 5.10 Flow pattern of an under-expanded jet

5.2.1 The effect of ambient pressure on the nozzle flow

In Section 5.1.5, we have seen that maximum thrust occurs when the exit pressure, p_e , equals the ambient pressure, p_a . The case that $p_e > p_a$ is called *under-expansion*, as more expansion is still possible. The expansion of the free jet will continue downstream of the exit section by a series of *expansion* and *compression waves*, which reflect at the free jet boundaries, Fig. 5.10. The under-expansion has no influence on the thrust as computed from Eq. (5.1-51). In the case that $p_e < p_a$, one speaks of *over-expansion*.

Because of the decrease of ambient pressure with altitude, both under-expansion and over-expansion actually occur during the powered flight of the rocket vehicle. The phenomenon of over-expansion is more complicated than under-expansion. If the over-expansion is too large, normal shock waves may occur. The shock wave itself is due to viscous effects. Across the normal shock there is a sudden rise in pressure, temperature and density, while the velocity has decreased. The compression by the shock is a non-isentropic process. Therefore, the entropy after the shock, which itself is a very thin region, has increased. The three one-dimensional steady-state conservation equations (with the same assumptions about the flow before and after the shock as in Section 5.1), can be written down just before (index 1), and just after (index 2) the normal shock, and one can easily verify that this system of equations:

$$\rho_1 V_1 = \rho_2 V_2, \quad (5.2-4)$$

$$(\rho_1 V_1^2 + p_1) = (\rho_2 V_2^2 + p_2), \quad (5.2-5)$$

$$\frac{\gamma}{\gamma-1} \frac{p_1}{\rho_1} + \frac{1}{2} V_1^2 = \frac{\gamma}{\gamma-1} \frac{p_2}{\rho_2} + \frac{1}{2} V_2^2, \quad (5.2-6)$$

allows for two different solutions. A trivial solution of the Eqs. (5.2-4) through (5.2-6) is $V_1 = V_2$, $p_1 = p_2$, etc.

The non-trivial solution is

$$\frac{p_2}{p_1} = \frac{2}{\gamma+1} \frac{\rho_1 V_1^2}{p_1} - \frac{\gamma-1}{\gamma+1} = \frac{2\gamma}{\gamma+1} M_{a_1}^2 - \frac{\gamma-1}{\gamma+1}, \quad (5.2-7)$$

$$\frac{p_1}{\rho_2} = \frac{V_2}{V_1} = \frac{2\gamma}{\gamma+1} \frac{p_1}{\rho_1 V_1^2} + \frac{\gamma-1}{\gamma+1} = \frac{2}{\gamma+1} \frac{1}{M_{a_1}^2} + \frac{\gamma-1}{\gamma+1}. \quad (5.2-8)$$

These equations give relations between the flow variables before and after the shock.

Let us now consider what may happen in an over-expanded nozzle, i.e. $p_e < p_a$. The design exit pressure, according to Eq. (5.1-42), is p_{ex} . For $p_c > p_a > p_{a_1}$, the flow is entirely subsonic, curve *a* in Fig. 5.11. For $p_c > p_a = p_{a_1}$, the flow just becomes sonic at the throat, but the flow in the divergent part of the nozzle is subsonic, curve *b*. If the ambient pressure $p_{a_1} > p_a > p_e$, a normal shock may occur. The pressure follows the ideal expansion curve *ex* up to a certain point *S*. Here, a normal shock develops. After the shock, a subsonic compression takes place such that the exit pressure equals the ambient pressure p_{a_2} . For lower ambient pressures, the point *S*, where the shock occurs, is located more downstream, until at an ambient pressure p_{a_3} the normal shock is located just at the exit of the nozzle. The pressure ratio for which this happens follows immediately from Eq. (5.2-7). We remember that in this case $p_2 = p_{a_3}$ and $p_1 = p_e$. Substitution of the Eqs. (5.1-13) and (5.1-15) into Eq. (5.2-7) then leads to

$$\frac{p_{a_3}}{p_e} = \frac{4\gamma}{\gamma^2 - 1} \left(\frac{p_c}{p_e} \right)^{(\gamma-1)/\gamma} - \frac{\gamma + 1}{\gamma - 1}. \quad (5.2-9)$$

For ambient pressures $p_{a_3} > p_a > p_e$ the flow in the nozzle is fully supersonic, the exhaust velocity is to be computed according to Eq. (5.1-15) and the thrust according to Eq. (5.1-51). Now, the ambient pressure is higher than the free jet pressure. The exhaust jet is compressed by an *oblique shock*, originating at the nozzle exit. This compression is followed by a series of expansion and compression waves, Fig. 5.12.

Until now, we have only considered ideal non-viscous gases as propulsive fluid. Because of viscous effects, a *boundary layer* builds up. The boundary layer thickness depends on the nozzle shape and, generally, increases with nozzle length. For nozzles of the same shape but of different sizes, we have to realize that the nozzle length increases with the square root of the mass

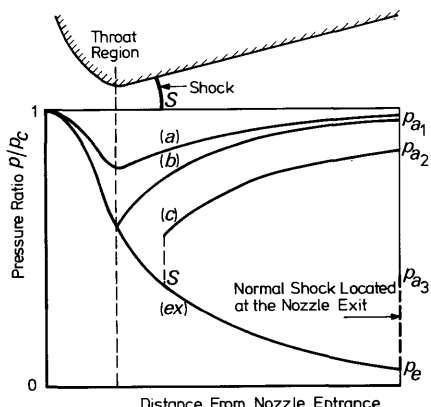


Fig. 5.11 Over-expansion of the flow in a converging-diverging nozzle

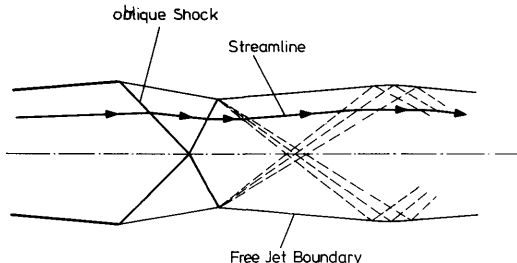


Fig. 5.12 Flow pattern of an over-expanded jet

flow. Therefore the boundary layer influence is relatively small for the larger size nozzles. As the velocity in the boundary layer is subsonic, the outside conditions can influence the flow upstream in the nozzle through the boundary layer. In the case of over-expansion, the ambient pressure has an influence on the boundary layer upstream. If the pressure gradient is too small to let the flow overcome the higher ambient pressure, the flow may separate locally from the nozzle wall and form an oblique shock. The separation may be symmetric but also asymmetric and it may be steady but also fluctuating. Behind the oblique shock wave the jet *contracts* and a *wake* with approximately atmospheric pressure arises, Fig. 5.13. The nozzle now acts as if it had a smaller expansion ratio. Point S where the oblique shock is attached to the nozzle wall moves upstream with increasing p_a/p_e . There is a classical rule of thumb, which indicates when separation may occur [12]:

$$\left(\frac{p_e}{p_c}\right) \leq \alpha \cdot \left(\frac{p_a}{p_c}\right), \quad (5.2-10)$$

where α lies somewhere between 0.25 and 0.35. The coefficient α will depend mainly on the *surface roughness* of the nozzle wall, the expansion ratio, the pressure gradient, and the viscosity of the combustion products.

It should be noted that the presence of particles reduces over-expansion ratios possible without separation occurring. Values of α in Eq. (5.2-10) may become as high as 0.6. Equation (5.2-10) is known as the *Summerfield criterion*. Originally, this criterion stated that for a divergence half-cone angle of 15° separation may occur if p_e/p_a as computed from Eq. (5.2-10) is smaller than 0.4. From Fig. 5.14 we can deduce that the idealized theory

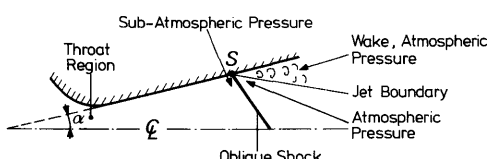


Fig. 5.13 Separation and oblique shockwave in a nozzle due to over-expansion

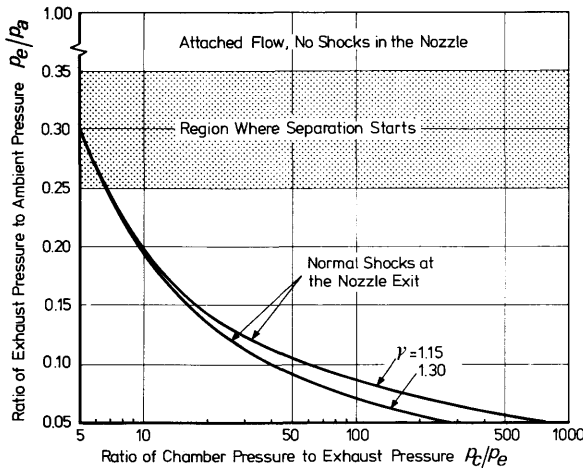


Fig. 5.14 Over-expanded nozzle flow. Separation may take place in the shaded region. The full lines give the pressure ratio p_e/p_a versus p_c/p_e for which the normal shock is located at the nozzle exit

gives good results for $p_e/p_a > 0.35$, and the whole effect of over-expansion is taken into account by the pressure term in Eq. (5.1-51). For lower exit pressures, $0.25 < p_e/p_a < 0.35$, we may expect separation and oblique shock waves in the nozzle. There are also other criteria for the occurrence of separation, for instance as a function of the Mach number [13].

Behind the separation region there is a wake where the pressure equals the ambient pressure, while the pressure in the jet is near to ambient pressure too. The effect of separation therefore is to reduce the effective exit area, and the thrust follows from the conditions at the point of separation. The separation has the effect that the thrust remains nearly constant with increasing p_a , after separation has occurred. If the ratio of exit pressure to ambient pressure is further decreased, we may get normal shocks in the nozzle. The normal shock starts, according to the idealized theory, with decreasing p_e/p_a at the nozzle exit, and moves further upstream with p_e/p_a decreasing more and more. If one were to expect a normal shock by theoretical considerations, while there is separation already, the oblique shock at some position in the nozzle may become a normal shock [14] and then move upstream. However, as Fig. 5.14 shows, the over-expansion has to be extremely large in this case, which is seldom met in practice. With the help of the Eqs. (5.2-7) and (5.2-8) one can determine the conditions directly after the shock. From these the stagnation conditions after the shock follow by Eq. (5.1-8) and the Poisson relations, Eqs. (3.7-20). The exhaust velocity then follows from Eq. (5.1-15) where instead of chamber conditions (index c), the stagnation conditions are to be used.

5.2.2 Other nozzle designs

Apart from the conical De Laval nozzle, we have mentioned the *contour* or *bell-shaped* nozzle. One of its advantages is its lower divergence loss and reduced length as compared to the conical nozzle. Other types of nozzles which adapt better to different ambient pressures are proposed for a good many years [15]. The expansion is fairly complicated. For all these nozzles at least one of the exhaust jet boundaries is a free jet boundary that adapts to different pressure ratios, p_e/p_a . Though much research has been devoted to the development of these types of nozzles, they have not yet found a widespread application. The most important types are:

1. The *Expansion-Deflection (E-D) nozzle* [16] (Fig. 5.15a). In this case a wake behind the plug forms the free jet boundary.
2. The *plug nozzle* (Fig. 5.15b). For this nozzle the free jet boundary is at the outside of the exhaust jet.
3. The *truncated plug nozzle* (Fig. 5.15c). This nozzle is roughly the same as the plug nozzle. Behind the plug there is a wake now too.

The thrust of these nozzles is a little less than the thrust of the classical nozzle in the case of ideal expansion. They give a higher thrust than the classical nozzle if we have non-ideal expansion. The analysis of the flow in these nozzles is rather complicated [17, 18, 19]. In general, all these nozzles are annular. Rectangular or linear configurations have been tested successfully too [20]. Instead of a rotational symmetric nozzle, the nozzle is essentially two-dimensional. These types of nozzles look well-suited for Space Shuttle-like vehicles. The non-conventional types of nozzles have two advantages:

1. For the same expansion ratio, they are much shorter than the De Laval or contour nozzle.
2. They adapt better to under- and over-expansion on the whole.

Important additional advantages are that for liquid-propellant motors, annular combustion chambers can be used, and that pumps, turbines and other

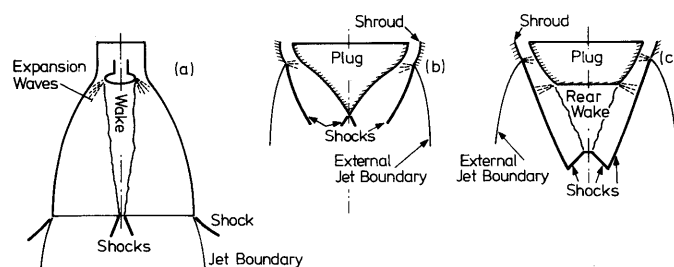


Fig. 5.15 The Expansion-Deflection (E-D) nozzle (a), the plug nozzle (b), and the truncated plug nozzle (c)

engine systems can be housed in the central (truncated) plug [21]. Apart from the reduction in nozzle length this reduces the overall motor length considerably.

The application of these types of nozzles to solid-propellant rocket motors looks promising too [22, 8]. However, the support of the central plug here poses structural problems, as this support is strongly heated. Moreover, the support struts disturb the flow field.

5.2.3 Thrust misalignment

If the thrust vector, \mathbf{F} , due to production inaccuracies in the rocket vehicle for instance, does not pass through the center of mass of the rocket we speak of *thrust misalignment*. The main causes are that the flow is not symmetrical, the center of mass may be off-set, or the nozzle may be tilted with respect to the rockets' center line. The moment due to thrust misalignment is, according to Eq. (4.2-51),

$$\mathbf{M}_F = \mathbf{r}_e \times \mathbf{F}, \quad (5.2-11)$$

where \mathbf{r}_e is the position vector of the center of mass flow, defined by Eq. (4.2-10) as

$$\mathbf{r}_e = \frac{1}{m} \int_{A_e} \mathbf{r} (\rho \mathbf{V} \cdot \mathbf{n}) dA_e. \quad (5.2-12)$$

Making the same assumptions as in Section 5.1 and taking for the exit surface a spherical surface of constant properties, A_s , we can determine the position vector of the center of mass flow. We assume the center of mass on the centerline of the rocket which coincides with the nozzle axis. Then,

$$\mathbf{r}_e = \frac{1}{A_s} \int_{A_s} \mathbf{r} dA_s. \quad (5.2-13)$$

The position vector of the apex of the diverging nozzle cone is \mathbf{d} , Fig. 5.16. Thus

$$\mathbf{r}_{se} = \mathbf{r}_e - \mathbf{d}, \quad (5.2-14a)$$

$$\mathbf{r} = \mathbf{d} + \mathbf{r}_s, \quad (5.2-14b)$$

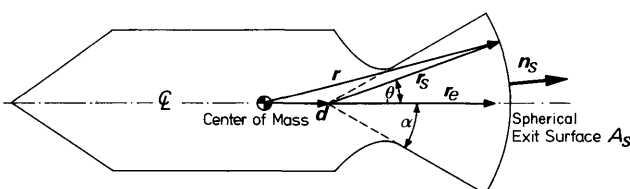


Fig. 5.16 The position vector of the center of mass flow, \mathbf{r}_e

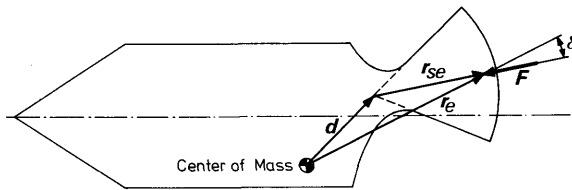


Fig. 5.17 Definition of the thrust misalignment angle, δ

and from Eq. (5.2-13) and Eqs. (5.2-14) follows

$$\mathbf{r}_{se} = \frac{1}{A_s} \int_{A_s} \mathbf{r}_s dA_s. \quad (5.2-15)$$

If we remember that $\mathbf{r}_s = r_s \mathbf{n}_s$ and substitute the Eqs. (5.1-46) and (5.1-47) into Eq. (5.2-15) we find that

$$\mathbf{r}_{se} = r_s \frac{1 + \cos \alpha}{2} \mathbf{e}_{z_s}, \quad (5.2-16)$$

and

$$\mathbf{r}_e = \mathbf{d} + r_s \frac{1 + \cos \alpha}{2} \mathbf{e}_{z_s}, \quad (5.2-17)$$

where \mathbf{e}_{z_s} is defined as in Section 5.1.4 and Fig. 5.8.

For a flat exit surface, we find in the same way

$$\mathbf{r}_e = \mathbf{d} + r_f \mathbf{e}_{z_s}, \quad (5.2-18)$$

where r_f is the distance of the apex of the diverging cone to the exit surface.

If the nozzle is tilted with respect to the longitudinal axis, if the center of mass does not lie on the longitudinal axis of the rocket, or if the apex of the diverging cone of the nozzle does not lie on that axis the foregoing derivation remains exactly the same. However as the thrust, \mathbf{F} , is not collinear now with the position vector of the center of mass flow, \mathbf{r}_e , the moment, \mathbf{M}_F , is different from zero. If the angle between \mathbf{F} and \mathbf{r}_e is δ (Fig. 5.17), the magnitude of the thrust misalignment moment, \mathbf{M}_F , is

$$M_F = Fr_e \sin \delta. \quad (5.2-19)$$

For a well-manufactured rocket, in general, $\delta \leq 0.1^\circ$.

5.2.4 Thrust vector control

Thrust vector control (TVC) is the intentional change of direction of the thrust vector with respect to the symmetry axis of the rocket. By changing the direction of the thrust vector, a control moment about a lateral axis of the rocket can be generated. There are three basically different methods [23, 24] by which this can be achieved.

Jet exhaust deflection. The most used systems are:

Jet vanes placed in the exhaust flow of the nozzle. This system also allows for roll control. It was used on the German V-2 rocket of World War II, and a modern example is the Scout first stage.

Jetavator, an annular ring is located at the nozzle exit. The exhaust jet is deflected by tilting the ring. There are a good many variations to this principle.

Spoilers at the nozzle exit can be used to block-off a part of the exit area. Due to the resulting shock waves, the flow becomes asymmetrical and side forces are produced.

All these systems more or less permanently influence the exhaust flow and cause losses in thrust. The thrust loss during deflection may become as high as 25%. The maximum jet deflection angle depends on the system used, but lies in the range of 20° to 30°.

Fluid injection. A fluid is injected at one or more points in the nozzle. A local shock wave results, causing the flow to become asymmetrical. The fluid used, is either hot gas from the combustion chamber, or a (inert) liquid or gas, stored in separate tanks. The system is used, for instance, on the solid boosters of the Titan launch vehicle. Fluid injection also offers the possibility of roll control [25]. If fluid is injected through the ports A and A' in Fig. 5.18, the pressure on the fins in the nozzle create a roll torque. If an inert fluid is used, the deflection angle of the jet may be of the order of 5°. A slight increase in thrust can be expected. Hot gas injection will result in deflection angles in the order of 10° while a slight loss in thrust can be expected.

Nozzle deflection. In the oldest system, used on many liquid-propellant rockets, the whole rocket motor was tilted. This system, however, is not suitable for solid-propellant motors. Other systems to deflect the whole nozzle or a part of the nozzle are:

The ball and socket type. The nozzle, or a part of it, is supported within a

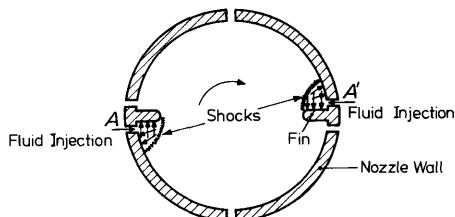


Fig. 5.18 Generation of roll torque by fluid injection

gimbal ring and pivoted about a central point. The leakage of combustion gas is prevented by a special seal.

The fluid-bearing nozzle. Instead of a gimbal ring a fluid bearing is used.

The flexible-seal nozzle. The nozzle is mounted to the structure by a seal which is stiff in one direction, but easily allows rotational motion to deflect the nozzle.

The flexible exit is another recent development [26]. Here the divergent section of the nozzle is made of flexible material, such that it can be deflected like a hose.

The bearing type deflection systems (ball and socket and fluid bearing) allow for deflections up to 20° , however, leakage sometimes poses difficulties. The flexible systems (flexible seal, flexible exit) demand relatively high actuation forces. They allow for nozzle deflections up to 12° . The thrust loss with these systems is negligible.

A completely different approach to the TVC problem is the *rotating nozzle*. If more nozzles on one motor are used, one can mount the nozzles in such a way that they can rotate about an axis that is inclined with respect to the symmetry axis of the rocket. By rotating one of the nozzles, a side force can be produced.

5.2.5 Thrust magnitude control

Thrust magnitude control (TMC) allows for large thrust variations usually with small variations in chamber pressure. In some liquid-propellant rocket motors, TMC has been used without varying the throat area by reducing the mass flow into the chamber. As a result of the reduced mass flow, the chamber pressure decreases too. This may cause irregular combustion, or even extinguishment. Apart from this, the exhaust velocity is also lowered. Two possible systems without these adverse effects are *the translating inlet nozzle* and *the pintle nozzle*. Both systems vary the throat to modulate the thrust. The translating nozzle is primarily designed for two different thrust magnitudes. An outline is given in Fig. 5.19a. The port, A, is either closed or fully opened. If the port, A, is closed, the sustain throat is the only way through which propulsive gases can leave the rocket engine. If port A is opened, an extra boost flow can leave the combustion chamber and the boost throat acts as nozzle throat.

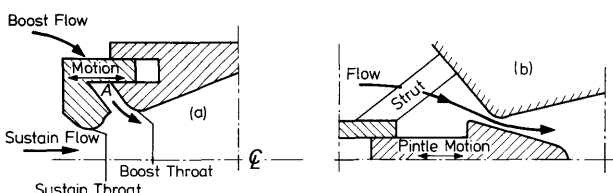


Fig. 5.19 The translating inlet nozzle (a) and the pintle nozzle (b)

The pintle nozzle employs a center body that can move in an axial direction, thereby continuously varying the throat area, Fig. 5.19b. The central body which holds the movable pintle is mounted on struts on the nozzle inlet. It is, of course, possible to combine TVC and TMC to obtain real thrust vector control, i.e. both magnitude and direction of the thrust can be varied.

Another TMC device that should be mentioned in this section is the *extendable exit cone*. If during powered flight under-expansion losses become unacceptably large, one can increase the thrust by lengthening the exit cone. This may be done by moving aft an extension to the divergent part of the nozzle. This concept was planned for the Space Shuttle Main Engine, SSME, but has been abandoned to keep the mechanism simple.

References

- 1 Liepmann, H. W. and Roshko, A. (1957), *Elements of Gasdynamics*, John Wiley, New York.
- 2 Malina, F. (1940), Characteristics of the rocket motor unit based on the theory of perfect gases, *J. Franklin Institute*, **230**, 433–454.
- 3 Harrje, D. T. and Reardon, F. H. (1972), *Liquid Propellant Rocket Combustion Instability*, NASA SP-194, Washington.
- 4 Culick, F. E. C. (1968), A review of calculations for unsteady burning of a solid propellant, *AIAA J.*, **6**, 2241–2255.
- 5 Rubin, S. (1972), *Analysis of POGO-Stability*, paper presented at the 23rd IAF Congress, Vienna.
- 6 Schöyer, H. F. R. (1971), *Report on Low Frequency Oscillatory Combustion Experiments*, Daniel and Florence Guggenheim Jet Propulsion Center, California Institute of Technology, Pasadena.
- 7 Norton, D. J. and White, R. E. (1973), Striated nozzle flow with small radius of curvature ratio throats, *J. Spacecraft*, **10**, 747–750.
- 8 Williams, F. A., Barrère, M. and Huang, N. C. (1969), *Fundamental Aspects of Solid Propellant Rockets*, AGARDograph #116, Technivision Services, Slough.
- 9 Benison, G. J. and Rubin, E. L. (1971), A time-dependent analysis for quasi-one-dimensional, viscous, heat conducting, compressible laval nozzle flows, *J. Eng. Math.*, **5**, 39–49.
- 10 Scaccia, C. and Kennedy, L. A. (1974), Calculating two-dimensional chemically reacting flows, *AIAA J.*, **12**, 1268–1272.
- 11 Kliegel, J. R. and Quan, V. (1968), Convergent-divergent nozzle flows, *AIAA J.*, **6**, 1728–1734.
- 12 Bloomer, H. E., Antl, R. J. and Renas, P. E. (1961), *Experimental Study of Effects of Geometric Variables on Performance of Conical Rocket-engine Exhaust Nozzles*, NASA TN D-846, Washington.
- 13 Arens, M. and Spiegler, E. (1963), Shock-induced boundary layer separation in over-expanded conical exhaust nozzles, *AIAA J.*, **1**, 578–581.

112 Rocket Propulsion & Spaceflight Dynamics

- 14 Nave, L. H. and Coffey, G. A. (1973), *Sea Level Sideloads in High-Area-Ratio Rocket Engines*, AIAA Paper 73-1284, New York.
- 15 Rao, G. V. R. (1961), Recent developments in rocket nozzle configurations, *A.R.S. J.*, **31**, 1488–1494.
- 16 Rao, G. V. R. (1960), The E-D nozzle, *Astronautics*, **5**, September 28–29, 50.
- 17 Hopkins, D. F. and Hill, D. E. (1968), Transonic flow in unconventional nozzles, *AIAA J.*, **6**, 838–842.
- 18 Migdal, D. (1972), Supersonic annular nozzles, *J. Spacecraft*, **9**, 3–6.
- 19 Sule, W. P. and Mueller, T. J. (1973), Annular truncated plug nozzle flowfield and base pressure characteristics, *J. Spacecraft*, **10**, 689–695.
- 20 Fuller, P. N. (1973), *Linear Rocket Engine Design-Fabrication-Testing*, AIAA Paper 73-1179, New York.
- 21 Lamont, E. A. (1973), *The Aerospike Engine System for the Space Tug—A Status Report*, AIAA Paper 73-1245, New York.
- 22 Casci, C., Gismond, E. and Angelino, G. (1968), An experimental study on the application of plug nozzles to solid-propellant rockets—2, *Spaceflight*, **10**, 33–36.
- 23 Ellis, R. A. (1972), *Continuing Evaluation of Nozzle Design and Analysis Techniques*, AIAA Paper 72-1190, New York.
- 24 Burgess, B. (1972), Recent advances in thrust vector control for tactical missiles (supplementary paper), *Aeronautical J.*, **77**, 429–433.
- 25 Zeierman, I. and Manheimer-Timnat, Y. (1973), Full control of solid propellant rockets by secondary injection, *J. Spacecraft*, **10**, 161–162.
- 26 Cauza, J. H. and Mockenhaupt, J. D. (1973), *The Integrated Omni-Vector Cone (INOVEC)™ Thrust Vector Control System*, AIAA Paper 73-1204, New York.

6 Characteristic Coefficients and Parameters of the Rocket Motor

It is possible to define some quantities which are characteristic for the rocket motor or its components. They are useful for outline information about the rocket motor, but they also allow comparison, in certain respects, of rocket engines of different sizes. Some other, dimensionless quantities, are useful to compare theoretical and experimental results. For a better understanding of how the latter quantities can be used to interpret test results, we will first briefly discuss the testing of rockets.

6.1 Some notes on rocket testing

The most important performance parameter of the rocket motor is the thrust. To measure the thrust, the rocket motor is fired on a *test stand*. As the rocket performances are dependent on the burning-time, t_b , the chamber pressure, p_c , and chamber temperature, T_c , these quantities are measured too. If heat transfer, deformation, etc., are important factors, it is obvious that many more variables have to be measured. We will concern ourselves, in this section, only with those quantities, that determine the rocket performances directly.

The rocket motor may be placed either in a horizontal, vertical or inclined position. If the rocket is in a pure horizontal position and the thrust is directed along the axis of symmetry, the weight of the rocket motor can be measured by the vertical support. In this position, the main components of weight and thrust are orthogonal. If the rocket is in a vertical position, the weight vector is in the same (or opposite) direction as the thrust vector, and a combination of thrust and weight is measured. This may pose difficulties for solid-propellant rockets, as it is not possible to determine exactly their mass flow at any instant. For a liquid-propellant rocket this information is easily obtained by measuring the mass flow from the propellant tanks.

Although horizontal testing may be easier, for large rocket motors the rocket structure may not be suited very well for testing in such a position, or the liquids injected in the combustion chambers of liquid-propellant rockets may stay there while not yet burned, due to the ignition time lag. This may lead to an explosion. One can avoid this risk by putting the rocket motor in a vertical position. It is clear that, especially for very large rockets, this leads to more complicated structures of the teststand.

By measuring the forces on the rocket in three orthogonal directions, at least at two different points for each direction, one can determine the forces

and moments on the rocket in all directions. This yields information about thrust misalignment and is also important in the case of thrust vector control.

Static rocket testing is a specialized technique and we will not discuss the various ways of measuring the important parameters. We will assume that it is possible to measure all these quantities more or less accurately. If a rocket engine does not meet its specifications, it is necessary to determine the cause of this shortcoming. It is here that the quantities to be discussed in this chapter turn out to be convenient, because they yield specific information.

6.2 Total and specific impulse

A rocket motor, which during a time interval, t_b , exerts a thrust, $F(t)$, delivers a total impulse, I ,

$$I = \int_0^{t_b} F(t) dt. \quad (6.2-1)$$

The propellant mass which was needed for this is M_p , and hence, the impulse per unit weight of the propellant, the *specific impulse*, I_{sp} , is

$$I_{sp} = \frac{\int_0^{t_b} F(t) dt}{M_p g_0} = \frac{\int_0^{t_b} F(t) dt}{\int_0^{t_b} g_0 m(t) dt}, \quad (6.2-2a)$$

where g_0 is the standard surface gravity. Another often used definition of specific impulse, is the ratio of the impulse delivered during an infinitesimal time interval, δt , $F \delta t$, and the propellant weight consumed during that time interval, $m g_0 \delta t$,

$$I_{sp} = F/(m g_0). \quad (6.2-2b)$$

This quantity is also referred to as the *specific thrust*, as it is the thrust per propellant weight flow rate. Both definitions are more or less equivalent, and are identical if F and m are constant.

The specific impulse shows how much impulse can be obtained from a unit weight of propellant, and as one tries to keep weights as low as possible in rocket technology, it is evident that a high specific impulse is desirable. The specific impulse may also be interpreted as the time during which a propellant can deliver a force which equals the propellants' initial weight. As the specific impulse is expressed in seconds, it has the same numerical value, in both English and SI units. The specific impulse depends on both the propellant and the motor configuration. This can be seen from Eq. (5.1-51) with $V_s = V_e$, and $p_s = p_e$,

$$F = \lambda m V_e + (p_e - p_a) A_e. \quad (6.2-3)$$

According to Chapter 5, the reduction factor, λ , depends on the nozzle shape, while the exhaust velocity, V_e , and the exhaust pressure, p_e , depend on the expansion ratio, A_e/A_t , and chamber pressure, p_c . Using the second definition, Eq. (6.2-2b), of the specific impulse, and assuming ideal expansion, i.e. $p_e = p_a$, we find, taking $\lambda = 1$,

$$I_{sp} = \frac{mV_e}{mg_0} = \frac{V_e}{g_0}. \quad (6.2-4)$$

Then, the specific impulse equals the ratio of the exhaust velocity and the standard surface gravity. The specific impulse attains its maximum value in the case that we expand to vacuum, i.e. $p_e = p_a = 0$. We then find

$$I_{sp_{max}} = \frac{V_L}{g_0}. \quad (6.2-5)$$

This value is a true propellant characteristic, as it is not dependent on pressure or expansion ratio. The direct measurement of the vacuum specific impulse is difficult, however; therefore one always should indicate the pressure ratio p_c/p_e and the ambient pressure if one lists values of the specific impulse. For solid propellants, I_{sp} attains values roughly between 200 s and 300 s. Modern liquid propellants exhibit higher values, somewhere between 250 s and 460 s. The values of I_{sp} for hybrid propellant combinations are, in general, a little higher than those for solids.

The *specific consumption* is defined as the ratio of propellant weight consumed and the total impulse delivered. Therefore, it is the inverse of the specific impulse:

$$c_s = \frac{1}{I_{sp}} = \frac{g_0 M_p}{\int_0^{t_b} F(t) dt}. \quad (6.2-6)$$

6.3 The volumetric specific impulse

The *volumetric specific impulse*, I_δ , is a measure for the influence of different propellants on the performance of a vehicle of fixed dimensions. It is defined as

$$I_\delta = \rho_p I_{sp}, \quad (6.3-1)$$

where ρ_p stands for the average density of the propellants.

In Chapters 11 and 12 it will be shown that ΔV_{id} , i.e. the velocity increment of a rocket vehicle in absence of drag and gravitational forces,

$$\Delta V_{id} = I_{sp} g_0 \ln \left(\frac{M_e + M_p}{M_e} \right), \quad (6.3-2)$$

is a very important performance parameter. In Eq. (6.3-2) M_p is the total

propellant mass, and M_e is the empty (final) mass of the vehicle. Then

$$M_p = \rho_p V_p, \quad (6.3-3)$$

where V_p is the volume available to store propellants. This volume is thought of as a fixed quantity, as we consider a rocket of fixed dimensions, and study the propellant influence on rocket performance. Now, if $M_p/M_e \ll 1$, we approximate the logarithm in Eq. (6.3-2) and find

$$\Delta V_{id} = I_{sp} g_0 \rho_p \frac{V_p}{M_e}. \quad (6.3-4)$$

This equation shows that for a rocket of fixed dimensions and $M_p/M_e \ll 1$, the ideal velocity increment, ΔV_{id} , depends on the volumetric specific impulse, I_{sp} . These small ratios of propellant mass over final mass are encountered in JATO (Jet Assisted Take-Off) rockets and small rocket weapons. The ratio $M_p/M_e \ll 1$ is one extreme, the other extreme is $M_p/M_e \gg 1$.

Then $\ln\left(1 + \frac{M_p}{M_e}\right)$ is not very sensitive anymore to changes in M_p/M_e .

Therefore, for very large ratios of propellant mass and final mass the specific impulse, I_{sp} is the prime factor that determines the performance parameter, ΔV_{id} . In many practical cases, M_p/M_e lies somewhere between these extremes. Then, both effects are noticeable. Thus, both the volumetric specific impulse and the specific impulse determine the performance. The case may as well be reversed: if a specified ideal velocity increment, ΔV_{id} , is required, which propellant combination yields the smallest vehicle possible? Solid propellants, which are much denser, exhibit higher volumetric specific impulses than liquid propellants. This is one of the reasons that solid propellants, in spite of their lower specific impulse, as compared to liquid propellants, find so much use.

6.4 The thrust coefficient

If the diverging part of the nozzle did not contribute to the thrust, and if there were no flow in the combustion chamber, the thrust delivered by the rocket motor in vacuum, F_0 , would be (Fig. 6.1),

$$F_0 = p_c A_r. \quad (6.4-1)$$

As the divergent section of the nozzle does contribute to the thrust, and as there is a flow in the combustion chamber, the thrust, F , differs from F_0 . The *thrust coefficient* is defined as the ratio of actual thrust and the thrust as defined by Eq. (6.4-1):

$$C_F = \frac{F}{p_c A_t}. \quad (6.4-2)$$

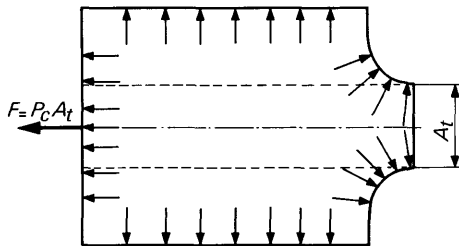


Fig. 6.1 The combustion chamber without the nozzle. The wall pressure is assumed constant all over the walls

With the Eqs. (5.1-15), (5.1-39) and (6.2-3), we find,

$$C_F = \lambda \Gamma \sqrt{\frac{2\gamma}{\gamma-1} \left[1 - \left(\frac{p_e}{p_c} \right)^{(\gamma-1)/\gamma} \right] + \left(\frac{p_e - p_a}{p_c} \right) \frac{A_e}{A_t}}. \quad (6.4-3)$$

In general, one will assume \$\lambda\$ unity. The expansion ratio, \$A_e/A_t\$, being only a function of the pressure ratio, \$p_e/p_c\$, and \$\gamma\$, (Eq. (5.1-41)), means that \$C_F\$ is a function of the pressure ratio, \$p_e/p_c\$, the ambient pressure, \$p_a\$, \$\gamma\$ and, \$p_c\$. If we have ideal expansion, i.e. \$p_e = p_a\$, the thrust, \$F\$, and therefore the thrust coefficient, \$C_F\$, reaches its maximum value (Section 5.1.5). In general, \$C_F\$ decreases with increasing values of \$\gamma\$ for the same expansion and pressure ratios. The maximum value of \$C_F\$ is called the *characteristic thrust coefficient*, and indicated as \$C_F^o\$. From Eq. (6.4-3), we obtain, taking \$\lambda = 1\$,

$$C_F^o = \Gamma \sqrt{\frac{2\gamma}{\gamma-1} \left[1 - \left(\frac{p_e}{p_c} \right)^{(\gamma-1)/\gamma} \right]} \quad (6.4-4)$$

In Fig. 6.2 \$C_F\$ and \$C_F^o\$ are plotted versus the expansion ratio, \$A_e/A_t\$, for various pressure ratios. The dotted region indicates where separation usually occurs. After separation has taken place (Section 5.2.1), thrust, and thrust coefficient remain approximately constant. The maximum value for \$C_F^o\$ occurs when \$p_e = p_a = 0\$ (expansion to vacuum),

$$C_{F_{max}}^o = \Gamma \sqrt{\frac{2\gamma}{\gamma-1}}. \quad (6.4-5)$$

The thrust coefficient can be used to compute a rocket's thrust, but also to determine the nozzle efficiency. To get an impression of the nozzle efficiency, one can determine experimentally the thrust coefficient according to Eq. (6.4-2) and compare this value with the theoretical thrust coefficient as determined by Eq. (6.4-3) or Fig. 6.2. The ratio of the experimental thrust coefficient and the theoretical one can be interpreted as a nozzle efficiency, \$\xi_F\$. From Eq. (5.2-1) and the foregoing reasoning it will be clear that

$$\xi_F = \frac{C_{F_{exp}}}{C_{F_{th}}}. \quad (6.4-6)$$

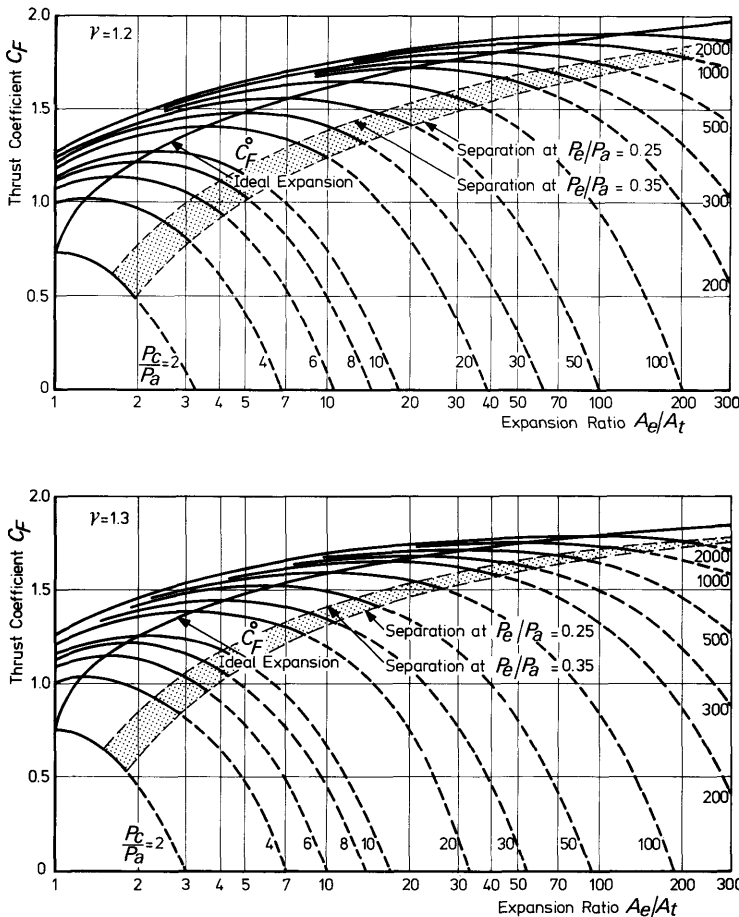


Fig. 6.2 The thrust coefficient versus the expansion ratio for various pressure ratios. (a) For $\gamma = 1.2$; (b) for $\gamma = 1.3$

6.5 The characteristic velocity

According to Eq. (6.4-2), the thrust, F , is

$$F = C_F p_c A_r \quad (6.5-1)$$

In the case of ideal expansion and again taking $\lambda = 1$, we also have, according to Eq. (6.2-3)

$$F = m V_e. \quad (6.5-2)$$

We may ask ourselves: what would the exhaust velocity be if the diverging

part of the nozzle does not contribute to the thrust, i.e. $C_F=1$? We will denote this exhaust velocity by c^* , and find

$$F = mc^* = p_c A_t, \quad (6.5-3)$$

from which follows

$$c^* = \frac{p_c A_t}{m}. \quad (6.5-4)$$

The quantity, c^* , is called the *characteristic velocity*, and we will show that it is a propellant property, which, as distinct from the specific impulse, is independent of pressure ratio. To see this, consider the mass flow through the nozzle, Eq. (5.1-39). Combination of this equation and Eq. (6.5-4) gives

$$c^* = \frac{1}{\Gamma} \sqrt{\frac{R_0 T_c}{m}}, \quad (6.5-5)$$

which is dependent only on chamber temperature and the properties of the combustion products. The theoretical value of c^* , as computed from Eq. (6.5-5), can be compared with the value determined by a test. The ratio of those two values is an indication of how efficiently the combustion process takes place within the rocket motor.

It follows immediately from Eq. (6.4-2) and Eq. (6.5-4) that

$$F = C_F c^* m. \quad (6.5-6)$$

We now have split the thrust into two contributing factors:

1. The thrust coefficient, C_F , which is a nozzle quality factor.
2. The characteristic velocity, c^* , which is a propellant and combustion quality factor.

This is indicated schematically in Fig. 6.3.

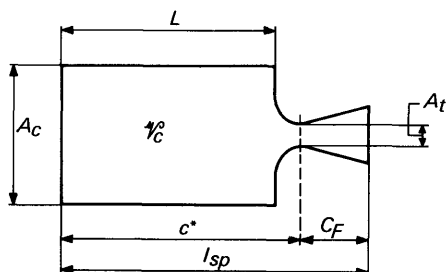


Fig. 6.3 The cylindrical combustion chamber, and the regions which are of importance for the characteristic velocity and the thrust coefficient

Directly related to the characteristic velocity is the *mass flow factor*, C_D , defined as

$$C_D = \frac{m}{p_c A_t} = 1/c^*. \quad (6.5-7)$$

The mass flow factor, C_D , can be computed theoretically from Eq. (6.5-5) by using the fact that $C_D = 1/c^*$, and determined experimentally according to Eq. (6.5-7). Comparing the experimental and theoretical values leads to

$$\xi_m = \frac{C_{D_{exp}}}{C_{D_{th}}} = \frac{c_{th}^*}{c_{exp}^*}, \quad (6.5-8)$$

where use is made of Eq. (5.2-3).

6.6 The effective exhaust velocity

Because Eq. (6.2-3) for the thrust of a rocket engine is not very convenient for analytical calculations, a simpler form, that avoids the pressure terms, is often used. One introduces the *effective exhaust velocity*, c , defined as

$$c = -\mathbf{F}/m. \quad (6.6-1)$$

From Eqs. (5.1-39) and (6.2-3) we can derive

$$c = V_e + \left(\frac{p_e - p_a}{p_c} \right) \frac{A_e}{A_t} \frac{\sqrt{RT_c}}{\Gamma}. \quad (6.6-2)$$

By use of the characteristic velocity, c^* , we may also write

$$c = V_e + \left(\frac{p_e - p_a}{p_c} \right) \frac{A_e}{A_t} c^*. \quad (6.6-3)$$

Combination of the Eqs. (6.5-6) and (6.6-1) yields

$$c = C_F c^*. \quad (6.6-4)$$

From Eqs. (6.6-2) and (6.6-3) it is clear that the effective exhaust velocity is dependent on the atmospheric pressure and thus will not be constant during a rocket's ascent. However, the exhaust velocity, V_e , is about constant and the contribution of the pressure thrust to the total thrust is small. Therefore, it is admissible in analytical approximations, to assume a constant effective exhaust velocity c . In that case, we find from the equation for the specific impulse, Eq. (6.2-2b),

$$I_{sp} = \frac{c}{g_0}. \quad (6.6-5)$$

6.7 Characteristic length and residence time

Consider a cylindrical combustion chamber with length, L , and cross-sectional area, A_c (Fig. 6.3). The volume of the converging part of the

nozzle is thought of as negligible as compared to the chamber volume, \mathcal{V}_c . In foregoing sections, we assumed the kinetic energy of the gas in the chamber small as compared to the total enthalpy. Let us now consider the gas velocity in the chamber. The steady-state continuity equation states for the mass flow

$$m = \rho_c V_c A_c = \rho_t V_t A_t. \quad (6.7-1)$$

Assuming a constant velocity in the chamber, the *residence time*, τ^* , that is the average time a particle will stay in the combustion chamber, follows from

$$\tau^* = \frac{L}{V_c} = \frac{\mathcal{V}_c}{V_c A_c}, \quad (6.7-2)$$

where L stands for the length of the chamber and \mathcal{V}_c for the chamber volume. Multiplication of the right-hand side of Eq. (6.7-2) with ρ_c/ρ_t and using the fact that the chamber mass flow equals the mass flow through the throat, Eq. (5.1-39) then leads to

$$\tau^* = \frac{\mathcal{V}_c}{A_t} \frac{1}{\Gamma \sqrt{RT_c}}. \quad (6.7-3)$$

The ratio of chamber volume to throat area is called the *characteristic length*, L^* , of a rocket motor and is defined, even in the case that the rocket motor is not cylindrical, as,

$$L^* = \frac{\mathcal{V}_c}{A_t}. \quad (6.7-4)$$

The characteristic length, L^* , is an important parameter in *combustion analysis* [1], and it also plays an important role in certain types of combustion instability analysis [2] which, however, is beyond the scope of this book. It should be emphasized that L^* is a constant for a liquid-propellant motor, but increases with time for solid- and hybrid-propellant motors because, owing to the propellant consumption, the chamber volume increases. It will be clear that if one wants to have a good utilization of the propellants, the whole combustion should take place within the combustion chamber. Therefore, the residence time, τ^* , should at least equal the time needed for vaporization and complete reaction of the propellants. For solid propellants, where the combustion [3, 4] is different from the combustion of liquid propellants [5], the residence time is usually large enough. By use of Eq. (6.5-5) we get a relation between residence time, characteristic velocity and characteristic length,

$$\tau^* = \frac{L^* c^*}{RT_c}. \quad (6.7-5)$$

References

- 1 Barrère, M., Jaumotte, A., Fraeijs de Veubeke, B. and Vandenkerckhove, J., (1960), *Rocket Propulsion*, Elsevier, Amsterdam, p. 398–403.
- 2 Strand, L. D. (1968), *Summary of a Study of the Low-pressure Combustion of Solid Propellants*, Techn. Rpt. 32-1242, Jet Propulsion Laboratory, California Institute of Technology, Pasadena.
- 3 Dadieu, A., Damm, R. and Schmidt, E.W. (1968), *Raketentreibstoffe*, Springer, Vienna, p. 160–164.
- 4 Price, E. W. and Culick, F. E. C. (1969), *Combustion of Solid Rocket Propellants*, AIAA professional study series, New York.
- 5 Harrje, D. T. (ed.) (1972), *Liquid Propellant Rocket Combustion Instability*, NASA SP-194, Washington, p. 74–100.

7 Thermochemistry of the Rocket Motor

In Chapter 5 we discussed methods to determine thrust and exhaust velocity from the chamber conditions, i.e. the chamber temperature, T_c , the mean molecular weight of the combustion products, M , and the ratio of specific heats, γ . These quantities were supposed to be known. However, in general, we only know the propellant combination used, and we have to determine the composition and temperature of the combustion products in the chamber at a prescribed chamber pressure.

Moreover, we assumed the ratio of specific heats and the composition of the combustion products constant during the expansion through the nozzle. In real rocket motors, there will be deviations from this idealized situation due to *dissociation and recombination, variation of specific heats with temperature, condensation, incomplete reactions, and ionization*. Generally, the first two effects dominate.

Because of dissociation and recombination, the molecular weight of the combustion products, as well as the ratio of specific heats, is not constant. Moreover, dissociation and recombination are attended with large heat absorptions or releases.

Even if no reactions take place in the nozzle, γ will vary during expansion, as the specific heats depend on the temperature.

Because of condensation, which involves heat releases, the density of the combustion products increases. Other effects of two-phase flow have been discussed in Section 5.2.

In general, the residence time of the species in the combustion chamber is rather short, usually less than a few milliseconds. The time required for the formation of a chemical substance may be much larger, and such a substance may be formed only in small quantities or not at all.

Ionization becomes an important factor at temperatures in the order of 5000 K. As in chemical rockets the temperature does not exceed 4000 K, ionization is of minor importance and is not treated in this chapter.

7.1 Concepts of chemical thermodynamics

7.1.1 General definitions

Molar quantities. In chemistry and physics, it is convenient to base the extensive quantities, such as enthalpy, entropy, etc., on a basic amount of matter. The basic amount of matter to be used as unit is the mol (mole in

older notations). One mol of matter contains the same number of particles (molecules, atoms, etc.) as there are atoms in exactly 12 g of the isotope ^{12}C . (In older definitions hydrogen and oxygen have been used as a reference substance). This number is called *Avogadro's number*, N_A , Table T.1. The molecular weight, M , of a substance is defined as the mass of one mol of that substance. It follows from this definition that the molecular weight of the isotope ^{12}C is 12 g/mol. Extensive quantities, based on the mol (kmol) instead of the gram (kg) are called *molar quantities*.

Instead of expressing the amount of chemicals considered in mols, we may as well express them in mols per unit volume. In that case we speak of *concentration*.

Compounds. A molecule of a *compound* consists of one or more atoms of one or more elements, i.e. H as well as NH_4ClO_4 are regarded as compounds.

The reaction equation. Consider a system initially containing the substances A_r . We observe that other substances A_p are formed and express this by the reaction equation

$$\sum_r n_r A_r \rightarrow \sum_p n_p A_p; \quad r = 1, 2, \dots, R \quad \text{and} \quad p = R + 1, R + 2, \dots, P. \quad (7.1-1)$$

The substances A_r are called the *reactants*, and A_p the *products*. The coefficients n_j indicate the concentration or number of mols of A_j , where $j = 1, 2, \dots, P$. An example may clarify this. Consider the reaction $2\text{H}_2 + \text{O}_2 \rightarrow 2\text{H}_2\text{O}$. Here H_2 and O_2 are the reactants, H_2O is the product, and 2, 1, and 2, respectively, are the concentrations or the number of mols of reactants and products. The equation expressing the formation of products from the reactants is called the *forward reaction*. Another reaction is usually going on simultaneously: the *back reaction*

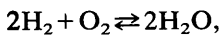
$$\sum_r n_r A_r \leftarrow \sum_p n_p A_p, \quad (7.1-2)$$

describing the conversion of products into reactants. The Eqs. (7.1-1) and (7.1-2) can be combined to give

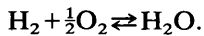
$$\sum_r n_r A_r \rightleftharpoons \sum_p n_p A_p. \quad (7.1-3)$$

Chemical equilibrium. If the concentrations of products and reactants remain constant, the two reactions (forward and back) are in equilibrium with each other. We define the *state of chemical equilibrium* as the state in which there is no spontaneous tendency of the system to change its internal composition, either by diffusion or by chemical reactions.

Stoichiometric coefficients. If it is conceivable that all reactants in Eq. (7.1-3) disappear to form products, n_r and n_p are called *stoichiometric coefficients*, which will be indicated as ν_r and ν_p . In the equation

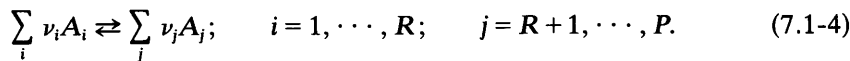


the stoichiometric coefficients are 2, 1 and 2. However, we could write as well

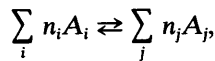


In this case, the stoichiometric coefficients are 1, $\frac{1}{2}$ and 1. We thus note that the important thing about the stoichiometric coefficients is their ratio, and not their magnitude. A mixture, such that the concentrations of the various species are proportional to the respective stoichiometric coefficients, is called a *stoichiometric mixture*.

Consider a system initially containing n_{i_0} mols of A_i . These substances, A_i , react with each other to form products, A_j , according to the stoichiometric equation



The numbers of mols of the substances A_i and A_j actually present are indicated by n_i and n_j , respectively. If no chemical equilibrium is reached yet, the reaction



will proceed to the right according to Eq. (7.1-4) in such a way that

$$\frac{dn_j}{\nu_j} = -\frac{dn_i}{\nu_i} = d\xi \quad (7.1-5)$$

and ξ is called the *extent of reaction*.

In this case we assumed that the reaction was progressing to the right, thus $dn_i < 0$. If the reaction progresses to the left and the substances A_j are disappearing, $dn_j < 0$. The Eq. (7.1-5) states that the change in concentration or number of mols of chemical substances during a reaction is proportional to their respective stoichiometric coefficients.

Heat of reaction. The first law of thermodynamics (Appendix 3) for systems involving only compression and expansion work, and thus applicable to the rocket motor, states:

$$dQ = dE + p \, dV, \quad (7.1-6)$$

i.e. the heat input dQ into the system balances the increase dE of internal energy and the work, $p \, dV$, performed on the surroundings. The enthalpy,

H , is defined as

$$H = E + pV, \quad (7.1-7)$$

and the first law can also be written as

$$dQ = dH - Vdp. \quad (7.1-8)$$

Now, consider a chemical reaction taking place at constant pressure and at a specified temperature. The index o indicates the state before the reaction, the index e the state after the reaction. The heat put into the system during the reaction is denoted by Q . According to Eq. (7.1-8), we find

$$Q = H_e - H_o = \Delta H. \quad (7.1-9)$$

Here ΔH is called the *heat change at constant pressure*, or commonly *the heat of reaction*.

The reaction is called *endothermal* if $Q > 0$, and *exothermal* if $Q < 0$. A combustion process, in general, generates heat and thus is exothermal.

If one considers reactions taking place at constant volume and a specified temperature, the heat Q put into the system during the reaction, according to Eq. (7.1-6) is

$$Q = E_e - E_o = \Delta E, \quad (7.1-10)$$

where ΔE is called the *heat change at constant volume*.

There is a direct relationship between the changes in enthalpy and internal energy. Consider a reaction at constant pressure. The volumes of the system before and after the reaction are indicated by V_o and V_e , respectively. It then immediately follows from Eq. (7.1-7) that

$$\Delta H = \Delta E + p(V_e - V_o), \quad (7.1-11)$$

For reactions involving only liquids or solids, the term $p(V_e - V_o)$, in general, is negligible small as compared to ΔE . For reactions involving gases too, this is not the case. The ideal gas law states

$$pV = nR_0T, \quad (7.1-12)$$

where n is the number of gaseous mols in the total volume V . A reaction, taking place at constant pressure and constant temperature, involving ideal gases thus yields

$$p(V_e - V_o) = (n_e - n_o)R_0T = \Delta nR_0T,$$

or, with Eq. (7.1-11),

$$\Delta H = \Delta E + \Delta nR_0T. \quad (7.1-13)$$

The amount of propellants that enter the combustion chamber of a rocket motor during the time interval Δt is $m\Delta t$. After combustion has taken place, the volume of this amount of matter has increased considerably, as, in general, liquids or solids are converted into gases. The pressure in the

combustion chamber has remained the same, all the time. Therefore, the combustion in a rocket motor essentially is a constant pressure reaction. In the following, we therefore will restrict ourselves to constant pressure reactions.

Hess' law. A direct consequence of the first law of thermodynamics, and H and E being state variables, is that the heat change is the same whether the reaction takes place in one or in several steps. This is known as *Hess' law*, or the *law of constant heat summation*.

Kirchhoff's equation. The heat of reaction depends on the temperature at which the reaction takes place. For a constant pressure reaction, we have

$$\Delta H(T) = H_e(T) - H_o(T), \quad (7.1-14)$$

where the enthalpies are evaluated at the temperature T . Differentiating both sides with respect to temperature leads to

$$\left(\frac{\partial \Delta H}{\partial T}\right)_p = \left(\frac{\partial H_e}{\partial T}\right)_p - \left(\frac{\partial H_o}{\partial T}\right)_p,$$

and as $(\partial H/\partial T)_p = C_p$, we have

$$\left(\frac{\partial \Delta H}{\partial T}\right)_p = C_{p_e} - C_{p_o} = \Delta C_p, \quad (7.1-15)$$

This result is known as *Kirchhoff's equation*. Integration leads to

$$\Delta H(T_2) - \Delta H(T_1) = \int_{T_1}^{T_2} \Delta C_p dT. \quad (7.1-16a)$$

In those cases where it is admissible to assume ΔC_p constant, this equation simplifies to

$$\Delta H(T_2) - \Delta H(T_1) = \Delta C_p (T_2 - T_1). \quad (7.1-16b)$$

In general, the heats of reaction at different temperatures are related by

$$\Delta H(T_2) = \Delta H(T_1) + [H(T_2) - H(T_1)]_e - [H(T_2) - H(T_1)]_o. \quad (7.1-16c)$$

For constant volume reactions, identical results hold if one replaces H by E and C_p by C_v , as the reader can verify himself.

Standard heat of formation. The heats of reaction can be calculated theoretically, or be determined by experiments. It would be convenient, of course, to have these heats of reaction in tabular form. It is, however, not possible to list all possible heats of reactions for a certain substance, as it may be formed in infinitely many different ways. Besides, the heats of reaction depend on the state of aggregation of the products and reactants, the temperature and the number of mols involved. As a result of Hess' law, however, it suffices to list the heat of reaction for the formation of one mol

of a substance from its elements, at a certain reference temperature, while we take the elements and the products in a *standard reference state*. This heat of reaction is called the standard heat of formation, and is denoted by ΔH_f° . The standard reference state for a solid or a liquid is its most stable state at a certain specified temperature and a pressure of 0.101325 MPa (1 atm). For gases, it is convenient and customary to take the standard reference state as the (hypothetical) ideal gas condition at a certain specified temperature and at a pressure of 0.101325 MPa (1 atm). To indicate that a thermodynamic quantity corresponds to the standard reference state, the superscript $^\circ$ is used; so we write H° , E° , etc. One finds the heats of formation listed in thermochemical tables [1, 2, 3]. From its definition, it follows that $\Delta H_f^\circ = 0$ for all elements. The reference temperature at which ΔH_f° is listed, is mostly 0 K or 298.15 K. It should be mentioned that, while the above definitions are the most common ones, some tables use other definitions.

Just like potential functions, H and E are fully determined, except for a constant. Often, this constant is taken zero for the elements, either at 0 K or at 298.15 K. For a particular substance, the values of the *absolute enthalpy*, H° , may differ from table to table, depending on the reference temperature and the assigned value of the numerical constant. In general, the tables also list the *sensible enthalpy*, $H^\circ(T) - H^\circ(0)$. These values will be the same for all tables.

From the definition of the standard heat of formation and Eq. (7.1-14) it immediately follows that

$$\Delta H^\circ(T) = \sum [n \Delta H_f^\circ(T)]_e - \sum [n \Delta H_f^\circ(T)]_o, \quad (7.1-17)$$

where n indicates the number of mols considered and the indices e and o indicate the final and initial state respectively.

If the heats of formation are given at a reference temperature T_1 , while the heat of reaction is evaluated at a temperature T_2 , and the reactants initially had the temperature T_3 , one finds

$$\begin{aligned} \Delta H^\circ(T_2) = & \sum n_e [\Delta H_f^\circ(T_1) + (H^\circ(T_2) - H^\circ(0)) - (H^\circ(T_1) - H^\circ(0))]_e \\ & - \sum n_o [\Delta H_f^\circ(T_1) + (H^\circ(T_3) - H^\circ(0)) - (H^\circ(T_1) - H^\circ(0))]_o, \end{aligned} \quad (7.1-18a)$$

where the equation is written in sensible enthalpies. In the case that one uses absolute enthalpies, Eq. (7.1-18a) can be written as

$$\Delta H^\circ(T_2) = H_e^\circ(T_2) - H_o^\circ(T_3). \quad (7.1-18b)$$

If all heat is used to heat up the products, i.e. $\Delta H^\circ(T_2) = 0$, then T_2 is called the *adiabatic flame temperature* or *combustion temperature*.

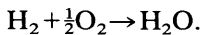
A few examples may illustrate how the above derived equations can be used to compute the heat of reaction, or the adiabatic flame temperature. First consider the formation of water from its elements at 500 K. We want

Table 7.1 Sensible and absolute enthalpies for H₂O, H₂ and O₂

Temperature	H ₂ O(gas)		H ₂ (gas)		O ₂ (gas)	
	H°(T) – H°(0) (kJ/mol)	H°(T) (kJ/mol)	H°(T) – H°(0) (kJ/mol)	H°(T) (kJ/mol)	H°(T) – H°(0) (kJ/mol)	H°(T) (kJ/mol)
(K)						
298.15	9.9065	57.3158	8.4676	290.5399	8.6805	17.2000
500	16.8427	64.2520	14.3490	296.4236	14.7645	23.2840
2700	118.6197	166.0291	85.1866	368.2589	94.8766	103.3963
2800	123.9543	171.3637	89.8342	371.9066	98.8223	107.3418
2900	129.3178	176.7271	93.5061	375.5784	102.7883	111.3078

$$(\Delta H_f^\circ(298.15))_{H_2O} = -241.8264 \text{ kJ}; H^\circ(298.15)_{H_2O,\text{Liquid}} = 13.3001 \text{ kJ/mol}$$

to find the heat of reaction and will use the following reaction equation:



From Table 7.1 we see $(\Delta H_f^\circ(298.15))_{H_2O} = -241.8264 \text{ kJ}$. So, using sensible enthalpies, Eq. (7.1-18a) with $T_3 = T_2 = 500 \text{ K}$ yields

$$\Delta H^\circ(500) = [-241.8264 + 16.8427 - 9.9065] - [14.3490 - 8.4676] - \frac{1}{2}[14.7645 - 8.6805] = -243.8136 \text{ kJ}.$$

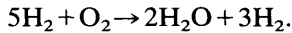
Using absolute enthalpies, Eq. (7.1-18b) with $T_3 = T_2 = 500 \text{ K}$ yields

$$\Delta H^\circ(500) = 64.2520 - 296.4236 - \frac{1}{2} \times 23.2840 = -243.8136 \text{ kJ}.$$

If a phase transition takes place, i.e. a transition of liquid to gas, etc., this is accompanied by a change in enthalpy: the heat of transition, also denoted by ΔH_f° . The heat of transition at a temperature T can be determined with Eq. (7.1-18a) or Eq. (7.1-18b) where one phase of the substance is regarded as reactant and the other one as product. For example, for the transition of water vapor to water, at 298.15 K,

$$\Delta H_f^\circ = H_{H_2O,\text{gas}}^\circ - H_{H_2O,\text{liquid}}^\circ = 57.3158 - 13.3001 = 44.0157 \text{ kJ}.$$

Let us now compute the flame temperature of a mixture of gaseous hydrogen and gaseous oxygen, at an initial temperature of 298.15 K, which reacts according to



Using sensible enthalpies, we have according to Table 7.1,

$$2 \times [-241.8264 + (H^\circ(T_2) - H^\circ(0))_{H_2O} - 9.9065] + 3 \times [(H^\circ(T_2) - H^\circ(0))_{H_2} - 8.4676] = 0.$$

There is no other contribution from H₂ and O₂ because $T_1 = T_3$ and the

heat of formation for the elements equals zero. So, we are left with

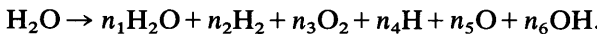
$$2 \times [H^\circ(T_2) - H^\circ(0)]_{H_2O} + 3 \times [H^\circ(T_2) - H^\circ(0)]_{H_2} = 528.8686 \text{ kJ.}$$

By interpolation in Table 7.1 we find for the combustion temperature, $T_2 = 2853 \text{ K}$. Using absolute enthalpies we have

$$2 \times (H^\circ(T_2))_{H_2O} + 3 \times (H^\circ(T_2))_{H_2} = 5 \times 290.5399 + 17.200 = 1469.6995 \text{ kJ,}$$

and by interpolation we find $T_2 = 2852 \text{ K}$.

At these elevated temperatures, however, another phenomenon takes place: *dissociation*. Compounds will partially break up into electrically-neutral fractions called *radicals*. Water, for instance, may break up according to the reaction



The last three species in this equation are the radicals mentioned. As dissociation is a highly endothermal process, the flame temperature may drop much below the value as computed by the above method. In rocket motors, the combustion temperatures are so high that the effects of dissociation cannot be ignored and we will deal with this in the next section. The opposite of dissociation is *recombination*. This phenomenon is important, for determining the performance of a rocket motor, as it may take place in the nozzle. Thermodynamic properties of radicals are, like those for compounds, listed in thermochemical tables.

7.1.2 Chemical equilibrium

The state of chemical equilibrium is defined in Section 7.1.1. In this section we will discuss thermodynamic relationships for chemical equilibrium reactions.

The second law of thermodynamics states for a change between state 1 and state 2:

$$S_2 - S_1 \geq \int_1^2 \frac{dQ}{T}. \quad (7.1-19)$$

As for an isolated system $dQ = 0$, the *entropy*, S , will increase until it has reached its maximum value for that system. In the state of equilibrium, where no *irreversible processes* take place

$$S = S_{max}. \quad (7.1-20)$$

Combining the first and second law of thermodynamics for a system at constant temperature yields

$$S_2 - S_1 \geq \frac{1}{T} \int_1^2 (dH - \gamma dp). \quad (7.1-21)$$

If the pressure is also kept constant, we find

$$H_2 - TS_2 \leq H_1 - TS_1.$$

Now the *Gibbs free energy*, F , (also often denoted by G and often called the *free enthalpy*) is defined as

$$F = H - TS, \quad (7.1-22)$$

and we may also write

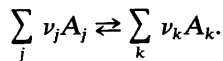
$$F_2 \leq F_1.$$

In the state of equilibrium the free energy reaches its minimum value $F = F_{\min}$. The state of equilibrium for a system at constant pressure and temperature thus can be characterized by

$$(dF)_{p,T} = d(H - TS)_{p,T} = 0. \quad (7.1-23)$$

As we will consider equilibrium reactions at constant pressure and temperature, this is the criterion to be used.

Consider the equilibrium reaction



Denoting the molar free energy of the species i by F_i , we have

$$F = \sum_i n_i F_i, \quad (7.1-24)$$

The reader is warned that this molar free energy is to be evaluated at the *partial pressure*, p_i , of the species i . Now, if we consider the change in free energy of one mol of a substance, we have for a reversible process at constant temperature,

$$dF = dH - T dS = \mathcal{V} dp.$$

It is customary to relate the free energy to the free energy in the standard state, i.e. at a reference pressure, p_o , of 0.101325 MPa. Thus

$$F - F^\circ = \int_{p_o}^p \mathcal{V} dp. \quad (7.1-25a)$$

For solids and liquids, the volume of one mol usually is very small, and is hardly sensitive to changes in pressure. Therefore, one can approximate the free energy change for solids and liquids by

$$F(p, T) - F^\circ(T) = 0, \quad (7.1-25b)$$

or

$$(dF)_T = 0. \quad (7.1-25c)$$

For ideal gases, this is not the case, there we find

$$F - F^\circ = \int_{p_o}^p \frac{R_0 T}{p} dp = R_0 T \ln(p/p_o). \quad (7.1-26)$$

As we will often deal with the pressure ratio p/p_o , we will use the notation $P = p/p_o$, and if we specifically denote a species i , we indicate the ratio of partial pressure and reference pressure as

$$P_i = p_i/p_o.$$

Hence, in Eq. (7.1-24), the molar free energy, F_i , stands for

$$F_i = F_i^\circ(T) + R_0 T \ln P_i. \quad (7.1-27)$$

Now, the condition for chemical equilibrium was, Eq. (7.1-23)

$$(dF)_{p,T} = \sum_i [n_i dF_i + F_i dn_i]_{p,T} = 0. \quad (7.1-28)$$

As $F_i^\circ(T)$ is a function of the temperature only, we find that

$$\left(\sum_i n_i dF_i \right)_{p,T} = R_0 T \sum_i \left(\frac{n_i}{p_i} dp_i \right)_{p,T}.$$

According to *Dalton's law*,

$$p = \sum_i p_i, \quad (7.1-29)$$

and if we consider a mixture of ideal gases we have

$$p_i \mathcal{V} = n_i R_0 T, \quad (7.1-30)$$

for the species i , and

$$p \mathcal{V} = \sum_i n_i R_0 T, \quad (7.1-31)$$

for the whole mixture. So

$$\frac{p_i}{n_i} = \frac{p}{\sum n_i}. \quad (7.1-32)$$

Hence,

$$\sum_i \left(\frac{n_i}{p_i} dp_i \right)_{p,T} = \frac{\sum n_i}{p} \left(\sum_i dp_i \right)_{p,T} = 0. \quad (7.1-33)$$

Inserting the result that $(\sum_i n_i dF_i)_{p,T} = 0$ into Eq. (7.1-28), the condition for chemical equilibrium, leads to

$$\sum_i (F_i dn_i)_{p,T} = 0. \quad (7.1-34)$$

Now, according to Eq. (7.1-5) we have for the products, k ,

$$dn_k = + \nu_k d\xi \quad (7.1-35a)$$

and for the reactants, j ,

$$dn_j = -\nu_j d\xi, \quad (7.1-35b)$$

where ν_k and ν_j denote the stoichiometric coefficients of the reaction. So the condition for chemical equilibrium at constant pressure and temperature is, using Eq. (7.1-27) for the molar free energy,

$$\sum_k \nu_k F_k^\circ - \sum_j \nu_j F_j^\circ = -R_0 T \left[\sum_k \nu_k \ln P_k - \sum_j \nu_j \ln P_j \right], \quad (7.1-36)$$

or

$$\sum_k \nu_k F_k^\circ - \sum_j \nu_j F_j^\circ = -R_0 T \ln \left(\frac{\prod_k P_k^{\nu_k}}{\prod_j P_j^{\nu_j}} \right). \quad (7.1-37)$$

The *equilibrium constant*, K_p , is defined as

$$K_p = \frac{\prod_k P_k^{\nu_k}}{\prod_j P_j^{\nu_j}}. \quad (7.1-38)$$

As the standard free energy, F_i° , and the stoichiometric coefficients, ν_i , are independent of the pressure at which the reaction takes place, it follows that K_p is only a function of the temperature, T , and not of the pressure, p . If $\alpha \nu_i$ instead of ν_i were taken as stoichiometric coefficients, the equilibrium constant, K_p , would be raised to the power α .

As for the heat of formation, we have only to know the K_p for the formation of one mol of compound from its elements either in their standard reference state or from atomic gases at 0.101325 MPa. This equilibrium constant is indicated as K_{pf} and called the *equilibrium constant of formation*. The K_{pf} 's are listed in thermodynamic reference tables [1, 2, 3]. In general, values for $\log_{10} K_{pf}$ are listed as this is advantageous for numerical work. The different definitions of K_{pf} will lead to different numerical values. Therefore, one should always check the definitions in the tables used. The numerical values of K_{pf} are determined from the change in free energy, Eq. (7.1-37). The change in free energy can be obtained from spectroscopic data [4] or statistical calculations [5]. The equilibrium constant for a specific reaction can be obtained by a suitable combination of the K_{pf} 's.

In practice, one often prefers to use the number of mols considered, n_i , or the mol fractions, $n_i/\sum_i n_i$, instead of the partial pressures. Using the relations $p_i = n_i p/N$, where $p = \sum_i p_i$, and $N = \sum_i n_i$, one may write for the equilibrium constant

$$K_p = \left(\frac{P}{N} \right)^{\sum_k \nu_k - \sum_j \nu_j} \times \frac{\prod_k n_k^{\nu_k}}{\prod_j n_j^{\nu_j}}. \quad (7.1-39)$$

The equilibrium constant, K_n , in terms of the number of mols considered, is defined as

$$K_n = \frac{\prod_k n_k^{\nu_k}}{\prod_j n_j^{\nu_j}}. \quad (7.1-40)$$

It was found that K_p is only a function of the temperature, T , at which the reaction takes place. However, only in those cases that $\sum_j \nu_j = \sum_k \nu_k$, a pressure independent reaction, this holds for K_n too, as is easily seen from the Eqs. (7.1-39) and (7.1-40).

Large values of K_p indicate that the reaction is accompanied by a significant decrease in the free energy and the forward reaction is favored. Values of $K_p < 1$ indicate that the back reaction is favored. If one deals with more reactions taking place simultaneously, as is usually the case, the relative magnitudes of the K_{pf} 's are an indication of which of the species will dominate. The reaction with the largest K_{pf} will yield the dominating species.

Differentiating $\ln K_p$ with respect to the temperature yields

$$\left(\frac{\partial \ln K_p}{\partial T} \right)_p = -\frac{1}{R_0} \frac{\partial}{\partial T} \left(\frac{\Delta F^\circ}{T} \right) = -\frac{1}{R_0 T} \left[\frac{\partial \Delta F^\circ}{\partial T} - \frac{\Delta F^\circ}{T} \right]_p. \quad (7.1-41)$$

From Eq. (7.1-23) follows for an equilibrium reaction at constant temperature

$$T \left(\frac{\partial \Delta S^\circ}{\partial T} \right)_p = \left(\frac{\partial \Delta H^\circ}{\partial T} \right)_p.$$

With Eq. (7.1-22) we then find

$$\left(\frac{\partial \Delta F^\circ}{\partial T} \right)_p = -\Delta S^\circ,$$

and so

$$\left(\frac{\partial \ln K_p}{\partial T} \right)_p = \frac{\Delta H^\circ}{R_0 T^2}, \quad (7.1-42)$$

where ΔH° , ΔF° and ΔS° stand for the changes in standard enthalpy, free energy and entropy as a result of the reaction. This equation, due to van't Hoff, is known as *the van't Hoff reaction isobar*. For exothermal reactions: $\Delta H^\circ < 0$ and $\ln K_p$ will decrease with increasing temperature. Integration of Eq. (7.1-42) yields

$$\ln \left(\frac{K_p(T_2)}{K_p(T_1)} \right) = \frac{1}{R_0} \int_{T_1}^{T_2} \frac{\Delta H^\circ}{T^2} dT. \quad (7.1-43)$$

For small temperature intervals over which ΔH° may be assumed constant, Eq. (7.1-43) can be approximated by

$$\ln \left(\frac{K_p(T_2)}{K_p(T_1)} \right) = -\frac{\Delta H^\circ}{R_0} \left[\frac{1}{T_2} - \frac{1}{T_1} \right]. \quad (7.1-43a)$$

Equilibrium reactions involving non-ideal gases, liquids and solids. In the rocket motor condensed (mostly solid) particles may be present. Examples of substances that may be present as condensed phases are carbon (C) or aluminum oxide, (Al_2O_3). Exact integration of the term, $\mathcal{V}dp$, in Eq. (7.1-25a) for non-ideal gases, liquids or solids, would lead to complicated expressions. Lewis [6] therefore introduced the concept of *fugacity*, f , which has the dimension of a pressure. For our purpose it is sufficient to note that the fugacity is defined by the relation

$$\ln \frac{f_2}{f_1} = \frac{1}{R_0 T} \int_{p_1}^{p_2} \mathcal{V} dp, \quad (7.1-44)$$

where the temperature, T , is constant. So for non-ideal gases, liquids, or solids, one has

$$F_i = F_i^\circ + R_0 T \ln f_i/f_i^\circ. \quad (7.1-45)$$

Here f° is the *fugacity in the standard state*. For the gaseous phases the fugacity in the standard state equals the standard reference pressure, i.e. $f^\circ = p_o = 0.101325 \text{ MPa}$. For the liquid and solid phases the fugacity of the standard state, in general, will have a different value, usually $f^\circ < 0.101325 \text{ MPa}$ [7]. The ratio f_i/f_i° is called the *activity*, a_i . The fugacities can be thought of as 'corrected' or 'active' pressures [8]. For an ideal gas $f_i \equiv p_i$, while for other gases

$$\lim_{p_i \rightarrow 0} f_i/p_i = 1 \quad \text{and} \quad f^\circ = p_o.$$

The fugacity can be used for the treatment of condensed phases. Consider two phases of the same substance being in equilibrium with each other. We assume one phase to be gaseous. The work involved in the quasi-steady, isothermal and isobaric process of evaporation, condensation or sublimation, follows from

$$(dW)_{T,p} = T dS - dE = p d\mathcal{V}.$$

or

$$d(E + p\mathcal{V} - TS)_{p,T} = dF = 0.$$

Therefore, the free energy of both phases is the same. If we replace the pressure ratio, P_i , in Eq. (7.1-37) by the activity, a_i , we conclude, as the free energy is the same in both phases, that

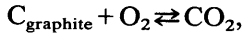
$$a_c^v = a_g^v, \quad (7.1-46)$$

where the index c indicates the condensed phase and g the gas phase. In many cases $\nu_c = \nu_g$ and thus $a_c = a_g$.

We mentioned already that the free energy for liquids and solids is approximately independent of pressure, i.e. $F = F^\circ$. With the concept of activity, Eq. (7.1-30) becomes

$$F_i - F_i^\circ = R_0 T \ln a_i = 0.$$

Thus, the activity of the condensed phases is unity, and therefore the fugacity equals the fugacity in the standard state. If one now considers the reaction



the equilibrium constant, involving the condensed graphite phase, becomes

$$K_{pf} = \frac{P_{\text{CO}_2}}{P_{\text{O}_2} \cdot a_{\text{C}}} = \frac{P_{\text{CO}_2}}{P_{\text{O}_2}},$$

where tacitly is assumed that both O_2 and CO_2 behave like ideal gases.

To determine, whether or not condensed phases will be present, one first assumes that no condensation has taken place. If the calculated partial pressure exceeds the vapor pressure, condensation must have taken place.

7.2 Combustion in the rocket motor

In order to determine either the performance of a rocket motor for a given propellant combination and mass flow, or the geometry of such a motor for a given chamber pressure, exit pressure, mass flow and mixture ratio, we will assume that the composition of the combustion products is according to chemical equilibrium. The theory, presented in Section 7.1.2, enables us to determine the composition and the adiabatic flame temperature.

In principle, one would have to consider the formation of all possible species. However, some of these species will have such low K_{pf} 's that the presence of these species can be ignored. For instance, in a $\text{H}_2\text{-O}_2$ rocket motor the amount of H_2O_2 present, will be negligible. In addition, we will make the following assumptions:

1. The chamber conditions are uniform.
2. Steady-state operation.
3. In the combustion chamber, the kinetic energy of the combustion products is negligible.
4. In the nozzle, there exist surfaces of constant properties.
5. Condensed particles have the same velocity and temperature as the surrounding gaseous species.
6. There are no heat losses.

Actually, one might account for heat losses by assuming enthalpy losses.

In practice, the assumption that we have an equilibrium composition in the chamber means that the *reaction times* are small as compared to the residence time in the chamber. This may not always be the case; for instance, if one has a motor with a small characteristic length, L^* .

For a fuel rich mixture, containing carbon- and oxygen-compounds, the theory may predict the formation of solid carbon according to the reaction



As the *rate of formation* of carbon is rather slow, less carbon may actually be present than predicted by equilibrium considerations.

One of the combustion products of hydrazine motors is ammonia. Now, NH_3 will dissociate according to the reaction



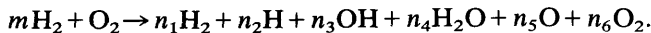
The *dissociation rate* of ammonia being small, an excess of ammonia may be present over that predicted by equilibrium calculations. Whether or not the theory of equilibrium reactions is applicable to certain products depends on the reaction rates of the species under consideration and the chamber geometry. Unfortunately, there does not exist, at the present time, a set of standard reaction rates, analogous to the sets of thermodynamic properties of species, and the rate constants have to be compiled from various sources.

For the flow through the nozzle we have to include the kinetic energy of the gases and we will have to make specific assumptions concerning the behavior of the combustion products.

7.2.1 The composition in the combustion chamber and the adiabatic flame temperature

To compute the adiabatic flame temperature and the composition of the combustion products, the following equations are available. From the known mixture ratio of the propellants we can write down the equations for the *conservation of elements*. If e elements are involved, this yields e equations. If there are c compounds under consideration, there are $c - e$ independent equations for the equilibrium constants of formation. Finally, there is the energy equation, Eq. (7.1-18a) or Eq. (7.1-18b) with $\Delta H^\circ(T) = 0$. So, we have $c + 1$ equations for the number of mols, $n_1 \cdots, n_c$, and the adiabatic flame temperature, T_f . In general, these equations cannot be solved analytically, and one must resort to numerical techniques [9, 10, 11, 12].

As an example, we will give the equations for a rocket motor using H_2 and O_2 as propellants. The combustion products will be: H_2 , H , OH , H_2O , O and O_2 . The reaction equation can be written as



The equations for the conservation of elements are

$$2m = 2n_1 + n_2 + n_3 + 2n_4,$$

$$2 = n_3 + n_4 + n_5 + 2n_6.$$

We assume the chamber pressure being known. Then it is convenient to write the equilibrium constants of formation in terms of the chamber pressure, p_c , and the number of mols n_1, \dots, n_6, N , where

$$N = \sum_{i=1}^6 n_i,$$

may be regarded as an additional unknown. The equilibrium constants of formation for this system are

$$2\text{H} + \text{O} \rightleftharpoons \text{H}_2\text{O}; \quad K_{pf_1} = \frac{n_4}{n_2^2 n_5} \left(\frac{N}{P_c} \right)^2,$$

$$\text{H} + \text{O} \rightleftharpoons \text{OH}; \quad K_{pf_2} = \frac{n_3}{n_2 n_5} \left(\frac{N}{P_c} \right),$$

$$2\text{H} \rightleftharpoons \text{H}_2; \quad K_{pf_3} = \frac{n_1}{n_2^2} \left(\frac{N}{P_c} \right),$$

$$2\text{O} \rightleftharpoons \text{O}_2; \quad K_{pf_4} = \frac{n_6}{n_5^2} \left(\frac{N}{P_c} \right),$$

where $P_c = p_c/p_o$, the ratio of chamber pressure to reference pressure. Finally, we have the energy equation

$$mH^\circ(T_r)_{\text{H}_2} + H^\circ(T_r)_{\text{O}_2} = n_1 H^\circ(T_f)_{\text{H}_2} + n_2 H^\circ(T_f)_{\text{H}} + n_3 H^\circ(T_f)_{\text{OH}} + n_4 H^\circ(T_f)_{\text{H}_2\text{O}} + n_5 H^\circ(T_f)_{\text{O}} + n_6 H^\circ(T_f)_{\text{O}_2}.$$

Here, T_r is the temperature at which the respective propellants, H_2 and O_2 , enter the combustion chamber, and T_f is the adiabatic flame temperature, which is to be determined. So, now we have the complete set of equations for the composition and the adiabatic flame temperature. These equations have to be solved numerically.

7.3 Expansion through the nozzle

The thrust of a rocket motor is, according to Eq. (6.2-3), given by

$$F = \lambda m V_e + (p_e - p_a) A_e. \quad (7.3-1)$$

The mass flow, m , equals the rate of propellant flowing into the combustion chamber, while λ depends on the nozzle shape.

For a given rocket motor, the area of the exit surface, A_e , in combination

with the chamber pressure, p_c , determines the exhaust velocity, V_e , and the exhaust pressure, p_e . If one, on the other hand, wants to design a nozzle for a given chamber pressure, pressure ratio and mass flow, the area of the exit surface and the exhaust velocity follow from the chamber pressure, pressure ratio, and mass flow. In both cases, the ambient pressure, p_a , is an independent variable that will not interfere with the nozzle flow as long as no shock waves occur. It is convenient to take the pressure, and not the area of a surface of constant properties, as an independent variable, as the pressure appears in the equations for the equilibrium constants and the entropy equation. Therefore, we will determine the local velocity and the local area of a surface of constant properties as a function of the local pressure.

In general, the composition of the combustion products will change during the expansion through the nozzle. For an exact determination of how the composition changes, the integration of the differential equations for the chemical kinetics and hydrodynamics is necessary. This is beyond the scope of this book. We can, however, distinguish between two extreme cases:

1. There is no effective change in composition during the expansion through the nozzle.
2. The composition at any location in the nozzle is according to chemical equilibrium.

In the first extreme case, one assumes the residence time in the nozzle to be very short, as compared to the time needed to change the composition effectively. Moreover, if we assume that the heat capacity of the mixture of combustion products is constant too, we can use the theory as developed in Chapter 5. We call this the *constant properties flow*. If we do assume a constant composition throughout the nozzle, but take into account the variation of the heat capacities with temperature, we speak of a *frozen flow*.

In the second extreme case, one assumes the reaction rates to be infinite, so that the composition changes immediately to the one dictated by equilibrium conditions. In this case we speak of *equilibrium flow*.

7.3.1 Constant properties flow

This is the most simple approach. The composition and heat capacities, which remain constant during the expansion through the nozzle, are known from the chamber conditions. The mean molecular weight, \mathcal{M} , of the combustion products, follows from

$$\mathcal{M} = \sum_k (n_k \mathcal{M}_k) / \sum_k n_k, \quad (7.3-2)$$

where $n_k / \sum_k n_k$ and \mathcal{M}_k stand for the mol fraction and the molecular weight,

respectively, of the combustion products A_k . The mean molar heat capacity at constant pressure, C_p , follows from

$$C_p = \sum_k (n_k C_{p_k}) / \sum_k n_k, \quad (7.3-3)$$

and the gas constant, R , of the mixture from

$$R = R_0 / M. \quad (7.3-4)$$

The ratio of specific heats, γ , is determined by

$$\gamma = \frac{C_p}{C_p - R_0}. \quad (7.3-5)$$

We assumed no heat losses in the combustion chamber, therefore, the adiabatic flame temperature equals the temperature of the gases in the combustion chamber, i.e. $T_f = T_c$.

Now that p_c , T_c , R and γ are known, the equations in the Sections 5.1.1 and 5.1.3 allow the direct computation of the velocity, V , the local expansion ratio, A/A_e , and the ratio m/A for a given local pressure, p . If this pressure is taken as the exit pressure, p_e , one finds the exhaust velocity, V_e , with Eq. (5.1-15), the expansion ratio, A_e/A , by Eq. (5.1-42) and the ratio m/A_e with Eq. (5.1-37).

7.3.2 Frozen flow

The main difference of this model with the one above, is that the heat capacities of the various substances are a function of the local temperature. Therefore, the simple equations, as derived in the Sections 5.1.1 and 5.1.3 cannot be applied anymore. The expansion process through the nozzle is assumed adiabatic and reversible, i.e. the entropy remains constant. This means that all heat transfer and frictional effects are neglected. For the amount of matter considered, the entropy at any position in the nozzle thus equals the entropy in the combustion chamber, or at the nozzle entrance. In Eq. (7.1-27) we showed that

$$F_i - F_i^\circ = R_0 T \ln P_i. \quad (7.3-6)$$

With the definition of free energy, Eq. (7.1-22), and as $H(T) = H^\circ(T)$, we find

$$S_i^\circ(T) - S_i(T) = R_0 \ln P_i. \quad (7.3-7)$$

As condensed phases do not contribute to the total pressure, the entropy is found from

$$S(T) = \sum_g n_g \left(S_g^\circ(T) - R_0 \ln \left(P \frac{n_g}{\sum_g n_g} \right) \right) + \sum_s n_s S_s^\circ(T), \quad (7.3-8)$$

Here, the index g denotes the gaseous species and the index s the condensed species. For a given pressure, the temperature is determined from this last equation.

In Section 3.7 we derived the energy equation; for stationary flows

$$\mathbf{V} \cdot \nabla(h + \frac{1}{2}\mathbf{V} \cdot \mathbf{V}) = 0. \quad (7.3-9)$$

Using the same arguments as in Section 5.1.1 we have

$$h(T) + \frac{1}{2}\mathbf{V} \cdot \mathbf{V} = h(T_c), \quad (7.3-10)$$

i.e. the sum of the enthalpy and kinetic energy per unit mass of the combustion products is constant and equals the enthalpy per unit mass in the combustion chamber. In this chapter, we use the molar enthalpy and Eq. (7.3-10) becomes

$$\sum_r n_r H_r^\circ(T_r) = \sum_k n_k H_k^\circ(T_c) = \sum_k n_k H_k^\circ(T) + \frac{1}{2} \sum_k n_k M_k V^2. \quad (7.3-11)$$

Here, T_r is the temperature at which the propellant, A_r , enters the combustion chamber. T_c is the temperature of the combustion products in the combustion chamber. If there are no heat losses $T_c = T_f$, the adiabatic flame temperature. T and V stand for the temperature and velocity, respectively, of the combustion products, A_k in the nozzle, while n_k stands for the number of mols considered, of the combustion products. The (numerical) solution of Eq. (7.3-11) yields the velocity, V , as for a given pressure, p , Eq. (7.3-8) yields the temperature, T . If $p = p_e$, one finds the exit temperature, T_e . The exhaust velocity, V_e , follows from Eq. (7.3-11):

$$V_e = \left[\frac{2 \left(\sum_r n_r H_r^\circ(T_r) - \sum_k n_k H_k^\circ(T_e) \right)}{\sum_k n_k M_k} \right]^{1/2} \quad (7.3-12)$$

The area of the surface of constant properties per unit mass flow, A/m , is determined from the continuity equation, Eq. (5.1-35). For the nozzle we have

$$m = \rho V A, \quad (7.3-13)$$

where m is known. Because the combustion products in the nozzle may contain condensed particles, we write

$$\rho = \frac{\sum_g n_g M_g + \sum_s n_s M_s}{\gamma}, \quad (7.3-14)$$

As the condensed particles do not contribute to the pressure, the volume, γ ,

considered, follows from

$$\mathcal{V} = \frac{R_0 T \sum_g n_g}{\frac{g}{p}}. \quad (7.3-15)$$

From the Eqs. (7.3-13) to (7.3-15) follows

$$\frac{A}{m} = \frac{R_0 T \sum_g n_g}{\left(\sum_g n_g M_g + \sum_s n_s M_s \right) V p}. \quad (7.3-16)$$

Now that temperature and velocity at a position in the nozzle are known, the area of the surface of constant properties follows from Eq. (7.3-16). If no condensed phases are present, Eq. (7.3-16) reduces to

$$\frac{A}{m} = \frac{R_0 T}{M V p}, \quad (7.3-17)$$

where M is the mean molecular weight of the combustion products as given by Eq. (7.3-2).

The calculations for the frozen flow require the numerical solution of equations. The constant properties flow can be determined analytically. In cases that a frozen flow performance calculation is available, while a neighboring solution is required, the following simple computational scheme can be applied. First, the average heat capacity ratio, $\bar{\gamma}$, for which both the frozen flow and the constant properties flow yield the same results for a given pressure ratio, p_c/p , is determined with the help of the Poisson relations, Eq. (3.7-20), from which follows

$$\bar{\gamma} = \frac{\ln(p_c/p)}{\ln(p_c/p) - \ln(T_c/T)}, \quad (7.3-18)$$

where T_c/T is the temperature ratio, as determined by the frozen flow calculations. As $\bar{\gamma}$ is only slowly varying with temperature, especially at lower temperatures, a constant properties analysis, using $\bar{\gamma}$ as determined by Eq. (7.3-18) will yield accurate results for nearby pressure ratios, as compared to the frozen flow analysis.

There is no direct way to determine the expansion ratio A_e/A_r . One can, for instance, approximate the throat conditions by those that follow from the constant properties flow. These can be used as initial values to determine the throat as the location where $M_a = 1$ by an iterative procedure [9].

In general, one will compute the ratio A/m for various pressures, lying between chamber and exit pressures. These data can be used to determine a minimum of A/m . This method also immediately yields p_t [13].

The throat conditions are determined by A/m being a minimum, i.e.

$$\frac{d}{dp} \left(\frac{R_0 T}{\mathcal{M} V p} \right) = 0. \quad (7.3-19)$$

For the frozen flow, \mathcal{M} is constant, and the requirement comes down to

$$\frac{dT}{dp} \left(1 - \frac{T}{V} \frac{dV}{dT} \right) - \frac{T}{p} = 0, \quad (7.3-20)$$

where use is made of $V = V\{T(p)\}$. As the flow is assumed isentropic, we also have,

$$T dS = C_p dT - \gamma dp = 0, \quad (7.3-21)$$

which gives

$$\left(\frac{dT}{dp} \right)_s = \frac{\gamma}{\sum_k n_k C_{p_k}} = \frac{\sum_k n_k R_0 T}{\sum_k n_k C_{p_k} p}. \quad (7.3-22)$$

From Eq. (7.3-11) it follows that

$$\frac{dV}{dT} = - \frac{\sum_k n_k C_{p_k}}{V \sum_k n_k \mathcal{M}_k}, \quad (7.3-23)$$

Combination of the Eqs. (7.3-20) to (7.3-23) yields

$$\frac{R_0 \sum_k n_k}{\sum_k n_k C_{p_k}} + \frac{T}{V^2} \frac{\sum_k n_k R_0}{\sum_k n_k \mathcal{M}_k} - 1 = 0. \quad (7.3-24)$$

The simultaneous solution of the Eqs. (7.3-8), (7.3-12) and (7.3-24) yields p_t , T_t and V_t . The ratio A_t/m is found from

$$\frac{A_t}{m} = \frac{R_0 T_t}{\mathcal{M} V_t p_t}. \quad (7.3-25)$$

The throat conditions, being determined by one method or another, yield, in combination with the values of A_t/m , the local expansion ratio

$$\frac{A}{A_t} = \frac{A_t/m}{A/m}. \quad (7.3-26a)$$

The expansion ratio, A_e/A_t , is found by setting $A = A_e$

$$\frac{A_e}{A_t} = \frac{A_e/m}{A_t/m}. \quad (7.3-26b)$$

An advantage of this last method is that the throat conditions can be determined beforehand, while some of the other methods require computation of A/m before the throat conditions can be determined.

7.3.3 Equilibrium flow

In this case we assume infinitely fast reaction rates, so that the composition of the combustion products is a function of chemical equilibrium at any location in the nozzle. Thus, not only the heat capacities, but also the composition, are dependent on the location in the nozzle. Again, we assume an isentropic flow through the nozzle.

To determine the velocity, temperature and composition for a given pressure ratio, the following equations have to be solved:

1. The equations for the conservation of elements. If e different elements are involved, there are e equations.
2. The equations for the equilibrium constants of formation. If c compounds are involved, there are $c - e$ equations.
3. The entropy equation

$$S(T_c) = \sum_g n_g \left(S_g^\circ(T) - R_0 \ln \left(P \frac{n_g}{\sum_g n_g} \right) \right) + \sum_s n_s S_s^\circ(T), \quad (7.3-27)$$

which equates the total entropy in the chamber to the total entropy at some location in the nozzle for the amount of matter considered.

4. The energy equation from which the velocity, V , follows:

$$V = \left[\frac{2 \left(\sum_r n_r H_r^\circ(T_r) - \sum_k n_k H_k^\circ(T) \right)}{\sum_k n_k M_k} \right]^{1/2}. \quad (7.3-28)$$

The exhaust velocity, V_e , exit temperature, T_e , and the composition at the nozzle exit, are found by setting $p = p_e$. The area of a surface of constant properties is found by Eq. (7.3-17). The average heat capacity ratio, $\bar{\gamma}$, is found by Eq. (7.3-18), with T_e/T now as determined by the equilibrium flow calculations.

To determine the throat conditions, we can use the same iterative procedures as were indicated to compute the throat conditions for the frozen flow. We can also use the simple condition of A/m being at a minimum. As the composition now varies according to chemical equilibrium, one also has to determine the differential quotients dn_k/dp from algebraic equations. These equations are found by differentiating the e equations for the conservation of elements and the $c - e$ equations for the K_{pf} 's with respect to pressure. One should be aware that $K_{pf}(T) = K_{pf}\{T(p)\}$ if the local pressure, p , instead

of the location in the nozzle is taken as an independent variable. By Eq. (7.1-42) one then finds a relation between dn_k/dT and $\Delta H_{f_k}^\circ$. The solution of the equations in the unknowns n_k , dn_k/dp , T and V yields the throat conditions [14].

We have discussed three methods that yield results, which are more or less in agreement with experimental results. The equilibrium flow method, accounting for many variations, requires much computer time. As it is based on the assumption that the composition varies according to chemical equilibrium, there is no guarantee that its results are a better approximation of reality than the frozen flow. The frozen flow requires less computing time, but assumes a constant composition throughout the nozzle. In fact, the real composition will lie somewhere between the results as computed by the frozen flow and equilibrium flow method. There is a fourth method, however, that combines both methods mentioned previously, which we will discuss below.

7.3.4 The modified Bray approximation

In a classical article, Bray [15] studied the effects of recombination in the nozzles of hypersonic windtunnels. He showed that, by good approximation, the flow in the nozzle can be divided into three regions: *equilibrium flow*, *transition region*, and *frozen flow*. The transition region, in general, is very small and may be approximated by an infinitely small region, the *Bray freezing point*. The various reactions taking place in the nozzle will yield freezing points at different locations. In general, however, there is one *dominating reaction* with respect to *energy release*, and this is the one that determines the Bray freezing point for the rocket motor [13].

Reaction rates increase with temperature, while the recombination rates increase with pressure. It is these recombinations that yield the high energy release. For moderate chamber pressures (~ 5.5 MPa) it is possible to avoid the exact determination of the Bray freezing point, which requires knowledge of the reaction rates, but to assume the freezing point location at the throat. The justification is that temperatures and pressures before the throat remain relatively high, while they rapidly drop after the throat. The reverse is the case for the fluid velocity. Experience shows this approximation to be very good [13].

For this *modified Bray approximation* an equilibrium flow calculation is performed from the chamber to the throat. It is followed by a frozen flow calculation from the throat to the exit. The throat conditions are determined according to equilibrium flow calculation.

The Figs. 7.1 to 7.3 show the results of performance computations for a $\text{H}_2\text{-O}_2$ rocket motor (based on LH_2 and LOX).

As recombination is accompanied by energy release, the calculations for the equilibrium flow yield higher specific impulses than for the frozen flow. The dependence of the maximum specific impulse on the mixture ratio and

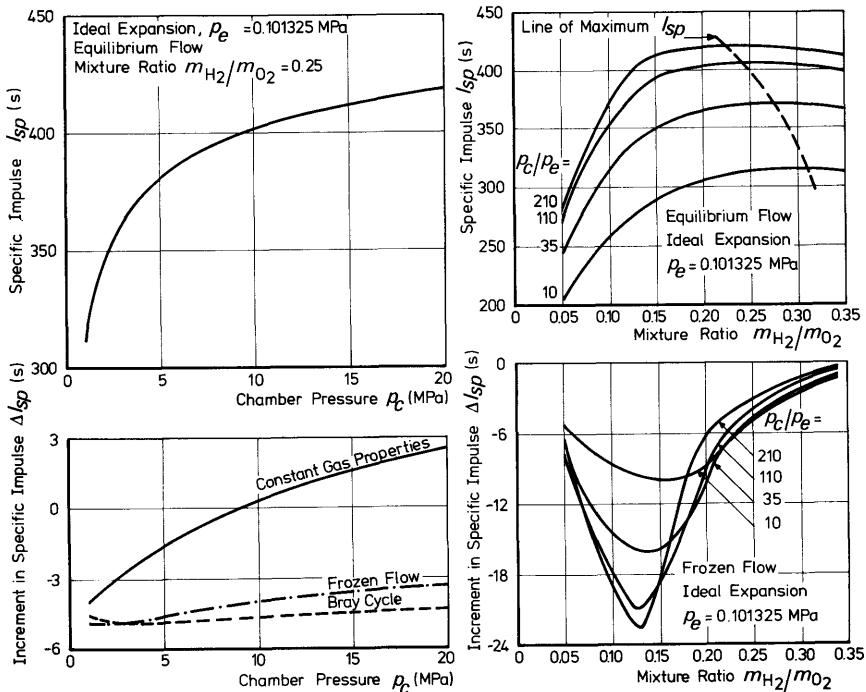


Fig. 7.1 The specific impulse of an ideal H₂-O₂ rocket motor versus chamber pressure and mixture ratio. The increments in specific impulse are plotted with respect to the equilibrium flow results

chamber pressure is shown for the equilibrium flow. With increasing chamber pressures, the optimum mixture ratio shifts towards the stoichiometric mixture ratio, $m_{H_2}/m_{O_2} = 0.125$.

As the degree of dissociation increases with temperature, one finds the largest differences between the frozen and equilibrium flow calculations around the stoichiometric mixture ratio.

For a mixture ratio 0.25, the differences between the Bray cycle and the frozen flow are small, while the I_{sp} computed according to the method of constant gas properties does not differ much from those found by equilibrium or frozen flow calculations. The expansion ratio determined by the method of constant gas properties yields larger differences.

Finally, one can, by Fig. 7.3, determine the effect of a non-ideal expansion ratio on the exit pressure. For example, with $(p_c/p_e)_{ideal} = 110$, $m_{H_2}/m_{O_2} = 0.175$ and an offset from the ideal expansion ratio, $\Delta(A_e/A_t) = 10^{-1}$, we see from Fig. 7.3 that $\Delta(p_e/p_c)/\Delta(A_e/A_t) = 10^{-3}$ and hence, for $p_c = 11 \text{ MPa}$, we then find $p_e = -1.1 \times 10^{-3} \text{ MPa}$.

We have determined the rocket performance parameters either by assuming constant gas properties, frozen flow or equilibrium flow. It is possible,

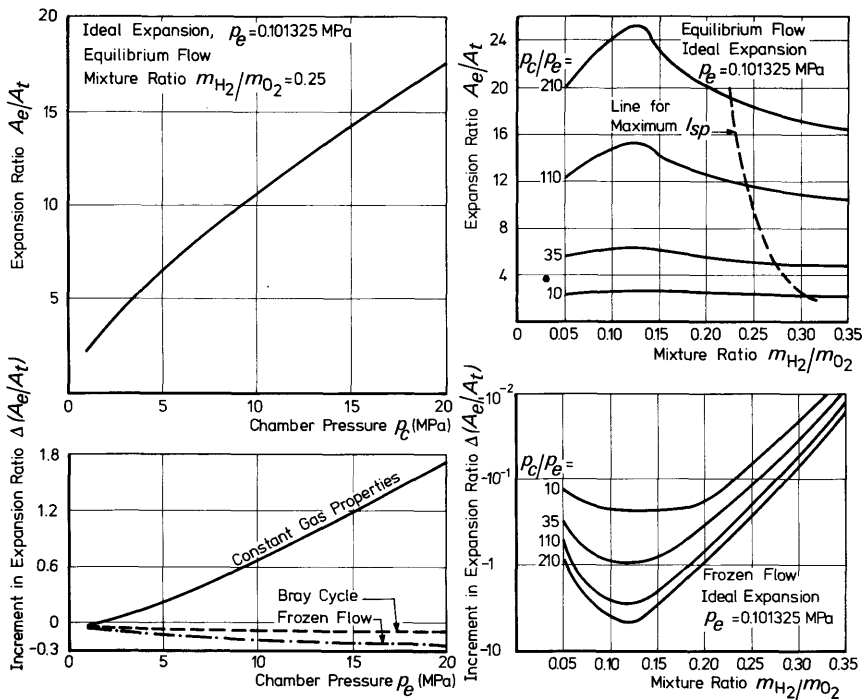


Fig. 7.2 The expansion ratio for an ideal $\text{H}_2\text{-O}_2$ rocket motor versus chamber pressure and mixture ratio. The increments in expansion ratio are plotted with respect to the equilibrium flow results

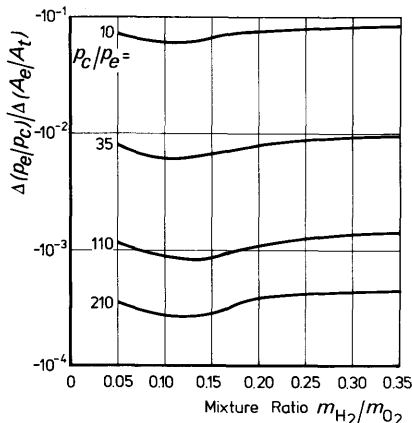


Fig. 7.3 The increment in the pressure ratio due to an increment in the expansion ratio for an ideal $\text{H}_2\text{-O}_2$ rocket motor, versus mixture ratio

however, to combine the equations of *chemical kinetics* and *hydrodynamics* [16] to obtain a better insight in the processes occurring in the nozzle. A different approach to obtain more accurate results for the nozzle flow is followed by Prud'homme [17], who uses a quasi-equilibrium method to obtain a more realistic picture of the composition. These techniques, however, are beyond the scope of this book. There is also the non-equilibrium effect due to the presence of condensed particles, and non-equilibrium chamber effects [13], which is not treated here either. It may be of importance, however. An excellent discussion on the calculation of the chemical equilibrium, especially with respect to rocket motors, is given by van Zeggeren and Storey [18]. These authors also pay much attention to various computational procedures and discuss the respective pros and cons.

References

- 1 Weast, R. C. (ed.) (1978), *Handbook of Chemistry and Physics*, 59th ed., C.R.C.-Press, Cleveland.
- 2 McBride, B. J., Heimel, S., Ehlers, J. G. and Gordon, S. (1963), *Thermodynamic Properties to 6000K for 210 Substances Involving the First 18 Elements*, NASA SP-3001, Washington.
- 3 Stull, D. R. and Prophet, H. (proj. dir.) (1971), *JANAF Thermochemical Tables*, 2nd edn, National Bureau of Standards NSRDS-NBS37, Washington.
- 4 Andrews, F. C. (1971), *Thermodynamics: Principles and Applications*, Wiley-Interscience, New York, p. 243.
- 5 Penner, S. S. (1957), *Chemistry Problems in Jet Propulsion*, Pergamon Press, London, p. 193.
- 6 Lewis, G. N. and Randall, M. (1923), *Thermodynamics and the Free Energy of Chemical Substances*, McGraw-Hill, New York, p. 190-202.
- 7 Rossini, F. D. (ed.) (1955), Thermodynamics and physics of matter, Vol. 1, in: *High Speed Aerodynamics and Jet Propulsion*, Princeton University Press, Princeton, p. 85-86.
- 8 Kestin, J. (1968), *A Course in Thermodynamics*, Vol. II, Blaisdell, Waltham, p. 257.
- 9 Gordon, S. and McBride, B. J. (1971), *Computer Program for Calculation of Complex Chemical Equilibrium Compositions, Rocket Performance, Incident and Reflected Shocks and Chapman-Jouguet Detonations*, NASA SP-273, Washington.
- 10 Svehla, R. A. and McBride, B. J. (1973), *Fortran IV Computer Program For Calculation of Thermodynamic and Transport Properties of Complex Chemical Systems*, NASA TN D-7056, Washington.
- 11 Huff, V. N., Gordon, S. and Morrel, V. E. (1951), *General Method and Thermodynamic Tables for Computation of Equilibrium Composition and Temperature of Chemical Reactions*, NACA Report 1037, Washington.

- 12 Barrère, M., Jaumotte, A., Fraeijis de Veubeke, B. and Vandenkerckhove, J. (1960), *Rocket Propulsion*, Elsevier, Amsterdam, p. 140-153.
- 13 Glassman, I. and Sawyer, R. F. (1970), *The Performance of Chemical Propellants*, AGARDograph 121, Technivision Services, Slough.
- 14 Schöyer, H. F. R. (1976), *The Determination of the Throat Conditions for Equilibrium and Frozen Flows in Rocket Motor Nozzles*, Rpt. VTH-209, Delft University of Technology, Dpt. of Aerospace Engineering, Delft.
- 15 Bray, K. N. C. (1959), Atomic recombination in a hypersonic wind-tunnel nozzle, *J. Fluid Mech.*, **6**, 1-32.
- 16 Bitther, D. A. and Scullin, V. J. (1972), *General Chemical Kinetics Computer Program for Static and Flow Reactions, with Application to Combustion and Shock-Tube Kinetics*, NASA TN D-6586, Washington.
- 17 Prud'homme, R. (1974), *Méthode de Quasi-Equilibre pour l'Etude des Ecoulements Relaxés*, paper presented at the 43rd P.E.P.-AGARD specialist meeting, Liège.
- 18 Van Zeggeren, F. and Storey, S. H. (1970), *The Computation of Chemical Equilibria*, Cambridge University Press, Cambridge.

8 Heat Transfer in Rocket Motors

Heat transfer is important in astronautics. For instance, the temperature of satellites and spacecraft has to be kept within certain limits to ensure a good operation. During the atmospheric flight of rockets and space vehicles, aerodynamic heating is important. To avoid damage to the structure or the payload one often has to take special precautions, such as the installment of heat shields. Another field of astronautics where heat transfer is very important is rocket motor technology. The high-temperature combustion products could raise the temperature of the engine structure in many cases to levels that exceed the melting point of the metals used, if no special precautions were taken. This often makes an active cooling system imperative. The heat absorbed by the coolant can be used to drive the turbines or to heat the pressurization gas in the propellant tanks. Evidently, a good knowledge of the amount of heat transfer in the rocket motor is a necessity for a successful design of the rocket motor.

In this chapter, we will restrict ourselves to the discussion of the most important aspects of heat transfer in the rocket motor, and leave out aerodynamic heating and thermal control of satellites and spacecraft. It is beyond the scope of this book to give an extensive treatment on heat transfer, and the reader is referred to the existing standard works [1, 2, 3].

8.1 The energy equation

In Section 3.7, we have derived the energy equation, assuming that there was no heat transfer. In this section, we will derive the energy equation for solids, including heat transfer. It is not practical to derive the full energy equation for fluids. The contribution of viscous effects to the equation for the conservation of energy for fluids is of the same order as heat transfer. If one includes these viscous effects in the energy equation, they must also be accounted for in the momentum equation, which leads to the *Navier-Stokes equation*. No general solutions are known to this equation; there are only exact solutions known for some special cases and there exist many approximate solutions. Heat transfer problems in fluids will be treated by means of the theory of convective heat transfer. The solutions to this last type of heat transfer problems are partly based on approximate solutions of the conservation equations, and partly on experimental results. Therefore, we will derive the energy equation which in principle allows for heat transfer effects in solids. We will not account for viscous or elastic forces. Therefore, the

equation will not hold if large *internal forces* are created by thermal effects. For most solids (and many liquids) the energy involved in the thermal expansion is very small as compared to the internal energy of the substance. Therefore, internal energy and enthalpy are approximately equal, and most solids (and many liquids) only have one specific heat capacity, $c = c_p \approx c_v$.

To derive the energy equation for a solid, we can follow exactly the same reasoning as in Section 3.7. The reader should keep in mind that the conservation equations in that section, though derived to be applied to fluids, also hold for solids. Thus, consider a material volume, \mathcal{V} . A closed surface, S , bounds this volume. There is a heat flux, \mathbf{q} , through S into \mathcal{V} , and thus we find, in the same way as in Section 3.7.3,

$$\frac{D}{Dt} \int_{\mathcal{V}} \rho(e + \frac{1}{2}V^2) d\mathcal{V} + \int_S p\mathbf{n} \cdot \mathbf{V} dS = - \int_S \mathbf{q} \cdot \mathbf{n} dS.$$

The minus sign at the right-hand side occurs as the unit normal, \mathbf{n} , is directed outward. In exactly the same way as in Section 3.7.3 we can evaluate this equation to find,

$$\frac{\partial}{\partial t}(e + \frac{1}{2}V^2) + \mathbf{V} \cdot \nabla(e + \frac{1}{2}V^2) + \frac{1}{\rho} \nabla \cdot (p\mathbf{V}) + \frac{1}{\rho} \nabla \cdot \mathbf{q} = 0. \quad (8.1-1)$$

Scalar multiplication of the momentum equation, Eq. (3.7-12), by \mathbf{V} , and subtracting the result from Eq. (8.1-1) yields

$$\frac{\partial}{\partial t}(cT) + (\mathbf{V} \cdot \nabla)(cT) + \frac{P}{\rho} \nabla \cdot \mathbf{V} + \frac{1}{\rho} \nabla \cdot \mathbf{q} = 0, \quad (8.1-2)$$

where use is made of $h = e = \int_{T_0}^T c dT$. As for solids $\nabla \cdot \mathbf{V}$, in general, is very small as it represents the velocity divergence due to thermal expansion, or due to the stresses caused by external forces, the term $\frac{P}{\rho} \nabla \cdot \mathbf{V}$ can be neglected to yield as a final result

$$\frac{\partial}{\partial t}(cT) + (\mathbf{V} \cdot \nabla)(cT) + \frac{1}{\rho} \nabla \cdot \mathbf{q} = 0. \quad (8.1-3)$$

The velocity \mathbf{V} represents the velocity of the particles with respect to the coordinate system chosen. In general one will choose a coordinate system fixed to the solid, making \mathbf{V} extremely small or zero, thus one may write

$$\frac{\partial}{\partial t}(cT) + \frac{1}{\rho} \nabla \cdot \mathbf{q} = 0. \quad (8.1-4)$$

In the case of a burning solid propellant it can be advantageous to fix the coordinate system to the burning surface. If this has a constant velocity \mathbf{r} with respect to a fixed point of the solid, the solid has a velocity $-\mathbf{r}$ with respect to the burning surface, and Eq. (8.1-3) becomes

$$\frac{\partial}{\partial t}(cT) - (\mathbf{r} \cdot \nabla)(cT) + \frac{1}{\rho} \nabla \cdot \mathbf{q} = 0. \quad (8.1-5)$$

8.2 Heat transfer processes

In principle, heat transfer is possible by two basically different processes: *radiation* and *conduction*. A third process is *convection*, which involves radiative or conductive heat transfer accompanied by the transport of the cooled or heated matter. In the following sections we will briefly discuss these three forms of heat transfer.

8.2.1 Conductive heat transfer

The mechanism of conductive heat transfer is one of the most complicated problems in modern physics. It is different for different states of aggregation and it may even be different for two different substances in the same state of aggregation. However, a full understanding of the mechanism is not necessary to achieve meaningful, practical results. In 1822, Fourier [4] stated his law about heat conduction, which is usually expressed nowadays as

$$\mathbf{q} = -k \nabla T. \quad (8.2-1)$$

The thermal conductivity, k , is dependent on the temperature, T , and is a physical property of the material. For not too large temperature intervals, k and the heat capacity, c , may be assumed constant and Eq. (8.1-4) can be written as

$$\frac{\partial T}{\partial t} - \kappa \nabla^2 T = 0, \quad (8.2-2)$$

where $\kappa = k/(\rho c)$, is the *thermal diffusivity* of the material. In the same way, Eq. (8.1-5) and Eq. (8.2-1) yield

$$\frac{\partial T}{\partial t} - (\mathbf{r} \cdot \nabla) T - \kappa \nabla^2 T = 0. \quad (8.2-3)$$

8.2.2 Radiative heat transfer

In 1879, Stefan determined from experiments, that the amount of heat radiated by a body of temperature T , was proportional to T^4 . In 1884, Boltzmann [5] proved this by thermodynamic considerations. Planck [6] in 1901 showed that the energy flux, q_λ , emitted in the wavelength λ , by a body of temperature T , ideally equals

$$q_\lambda = \frac{2\pi h c^2}{\lambda^5 (e^{hc/\lambda kT} - 1)}. \quad (8.2-4)$$

In this equation, k is *Boltzmann's constant*, h is *Planck's constant* and c is the velocity of light in vacuum. Their respective values are given in Table

T.1. Integration of Eq. (8.2-4) from $\lambda = 0$ to $\lambda \rightarrow \infty$ yields

$$q = \sigma T^4, \quad (8.2-5)$$

which is known as the *Stefan–Boltzmann equation*. The *Stefan–Boltzmann constant*, σ , equals

$$\sigma = \frac{2 \pi^5 k^4}{15 h^3 c^2}. \quad (8.2-6)$$

The wavelength $\lambda_{q_{max}}$ at which an ideal radiator of constant temperature T radiates most of its energy per unit wavelength, is found by differentiating Eq. (8.2-4) with respect to λ , and putting the result equal to zero,

$$\lambda_{(q_s)_{max}} T = c_1 = 2.8978 \times 10^{-3} \text{ mK}. \quad (8.2-7)$$

This result is known as *Wien's law*. Insertion of Eq. (8.2-7) into Eq. (8.2-4) yields

$$(q_s)_{max} = c_2 T^5 = 1.2865 \times 10^{-5} T^5 \text{ W/m}^3. \quad (8.2-8)$$

The Eqs. (8.2-4) and (8.2-8) are plotted in Fig. 8.1.

If a body radiates according to the Stefan–Boltzmann law, Eq. (8.2-5), it is called an ideal radiator. If it emits less energy, this is accounted for by the *emittance*, $\varepsilon < 1$

$$q = \varepsilon \sigma T^4. \quad (8.2-9)$$

The emittance is the ratio of the actual radiant energy flux to the energy flux from an ideal radiator at the same temperature.

Radiant energy on matter can either be *absorbed*, *transmitted* or *reflected*. The *absorptance*, α , is defined as the *ratio of absorbed to total radiant energy*. The *reflectance*, ρ , and *transmittance*, τ , are defined correspondingly. Thus,

$$\alpha + \rho + \tau = 1. \quad (8.2-10)$$

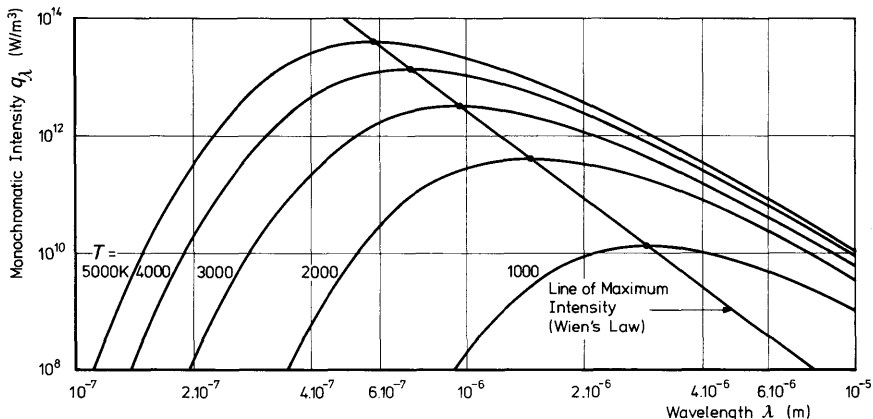


Fig. 8.1 The monochromatic intensity, q_λ , versus the wavelength, λ , for black-body radiation

If $\alpha = 1$, i.e. if all radiant energy is absorbed, the body is called a *black-body*. Black-bodies can closely be approximated by a small hole in a closed hollow surface for which $\tau = 0$, as only an extremely small portion of the radiant energy falling into the hole will be reflected back through it [1, 2], and nearly all energy is absorbed by the walls of the volume. If one considers monochromatic radiation of wavelength λ one can define the *monochromatic emittance*, ε_λ , and *monochromatic absorptance*, α_λ , analogous to the emittance and absorptance and show that $\alpha_\lambda = \varepsilon_\lambda$ [1, 2]. For most materials α_λ and ε_λ depend strongly on λ . Under some special restrictions, one can show that also $\alpha = \varepsilon$, Kirchhoff's law [1]. In general the absorptance is dependent on the spectrum of the incident radiation, and α and ε can differ considerably. For a black-body, by definition, $\alpha = \varepsilon = 1$. So, a black-body is also an ideal radiator and vice versa.

Let us now consider a radiating surface of which the emissive properties are not directional dependent. The amount of radiated energy, however, will show a directional dependency as will be shown below. Consider a surface element ΔS radiating in all directions. All radiation will pass through a hemisphere, with unit radius, centered around ΔS , Fig. 8.2. The radiative flow, received in the point $P(\varphi, \theta)$ on the hemisphere from the element ΔS is

$$dq = \varepsilon_d \sigma T^4 \Delta S \cos \varphi,$$

where ε_d is the *directional emittance*. The total radiation passing through the hemisphere is

$$q = \Delta S \int_{\varphi=0}^{\pi/2} d\varphi \int_{\theta=0}^{2\pi} \varepsilon_d \sigma T^4 \cos \varphi \sin \varphi d\theta = \pi \varepsilon_d \sigma T^4 \Delta S,$$

as ε_d is constant for a surface which shows no directional dependence in its emissive properties. As $q = \varepsilon \sigma T^4 \Delta S$, it follows that

$$\varepsilon_d = \varepsilon / \pi. \quad (8.2-11)$$

The emittance ε is often denoted as the *hemispherical emittance*. Analogous to the above reasoning $\varepsilon_{d\lambda} = \varepsilon_\lambda / \pi$.

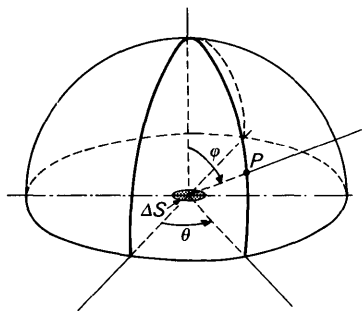


Fig. 8.2 Nomenclature for emittance

8.2.3 Radiating gases

While liquids and solids usually have a uniform radiation spectrum, gases often emit in narrow wavebands, which are characteristic for the gases under consideration. At high pressures, these bands tend to broaden.

As far as radiative heat transfer is concerned, the hot combustion products in the rocket motor can often be regarded as a radiating black-body of temperature T_c . By the walls, an amount of heat per unit area, $\alpha_w \sigma T_c^4$, is absorbed, while $\varepsilon_w \sigma T_w^4$ is emitted. So, the total heat flux into the chamber walls equals

$$q = \alpha_w \sigma T_c^4 - \varepsilon_w \sigma T_w^4. \quad (8.2-12)$$

In those cases that the combustion products hardly contain solid particles, such as soot or metal oxides, the assumption of black-body radiation from the combustion products may not be correct, and Eq. (8.2-12) will predict wall temperatures which are too high.

Emission and absorption in gases involve the interaction of gas molecules. Let us therefore consider a narrow beam of monochromatic radiation in a volume filled with a gas. We assume that the amount of emission (absorption) is proportional to the number of molecules within the beam. For an ideal gas the number of molecules per unit volume is proportional to the pressure, p . The energy flux $-dq_\lambda$, absorbed in a layer of gas of thickness, dL , is proportional to the total flux q_λ

$$-dq_\lambda = q_\lambda k_\lambda p dL,$$

leading to

$$(q_\lambda)_0 - (q_\lambda)_L = (1 - e^{-k_\lambda p L})(q_\lambda)_0 \quad (8.2-13)$$

where $(q_\lambda)_0$ stands for the flux at zero distance, and $(q_\lambda)_L$ for the flux at a distance L . The constant, k_λ , is the *spectral absorption coefficient* of the gas, and pL is called the optical density. In many cases the quantity $-k_\lambda p L$ is so small that, using the definition of absorptance, Eq (8.2-13) can be approximated by

$$\alpha_\lambda = \varepsilon_\lambda = k_\lambda p L. \quad (8.2-14)$$

The monochromatic emittance (absorptance) of a layer of gas of unit length is called the *monochromatic emissivity*, $\bar{\varepsilon}_\lambda$, (*absorptivity*, $\bar{\alpha}_\lambda$) and

$$\bar{\alpha}_\lambda = \bar{\varepsilon}_\lambda = k_\lambda p. \quad (8.2-15)$$

Now again consider a closed volume filled with radiating gas. From a layer of gas with thickness L , a surface element dS will receive an amount of radiative energy

$$dq_\lambda = \sigma T^4 k_\lambda p L dS.$$

With the approximations made, the total amount of monochromatic radiative energy from all the gas in the volume, can be expressed as

$$q_\lambda = \sigma T^4 k_\lambda p L_{eq} S = \sigma T^4 \bar{\varepsilon}_\lambda L_{eq} S, \quad (8.2-16)$$

where L_{eq} stands for an ‘equivalent beam length’.

On the other hand, the monochromatic radiation received by the wall from a volume element dV of the gas is

$$d^2 q_\lambda = \bar{\varepsilon}_{\lambda_d} dV d\Omega \sigma T^4,$$

where $d\Omega$ is the solid angle under which the wall is seen by the volume element. Thus,

$$q_\lambda = \bar{\varepsilon}_{\lambda_d} V 4 \pi \sigma T^4 = 4 \bar{\varepsilon}_\lambda V \sigma T^4. \quad (8.2-17)$$

Equating the Eqs. (8.2-16) and (8.2-17) yields an expression for the equivalent beam length, L_{eq}

$$L_{eq} = \frac{4V}{S}. \quad (8.2-18)$$

In those cases that the combustion products cannot be regarded as a radiating black-body, the heat flux to the chamber walls can be calculated with Eq. (8.2-16) where L_{eq} follows from Eq. (8.2-18). If the reflectance ($\rho = 1 - \alpha$) of the chamber walls is taken into account, the problem becomes more complex. According to Zieblund [7], the effective monochromatic gas emittance, ε_{λ_g} , follows from

$$\frac{1}{\varepsilon_{\lambda_g}} = \frac{1}{\varepsilon_\lambda} + \frac{1 - \alpha}{\alpha - \varepsilon_{\lambda_\infty}} \quad (8.2-19)$$

Here $\varepsilon_\lambda = \bar{\varepsilon}_\lambda L$, $\varepsilon_{\lambda_\infty}$ is the monochromatic emittance of an infinitely thick layer of gas, while the absorptance, α , of the grey wall may be assumed to be independent of the wavelength.

8.2.4 Convective heat transfer

If heat transfer is due to the transport of heat containing matter, one speaks of convection. This phenomenon takes place in fluids. In Section 8.1, we mentioned already that the complete solution of the fluid dynamic equations, including heat transfer and viscosity, is not possible. Prandtl has shown that approximate solutions can be found for specific regions in the fluid, the *boundary layers*. These are thin regions between the wall and the main flow, in which temperature and velocity differ considerably from the main flow values. Solution of the boundary layer equations is of a very specialized character and falls beyond the scope of this book. We restrict ourselves to give results, which partially stem from theoretical considerations and partially from experiments.

The importance of the boundary layer is illustrated by a stationary flow along a flat plate, through which there is no heat transfer (*adiabatic wall*). In absence of viscosity, the velocity, V , the temperature, T , and the total temperature, T_{tot} , are constant, Fig. 8.3a. Because of viscosity, at the wall, $V = 0$, while V increases with increasing distance from the wall until the main stream velocity is reached. The velocity and temperature profiles become as shown in Fig. 8.3b. Note that T_{tot} remains constant. As now $\nabla T \neq 0$, heat will be conducted towards the main flow, according to Fourier's law, Eq. (8.2-1). Thus the wall temperature decreases while T_{tot} attains a maximum somewhere in the boundary layer, Fig. 8.3c.

Newton, in 1701, proposed the following relationship for the convective heat transfer flux:

$$q = h_c \Delta T, \quad (8.2-20)$$

Here ΔT is a temperature difference and h_c is the *convective heat transfer coefficient*, which is dependent on fluid properties. We will now introduce a series of dimensionless numbers, by which h_c can be determined.

The available heat flow parallel to the wall is $\rho V c_p (T_g - T_w)$, where T_w is the gas temperature at the wall and T_g is the main flow gas temperature. The heat flow, normal to the wall, according to Newton's equation, is $q_w = h_c (T_g - T_w)$ and the ratio of these two heat flows is the *Stanton number*, St ,

$$St = \frac{h_c}{\rho V c_p}. \quad (8.2-21)$$

A number expressing the relative importance of viscosity and conductivity in a fluid is the *Prandtl number*, Pr , which is a fluid property,

$$Pr = \frac{c_p \mu}{k}, \quad (8.2-22)$$

where μ is the dynamic viscosity of the fluid. The relative importance of

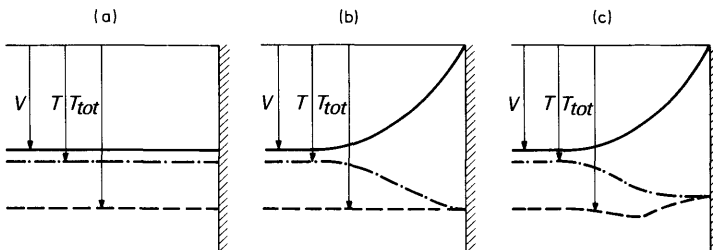


Fig. 8.3 The effect of the boundary layer on the temperature distribution of a flow parallel to an adiabatic wall

inertial forces with respect to viscous forces is given by the *Reynolds number*, Re ,

$$Re = \frac{\rho VL}{\mu}, \quad (8.2-23)$$

where L is a suitable chosen reference length. Comparing the relative importance of convective and conductive heat transfer yields the *Nusselt number*, Nu ,

$$Nu = \frac{h_c L}{k} = St \cdot Re \cdot Pr \quad (8.2-24)$$

For flows through a pipe, there exist experimental relationships of the form $St = St(Re, Pr)$ or $Nu = Nu(Re, Pr)$ by which h_c can be determined, for instance,

$$St = a Re_D^{-1/5} Pr^{-2/3}, \quad (8.2-25a)$$

$$Nu = a Re_D^{4/5} Pr^{1/3}, \quad (8.2-25b)$$

where a is a coefficient. The Reynolds number, Re_D , is based on the pipe diameter. For the divergent part of the nozzle, better correlations are obtained by expressions of the form,

$$St = B Re_x^b Pr^{-2/3}, \quad (8.2-26a)$$

$$Nu = B Re_x^{b+1} Pr^{1/3}. \quad (8.2-26b)$$

Here, B and b are constants, and the Reynolds number, Re_x , is based on the distance x from the throat.

To determine Re , Pr , Nu or St , the values of k , c_p , μ and ρ of the fluid have to be known. These quantities depend, among others, on the temperature, which is not constant over the boundary layer. It is customary to evaluate these quantities at a reference temperature, the *film temperature*, T_f . This T_f may be taken as the average of the wall temperature, T_w , and the free stream temperature, T ,

$$T_f = \frac{T + T_w}{2}. \quad (8.2-27)$$

Though the wall temperature is not known *a priori*, but has to be determined, it should not exceed certain limits, determined for instance by strength and stiffness considerations. As convective heat transfer calculations are of an iterative type, it is convenient to assume for T_w the maximum allowable wall temperature as a first guess.

A more refined determination of T_f includes the *recovery temperature*, T_r , which is the *stagnation temperature at the adiabatic wall*. As we have seen, this temperature is lower than the main flow stagnation temperature. This is

expressed by the *recovery factor*, r ,

$$r = (T_r - T) / (T_{tot} - T). \quad (8.2-28)$$

For a laminar boundary layer:

$$r = \sqrt{Pr}, \quad (8.2-29)$$

and for a turbulent boundary layer:

$$r = Pr^{1/3}. \quad (8.2-30)$$

For rocket motors, r usually lies between 0.86 and 0.93.

According to Zieblund [7], T_f is given by

$$T_f = 0.5 T_w + 0.28 T + 0.22 T_r. \quad (8.2-31)$$

With the determined value of T_f , Re , Pr and Nu follow, and h_c can be computed from the Nusselt number.

Finally, the convective heat transfer flux, q , normal to the wall follows from

$$q = h_c(T - T_w). \quad (8.2-32)$$

To determine the values of c_p , μ and k for a mixture of gases, such as the combustion products, the following expressions can be used. In Chapter 7 we have shown for a mixture of gases

$$c_p = \frac{\sum n_i C_{pi}}{\sum n_i M_i} = \frac{\bar{C}_p}{\bar{M}}. \quad (8.2-33)$$

In the same way the conductivity, k , and dynamic viscosity, μ , follow from:

$$k = \frac{\sum n_i k_i}{\sum n_i}, \quad (8.2-34)$$

$$\mu = \frac{\sum M_i n_i}{\sum \frac{M_i n_i}{\mu_i}}. \quad (8.2-35)$$

The temperature dependence of C_{pi} is given in the thermodynamic tables mentioned in Chapter 7. Hirschfelder [8] gives the temperature dependence of μ_i . However, a simple, rough approximation, such as

$$\mu(T_1)/\mu(T_2) = \sqrt{T_1/T_2}, \quad (8.2-36)$$

often will suffice.

There is a direct relationship between the thermal conductivity, viscosity and heat capacity of gases, due to Eucken [9],

$$k_i = \frac{1}{4}(9\gamma_i - 5)\mu_i c_{pi}, \quad (8.2-37)$$

which yields for the Prandtl number of a single gas,

$$Pr = \frac{4\gamma}{9\gamma - 5}. \quad (8.2-38)$$

8.3 Heat transfer in the rocket motor

In the liquid motor, the nozzle and chamber walls are exposed to hot combustion products. Usually these walls are provided with ducts through which propellant flows to keep material temperatures within acceptable limits. This method is known as *active cooling* (Section 10.5.1). In the solid motor, the propellant usually insulates the chamber walls from the hot combustion products, (Section 9.3), but the nozzle is exposed to the hot combustion products. As active cooling is not possible, one has to select special materials, such as graphite, ceramics or refractory metals for the hot parts. Moreover, radiation cooling and heat sinks, consisting of a piece of material with a high heat capacity, are often used (*passive cooling*).

Concerning heat transfer in the rocket motor, we will distinguish between the following regions: heat transfer from the combustion products to the wall (the gas-side heat transfer), heat transfer in the wall, heat transfer from the wall to the coolant (liquid or coolant-side heat transfer) and the radiative heat transfer of hot walls into space, usually called radiation cooling. An exact analysis of the spatial and time-dependent distribution of temperature and heat fluxes is very complex. As most rocket engines are about axial-symmetric, it is customary for a first analysis to consider the rocket motor as consisting of many annular elements for which the axial heat transfer is negligible. This may be done because the change in radial heat flux does not vary strongly in the axial direction. The distribution of temperatures and heat fluxes thus obtained is a first approximation of the real distribution.

8.3.1 Gas-side heat transfer

In the combustion chamber and nozzle, both convection and radiation contribute to heat transfer. If the emissivity, $\bar{\epsilon}$, of the combustion products is not well known, the radiative heat transfer can be estimated with Eq. (8.2-12). The convective heat transfer is found by the method outlined in Section 8.2.4. For the chamber and nozzle throat region, the convective heat transfer is predicted fairly well if the constant a in Eq. (8.2-25) is taken $a = 0.023$ and the *local diameter* is taken as the *characteristic length*. The throat region extends to about one throat diameter downstream of the throat and the result holds for a throat with a radius of curvature equal to, or larger than the throat diameter. In sharp throats the heat transfer will be higher. From about one throat diameter downstream of the throat, the heat transfer can be calculated with Eq. (8.2-25) with $a = 0.025$ to 0.028 , and the characteristic length is the distance from the throat.

By combining the Eqs. (8.2-21) to (8.2-25), one finds for the convective heat transfer coefficient, h_c ,

$$h_c = ap^{0.8} \left(\frac{V}{RT} \right)^{0.8} \frac{1}{D^{0.2}} \frac{k Pr^{0.33}}{\mu^{0.8}} \quad (8.3-1)$$

Thus h_c is about proportional to $p^{0.8}$. Figure 8.4 shows how the heat fluxes in rocket motors have increased steadily over the years, which is mainly due to the increase in chamber pressure. Modern high-pressure rocket motors, such as the Space Shuttle Main Engine, encounter very high heat fluxes.

The Eqs. (8.2-21) to (8.2-25) can also be combined to give

$$h_c = 1.213 am^{0.8} \mu^{0.2} c_p Pr^{-2/3} D^{-1.8}. \quad (8.3-2)$$

For a given rocket motor the mass flow, m , is constant, and μ , c_p , and Pr are only weak functions of the temperature. The diameter, D , varies from section to section. Hence, the largest convective heat flux can be expected at the throat where D is at a minimum. This is in good agreement with experimental data which show the maximum heat flux to occur just before the throat.

Another semi-empirical relationship that is often used for the determination of h_c is due to Bartz [10]:

$$h_c = 0.026 \left(\frac{\mu^{0.2} c_p}{Pr^{0.6}} \right) \cdot \frac{(\rho V)^{0.8}}{D^{0.2}} \left(\frac{\rho_f}{\rho} \right) \left(\frac{\mu_f}{\mu} \right), \quad (8.3-3)$$

where f indicates that the variable is to be evaluated at the film temperature, T_f .

To show the influence of the chamber pressure on the heat flux in the combustion chamber, Table 8.1 summarizes the results of heat transfer calculations made for two different chamber pressures. A combustion temperature of 3000 K was assumed. Since, at low pressures, the dissociation is more pronounced, the composition is slightly different for the two cases. In both cases, a gas-side wall temperature of 850 K, and a chamber diameter of 0.5 m, were assumed. The radiative heat flux, q_r , was calculated on the

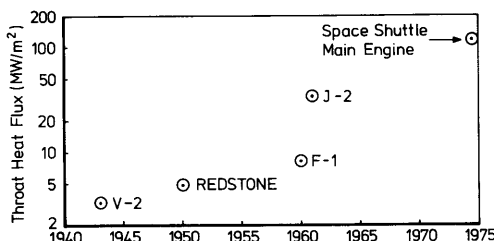


Fig. 8.4 The heat flux in rocket motors has steadily increased over the years

Table 8.1 The influence of chamber pressure on the convective heat flux

Chamber pressure, p_c (MPa)	20	3.5
Chamber temperature, T_c (K)	3000	3000
Wall temperature, T_w (K)	850	850
Chamber diameter, D_c (m)	0.5	0.5
Main stream velocity, V (m/s)	50	50
Mass flow, m (kg/s)	186.5	32.4
Molecular weight, \mathcal{M} (kg/kmol)	23.7	23.5
Ratio of specific heats, γ	1.207	1.21
C_v (J/(kmol.K))	1694	1695
R (J/(kmol.K))	351	354
Viscosity, μ (kg/(m.s))	6.62×10^{-5}	6.59×10^{-5}
Film temperature, T_f (K)	1925	1925
Film viscosity, μ_f (kg/(m.s))	5.07×10^{-5}	5.05×10^{-5}
Film conductivity, k_f (W/(m.K))	0.126	0.126
Convective heat transfer coefficient, h_c (W/(K.m ²))	2927	721
Convective heat flux, q_c (W/m ²)	7.12×10^6	1.81×10^6
Wall emittance, ε_w	1	0.75
Radiative heat flux, q_r (W/m ²)	4.56×10^6	3.42×10^6
	0.5	0.25
	2.28×10^6	1.14×10^6

assumption that the combustion products produce a black-body radiation, and $\alpha_w = \varepsilon_w$. The absorptance, α_w , of the walls depends on the surface conditions and whether or not there are deposits of soot or oxides. Therefore, q_r values for four different values of α_w are tabulated. It is seen that convective and radiative heat fluxes in the combustion chamber are of the same order of magnitude.

During the expansion through the nozzle, the radiative heat flux decreases with the gas temperature. Indicating the radiative heat flux, q_r , in the chamber with the index c and at the throat with the index t , we find by linearization that the ratio

$$\frac{q_{r_c}}{q_{r_t}} = \frac{T_c^4 - T_{w_g}^4}{\left(\frac{2}{\gamma + 1} T_c\right)^4 - T_{w_g}^4} \approx 2\gamma - 1 > 1. \quad (8.3-4)$$

Here, T_{w_g} stands for the gas-side wall temperature. Thus, the radiative heat flux at the throat is less than in the chamber. On the other hand, as shown by Eq. (8.3-2), the convective heat flux is at a maximum at the throat. Thus in the throat region the convective heat flux is the main source of heat transfer.

8.3.2 Heat transfer in the wall

For steady-state conditions the main heat conduction is in a radial direction. We will therefore consider the lateral heat conduction in a cylindrical ring,

with a wall thickness, δ (Fig. 8.5). At the left-hand side of the wall there is the flow of hot combustion products, which yields a heat flux q_g into the wall. At the right-hand side there is the flow of coolant, extracting a heat flux q_l from the wall. The gas-side wall temperature is T_{wg} and the coolant-side wall temperature is T_{wl} . The radius of the ring is r_c . For steady-state conditions it follows immediately that

$$r_c q_g = (r_c + \delta) q_l \quad (8.3-5)$$

The heat conduction equation, Eq. (8.2-2), for a steady state becomes

$$\kappa \nabla^2 T = 0. \quad (8.3-6)$$

In cylindrical coordinates, with the assumption that the heat transfer is uniform around the wall, and negligible in an axial direction, we then find

$$\frac{\kappa}{r} \frac{\partial}{\partial r} \left(r \frac{\partial T}{\partial r} \right) = 0. \quad (8.3-7)$$

With the boundary conditions $T(r_c) = T_{wg}$, $T(r_e) = T_{wl}$, this leads to

$$\frac{T - T_{wl}}{T_{wg} - T_{wl}} = \frac{\ln \left(\frac{r}{r_c + \delta} \right)}{\ln \left(\frac{r_c}{r_c + \delta} \right)}, \quad r_c \leq r \leq r_e \quad (8.3-8)$$

where $r_e = r_c + \delta$. This temperature dependence is schematically shown in Fig.

8.5b. If $\frac{\delta}{r_c} \ll 1$, Eq. (8.3-8) can be linearized

$$\frac{T - T_{wl}}{T_{wg} - T_{wl}} = 1 - \frac{r - r_c}{\delta}, \quad (8.3-9)$$

and the temperature decreases linearly with r as shown in Fig. 8.5a.

In solid motors, sometimes a heat sink is used. It absorbs the heat that flows into the wall, thereby raising its own temperature. The maximum

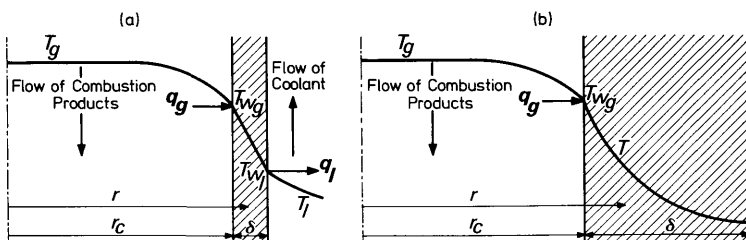


Fig. 8.5 Steady-state heat conduction through an annular wall; (a) for small δ/r_c , (b) for large values of δ/r_c

allowable temperature, for instance the melting temperature, should not be exceeded, and the time it takes to reach this maximum temperature, which will occur at the gas-side of the wall, in fact determines the maximum possible operation time of the motor. To determine this time, we take a cylindrical ring with a thickness δ . Again, we only consider radial heat transfer from the combustion products into the wall. As in the throat area, where heat sinks are most often used, the radiative heat transfer is small as compared to the convective heat transfer, we will only account for this last type of heat transfer. Moreover, we neglect heat fluxes at the outside of the ring. Thus at $r = r_e = r_c + \delta$, $\frac{\partial T}{\partial r} = 0$. For simplicity, we will assume h_c and k constant. Thus at $r = r_c$ the boundary condition is:

$$-k\left(\frac{\partial T}{\partial r}\right)_{r=r_c} = q_g = h_c(T_g - T_{w_s})$$

and the heat conduction equation can be written as

$$\frac{\partial T}{\partial t} - \frac{\kappa}{r} \frac{\partial}{\partial r} \left(r \frac{\partial T}{\partial r} \right) = 0. \quad (8.3-10)$$

This equation can be solved by standard methods, such as separation of variables [11]. We will not go into the details of this solution, but only state that the temperature in the wall can be written as a function of the dimensionless quantities $\kappa t/\delta^2$, $h_c \delta/k$ and r_c/δ .

In Fig. 8.6 the dimensionless temperature $\frac{T_g - T}{T_g - T_o}$ at the inner radius, r_c , of the cylindrical ring is plotted versus these quantities.

8.3.3 Coolant-side heat transfer

The liquid coolant, in contact with the hot wall of the cooling jacket, absorbs heat, thereby raising the bulk coolant temperature, T_b . Figure 8.7 schematically shows the heat flux q_l from the wall into the coolant versus the temperature difference $T_w - T_b$. For small values of $T_w - T_b$ the heat transfer is entirely due to convection. This is indicated by the line up to *NB*. If the coolant pressure is below the critical pressure, at the point *NB* the wall temperature becomes such high, that vapor bubbles are formed at the hot wall. These bubbles move into the cooler liquid, where condensation takes place. This strongly increases the heat flux into the coolant as is shown by the curve *NB-FB*. The phenomenon is known as *nucleate boiling*. If the wall temperature, T_w , rises still more, so many vapor bubbles are formed, that a stable, gaseous boundary layer is created at the hot wall. This is known as *film boiling*. The convective heat transfer now is governed by the temperature difference across the gaseous boundary layer, which has a much lower conductivity than the liquid. Therefore, the heat flux into the coolant is

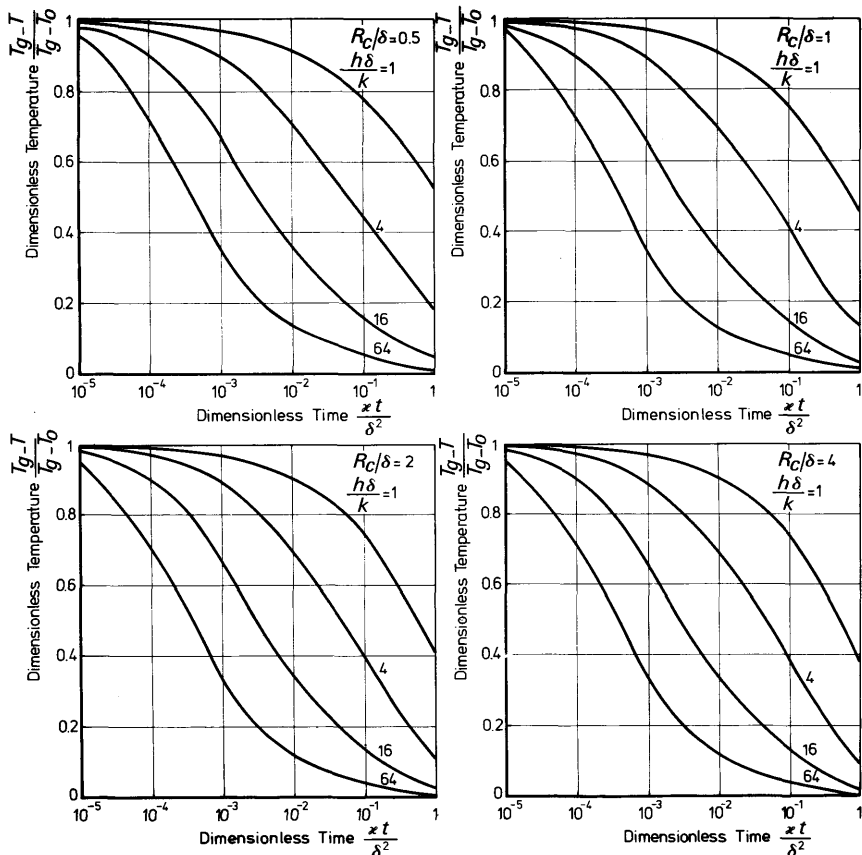


Fig. 8.6 The temperature history at the inner radius, r_c , of a cylinder, internally heated by convection, for some values of r_c/δ and $h_c\delta/k$

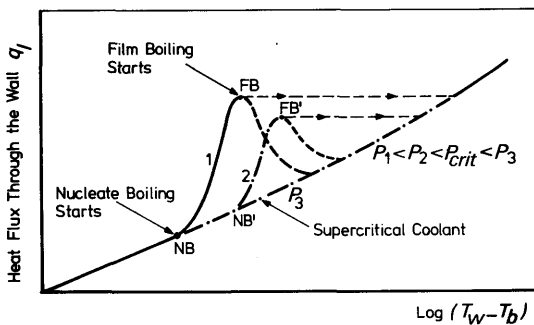


Fig. 8.7 The heat flux through the hot wall of a cooling jacket versus the difference between hot wall temperature, T_w , and bulk coolant temperature, T_b , for pressures below and above the critical pressure, p_{crit}

strongly reduced and the wall temperature will rise to a much higher value, often so high that structural failure may result. Nucleate boiling is a very effective way of cooling. The point *FB* where film boiling, which we want to avoid, starts is difficult to predict and has to be determined experimentally. When the pressure is increased, but still remains lower than the critical pressure, nucleate boiling will start at higher wall temperatures (point *NB'*), while the maximum heat flux that can be attained (point *FB'*) is apt to be somewhat less.

For supercritical pressures (line for p_3), the liquid will, upon reaching the critical pressure, transform into gas without evaporation. If the pressure is near to the critical pressure (i.e. $p/p_{crit} < \sim 3$) still large changes in density, and hence in flow velocities may take place. This has to be analysed carefully to ascertain that pressure drops do not become too large.

To determine the fluid heat transfer, use can be made of the Sieder-Tate [7] equation, which allows for the large temperature difference, $T_w - T_b$, by the factor $(\mu/\mu_w)^{0.14}$,

$$St = 0.027 Re_D^{-0.2} Pr^{-0.67} \left(\frac{\mu}{\mu_w} \right)^{0.14}. \quad (8.3-11)$$

All variables are evaluated at the bulk temperature, T_b , of the coolant except μ_w , which is evaluated at the wall temperature, T_w .

For supercritical hydrogen, helium and nitrogen, Taylor [12] recommends the use of

$$Nu = 0.023 Re_D^{0.8} Pr^{0.4} \left(\frac{T_w}{T_b} \right)^{[1.59/(x/D) - 0.57]}, \quad (8.3-12)$$

where again, with the exception of T_w , all physical properties are evaluated at the bulk temperature, T_b . The equation allows for entrance effects by the factor x/D . Here x stands for the distance from the entrance of the duct, D is the equivalent duct diameter, $D = \sqrt{4A/\pi}$ and A is the cross-sectional area of the duct.

8.3.4 Radiation cooling

For rocket motors, radiation cooling is especially important for extremely hot parts, such as the nozzle extension skirt, and sometimes the combustion chamber, if no active cooling system is used. This is often the case with satellite and spacecraft rocket engines, and with many solid motors. If the motor radiates into empty space (the atmosphere during atmospheric flight can often be regarded as 'empty space' in so far as radiation is concerned) the heat flow dq radiated by a surface element dS with temperature T_w and emittance ϵ , equals

$$dq = \sigma \epsilon T_w^4 dS. \quad (8.3-13)$$

However, such an element dS also receives radiation from other hot parts of the motor-nozzle configuration, which makes an accurate calculation complicated.

Consider two elementary surfaces dS_1 and dS_2 a distance r apart from each other (Fig. 8.8), of temperatures T_1 and T_2 . The respective unit normals \mathbf{n}_1 and \mathbf{n}_2 make angles φ_1 and φ_2 with the line connecting dS_1 and dS_2 . The heat flow dq_{12} , received by the element dS_2 from the element dS_1 , equals

$$dq_{12} = \sigma \varepsilon_1 T_1^4 dS_1 \frac{dS_2 \cos \varphi_2}{\pi r^2} \cos \varphi_1, \quad (8.3-14)$$

and, in the same way, the heat flow dq_{21} received by element dS_1 from element dS_2 equals

$$dq_{21} = \sigma \varepsilon_2 T_2^4 dS_2 \frac{dS_1 \cos \varphi_1}{\pi r^2} \cos \varphi_2. \quad (8.3-15)$$

Thus, there is an interchange of radiant energy flow between dS_1 and dS_2 .

$$dq = \sigma (\varepsilon_1 T_1^4 - \varepsilon_2 T_2^4) \frac{dS_1 dS_2 \cos \varphi_1 \cos \varphi_2}{\pi r^2}. \quad (8.3-16)$$

If dS_1 and dS_2 belong to surfaces S_1 and S_2 with a constant temperature, the total radiation interchange between these surfaces is

$$q = \sigma (\varepsilon_1 T_1^4 - \varepsilon_2 T_2^4) \int_{S_1} \int_{S_2} \frac{\cos \varphi_1 \cos \varphi_2}{\pi r^2} dS_1 dS_2. \quad (8.3-17)$$

The integral

$$E_{12} = \int_{S_1} \int_{S_2} \frac{\cos \varphi_1 \cos \varphi_2}{\pi r^2} dS_1 dS_2 \quad (8.3-18)$$

is called the *transfer function* and depends on the shape of the body considered, and the visibility of a point on that surface by another point. Hence, the determination of the transfer function E_{12} is a geometrical problem.

The concept of the transfer functions is very useful in radiative, thermal analysis. Transfer functions for various nozzle and rocket motor shaped axisymmetric surfaces, have been computed by Bernard and Génot [13].

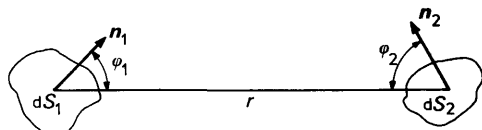


Fig. 8.8 Elementary radiating surfaces

Using these transfer functions, radiative heat transfer calculations are strongly simplified.

In this chapter, we had to limit ourselves to a general discussion of heat transfer in rocket engines. Without going into detail we mentioned some methods that can be applied quickly to get an estimate of heat fluxes and temperatures, or methods that give some insight in the processes going on. A more detailed discussion of heat transfer in the rocket motor is given by Ziebland [7].

References

- 1 Eckert, E. R. G. and Drake Jr., R. M. (1973), *Analysis of Heat and Mass Transfer*, McGraw-Hill, New York.
- 2 Kreith, F. (1969), *Principles of Heat Transfer*, Int. Textbook Co., fifth printing, Scranton.
- 3 Gebhart, B. (1961), *Heat Transfer*, McGraw-Hill, New York.
- 4 Fourier, J. (1878), *The Analytical Theory of Heat*, Cambridge University Press, (English translation by A. Freeman).
- 5 Boltzmann, L. (1884), Ableitung des Stefan'schen Gesetzes, *Ann. d. Physik*, Ser. 2, **22**, 291–294.
- 6 Planck, M. (1901), Ueber das Gesetz der Energieverteilung im Normalspectrum, *Ann. d. Physik*, Ser. 4, no. 3, 553–563.
- 7 Ziebland, H. and Parkinson, R. C. (1971), *Heat Transfer in Rocket Engines*, AGARDograph 148, NATO, Neuilly-sur-Seine.
- 8 Hirschfelder, J. O., Bird, R. B. and Curtiss, C. F. (1954), *Molecular Theory of Gases and Liquids*, John Wiley, New York, p. 533.
- 9 Eucken, A. (1913), Ueber das Wärmeleitvermögen, die spezifische Wärme und die innere Reibung der Gase, *Physik. Zeitschr.*, **14**, 324–332.
- 10 Bartz, D. R. (1957), A simple equation for rapid estimation of rocket nozzle convective heat transfer coefficients, *Jet Propulsion*, **27**, 49–51.
- 11 Schöyer, H. F. R. (1977) *The Determination of Temperature Histories in a Cylindrical Ring, Heated by Convection*, Rpt. LR-253, Delft University of Technology, Dpt. of Aerospace Engineering, Delft.
- 12 Taylor, M. F. (1968), *Correlation of Local Heat-Transfer Coefficients for Single-Phase Turbulent Flow of Hydrogen in Tubes with Temperature Ratio's to 23*, NASA TN D-4332, Washington.
- 13 Bernard, J. J. and Génot, J. (1975), *Radiation Cooling of Thrust Nozzles*, AGARDograph 184, NATO, Neuilly-sur-Seine.

9 The Solid-Propellant Rocket Motor

In discussing the general characteristics of the solid-propellant rocket motor, or solid rocket, it will prove useful to compare it with its liquid counterpart. Advantages of the solid rocket are:

1. *Long storage life* even for high-performance rockets; this makes the type well suited for military purposes.
2. The propellants are harmless in human contact, this in contrast to many liquid propellants.
3. No active cooling system is needed, nor a propellant feed system; this leaves out complicated parts, such as pumps, turbines, etc, and makes low cost production possible.
4. Solid rockets are immediately ready for firing and have, due to their small number of components, a high reliability.

Many of the advantages are off-set, more or less, by disadvantages:

1. Relatively low I_{sp} for the solid propellants. This is partly compensated by a high I_g .
2. Some solid propellants become *brittle* below certain temperatures and then are *liable to crack*. These cracks may cause such high chamber pressures after ignition that an explosion results.
3. Thrust modulation, and thrust vector control are more difficult for the solid motor.
4. Extinguishment and re-ignition, though possible, are difficult.
5. Careful nozzle construction design is required as there is no active cooling system. The situation is often aggravated by the presence of solid particles in the combustion products; in most cases metal oxides that may cause serious nozzle erosion, or that may form deposits on the nozzle.

Combustion instability is a major problem in solid rocketry. It occurs frequently in newly developed rocket motors [1]. Prevention is still difficult and curing often weight consuming.

Solid rockets find widespread military and civil applications as: tactical weapons, sounding rockets, boosters for launch vehicles, including man-rated vehicles, such as the Space Shuttle, strategical weapons (ICBM), spacecraft launch vehicles and motors for stage separation.

9.1 Solid propellants

The solid propellant family basically consists of two entirely different types: the *homogeneous* or *colloidal propellant* and the *composite propellant*. There is a mixed form too, where ingredients of the first type are used in the second one. These are called *Composite Modified Double-Base* (CMDB).

9.1.1 Double-Base propellants

The most important homogeneous propellant is the *Double-Base* (DB) propellant. It was invented in 1888 by Nobel and has since been used as a gunpowder. It mainly consists of *nitrocellulose* (NC), a better name of which is *cellulose-nitrate* (CN) and *nitroglycerine* (NG), a better name of which is *glyceroltrinitrate* (GN). The first is a solid material, prone to detonation. It plasticizes with the highly explosive, liquid NG to a relatively stable solid propellant. When the propellant plasticizes the two ingredients form a gel and the propellant gets a homogeneous structure. Both NG and NC combine oxidizer and fuel in one molecule. DB propellants decompose completely into gases and therefore are smokeless. For *military purposes* this can be of importance. Often, besides stabilizers to prevent self-ignition, substances are added to the mixture, either to improve the mechanical properties, or to influence the burning characteristics. If these additives, such as

Table 9.1 Properties of some double-base propellants

Propellant	Composition (% by weight)	M (kg/kmol)	γ	T_c (K)
AHH	NC 55.2; NG 32.7; Triacetin 8.1; 2-Nitro- diphenyl amine 1; Lead salicylate 1.5; L-26 1.5	24.56	1.23	2485
ATN	NC 40; NG 48.4; Triacetin 6.4; 2-Nitro-diphenyl amine 1; Lead beta-resorcylate 2; Lead salicylate 2; Carbolac I 0.2	26.10	1.22	2822
AFU	NC 54.5; NG 23.1; Triacetin 18.1; Ethyl Centralite 0.6; 2-Nitro- Diphenyl amine 0.3; Lead stearate 3.4	21.55	1.26	1693
JPN (Ballistite)	NC 51.22; NG 43; Diethylphthalate 3.25; Ethyl Centralite 1; K_2SO_4 1.25; Carbon Black 0.2, wax 0.08	26.4	1.215	3125

carbon black, or aluminum powder do not form gaseous combustion products, the DB propellant may produce smoke. Table 9.1 gives the composition of some DB propellants, some thermochemical properties and some performance properties such as I_{sp}^o and c^* . Here I_{sp}^o indicates I_{sp} at ideal expansion. The volumetric specific impulse is found from ρ_p and I_{sp}^o . The burning rate versus the chamber pressure and the burning rate sensitivity for the initial temperature, are given in the last columns.

In some cases, the NG in DB propellants are replaced by other constituents such as di- or tri-nitrodiethyleneglycol.

Nitroglycerine has an excess of oxygen while NC is deficient in oxygen. The mixture ratio yielding the highest I_{sp} is about stoichiometric, i.e. the ratio of NG mass to NC mass should be about 8.6. Presently it is not possible to obtain a propellant gel with good mechanical properties at NG mass fractions exceeding 0.5.

9.1.2 Composite propellants

These usually are a mixture of an *anorganic salt*, serving as an *oxidizer*, and an *organic fuel* or *binder*, *plastic* or *rubber* in most cases. The following qualities are important for selecting an oxidizer: high heat of formation, high amount of available oxygen, high density, not or slightly hygroscopic and smooth burning characteristics over a wide pressure range. Most propellants nowadays use NH_4ClO_4 , *ammonium perchlorate* or AP, while sometimes

I_{sp}^o (s)	c^* (m/s)	ρ_p (kg/m ³)	Pressure Range (MPa)	$r = ap^n$		π_K (K ⁻¹)
				a	n	
225 $p_c = 7 \text{ MPa}$ $p_e = 0.1 \text{ MPa}$	1402	1601	2.76– 4.83	39.77	0.7	
			4.83– 5.21	8.74	0.2	1.26×10^{-3}
			5.21– 7.58	21.67	-0.35	0.81×10^{-3}
			7.58– 8.62	39.64	-0.65	1.53×10^{-3}
			8.62–10	5.98	0.23	
			10 –25	1.40	0.86	
235 $p_c = 7 \text{ MPa}$ $p_e = 0.1 \text{ MPa}$	1453	1602	at 293 K			
			3.10– 7.58	7.01	0.49	5.04×10^{-3}
			7.58–13.10	116.42	0.07	2.34×10^{-3}
			13.10–16.89	4.31	0.59	4.32×10^{-3}
			at 293 K			
196 $p_c = 7 \text{ MPa}$ $p_e = 0.1 \text{ MPa}$	1225	1514	3.79– 6.21	4	0.24	
			6.21– 9.65	112.87	-0.4	2.16×10^{-3}
			9.65–17.24	6.35	0.56	6.66×10^{-3}
						at 293 K
250	1523	1620		8.9	0.69	12.26×10^{-3}

Table 9.2 Properties of some composite propellants

Propellant	Composition (% by weight)	M (kg/kmol)	γ	T_c (K)	I_{sp}^o (s)
JPL 540A	PU 20; AP 80.	25	1.2	2600	231 $p_c = 6 \text{ MPa}$ $p_e = 0.1 \text{ MPa}$
Propellant proposed for Space Shuttle Boosters	PBAN 12.5; Al 16; Epoxy Curative 1.5; Ferric Oxide 0.1; AP 69.9.	27.8	1.18	3480	260 $p_c = 7 \text{ MPa}$ $p_e = 0.1 \text{ MPa}$
ANP-2639AF	PU 24.1; Al 15; Carbon Black 0.5; Copper-Chromite 0.4; AP 60.	24.7	1.18	2703	254 $p_c = 7 \text{ MPa}$ $p_e = 0.1 \text{ MPa}$
Arcite 373	AP 58.9; Al 21; PVC 8.62; Diethyl Adipate 10.79; XB82 0.17; X23-74 0.17; British Detergent 0.25.	29.06	1.18	3370	242 $p_c = 7 \text{ MPa}$ $A_e/A_t = 9$ 266 $p_c = 7 \text{ MPa}$ $A_e/A_t = 9.8$ (theoretical)
CDT (80)	NC 26; NG 27.2; AP 19.5; Al 18.9; 2-Nitro diphenyl amine 1; Triacetin 6.4; Magnesium Oxide 1.	30.18	1.168	4000	263
H-3515	AP 35; Pentaeritritol-trinitrate 35; NC 14.25; Al 15; Ethylcentralite 0.75.			3450	255
TRX-H609	AP 70; Al 16; PBAA 11.05; ERL-2795 2.94.	25.97	1.21	3040	245
Flexadyne RDS-509 (Rocketdyne)	CTPB 12; AP 82; Al 4; Additive 2.	27.16	1.20	3176	248 $p_c = 7 \text{ MPa}$ $p_e = 0.1 \text{ MPa}$
Flexadyne RDS-556 (Rocketdyne)	CTPB 15; AP 69; Al 14; Additive 2.	26.92	1.20	3246	252 $p_c = 7 \text{ MPa}$ $p_e = 0.1 \text{ MPa}$

Al aluminum

AP ammonium perchlorate

NC nitrocellulose

NG nitroglycerin

c^* (m/s)	ρ_p (kg/m ³)	Pressure Range (MPa)	$r = a \cdot p^n$		π_K (K ⁻¹)
			a	n	
1434	1660	0.1 – 0.45	5.13	0.679	
		0.45– 1.65	4.13	0.406	
		1.65– 5.5	4.6	0.189	
1583	1772	5– 7	7.35 at 294 K	0.33	8.3×10^{-4}
1480	1669	1.38– 4.14	4.5	0.3135	$2.8 \times 10^{-3}; 255 \text{ K} < T_i < 289 \text{ K}$
		4.14– 8.96	5.61 at 289 K	0.159	$1.9 \times 10^{-3}; 289 \text{ K} < T_i < 316 \text{ K}$
1523	1772	3.45– 4.83	6.74	0.176	
		4.83–13.1	5.64 at 294 K	0.295	19.8×10^{-4}
					at 294 K; $K = 300$ $p = 7 \text{ MPa}$
1635	1745	4.14–20.68	6.99 at 294 K	0.48	8.46×10^{-3} at 7 MPa 8.1×10^{-3} at 10.5 MPa
1772		4.14–13.79	2.87 at 294 K	0.68	12.4×10^{-3}
1517	1760	2.07–13.79	4.92 at 294 K	0.297	19.8×10^{-4}
1518	1758		8.25	0.39	2.11×10^{-3}
1544	1747	2.76– 6.85	10.79	0.65	2.48×10^{-3}
		6.85–20.68	18.86	0.36	2.10×10^{-3}

- CTPB carboxyl terminated polybutadiene
 PBAA polybutadiene-acrylic acid polymer
 PBAN polybutadiene-acrylic acid-acrylonitrile terpolymer
 PU polyurethane
 PVC polyvinyl chloride

NH_4NO_3 , ammonium nitrate, and KClO_4 , potassium perchlorate are used. Other possible oxidizers which have been proposed for instance are NO_2ClO_4 , nitronium perchlorate [2], and $\text{N}_2\text{H}_5\text{ClO}_4$, hydrazine perchlorate [3] while also organic oxidizers are considered. Nevertheless, AP at the present time is the most commonly used oxidizer for composite propellants.

The choice of the fuel is mainly determined by mechanical properties, such as strength, elasticity and thermal properties at low and high environmental temperatures, a high energy content and good aging and burning characteristics. An essential feature of the binder is an initial liquid state of its components (prepolymers), as this facilitates the mixing of oxidizer and fuel. The mixing is followed by a curing process during which the binder becomes a solid. By adding powdered metals, such as Al, aluminum, to the propellant the flame temperature, and thus I_{sp} , can be increased considerably. Table 9.2 lists compositions and characteristics of some typical composite propellants. Like Table 9.1, this table gives the propellant composition, some thermochemical properties, the burning rate behavior and the temperature sensitivity.

Composite modified double-base propellants contain NC, NG, an anorganic salt, such as AP and a powdered metal, such as Al, and in some cases a polymer. In general, these propellants have high flame temperatures; their burning rates are very sensitive to pressure. They are not used in large quantity as yet.

9.1.3 The burning rate

Solid propellant burns normal to its surface. The (average) *burning rate*, r , is defined as the regression of the burning surface per unit time. For a given propellant, the burning rate is mainly dependent on the pressure, p , and the initial temperature, T_i , of the propellant. One determines $r(p)$ by measurements in a *Crawford bomb* or *strand burner* (Fig. 9.1). In this vessel, in which the pressure can be adjusted, a strand of propellant is burnt. Often a gas, mostly N_2 , which does not influence the propellant burning, ventilates the vessel. The propellant strand is inhibited such that burning will only take place in the longitudinal direction. Two electrical wires are fixed to the strand at a mutual distance L . The melting of those two wires will start and stop, respectively, a chronometer. From the time measured and the distance, L , the average burning rate is determined. By repeating this procedure at different pressures and temperatures T_i , one obtains $r(p, T_i)$. It should be emphasized here that the relationship obtained this way only holds for stationary conditions. As the burning rate is also strongly dependent on non-stationary effects, this relationship cannot be applied to non-steady situations.

It turns out that the burning rate dependence on pressure can be expressed as

$$r = a + bp^n, \quad (9.1-1)$$

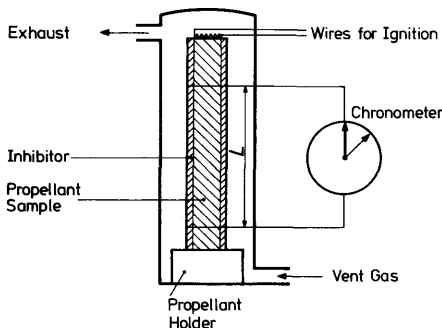


Fig. 9.1 Schematic drawing of the Crawford bomb or strand burner

which is known as *De Vieille's* or *St. Robert's* law. However, for all types of propellant the simpler relationship

$$r = ap^n, \quad (9.1-2)$$

turns out to be very accurate, and is generally used. The exponent n is called the *pressure exponent*. In general, the parameters a and n in Eq. (9.1-2) only have constant values over certain pressure intervals, thus for one propellant,

$$r = a_1 p^{n_1}, \quad p \leq p_1,$$

$$r = a_2 p^{n_2}, \quad p_1 \leq p \leq p_2,$$

In general, r lies between 3 and 250 mm/s. Plots of r versus p are generally given on a double logarithmic scale, as $\log r$ is about linearly dependent on $\log p$. In that case, any change in the burning rate exponent, n , is coupled with a change in the slope of the curve. The dependence of r on p for a typical composite propellant is given in Fig. 9.2.

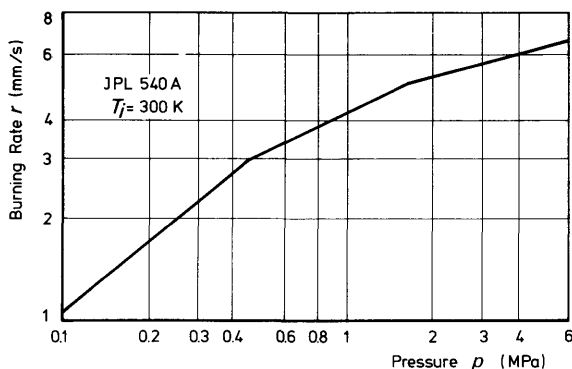


Fig. 9.2 Burning rate versus pressure for JPL 540 A composite propellant

In some cases, r is independent of p over a certain interval, i.e. $n = 0$. In this case one speaks of *plateau-burning* (Fig. 9.3a). In those cases that r decreases with increasing p , i.e. $n < 0$, one speaks of *mesa-burning* (Fig. 9.3b). The dependence of r on the initial temperature T_i is depicted in Fig. 9.3c. In general, r will increase with increasing T_i . This dependence is expressed by one of the following empirical relationships

$$a = a_0 e^{\tau(T_i - T_{i0})}, \quad (9.1-3)$$

or

$$a = \frac{a'}{T' - T_i}. \quad (9.1-4)$$

Here T_{i0} is a reference temperature, T' is the auto-ignition temperature and a_0 , τ and a' are constants. Sometimes different values for a_0 are used for $T_i < T_{i0}$ and $T_i > T_{i0}$.

It may seem strange that the initial temperature of the propellant has such a strong influence on the burning rate, as one would expect the propellant to heat up during the combustion process. Being the major source of heat transfer, we will consider the one-dimensional steady-state heat conduction in a propellant slab, burning steadily. The heat conduction equation, Eq. (8.2-3), then states

$$r \frac{dT}{dx} = \kappa \frac{d^2T}{dx^2} \quad (9.1-5)$$

where $\kappa = k/(\rho_p c)$ stands for the thermal diffusivity. The origin of the coordinate system is fixed to the burning surface (Fig. 9.4). So with respect to a fixed point in the propellant, the origin moves to the left at a rate r . For $x \rightarrow -\infty$ the temperature in the solid is constant and equals T_i , the initial temperature. At $x = 0$ the temperature is the surface temperature, T_s , which may be in the order of 1000 K. Integration of Eq. (9.1-5), and using the fact that for $x \rightarrow -\infty$: $\frac{dT}{dx} = 0$, $T = T_i$, yields

$$T - T_i = -\frac{\kappa}{r} \frac{dT}{dx}.$$

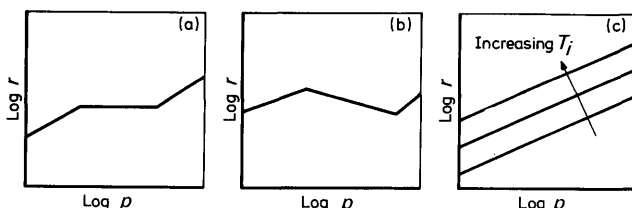


Fig. 9.3 Burning rate versus pressure; (a) plateau-burning, (b) mesa-burning, (c) dependence on the initial temperature, T_i , of the propellant

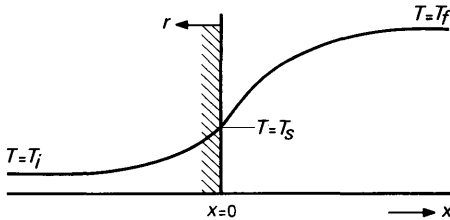


Fig. 9.4 Coordinate system and temperature profile for a stationary burning solid propellant

A second integration and subsequent substitution of the boundary condition, $T = T_s$ at $x = 0$ yields

$$\frac{T - T_i}{T_s - T_i} = e^{rx/\kappa}, \quad x \leq 0 \quad (9.1-6)$$

which represents the temperature profile in the solid.

The order of magnitude of the thermal diffusivity is $\kappa \approx 10^{-7} \text{ m}^2/\text{s}$ [4]. For a burning rate of 5 mm/s, $(T - T_i)/(T_s - T_i)$ is only 0.001 at $x = -0.14 \text{ mm}$. Thus only a very thin zone of the propellant is effectively heated and therefore it is conceivable that the initial temperature acts as a rate controlling factor.

The sensitivity of r to variations in T_i is expressed by

$$(\pi_r)_p = \frac{1}{r} \left(\frac{dr}{dT_i} \right)_p. \quad (9.1-7)$$

Inserting Eq. (9.1-3) yields

$$(\pi_r)_p = \tau, \quad (9.1-8)$$

while by the use of Eq. (9.1-4) we find

$$(\pi_r)_p = \frac{1}{T' - T_i}. \quad (9.1-9)$$

In Section 9.2.1, we will define three other useful temperature sensitivity coefficients.

9.1.4 Combustion models

The burning rate law, Eq. (9.1-1) or Eq. (9.1-2), is a quantification of measurements. It does not take into account any of the chemical and physical phenomena that take place on a microscopic scale at or near the burning surface. Based on observations, a good many more or less detailed propellant combustion models have been formulated [4, 5]. As the structures of DB and composite propellant are quite different, it is not surprising that there are different combustion models for both types of propellant.

Combustion of Double-Base propellants. The various models for the combustion of DB propellant all assume a combustion process in four steps [5, 6]. In a very thin (10^{-5} – 10^{-4} m) surface layer, the *foam region*, the propellant decomposes into gaseous products. The decomposition rate is controlled by the heat input (mainly conduction) from the burning gases into the propellant. The gases leaving the foam region react exothermally in a thin region, the *fizz zone*. The temperature increases with increasing distance from the burning surface. The fizz zone is followed by the *dark zone* or *preparation zone*. Here, activated products are formed, but the temperature remains about constant. The dark zone is followed by the *flame zone* where the *final combustion* takes place and the temperature increases to the adiabatic flame temperature.

At pressures above roughly 2 MPa, there is a luminous flame. With increasing pressures the thicknesses of the zones decrease. At very high pressures, the dark zone disappears almost completely. At high pressures the flame zone is nearer to the burning surface, so the heat input into the propellant, being proportional to dT/dx , is increased, leading to higher burning rates. The pressure dependence of the burning rate, however, is rather complex, and also depends strongly on the propellant composition, such as mixture ratio, NG/NC, and the presence of additives.

Combustion of AP-based composite propellants. Like in the case of DB propellant, conduction of heat into the propellant causes the propellant to decompose. At the surface, the oxidizer crystals and binder matrix form gaseous products, but usually not at the same rate for the same surface temperature. Therefore, the surface will become rough. On the average, however, flat surfaces remain flat, because if one assumes that the component with the lower burning rate protudes above the mean surface, it will obtain a higher surface temperature leading to a higher pyrolysis rate. The surface temperature of the burning surface therefore stands for an average value.

Based on visual observations, usually the following assumptions are made to analyse the combustion process. The surface remains dry, and there is no mixing of oxidizer and fuel on the surface. The gas flow from the surface is laminar. There are separate flows of oxidizer and fuel gases. At low pressures, the gases mix very rapidly before combustion takes place, the *premixed flame*. For moderate and high pressures there are many different models [4, 5]. We will briefly discuss two of them. The first one is the *granular diffusion flame* (GDF) model by Summerfield [7, 8]. The basic features of the GDF model are depicted in Fig. 9.5a. Directly after the burning surface there is an endothermal reaction involving the pyrolysis of the binder to form fuel gases and the dissociation of AP into NH_3 and HClO_4 . This is followed by an exothermal premixed reaction between NH_3 and HClO_4 (the A/PA reaction). The fuel gases form *pockets* in the oxygen-rich A/PA combustion products. At their surface these fuel pockets

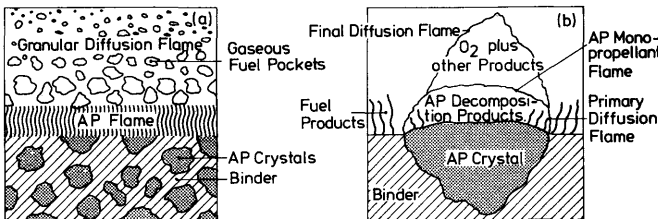


Fig. 9.5 (a) The Granular Diffusion Flame model; (b) The Multiple Flames model.

react with the oxidizer products, the *oxidizer/fuel* (O/F) flame. At low pressures, the O/F flame is controlled by the chemical reaction rate. At high pressures, the O/F flame is controlled by the diffusional mixing rate. The GDF model eventually yields a relation between burning rate and pressure

$$\frac{1}{r} = \frac{a}{p} + \frac{b}{p^{1/3}}. \quad (9.1-10)$$

The second model we will mention is the *multiple flames* (MF) model by Beckstead, Derr and Price [9]. Its basic features are depicted in Fig. 9.5.b. It assumes a flow of AP decomposition products above the oxidizer crystal. Only at the boundaries, where there is a contact with the fuel products, there is a diffusion flame. The AP products react to form an *AP mono-propellant flame*. This is followed by a *final diffusion flame* where the oxygen-rich products of the monopropellant flame react with the fuel pyrolysis products. The mixing of this flame is assumed to be diffusion controlled. The MF model accounts for propellant composition, oxidizer crystal size, and oxidizer crystals protruding above, or recessing below the surface. As it does not yield a simple relation between r and p , $r(p)$ has to be computed numerically.

Both models, which have been formulated for non-metallized AP-based composite propellants, have yielded satisfactory results. While the GDF model has the charm of yielding a simple relationship between r and p , the MF model is liable to give better predictions, as more important variables, such as oxidizer crystal size, mixture ratio, etc., are accounted for explicitly. According to the MF model, one would expect the burning rate to increase with smaller oxidizer crystal size, which, in general, is the case. A comparison of both models has been made by Stamets and Weiss [10] and Hamann [11]. The last author also extends the MF model by small perturbation techniques to non-steady cases. An excellent compilation of our knowledge about the mechanisms of combustion of composite propellants is given by Boggs [12].

9.2 Internal ballistics

The solid rocket motor is essentially a pressure vessel, with a nozzle at one end, partially filled with one or more blocks of solid propellant, called the grain, plus an ignition device. Those parts of the motor case exposed to the combustion products are usually thermally insulated. The grain is fabricated to a configuration that produces a specific thrust-time history (Section 9.3), and a typical motor with a slotted tube grain is illustrated in Fig. 9.6. As shown, the surface of the propellant is ignited by a pyrotechnic device although other techniques are occasionally employed. Combustion can be restricted to specified surfaces by bonding an inhibitor to selected areas of the grain (*restricted burning*). During the ignition transient, chamber pressure increases and stable operating pressure is obtained when the uninhibited propellant surface is fully ignited. Exclusion of moisture and foreign matter, plus a rapid pressure build-up, can be achieved by sealing the nozzle with a rupture disk, designed to fail at a predetermined pressure, typically 50 to 90 percent of operating pressure. This application is common for upper-stage motors that must ignite at low ambient pressure and temperature.

9.2.1 Equilibrium chamber pressure

We will assume the combustion products to be ideal gases and the chamber conditions to be uniform. As we will see later (Section 9.2.2), the assumption of uniform chamber conditions certainly is a simplification. The chamber volume, V_c , is the volume available to the combustion products. Usually it is taken up to the surface of constant properties at the throat. We indicate the volume taken up by the propellant by V_p . We can apply the equation of continuity, Eq. (3.7-1), which was formulated for a constant volume, to the total volume of the solid motor:

$$\frac{\partial}{\partial t} \left\{ \int_{V_c} \rho dV + \int_{V_p} \rho dV \right\} = - \int_{S_w} \rho \mathbf{V} \cdot \mathbf{n} dS - \int_{A_t} \rho \mathbf{V} \cdot \mathbf{n} dS. \quad (9.2-1)$$

In this equation, S_w stands for the walls of the solid motor, and as at the motor walls $\mathbf{V} \cdot \mathbf{n} = 0$, we have

$$\int_{S_w} \rho \mathbf{V} \cdot \mathbf{n} dS = 0. \quad (9.2-2)$$

Owing to the combustion of propellant, the chamber volume increases, while the propellant volume decreases. During a time interval Δt , a propellant mass

$$\Delta M = \rho_p r S_b \Delta t, \quad (9.2-3)$$

is consumed; where S_b is the area of the burning surface. Thus:

$$\partial V_c / \partial t = r S_b, \quad (9.2-4)$$

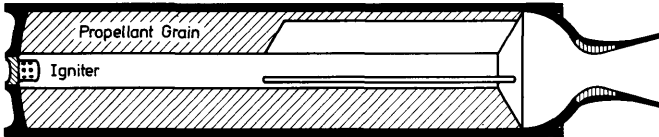


Fig. 9.6 Cross-section of a solid rocket motor

and

$$\frac{\partial \mathcal{V}_p}{\partial t} = -rS_b. \quad (9.2-5)$$

Combining these results with Eq. (9.2-1), while considering that the propellant density is constant, we are left with

$$\frac{\partial}{\partial t} \left\{ \int_{\mathcal{V}_c} \rho d\mathcal{V} + \int_{\mathcal{V}_p} \rho d\mathcal{V} \right\} = \int_{\mathcal{V}_c} \frac{\partial \rho}{\partial t} d\mathcal{V} + \rho_c r S_b - \rho_p r S_b = - \int_{A_t} \rho \mathbf{V} \cdot \mathbf{n} dS. \quad (9.2-6)$$

The last integral stands for the mass flow through the nozzle, and by Eq. (5.1-39) we have

$$\int_{A_t} \rho \mathbf{V} \cdot \mathbf{n} dS = \Gamma \frac{p_c A_t}{\sqrt{RT_c}}. \quad (9.2-7)$$

Inserting this result into Eq. (9.2-6) and rearranging the terms leaves us with

$$\int_{\mathcal{V}_c} \frac{\partial \rho}{\partial t} d\mathcal{V} = (\rho_p - \rho_c) S_b r - \Gamma \frac{p_c}{\sqrt{RT_c}} A_t, \quad (9.2-8)$$

where ρ_c is the gas density in the chamber. The order of magnitude of the propellant density is $\rho_p = 1600 \text{ kg/m}^3$, while $\rho_c \approx 3 - 10 \text{ kg/m}^3$. As $\rho_c \ll \rho_p$, Eq. (9.2-8) can be simplified to

$$\int_{\mathcal{V}_c} \frac{\partial \rho}{\partial t} d\mathcal{V} = \rho_p S_b r - \Gamma \frac{p_c}{\sqrt{RT_c}} A_t. \quad (9.2-9)$$

For steady-state operations the mass balance for the rocket motor is given by

$$\rho_p S_b r = \Gamma \frac{p_c}{\sqrt{RT_c}} A_t. \quad (9.2-10)$$

Inserting $r = ap_c^n$, and using $c^* = \sqrt{RT_c}/\Gamma$, yields the equilibrium pressure for the quasi-steady operation of a solid rocket motor

$$p_c = (a \rho_p c^* K)^{1/(1-n)}. \quad (9.2-11)$$

Here K is the ratio of the area of the burning surface and the throat area,

called the '*klemmung*', which means *pinching*,

$$K = S_b/A_r. \quad (9.2-12)$$

We see that for $n = 0$, p_c is proportional with K , while for $0 < n < 1$, p_c is more than proportional with K . For $n \uparrow 1$, the right-hand side of Eq. (9.2-11) tends to infinity. Logarithmic differentiation of Eq. (9.2-11) leads to

$$\frac{dp_c}{p_c} = \frac{1}{1-n} \frac{dK}{K}, \quad (9.2-13)$$

which illustrates the same result as discussed above. For most solid motors, K lies somewhere between 200 and 1000.

In Section 9.1.3 we have defined a temperature sensitivity coefficient $(\pi_r)_p$ for the propellant. We now can define three more temperature sensitivity coefficients. They express the pressure change, or the change in the burning rate with a change in the initial temperature. The first one, defined at a particular value of the *klemmung*, K , is

$$(\pi_p)_K = \frac{1}{p_c} \left(\frac{\partial p_c}{\partial T_i} \right)_K, \quad (9.2-14)$$

and expresses the relative variation in chamber pressure, p_c , with a change in the initial temperature, T_i . The second one expresses the relative variation in burning rate with a change in initial temperature, at a particular value of the *klemmung*, K ,

$$(\pi_r)_K = \frac{1}{r} \left(\frac{\partial r}{\partial T_i} \right)_K. \quad (9.2-15)$$

With the Eqs. (9.2-12), (9.2-14), (9.2-15) and (9.1-7), one easily shows that

$$(\pi_p)_K = (\pi_r)_K = \pi_K = \frac{1}{1-n} (\pi_r)_p.$$

Often $(\pi_r)_K$ is denoted as σ_K . Thus, the sensitivity of combustion pressure to grain temperature is greater than the sensitivity of the burning rate to the grain temperature at constant pressure, by the factor $1/(1-n)$. Therefore, in addition to a high T' , a desirable propellant should have a low value of n .

The last temperature sensitivity coefficient that is used sometimes is $(\pi)_{p/r}$, which is the temperature sensitivity coefficient of pressure at a particular value of p_c/r [13]

$$(\pi)_{p/r} = \frac{1}{p_c} \left(\frac{\partial p_c}{\partial T_i} \right)_{p_c/r} = \frac{1}{1-n} (\pi_r)_p. \quad (9.2-16)$$

In general π_K is given as a propellant variable. For modern composite propellants, π_K may be about $5 \times 10^{-3} \text{ K}^{-1}$ to $5 \times 10^{-4} \text{ K}^{-1}$. For DB propellants, π_K is generally between 10^{-2} K^{-1} to 10^{-3} K^{-1} .

For a stable operation of the motor, the pressure exponent, n , should

satisfy certain requirements. An indication for this was found already in Eq. (9.2-13) where $d\rho_c$ tends to infinity for $n \uparrow 1$. Consider the equation for the conservation of mass for the rocket motor, Eq. (9.2-9). We assume uniform chamber conditions, and therefore we can write

$$\gamma_c \frac{d\rho_c}{dt} = \rho_p S_b a p_c^n - \Gamma \frac{p_c}{\sqrt{RT_c}} A_t. \quad (9.2-17)$$

We will now consider a perturbed steady-state process. A small pressure perturbation, p'_c , will be accompanied by perturbations ρ'_c and T'_c in the density and chamber temperature, respectively. The steady-state chamber variables are denoted by \bar{p}_c , $\bar{\rho}_c$ and \bar{T}_c . Thus,

$$p_c = \bar{p}_c + p'_c, \quad \rho_c = \bar{\rho}_c + \rho'_c \quad \text{and} \quad T_c = \bar{T}_c + T'_c.$$

As $\frac{d\bar{\rho}_c}{dt} = 0$, we have

$$\rho_p S_b a \bar{p}_c^n = \Gamma \frac{\bar{p}_c}{\sqrt{R\bar{T}_c}} A_t = \bar{m}. \quad (9.2-18)$$

Linearization, and the use of Eq. (9.2-18) yields

$$\bar{\rho}_c \gamma_c \frac{d}{dt} \left(\frac{\rho'_c}{\bar{\rho}_c} \right) = \rho_p S_b a \bar{p}_c^n \left(\frac{p'_c}{\bar{p}_c} \right) n - \Gamma \frac{\bar{p}_c A_t}{\sqrt{R\bar{T}_c}} \left(\frac{p'_c}{\bar{p}_c} - \frac{T'_c}{2\bar{T}_c} \right). \quad (9.2-19)$$

Now, if the change of state in the motor is isentropic, i.e. if the compression or expansion is not accompanied by heat transfer or other irreversible processes, the Poisson relations, Eq. (3.7-20), will hold

$$\frac{\rho_c}{\bar{\rho}_c} = \left(\frac{p_c}{\bar{p}_c} \right)^{1/\gamma}, \quad \text{and} \quad \frac{T_c}{\bar{T}_c} = \left(\frac{p_c}{\bar{p}_c} \right)^{(\gamma-1)/\gamma}.$$

If the change of state is isothermal, i.e. the temperature remains constant, we may express this by

$$\rho_c \propto p_c, \quad \text{and} \quad T_c = \text{constant}.$$

It is conceivable that in practice the change of state will be in between isothermal and isentropic. We will express this by

$$\frac{\rho_c}{\bar{\rho}_c} = \left(\frac{p_c}{\bar{p}_c} \right)^{1/\delta}, \quad \text{and} \quad \frac{T_c}{\bar{T}_c} = \left(\frac{p_c}{\bar{p}_c} \right)^{(\delta-1)/\delta},$$

with $\delta = 1$ for an isothermal change of state and $\delta = \gamma$ for an isentropic one. Again, linearizing leads to

$$\frac{p'_c}{\bar{p}_c} = \delta \frac{\rho'_c}{\bar{\rho}_c} \quad \text{and} \quad \frac{T'_c}{\bar{T}_c} = \frac{\delta-1}{\delta} \frac{p'_c}{\bar{p}_c}. \quad (9.2-20)$$

Inserting these relations into Eq. (9.2-19), gives a differential equation in $\frac{p'_c}{\bar{p}_c}$,

$$\frac{\bar{\rho}_c \mathcal{V}_c}{\delta} \frac{d}{dt} \left(\frac{p'_c}{\bar{p}_c} \right) = \bar{m} \left(n - \frac{\delta + 1}{2\delta} \right) \frac{p'_c}{\bar{p}_c}, \quad (9.2-21)$$

the solution of which is

$$(p'_c/\bar{p}_c) = (p'_c/\bar{p}_c)_{t=0} \times \exp \left[\frac{\delta \bar{m}}{\bar{\rho}_c \mathcal{V}_c} \left(n - \frac{\delta + 1}{2\delta} \right) t \right]. \quad (9.2-22)$$

This equation describes the initial growth of a pressure fluctuation with time. For a stable operation of the motor, according to this first-order theory, we require the fluctuation to damp out, i.e.

$$n - \frac{\delta + 1}{2\delta} < 0.$$

Thus for a stable motor operation, the pressure exponent, n , should satisfy the relation

$$n < \frac{\delta + 1}{2\delta}. \quad (9.2-23)$$

If the change of state is isothermal, which means that T_c , and consequently c^* is constant, the requirement is the well-known criterion $n < 1$. This may, however, over-estimate the admissible value of n , as for an isentropic change of state one finds $n < (\gamma + 1)/2\gamma$, which, for $\gamma = 1.25$, yields $n < 0.9$. In practice $n < 0.8$ for most propellants.

The criterion $n < 1$ is also obtained by the following reasoning. If we assume T_c constant, the mass flow through the nozzle is proportional to p_c . In Fig. 9.7 the straight line through the origin and S depicts the mass flow

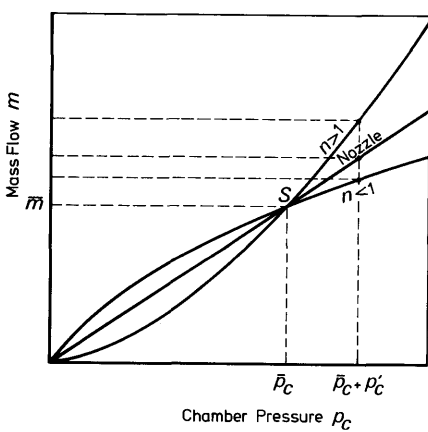


Fig. 9.7 The balance of mass in a solid rocket motor

through the nozzle as a function of p_c . The two curves through the origin and S represent the mass produced at the burning surface, for the cases $n < 1$ and $n > 1$. At S there is a balance between mass production and outflux of mass. At a pressure $\bar{p}_c + p'_c$, the mass flow through the nozzle is larger than the production at the burning surface in case $n < 1$ and the reverse happens for $n > 1$. Thus if $n < 1$ the pressure will drop to its steady-state value \bar{p}_c . For $p'_c < 0$ the same reasoning shows that the pressure will return to \bar{p}_c for $n < 1$ and continue dropping in case $n > 1$. Thus, $n < (\delta + 1)/2\delta$ produces a stable operation while $n > (\delta + 1)/2\delta$ will probably lead to over-pressurization and rupture of the motor or depressurization and flame out.

9.2.2 The flow in a cylindrical grain

In many cases the propellant grain is cylindrical or nearly cylindrical. In other cases the grain may be composed of a succession of cylindrical, or nearly cylindrical parts. The cross-section of the grain may have any shape. The cross-sectional area of the flow channel is called the *port area*, A_p , which we will assume constant along the grain. In those cases that the port area varies along the grain one could either approximate the grain by cylindrical parts, or take this variation into account by a two- or three-dimensional analysis. For the sake of simplicity we will make the following assumptions: the burning rate, r , is independent of the location, x , in the grain; the perimeter, l_b , of the cross-section of the perforation is constant along the grain; the change of A_p , l_b , and V_c per unit time is small and a quasi-steady analysis suffices; c_p and γ are constant, except directly at the burning surface; the local cross-section of the tube can be regarded as a surface of constant properties; the gas temperature at the burning surface equals the flame temperature, T_f , everywhere.

Conservation of mass. We consider a small section of the grain (Fig. 9.8). The equation for the conservation of mass, Eq. (3.7-1), applied to this section between the positions x and $x + \Delta x$ is

$$\frac{\partial}{\partial t} \int_V \rho dV + \int_S \rho \mathbf{V} \cdot \mathbf{n} dS = 0. \quad (9.2-24)$$

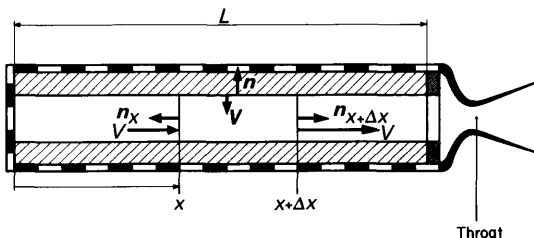


Fig. 9.8 Nomenclature for the cylindrical grain

The volume \mathcal{V} consists of the volume taken up by the propellant, \mathcal{V}_p , and the volume containing the combustion products, \mathcal{V}_c . In the same way as in Section 9.2.1, we find

$$\partial \mathcal{V}_c / \partial t = r S_b = r l_b \Delta x, \quad (9.2-25)$$

and

$$\partial \mathcal{V}_p / \partial t = -r S_b = -r l_b \Delta x. \quad (9.2-26)$$

At the walls of the rocket motor $\mathbf{V} \cdot \mathbf{n} = 0$ and at the control surface A_x we have $\mathbf{V} = -\mathbf{V} \cdot \mathbf{n}_x$ while at $A_{x+\Delta x}$, we have $\mathbf{V} = \mathbf{V} \cdot \mathbf{n}_{x+\Delta x}$. For steady-state, $\partial \rho / \partial t = 0$ and hence, in the same way as in Section 9.2.1, we find, as $\Delta x \rightarrow 0$,

$$\rho r l_b - \rho_p r l_b + \frac{d}{dx} (\rho V) A_p = 0.$$

Note that the index ρ here is used to indicate both port and propellant. As $\rho \ll \rho_p$, we can write the equation of continuity for a cylindrical channel with uniform mass addition as

$$\rho V = cx, \quad (9.2-27)$$

with

$$c = \frac{\rho_p r l_b}{A_p}. \quad (9.2-28)$$

The momentum equation, Section 3.7.2, can be written as

$$\int_{\mathcal{V}} \frac{\partial}{\partial t} (\rho \mathbf{V}) d\mathcal{V} + \int_S \{(\rho \mathbf{V} \cdot \mathbf{n}) \mathbf{V} + \mathbf{n} p\} dS = 0.$$

Applying this to the section depicted in Fig. 9.8 we find for the steady-state case

$$\begin{aligned} \int_{A_x} \{(\rho \mathbf{V} \cdot \mathbf{n}) \mathbf{V} + \mathbf{n} p\} dA + \int_{A_{x+\Delta x}} \{(\rho \mathbf{V} \cdot \mathbf{n}) \mathbf{V} + \mathbf{n} p\} dA + \\ + \int_{S_b} \{(\rho \mathbf{V} \cdot \mathbf{n}) \mathbf{V} + \mathbf{n} p\} dS_b = 0. \end{aligned} \quad (9.2-29)$$

At the burning surface we have $\rho \mathbf{V} \cdot \mathbf{n} = -\rho_p r$. Using this relation and the assumption that the control surfaces, A_x , and $A_{x+\Delta x}$, are surfaces of constant properties, we can evaluate Eq. (9.2-29) to

$$\mathbf{n}_{x+\Delta x} [(\rho V^2 + p)_{x+\Delta x} - (\rho V^2 + p)_x] A_p + \int_{\Delta x} dx \oint_{l_b} \left(-\frac{\rho_p^2 r^2}{\rho} + p \right) \mathbf{n} dl = 0.$$

As ρ_p and r are constant and p and ρ are constant over any cross-sectional area we have

$$\oint_{l_b} \left(-\frac{\rho_p^2 r^2}{\rho} + p \right) \mathbf{n} dl = \left(-\frac{\rho_p^2 r^2}{\rho} + p \right) \oint_{l_b} \mathbf{n} dl = 0.$$

Now let $\Delta x \rightarrow 0$, then we find for the momentum equation in a cylindrical grain

$$\frac{d}{dx} (\rho V^2 + p) = 0, \quad (9.2-30)$$

or

$$\rho V^2 + p = \text{constant.}$$

At the front end of the grain, i.e. at $x = 0$, the velocity is zero, or practically zero, and the pressure is the front-end stagnation pressure, p_0 , thus

$$\rho V^2 + p = p_0. \quad (9.2-31)$$

The energy equation, Eq. (3.7-15), can be written in a slightly different form,

$$\frac{\partial}{\partial t} \int_V \rho(e + V^2/2) dV = - \int_S [(\rho \mathbf{V} \cdot \mathbf{n})(e + V^2/2) + p \mathbf{V} \cdot \mathbf{n}] dS. \quad (9.2-32)$$

We now apply Eq. (9.2-32) to the cavity enclosed by the burning propellant and the surfaces of constant properties, A_x and $A_{x+\Delta x}$, (Fig. 9.8) which yields,

$$\begin{aligned} \int_V \frac{\partial}{\partial t} [\rho(e + V^2/2)] dV + rl_b \rho(e + V^2/2) \Delta x &= \{(\rho V)(e + V^2/2 + p/\rho)\}_x \\ &- \{(\rho V)(e + V^2/2 + p/\rho)\}_{x+\Delta x} A_p - \int_{\Delta x} dx \oint_{l_b} [(\rho \mathbf{V} \cdot \mathbf{n})(e + V^2/2 + p/\rho)] dl. \end{aligned} \quad (9.2-33)$$

At the burning surface, $V^2 \ll e$, the temperature is the flame temperature, T_f , and

$$e = e_f = \int_0^{T_f} c_v dT.$$

Moreover, we make use of the fact that at the burning surface,

$$\rho \mathbf{V} \cdot \mathbf{n} = -\rho_p r. \quad (9.2-34)$$

Substituting these relations into Eq. (9.2-33), and letting $\Delta x \rightarrow 0$, this equation can be evaluated for a steady-state flow, to yield

$$\frac{d}{dx} [(\rho V)(e + V^2/2 + p/\rho)] A_p = rl_b [\rho_p (e_f + RT_f) - \rho e_f]. \quad (9.2-35)$$

Use has been made of the ideal gas law and the fact that at the burning surface the gas temperature equals T_f . Neglecting ρ with respect to ρ_p , finally gives

$$\frac{d}{dx} [(\rho V)(e + V^2/2 + p/\rho)] = \frac{\rho_p r l_b}{A_p} (e_f + RT_f).$$

Making use of the concept of enthalpy and Eq. (9.2-27) thus leads to

$$cx(h + \frac{1}{2}\mathbf{V} \cdot \mathbf{V} - h_f) = \text{constant}.$$

As this last equation must also hold for $x = 0$, the constant at the right-hand side is zero, which finally yields the energy equation for the flow in the tubular grain:

$$h + \frac{1}{2}V^2 = h_f. \quad (9.2-36)$$

In addition to the Eqs. (9.2-27), (9.2-31) and (9.2-36) we have the perfect gas law, $p = \rho RT$, as a fourth equation to describe the flow in the tubular grain. As the flow is not isentropic anymore, the Poisson relations, Eq. (3.7-20), do not hold for the whole field. However, we still can define the *local velocity of sound* as

$$a = \sqrt{\left(\frac{\partial p}{\partial \rho}\right)_s} = \sqrt{\gamma \frac{p}{\rho}}. \quad (9.2-37)$$

The local Mach number, M_a , is given by

$$M_a = V/a. \quad (9.2-38)$$

The momentum equation, Eq. (9.2-31), then can be written as

$$1 + \gamma M_a^2 = p_0/p. \quad (9.2-39)$$

By using $c_p = \frac{\gamma R}{\gamma - 1}$, the energy equation transforms into

$$\frac{2\gamma}{\gamma - 1} \frac{p}{\rho} + V^2 = \frac{2\gamma}{\gamma - 1} \frac{p_0}{\rho_0} \quad (9.2-40)$$

or

$$\frac{T_0}{T} = \frac{a_0^2}{a^2} = 1 + \frac{\gamma - 1}{2} M_a^2, \quad (9.2-41)$$

where the index 0 denotes front-end conditions. By the use of the perfect gas law, Eq. (9.2-39) and Eq. (9.2-41), the ratio ρ_0/ρ can be related to the local Mach number

$$\frac{\rho_0}{\rho} = \frac{T}{T_0} \frac{p_0}{p} = \frac{1 + \gamma M_a^2}{1 + \frac{\gamma - 1}{2} M_a^2}. \quad (9.2-42)$$

The local pressure in the grain is found from the three conservation equations, Eqs. (9.2-27), (9.2-31) and (9.2-36). From Eq. (9.2-27) we have $\rho = cx/V$, and from Eq. (9.2-31), $V = (p_0 - p)/(cx)$. Substitution into the energy equation, Eq. (9.2-36) leads to

$$2h_f = \frac{2\gamma}{\gamma - 1} \left(\frac{p_0}{cx} \right)^2 (1 - p/p_0)(p/p_0) + \left(\frac{p_0}{cx} \right)^2 (1 - p/p_0)^2,$$

which is a quadratic equation in p/p_0 with two different solutions. As for $x = 0$, $p/p_0 = 1$, the solution sought is

$$\frac{p}{p_0} = \frac{1}{\gamma + 1} \left[1 + \sqrt{1 + (\gamma^2 - 1) \left(1 - 2h_f \left(\frac{cx}{p_0} \right)^2 \right)} \right]. \quad (9.2-43)$$

Now, according to Eq. (9.2-39)

$$\frac{p}{p_0} = \frac{1}{1 + \gamma M_a^2}.$$

For brevity, we will write

$$D = 1 + (\gamma^2 - 1) \left(1 - 2h_f \left(\frac{cx}{p_0} \right)^2 \right), \quad (9.2-44)$$

and as for real solutions of Eq. (9.2-43), $D \geq 0$ it follows that

$$\frac{1}{1 + \gamma M_a^2} \geq \frac{1}{\gamma + 1}.$$

This inequality immediately yields the important conclusion that for the flow in a cylindrical grain, with uniform mass addition

$$M_a \leq 1, \quad (9.2-45)$$

and thus, the flow cannot change from subsonic to supersonic.

We will now investigate the occurrence of $M_a = 1$. By equating the Eqs. (9.2-39) and (9.2-43) we immediately see that $D = 0$ in this case. Moreover, as can be seen from Eq. (9.2-44), $\frac{dD}{dx} < 0$ for $x > 0$. If for $x = x_1$, $M_a = 1$,

then for $x = x_2 > x_1$: $D < 0$, which would yield complex solutions of Eq. (9.2-43). The only way to obtain real solutions is increasing the discriminant D by an increasing pressure p_0 (as T_f is constant). The location where $M_a = 1$ then shifts toward the end of the grain, until $M_a = 1$ is reached at $x = L$; i.e. at the grain end. For $M_a = 1$ the channel is choked, which is fully equivalent to the choking of the throat of a supersonic nozzle.

The mass flow at every location in the channel is given by

$$\rho V A_p = \rho_0 \frac{\rho}{\rho_0} \frac{V}{a} a_0 A_p = p_0 \sqrt{\frac{\gamma}{RT_0}} M_a \sqrt{\frac{1 + \frac{\gamma - 1}{2} M_a^2}{(1 + \gamma M_a^2)^2}} A_p. \quad (9.2-46)$$

For $M_a = 1$, this becomes

$$(\rho V A_p)_{M_a=1} = p_0 \sqrt{\frac{\gamma}{2RT_0(\gamma + 1)}} A_p, \quad (9.2-47)$$

which should be compared with the mass flow through the nozzle,

$$\rho V A = \Gamma \frac{p_c A_t}{\sqrt{RT_c}}. \quad (9.2-48)$$

Directly after the grain, where there is zero mass addition, one has

$$h_c = h_f = h + \frac{1}{2}V^2.$$

The assumption of a zero velocity at the nozzle entrance, or the definition of the chamber temperature as the isentropic stagnation temperature, thus leads to

$$T_0 = T_f = T_c. \quad (9.2-49)$$

The stagnation temperature in the channel is $T_s = T_f$, and the *local stagnation pressure*, p_s , is found by applying the Poisson relations Eq. (3.7-20)

$$\frac{p_s}{p} = \left(\frac{T_f}{T} \right)^{\gamma/(\gamma-1)}. \quad (9.2-50)$$

By virtue of the Eqs. (9.2-39) and (9.2-40) we have

$$\frac{p_s}{p_0} = \frac{p_s}{p} \frac{p}{p_0} = \frac{\left(1 + \frac{\gamma-1}{2} M_a^2 \right)^{\gamma/(\gamma-1)}}{1 + \gamma M_a^2}. \quad (9.2-51)$$

In those cases that $M_a^2 \ll 1$ we find by a series expansion, neglecting higher-order terms

$$\frac{p_s}{p_0} = \frac{1 + \gamma/2 M_a^2}{1 + \gamma M_a^2} = \frac{1}{2}(p/p_0 + 1).$$

Thus, for small local Mach numbers, the local stagnation pressure is the average of the local pressure, p , and p_0 ,

$$p_s = \frac{p + p_0}{2}. \quad (9.2-52)$$

This is an important relationship. If one measures the total pressure, Eq. (9.2-52) shows the measured value to depend strongly on the location of the pressure transducer. The front-end stagnation pressure, p_0 , is higher than the stagnation pressure, p_c , just before the nozzle. By measuring the local pressure at the grain and p_0 , one can, by Eq. (9.2-52) determine the local total chamber pressure, p_s , for low Mach numbers. In Fig. 9.9 the pressure ratio p_s/p_0 as determined by Eq. (9.2-51) and by Eq. (9.2-52) are given as a function of the local Mach number, M_a . It is evident that the error made by using Eq. (9.2-52) even for high M_a remains small.

There is a relation between the pressure at the end of the grain and the chamber pressure p_c . We denote conditions at the grain end by the index g , thus p_g is the pressure at the end of the grain. The mass flow at the end of the grain, m_g , is

$$m_g = \rho_g V_g A_p = \left(\frac{p_g}{p_c} \right)^{1/\gamma} \frac{p_c}{\sqrt{RT_c}} \sqrt{\frac{2\gamma}{\gamma-1} \left(1 - \left(\frac{p_g}{p_c} \right)^{(\gamma-1)/\gamma} \right)} A_p,$$

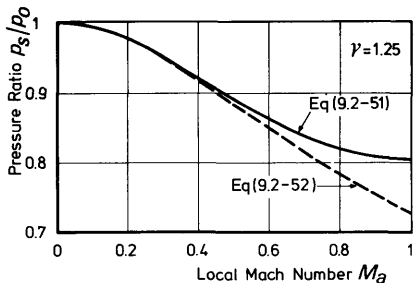


Fig. 9.9 The ratio of local stagnation pressure to front-end stagnation pressure versus local Mach number for a cylindrical grain

where use is made of the Poisson relations, Eq. (3.7-20). Equating the mass flow at the end of the grain to the mass flow through the nozzle, Eq. (9.2-48) yields

$$\Gamma J = \left(\frac{p_g}{p_c} \right)^{1/\gamma} \sqrt{\frac{2\gamma}{\gamma-1} \left(1 - \left(\frac{p_g}{p_c} \right)^{(\gamma-1)/\gamma} \right)}, \quad (9.2-53)$$

where

$$J = A_g/A_p. \quad (9.2-54)$$

For low gas velocities at the grain end, i.e. for small Mach numbers, or low values of J , p_g will not differ much from p_c . By writing $p_g = p_c - \Delta p$, where $\Delta p \ll p_c$, one can linearize Eq. (9.2-53), yielding

$$p_g/p_c = 1 - \frac{1}{2}\Gamma^2 J^2. \quad (9.2-55)$$

Now, if one assumes the flow after the grain end to be isentropic, it follows that $p_{s_g} = p_c$. The combination of the Eqs. (9.2-52) and (9.2-55) then yields a direct relation between the chamber pressure, p_c , and the front-end stagnation pressure, p_0 , provided that M_a is small

$$p_c = \frac{p_0}{1 + \frac{1}{2}\Gamma^2 J^2}. \quad (9.2-56)$$

In Fig. 9.10, the pressure ratios, p/p_0 , p_s/p_0 and the Mach number, M_a , in the channel are plotted versus the location x/L in the grain for some values of the ratio m/m_{max} . Here m is the actual local mass flow, while m_{max} is the mass flow for which, at the end of the grain, i.e. at $x = L : M_a = 1$.

9.2.3 The flow between the grain end and the nozzle

Though there may be a smooth fairing from the charge towards the nozzle, an abrupt enlarging of the cross-sectional area, directly after the grain,

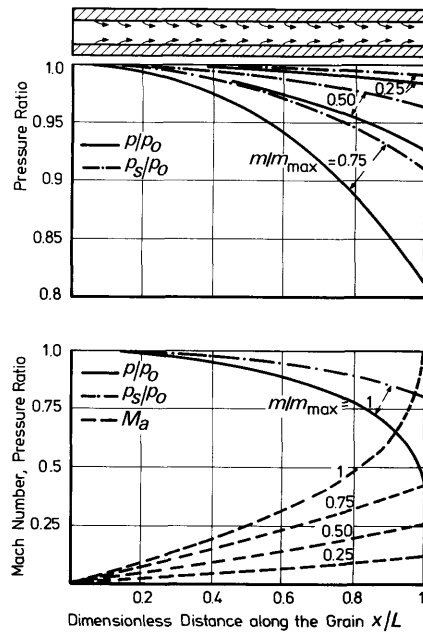


Fig. 9.10 The pressure ratios, stagnation pressure ratios and Mach number as a function of the position in a cylindrical grain for some mass ratios

causing swirl and mixing losses, is also found in solid motors. One can, if necessary, account for these losses by introducing a recovery factor. We will, however, assume the flow after the grain to be isentropic.

The Mach number at the end of the charge, $M_{a_g} \leq 1$ as we found in the previous section. The mass flow m_g equals

$$m_g = \rho_g V_g A_p = \sqrt{\gamma} \frac{p_0}{\sqrt{RT_c}} \frac{M_{a_g}}{1 + \gamma M_{a_g}^2} \sqrt{\left(1 + \frac{\gamma - 1}{2} M_{a_g}^2\right)} A_p. \quad (9.2-57)$$

At any arbitrary section after the charge, the mass flow through a surface of constant properties equals

$$m = \sqrt{\gamma} \frac{p_0}{\sqrt{RT_c}} \frac{M_a}{\left(1 + \frac{\gamma - 1}{2} M_a^2\right)^{(y+1)/(2(y-1))}} \frac{\left(1 + \frac{\gamma - 1}{2} M_{a_g}^2\right)^{y/(y-1)}}{(1 + \gamma M_{a_g}^2)} A. \quad (9.2-58)$$

where M_a is the Mach number at the surface of constant properties. Equation (9.2-51) relates p_c to p_0 with $p_{g_s} = p_c$ at the end of the grain. For

stationary conditions, the mass flows as determined by the Eqs. (9.2-57) and (9.2-58) are equal and we evaluate Eq. (9.2-58) at the throat, allowing for $M_{a_t} \neq 1$, where M_{a_t} is the Mach number at the throat

$$\frac{M_{a_t}}{\left(1 + \frac{\gamma-1}{2} M_{a_t}^2\right)^{(\gamma+1)/(2(\gamma-1))}} A_t = \frac{M_{a_g}}{\left(1 + \frac{\gamma-1}{2} M_{a_g}^2\right)^{(\gamma+1)/(2(\gamma-1))}} A_p.$$

We define

$$f(M_a) = \frac{M_a}{\left(1 + \frac{\gamma-1}{2} M_a^2\right)^{(\gamma+1)/(2(\gamma+1))}}, \quad (9.2-59)$$

and thus we have, by the use of Eq. (9.2-54),

$$J = \frac{A_t}{A_p} = \frac{f(M_{a_g})}{f(M_{a_t})}. \quad (9.2-60)$$

In Fig. 9.11, $f(M_a)$ is given as a function of M_a . We see that $f(M_a) > 0$, $f(0) = 0$, $\lim_{M_a \rightarrow \infty} f(M_a) = 0$. Moreover, we see that $f(M_a)$ reaches its maximum for $M_a = 1$, $f(1) = \Gamma/\sqrt{\gamma}$.

For $J < 1$: $f(M_{a_g}) < f(M_{a_t})$ and as $0 \leq M_{a_g} \leq 1$ we find $M_{a_t} > M_{a_g}$. Thus, if the pressure ratio p_c/p_e exceeds the critical pressure ratio, $M_{a_t} = 1$ and $0 < M_{a_g} < M_{a_t} = 1$. For $p_c/p_e < (p_c/p_e)_{cr}$ we find: $0 < M_{a_g} < M_{a_t} < 1$.

For $J = 1$: $M_{a_g} = M_{a_t}$, and for $(p_c/p_e) \geq (p_c/p_e)_{cr}$ we have $M_{a_g} = M_{a_t} = 1$.

For $J > 1$: $f(M_{a_g}) > f(M_{a_t})$. For one value of M_{a_g} , there are two possible values of M_{a_t} . One being $M_{a_t} < M_{a_g}$ and the other one $M_{a_t} > M_{a_g}$. For an isentropic flow, we have, Eq. (5.1-33),

$$\frac{dV}{V} (1 - M_a^2) = - \frac{dA}{A}. \quad (9.2-61)$$

For $M_{a_g} < 1$ directly after the charge where the cross-sectional area generally increases one has, as $\frac{dA}{A} > 0$, $\frac{dV}{V} < 0$, i.e. the flow decelerates. For $J > 1$ the velocity increase in the converging section to the throat is less than the decrease of the velocity after the grain. For, integrating the right-hand side

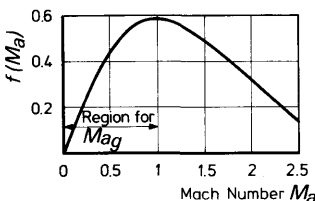


Fig. 9.11 The Mach number function $f(M_a)$

of Eq. (9.2-61) yields

$$\int_{A_p}^{A_{max}} \frac{dA}{A} + \int_{A_{max}}^{A_t} \frac{dA}{A} = \int_{A_p}^{A_t} \frac{dA}{A} = \ln J > 0.$$

Thus for $M_{a_t} < 1$ the velocity must have decreased. We have $M_{a_t} < M_{a_g} < 1$ and in this case we have only one possible solution for M_{a_t} . If $M_{a_g} = 1$ the possibilities are:

(a) Directly after the grain the flow becomes supersonic and it remains supersonic. Then, there is a local minimum in the Mach number at the throat and one has $M_{a_t} > M_{a_g} = 1$.

(b) The flow becomes subsonic directly after the grain and remains subsonic, $M_{a_t} < M_{a_g} = 1$. Which will be the case, will strongly depend on the shape of the duct, losses, etc.

We thus conclude that the conditions, ensuring a supersonic nozzle flow are:

$$p_c/p_e \geq \left(\frac{\gamma+1}{2}\right)^{\gamma/(\gamma-1)}, \quad \text{and} \quad J \leq 1.$$

High J numbers, are attended with high gas velocities at the end of the grain. This may cause *erosive burning* (Section 9.4.1), a phenomenon one usually tries to avoid as much as possible.

As, in general, $J < 1$ and $p_c/p_e > (p_c/p_e)_{cr}$, the Mach number at the end of the grain, M_{a_g} is less than unity.

9.3 Propellant grains

Modern solid rockets mostly use internal burning grains that more or less insulate the chamber wall from hot combustion products. Many grains are cylindrical (two-dimensional grain) or consist of cylindrical parts. To determine the burning surface, S_b , of a cylindrical grain with length, L , it suffices to determine the *burning perimeter*, l_b , of the cross-sectional area, and S_b follows from

$$S_b = l_b L. \quad (9.3-1)$$

The determination of the burning surface of three-dimensional grains, is more complicated.

As a propellant burns normal to its surface, a curved surface will propagate as a parallel curved surface, which is known as *Pioberi's law*. A surface convex towards the gas phase remains convex (Fig. 9.12a), and a surface concave towards the gas phase remains concave towards the gas phase (Fig. 9.12b). A cusp, initially concave towards the gas phase will become an arc of a circle or sphere with its center at the original cusp (Fig. 9.12b). The determination of l_b or S_b is a geometrical problem that can be solved by (analytical) geometry, graphical techniques or numerical procedures [13, 14]. With these methods one can determine S_b as a function of the distance

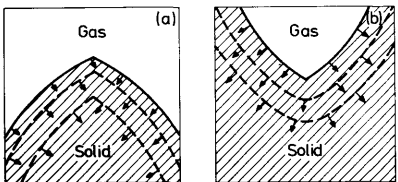


Fig. 9.12 Illustration of Piobert's law; (a) convex surfaces remain convex, (b) concave surfaces remain concave

burnt. As there is a direct relationship between the distance burnt, the burning rate, r , and the local pressure, p , the method is only applicable if there are no great differences in the burning rate along the grain, if the pressure is about constant along the grain length and in the absence of erosive burning. If this is not the case, one has to incorporate the internal ballistic properties of the motor in the analysis. In this case one usually has to resort to numerical methods.

In some cases a sudden decrease in burning surface may occur. In such a case the chamber pressure may become so low that either the combustion ceases, or that no effective thrust results anymore. Hence, the propellant left does not contribute to the propulsion anymore and should be considered as a dead weight. This amount of propellant is called the *sliver*. Grains that, by their geometry, exhibit a sliver, can be made sliverless by using two distinct propellants with different burning rates (Fig. 9.13).

Failures in the grain that may occur, are *cracking*, *debonding*, *deformation* and *auto-ignition*. Cracking and debonding are caused by high stresses due to ignition pressurization, temperature changes and accelerations. As a result of aging, which usually is accompanied by a deterioration of the mechanical properties, these last failures can be enhanced. They may lead to an undesired burning geometry and over-pressurization, or structural

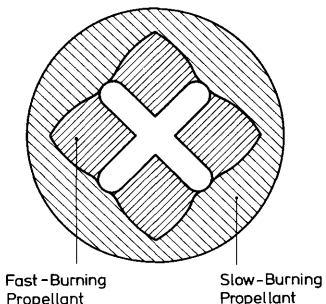


Fig. 9.13 Cross-section of a grain composed of two different propellants to avoid slivers

failure from premature exposure of the motor case to hot combustion products. Deformations may either be a result of *creep*, or of inertial forces, generated by high accelerations. The deformations may alter the port area, thus affecting the internal ballistics significantly. Auto-ignition may result from a heat build-up in the propellant, caused by internal viscous forces due to vibrations for instance.

Stress relief, by rounding off sharp corners, or by special slots will reduce the risk of cracking. Large L/D ratios or large w/D ratios (Section 9.3.1) are not favorable as internal stresses are concerned. This is one of the reasons to use *segmented grains* with relatively low L/D ratios in modern motors. A review on the structural integrity of the grain is given in Reference [15].

Apart from structural considerations, high L/D ratios are also unfavorable with respect to erosive burning and combustion instability.

9.3.1 Definitions

Before discussing the specific grain geometries we will first give some general definitions.

The change in chamber pressure during motor operation is a very important quantity. The maximum chamber pressure determines the required strength and therefore the weight of the motor case. Equation (9.2-10) directly relates p_c and S_b . For S_b constant, p_c will be constant too, for A_t constant. This is called *neutral burning*. If S_b increases with time one speaks of *progressive burning*, while a decrease of S_b with time is called *regressive burning*.

The thickness of the grain that determines the burning-time, is called the *web thickness*, w . It is defined by

$$w = \int_0^{t_b} r dt. \quad (9.3-2)$$

It is convenient to use dimensionless quantities. Lengths are non-dimensionalized by division by half the outer diameter D of the grain. We will define the *web fraction*, w_f , as

$$w_f = \frac{2w}{D}, \quad (9.3-3)$$

and the dimensionless distance burnt, y , as

$$y = \frac{2 \int_0^t r dt}{D}. \quad (9.3-4)$$

The dimensionless burning surface, Σ , is defined by

$$\Sigma = \frac{4S_b}{D^2}, \quad (9.3-5)$$

and is a function of y .

The *volumetric loading fraction*, V_l , is defined as

$$V_l = \frac{V_p}{V_c}. \quad (9.3-6)$$

where V_p is the propellant volume and V_c is the total chamber volume. It is evident that an effective use of the chamber volume, V_c , dictates V_l to be as high as possible. The *initial throat to port area ratio*, J_i , is defined as

$$J_i = \frac{A_t}{A_{p_i}}, \quad (9.3-7)$$

where A_{p_i} is the initial port area. As was shown in Section 9.2.3, preferably $J_i < 1$.

For strictly cylindrical grains, Eq. (9.3-7) can be approximated by

$$J_i = \frac{A_t}{\pi/4 D^2(1 - V_l)}. \quad (9.3-8)$$

High values of V_l will yield high values of J_i and make the motor sensitive to erosive burning (Section 9.4.1) and hence initial pressure peaks may be expected.

9.3.2 Cylindrical grains

The *endburning grain*, or *cigarette burning grain*, is the simplest cylindrical grain. Its burning surface equals its cross-sectional area. The required insulation of the motor case from hot combustion gases is rather weight consuming. The upper limits on burning rates in combination with the grain diameter limit the mass flow and consequently the obtainable thrust. The use of the endburning grain therefore is restricted to some very special applications.

Heat transfer to the propellant along the chamber wall, either from aerodynamic heating or from combustion gases, may cause higher burning rates at the wall, leading to a more or less conical burning surface. By embedding in the propellant heat conducting metal wires [16], or tubes through which hot combustion gases flow [17], one can increase the burning rate. In these cases the burning surface will consist of intersecting cones with the wires or tubes as axes.

The *tubular grain* (Fig. 9.14) will burn progressively if the ends are restricted, as the burning perimeter, l_b , increases linearly with y . If both ends, which burn regressively, are not restricted, it in fact becomes a three-dimensional burning grain, which, depending on the L/D ratio, can exhibit a fair degree of neutrality. In Fig. 9.15a the dimensionless burning surface, Σ , is depicted as a function of y for some L/D ratios and fixed d/D . From this figure we conclude that for L/D around 2 fairly neutral burning can be obtained. The burning becomes more and more progressive with increasing

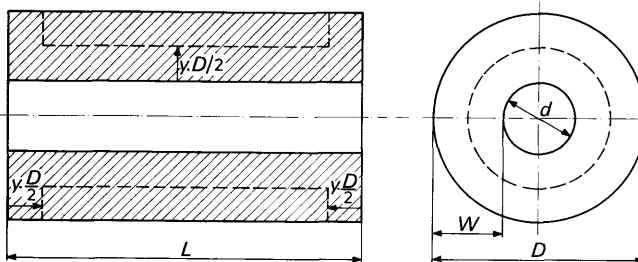


Fig. 9.14 The tubular grain

L/D . However, for chambers exhibiting a large L/D the grain can be segmented, each segment exhibiting an L/D that ensures neutral burning. This method is applied to many segmented motors. Of course, those parts of the chamber walls exposed to hot combustion gases have to be insulated in proportion to their time of exposure. Figure 9.15b depicts Σ versus y for various values of d/D and fixed L/D . The curve for $d/D = 0$ is a limiting case; it represents a massive cylinder, which is assumed to ignite along its central axis and both its end surfaces. The neutrality increases with increasing d/D .

Grains that exhibit pure neutral burning are the *tubular grain with restricted ends*, burning radially at its inner and outer surface (Fig. 9.16a) and the *rod and shell*, also with restricted ends (Fig. 9.16b). The first configuration exposes the chamber walls to the hot combustion products, while in both the configurations the support is difficult and complicated, and maintaining the structural integrity until burnout gives rise to serious problems.

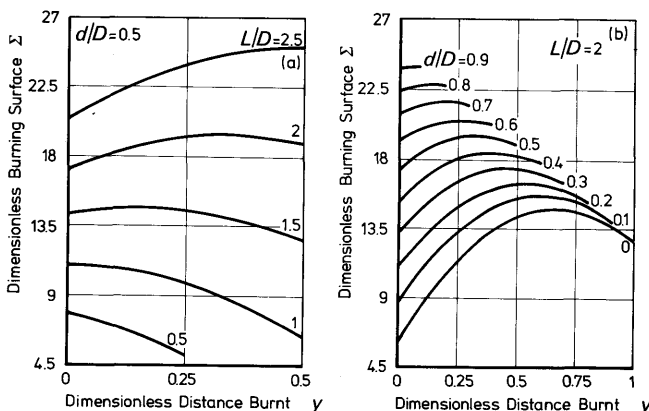


Fig. 9.15 The dimensionless burning surface of a tubular grain with non-restricted ends versus the dimensionless distance burnt; (a) for some length over diameter ratios and (b) for some inner over outer diameter ratios

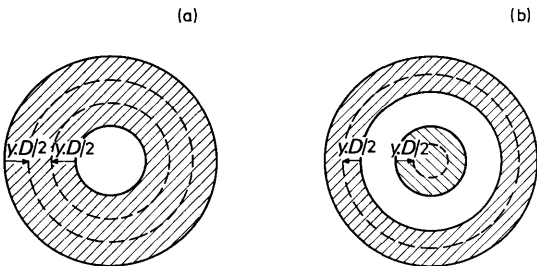


Fig. 9.16 Neutral burning grains. (a) The tubular grain with restricted ends, burning at its inner and outer surface. (b) The rod and shell configuration

The *slotted tube grain*, which exhibits a high loading fraction, is depicted in Fig. 9.17. At its ends, it may either be restricted or not. In most cases at least one end is restricted and bonded to the front end of the chamber. The slotted portion of the grain provides regressive burning. The burning progresses in radial, tangential and longitudinal directions. The number of slots, N , the slot length, l , and the width of the slots, $2r$, are independent variables, together with the grain length, L , the outer diameter, D , and the inner diameter d . As the port area in the slotted portion is increased with respect to that in the tubular section, this provides a way to avoid high gas velocities. Stone [18] has analysed the geometry of the slotted tube in detail and gives excellent graphs that can be used in slotted tube grain design [19]. As an example, Fig. 9.17 shows the variation of Σ with y for two specific slotted tube grains.

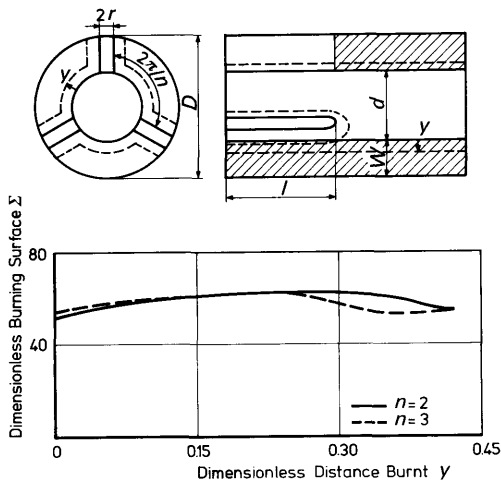


Fig. 9.17 The slotted tube grain; its configuration and an example of its burning surface versus the dimensionless distance burnt for $d/D = 0.16$; $L/D = 8.3$; $l/D = 5.32$; $2r/D = 0.06$ and $N = 2$ and $N = 3$ (Reference [20])

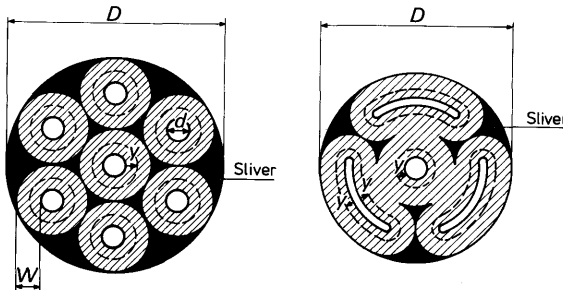


Fig. 9.18 Some multiperforated grains

The grain geometries discussed so far had no sliver. *Multiperforated grains*, such as the ones depicted in Fig. 9.18, exhibit slivers. At the end of the burning, the grain may collapse. If the pressures in the various ports are different from each other, grain collapse may occur before burnout. It is easily shown that for a multiperforated grain a sufficient condition for equal pressures in all ports is that all channels exhibit the same S_b/A_p ratio.

The *star configuration* (Fig. 9.19) has been used in many solid motors. It is a radially burning cylindrical grain. Neutrality can be obtained by the interaction of the regressive burning star points and the progressive burning tube. As is obvious from Fig. 9.19b, the star is defined by six independent variables: N , ε , η , r , w and D . Stone [21] gives an extensive description of the calculation of the burning surface of the star. A slightly different approach is followed by Vandekerckhove [22]. The burning perimeter of the star can be determined by analysing a section such as depicted in Fig. 9.19b. There are three different *regions* or *phases*: I, II and III. Region I will either burn regressively, neutrally or progressively, depending on η , r and ε . Region II will burn progressively, while region III, the sliver, will burn regressively, if it burns at all. In Fig. 9.20, the burning surfaces of two specific stars are depicted as a function of y .

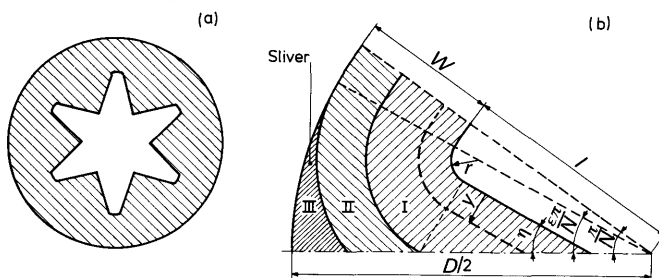


Fig. 9.19 The star configuration and its nomenclature

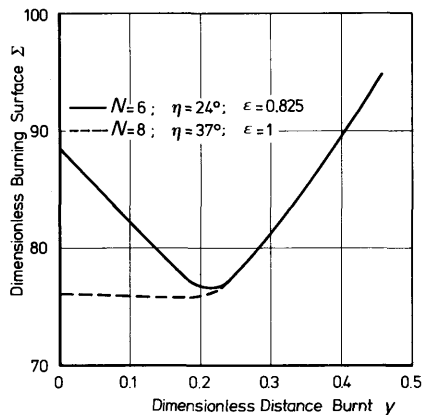


Fig. 9.20 The dimensionless burning surface versus the dimensionless distance burnt for two specific star configurations for $2l/D = 0.54$; $2r/D = 0.049$; $2w/D = 0.46$ and $L/D = 15.2$ (Reference [20])

The *wagon-wheel* (Fig. 9.21a) is another often used grain configuration, with two more variables than the star: the length and angle, β , of the spokes. The wagon-wheel is used if small web fractions are required. Vandenkerckhove [22] gives an analysis of the wagon-wheel geometry. Next to the conventional wagon-wheel there is also the *dendrite* or *forked wagon-wheel* (Fig. 9.21b). It may exhibit a higher volumetric loading fraction. The important variables can be calculated according to Peretz [23]. The wagon-wheel configuration can exhibit more phases than the star as the number of phases increases with the number of independent variables. It is possible for the wagon-wheel that, when the spokes are all burnt, the burning perimeter decreases discontinuously. Therefore the wagon-wheel is suitable as a boost-sustain grain.

In those cases that the gas velocities become too high, and erosion is to be expected, the tapering of the end port of the grain provides means to reduce the gas velocities and thus the danger of erosive burning.

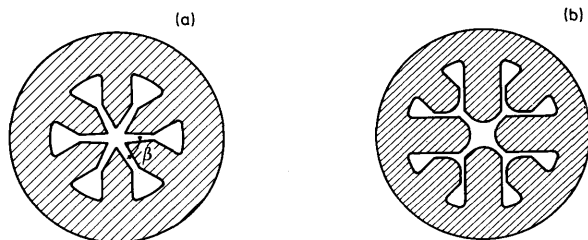


Fig. 9.21 (a) The wagon-wheel configuration, (b) The dendrite or forked wagon-wheel

9.3.3 Three-dimensional grains

In the foregoing section we discussed cylindrical grains. Some of them, the tubular grain with unrestricted ends, and the slotted tube, exhibited three-dimensional characteristics. There are non-cylindrical grains in use whose burning characteristics depend strongly on the shape of the outer surface too. The *spherical grains*, an example of which is depicted in Fig. 9.22, form an important class. They may be used if *aerodynamic drag* is not important. Also, if system requirements dictate limits on the moment of inertia and weight, a spherical motor may be a favorable solution. These motors are used or have been proposed as *apogee-kick motors*, *final stage motors* or *motors for interplanetary spacecraft*. They have the potential of a high volumetric loading fraction. Methods to determine the ballistic properties of spherical motors are given by Segal [24] and Berti [25]. A simple criterion to ensure the structural integrity of the spherical grain is discussed by Toda [26].

The *conocyl* (Fig. 9.23a) is another three-dimensional grain. The name stems from cone-in-cylinder. Both conical burning surfaces burn regressively, while the central perforation burns progressively. In combination with the chamber envelope the charge can provide neutrality for a range of L/D values up to about 4. Those areas of the chamber that will be exposed to hot combustion gases have to be insulated, in direct proportion to their time of exposure.

The *finocyl*, an acronym for fin-in-cylinder (Fig. 9.23b) is used in modern ICBM systems. The finocyl can provide long burning-times for relatively low L/D ratios. Instead of the radial slot of the concoyl, the finocyl has axial slots to provide regressive burning. The ballistics of the finocyl do not differ much from those of the concoyl, but in some cases fabrication is considered easier. Other system requirements, however, such as thrust reversal, or thrust termination ports at the front end of the chamber, require an added flow channel volume in the forward end, which may make the concoyl a desirable configuration.

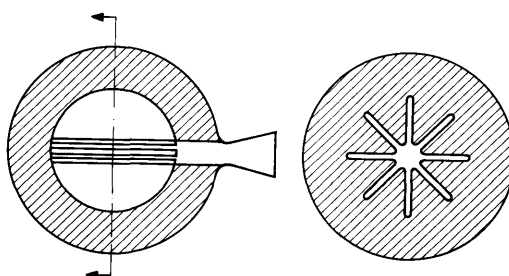


Fig. 9.22 An example of a spherical grain

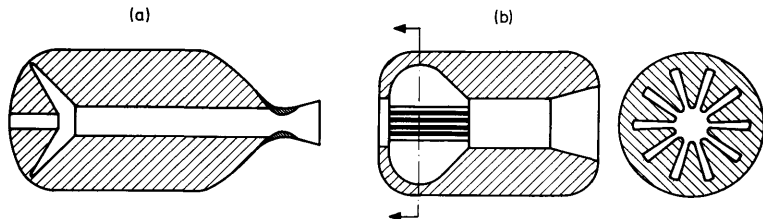


Fig. 9.23 (a) The conocyl design, (b) The finocyl design

Apart from the geometries mentioned, many more configurations exist. An excellent survey is given by Billheimer and Wagner [27], while Williams [3] also gives extensive information on the determination of burning surface, port area and other ballistic properties. Reference [13] provides excellent general information on grain geometries, design and verification and analysis, while reference [15] discusses the structural integrity of solid propellant grains.

9.4 Burning rate augmentation

In the previous sections, we assumed the actual burning rate in rocket motors to equal the one measured in a strand burner. This is not always the case. If high gas velocities, or high *mass flow densities*, ρV , are encountered, the actual burning rate may substantially exceed the burning rate as measured in the Crawford bomb. This is due to *erosive burning*. The burning rate can also be affected by introducing a fluid into the thrust chamber. This is sometimes done to provide thrust magnitude control. The fluid may either be inert or may be a high-energy liquid oxidizer which, in combination with a propellant exhibiting an exponent near unity, produces a wide range of throttling [28].

Another factor that influences the burning rate is a time dependent pressure. We mentioned already in Section 9.1.3, that burning rate data, as obtained from strand burner measurements, only hold for constant pressure processes.

Accelerations, internal stresses in the propellant and specific motor effects can also affect the propellant combustion. It is current practice, therefore, to determine r over specified operational pressure and temperature ranges in small rocket motors, *Ballistic Evaluation Motors*, or BEM's, too [29].

We will not discuss the above mentioned effects in detail, as this goes beyond the scope of this book, but restrict ourselves to some general remarks.

9.4.1 Erosive burning

Most of the work on erosive burning, which is still a field of experimental and theoretical research, is on a semi-empirical basis. If high gas velocities

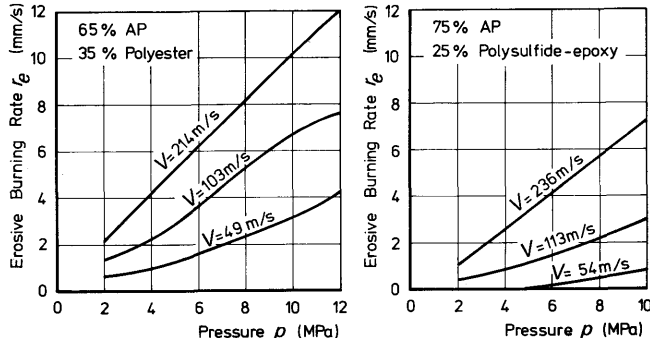


Fig. 9.24 The dependence of erosion on the velocity and pressure, or density (Reference [31])

or mass flow densities are met in the propellant grain, there will be a strong heat transfer into the propellant. In Sections 9.1.3 and 9.1.4, we saw that heat transfer is a prime rate controlling factor.

Formulae that correlate erosive burning rate data, generally, are of one of the following forms:

$$r_b = r + r_e, \quad (9.4-1)$$

or

$$r_b = \varepsilon r. \quad (9.4-2)$$

Here r_b is the actual burning rate, r stands for the burning rate as obtained from strand burner data, r_e is the *erosive burning rate*, and ε is called the *erosion function*. Both Lenoir and Robillard [30], and Marklund and Lake [31] give semi-empirical expressions for the erosive burning rate. These expressions relate the effect of erosion to the mass flow density ρV . If the chamber temperature, T_c , is about constant, the density is proportional to the pressure. Figure 9.24 clearly illustrates that the erosion increases with increasing pressure, or density and velocity. The erosion function, ε , is more widely used than the erosive burning rate. Kreidler [32] gives a relation between mass flow density and the erosion function. It has been observed too that the Mach number, M_a , may influence the erosion. For more information the reader is referred to Williams [3].

9.4.2 Pressure-induced burning rate changes

If the pressure is not constant, but varies with time, the burning rate will be time dependent too. In general, $r(t)$ will not follow the simple steady-state burning rate laws, Eq. (9.1-1) or Eq. (9.1-2). From combustion models [7, 9, 11] a theoretical non-stationary burning rate can be determined. A thorough experimental check, however, is a necessity.

If one deals with fluctuating pressures, it is, in many cases, customary and convenient to use, instead of the burning rate, related complex functions [4]: the *admittance*, A_b , or the *response*, R_b , of the propellant. In principle, the admittance and response functions of propellants, can be deduced from combustion models. In practice they have to be measured in special devices such as *T*- or *L*^{*}-*burners*.

For non-oscillatory pressure changes, the GDF model sometimes yields satisfactory predictions of the burning rate behavior of composite propellants. Von Elbe [33] first derived a simple expression for the burning rate, r , valid both for composite and double-base propellants, which has been improved by others [4, 10],

$$r = ap^n \left(1 + n \frac{\kappa}{a^2 p^{2n+1}} \frac{dp}{dt} \right). \quad (9.4-3)$$

Here κ is the thermal diffusivity of the propellant, n is the pressure exponent from the steady-state burning rate law, and a is the coefficient in this law. In many cases Eq. (9.4-3) yields fairly good correlations between pressure and burning rate.

In case of large negative values of dp/dt , *propellant extinction* may take place; the phenomenon is known as *dp/dt extinguishment*.

The dependence of the combustion on variable pressures is of a highly complicated character and cannot be given in this chapter. It is mentioned here, because the reader should be aware that non-stationary problems in solid-propellant rocketry are not merely a simple extension of the existing stationary theory.

9.4.3 Acceleration-induced burning rate augmentation

It is a well-known fact that accelerations may influence the burning rate. These accelerations, as experienced by the propellant, are caused by the acceleration of the whole vehicle, but can also be spin-induced. For a specific propellant the burning rate augmentation is dependent on the *magnitude* and *orientation* of the acceleration vector with respect to the burning surface, and the *pressure level* [34]. It has also been shown that the *composition* of the propellant has much to do with the *acceleration-induced burning rate augmentation* [35].

Not only the burning rate itself, but also the burning rate exponent may change due to acceleration. In general, the accelerations have to be of the order of about 100 m/s^2 before a noticeable deviation from the burning rate occurs. By how much the rate augmentation is also due to strain induced in the propellant itself, and to what extent to different flame structures, cannot be said at the present time. In most cases, *propellant strain* will also lead to different burning rates. As no general theories are available, the influence of the acceleration on the burning rate has to be determined experimentally for the propellant under consideration.

References

- 1 Karnesky, A. L. and Colucci, S. E. (1975), Recent occurrences of combustion instability in solid rocket motors—an overview, *J. Spacecraft*, **12**, 33–38.
- 2 Shorr, M. and Zaehringer, A. J. (ed.) (1967), *Solid Rocket Technology*, John Wiley, New York, p. 50.
- 3 Williams, F. A., Barrère, M. and Huang, N. C. (1969), *Fundamental Aspects of Solid Propellant Rockets*, AGARDograph 116, Technivision Services, Slough.
- 4 Price, E. W. and Culick, F. E. C. (1969), *Combustion of Solid Rocket Propellants*, AIAA, New York.
- 5 Dadieu, A., Damm, R. and Schmidt, E. W. (1968), *Raketentreibstoffe*, (in German), Springer, Vienna.
- 6 Barrère, M., Jaumotte, A., Fraeijs de Veubeke, B. and Vandenerckhove, J. (1960), *Rocket Propulsion*, Elsevier, Amsterdam.
- 7 Summerfield, M. (ed.) (1960), *Solid Propellant Rocket Research*, Academic Press, New York, p. 141–182.
- 8 Steinz, J. A., Stang, P. L. and Summerfield, M. (1968), *The Burning Mechanism of AP-based Composite Solid Propellants*, AIAA Paper 68-658, AIAA, New York.
- 9 Beckstead, M. W., Derr, R. L. and Price, C. F. (1968), A model of composite solid propellant combustion based on multiple flames, *AIAA J.*, **6**, 2200–2207.
- 10 Stamets, L. E. and Weiss, R. R. (1971), *Analytical Models of Solid Propellant Combustion*, paper presented at the 22nd I.A.F. Congress, Brussels.
- 11 Hamann, R. J. (1974), *Three Solid Propellant Combustion Models, A Comparison and Some Applications to Non-Steady Cases*, Memorandum M-215, Delft University of Technology, Dept. of Aeron. Eng., Delft.
- 12 Boggs, T. L., Zurn, D. E., Strahle, W. C., Handley, J. C. and Milkie, T. T. (1973), *Mechanisms of Combustion*, Final Report, NWC TP-5514, Naval Weapons Center, China Lake.
- 13 Anon. (1972), *Solid Propellant Grain Design and Internal Ballistics*, NASA SP-8076, Washington.
- 14 Peterson, E. G., Nielsen, C. C., Johnson, W. C., Cook, K. S. and Barron, J. G. (1968), *Generalized Coordinate Grain Design and Internal Ballistics Evaluation Program*, AIAA Paper 68-490, AIAA, New York.
- 15 Anon. (1973), *Solid Propellant Grain Structural Integrity Analysis*, NASA SP-8073, Washington.
- 16 Schaefer, J. (1973), Schuboptimierung von Feststoffraketen, *Z. Flugwiss.*, **21**, 195–202.
- 17 Caveny, L. H. and Sowyer, T. T. (1967), *Solid Propellant Burning Along a Tube Heated by Combustion Gas Influx*, AIAA Paper 67-102, AIAA, New York.

- 18 Stone, M. W. (1961), Slotted tube grain design, *A.R.S. J.*, **31**, 223–228.
- 19 Stone, M. W. (1960), *The Slotted Tube Grain Design*, Rep. S-27, Rohm & Haas Comp., Huntsville.
- 20 Schöyer, H. F. R. (1968), *The Design of a Rocket Motor for the Second Stage of a Two Stage Sounding Rocket* (in Dutch), Memorandum M-131, Delft University of Technology, Dept. of Aeron. Eng./Royal Naval Institute, Delft/Den Helder.
- 21 Stone, M. W. (1958), A practical mathematical approach to grain design, *Jet. Prop.*, **28**, 236–244.
- 22 Vandenkerckhove, J. (1958), *Internal-Burning Star and Wagon-Wheel Designs for Solid-Propellant Grains*. Publication of the Université Libre de Bruxelles, Institute d'Aeronautique, Brussels.
- 23 Peretz, A. (1969), A practical mathematical approach to the dendrite design of solid propellant grains, *J. Spacecraft*, **6**, 944–946.
- 24 Segal, H. M. (1960), Design method for spherical grains, *A.R.S. J.*, **30**, 370–371.
- 25 Berti, J. W. and Wrubel, J. A. (1962), Calculating burning surface areas of internal burning spherical propellant charges, *A.R.S. J.*, **32**, 1283–1285.
- 26 Toda, Y., Nagaoka, T., Ueno, L., Orado, Y. and Kunio, T. (1973), Failure criterion for a propellant of spherical solid rocket motor, *J. Spacecraft*, **10**, 807–808.
- 27 Billheimer, J. S. and Wagner, F. R. (1970), *The Morphological Continuum in Solid Propellant Grain Design*, Proceedings of the 19th IAF Congress, Vol 3, Pergamon Press/PWN-Polish Scientific Publishers, Oxford, p. 153–188.
- 28 McDonald, A. J. (1971), *On-Off and Acceleration Control of Solid Rockets*, SAE Paper 710767, SAE, New York.
- 29 Miller, W. H. and Barrington, D. K. (1970), A review of contemporary solid rocket motor performance prediction techniques, *J. Spacecraft*, **7**, 225–237.
- 30 Lenoir, J. M. and Robbillard, G. (1957), *A Mathematical Method to Predict the Effects of Erosive Burning in Solid Propellant Rockets*, Proceedings of the Sixth Symposium on Combustion, Reinhold, New York, p. 663–667.
- 31 Marklund, T. and Lake, A. (1960), Experimental investigation of propellant erosion, *A.R.S. J.*, **30**, 173–178.
- 32 Kreidler, J. W. (1964), *Erosive Burning; New Experimental Techniques and Methods of Analysis*, AIAA Paper 64-155, AIAA, New York.
- 33 von Elbe, G. (1966), *Solid Propellant Ignition and Response of Combustion to Pressure Transients*, AIAA Paper 66-668, AIAA, New York.
- 34 Northam, G. B. (1972), *Effects of Orientation of the Acceleration Vector on Burning-Rate Augmentation*, NASA TN D-6952, Washington.
- 35 Northam, G. B. (1972), *Effects of Propellant Composition Variables on Acceleration Induced Burning-Rate Augmentation*, NASA TN D-6923, Washington.

10 The Liquid-Propellant Rocket Motor

In Chapter 9 we discussed the solid rocket motor and also paid brief attention to the merits of the liquid motor. In this chapter we will give an overview of the liquid propulsion system. The liquid motor (Fig. 10.1) consists of one or more propellant tanks, a feed system, a combustion chamber and an expansion nozzle. If monopropellants are used, only one tank is needed. In other cases, fuel and oxidizer are stored in separate tanks. Smaller rockets often use (inert) pressurization gas to force the propellants into the combustion chamber (*pressure fed*). The larger engines use pumps, driven by turbines, to feed the combustion chamber. In modern staged-combustion motors, *precombustion chambers* may be used. In this precombustion chamber the fuel and part of the oxidizer react, and the precombustion products drive the turbines before entering the main combustion chamber, where the remainder of the oxidizer reacts with the precombustion products (Fig. 10.2a). If the turbines are not driven by precombustion products, they may then use combustion gases from the main combustion chamber, *tap-off* system (Fig. 10.2b), or the cooling fluid from the combustion chamber or nozzle, *topping cycle* (Fig. 10.2c), or *bleed-off* system in which case the turbine gases are dumped, or a separate gas generator (Fig. 10.2d).

Except for motors with a low combustion temperature, or short burning times, active cooling by one of the propellants is imperative in most cases. In absence of an active cooling system, either heat sink, radiation cooling or other means of cooling are used (Section 10.5).

A regulating system to keep the pressures and mass flows within their required range is needed, just like a control system for the starting and shut-down sequence of the motor. The starting of the motor usually is accomplished by means of a separate gas generator or by stored pressure gas which starts the turbines, whereafter the propellants are injected into the combustion chamber and subsequently ignited.

In this chapter we will devote our attention to those subjects that directly determine the performance of the liquid motor, such as propellants, pumps and turbines, and to typical liquid motor components such as tanks, injectors and cooling systems. We will avoid going into details, such as feedline dynamics, valves and seals, or injector performance analysis. These subjects, though of high interest to the rocket engineer are of too specialized a character and often rely heavily on experiments.

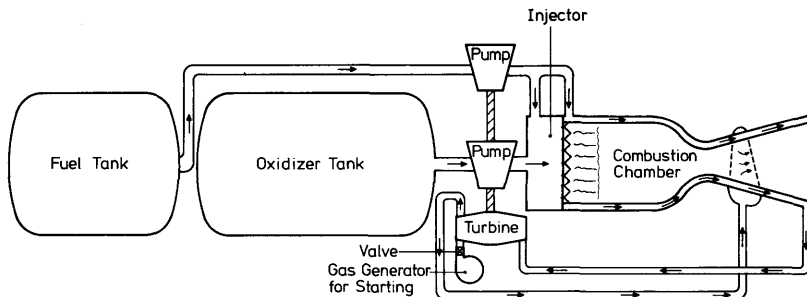


Fig. 10.1 Outline of a liquid-propellant rocket motor

10.1 Liquid propellants

Liquid propellants can be divided into *monopropellants* and *bipropellants*. Monopropellants, such as hydrogen peroxide (H_2O_2) and hydrazine (N_2H_4) decompose by means of a catalyst, producing gases of high temperature and pressure. While the monopropellant rocket has the advantage of simplicity, the available I_{sp} is low, up to about 250 s.

The bipropellants usually are divided into *cryogenic* and *storable propellants*. Cryogenic propellants, such as liquid oxygen (LOX) and liquid hydrogen (LH₂), are liquids only at extremely low, or cryogenic, temperatures. The storable propellants are liquids at normal temperatures and can be stored for long periods of time at those temperatures without any significant loss of performance.

Many propellant combinations need an ignition device to start the combustion. Some combinations, however, ignite spontaneously. These are called *hypergolic* propellants. Examples are (with or without catalyst) Hydrogen–Fluorine (H_2/F_2), Ammonia–Fluorine (NH_3/F_2), Hydrazine–Nitric Acid (N_2H_4/HNO_3), Unsymmetrical Dimethyl Hydrazine–Nitric Acid (UDMH/ HNO_3). The choice of a particular propellant combination will be affected by various considerations: the heat of formation, ΔH_f° , the combustion temperature, T_c , the molecular weight of the combustion products, M ,

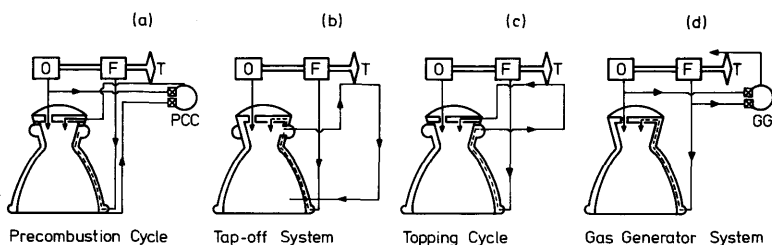


Fig. 10.2 Turbine-driven propellant feed systems. O = oxidizer pump; F = fuel pump; T = turbine; PCC = precombustion chamber; GG = gas generator

the density of the propellant combination, ρ , availability, compatibility with materials and the environment, handling and storage qualities and price. Table 10.1 lists a few propellant combinations, and a few of the properties mentioned. Instead of the characteristic velocity, the specific impulse for a chamber pressure of 7 MPa and an ideal expansion to 0.1 MPa is listed as a performance parameter at the given mixture ratio. It appears that liquid propellants yield higher I_{sp} than the solid ones, and that the cryogenic combinations, H₂/F₂ and H₂/O₂ yield the highest I_{sp} . For chamber pressures

Table 10.1. Properties of some liquid propellant combinations

Fuel	Oxidizer	Mixture ratio	Molecular weight of the combustion products	Combustion temperature	Specific impulse	Mean density of the propellants	Volumetric specific impulse
		$r = \frac{m_{ox}}{m_{fuel}}$	M_c (kg/kmol)	T_c (K)	I_{sp}^o (s)	ρ (kg/m ³)	I_s^o (kg.s/m ³)
Hydrogen, H ₂	Oxygen, O ₂	4	10	2980	390	280	109.2×10^3
	Fluorine, F ₂	8	12.8	4117	410	460	188.6×10^3
	Oxygendifluoride, OF ₂	5.9	11	3590	410	390	159.9×10^3
Kerosine	Oxygen, O ₂	2.45	23.4	3687	301	1020	307×10^3
	Fluorine, F ₂	2.8	23.9	3917	320	1230	393.6×10^3
	Red Fuming Nitric Acid (RFNA)	4.8	25.7	3156	268	1355	369.1×10^3
	Nitrogen Tetroxide, N ₂ O ₄	4.3	26.2	3460	276	1260	347.8×10^3
	Hydrogen Peroxide H ₂ O ₂	7	22.2	3008	278	1362	378.5×10^3
	Hydrazine, N ₂ H ₄	0.9	19.4	3410	313	1070	334.9×10^3
Unsymmetrical Di-Methyl Hydrazine (UDMH), (CH ₃) ₂ NNH ₂	Fluorine, F ₂	2.18	19.4	4687	364	1310	476.8×10^3
	Nitric Acid, HNO ₃	1.3	20	2967	278	1310	364.2×10^3
	Nitrogen Tetroxide, N ₂ O ₄	1.3	20.7	3255	291	1225	356.5×10^3
	Oxygen, O ₂	1.67	21.5	3623	310	970	300.1×10^3
Ammonia, NH ₃	Fluorine, F ₂	2.5	21.3	4183	313	1119	350.2×10^3
	Nitric Acid, HNO ₃	3	23.7	3222	276	1220	336.7×10^3
	Nitrogen Tetroxide, N ₂ O ₄	2.65		3436	286	1185	338.9×10^3
	Oxygen, O ₂	1.36	19.8	3104	295	890	262.6×10^3
Monopropellants:		Fluorine, F ₂	3.15	4576	330	1170	386.1×10^3
Nitromethane, CH ₃ NO ₂				20.3	2646	1137	290×10^3
Hydrazine, N ₂ H ₄				10.29	966	1011	201.2×10^3
Hydrogen peroxide, H ₂ O ₂				22.7	1278	1442.2	238×10^3

All values are given for $p_e = 7$ MPa, and ideal expansion to $p_e = 0.1$ MPa

of 20 MPa, the I_{sp} of the LH₂-LOX combination can even be raised to 460 s. Systems using a fluorine compound as oxidizer yield very high specific impulses. Though numerous experiments with fluorine or fluorine-oxygen propellants have been carried out, they have not achieved operational use as yet. Partly this is due to technical difficulties (the corrosive and aggressive nature), partly to the hazards the combustion products yield for the environment [1]. Therefore, it is doubtful whether fluorine-based propellants will ever be used at low altitudes.

Metal additives, such as aluminum, boron and lithium, are widely used in solid propellants. Both combustion temperature and molecular weight are raised, but the overall effect is an increased I_{sp} . For liquid propellants, metal additives also look promising, but up to now they have not found a widespread operational use.

A new promising development, which is still in the research stage, is the use of atomic hydrogen as propellant. The H is trapped in a matrix of frozen H₂ at temperatures below 1.5 K. A H₂-H matrix, containing 15 percent H by weight would yield an I_{sp} of about 740 s [2].

10.2 Propellant tanks

For the storage of a given amount of propellant a spherical tank will yield the largest volume for a given tank weight. Because of diameter constraints, however, one often has to apply cylindrical tanks. A common situation is the tandem configuration of two tanks with a common bulkhead (Fig. 10.3a). In this case, p_1 must be greater than p_2 as otherwise there is danger of buckling of the common bulkhead. Another often used tandem configuration is shown in Fig. 10.3b. Though this configuration is heavier than the

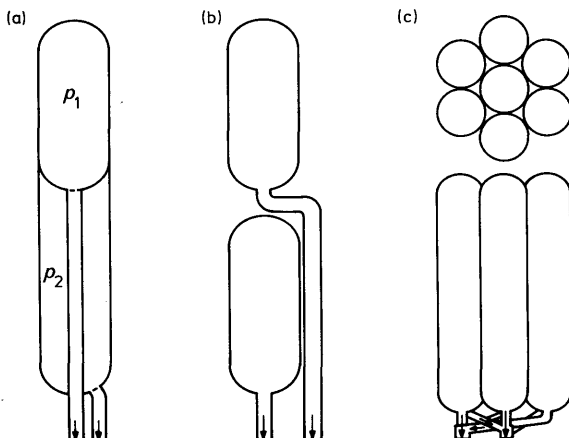


Fig. 10.3 Some possible propellant tank arrangements

one with the common bulkhead, it is easier to produce. A multi-tank arrangement, such as used on the Saturn IB, is depicted in Fig. 10.3c.

In most cases, the walls of the tanks are the outer-walls of the vehicle. They have to provide the necessary strength to bending moments on the vehicle and they have to transfer the thrust. Often they are subjected to aerodynamic heating. A short total tank length is attractive from the viewpoint of strength and weight. It can be achieved, for instance, by the use of a common bulkhead, or by careful shaping of the bulkheads [3].

Depending on the feed system, the tank will be submitted to high or moderate internal pressures. For pressure-fed engines, where the tank pressure has to overcome the chamber pressure and the pressure loss in ducts and injector, the tank pressure may be as high as 6 MPa. For pump-fed systems lower pressures suffice, up to 0.5 MPa. These tank pressures are necessary to suppress *cavitation* (Section 10.3.1) in the pumps, but also to provide the vehicle with the necessary stiffness.

The total tank volume required consists of the volume of the propellant that is used for propulsion, the propellant volume left in tanks, ducts and cooling system after shut-down, the boiled-off propellant volume, and the tank *ullage* volume, i.e. the tank volume filled with gas.

Because of the vehicle's motion, sloshing of the propellant will occur. This may have three different, unfavorable effects: it may adversely affect the vehicle's stability, it causes structural loads, and it will cause a severe mixing of gas and liquids. To suppress sloshing, baffles are installed in the tank to dampen the fluid motion. An analysis of slosh loads is given in Reference [4] and by Woodward [5]. Even if baffles are present, special precautions must be taken to ensure that most of the gas bubbles are removed from the propellant before it enters the feedlines [6].

If the rocket coasts, the propellant may, if no special precautions are taken, not be near the sump, so that no ignition is possible. To ensure positive propellant expulsion, inflatable diaphragms or a piston between the ullage and the propellant can be used, which will also suppress sloshing. Another way to ensure positive expulsion is by means of a *capillary barrier*. This device consists of a plate with many orifices located near the sump, and the fluid surface tension will prevent the gas entering under the plate [6, 7]. A third method to ensure ignition after coasting is the use of small (Vernier) rockets, which give the vehicle a sufficiently large acceleration to position the propellant at the sump.

Special provisions have to be taken to minimize the dip in the propellant surface near the sump when the tank is being emptied. If this dip becomes too large, gas may enter the feedlines, causing a motor malfunction. This phenomenon is known as '*vapor pull through*' [8].

To pressurize the tank, an inert pressurization gas can be used. In former days N₂ was widely used, nowadays mostly He is used, which, due to its low molecular weight requires less mass. For LH₂ tanks compressed H₂ can be used. As during the expansion from the storage bottles the gas cools,

especially for pressure-fed systems, the pressure of the stored gas must be sufficiently high, often as high as 30 MPa, and heating of the gas by thrust chamber heat exchangers may be necessary. As during propellant expulsion the gas in the propellant tanks also cools down, the tanks are often provided with a heating system too. Tank pressurization can also be achieved by *Main Tank Injection* (MTI). This system, which can be used for hypergolic propellant combinations, employs the injection of small quantities of fuel and oxidizer into the main oxidizer and fuel tanks respectively. Only a small bottle of pressure gas is needed now to overcome the tank pressure.

10.3 The propellant feed system

In order to enter the combustion chamber, the propellant pressure at the chamber entrance has at least to equal the chamber pressure. This is achieved either by means of pumps (*pump-fed*) or by pressurized tanks (*pressure-fed*). The tank pressure at the sump consists of the ullage pressure p_u and the hydrostatic pressure p_h , which depends on the vehicle acceleration.

For pump-fed systems, the pumps are usually located near the combustion chamber and the tank pressure has to overcome the pressure losses in the feedlines. The pressure at the pump entrance has to be sufficiently high to avoid *cavitation*.

As for the pressure-fed system all pressure losses and the chamber pressure have to be overcome by a fairly high tank pressure, the tanks become relatively heavy. Which system is chosen for a particular vehicle will depend on a performance and cost analysis. For motors having low chamber pressures and short operation times, and for small rockets and upper stages, the pressure-fed system may prove to be the most suitable one; in other cases one will usually prefer a pump-fed system.

The feedlines transport the propellants to the thrust chamber or to the turbopumps. As neither the vehicle nor the feedlines are infinitely stiff, a closed-loop coupling between the vehicle's longitudinal structural modes, the feed system and the chamber pressure may result, a phenomenon which is known as *POGO*, and which is described lucidly by Rubin [9] and Rasumoff and Winje [10]. Feedline dynamics and instabilities in liquid rocket motors are treated by various authors [11, 12, 13]. A general discussion of these instabilities is given by Harrje and Reardon [14].

10.3.1 Pumps

Most liquid-propellant rockets use pumps of the centrifugal type, as these are light-weight, high-performance, small-volume pumps. The required power is delivered by one or more turbines. Usually, pumps and turbines are built together to compact *turbopump* units.

To analyse the pumping process, we will make the following assumptions: the flow is isothermal and incompressible. We can neglect friction and viscous forces, and there is no swirl in the incoming flow.

The conditions before and after the pump are indicated by the indices 1 and 2 respectively. The rise in stagnation pressure, Δp_t , due to the pump is

$$\Delta p_t = (p_2 - p_1) + \frac{1}{2}\rho(V_2^2 - V_1^2). \quad (10.3-1)$$

At sea level a fluid column of height H_e would exert the same pressure if

$$H_e = \frac{\Delta p_t}{\rho g_0}. \quad (10.3-2)$$

The quantity H_e , the *pumphead*, is a pump quality parameter, and g_0 is the standard surface gravity. The increase in energy, per unit mass of the fluid is

$$\Delta e = h_2 - h_1 + \frac{1}{2}(V_2^2 - V_1^2) = \frac{p_2 - p_1}{\rho} + \frac{1}{2}(V_2^2 - V_1^2).$$

Thus the power, P , delivered to the fluid is

$$P = m \Delta e = m \frac{\Delta p_t}{\rho} = mg_0 H_e, \quad (10.3-3)$$

and the required power per unit weight flow of the fluid is

$$\frac{P}{mg_0} = H_e, \quad (10.3-4)$$

which for any value of P/m is independent of the fluid itself and hence the head is a pump quality factor which can, in principle, be determined with any fluid.

Figure 10.4 gives an outline of a centrifugal pump. It consists of a rotating impeller, an *impeller shroud*, and a *diffuser*. On the impeller, vanes are

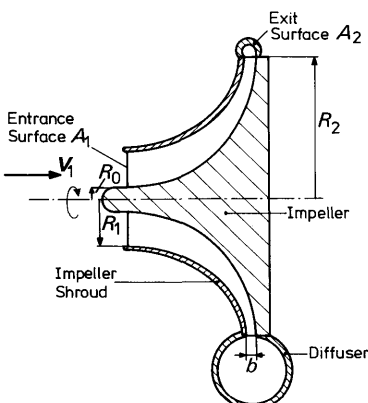


Fig. 10.4 Outline of a centrifugal pump

mounted which whirl the fluid around. The centrifugal forces move the fluid into the diffuser or collector, where it is decelerated and where the static pressure rises. To analyse the performance of the centrifugal pump, we will make the following additional assumptions: the flow enters the pump in the axial direction, the fluid leaves the impeller tangential to the vanes, and the velocity distribution at the entrance and exit surface is uniform. The cavity enclosed between the impeller, impeller shroud and the entrance and exit surfaces, A_1 and A_2 (Fig. 10.4) will be taken as control volume. According to the equation for conservation of angular momentum, Eq. (3.7-25), for stationary flow, we have

$$\int_S \{(\rho \mathbf{V} \cdot \mathbf{n})(\mathbf{r} \times \mathbf{V}) + \mathbf{r} \times \mathbf{n}p\} dS = 0. \quad (10.3-5)$$

For all surfaces, except A_1 and A_2 , the term $\rho \mathbf{V} \cdot \mathbf{n} = 0$. The integral $\int_S \mathbf{r} \times \mathbf{n}p dS$ represents the torque of the fluid on the impeller, thus the torque, \mathbf{T} , from the impeller on the fluid with respect to the axis of rotation, as the impeller is rotational symmetric, equals

$$\mathbf{T} = - \int_S (\mathbf{r} \times \mathbf{n}p) dS,$$

and it follows that

$$\mathbf{T} = \int_{A_1} (\rho \mathbf{V} \cdot \mathbf{n})(\mathbf{r} \times \mathbf{V}) dA + \int_{A_2} (\rho \mathbf{V} \cdot \mathbf{n})(\mathbf{r} \times \mathbf{V}) dA. \quad (10.3-6)$$

Using cylindrical coordinates (Fig. 10.5), where the positive z -axis coincides with the rotational axis of the impeller, in the sense of the rotation, and where the origin can be chosen arbitrarily on the axis of rotation, we have:

$$\mathbf{V}_1 = V_{1z} \mathbf{e}_z, \quad \mathbf{V}_2 = V_{2R} \mathbf{e}_R + V_{2\phi} \mathbf{e}_\phi + V_{2z} \mathbf{e}_z,$$

$$\mathbf{n}_1 = \mathbf{e}_z, \quad \mathbf{n}_2 = \mathbf{e}_R,$$

$$dA_1 = R d\varphi dR, \quad dA_2 = R_2 d\varphi dz,$$

$$\mathbf{r} = R \mathbf{e}_R + z \mathbf{e}_z.$$

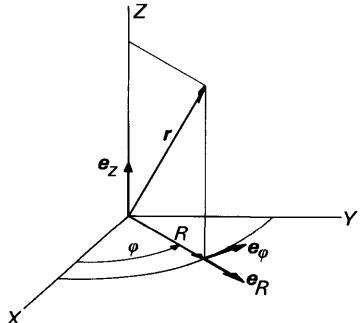


Fig. 10.5 Cylindrical coordinates

Evaluation of Eq. (10.3-6) yields

$$\mathbf{T} = -\rho \left[- \int_{\varphi=0}^{2\pi} d\varphi \int_{R=R_0}^R R^2 V_{1z}^2 \mathbf{e}_\varphi dR + \int_{\varphi=0}^{2\pi} d\varphi \int_{z=z_0}^{z_0+b} \times \right. \\ \left. \times V_{2R} \{ \mathbf{e}_R z V_{2\varphi} + \mathbf{e}_\varphi (R_2 V_{2z} - z V_{2R}) - \mathbf{e}_z R_2 V_{2\varphi} \} R_2 dz \right].$$

Now, it is easily seen that

$$\mathbf{e}_\varphi(\varphi) = -\mathbf{e}_\varphi(\varphi + \pi), \quad \text{and} \quad \mathbf{e}_R(\varphi) = -\mathbf{e}_R(\varphi + \pi).$$

Thus

$$\int_0^{2\pi} \mathbf{e}_\varphi d\varphi = \int_0^\pi \mathbf{e}_\varphi d\varphi + \int_\pi^{2\pi} \mathbf{e}_\varphi d\varphi = \int_0^\pi (\mathbf{e}_\varphi(\varphi) + \mathbf{e}_\varphi(\varphi + \pi)) d\varphi = 0,$$

and in the same way $\int_0^{2\pi} \mathbf{e}_R d\varphi = 0$. We then find for the torque, \mathbf{T} , delivered by the impeller

$$\mathbf{T} = \rho R_2^2 V_{2R} V_{2\varphi} 2\pi b \mathbf{e}_z = m V_{2\varphi} R_2 \mathbf{e}_z, \quad (10.3-7)$$

where m is the mass flow through the pump. If the flow entering the pump has an angular momentum, \mathbf{B} , per unit mass in z -direction, one can show that

$$\mathbf{T} = m(V_{2\varphi} R_2 - \mathbf{B}) \mathbf{e}_z$$

The power, P , delivered by the pump is

$$P = \mathbf{T} \cdot \boldsymbol{\omega} = m V_{2\varphi} \omega R_2 = m V_{2\varphi} V_{2e}, \quad (10.3-8)$$

where ω is the angular velocity and V_{2e} the impeller tip speed.

The influence of the shape of the vanes. Until now we considered the absolute velocity of the fluid. We will now consider the fluid velocity V_r relative to the impeller. Figure 10.6 presents a typical velocity diagram and top view of the impeller. From this figure, we see

$$V_r \sin \beta = V_R = V_a \sin \alpha, \quad (10.3-9a)$$

$$V_r \cos \beta = V_e - V_a \cos \alpha, \quad (10.3-9b)$$

$$V_\varphi = V_a \cos \alpha. \quad (10.3-9c)$$

where V_a is the absolute fluid velocity, $V_e = \omega R = 2\pi N R$, and N is the number of revolutions per second of the pump. Combination of the Eqs. (10.3-2), (10.3-4) and (10.3-7) to (10.3-9) yields, omitting the index 2

$$P = m V_e^2 (1 - \mu \cot \beta) = m V_e^2 \psi, \quad (10.3-10)$$

$$H_e = \frac{V_e^2}{g_0} (1 - \mu \cot \beta) = \frac{V_e^2}{g_0} \psi, \quad (10.3-11)$$

$$\Delta p_t = \rho V_e^2 (1 - \mu \cot \beta) = \rho V_e^2 \psi, \quad (10.3-12)$$

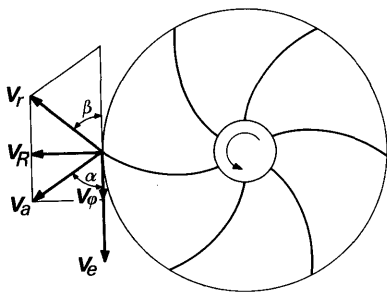


Fig. 10.6 Top view of an impeller, and a typical velocity diagram

Here, μ is the *mass flow parameter*, $\mu = m/(2\pi R b \rho V_e)$ and b is the width of the impeller as indicated in Fig. 10.5. The *pressure parameter*, ψ , is defined by the above equations. Equation (10.3-10) shows that the power P , required by the pump is proportional to mV_e^2 . The maximum pump efficiency is obtained if no separation of the flow from the blades occurs, i.e. V_t is tangential to the blades (Fig. 10.6). This is called the *design point* of the pump. If one increases the rotational speed then, to keep the pump in its design point, the mass flow, m , has to be increased in proportion. Thus, for pumps operating at their design point, $m \propto N$ and thus the power $P \propto N^3$. The mass flow parameter, μ , at the design point is independent of N . Equation (10.3-12) also yields the increase in stagnation pressure, Δp_0 , at any location of the impeller if R , V_e , b and β are regarded as local variables. It is seen that the pressure parameter ψ decreases with increasing mass flow for *backward-leaning* vanes, i.e. $0 < \beta < \pi/2$, is independent of the mass flow for *radial* vanes, i.e. $\beta = \pi/2$ and increases with the mass flow for *forward-leaning* blades, i.e. $\pi/2 < \beta < \pi$. This effect is illustrated in Fig. 10.7.

The high pressures and the centrifugal forces induce high bending stresses in the impeller blades. For forward-leaning blades, the pressure rise may lead to an unstable flow, and as the absolute impeller exit velocity is also

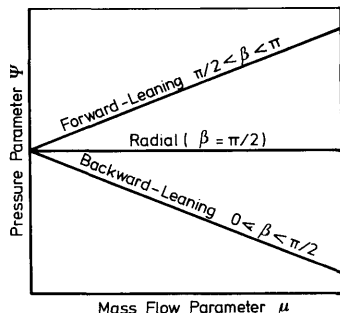


Fig. 10.7 The pressure parameter, ψ , versus the mass flow parameter, μ , for forward-leaning, radial, and backward-leaning blades

higher than for radial or backward-leaning vanes, there is a larger pressure rise in the diffuser too. In general, the diffuser losses are proportional to V_a^2 , thus the efficiency of the impeller with forward-leaning vanes may be lower than the efficiency of the other types. Therefore, rocket turbopumps often have radial or backward-leaning blades.

The pump specific speed. We compare two geometrically similar pumps, *A* and *B*, with volumetric flow rates $Q_A = (m/\rho)_A$ and $Q_B = (m/\rho)_B$. Now $m/\rho = 2\pi R b V_s \sin \beta$. For geometrically similar pumps $\frac{b}{R}$ is the same and $V_s \sin \beta$ is proportional to $V_e = 2\pi N R$. Thus we have

$$Q_A/Q_B = (N_A R_A^3)/(N_B R_B^3).$$

The ratio of the respective rise in stagnation enthalpy is

$$\frac{(\Delta p_v/\rho)_A}{(\Delta p_v/\rho)_B} = \frac{N_A^2 R_A^2}{N_B^2 R_B^2}.$$

Elimination of R_A/R_B yields

$$\frac{N_B}{N_A} = \sqrt{\frac{Q_A}{Q_B}} / \left(\frac{(\Delta p_v/\rho)_A}{(\Delta p_v/\rho)_B} \right)^{3/4}.$$

If pump *B* is taken as reference pump, with $Q_B = 1 \text{ m}^3/\text{s}$ and $(\Delta p_v/\rho)_B = 1 \text{ J/kg}$, the number of revolutions per second of pump *B* is called the *pump specific speed*, N_s . Omitting the indices, we find

$$N_s = N \sqrt{Q} / (\Delta p_v/\rho)^{3/4} \quad (10.3-13)$$

The pump specific speed, N_s , is a dimensionless performance parameter, which does not vary significantly for geometrically similar impellers. Figure 10.8 shows some types of impellers with the general range of specific speeds.

From Eq. (10.3-13) we see that the pump specific speed increases with the flow rate and decreases with the rise in stagnation enthalpy required. The number of revolutions at which the pump is to operate should, according to

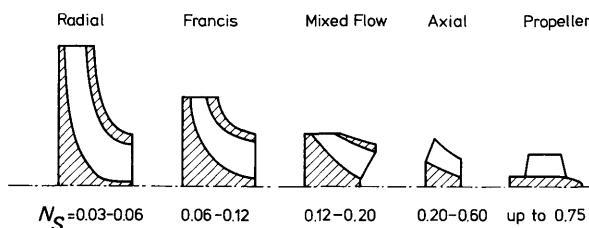


Fig. 10.8 Some impeller types with their specific speeds

Eq. (10.3-12) with $V_e = 2\pi NR$ be as high as possible to minimize the pump dimensions. The angular velocity is limited in most cases either by the allowable material stresses or by cavitation, which will be discussed later. Therefore, the maximum allowable rotational speed, N , in combination with the volumetric flow rate, Q , and the stagnation enthalpy rise will roughly determine the impeller shape.

Losses can be attributed to the following causes: *friction and viscous forces*, *leakage*, *slip*, and *cavitation*. The losses due to friction and viscous effects arise in the mechanical parts (bearings) and the flow, respectively. After the flow has become fully turbulent, a further increase in flow velocity through the pump hardly affects the performance. By means of special mechanical devices, leakage can be kept to a minimum, but cannot always be avoided. If the main flow, locally, is not tangential to the blade, one speaks of *slip*. It can be kept to a minimum by operating the pump near to its design conditions.

We have ignored the blade thickness in the performance analysis. The finite blade thickness slightly reduces the performance, with respect to the analysis given above, but is easily accounted for.

Cavitation is the boiling of the liquid at low pressures and the release of dissolved gas from the liquid. Small gas bubbles grow in the liquid and then collapse within a few milliseconds. This is accompanied by high temperature rises, up to $\sim 10,000$ K, and pressure rises up to ~ 400 MPa. A general discussion on cavitation is given by Pearsall [15]. Brennen and Acosta [16] discuss some aspects of cavitation in turbopumps, especially its relation with the mass flow through the pump, by which it may contribute to the POGO phenomenon. Apart from affecting the mass flow through the pump, the high pressures and temperatures which may occur locally may cause serious damage.

Cavitation can be suppressed by ensuring that everywhere in the flow the static pressure is well above the vapor pressure. This can be achieved by avoiding high flow velocities, or by using high fluid pressures, or by a combination of both. The high fluid pressures in the turbopumps are achieved by high tank pressures, possibly in combination with booster-pumps. Dissolved gas should be removed from the liquid as much as possible.

A measure for the occurrence of cavitation is the *Net Positive Suction Energy*, NPSE. (In older literature *Net Positive Suction Head NPSH*.) The NPSE is defined as

$$NPSE = \frac{p_{t_1} - p_v}{\rho}, \quad (10.3-14)$$

where p_{t_1} is the stagnation pressure at the suction or pump inlet and p_v is the vapor pressure. The NPSE value at which, for the first time cavitation

occurs in the pump is the *critical NPSE*, indicated as $(NPSE)_c$. To avoid cavitation, $NPSE > (NPSE)_c$. Analogous to the pump specific speed N_s , the *suction specific speed* N_{ss} is defined as

$$N_{ss} = \frac{N\sqrt{Q}}{(NPSE)^{3/4}}. \quad (10.3-15)$$

The ratio $(N_s/N_{ss})^{4/3}$ is the *Thoma parameter*, τ , which is often used in pump design

$$\tau = \frac{NPSE}{(\Delta p_t/\rho)} = \left(\frac{N_s}{N_{ss}} \right)^{4/3}. \quad (10.3-16)$$

For a given suction pressure, the pump suction characteristics, in combination with the required flow rate, determine the maximum rotational speed. A high N_{ss} permits a high angular velocity, which makes small, lightweight pumps possible. Modern pumps, such as for the Space Shuttle or third stage of the L III S Ariane have $N \approx 1000 \text{ s}^{-1}$. The effect of cavitation on performance is schematically shown in Fig. 10.9. The stagnation enthalpy is shown versus the *NPSE*. The line $(NPSE)_c$ connects the points where there is a loss of a certain percentage in stagnation enthalpy.

For motors with a short operation time, the damage due to cavitation often did not create too serious a problem, but for reusable motors, such as for the Space Shuttle, the avoidance of cavitation is of utmost importance.

The total efficiency, η , of the pump is defined as

$$\eta = \frac{P_u}{P_i}. \quad (10.3-17)$$

Here P_u is the useful power, and P_i is the power delivered to the pump. It immediately follows that

$$\Delta p_t = \eta \frac{\rho P_i}{m} = \eta \frac{P_i}{Q}. \quad (10.3-18)$$

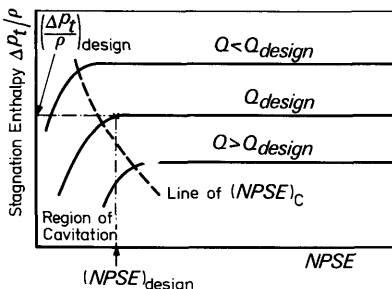


Fig. 10.9 The effect of cavitation on pump performance

For modern rocket motors the total pump efficiency ranges between 0.45 and 0.65.

10.3.2 Turbines

The power to drive the pumps is generated by one or more turbines. These turbines usually are of the axial flow type, i.e. the main direction of the flow is parallel to the axis of rotation. They can be divided into two basic classes: *impulse turbines* and *reaction turbines*. Impulse turbines can either be *single-* or *multi-stage*. The reaction turbine usually is multi-stage.

In the ideal impulse turbine, gas is accelerated by stationary nozzles and fed into the blades of the *rotor*. While the gas is passing through the rotor, the static pressure remains constant while the kinetic energy of the gas is imparted to the rotor (Fig. 10.10).

In the reaction turbine, the expansion of the gas takes place in the rotor. It is the reaction force due to the gas expansion, similar to the expansion of gas in the rocket nozzle, that drives the rotor. As the gas velocity is relatively low in the reaction turbine, viscous losses can also be kept low and the efficiency may be somewhat higher than for the impulse turbine. As the pure reaction turbine requires more stages for an equal power output than the impulse turbine, this last type is preferred for applications in rocket engines. The outlines of some types of impulse turbines are sketched in Fig. 10.10. In the *single-stage, single-rotor impulse turbine*, the gas is expanded by stationary nozzles and drives the rotor (Fig. 10.10a). The *single-stage, two-rotor velocity compound impulse turbine* (Fig. 10.10b) has one row of expansion nozzles. After leaving the first rotor, the gas passes through a stator to enter the second rotor. The turbine is called *single-stage*, as there is

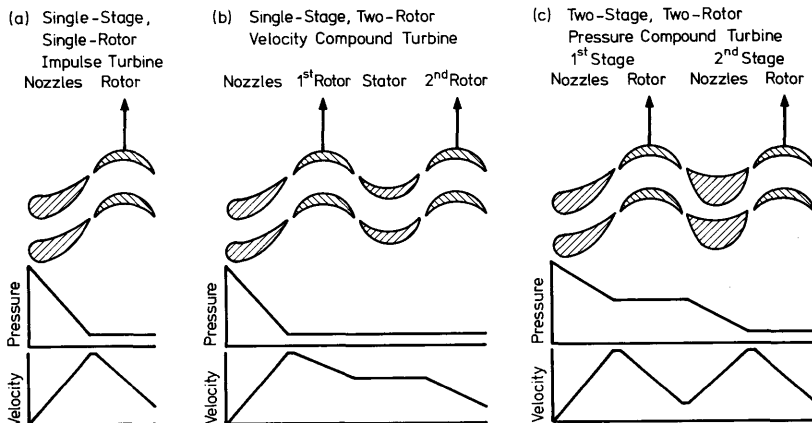


Fig. 10.10 Schematic representation of some types of impulse turbines, and their velocity and pressure profiles

only one expansion cycle. The *two-stage pressure compound impulse turbine* (Fig. 10.10c) consists of two rows of stationary nozzles. After the first rotor the gas expands through the second row of nozzles and drives the second rotor. The objective is to have identical entrance velocities at both rotors, such that both rotors are identical and absorb the same amount of energy.

To determine the power output of an ideal impulse turbine, consider the flow between two rotor blades (Fig. 10.11). We assume a constant cross-sectional area between the blades, hence the gas velocity, V_r , with respect to the blades is of a constant magnitude and the pressure is constant. Moreover, we assume that the width of the blades is small with respect to the diameter, so we can assume a uniform circumferential velocity, V_e . The absolute gas velocity is indicated by V_a ; the z -axis coincides with the axis of rotation. By the same arguments as for the centrifugal pump, we find

$$\mathbf{T} = \int_{A_1} (\rho \mathbf{V}_a \cdot \mathbf{n}) (\mathbf{r} \times \mathbf{V}_a) dA + \int_{A_2} (\rho \mathbf{V}_a \cdot \mathbf{n}) (\mathbf{r} \times \mathbf{V}_a) dA. \quad (10.3-19)$$

Here, A_1 and A_2 are the entrance and exit surface areas of the turbine wheel. Integration yields

$$T = rm(V_{a_1} \cos \alpha_1 - V_{a_2} \cos \alpha_2), \quad (10.3-20)$$

$$P = \mathbf{T} \cdot \boldsymbol{\omega} = mV_e(V_{a_1} \cos \alpha_1 - V_{a_2} \cos \alpha_2), \quad (10.3-21)$$

where α_1 and α_2 follow from Fig. 10.11.

The specific power, P_{sp} , i.e. the power per unit mass flow, equals

$$P_{sp} = V_e(V_{a_1} \cos \alpha_1 - V_{a_2} \cos \alpha_2).$$

The available power per unit mass flow is $\frac{1}{2}V_{a_1}^2$, so the turbine efficiency, η_T , is

$$\eta_T = \frac{2V_e}{V_{a_1}^2} (V_{a_1} \cos \alpha_1 - V_{a_2} \cos \alpha_2). \quad (10.3-22)$$

By using the blade angles β_1 and β_2 , as defined in Fig. 10.11, we can write

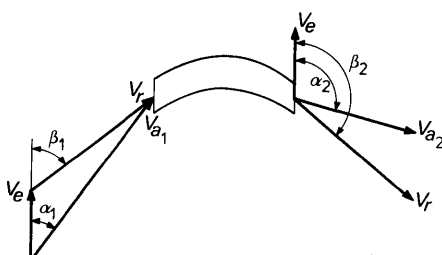


Fig. 10.11 Velocity diagram for the flow between the rotor blades of an ideal impulse turbine

Eq. (10.3-22) as

$$\eta_T = \frac{2V_e}{V_{a_1}} \left(\cos \alpha_1 - \frac{V_e}{V_{a_1}} \right) \left(1 - \frac{\cos \beta_2}{\cos \beta_1} \right),$$

and for symmetrical blades, i.e. $\beta_2 = 180^\circ - \beta_1$, we find

$$\eta_T = \frac{4V_e}{V_{a_1}} \left(\cos \alpha_1 - \frac{V_e}{V_{a_1}} \right). \quad (10.3-23)$$

The circumferential velocity, V_e , is determined by the rotor diameter and the angular velocity. The absolute entrance velocity, V_{a_1} , is determined by the gas expansion in the nozzles. The turbine efficiency thus follows from the ratio V_e/V_{a_1} and the angle α_1 under which the flow enters the rotor. The maximum efficiency for a fixed nozzle angle α_1 follows from differentiation of Eq. (10.3-23) with respect to V_e/V_{a_1} and equating the result to zero

$$V_e/V_{a_1} = \frac{1}{2} \cos \alpha_1. \quad (10.3-24)$$

Thus the maximum efficiency is

$$\eta_{T_{max}} = \cos^2 \alpha_1. \quad (10.3-25)$$

It tends to unity for small angles α_1 . Small nozzle angles α_1 mean that the expanding gas has to follow a strongly curved path, which is difficult to achieve in practice. Moreover, it is difficult to reach values of $V_e/V_{a_1} \approx \frac{1}{2}$. Generally, these values are somewhat lower.

In practice, α_1 lies between 15° and 30° , which yields a maximum theoretical turbine efficiency of 0.94 to 0.75.

In the beginning of this chapter, we have briefly discussed the sources of the high pressure gas which drives the turbines. The gas is expanded between the nozzle blades. Analogous to the expansion in the rocket nozzle, we find

$$V_{a_1} = \sqrt{\frac{2\gamma}{\gamma-1} RT_{tot} \left[1 - \left(\frac{p_1}{p_{tot}} \right)^{(\gamma-1)/\gamma} \right]}, \quad (10.3-26)$$

where the index *tot* indicates the stagnation conditions and the index 1 the conditions at the nozzle exit or rotor entrance. The throat area, A_t , of the nozzles is given by the well-known relation

$$A_t = \frac{m \sqrt{RT_{tot}}}{\Gamma p_{tot}}. \quad (10.3-27)$$

For η_T being at a maximum, it follows that

$$m = \rho V_s \sin \beta_1 A_1 = \rho V_{a_1} \sin \alpha_1 A_1 = 2\rho V_e \tan \alpha_1 A_1, \quad (10.3-28)$$

where use is made of Eq. (10.3-24).

From the Eqs. (10.3-21) and (10.3-28) it is clear that for a fixed turbine mass flow, the power output of a turbine wheel is proportional to V_e^2 or N^2 .

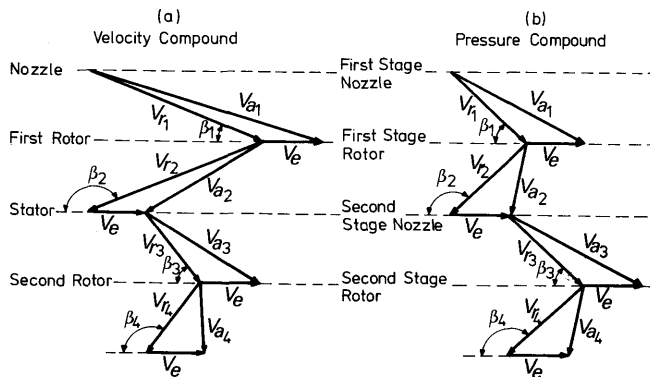


Fig. 10.12 Velocity diagrams for velocity compound and pressure compound turbines

Now, the rotational speed is limited by the allowable material stresses. Thus if the required power output exceeds the maximum power output of one turbine wheel, one has to add one or more rotors to the turbine. In Section 10.3.1, we have seen that the power required by the pump, is proportional to N^3 . So, with increasing N a point will be reached where the available and required power balance each other.

If two or more rotors are necessary, one has the choice between a velocity compound and a pressure compound turbine. The velocity diagrams for both types are sketched in Fig. 10.12. As Fig. 10.12a shows, the blade angles of both the rotors of the velocity compound turbine have to be different, while Fig. 10.12b shows that the pressure compound turbine has rotors with the same blade angles. On the other hand, the pressure differences between the two stages in the pressure compound turbine require a very good sealing between the stages to avoid leakage. To minimize exhaust problems, one always tries to have the final absolute gas velocity V_{a4} about parallel to the axis of rotation, as indicated in Fig. 10.12.

10.3.3 The injector

After their passage through the pumps, the propellants are injected into the thrust chamber. They pass through the *injector*, which is a plate with many orifices. The purpose of the injector is to *atomize* the propellants, and to ensure an even mixing and propellant distribution, such that a smooth and stable combustion will take place. The spatial distribution of the orifices in the injector can have a profound influence on the combustion characteristics of the rocket engine, especially in regard to stable combustion [14].

A good mixing usually is achieved by letting the streams of propellant impinge on each other, but also other methods, such as the splash plate, have been used. Some of the various possible patterns are depicted in Fig. 10.13.

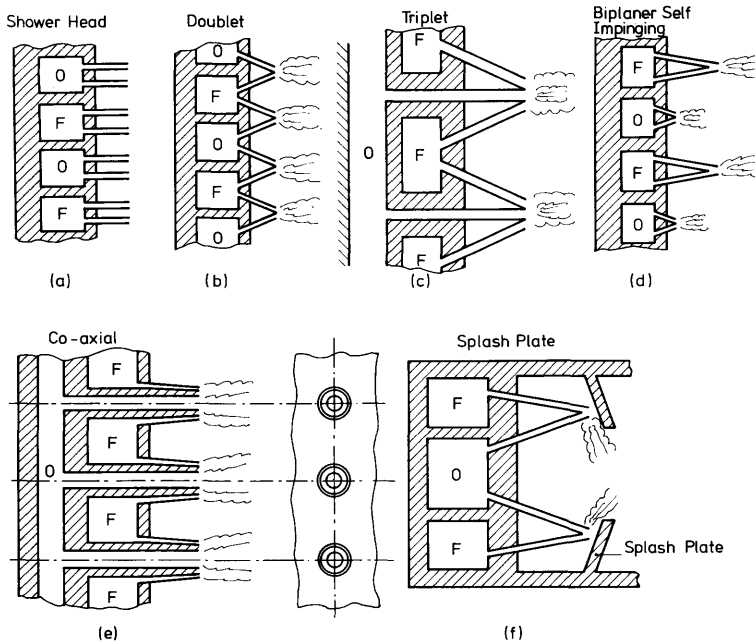


Fig. 10.13 Some injector impinging patterns

Here O stands for the oxidizer ducts and F for the fuel ducts. The choice of the spacing and the pattern of the orifices in the injector design depend on many factors, such as heat transfer characteristics, the spatial distribution of the energy release and combustion characteristics, and are related to the breaking-up of liquid jets and droplet formation. Theoretical work on these items has advanced in recent years [14], but still much of the work must be carried out experimentally or by a combination of experiments and theory [17, 18, 19, 20, 21].

Often supplementary or larger fuel orifices are placed near the injector periphery in order to get a higher fuel concentration near the chamber walls. This higher fuel concentration may be desirable, because it lowers the local combustion temperature and the heat transfer to the chamber walls. To dampen the tangential pressure oscillations, which can occur in certain types of oscillatory combustion, sometimes radial baffles are mounted on the injector.

The heat transfer to the gas-side of the injector is due to radiation, and convection from the combustion products and propellants. Recirculation patterns of the fluid between the injector orifices complicate an accurate prediction of heat transfer rates. Also the radiative heat transfer from both the hot chamber walls and the combustion products is difficult to analyse precisely. A more detailed discussion of heat transfer to the injector is given by Zie bland and Parkinson [22].

The propellant injection velocity, V_i , follows from the equation for the conservation of mass (either for the fuel or the oxidizer),

$$V_i = \frac{m}{\rho A}, \quad (10.3-29)$$

where m stands for the fuel or oxidizer mass flow through an orifice, A is the cross-sectional area of the orifice and ρ the appropriate density. Because of viscous forces there is a strong pressure drop, Δp_i , over the injector. This pressure drop is related to the injection velocity, V_i , by the relationship

$$\Delta p_i = \rho/2 \left(\frac{V_i}{c_d} \right)^2, \quad (10.3-30)$$

where c_d is a discharge coefficient which can be determined quite accurately by means of waterflow tests. Values for c_d range from about 0.5 to a little over 0.9, depending on the shape and length of the orifice.

Upper-stage engines, space engines or motors for landers are often designed to provide a variable thrust. Since the flow into the chamber depends on the pressure drop, Δp_i , across the injector orifice, a significant variation in the flow rate seriously affects the pressurization system and the injector performance. To avoid this, for variable-thrust rocket motors, special injectors, such as *multi-manifold injectors*, *variable-area injectors* or *aeration injectors* may be used. The multi-manifold injectors employ two or more sets of propellant manifolds, each set connected to its own injector orifices. By closing propellant manifolds, one can obtain a reduced propellant flow rate at a satisfactory Δp_i . The variable-area injector employs a pintle to vary the injector area, while controlling the pressure drop. The aeration injector employs fixed area orifices, but it is possible to inject an inert gas in the propellant manifold, replacing part of the propellants in the ducts. By changing the amount of gas injected, the propellant flow may be varied, thus providing throttling capability. It was shown in experiments that with aeration injection, thrust modulation between 4% and 100% was possible, while, even in the worst case, losses did not exceed 10%.

Injector design itself is of a fairly complicated and specialized character, a full discussion of which cannot be given at this place.

10.4 The thrust chamber

After the propellants have entered the combustion chamber, they vaporize, mix and react. Part of the combustion reaction may already take place in the liquid state. In some cases one, or both, of the propellants are injected in gaseous form, which reduces the time necessary to complete the combustion, leading to relatively short motors.

It is possible that a non-uniform mixture ratio exists in the combustion chamber. It has been observed that regions of identifiable mixture ratios,

larger than a typical molecular mixing length (~ 1 cm), may maintain their identity throughout the chamber and nozzle. This may result in performance losses up to 5%.

10.4.1 Aspects of oscillatory combustion

Apart from the POGO phenomenon mentioned already, other types of combustion instability are encountered in liquid motors. Frequencies ranging from a few Hertz up to 15,000 Hz have been observed, with pressure amplitudes ranging from 0.1 to 10 times the chamber pressure. Oscillatory operation of the rocket motor is undesirable, as it causes severe vibrations (up to $10,000 \text{ m/s}^2$) and as it is accompanied by a strong increase in heat transfer.

Some well-known instabilities are *chugging* and *screaming*. Chugging takes place at low frequencies (less than a few hundred Hertz). It may be due to an interaction between the propellant flow rate entering the chamber and the chamber pressure, but also a coupling between the injector structure and the combustion process has been traced as a cause. Screaming is a high-frequency acoustic or resonant combustion. Longitudinal, radial and tangential pressure oscillations have been observed. The energy to drive the oscillations stems from the propellant combustion.

Combustion instabilities can be eliminated by changing the chamber geometry, the pattern and size of the injector orifices, or by mounting baffles. An extensive treatment on oscillatory combustion in liquid motors is given by Harrje and Reardon [14].

10.4.2 The shape of the combustion chamber

The most commonly used shapes of combustion chambers are spherical, near spherical and cylindrical. The spherical shape yields the smallest surface area for a given volume, and thus is attractive from the viewpoint of cooling and weight. It is also an attractive shape from strength considerations. However, it is more difficult to produce than a cylindrical chamber, while also its performance is less than that of the cylindrical chamber.

If annular nozzles, such as plug or E-D nozzles, are used, an annular or toroidal type of chamber is an obvious choice.

10.4.3 The chamber volume

The propellants, after entering the combustion chamber, need some time for vaporization, mixing and reaction. We will denote this time interval by τ_c . The residence time, τ^* , has to be equal to or larger than τ_c to ensure a

satisfactory performance. The minimum chamber volume \mathcal{V}_c therefore directly follows from Eq. (6.7-3), with $\tau^* = \tau_c$,

$$\mathcal{V}_c = \tau_c A_t \Gamma \sqrt{RT_c}, \quad (10.4-1)$$

or with Eq. (5.1-39)

$$\mathcal{V}_c = \tau_c m \frac{RT_c}{p_c} = \tau_c m \frac{R_0 T_c}{M p_c}. \quad (10.4-2)$$

From this equation, we immediately see that the minimum chamber volume is proportional to τ_c , m and T_c and inversely proportional to M and p_c . The combustion temperature and the molecular weight of the combustion products do not vary strongly with p_c . Thus, by increasing the chamber pressure, p_c , one can reduce the required chamber volume and consequently the weight of the whole system. The weight benefit, however, is partly off-set by the larger expansion nozzle which is necessary to achieve the same exit pressure as for an engine with a lower chamber pressure.

10.5 Cooling of liquid engines

In Chapter 8 we discussed some of the most important aspects of heat transfer in rocket motors. In this section we will discuss some of the most used cooling techniques for liquid engines.

Cooling is necessary mainly from strength considerations. The strength of materials decreases with increasing temperatures, but even before the allowable stress is reduced to an unacceptable low level, creep may occur. For reusable engines, the fatigue life, which depends on temperature and stress levels, will also put an upper limit on the allowable material temperature. There are no materials available which combine good strength, creep and fatigue qualities at elevated temperatures, with good manufacturing characteristics and low costs.

Hence, for rocket motors in which temperatures of over 2000 K are common, the only way to avoid structural parts getting too weak due to high temperature levels, is cooling. This can be achieved by a great variety of methods or combinations of these.

The various cooling techniques that are in use in rocket technology have been discussed by Sutton [23] in 1966, and since, no basically new techniques have been developed. We can distinguish between *active* and *passive* cooling techniques. The active cooling methods use a forced convection heat transport, as to actively cool the hot spots. Passive cooling systems do not make use of a special heat transport system but are designed such that during motor operation they prevent structural parts becoming too hot. Some of the passive cooling systems do not actually cool, but only reduce heat fluxes into the structure (insulation cooling). Other methods, such as radiation cooling and ablative cooling are real cooling methods.

10.5.1 Active cooling systems

The four most important active cooling methods, *regenerative*, *film*, *transpiration* and *dump cooling* are schematically depicted in Fig. 10.14.

Regenerative cooling is one of the most efficient and sophisticated means of cooling. The method (Fig. 10.14a) is used on many of the large rocket engines. The thrust chamber and nozzle wall contain passages through which one of the propellants, usually the fuel, flows. The passages may either be formed by a simple, double-wall construction, by composing the thrust chamber and nozzle of a bundle of coolant tubes, or by milling out the coolant ducts in the wall of the chamber and nozzle [24]. The coolant, passing at high pressures through the ducts (~ 40 MPa for the SSME) then is injected into the combustion chamber. In some cases, if the coolant is at a supercritical pressure, it is possible to use the absorbed energy to drive a turbopump unit before the coolant is injected into the combustion chamber. The size of the coolant ducts and the coolant flow rate are determined by the following considerations: the total amount of heat absorbed should not raise the bulk temperature to the boiling point, or to such a level that propellant decomposition takes place; the local heat transfer rate should not exceed the maximum nucleate boiling heat transfer rate (Section 8.3.3); the pressure in the cooling jacket should not become too low.

Coolant boiling is accompanied with the formation of large vapor bubbles and a strong decrease in density and cooling capacity. Moreover, a blockage of the flow may occur. Propellant decomposition may form deposits on the hot walls of the cooling jacket, thus effectively reducing the conductivity of the wall, and hence the heat transfer rate.

Local nucleate boiling strongly increases the heat transfer rate, however, if film boiling takes place, an insulating vapor film at the wall reduces the possible heat fluxes strongly. If the fluids are at supercritical pressures, neither boiling nor nucleate or film boiling will occur and high heat transfer rates are possible: for modern engines up to 150 MW/m^2 . Table 10.2 shows

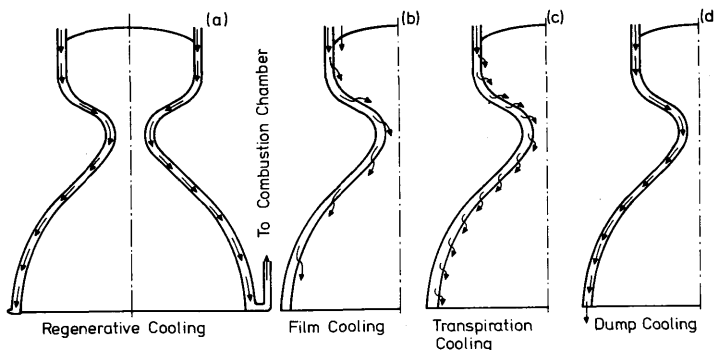


Fig. 10.14 Some active cooling methods

Table 10.2. The critical temperatures and pressures of some rocket propellants

Propellant	Critical temperature T_{cr} (K)	Critical pressure p_{cr} (MPa)
Ammonia (NH_3)	406	11.1
Fluorine (F_2)	145	5.4
Hydrazine (N_2H_4)	654	14.7
Hydrogen (H_2)	34	1.3
Kerosine*	622	2.2
Nitrogen Tetroxide (N_2O_4)	432	10.1
Oxygen (O_2)	154	5.1
Red Fuming Nitric Acid*	545	8.9
UDMH[$(\text{CH}_3)_2\text{NNH}_2$]	524	5.3

* Denotes average values

the critical temperatures and pressures for some propellants. It is seen that at low and moderate pressures only hydrogen and kerosine offer the opportunity of supercritical cooling, but at higher pressures many more propellants have this potential.

Regenerative cooling is very effective as nearly all heat energy that was transferred to the wall is fed back into the thrust chamber and hence is available for propulsion. The system, however, requires a complicated construction and there is a large pressure drop along the coolant jacket, in the case of the SSME about 10 MPa, which makes very high pump pressures necessary. Moreover, some propellants only allow low wall temperatures as decomposition may take place otherwise.

Film cooling (Fig. 10.14b) is suited to be used in combination with other methods, such as regenerative cooling or insulation cooling. Pure film cooling permits a relatively simple chamber and nozzle design. The coolant is injected along the gas-side wall surface by means of tangential slots. The coolant forms a cool boundary layer between the gas-side wall surface and the hot gases. As this boundary layer gradually mixes with the main flow, its temperature rises and downstream of the slot new coolant has to be injected.

Transpiration cooling (Fig. 10.14c) is quite similar to film cooling. Through a porous wall, coolant is injected continuously along the gas-side wall surface, forming a cool boundary layer at the wall.

Dump cooling (Fig. 10.14d) resembles regenerative cooling, but after having performed its cooling function, the coolant is dumped overboard at the

nozzle exit. Many of the restrictions for regenerative cooling also hold for dump cooling. The heated, gasified coolant can be accelerated to supersonic speeds thus providing a small extra thrust. The method is especially suited for low-pressure engines, using low molecular weight propellants, but yields a performance loss as compared to regenerative cooling. On the other hand, the construction is simpler as compared to regeneratively cooled engines.

10.5.2 Passive cooling systems

Among these systems, the most important ones are: *insulation cooling*, *heat sink cooling*, *ablative cooling* and *radiation cooling*.

Insulation cooling. Here liners are used with an extremely low thermal conductivity, thus reducing the heat flux into the wall. As it is not a real cooling method by itself, it is mostly used in combination with other cooling techniques, such as heat sink, radiation or regenerative cooling. A very special material is *pyrolytic graphite*. This material has high and low conductivity directions. While the conductivity parallel to the layer planes is in the order of 2×10^3 W/(m.K), the conductivity perpendicular to the layer planes is only 5.75 W/(m.K). This makes it possible to conduct the heat in preferred directions, and so to avoid the heating of critical parts.

Heat sink cooling is mostly used in solid rockets. The method consists of applying a piece of solid material with good conductivity and a high specific heat capacity to certain hot spots. The heat sink absorbs the heat from the hot gases, thereby raising its own temperature but keeping the wall relatively cool. The method is only suitable for short-duration applications, but is sometimes used in combination with insulation cooling for small liquid rocket engines.

Ablative cooling consists of covering the hot gas-side of the engine wall with a material that decomposes endothermally at high temperatures, while forming a insulating char layer. It is often used in combination with radiation and insulation cooling and chosen for upper-stage motors and reaction control engines for the sake of simplicity [25]. It is also an effective means to keep the temperature of variable-thrust motors within an acceptable range. Regenerative cooling often poses a problem for variable-thrust motors, because of the variable chamber pressure and flow rate. Therefore, ablative cooling offers a simple and efficient way to keep the engine wall relatively cool.

Radiation cooling is often used for upper-stage engines and reaction control engines in combination with insulation and ablative cooling. The hot walls radiate the heat to the surroundings. As the radiative heat flux is proportional to T^4 , the material temperature must be high to obtain a large

Table 10.3. The melting point and density of some metals used for rocket motor construction

Metal	Melting temperature (K)	Density* (kg/m ³)
Copper (Cu)	1356	8.89×10^3
Iron (Fe)	1812	7.87×10^3
Molybdenum (Mo)	2890	10.22×10^3
Nickel (Ni)	1726	8.9×10^3
Niobium (Nb) (Columbium)	2741	8.57×10^3
Tantalum (Ta)	3269	16.65×10^3
Wolfram (W) (Tungsten)	3683	19.3×10^3

* At room temperature

radiative heat flux. Refractory metals, such as molybdenum, niobium (columbium), etc. can withstand high temperatures without losing their strength. Table 10.3 lists the melting points and densities of some metals which are used for rocket motor construction.

Some refractory metals easily react with the combustion products. As the melting point of their oxides or compounds often is much lower than that of the metals, coatings have to be applied in many cases. The refractory alloys based on tantalum, niobium and molybdenum, in particular, have found successful applications as nozzle construction material. Wolfram (tungsten) alloys have found applications for nozzle inserts. More specific information on alloys of refractory metals can be found in Reference [26].

References

- 1 Schmidt, H. W. and Harper, J. T. (1967), *Handling and Use of Fluorine and Fluorine-Oxygen Mixtures in Rocket Systems*, NASA SP-3037, Washington.
- 2 Rosen, G. (1974), Manufacture and deflagration of an atomic hydrogen propellant, *AIAA J.*, **12**, 1325–1330.
- 3 Bernstein, A. L. and Blumrich, J. F. (1968), Concepts for more efficient bulkhead designs for launch and space vehicles, *J. Spacecraft*, **5**, 1404–1410.
- 4 Anon. (1968), *Propellant Slosh Loads*, NASA SP-8009, Washington.
- 5 Woodward, J. H. and Bauer, H. F. (1970), Fluid behavior in a longitudinally excited cylindrical tank of arbitrary sector-annular cross section, *AIAA J.*, **8**, 713–719.
- 6 DeBrock, S. C. and Rudey, C. J. (1974), Agena primary and integrated secondary propulsion systems, *J. Spacecraft*, **11**, 769–777.
- 7 Gluck, D. F. (1970), Propellant position control by capillary barriers during spacecraft rotational manuevres, *J. Spacecraft*, **7**, 242–247.

- 8 Easton, C. R. and Catton, I. (1970), Nonlinear free surface effects in tank draining at low gravity, *AIAA J.*, **8**, 2195–2199.
- 9 Rubin, S. (1972), *Analysis of POGO Stability*, paper presented at the 23rd IAF-Congress, Vienna.
- 10 Rasumoff, A. and Winje, R. (1971), *The POGO Phenomenon: Its Causes and Cure*, paper presented at the 22nd IAF-Congress, Brussels.
- 11 Holster, J. L. and Astleford, W. J. (1974), Analytical model for liquid rocket propellant feedline dynamics, *J. Spacecraft*, **11**, 180–187.
- 12 Astleford, W. J., Holster, J. L., and Gerlach, C. R. (1972), *Analysis of Propellant Feedline Dynamics*, NASA CR-123913, Washington.
- 13 Powell, E. A. and Zinn, B. T. (1974), Theoretical investigation of nonlinear three-dimensional instabilities in liquid rockets with real nozzles, *Acta Astronautica*, **1**, 1051–1073.
- 14 Harrje, D. T. and Reardon, F. H. (eds) (1972), *Liquid Propellant Rocket Combustion Instability*, NASA SP-194, Washington.
- 15 Pearsall, I. S. (1975), Cavitation, Technical File no 14, *Engineering*, **215**, I-VIII.
- 16 Brennen, C. and Acosta, A. J. (1973), Theoretical quasi-static analysis of cavitation compliance in turbopumps, *J. Spacecraft*, **10**, 175–180.
- 17 Bracco, F. V. (1973), An experimental-analytical method to study steady spray combustion, *J. Spacecraft*, **10**, 353–354.
- 18 Burick, R. J. (1972), Atomization and mixing characteristics of gas/liquid coaxial injector elements, *J. Spacecraft*, **9**, 326–331.
- 19 Burick, R. J. (1973), Optimum design of space storable gas/liquid coaxial injectors, *J. Spacecraft*, **10**, 663–670.
- 20 Wong, J. K. S., Sandri, R. and Newman, J. A. (1974), A new experimental method for the investigation of fuel spray evaporation, *AIAA J.*, **12**, 269–274.
- 21 George, D. J. (1973), *Rocket Injector Hot Firing and Cold Flow Spray Fields*, AIAA Paper 73-1192, AIAA, New York.
- 22 Ziebland, H. and Parkinson, R. C. (1971), *Heat Transfer in Rocket Engines*, AGARDograph No. 148, NATO, Neuilly-sur-Seine, p. 77–86.
- 23 Sutton, G. P., Wagner, W. R. and Seader, J. D. (1966), Advanced cooling techniques for rocket engines, *Astronautics and Aeronautics*, **4**, no. 1, 60–71.
- 24 Cook, R. T. and Coffey, G. A. (1973), *Space Shuttle Orbiter Engine Main Combustion Chamber Cooling and Life*, AIAA Paper 73-1310, AIAA, New York.
- 25 Park, L. T., Corbin, J. D. and Ernst, R. D. (1973), *Titan Transtage Spacecraft Propulsion System*, AIAA Paper 73-1210, AIAA, New York.
- 26 Anon. (1970), *Recent Advances in Refractory Alloys for Space Power Systems*, NASA SP-245, Washington.

11 Two-dimensional Rocket Motion in Vacuum

In Chapter 4 the equations of motion for a rigid rocket were derived. These equations can only be solved by numerical methods. As, in practice, rocket motion will be nearly two-dimensional in many cases, and as the assumption of a pure two-dimensional motion will greatly simplify the treatment of rocket motion, we will assume in this chapter that the complete trajectory of the center of mass of the vehicle lies in a single plane. In that case, there are only three degrees of freedom: two for the position of the center of mass and one for the orientation of the rocket.

Such a pure two-dimensional motion is, of course, only possible if all forces acting on the rocket, including the apparent forces, lie in the plane of motion. Consequently, the resulting moment is perpendicular to that plane. In practice, pure two-dimensional motion does not occur because of the presence of forces perpendicular to the instantaneous plane of motion, such as aerodynamic forces, gravitational forces, or components of the thrust. The aerodynamic forces may be caused by cross-wind, misalignments or by the deflection of control surfaces. The gravitational forces may appear if the instantaneous plane of the trajectory does not coincide with the direction of the gravitational field. Thrust forces normal to the plane of motion may be caused either by thrust misalignment or by thrust vector control. For an uncontrolled rocket, flying in a central or homogeneous gravitational field, one may assume that no forces are acting normal to the instantaneous plane of motion, making the nominal trajectory to lie in the nominal plane of motion. Wind, thrust misalignment, aiming error, launcher deflection, etc., cause the real trajectory to deviate from the nominal one. This is called the *dispersion*, which can be divided into lateral or out-of-plane dispersion, and in-plane dispersion. In this chapter we will only discuss nominal trajectories.

11.1 The equations of motion

To describe the motion of the rocket vehicle we need the following reference frames:

Inertial frame OXYZ. This frame is chosen such that the trajectory of the center of mass of the vehicle lies in the XZ -plane. So this plane is determined by the launch direction (initial velocity) and the direction of the gravitational field. The inertial frame will be specified further where necessary. The unit vectors along the axes of the inertial frame will be denoted by e_x , e_y and e_z .

Vehicle reference frame oxyz. The origin of this frame is the center of mass of the rocket. The x -axis coincides with the longitudinal axis of the rocket and is positive forwards. The y - and z -axes are chosen such that they form an orthogonal right-handed Cartesian frame, the xz -plane coinciding with the XZ -plane. The unit vectors along the axes of the vehicle reference frame are \mathbf{e}_x , \mathbf{e}_y and \mathbf{e}_z .

The position of the rocket is determined by the X - and Z -coordinates of its center of mass, while the orientation is determined by the angle between the x -axis and the X -axis: the *pitch angle* θ (Fig. 11.1).

The equations of two-dimensional motion (along the axes of the vehicle reference frame) can be obtained by substitution of $v = p = r = 0$ into Eqs. (4.2-58). However, in this simple case, we prefer to express the equations in components along the axes of the inertial frame. The equations for translational motion can be obtained from the vector equation, Eq. (4.2-52),

$$M \frac{d\mathbf{V}_{cm}}{dt} = \mathbf{F} + \mathbf{W} + \mathbf{F}_a. \quad (11.1-1)$$

As we will only consider nominal trajectories, the thrust is assumed to act along the x -axis, i.e. $F_y = F_z = 0$, while its application point (the center of mass flow as defined by its coordinates x_e , y_e and z_e relative to the vehicle reference frame) will be assumed to lie on the (negative) x -axis, i.e. $y_e = z_e = 0$. Then according to Eqs. (4.2-57), the thrust, \mathbf{F} , and the aerodynamic force, \mathbf{F}_a , are given by

$$\mathbf{F} = F \mathbf{e}_x, \quad (11.1-2)$$

$$\mathbf{F}_a = X_a \mathbf{e}_x + Z_a \mathbf{e}_z. \quad (11.1-3)$$

The gravitational field strength \mathbf{g} , and the position vector, \mathbf{R}_{cm} , of the

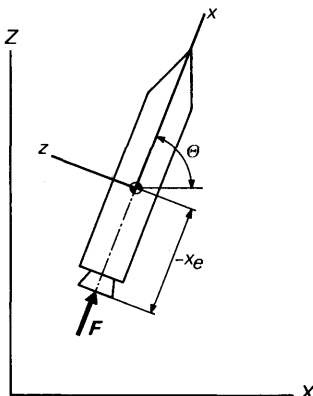


Fig. 11.1 Coordinate systems to describe the two-dimensional rocket motion

center of mass are resolved into components along the inertial axes

$$\mathbf{g} = g_x \mathbf{e}_x + g_z \mathbf{e}_z, \quad (11.1-4)$$

$$\mathbf{R}_{cm} = X \mathbf{e}_x + Z \mathbf{e}_z. \quad (11.1-5)$$

By substitution of Eqs. (11.1-2) to (11.1-5) into Eq. (11.1-1), and using the relation between the unit vectors in both reference frames,

$$\begin{bmatrix} \mathbf{e}_x \\ \mathbf{e}_y \\ \mathbf{e}_z \end{bmatrix} = \begin{bmatrix} \cos \theta & 0 & \sin \theta \\ 0 & 1 & 0 \\ -\sin \theta & 0 & \cos \theta \end{bmatrix} \begin{bmatrix} \mathbf{e}_X \\ \mathbf{e}_Y \\ \mathbf{e}_Z \end{bmatrix}, \quad (11.1-6)$$

we obtain

$$M \frac{d^2 X}{dt^2} = F \cos \theta + Mg_x + X_a \cos \theta - Z_a \sin \theta, \quad (11.1-7a)$$

$$M \frac{d^2 Z}{dt^2} = F \sin \theta + Mg_z + X_a \sin \theta + Z_a \cos \theta. \quad (11.1-7b)$$

The equation for rotational motion is obtained by substitution of $p = r = z_e = F_z = 0$ into Eq. (4.2-58e)

$$I_{yy} \frac{dq}{dt} = -q \frac{dI_{yy}}{dt} - mqx_e^2 + M'. \quad (11.1-8)$$

Letting V_X and V_Z be the velocity components of the center of mass along the X - and Z -axes respectively, and noting that the pitch rate, q , is related to the pitch angle, θ , by

$$q = -\frac{d\theta}{dt}, \quad (11.1-9)$$

the equations of motion can be written as

$$M \frac{dV_X}{dt} = F \cos \theta + Mg_x + X_a \cos \theta - Z_a \sin \theta, \quad (11.1-10a)$$

$$M \frac{dV_Z}{dt} = F \sin \theta + Mg_z + X_a \sin \theta + Z_a \cos \theta, \quad (11.1-10b)$$

$$\frac{dX}{dt} = V_X, \quad (11.1-10c)$$

$$\frac{dZ}{dt} = V_Z, \quad (11.1-10d)$$

$$I_{yy} \frac{d^2 \theta}{dt^2} = -\frac{d\theta}{dt} \left(\frac{dI_{yy}}{dt} + mx_e^2 \right) - M'. \quad (11.1-10e)$$

The instantaneous mass of the rocket follows from the differential equation

$$\frac{dM}{dt} = -m. \quad (11.1-10f)$$

According to Section 5.1.4 the thrust can be written as

$$F = mV_e + (p_e - p_a)A_e. \quad (11.1-10g)$$

The equations (11.1-10) are the complete equations for two-dimensional rocket motion. This system of equations is still rather complicated. The aerodynamic forces are dependent on velocity and position; the gravitational components are in general dependent on the position, while the thrust is dependent on the position owing to the atmospheric pressure term. In general, analytic solution of these equations is not possible and one must resort to numerical techniques. We will now make some further simplifications.

11.2 Rocket motion in free space

In this section we will consider the motion of a rocket in the absence of gravitational and aerodynamic forces. The equations of motion for this case are obtained from Eqs. (11.1-10) by setting $X_a = Z_a = M' = g_x = g_z = 0$. As we consider flight in vacuum the thrust is given by

$$F = mV_e + p_e A_e,$$

but we will use the more simple expression (Section 6.6)

$$F = mc = mg_0 I_{sp}, \quad (11.2-1)$$

where c and I_{sp} are effective exhaust velocity and specific impulse respectively, which are assumed to be constant, and g_0 stands for the standard surface gravity.

From inspection of the equation for rotational motion, Eq. (11.1-10e) with $M' = 0$, it will be clear that if initially $d\theta/dt = 0$, θ will remain constant during the flight. If we have a non-zero initial value of the pitch rate, the pitch angle will decrease, or increase monotonically. However, the rotational equation, Eq. (11.1-10e), is only valid for an uncontrolled rocket. As all rockets are stabilized and/or controlled during motor operation, a stabilizing or control moment has to be incorporated in the equation for rotational motion. For an aerodynamically stabilized, or controlled rocket flying through the atmosphere, the control moment is part of the total aerodynamic moment M' . For a mechanically stabilized and controlled vehicle, control moments are generated by thrust vector control, separate control rockets, control moment gyros, etc., and an additional term will appear in the equation for rotational motion. In general, the pitch angle-time history, *pitch-program*, of the rocket is specified and control moments will be

generated such that the required pitch-program is obtained. We will, therefore, assume in the following that the pitch-program is prescribed. We will start with the most simple pitch-program: *constant pitch angle*. If we assume moreover that the initial velocity of the rocket has the same direction as the thrust, the problem is purely one-dimensional. The rocket will travel along a straight line, making an angle θ_0 with the X-axis. The equations of motion for this case are

$$M \frac{dV}{dt} = F = mc, \quad (11.2-2a)$$

$$\frac{ds}{dt} = V, \quad (11.2-2b)$$

$$\frac{dM}{dt} = -m, \quad (11.2-2c)$$

where V is the velocity of the rocket and s is the distance travelled.

11.2.1 Tsiolkovsky's equation

The equation for the velocity in free space can be integrated directly. Combining Eqs. (11.2-2a) and (11.2-2c) leads to

$$\frac{dV}{dt} = -\frac{c}{M} \frac{dM}{dt}. \quad (11.2-3)$$

With the initial conditions

$$t = 0: \quad V = V_0, \quad M = M_0,$$

this equation can be integrated, yielding

$$\Delta V = V(t) - V_0 = c \ln \frac{M_0}{M(t)}. \quad (11.2-4)$$

This is *Tsiolkovsky's Equation* (1903), also called the *equation of Oberth*, for the velocity increment of a rocket in free space. Using the specific impulse instead of the effective exhaust velocity, this equation can also be written as

$$\Delta V = g_0 I_{sp} \ln \frac{M_0}{M}. \quad (11.2-5)$$

For a given rocket, ΔV is only a function of the instantaneous mass of the rocket. In order to determine ΔV (or V) as a function of time, it is necessary to know the mass as a function of time. The mass of the rocket follows from Eq. (11.2-2c)

$$M = M_0 - \int_0^t m dt. \quad (11.2-6)$$

So we see that mass and velocity, as a function of time are dependent on the mass flow-time history.

If the total useful propellant mass contained by the rocket is M_p , the mass at burnout (empty mass) is given by

$$M_e = M_0 - M_p. \quad (11.2-7)$$

The burning-time, t_b , is determined by

$$M_p = \int_0^{t_b} m \, dt. \quad (11.2-8)$$

We define the *mass ratio*, Λ , of the rocket as

$$\Lambda = \frac{M_0}{M_e}. \quad (11.2-9)$$

Then the velocity increment at burnout is given by

$$\Delta V_{id} = g_0 I_{sp} \ln \Lambda. \quad (11.2-10)$$

This velocity increment is called the *ideal velocity* of the rocket. It is only a function of specific impulse and mass ratio but is independent of the thrust-time history. Figure 11.2 gives ΔV_{id} as a function of Λ for various values of the specific impulse.

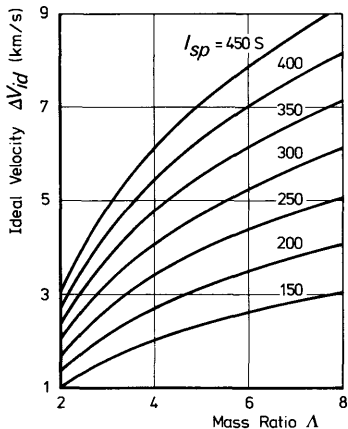


Fig. 11.2 The ideal velocity as a function of mass ratio and specific impulse

11.2.2 Rocket parameters

We have seen that the mass ratio of the rocket is a very important parameter in determining the ideal velocity of the rocket. Next to this mass ratio we can define other dimensionless quantities, which relate the rocket mass distribution and the rocket performance. We divide the initial mass of

the rocket, M_0 , into three parts: the *payload mass*, M_u , the *structural mass*, M_c , and the *useful propellant mass*, M_p . We then have

$$M_0 = M_u + M_c + M_p, \quad (11.2-11a)$$

$$M_e = M_u + M_c. \quad (11.2-11b)$$

The payload may be a satellite, a warhead, a scientific package, or, in some cases, a complete rocket vehicle. In this last case we speak of *multi-stage rockets*, which will be discussed in Chapter 12. The structural mass consists of the mass of the rocket structure, the mass of the auxiliary structure, such as pipes, cables, mountings and thermal insulation, the mass of the installed equipment, such as rocket motors, guidance and control systems, pressurizing systems and electrical and hydraulic power supply systems, and finally the mass of the unconsumed propellant. Note, that M_p is the mass of the useful propellant and not the total propellant mass. These two masses may differ owing to the fact that not all propellant is consumed in many cases. One of the most important causes for this is the extinction of the rocket motor when the vehicle has reached a prescribed velocity, while still propellant is left over. Other causes are the presence of residual propellant in the feed lines and turbopumps, and sometimes in the tanks because of imperfect mixture control. In a solid-propellant rocket there may be unconsumed propellant due to slivers (Section 9.3).

We now define the following parameters:

$$\text{payload ratio} \quad \lambda = \frac{M_u}{M_0}, \quad (11.2-12a)$$

$$\text{structural efficiency} \quad \varepsilon = \frac{M_c}{M_c + M_p}, \quad (11.2-12b)$$

$$\text{propellant ratio} \quad \varphi = \frac{M_p}{M_0}. \quad (11.2-12c)$$

Although these parameters, together with the mass ratio Λ , are used most commonly and will be used throughout this book, many other parameters, often with the same name, are in use [1, 2, 3, 4].

The mass ratio, Λ , is always larger than one, while payload ratio, λ , structural efficiency, ε , and propellant ratio, φ , are less than one. In general, the range of these parameters for single-stage rockets is:

$$2 < \Lambda < 10, \quad 0.08 < \varepsilon < 0.5, \quad 0.5 < \varphi < 0.9, \quad 0.01 < \lambda < 0.2.$$

It can be checked easily that the various parameters are related by

$$\varphi = (1 - \varepsilon)(1 - \lambda), \quad (11.2-13a)$$

$$\Lambda = \frac{1}{1 - \varphi} = \frac{1}{\varepsilon(1 - \lambda) + \lambda}. \quad (11.2-13b)$$

Figure 11.3 gives the mass ratio as a function of the payload ratio for various values of the structural efficiency.

Substitution of Eq. (11.2-13b) into Eq. (11.2-10) gives the ideal velocity as a function of λ and ε ,

$$\Delta V_{id} = -g_0 I_{sp} \ln \{\varepsilon(1-\lambda) + \lambda\}. \quad (11.2-14)$$

In Fig. 11.4 the dimensionless ideal velocity $V_{id}/g_0 I_{sp}$ is given as a function of λ and ε . If λ and ε increase the ideal velocity decreases. For a fixed structural efficiency the ideal velocity attains its maximum for $\lambda = 0$, i.e. no payload. In that case

$$(\Delta V_{id})_{max} = -g_0 I_{sp} \ln \varepsilon$$

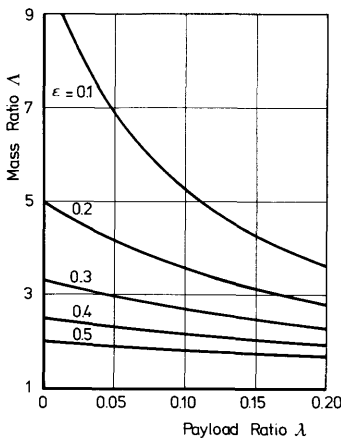


Fig. 11.3 The mass ratio as a function of payload ratio and structural efficiency

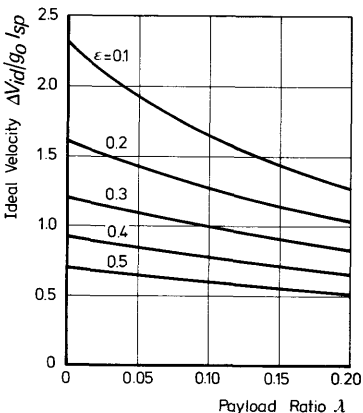


Fig. 11.4 The dimensionless ideal velocity as a function of payload ratio and structural efficiency

The structural efficiency, however, cannot be made arbitrarily small, as a minimum structural mass is necessary for housing the propellant and for a motor in which the combustion and expansion can take place. In general, $\varepsilon > 0.08$, which means that for every 92 kg propellant at least 8 kg structural mass is required. These low values of the structural efficiency can only be reached for large rockets, for which the mass of the motor is small relative to the mass of the tanks. For small rockets ε lies between 0.2 and 0.5.

For a given mission, the ideal velocity is known and the required propellant ratio is determined by

$$\varphi = 1 - \frac{1}{\Lambda} = 1 - \exp \left(-\frac{\Delta V_{id}}{g_0 I_{sp}} \right). \quad (11.2-15)$$

This relation is depicted in Fig. 11.5. If the structural efficiency is known too, the payload ratio follows from

$$\lambda = \frac{\exp(-\Delta V_{id}/g_0 I_{sp}) - \varepsilon}{1 - \varepsilon}. \quad (11.2-16)$$

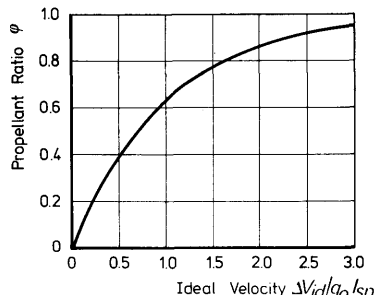


Fig. 11.5 The dependence of the propellant ratio on the dimensionless ideal velocity

Apart from the mass parameters, two other rocket parameters are frequently used. They relate thrust and mass,

$$\text{the specific thrust } \beta = \frac{F}{g_0 M}, \quad (11.2-17)$$

and in the case of a constant thrust

$$\text{the thrust-to-weight ratio } \psi_0 = \frac{F}{g_0 M_0}. \quad (11.2-18)$$

11.2.3 The burnout range

The distance covered at time t is given by

$$\Delta s = s - s_0 = \int_0^t V dt. \quad (11.2-19)$$

In order to evaluate the integral in Eq. (11.2-19) we have to know V as a function of time, which means that the propellant consumption as a function of time, $m = m(t)$, has to be known. In the following we will derive expressions for the range for two different propellant consumption histories. The first one yields a constant thrust and the second one a constant specific thrust.

Constant thrust. In this case the propellant consumption is

$$m = m_0 = \text{constant}; \quad 0 \leq t \leq t_b,$$

$$m = 0; \quad t > t_b.$$

Consequently, the instantaneous mass of the rocket during thrusting is

$$M = M_0 - m_0 t. \quad (11.2-20)$$

The burning-time, t_b , follows from

$$M_e = M_0 - m_0 t_b,$$

which yields, after solving for t_b and using Eqs. (11.2-18) and (11.2-9),

$$t_b = \frac{I_{sp}}{\psi_0} \left(1 - \frac{1}{\Lambda} \right). \quad (11.2-21)$$

We see that for fixed ψ_0 the burning-time increases with increasing specific impulse, and increasing mass ratio. The burning-time decreases if ψ_0 increases, and $t_b \rightarrow 0$ if $\psi_0 \rightarrow \infty$. In that case all propellant is consumed instantaneously. This is called an *impulsive shot*. If $\Lambda \rightarrow \infty$, meaning that the whole rocket consists of propellant, $t_b \rightarrow I_{sp}/\psi_0$. It thus follows that the specific impulse is the burning-time of a rocket consisting solely of propellant with a constant thrust equal to the initial weight of the propellant (Section 6.2).

The velocity as a function of time is given by (for zero initial velocity)

$$V = g_0 I_{sp} \ln \frac{M_0}{M_0 - m_0 t}. \quad (11.2-22)$$

Substitution of this last expression into Eq. (11.2-19) and evaluation of the integral leads to

$$\Delta s = \frac{g_0 I_{sp} M_0}{m_0} \left[\frac{M_0 - m_0 t}{M_0} \left\{ \ln \frac{M_0 - m_0 t}{M_0} - 1 \right\} \right]_0^t.$$

Introducing the *range function*, $p(t)$, defined as

$$p(t) = 1 - \frac{M_0 - m_0 t}{M_0} \left\{ \ln \frac{M_0}{M_0 - m_0 t} + 1 \right\}, \quad (11.2-23)$$

and using Eq. (11.2-18), the range can be written as

$$\Delta s(t) = \frac{g_0 I_{sp}^2}{\psi_0} p(t). \quad (11.2-24)$$

The burnout range, i.e. the distance covered at $t = t_b$, then is

$$\Delta s_b = \frac{g_0 I_{sp}^2}{\psi_0} p_b, \quad (11.2-25)$$

where

$$p_b = p(t_b) = 1 - \frac{1}{\Lambda} (\ln \Lambda + 1). \quad (11.2-26)$$

Figure 11.6 gives the dimensionless burnout range, $\Delta s_b / g_0 I_{sp}^2$, as a function of Λ and also depicts the range as a function of the instantaneous mass ratio $M_0 / (M_0 - m_0 t)$.

We see that the burnout range is proportional to the square of the specific impulse and inversely proportional to the thrust-to-weight ratio. For an impulsive shot: $\Delta s_b = 0$ (the total velocity increment is given instantaneously). If $\Lambda \rightarrow \infty$ the function p_b approaches unity and, consequently,

$$\Delta s_b \rightarrow g_0 I_{sp}^2 / \psi_0.$$

After burnout the velocity remains constant and Δs increases linearly with time.

The *dimensionless acceleration*, defined as

$$n = \frac{1}{g_0} \frac{dV}{dt}, \quad (11.2-27)$$

equals the specific thrust and is increasing monotonically from ψ_0 to $\Lambda \psi_0$ at burnout.

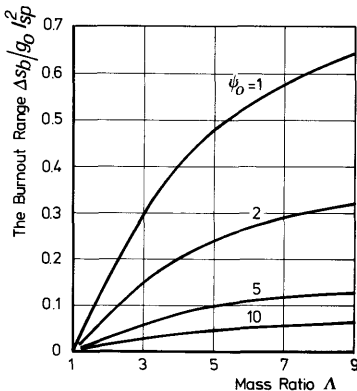


Fig. 11.6 The dimensionless burnout range in free space

Constant specific thrust. In this case

$$\beta = \frac{F}{g_0 M} = \beta_0 = \text{constant.} \quad (11.2-28)$$

The instantaneous mass of the rocket is obtained by integration of Eq. (11.2-28), leading to

$$\ln \frac{M_0}{M} = \frac{\beta_0}{I_{sp}} t. \quad (11.2-29)$$

So

$$M = M_0 \exp\left(-\frac{\beta_0}{I_{sp}} t\right). \quad (11.2-30)$$

By differentiation of Eq. (11.2-30), the propellant consumption as a function of time is found to be

$$m = \frac{M_0 \beta_0}{I_{sp}} \exp\left(-\frac{\beta_0}{I_{sp}} t\right), \quad (11.2-31)$$

and the burning-time follows from Eq. (11.2-29)

$$t_b = \frac{I_{sp}}{\beta_0} \ln \Lambda. \quad (11.2-32)$$

In this case too, the specific impulse can be interpreted as a burning-time, namely the burning-time of a rocket with mass ratio $\Lambda = e$ and a constant specific thrust of unity. As the acceleration is constant and equal to $g_0 \beta_0$, velocity and range are given by

$$V = g_0 \beta_0 t, \quad (11.2-33)$$

$$\Delta s = \frac{1}{2} g_0 \beta_0 t^2, \quad (11.2-34)$$

and thus at burnout

$$V_b = g_0 \beta_0 t_b = g_0 I_{sp} \ln \Lambda, \quad (11.2-35)$$

$$\Delta s_b = \frac{1}{2} g_0 \beta_0 t_b^2 = \frac{1}{2} g_0 \frac{I_{sp}^2}{\beta_0} \ln^2 \Lambda. \quad (11.2-36)$$

It can be verified easily that, in the case of constant specific thrust, burning-time and burnout range are larger than the corresponding quantities in the case of constant thrust with the same initial specific thrust. The burnout velocity, of course, is the same in both cases.

It follows from Eq. (11.2-31) that the mass flow is continuously decreasing from m_0 at ignition to m_0/Λ at burnout. As, for a fixed nozzle geometry, the chamber pressure is proportional to the mass flow, this pressure will have to decrease too during powered flight. As the strength of the combustion

chamber is determined by maximum chamber pressure, the combustion chamber will be oversized during the flight. In the case of constant thrust, the mass flow and so the chamber pressure are constant. From the viewpoint of combustion chamber weight this is optimal, and is encountered very much in practice, in contrast with the case of constant specific thrust. We have treated the case of constant specific thrust because for a rocket flying through the atmosphere there is an aerodynamic force, the drag, acting opposite to the thrust. We can define an *effective thrust*, equal to the actual thrust minus the drag. In the case of a constant actual thrust the velocity will increase and consequently the drag increases too. So the effective thrust is decreasing. However, the mass of the rocket will decrease too. For preliminary trajectory calculations the trajectory can be subdivided into portions along which the ratio of effective thrust and instantaneous weight (the effective specific thrust) can be assumed constant.

11.3 Rocket motion in a homogeneous gravitational field

In a homogeneous gravitational field the field strength, g , is constant. If we consider the Earth locally as being flat, the local gravitational field may be considered homogeneous. Actually, the Earth is nearly spherical and its gravitational field can be approximated very well by a central inverse square field (Section 18.6). However, as long as the altitude and range are small relative to the mean Earth's radius, the Earth may be considered flat and the field strength can be approximated very well by a constant. For small rockets, such as sounding rockets and tactical missiles this approximation yields good results. For launch vehicles and intercontinental ballistic missiles (ICBM's), the powered flight trajectory of the first stages can, in general, also be calculated by good approximation with the flat Earth assumption. For the upper stages, however, the velocity will be so large that the flat Earth approximation will lead to unacceptable deviations from the real trajectory. However, as most part of this trajectory is a coast phase, the trajectory can be approximated by a ballistic one and can be determined analytically in the case of a spherical Earth (Chapter 13).

If we choose the X -axis of the inertial system to coincide with the flat Earth surface and the Z -axis vertical, then $g_x = 0$ and $g_z = -g_0$, where it is assumed that motion takes place near the surface of the Earth. Then the equations of translational motion become

$$M \frac{dV_x}{dt} = F \cos \theta, \quad (11.3-1a)$$

$$M \frac{dV_z}{dt} = F \sin \theta - Mg_0, \quad (11.3-1b)$$

$$\frac{dX}{dt} = V_x, \quad (11.3-1c)$$

$$\frac{dZ}{dt} = V_Z, \quad (11.3-1d)$$

$$\frac{dM}{dt} = -m. \quad (11.3-1e)$$

As in the foregoing, the thrust is given by

$$F = mc = mg_0 I_{sp}. \quad (11.3-1f)$$

We will assume that the pitch program, $\theta = \theta(t)$, is known.

11.3.1 Vertical flight

If during the whole flight $\theta = 90^\circ$, and if we have zero initial horizontal velocity, the trajectory will be a straight line parallel to the Z -axis. In that case V_Z equals the total velocity V , and the equations of motion simplify to

$$\frac{dV}{dt} = -g_0 \left[\frac{I_{sp}}{M} \frac{dM}{dt} + 1 \right], \quad (11.3-2a)$$

$$\frac{dh}{dt} = \frac{dZ}{dt} = V. \quad (11.3-2b)$$

As initial conditions we will choose a zero velocity and altitude at $t = 0$. Equation (11.3-2a) can be integrated independently of the mass flow program, leading to

$$V = g_0 \left[I_{sp} \ln \frac{M_0}{M} - t \right]. \quad (11.3-3)$$

We see that, in order to determine V as a function of time, knowledge of the mass flow history is necessary. Even the burnout velocity in this case is dependent on the thrust program because the burning-time depends on it. Again we will assume a constant thrust, in which case the mass flow is given by

$$m = m_0; \quad 0 \leq t \leq t_b,$$

$$m = 0; \quad t > t_b.$$

For this case, the burning-time is already derived in Section 11.2.3 and is given by Eq. (11.2-21). Then we find for the velocity as a function of time

$$V = g_0 \left[I_{sp} \ln \frac{M_0}{M_0 - m_0 t} - t \right]; \quad 0 \leq t \leq t_b, \quad (11.3-4a)$$

$$V_b = g_0 I_{sp} \left[\ln \Lambda - \frac{1}{\psi_0} \left(1 - \frac{1}{\Lambda} \right) \right]; \quad t = t_b, \quad (11.3-4b)$$

$$V = g_0 [I_{sp} \ln \Lambda - t]; \quad t \geq t_b, \quad (11.3-4c)$$

According to Eq. (11.2-10) we can also write for $t \geq t_b$

$$V = \Delta V_{id} - g_0 t. \quad (11.3-5)$$

The dimensionless velocity at burnout, $V_b/g_0 I_{sp}$, is depicted in Fig. 11.7 as a function of ψ_0 for various values of Λ . The burnout velocity attains a maximum for an impulsive shot. In that case, the *gravity loss*, i.e. $g_0 t_b$, is zero and the burnout velocity equals the ideal velocity.

Maximum altitude is reached at $V=0$. For $\psi_0 \geq 1$ this will always occur for $t > t_b$ and we find for the *culmination time*

$$t_c = I_{sp} \ln \Lambda. \quad (11.3-6)$$

The culmination time does not depend on ψ_0 . In fact, it does not depend on the thrust-time history, for the velocity after burnout as given by Eq. (11.3-4c) is independent of the thrust program.

Integration of V with respect to time yields the altitude as a function of time. Using the range function p as defined in Section 11.2.3., Eqs. (11.2-23) and (11.2-26), the altitude is given by

$$h = \frac{g_0 I_{sp}^2}{\psi_0} p(t) - \frac{1}{2} g_0 t^2; \quad t \leq t_b, \quad (11.3-7a)$$

$$h_b = \frac{g_0 I_{sp}^2}{\psi_0} \left[p_b - \frac{1}{2\psi_0} \left(1 - \frac{1}{\Lambda} \right)^2 \right]; \quad t = t_b, \quad (11.3-7b)$$

$$h = h_b + V_b(t - t_b) - \frac{1}{2} g_0(t - t_b)^2; \quad t \geq t_b, \quad (11.3-7c)$$

$$h_c = \frac{g_0 I_{sp}^2}{\psi_0} \left[\frac{1}{2} \psi_0 \ln^2 \Lambda - \ln \Lambda - \frac{1}{\Lambda} + 1 \right]; \quad t = t_c. \quad (11.3-7d)$$

Figure 11.8 gives the burnout altitude and the culmination altitude in

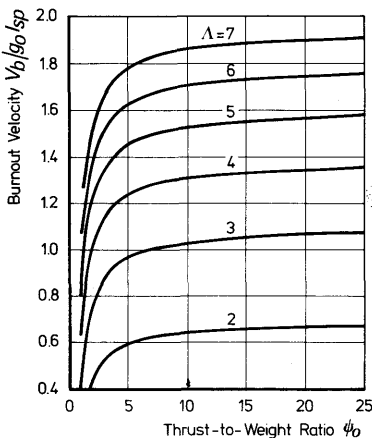


Fig. 11.7 The dimensionless burnout velocity for vertical ascent in a homogeneous gravitational field and in vacuum

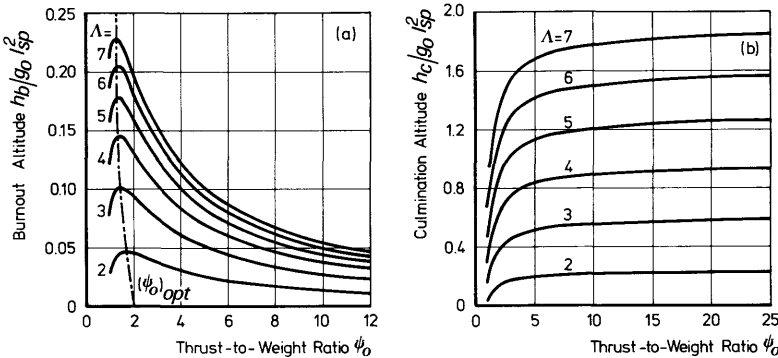


Fig. 11.8 The burnout and culmination altitudes for vertical ascent in a homogeneous gravitational field and in vacuum

dimensionless form as a function of ψ_0 for various values of Λ . From Eqs. (11.3-7) we conclude that, like the burnout range in free space, burnout altitude and culmination altitude are proportional to the square of the specific impulse.

It follows from Fig. 11.8a that there is an optimal thrust-to-weight ratio, yielding a maximum value of the burnout altitude. The optimal value of ψ_0 is found by differentiating the expression for h_b with respect to ψ_0 and setting the result equal to zero. Apart from the solution $\psi_0 \rightarrow \infty$, which yields a minimum burnout altitude, this leads to

$$(\psi_0)_{opt} = \frac{(1 - 1/\Lambda)^2}{p_b} < 2.$$

The corresponding value of the burnout altitude then is

$$(h_b)_{max} = \frac{g_0 I_{sp}^2}{2} \frac{p_b^2}{(1 - 1/\Lambda)^2}.$$

From inspection of Fig. 11.8b, or Eq. (11.3-7d), we conclude that the culmination altitude increases with increasing thrust-to-weight ratio and reaches a maximum for an impulsive shot:

$$(h_c)_{max} = \frac{1}{2} g_0 I_{sp}^2 \ln^2 \Lambda.$$

We have seen that both burnout velocity and culmination height increase with increasing ψ_0 . The reason for this is that both quantities are a measure for the energy that is transferred to the rocket vehicle structure and payload. Part of the available energy, however, is transferred to the propellant in the form of potential and kinetic energy of the propellant and this energy cannot be regained. By consuming the propellant as quick as possible, i.e. approaching an impulsive shot, the total amount of energy lost in this way is kept to a minimum. Thus, for high performances it is favorable to consume

the propellant as fast as possible. Note, however, that this is only true in vacuum. For an ascent through the atmosphere a large thrust-to-weight ratio causes a large acceleration and consequently a high velocity in the denser part of the atmosphere. This results in a large drag. In that case there will be a finite optimal thrust-to-weight ratio (Chapter 14).

11.3.2 Constant pitch angle

After having considered a special case with constant pitch angle ($\theta = 90^\circ$), we will now consider the more general case. The equations of motion are the Eqs. (11.3-1) with $\theta = \theta_0$. For simplicity, we assume that start takes place at $t = 0$, in the origin of the inertial frame, with zero initial velocity. The equations for the velocity components can be integrated directly, yielding

$$V_x = g_0 I_{sp} \ln \frac{M_0}{M} \cos \theta_0, \quad (11.3-8a)$$

$$V_z = g_0 I_{sp} \ln \frac{M_0}{M} \sin \theta_0 - g_0 t. \quad (11.3-8b)$$

With the use of Eq. (11.2-10) we can write for the burnout velocity,

$$V_b = \Delta V_{id} \sqrt{1 - 2 \frac{t_b \sin \theta_0}{I_{sp} \ln \Lambda} + \frac{t_b^2}{I_{sp}^2 \ln^2 \Lambda}}. \quad (11.3-9)$$

We see that gravity losses increase with increasing pitch angle, θ_0 , and increasing burning-time, t_b .

The flight path angle, being the angle between the velocity vector and the X -axis, and positive if V_z is positive, follows from

$$\tan \gamma = \frac{V_z}{V_x} = \tan \theta_0 - \frac{t}{I_{sp} \ln \frac{M_0}{M} \cos \theta_0}. \quad (11.3-10)$$

The *angle of attack*, i.e. the angle between the longitudinal axis of the rocket and the velocity vector, is given by

$$\alpha = \theta - \gamma.$$

By using Eq. (11.3-10) it can be derived that

$$\tan \alpha = \frac{t \cos \theta_0}{I_{sp} \ln \frac{M_0}{M} - t \sin \theta_0}. \quad (11.3-11)$$

We see that, in general, flight path angle and angle of attack will not be constant and the trajectory will be curved. Only in the case that $\ln M_0/M$ is proportional to t the flight path angle and the angle of attack are constant and the resulting trajectory will be a straight line. According to Eq. (11.2-29) this is the case for a constant specific thrust.

In the following we will again consider a constant thrust. Then the velocity components, the flight path angle and the angle of attack follow as a function of time by substitution of

$$M = M_0 - m_0 t; \quad 0 \leq t \leq t_b,$$

$$M = M_e; \quad t > t_b,$$

into Eqs. (11.3-8) to (11.3-11). We then find that during powered flight γ increases and the trajectory is curved upwards. By taking the limit for $t \rightarrow 0$ of Eq. (11.3-10) it follows that

$$\tan \gamma_0 = \tan \theta_0 - \frac{1}{\psi_0 \cos \theta_0}. \quad (11.3-12)$$

Consequently, the angle of attack decreases during powered flight. Its initial value is given by

$$\tan \alpha_0 = \frac{\cos \theta_0}{\psi_0 - \sin \theta_0} \quad (11.3-13)$$

In Fig. 11.9 the angle of attack is given as a function of the instantaneous mass ratio M_0/M for $0 \leq t \leq t_b$.

After burnout, γ decreases and α increases. Then the trajectory is curved downwards. Culmination altitude is reached if $\gamma = 0$, or equivalently if $V_Z = 0$, leading to

$$t_c = I_{sp} \ln \Lambda \sin \theta_0. \quad (11.3-14)$$

Again the culmination time is independent of the thrust program.

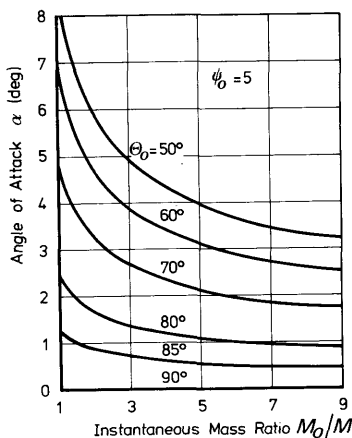


Fig. 11.9 The angle of attack for flights with constant pitch angle and constant thrust in a homogeneous gravitational field and in vacuum

Integration of the velocity components with respect to time yields the position of the vehicle. During powered flight, the coordinates are determined by

$$X = \frac{g_0 I_{sp}^2}{\psi_0} p(t) \cos \theta_0, \quad (11.3-15a)$$

$$Z = \frac{g_0 I_{sp}^2}{\psi_0} p(t) \sin \theta_0 - \frac{1}{2} g_0 t^2. \quad (11.3-15b)$$

The position at burnout is given by

$$X_b = \frac{g_0 I_{sp}^2}{\psi_0} p_b \cos \theta_0, \quad (11.3-16a)$$

$$Z_b = \frac{g_0 I_{sp}^2}{\psi_0} \left[p_b \sin \theta_0 - \frac{1}{2} \psi_0 \left(1 - \frac{1}{\Lambda} \right)^2 \right]. \quad (11.3-16b)$$

After burnout the position follows from

$$X = X_b + V_{X_b} (t - t_b), \quad (11.3-17a)$$

$$Z = Z_b + V_{Z_b} (t - t_b) - \frac{1}{2} g_0 (t - t_b)^2. \quad (11.3-17b)$$

The coordinates of the culmination point, finally, are obtained by substitution of $t = t_c$ in Eqs. (11.3-17):

$$X_c = \frac{g_0 I_{sp}^2}{\psi_0} \left[1 + \psi_0 \ln^2 \Lambda \sin \theta_0 - \frac{1}{\Lambda} - \ln \Lambda \right] \cos \theta_0, \quad (11.3-18a)$$

$$Z_c = \frac{g_0 I_{sp}^2}{\psi_0} \left[1 + \frac{1}{2} \psi_0 \ln^2 \Lambda \sin \theta_0 - \frac{1}{\Lambda} - \ln \Lambda \right] \sin \theta_0. \quad (11.3-18b)$$

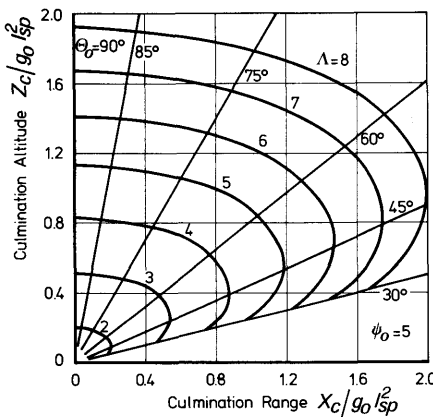


Fig. 11.10 The coordinates of the culmination point for flights with constant pitch angle and constant thrust in a homogeneous gravitational field and in vacuum

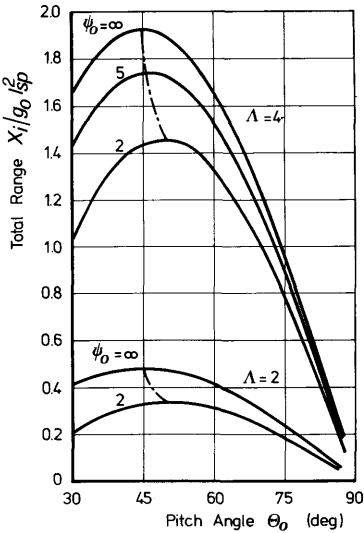


Fig. 11.11 The dimensionless range for flights with constant pitch angle and constant thrust in a homogeneous gravitational field and in vacuum.

Figure 11.10 gives the dimensionless coordinates of the culmination point for various values of mass ratio and pitch angle. From this figure we see that for pitch angles close to 90° a small variation in pitch angle results in a relatively large change in X_c while the culmination height Z_c hardly changes. For pitch angles close to 45° it is just the other way round.

The *impact point*, and therefore the total range, can be found by putting $Z=0$ into Eq. (11.3-17b) and then solving this equation for t . This gives the time of impact, t_i . Substitution of t_i into Eq. (11.3-17a) yields the X -coordinate of the impact point, X_i . In Fig. 11.11 the range is given as a function of pitch angle and thrust-to-weight ratio.

For an impulsive shot, i.e. for $\psi_0 \rightarrow \infty$, we get a ballistic trajectory with initial velocity

$$V_b = g_0 I_{sp} \ln \Lambda, \quad (11.3-19)$$

making an angle θ_0 with the horizontal. In that case the trajectory is a parabola, given by the equations

$$X = g_0 I_{sp} \ln \Lambda \cos \theta_0 t, \quad (11.3-20a)$$

$$Z = g_0 I_{sp} \ln \Lambda \sin \theta_0 t - \frac{1}{2} g_0 t^2, \quad (11.3-20b)$$

or by eliminating t ,

$$Z = X \tan \theta_0 \left[1 - \frac{X}{g_0 I_{sp}^2 \ln^2 \Lambda \sin 2\theta_0} \right]. \quad (11.3-21)$$

The impact point is found by putting $Z = 0$; this yields, apart from $X = 0$, which is the launching point,

$$X_i = g_0 I_{sp}^2 \ln^2 \Lambda \sin 2\theta_0 \quad (11.3-22)$$

From this we see the well-known result, that for an impulsive shot the range is a maximum if $\theta_0 = 45^\circ$. From Fig. 11.11 we see that for finite thrust too the optimum pitch angle for maximum range lies close to 45° .

In this section we have discussed flights with constant pitch angle. In vacuum this is a widely used steering program. The reasons for this are that such a steering program is relatively easy to realize, and that it is an optimal steering program, as will be explained now.

For a given mission the conditions at burnout are specified. Often, the values of flight path angle and burnout velocity are specified. For a given rocket, i.e. t_b , Λ and I_{sp} fixed, which is to have a specified flight path angle at burnout, the burnout velocity will be a function of the steering program. This velocity will be a maximum if the pitch angle is kept constant. The proof of this statement can be given with the help of the calculus of variations, which is a technique to determine optimal functions. In this case, a rather simple proof is possible using the $V_x - V_z$ hodograph plane. The curve in this plane, representing V_z as a function of V_x , is called the *hodograph* (Fig. 11.12). For an arbitrary steering program, the equations of motion can be written as

$$\frac{dV_z}{dV_x} = \tan \theta - g_0 \frac{dt}{dV_x}, \quad (11.3-23)$$

or, by integration

$$V_z(t) = \int_0^{V_x} \tan \theta dV_x - g_0 t. \quad (11.3-24)$$

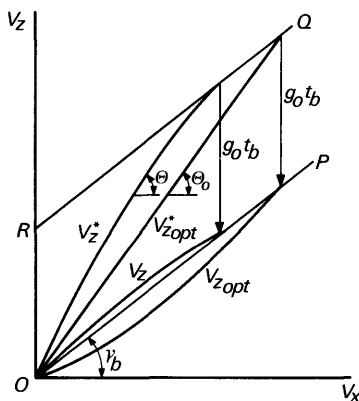


Fig. 11.12 The hodograph plane for flights over a flat Earth

Now define

$$V_Z^* = \int_0^{V_X} \tan \theta \, dV_X, \quad (11.3-25)$$

then, according to Eq. (11.3-24),

$$V_Z = V_Z^* - g_0 t. \quad (11.3-26)$$

As

$$\frac{dV_Z^*}{dV_X} = \tan \theta, \quad (11.3-27)$$

the slope of the line V_Z^* is just the pitch angle. Because at burnout the flight path angle is required to be γ_b , the burnout point of the hodograph must lie on the straight line OP , given by $V_{Z_b} = \tan \gamma_b V_{X_b}$. The burnout point of the curve V_Z^* then has to lie on the line RQ which is parallel to OP and given by

$$V_{Z_b}^* = \tan \gamma_b V_{X_b} + g_0 t_b.$$

The total length of the curve V_Z^* between $t = 0$ and $t = t_b$ is given by

$$s = \int_0^{t_b} \sqrt{1 + \left(\frac{dV_Z^*}{dV_X} \right)^2} dV_X = \int_0^{t_b} \frac{dV_X}{\cos \theta} = \int_0^{t_b} \frac{F}{M} dt = g_0 I_{sp} \ln \Lambda. \quad (11.3-28)$$

We see that s is independent of steering program and thrust-time history. As $V_b = V_{X_b}/\cos \gamma_b$, the burnout velocity is a maximum, for fixed γ_b , if V_{X_b} is a maximum. Consequently, for maximum burnout velocity, the burnout point of V_Z^* has to lie as far as possible to the right on the line RQ . As the length s of the curve V_Z^* is a constant, this is realized if, V_Z^* is represented by a straight line in the hodograph plane. Thus, for maximum burnout velocity the slope of V_Z^* and, consequently, the pitch angle has to be a constant. This result is independent of the thrust program.

11.3.3 Gravity turns

To reduce the aerodynamic forces on a rocket during its flight through the atmosphere, one will endeavor to keep the angle of attack as small as possible. For simple aerodynamically stabilized vehicles, this is accomplished by fixed fins. Vehicles that are mechanically stabilized use more or less complicated control systems to generate the moments necessary to keep the angle of attack as small as possible. This is of course not the case for aerodynamically controlled rockets, during maneuvering. For launch vehicles, ICBM's and uncontrolled aerodynamically stabilized rockets we can say that the flight through the atmosphere takes place with zero angle of attack. In that case there is no lift and the curvature of the trajectory is solely due to gravity, hence the name *gravity turn*, or *zero-lift trajectory*. In this section we will discuss some gravity turns in vacuum.

As the angle of attack is zero, the flight path angle equals the pitch angle:

$$\theta = \gamma = \arctan \frac{V_z}{V_x}. \quad (11.3-29)$$

Then the equations of motion become

$$M \frac{dV_x}{dt} = F \frac{V_x}{V}, \quad (11.3-30a)$$

$$M \frac{dV_z}{dt} = F \frac{V_z}{V} - Mg_0, \quad (11.3-30b)$$

where

$$V = \sqrt{V_x^2 + V_z^2}.$$

It is convenient in this case to use the total velocity, V , and the flight path angle, γ , as dependent variables, instead of V_x and V_z . Multiplication of Eq. (11.3-30a) by V_x , Eq. (11.3-30b) by V_z and summation yields

$$\frac{dV}{dt} = \frac{F}{M} - g_0 \sin \gamma. \quad (11.3-31)$$

The differential equation for γ is found by multiplication of Eq. (11.3-30a) by V_z , Eq. (11.3-30b) by V_x , and subsequently subtracting the results:

$$\frac{d\gamma}{dt} = - \frac{g_0}{V} \cos \gamma. \quad (11.3-32)$$

The equations for the gravity turn, in general, cannot be solved analytically. However, some special cases exist which allow for analytical solutions. These are *constant specific thrust* and *constant pitch rate*.

Constant specific thrust, $\beta = \beta_0$. In this case the equations of motion become

$$\frac{dV}{dt} = g_0 (\beta_0 - \sin \gamma), \quad (11.3-33a)$$

$$\frac{d\gamma}{dt} = - g_0 \frac{\cos \gamma}{V}. \quad (11.3-33b)$$

Elimination of t from Eqs. (11.3-33) leads to

$$\frac{dV}{V} = \left[\frac{\beta_0}{\cos \gamma} - \frac{\sin \gamma}{\cos \gamma} \right] d\gamma. \quad (11.3-34)$$

Integration of this equation yields

$$V \cos \gamma \left[\frac{1 + \sin \gamma}{1 - \sin \gamma} \right]^{\beta_0/2} = \text{constant}. \quad (11.3-35)$$

We now define a *velocity factor*, Γ

$$\Gamma = \frac{1}{\cos \gamma} \left[\frac{1 - \sin \gamma}{1 + \sin \gamma} \right]^{\beta_0/2}. \quad (11.3-36)$$

If V_0 and γ_0 are initial velocity and initial flight path angle respectively, then Eq. (11.3-35) in combination with Eq. (11.3-36), can be written as

$$\frac{\Gamma_0}{V_0} V = \Gamma. \quad (11.3-37)$$

The function Γ is given in Fig. 11.13a as function of γ for various values of β_0 . If the initial conditions V_0 and γ_0 are known, Eq. (11.3-37) gives V as a function of γ .

We cannot start the integration of the differential equations from initial conditions $V_0 = 0$ and $\gamma_0 = 90^\circ$ because for these conditions Eq. (11.3-37) is singular. All vehicles, following gravity turn trajectories directly after launch, are launched vertically and follow a vertical trajectory for a short period of time: *the vertical rise time* t_v . After the vertical rise there is a very short period of pitch-over after which the gravity turn starts. The pitch-over is necessary because if $\gamma_0 = 90^\circ$ and $V_0 \neq 0$, Eq. (11.3-37) can only be satisfied for $\gamma = 90^\circ$ and we get a vertical ascent. In preliminary trajectory calculations the pitch-over period is represented mathematically by an instantaneous rotation of both vehicle and velocity vector over an angle δ_0 , called the *kick angle*. The flight path angle then is

$$\gamma_0 = \frac{\pi}{2} - \delta_0.$$

The relation between time and flight path angle follows from Eq. (11.3-33b) when it is written as

$$dt = -\frac{V}{g_0 \cos \gamma} \frac{d\gamma}{.} \quad (11.3-38)$$

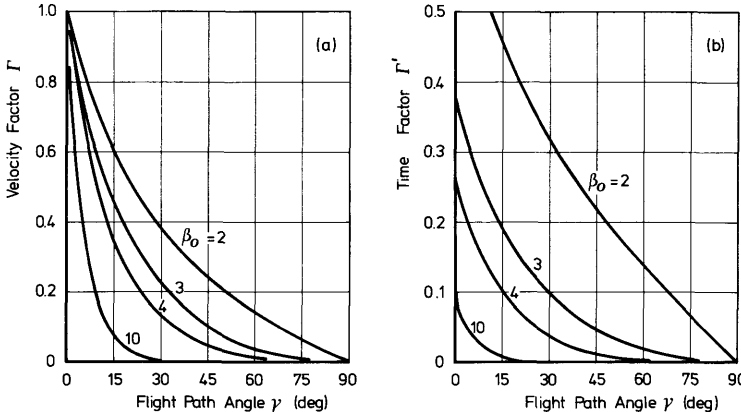


Fig. 11.13 The velocity factor and the time factor for the gravity turn with constant specific thrust in a homogeneous gravitational field

258 Rocket Propulsion & Spaceflight Dynamics

Substitution of $V = V(\gamma, \gamma_0, V_0)$ from Eq. (11.3-37) into Eq. (11.3-38) and changing to the variable q , defined as

$$q = \tan\left(\frac{\pi}{4} - \frac{\gamma}{2}\right), \quad (11.3-39)$$

simplifies integration of Eq. (11.3-38), which finally leads to

$$t - t_0 = \frac{1}{g_0(\beta_0^2 - 1)} [V(\beta_0 + \sin \gamma) - V_0(\beta_0 + \sin \gamma_0)]. \quad (11.3-40)$$

By introduction of a *time factor*, Γ' , defined as

$$\Gamma' = \frac{\beta_0 + \sin \gamma}{\beta_0^2 - 1} \Gamma, \quad (11.3-41)$$

Eq. (11.3-40) can be written as

$$\frac{g_0 \Gamma_0}{V_0} (t - t_0) = \Gamma' - \Gamma'_0 \quad (11.3-42)$$

The time factor Γ' is depicted in Fig. 11.13b as a function of γ .

For a rocket with β_0 , t_b and the initial conditions t_0 , V_0 and γ_0 known, the burnout conditions can be determined as follows. The values of Γ_0 and Γ'_0 follow from Fig. 11.13. Then the time factor at burnout, Γ'_b is determined by Eq. (11.3-42) and the flight path angle at burnout follows from Fig. 11.13b. The velocity factor at burnout, Γ_b , is determined with Fig. 11.13a, and Eq. (11.3-37) finally yields the burnout velocity. If the burnout conditions are specified, the initial conditions can be found using the described procedure the other way round.

As, in general, both V_0 and δ_0 are very small one can start with initial conditions $V_0 = 0$ and $\gamma_0 = 90^\circ$. In that case Γ_0/V_0 is undetermined. If, however, one of the burnout conditions is specified, for example the flight path angle γ_b , we can determine the other burnout condition, V_b , in this case, in the following way: for $\gamma_0 = 90^\circ$, $\Gamma'_0 = 0$ and as γ_b is known, Γ'_b is determined from Fig. 11.13b. From Eq. (11.3-42) the ratio Γ_0/V_0 is determined and V_b can be calculated with Eq. (11.3-37).

The coordinates X and Z follow from

$$X = - \int_{t_0}^t \frac{V^2}{g_0} d\gamma + X_0, \quad (11.3-43a)$$

$$Z = - \int_{t_0}^t \frac{V^2}{g_0} \frac{\sin \gamma}{\cos \gamma} d\gamma + Z_0. \quad (11.3-43b)$$

Again using the variable q defined in Eq. (11.3-39) we can derive

$$\frac{X - X_0}{V_0^2} \frac{\Gamma_0^2}{g_0} \frac{1}{4\beta_0^2 - 1} [\Gamma^2 \cos \gamma (2\beta_0 + \sin \gamma) - \Gamma_0^2 \cos \gamma_0 (2\beta_0 + \sin \gamma_0)], \quad (11.3-44a)$$

$$\frac{Z - Z_0}{V_0^2} \frac{\Gamma_0^2}{g_0} = \frac{1}{2(\beta_0^2 - 1)} [\Gamma^2 (\beta_0 \sin \gamma + 1 - \frac{1}{2} \cos^2 \gamma) - \Gamma_0^2 (\beta_0 \sin \gamma_0 + 1 - \frac{1}{2} \cos^2 \gamma_0)]. \quad (11.3-44b)$$

As mentioned before, for a flight through the atmosphere, the effective specific thrust can in some cases very well be approximated by a constant. In those cases the above discussed method will lead to rapid results.

Miele [5] gives analytical solutions for the gravity turn for constant specific thrust but uses different end conditions, namely the conditions $V = V_2$ at $\gamma = 0$. Then V_2 is the velocity that the rocket should have if the flight were continued until the trajectory had become horizontal.

In the case of a constant thrust, the equations for the gravity turn can only be solved numerically. Here the same difficulty, due to the singularity for vertical start with zero initial velocity, occurs. Both Seifert [2] and Culler and Fried [6] eliminate these singularities in an elegant way. Typical plots for gravity turn trajectories are given by White [7].

Constant pitch rate, $q = q_0$. Finally we should mention that a simple analytical solution for the gravity turn is possible in the case of a constant pitch rate. In that case

$$\frac{d\theta}{dt} = \frac{d\gamma}{dt} = -q_0 \quad (11.3-45)$$

and the equations of motion become

$$\frac{g_0 \cos \gamma}{V} = q_0 \quad (11.3-46)$$

$$\frac{dV}{dt} = \frac{F}{M} - g_0 \sin \gamma. \quad (11.3-47)$$

Differentiation of Eq. (11.3-46) yields

$$\frac{d}{dt} \left(\frac{\cos \gamma}{V} \right) = \frac{\cos \gamma}{V^2} \left(g_0 \sin \gamma - \frac{dV}{dt} \right) = 0. \quad (11.3-48)$$

Equation (11.3-48) can only be satisfied either if $\cos \gamma \equiv 0$, which means that we have a vertical ascent with zero pitch rate, or if

$$\frac{dV}{dt} = g_0 \sin \gamma. \quad (11.3-49)$$

By combining Eq. (11.3-47) and Eq. (11.3-49) we see that the specific thrust is determined by

$$\frac{F}{g_0 M} = 2 \sin \gamma. \quad (11.3-50)$$

As according to Eq. (11.3-45)

$$\gamma = \gamma_0 - q_0 (t - t_0), \quad (11.3-51)$$

Eq. (11.3-50) can be integrated, leading to

$$\ln \frac{M}{M_0} = \frac{2}{q_0 I_{sp}} (\cos \gamma_0 - \cos \gamma). \quad (11.3-52)$$

Thus, at burnout

$$\cos \gamma_b = \cos \gamma_0 + \frac{q_0 I_{sp}}{2} \ln \Lambda, \quad (11.3-53)$$

which determines γ_b . The burning-time follows from

$$t_b - t_0 = \frac{\gamma_0 - \gamma_b}{q_0}. \quad (11.3-54)$$

Substitution of Eq. (11.3-51) into Eq. (11.3-49) and integration of the resulting equation yields the velocity as a function of γ :

$$V = V_0 + \frac{g_0}{q_0} (\cos \gamma - \cos \gamma_0). \quad (11.3-55)$$

By using Eq. (11.3-52) one finds

$$V_b = V_0 + \frac{1}{2} g_0 I_{sp} \ln \Lambda, \quad (11.3-56)$$

or

$$\Delta V_b = \frac{1}{2} \Delta V_{id}. \quad (11.3-57)$$

So in this case gravity losses amount to 50% of the ideal velocity. This is a consequence of the low thrust ($\beta < 2$), and the resulting large burning-time. The trajectory is obtained by integrating

$$\frac{dX}{dt} = V \cos \gamma, \quad (11.3-58a)$$

$$\frac{dZ}{dt} = V \sin \gamma. \quad (11.3-58b)$$

These equations can also be integrated analytically. This will be left to the reader.

The methods discussed in this chapter can be used for a rough determination of the trajectory of a launch vehicle or ICBM until burnout of the first

stage(s). In most cases such a trajectory is composed of the following sub-arcs:

1. Vertical rise.
2. Pitch-over maneuver (mathematically represented by kick-angle).
3. Gravity turn to reduce aerodynamic forces in the lower part of the atmosphere
4. Flight with constant pitch angle to reach a maximum burnout velocity, or flight with constant pitch rate. However, other pitch programs are used too.

As all of these vehicles are multi-stage rockets, the next chapter will be devoted to the theory of the multi-stage rocket.

References

- 1 Vertregt, M. (1965), *Principles of Astronautics*, Elsevier, Amsterdam, p. 29.
- 2 Seifert, H. S. (1959), *Space Technology*, John Wiley, New York, p. 3–09, 4–10.
- 3 Williams, M. L. (1957), The calculation of fuel distribution in step-rockets, *J. Brit. Interplanet. Soc.*, **16**, No 4, 211–215.
- 4 Fraeijs de Veubeke, B. (1958), Performances ballistiques des fusées, *Revue Universelle des Mines*, **XIV**, No. 6, 174–193.
- 5 Miele, A. (1962), *Flight Mechanics I*, Addison-Wesley, Reading, p. 345.
- 6 Culler, G. S. and Fried, B. D. (1957), Universal gravity turn trajectories, *J. Appl. Physics*, **28**, 672–676.
- 7 White, J. F. (1963), *Flight Performance Handbook for Powered Flight Operations*. John Wiley, New York, p. 29A.

12 The Multi-Stage Rocket

During the powered flight of a single-stage rocket, part of its mass has become ‘superfluous’. As the propellant tanks are designed to contain the gross propellant mass, they will be ‘too large’ if part of the propellant is consumed. So an extra, in fact useless mass has to be accelerated by the rocket engine. Consequently, this superfluous mass absorbs energy, which otherwise could be utilized for the payload. So it should be advantageous if this useless mass could be discarded continuously during the flight. However, this is not feasible. We cannot continuously throw away parts of the propellant tanks. Therefore, a multi-stage rocket contains several propellant tanks, which are discarded when they are empty. As it is not possible to discard only a tank, in general a complete propulsion unit, i.e. tanks together with motor and propellant feed system, is thrown-off. This complete unit is called a *stage*. In this way we do not have the full advantage of the discarding of the ‘useless’ mass as more rocket engines and propellant feed systems will be necessary. Therefore, more stages will only be advantageous for relatively large rockets where the propulsion system mass is small as compared to the mass of the tanks. In addition to extra rocket engines and auxiliary equipment, special provisions for separation of the various stages, and consequently extra mass, will be required.

An additional advantage of this staging is the possibility of thrust-programming, as well as the possibility of adapting the engines of the subsequent stages to the altitude where they are fired, thus reducing losses due to non-ideal expansion.

12.1 Nomenclature of the multi-stage rocket

We distinguish between *rocket stages* and *sub-rockets*. A stage (also called *step* in older literature) is a complete propulsion unit (motor, propellant feed system, tanks, propellant) together with control equipment, which is discarded completely when all propellant of that stage is consumed (*staging*). A sub-rocket is a complete rocket vehicle, consisting of one or more stages together with the payload and the guidance and control system (*astrionics* system).

Figure 12.1 shows a three-stage rocket. In this case we have three stages and three sub-rockets. The first sub-rocket is the complete rocket vehicle. The second sub-rocket is the first sub-rocket minus the first stage. The third sub-rocket, finally, is the second sub-rocket minus the second stage, or,

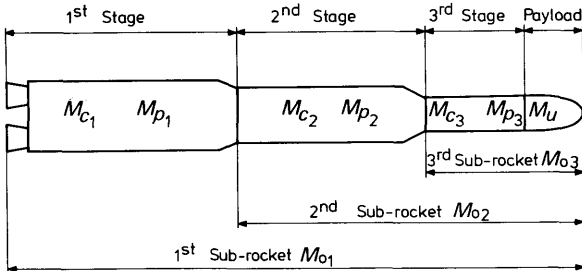


Fig. 12.1 Nomenclature for a three-stage rocket

equivalently, the payload plus the third stage. In general, for a N -stage rocket,

sub-rocket 1 = complete rocket,

sub-rocket $(i+1)$ = sub-rocket i – stage i ; $i = 1 \dots N-1$.

It should be noted that some authors use a different numbering system so that care has to be taken in using formulae and results from different sources.

In general, a rocket vehicle contains a propulsion unit and a payload. As the first stage is the propulsion unit of the first sub-rocket, we define the payload of the first sub-rocket to be the second sub-rocket. Then the payload of the second sub-rocket is the third sub-rocket, while in our example the payload of the third sub-rocket is the actual payload. In general, for a N -stage rocket,

payload sub-rocket i = sub-rocket $(i+1)$; $i = 1 \dots N-1$,

payload sub-rocket N = actual payload.

We will subdivide the total mass of the rocket vehicle in the same way as in Chapter 11 for single-stage rockets, i.e. payload mass, M_u , useful propellant mass, M_p , and structural mass, M_c . The total mass of stage i then consists of a structural mass, M_{ci} , and a propellant mass, M_{pi} . These are at the same time structural and propellant mass, respectively, of sub-rocket i . If we denote the initial mass of sub-rocket i with M_{0i} , we have

$$M_{0i} = M_{ci} + M_{pi} + M_{ui}, \quad (12.1-1)$$

where M_{ui} is the payload mass of sub-rocket i . So in view of the foregoing

$$M_{ui} = M_{0i+1}; \quad i = 1 \dots N-1, \quad (12.1-2)$$

$$M_{uN} = M_u,$$

where M_u is the actual payload mass.

We further define the same rocket parameters as in Section 11.2.2 for the

single-stage rocket. For sub-rocket i we have

$$\text{mass ratio} \quad \Lambda_i = \frac{M_{0_i}}{M_{0_i} - M_{p_i}}, \quad (12.1-3a)$$

$$\text{payload ratio} \quad \lambda_i = \frac{M_{u_i}}{M_{0_i}} = \frac{M_{0_{i+1}}}{M_{0_i}}, \quad (12.1-3b)$$

$$\text{propellant ratio} \quad \varphi_i = \frac{M_{p_i}}{M_{0_i}}, \quad (12.1-3c)$$

$$\text{structural efficiency} \quad \varepsilon_i = \frac{M_{c_i}}{M_{c_i} + M_{p_i}}. \quad (12.1-3d)$$

As we already mentioned in the discussion of rocket parameters of single-stage rockets, the above defined parameters are the ones most commonly used, there are, however, other parameters in use. Mass ratio, payload ratio and propellant ratio are related to sub-rockets only. The structural efficiency is related both to sub-rockets and to stages.

Just like for single-stage rockets, here too we have the following relations between the various rocket parameters

$$\varphi_i = (1 - \varepsilon_i)(1 - \lambda_i), \quad (12.1-4a)$$

$$\Lambda_i = \frac{1}{1 - \varphi_i} = \frac{1}{\varepsilon_i(1 - \lambda_i) + \lambda_i}. \quad (12.1-4b)$$

The *total payload ratio* is defined as the ratio of the actual payload mass and the total initial mass of the rocket,

$$\lambda_{tot} = \frac{M_u}{M_0} = \frac{M_{u_N}}{M_{0_1}}. \quad (12.1-5)$$

The inverse of this total payload ratio is called the *growth factor* and is denoted by G

$$G = \frac{M_0}{M_u} \quad (12.1-6)$$

The growth factor is an indication of the increase of the total initial mass as a result of an increase of payload mass. There is a simple relation between the total payload ratio and the payload ratios of the sub-rockets. Using Eq. (12.1-2) we can write

$$\frac{M_{u_N}}{M_{0_1}} = \frac{M_{u_1}}{M_{0_1}} \frac{M_{u_2}}{M_{0_2}} \cdots \frac{M_{u_N}}{M_{0_N}}. \quad (12.1-7)$$

So, in view of Eqs. (12.1-5) and (12.1-3b), the total payload ratio can be written as

$$\lambda_{tot} = \lambda_1 \lambda_2 \cdots \lambda_N. \quad (12.1-8)$$

Furthermore, we define the *total propellant ratio* as the ratio of total useful

propellant mass, M_p , and initial mass of the rocket

$$\varphi_{tot} = \frac{M_p}{M_0} = \frac{\sum M_{p_i}}{M_{0_i}}. \quad (12.1-9)$$

Now

$$\frac{M_{p_i}}{M_{0_i}} = \frac{M_{p_i}}{M_{0_i}} \frac{M_{0_i}}{M_{0_{i-1}}} \dots \frac{M_{0_2}}{M_{0_1}},$$

and by using Eqs. (12.1-3), we find

$$\frac{M_{p_i}}{M_{0_i}} = \varphi_i \lambda_1 \lambda_2 \dots \lambda_{i-1}. \quad (12.1-10)$$

Substitution of Eq. (12.1-10) into Eq. (12.1-9) leads to

$$\varphi_{tot} = \varphi_1 + \varphi_2 \lambda_1 + \dots + \varphi_N \lambda_1 \lambda_2 \dots \lambda_{N-1}. \quad (12.1-11)$$

Finally, we define a *total structural efficiency* as

$$\varepsilon_{tot} = \frac{M_c}{M_c + M_p} = \frac{\sum M_{c_i}}{\sum M_{c_i} + \sum M_{p_i}}, \quad (12.1-12)$$

where M_c is the total structural mass of the rocket. As the sum of total structural and total propellant mass equals the initial mass minus the payload mass, we may also write, using Eq. (12.1-5),

$$\varepsilon_{tot} = \frac{1}{1 - \lambda_{tot}} \sum \frac{M_{c_i}}{M_0}. \quad (12.1-13)$$

According to Eq. (12.1-3d)

$$M_{c_i} = \frac{\varepsilon_i}{1 - \varepsilon_i} M_{p_i},$$

and, using Eq. (12.1-10), we find

$$\frac{M_{c_i}}{M_0} = \frac{\varepsilon_i}{1 - \varepsilon_i} \varphi_i \lambda_1 \lambda_2 \dots \lambda_{i-1}. \quad (12.1-14)$$

Substitution of Eq. (12.1-14) into Eq. (12.1-13) and using Eq. (12.1-4a) finally gives

$$\varepsilon_{tot} = \frac{1}{1 - \lambda_{tot}} [\varepsilon_1(1 - \lambda_1) + \varepsilon_2(1 - \lambda_2)\lambda_1 + \dots + \varepsilon_N(1 - \lambda_N)\lambda_1\lambda_2 \dots \lambda_{N-1}]. \quad (12.1-15)$$

12.2 The ideal velocity of the multi-stage rocket

According to Eq. (11.2-10), the velocity increment of sub-rocket i during motor operation in free space is given by

$$\Delta V_i = c_i \ln \Lambda_i, \quad (12.2-1)$$

where c_i is the effective exhaust velocity of stage i . If $V_{b_{i-1}}$ is the burnout velocity of sub-rocket $(i-1)$, the burnout velocity of sub-rocket i is

$$V_{b_i} = V_{b_{i-1}} + \Delta V_i. \quad (12.2-2)$$

If the initial velocity of the rocket is zero, the burnout velocity of sub-rocket N , according to Eqs. (12.2-1) and (12.2-2), is

$$V_{id} = V_{b_N} = \sum_{i=1}^N \Delta V_i = \sum_{i=1}^N c_i \ln \Lambda_i. \quad (12.2-3)$$

This velocity is called the *ideal velocity of the N-stage rocket*. By using Eq. (12.1-4b), we may also write

$$V_{id} = - \sum_{i=1}^N c_i \ln \{\lambda_i + \varepsilon_i(1 - \lambda_i)\}. \quad (12.2-4)$$

Just as for the single-stage rocket, this ideal velocity is an important measure for the performance of the multi-stage rocket. A second important performance parameter is the total payload ratio. For a given ideal velocity, one will endeavor to have a payload ratio as large as possible. This means that we have a maximum payload mass for a given initial mass. This, of course, is equivalent to maximizing the ideal velocity for a given total payload ratio. From Eq. (12.2-4) we see that the ideal velocity is dependent on the effective exhaust velocities (i.e. the propellants) and the structural efficiencies of the stages, as well as on the payload ratio distribution. In general, we are free to choose this payload ratio distribution such that maximum performances are obtained. The structural efficiencies and the choice of propellants, however, are strongly dependent on operational aspects and on the state of the art of construction techniques. We may assume that in the design stage ε_i and c_i are known. Maximizing the ideal performances then is equivalent to maximizing the ideal velocity as a function of the λ_i 's only, for a given total payload ratio. So, this comes down to the determination of the payload ratios such that

$$V_{id}(\lambda_i) = - \sum_{i=1}^N c_i \ln \{\lambda_i + \varepsilon_i(1 - \lambda_i)\}, \quad (12.2-5)$$

is a maximum, with the side condition

$$\lambda_1 \lambda_2 \dots \lambda_N = \lambda_{tot} \quad (12.2-6)$$

This is a constrained optimization problem which can be solved by using the *method of Lagrange multipliers* [1]. Vertregt [2, 3] was the first to solve the multi-stage rocket optimization problem this way. We will follow this approach.

It will prove to be convenient to write the side condition, Eq. (12.2-6), as

$$\sum_{i=1}^N \ln \lambda_i - \ln \lambda_{tot} = 0. \quad (12.2-7)$$

Now we define an *augmented function*, F , as

$$F(\lambda_i) = V_{id}(\lambda_i) + \nu \left[\sum_{i=1}^N \ln \lambda_i - \ln \lambda_{tot} \right]. \quad (12.2-8)$$

The constant ν , to be determined later, is called a *Lagrange multiplier*. According to the theory of constrained maximization [1], a necessary condition for V_{id} to be a maximum, while Eq. (12.2-7) is satisfied, is

$$\frac{\partial F}{\partial \lambda_i} = 0; \quad i = 1, 2, \dots, N. \quad (12.2-9)$$

Elaboration of Eq. (12.2-9) yields as necessary conditions:

$$c_i \frac{1 - \varepsilon_i}{\lambda_i + \varepsilon_i(1 - \lambda_i)} - \frac{\nu}{\lambda_i} = 0. \quad (12.2-10)$$

Solution of these equations for λ_i leads to

$$\lambda_i = \frac{\nu \varepsilon_i}{(c_i - \nu)(1 - \varepsilon_i)}. \quad (12.2-11)$$

The value of the Lagrange multiplier, ν , is determined by substitution of Eq. (12.2-11) into the side condition, Eq. (12.2-7), yielding

$$\sum_{i=1}^N \ln \frac{\nu \varepsilon_i}{(c_i - \nu)(1 - \varepsilon_i)} = \ln \lambda_{tot} \quad (12.2-12)$$

which is an equation in ν only. Thus, the optimal payload ratio distribution and the corresponding maximum value of the ideal velocity are found by first solving Eq. (12.2-12) for ν . Then this solution is substituted into Eq. (12.2-11), yielding the λ_i 's. Finally, substitution of the obtained values of the payload ratios into Eq. (12.2-5) yields the maximum ideal velocity.

In general, Eq. (12.2-12) is a N th-order algebraic equation in ν , which cannot be solved analytically. As this equation has N roots, it will sometimes be necessary to check which root yields the maximum value of the ideal velocity. However, the solution is relatively simple if all stages have the same effective exhaust velocity. In that case $c_1 = c_2 = \dots = c_N = c$, and Eq. (12.2-12) leads to

$$\frac{\nu}{c - \nu} = \lambda_{tot} \left[\frac{(1 - \varepsilon_1)(1 - \varepsilon_2) \dots (1 - \varepsilon_N)}{\varepsilon_1 \varepsilon_2 \dots \varepsilon_N} \right]^{1/N}.$$

Substitution of this expression into Eq. (12.2-11) gives

$$\lambda_i = \frac{\varepsilon_i}{1 - \varepsilon_i} \left[\lambda_{tot} \frac{(1 - \varepsilon_1)(1 - \varepsilon_2) \dots (1 - \varepsilon_N)}{\varepsilon_1 \varepsilon_2 \dots \varepsilon_N} \right]^{1/N}. \quad (12.2-13)$$

Substitution of these values of the λ_i 's into Eq. (12.2-5) yields

$$(V_{id})_{max} = -c \ln \left[\varepsilon_1 \varepsilon_2 \dots \varepsilon_N \left\{ 1 + \left(\lambda_{tot} \frac{(1 - \varepsilon_1)(1 - \varepsilon_2) \dots (1 - \varepsilon_N)}{\varepsilon_1 \varepsilon_2 \dots \varepsilon_N} \right)^{1/N} \right\}^N \right]. \quad (12.2-14)$$

Conversely, if the ideal velocity is given, the solution of Eq. (12.2-14) for λ_{tot} gives the maximum payload ratio,

$$(\lambda_{tot})_{max} = \frac{[e^{-u/N} - (\varepsilon_1 \varepsilon_2 \dots \varepsilon_N)^{1/N}]^N}{(1 - \varepsilon_1)(1 - \varepsilon_2) \dots (1 - \varepsilon_N)} \quad (12.2-15)$$

Here, u is the *ideal velocity ratio*, i.e. the ratio of the ideal velocity and the exhaust velocity:

$$u = \frac{V_{id}}{c}. \quad (12.2-16)$$

For a two-stage rocket, the Eqs. (12.2-14) and (12.2-15) simplify to

$$(V_{id})_{max} = -2c \ln [\sqrt{\varepsilon_1 \varepsilon_2} + \sqrt{\lambda_{tot}(1 - \varepsilon_1)(1 - \varepsilon_2)}], \quad (12.2-17)$$

$$(\lambda_{tot})_{max} = \frac{[e^{-u/2} - \sqrt{\varepsilon_1 \varepsilon_2}]^2}{(1 - \varepsilon_1)(1 - \varepsilon_2)}. \quad (12.2-18)$$

Figure 12.2 gives the maximum payload ratio as a function of the ideal velocity ratio for a two-stage rocket. We see that for very small ideal velocity ratios, the total payload ratio is practically independent of the structural efficiencies.

The general solution for the optimal payload ratio distribution simplifies still more if not only the effective exhaust velocities, but also the structural efficiencies of all stages, are equal. In that case

$$\varepsilon_1 = \varepsilon_2 = \dots = \varepsilon_N = \varepsilon.$$

It then follows from Eq. (12.2-13), that all partial payload ratios are identical for maximum ideal velocity:

$$\lambda_i = \lambda_{tot}^{1/N} = \lambda \quad (12.2-19)$$

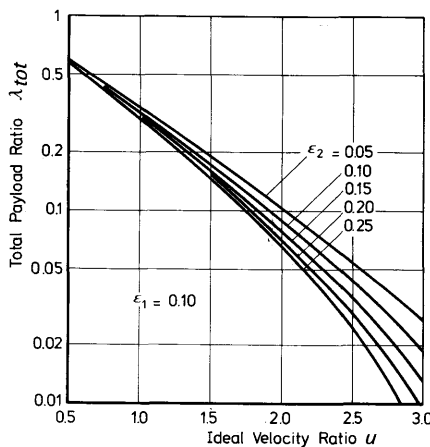


Fig. 12.2 The total payload ratio for a two-stage rocket

We then say that the rocket has *identical stages*. For a given total payload ratio, the maximum ideal velocity follows from Eq. (12.2-14):

$$(V_{id})_{max} = -cN \ln \{\varepsilon + \lambda_{tot}^{1/N}(1 - \varepsilon)\}. \quad (12.2-20)$$

For a given ideal velocity, the maximum total payload ratio is

$$(\lambda_{tot})_{max} = \left[\frac{e^{-u/N} - \varepsilon}{1 - \varepsilon} \right]^N, \quad (12.2-21)$$

where again u is the ideal velocity ratio. Figure 12.3a gives the total payload ratio for a rocket with identical stages, as a function of the ideal velocity ratio for various values of N . For given values of u and ε , the minimum numbers of stages is found for $\lambda_{tot} = 0$. It follows from Eq. (12.2-21) that

$$N_{min} = -\frac{u}{\ln \varepsilon}. \quad (12.2-22)$$

As, in general, the thus determined value of N_{min} will not be an integer, the real minimum number of stages will be the smallest integer equal to, or larger than N_{min} as determined by Eq. (12.2-22).

It can easily be proved that for given values of u and ε , the total payload ratio increases monotonically with the number of stages, and reaches its maximum value for $N \rightarrow \infty$. From Eq. (12.2-21) it is found that

$$\lim_{N \rightarrow \infty} \lambda_{tot} = e^{-u/(1-\varepsilon)}, \quad (12.2-23)$$

or, equivalently,

$$\lim_{N \rightarrow \infty} V_{id} = -c(1 - \varepsilon) \ln \lambda_{tot}. \quad (12.2-24)$$

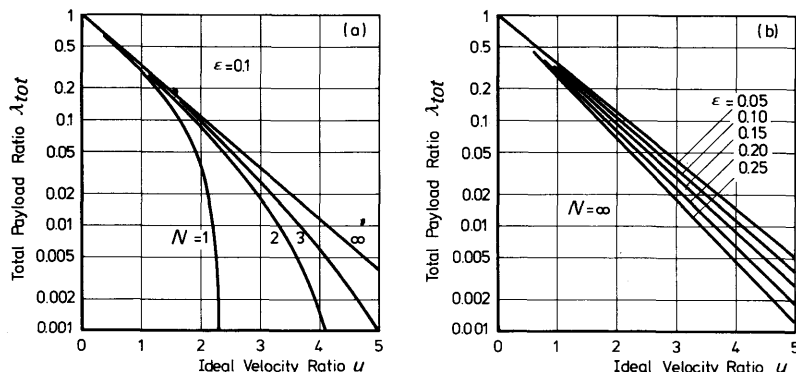


Fig. 12.3 The total payload ratio for a N -stage and for an infinitely staged rocket with identical stages

In Fig. 12.3b the total payload ratio is given as a function of the ideal velocity ratio for the case of infinite staging.

For a rocket with identical stages, the total propellant ratio is, according to Eq. (12.1-11),

$$\varphi_{tot} = \varphi(1 + \lambda + \lambda^2 + \dots + \lambda^{N-1}) = \frac{1 - \lambda^N}{1 - \lambda} \varphi, \quad (12.2-25)$$

or, by using Eqs. (12.1-4a) and (12.2-19),

$$\varphi_{tot} = (1 - \varepsilon)(1 - \lambda_{tot}). \quad (12.2-26)$$

We see that for a rocket with identical stages the total propellant ratio does not depend on the number of stages. So, if the total propellant mass is fixed, it is favorable in this case to distribute it over as many stages as possible.

From Eq. (12.1-15) we find the total structural efficiency to be

$$\varepsilon_{tot} = \varepsilon. \quad (12.2-27)$$

So, again for a rocket with identical stages, the total structural efficiency is independent of both the number of stages and the total payload ratio and equals the structural efficiency of the stages.

These results hold only if the structural efficiencies of the stages are independent of the number of stages. In practice, this is not possible. If, for a fixed initial gross mass, the number of stages increases, the propellant mass in each stage will decrease. Consequently, the mass of the tanks in each stage decreases too. In general, the mass of the motor and the propellant feed system will decrease too, however, not with the same rate as the propellant and tank mass. As a result of this, the structural efficiencies of the stages will increase with increasing number of stages and will approach unity for infinite staging. Therefore, there will be a finite optimum number of stages.

The derived results are also strongly dependent on the parameters used and on the assumptions made. If, instead of the structural efficiency, ε , the *structure ratio* s_i defined as

$$s_i = \frac{M_{c_i}}{M_{0_i}}, \quad (12.2-28)$$

is used and if it is assumed that s_i is independent of the number of stages, the results will differ considerably, as will be shown. In this case the relation between mass ratio, payload ratio and structure ratio is

$$\frac{1}{\Lambda_i} = \frac{M_{0_i} - M_{p_i}}{M_{0_i}} = \frac{M_{u_i} + M_{c_i}}{M_{0_i}} = \lambda_i + s_i. \quad (12.2-29)$$

Consequently, the ideal velocity of a N -stage rocket is

$$V_{ia} = - \sum_{i=1}^N c_i \ln (\lambda_i + s_i). \quad (12.2-30)$$

If effective exhaust velocity and structure ratio are the same for all sub-rockets, it can easily be proved that the ideal performance is at a maximum if the payload ratios are the same for all sub-rockets. Then, the ideal velocity is

$$V_{id} = -cN \ln(\lambda + s), \quad (12.2-31)$$

or

$$\lambda = e^{-u/N} - s, \quad (12.2-32)$$

and the total payload ratio is

$$\lambda_{tot} = (e^{-u/N} - s)^N. \quad (12.2-33)$$

In Fig. 12.4 the maximum total payload ratio is given as a function of the number of stages for various values of the ideal velocity ratio, u . Here N is considered a continuous variable, but in fact it can only have discrete values (integers). From this figure we see that there is a finite optimum number of stages. This optimum is determined by

$$\frac{d\lambda_{tot}}{dN} = 0.$$

Elaboration of this equation leads to

$$(1 - se^{u/N}) \ln(1 - se^{u/N}) + s \frac{u}{N} e^{u/N} = 0. \quad (12.2-34)$$

For a given value of s , Eq. (12.2-34) is an equation in u/N , the solution of which is given in Fig. 12.5. It follows from Eq. (12.2-34) that for a given value of s , the optimum number of stages increases linearly with increasing ideal velocity ratio, u . From Fig. 12.5 we see that the optimum value of u/N decreases almost linearly with increasing structure ratio, which means that

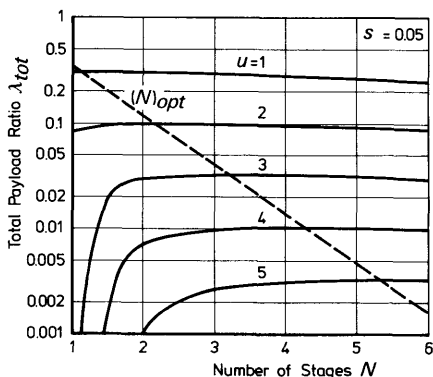


Fig. 12.4 The total payload ratio and the optimal number of stages for a rocket with identical sub-rockets

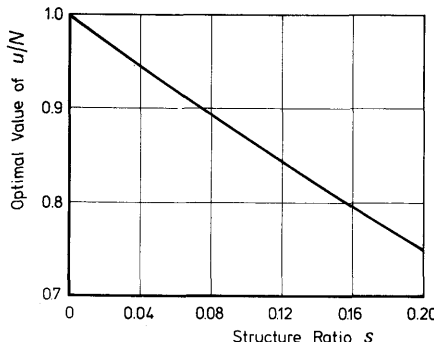


Fig. 12.5 The optimum value of u/N versus the structure ratio for a rocket with identical sub-rockets

for a given value of the ideal velocity ratio the optimum number of stages increases with increasing structure ratio. Cooper [4] gives a more extensive discussion on this optimization problem.

Coleman [5], in his optimization procedure for multi-stage rockets, uses a *structure factor* C_i , defined as

$$C_i = \frac{M_{c_i}}{(M_{c_i} + M_{p_i})^{\alpha_i}}.$$

Here an extra parameter α_i is introduced. As α_i can vary, depending on propellants used, etc., a better approximation of reality is obtained.

12.3 Vertical ascent in a homogeneous gravitational field and in vacuum

After having considered the flight of a multi-stage rocket in free-space, we will now take into account gravitational effects. The gravitational field will be assumed to be homogeneous (flat Earth). As is already explained in Section 11.3, this is a fairly good approximation of the gravitational field of the Earth as long as altitude differences and ranges covered are small relative to the radius of the Earth.

We will only consider the case where the thrust of each stage is constant. As for single-stage rockets, it will be convenient to use the thrust-to-weight ratio, defined for sub-rocket i as

$$\psi_i = \frac{F_i}{g_0 M_{0i}}, \quad (12.3-1)$$

The burning-time for sub-rocket i follows from

$$t_{bi} = \frac{c_i}{g_0 \psi_i} \left(1 - \frac{1}{\Lambda_i} \right) = \frac{c_i (1 - \varepsilon_i)(1 - \lambda_i)}{g_0 \psi_i}. \quad (12.3-2)$$

We further define V_{0_i} to be the velocity of sub-rocket i at ignition, taking place at time t_{0_i} and altitude h_{0_i} , while V_{b_i} is the burnout velocity of sub-rocket i , at an altitude h_{b_i} at time $t_{0_i} + t_{b_i}$. We will assume the initial velocity of the rocket, $V_0 = V_{0_1}$, to be zero.

12.3.1 The burnout velocity

The total velocity increment due to the motor operation of sub-rocket i is

$$\Delta V_i = V_{b_i} - V_{0_i} = c_i \ln \Lambda_i - g_0 t_{b_i}. \quad (12.3-3)$$

If t_{c_i} is the time between burnout of sub-rocket i and ignition of sub-rocket $(i+1)$, the *coast-time*, the velocity at ignition of sub-rocket $(i+1)$ is

$$V_{0_{i+1}} = V_{b_i} - g_0 t_{c_i}. \quad (12.3-4)$$

From Eqs. (12.3-3) and (12.3-4) we obtain the burnout velocity of the N th sub-rocket, the total burnout velocity

$$V_b = V_{b_N} = \sum_{i=1}^N \Delta V_i - g_0 \sum_{i=1}^{N-1} t_{c_i}. \quad (12.3-5)$$

We see that the burnout velocity decreases linearly with increasing coast-time between burnout and ignition of the next stage. Maximum burnout velocity is obtained if every stage is ignited directly after burnout of the previous one. For the time being we will assume that this is the case. The burnout velocity then follows from Eqs. (12.3-5) and (12.3-3):

$$V_b = \sum_{i=1}^N [c_i \ln \Lambda_i - g_0 t_{b_i}]. \quad (12.3-6)$$

Using Eqs. (12.1-4b) and (12.3-2), we obtain the burnout velocity as a function of effective exhaust velocity, thrust-to-weight ratio, structural efficiency and payload ratio of the various sub-rockets:

$$V_b = - \sum_{i=1}^N c_i \left[\ln \{\lambda_i + \varepsilon_i(1 - \lambda_i)\} + \frac{(1 - \varepsilon_i)(1 - \lambda_i)}{\psi_i} \right]. \quad (12.3-7)$$

As for single-stage rockets, we see that the gravitational losses approach zero, and consequently the burnout velocity approaches the ideal velocity, if $\psi_i \rightarrow \infty$, i.e. for impulsive shots. Here too we can ask for the optimal distribution of the partial payload ratios, such that for given c_i , ε_i , ψ_i and λ_{tot} , the burnout velocity reaches a maximum value. Again this is a constrained optimization problem, which can be solved by using Lagrange multipliers. We define the augmented function F as

$$F(\lambda_i) = V_b(\lambda_i) + \nu \left[\sum_{i=1}^N \ln \lambda_i - \ln \lambda_{tot} \right],$$

and the necessary conditions for maximum burnout velocity with total

payload ratio given, are

$$\frac{\partial F}{\partial \lambda_i} = 0; \quad i = 1, 2, \dots, N.$$

This leads to N quadratic equations in the payload ratios λ_i . Solution of these equations yields each λ_i as a function of the corresponding c_i , ε_i , ψ_i and the Lagrange multiplier ν . This multiplier is determined with the side-condition, Eq. (12.2-7). For a rocket with $\varepsilon_i = \varepsilon$, $c_i = c$ and $\psi_i = \psi$, it follows that the burnout velocity is maximized if all partial payload ratios are equal, i.e.

$$\lambda_i = \lambda = \lambda_{tot}^{1/N}. \quad (12.3-8)$$

Then, the burnout velocity is

$$V_b = -cN \left[\ln \{ \lambda_{tot}^{1/N} + \varepsilon (1 - \lambda_{tot}^{1/N}) \} + \frac{(1 - \varepsilon)(1 - \lambda_{tot}^{1/N})}{\psi} \right]. \quad (12.3-9)$$

In Fig. 12.6 the dimensionless burnout velocity, V_b/c , is given as a function of N and ψ . As we see, V_b does not increase monotonically with N for finite ψ . Thus, in this case there is a finite optimum number of stages.

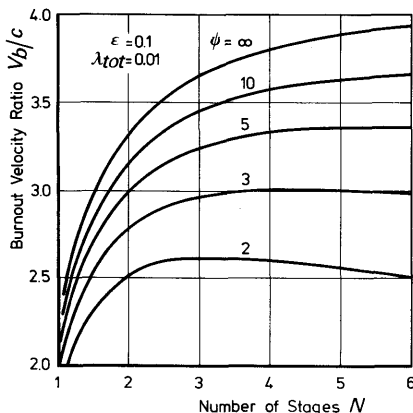


Fig. 12.6 The burnout velocity ratio for a N -stage rocket with identical stages ascending vertically in a homogeneous gravitational field

12.3.2 The culmination altitude

In this section, we will discuss a method to determine the culmination altitude of a N -stage rocket, ascending vertically in a homogeneous gravitational field and in vacuum.

During thrusting of stage i , i.e. for

$$t_{0_i} < t < t_{0_i} + t_{b_i},$$

the velocity is

$$V_i(t) = V_{0i} + c_i \ln \frac{M_{0i}}{M} - g_0(t - t_{0i}), \quad (12.3-10)$$

where M is the instantaneous mass of sub-rocket i . Thus, the altitude at burnout of stage i is

$$h_{bi} = h_{0i} + \int_{t_{0i}}^{t_{0i} + t_{bi}} V_i(t) dt, \quad (12.3-11)$$

or, by using Eq. (12.3-10)

$$h_{bi} = h_{0i} + V_{0i}t_{bi} + \int_0^{t_{bi}} \left(c_i \ln \frac{M_{0i}}{M} - g_0\tau \right) d\tau, \quad (12.3-12)$$

where $\tau = t - t_{0i}$. Now define

$$\Delta h_i = \int_0^{t_{bi}} \left(c_i \ln \frac{M_{0i}}{M} - g_0\tau \right) d\tau. \quad (12.3-13)$$

We then find for constant thrust

$$\Delta h_i = \frac{c_i^2}{g_0\psi_i} \left[1 - \frac{1}{\Lambda_i} (\ln \Lambda_i + 1) - \frac{1}{2\psi_i} \left(1 - \frac{1}{\Lambda_i} \right)^2 \right]. \quad (12.3-14)$$

At burnout of stage i , time, velocity and altitude are

$$t = t_{0i} + t_{bi}, \quad (12.3-15a)$$

$$V_{bi} = V_{0i} + \Delta V_i, \quad (12.3-15b)$$

$$h_{bi} = h_{0i} + V_{0i}t_{bi} + \Delta h_i. \quad (12.3-15c)$$

After burnout of stage i , this stage is discarded and sub-rocket $(i+1)$ remains. This rocket first coasts during a time t_{ci} . So, at ignition of stage $(i+1)$, time, velocity and altitude are

$$t_{0i+1} = t_{0i} + t_{bi} + t_{ci}, \quad (12.3-16a)$$

$$V_{0i+1} = V_{bi} - g_0 t_{ci}, \quad (12.3-16b)$$

$$h_{0i+1} = h_{bi} + V_{bi}t_{ci} - \frac{1}{2}g_0 t_{ci}^2. \quad (12.3-16c)$$

Now, for given initial conditions of the first sub-rocket, V_{bi} and h_{bi} are determined with Eqs. (12.3-15). Then V_{02} and h_{02} can be determined with Eqs. (12.3-16) and then V_{b2} and h_{b2} can again be determined, etc. Finally, V_{bn} and h_{bn} are found this way. This last sub-rocket then coasts during a time interval t_{cn} until culmination. In some cases, payload and last stage are separated too after burnout of the last stage. The time t_{cn} is determined with

$$t_{cn} = \frac{V_{bn}}{g_0}. \quad (12.3-17)$$

276 Rocket Propulsion & Spaceflight Dynamics

Then, the culmination altitude is

$$h_c = h_{b_N} + V_{b_N} t_{c_N} - \frac{1}{2} g_0 t_{c_N}^2,$$

or, with Eq. (12.3-17)

$$h_c = h_{b_N} + \frac{V_{b_N}^2}{2 g_0}. \quad (12.3-18)$$

The total time to culmination is

$$t_c = \sum_{i=1}^N (t_{b_i} + t_{c_i}),$$

or, using Eq. (12.3-17)

$$t_c = \sum_{i=1}^N t_{b_i} + \sum_{i=1}^{N-1} t_{c_i} + \frac{V_{b_N}}{g_0}. \quad (12.3-19)$$

Substitution of Eqs. (12.3-3) and (12.3-5) into Eq. (12.3-19), finally leads to

$$t_c = \frac{1}{g_0} \sum_{i=1}^N c_i \ln \Lambda_i. \quad (12.3-20)$$

We see that the total time to culmination is independent of the thrust-to-weight ratios and the intermediate coast-times.

12.3.3 Vertical ascent of a two-stage rocket

We will now apply the expressions derived in the preceding section to a two-stage rocket, and determine its culmination altitude. We assume lift-off taking place at $t_{b_1} = 0$ with $V_{0_1} = h_{0_1} = 0$. First, t_{b_1} and t_{b_2} are determined from Eq. (12.3-2). Then ΔV_1 , ΔV_2 , Δh_1 and Δh_2 can be determined from Eqs. (12.3-3) and (12.3-14). Thus, according to Eqs. (12.3-15), burnout velocity and burnout altitude of the first sub-rocket are

$$V_{b_1} = \Delta V_1, \quad (12.3-21a)$$

$$h_{b_1} = \Delta h_1. \quad (12.3-21b)$$

The second stage ignites at time $t_{0_2} = t_{b_1} + t_{c_1}$. Velocity and altitude at that time are

$$V_{0_2} = \Delta V_1 - g_0 t_{c_1}, \quad (12.3-22a)$$

$$h_{0_2} = \Delta h_1 + \Delta V_1 t_{c_1} - \frac{1}{2} g_0 t_{c_1}^2. \quad (12.3-22b)$$

Burnout velocity and altitude of the second sub-rocket again follow from Eqs. (12.3-15)

$$V_{b_2} = \Delta V_1 + \Delta V_2 - g_0 t_{c_1}, \quad (12.3-23a)$$

$$h_{b_2} = \Delta h_1 + \Delta h_2 + \Delta V_1 (t_{c_1} + t_{b_2}) - \frac{1}{2} g_0 t_{c_1} (t_{c_1} + 2t_{b_2}). \quad (12.3-23b)$$

The culmination altitude, finally, follows from Eq. (12.3-18)

$$h_c = \Delta h_1 + \Delta h_2 + \frac{1}{2g_0} (\Delta V_1 + \Delta V_2)^2 + \Delta V_1 t_{b_2} - \Delta V_2 t_{c_1} - g_0 t_{c_1} t_{b_2}. \quad (12.3-24)$$

Substitution of the expressions for t_{b_1} , t_{b_2} , ΔV_1 , ΔV_2 , Δh_1 and Δh_2 into Eq. (12.3-24) yields

$$h_c = \frac{c_1^2}{g_0 \psi_1} \left(1 + \psi_1 \frac{\ln^2 \Lambda_1}{2} - \frac{1}{\Lambda_1} - \ln \Lambda_1 \right) + \frac{c_2^2}{g_0 \psi_2} \left(1 + \psi_2 \frac{\ln^2 \Lambda_2}{2} - \frac{1}{\Lambda_2} - \ln \Lambda_2 \right) + \frac{c_1 c_2}{g_0} \ln \Lambda_2 \left[\ln \Lambda_1 - \frac{1}{\psi_1} \left(1 - \frac{1}{\Lambda_1} \right) \right] - c_2 \ln \Lambda_2 t_{c_1}. \quad (12.3-25)$$

We see that the culmination altitude, just like the burnout velocity, decreases with increasing coast-time between burnout of stage 1 and ignition of stage 2. So the best performance is obtained if the second stage is ignited directly after burnout of the first one. This also holds for a rocket with more than two stages. It should be realized, however, that this is only true in vacuum; the presence of an atmosphere may yield a non-zero optimal coast-time. From Eq. (12.3-25) we see that the culmination altitude increases if ψ_1 and ψ_2 increase. Maximum culmination height is reached if $\psi_1, \psi_2 \rightarrow \infty$, i.e. for impulsive shots. In that case, and for $t_{c_1} = 0$

$$h_c = \frac{1}{2g_0} (c_1 \ln \Lambda_1 + c_2 \ln \Lambda_2)^2. \quad (12.3-26)$$

For a rocket with identical stages, and zero coast-time, Eq. (12.3-25) simplifies to

$$h_c = \frac{c^2}{g_0 \psi} \left[2\psi \ln^2 \Lambda + 2 - \frac{2}{\Lambda} - \ln \Lambda \left(3 - \frac{1}{\Lambda} \right) \right]. \quad (12.3-27)$$

The dimensionless culmination altitude $h_c g_0 / c^2$, or equivalently $h_c / g_0 I_{sp}^2$, for a two-stage rocket with identical stages and zero coast-time is given in Fig. 12.7 as a function of thrust-to-weight ratio and mass ratio.

Finally, we will compare the performances of a two-stage rocket with identical stages with the performances of a single-stage rocket having the same initial mass, payload mass and total propellant mass as the two-stage rocket. If λ_{tot} is the total payload ratio of both the two-stage and the single-stage rocket, then, for a two-stage rocket with identical stages

$$\frac{M_u}{M_{0_2}} = \frac{M_{0_2}}{M_0} = \sqrt{\lambda_{tot}} \quad (12.3-28)$$

Let Λ be the mass ratio of each of the sub-rockets of the two-stage rocket. Then

$$\Lambda = \frac{M_0}{M_0 - M_{p_1}} = \frac{M_{0_2}}{M_{0_2} - M_{p_2}}. \quad (12.3-29)$$

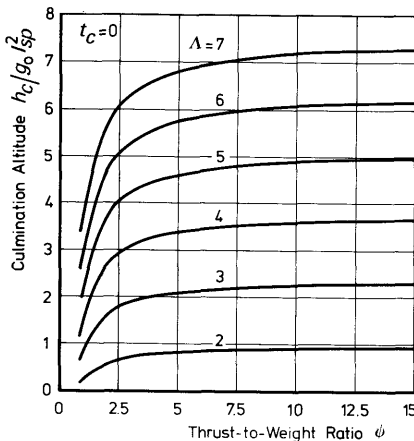


Fig. 12.7 The dimensionless culmination altitude for a two-stage rocket with identical stages ascending vertically in a homogeneous gravitational field ($t_c = 0$)

From Eqs. (12.3-28) and (12.3-29) follows

$$\frac{M_{p_2}}{M_{p_1}} = \sqrt{\lambda_{tot}} \quad (12.3-30)$$

and

$$\frac{M_{p_1}}{M_0} = \left(1 - \frac{1}{\Lambda}\right). \quad (12.3-31)$$

The mass ratio of the single-stage rocket is given by

$$\Lambda^{(1)} = \frac{M_0}{M_0 - M_{p_1} - M_{p_2}}, \quad (12.3-32)$$

and by using Eqs. (12.3-30) and (12.3-31), we obtain a relation between the mass ratio of the single-stage rocket, $\Lambda^{(1)}$, and the mass ratio, Λ , of the sub-rockets of the two-stage vehicle:

$$\Lambda^{(1)} = \frac{\Lambda}{1 - (\Lambda - 1)\sqrt{\lambda_{tot}}}. \quad (12.3-33)$$

This relation is depicted in Fig. 12.8. Note that $\lambda_{tot} = 0$ implies that $M_{p_2} = 0$ and our two-stage rocket has become a single-stage one.

For the same effective exhaust velocities, the ratio of the ideal velocities is

$$\frac{V_{id}^{(2)}}{V_{id}^{(1)}} = \frac{2 \ln \Lambda}{\ln \Lambda^{(1)}}, \quad (12.3-34)$$

and, as according to Eq. (12.3-33), Λ is a function of $\Lambda^{(1)}$ and λ_{tot} , this ratio

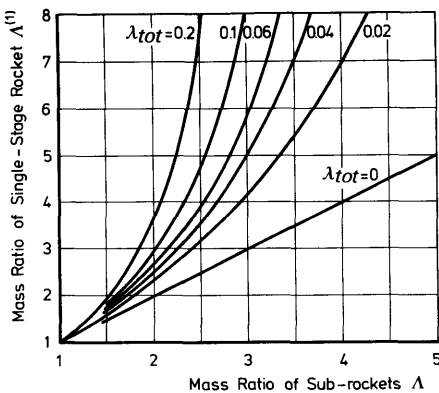


Fig. 12.8 The mass ratio of a single-stage rocket versus the mass ratio of the sub-rockets of a two-stage rocket with the same mass distribution

is also a function of $\Lambda^{(1)}$ and λ_{tot} . This ratio is depicted in Fig. 12.9a. Of course, this ratio becomes unity if $\Lambda^{(1)} = 1/\lambda_{tot}$. Then $M_c = 0$, which is not a real possibility, and there is no gain in using a two-stage rocket.

Using Eqs. (12.3-27) and (11.3-7d), we find for the ratio of culmination altitudes, for the same thrust-to-weight ratio

$$\frac{h_c^{(2)}}{h_c^{(1)}} = \frac{2\psi \ln^2 \Lambda + 2 - 2/\Lambda - (3 - 1/\Lambda) \ln \Lambda}{\frac{1}{2}\psi \ln^2 \Lambda^{(1)} - \ln \Lambda^{(1)} - 1/\Lambda^{(1)} + 1}. \quad (12.3-35)$$

This ratio is depicted in Fig. 12.9b as a function of $\Lambda^{(1)}$ and λ_{tot} , for $\psi = 5$.

From Fig. 12.9 we see that the performance gain by using a two-stage instead of a single-stage rocket increases with decreasing mass ratio and decreasing payload ratio. This is understandable as for a small mass ratio and a small payload ratio a large part of the initial mass is due to the

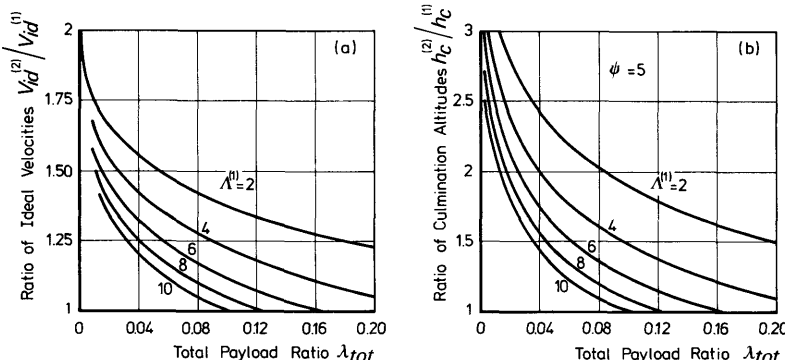


Fig. 12.9 The ratios of ideal velocities and culmination altitudes of a two- and a single-stage rocket having identical mass distribution

structure and consequently the useless mass of the single-stage rocket will be relatively large, thus absorbing a relatively large amount of energy. We also see that the performance improvement is larger if gravitation is taken into account. This is due to the fact that in that case the useless mass also represents a certain amount of potential energy in addition to its kinetic energy. The real performance improvement will be less than calculated here, owing to the fact that a two-stage rocket with the same payload mass and total propellant mass as a single-stage rocket will have a larger structural mass. This is due to the fact that instead of one, two complete propulsion units, as well as a mechanism for stage-separation, are required. For very small rockets these extra masses are so large as compared to the total mass, that staging hardly improves the performance. For large rockets, the extra masses are small as compared to the total mass and performance improvements of 25% to 80% are possible.

12.4 Parallel staging

Up to now, we have meant by staging the stacking of one stage on top of another. *Parallel staging* is defined as staging a vehicle such that the upper-stage engines are also used during lower stage operation. This is usually accomplished by arranging the stages alongside one another, hence the name parallel staging. To distinguish between the two methods of staging, the first one is often called *tandem staging*. The main advantage of parallel staging is the reduction of gravitational losses. As we already explained, in a gravitational field it is always advantageous to consume the propellant as fast as possible. Then, the amount of energy that is absorbed by the propellant as potential energy and cannot be recuperated anymore, is reduced. By parallel staging, a large propellant consumption is realized. A disadvantage is that the rocket is likely to be bulky, and for flight through the atmosphere the drag penalty may be large. This, however, is of minor importance for large rockets where the drag losses are very small as compared to gravitational losses (Chapter 14). A second disadvantage of parallel staging is the reduction in nozzle efficiency of the engines of the first stage. If these engines are used from the start, their expansion ratio is limited by the atmospheric pressure at low altitudes. Using tandem staging, the expansion ratio of the engines of the subsequent stages can be adapted to the altitude where they are fired.

Often, both methods of staging are applied in one vehicle. For large launch-vehicles, parallel staging is realized by placing boosters around the first stage. These boosters are often identified as stage zero. Examples are the Delta with three, six, or nine solid boosters, the Titan III with two or four solid boosters, the Space Shuttle with two solid boosters and the Russian Soyuz launch-vehicle with four boosters using kerosine and LOX as propellant.

In general, the burning-time of these boosters is shorter than the burning-time of the first stage. They are jettisoned after burnout.

The analysis of parallel staging is about analogous as for tandem staging and will not be presented here. Methods of optimal parallel staging are discussed by White [6, 7] and Barrère [8].

Finally, we have to remark that we discussed optimum staging such that the take-off mass is minimized. In practice one is perhaps more interested in minimization of cost than in minimization of take-off mass. A mathematical procedure whereby optimum staging for minimum cost may be computed, with minimum mass staging as a special case, is derived by Gray [9].

We have limited ourselves to rectilinear motion in vacuum, but pitching and drag may have considerable effects on the optimum mass distribution. Cobb [10] minimizes the gross take-off mass with the constraint that the total energy, i.e. kinetic and potential energy, imparted to the payload is fixed. In his paper, pitching is included by assuming an average attitude angle for each stage. Drag, however, is not included. Adkins [11], finally, takes both drag and varying attitude into account.

References

- 1 Leitmann, G. (1962), *Optimization Techniques*, Academic Press, New York, p. 1-31.
- 2 Vertregt, M. (1955), Calculation of step-rockets, *J. Brit. Interplanet. Soc.*, **14**, 20-25.
- 3 Vertregt, M. (1956), A method for calculating the mass ratio's of step-rockets, *J. Brit. Interplanet. Soc.*, **15**, 95-97.
- 4 Cooper, R. S. (1962), Performance of optimized multistage rockets, *J. Aerospace Sciences*, **29**, 1339-1343.
- 5 Coleman, J. J. (1961), Optimum stage-weight distribution of multistage rockets, *ARS J.*, **31**, 259-261.
- 6 White, J. F. (1959), *Method for Staging Parallel Boosters for Minimum Gross Weight*, Space Technology Lab. TM-59-0000-00399, Los Angeles.
- 7 White, J. F. (1963), *Flight Performance Handbook for Powered Flight Operations*, John Wiley, New York, p. 5-80.
- 8 Barrère, M., Jaumotte, A., Fraeijis de Veubeke, B. and Vandekerckhove, J. (1960), *Rocket Propulsion*, Elsevier, Amsterdam, p. 754.
- 9 Gray, J. S. and Alexander, R. V. (1965), Cost and weight optimization for multistage rockets, *J. Spacecraft*, **2**, 80-86.
- 10 Cobb, E. R. (1961), Optimum staging techniques to maximize payload total energy, *ARS J.*, **31**, 342-344.
- 11 Adkins, C. N. (1970), Optimization of multistage rockets including drag, *J. Spacecraft*, **7**, 751-755.

13 Ballistic Missile Trajectories

Ballistic missiles are used for transportation of a payload from one point on the Earth, the *launch site*, to another point on the surface of the Earth, the *impact point* or *target*. Long-range ballistic missiles became a practical reality in World War II with the German V2 and have developed rapidly in succeeding years.

It is characteristic of these ballistic missiles that during a relatively short period they are accelerated to a high velocity. Then a *re-entry vehicle*, containing the warhead, is released and this vehicle then simply coasts in a *ballistic* or *free-fall trajectory* to the final impact point. The older type ICBM's (Minuteman-2, Titan-2), carrying only one re-entry vehicle, release this vehicle after shut-down of the last stage. Modern vehicles (Minuteman-3, Polaris, Poseidon), carrying so-called *multiple independently targetable re-entry vehicles* (MIRV), have a *post-boost control system*. This system, which in fact is a low-thrust maneuverable rocket stage, allows for the accurate successive deployment of the re-entry vehicles against their pre-selected separate targets. After release of a re-entry vehicle no control can be exercised anymore and it will be clear that the position of the impact point is practically uniquely determined by position and velocity at release. Thus, the burden of establishing a proper ballistic trajectory resulting in impact at the desired point rests with the guidance and control of the relatively short powered flight phase. A recent development is the *advanced maneuverable re-entry vehicle* (AMARV) now being designed as a payload for the advanced MX missile and the Trident submarine-launched ballistic missile (SLBM). This re-entry vehicle, having its own full guidance system, will be able to maneuver during the terminal phase of the flight to avoid interception by anti-ballistic missile weapons as well as to eliminate some error factors, such as booster separation errors, wind shears and atmospheric behavior, that contribute to target misses.

In this chapter we will discuss the flight of a conventional ballistic missile, carrying only one re-entry vehicle, from launch until impact, with emphasis on the ballistic portion of the flight. Vehicles equipped with MIRV's distinguish themselves from conventional vehicles by a short low-thrust guided boost phase after last stage shut-down and the trajectory analysis will be roughly identical.

Figure 13.1 shows a typical ballistic missile trajectory. It can be divided into three phases:

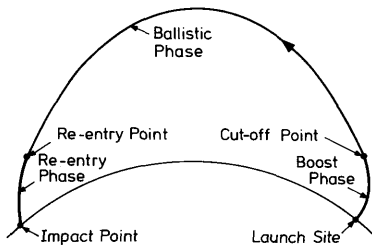


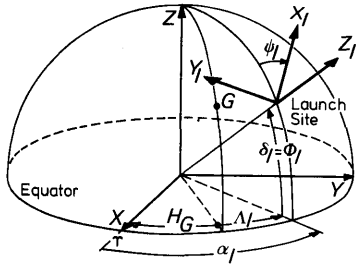
Fig. 13.1 Ballistic missile trajectory

1. The boost phase in which the vehicle is boosted by one or more rocket stages through the atmosphere until final shut-down or cut-off. Concerning guidance, which we will not discuss, the boost phase can be subdivided into an *open-loop phase* and a *closed-loop*, or *guidance phase*. The open-loop phase is pre-programmed and consists of a vertical lift-off, during which the rocket is rolled such that the thrust vector plane coincides with the desired plane of motion, followed by a pitch-over and gravity turn. The subsequent guidance phase is characterized by the computation of steering commands from the vehicle's actual location and velocity and the coordinates of the desired impact point. If at shut-down the atmospheric drag cannot be neglected with respect to the gravitational force, a subsequent atmospheric ascent phase follows the boost phase.
2. The ballistic phase covering the major part of the range and at the end of which the vehicle enters the atmosphere.
3. The re-entry phase is the subsequent passage downwards through the atmosphere until impact at the surface of the Earth.

13.1 The boost phase

As the total flight of an ICBM is of relatively short duration, about 30 minutes, the motion of the Earth about the Sun can be neglected and a geocentric non-rotating reference system will constitute a quasi-inertial frame for describing the motion. The main reference system we will use throughout this chapter will be the *geocentric equatorial mean-of-launch-date reference system*, with the *X-axis* pointing towards the *mean vernal equinox of date* (Section 2.3.6). With respect to this frame, the position of the launch site at launch time t_l is determined by the radius, r_l , the declination, δ_l , and the right ascension, α_l (Fig. 13.2). If Λ_l and Φ_l are known geographic longitude and geocentric latitude of the launch site respectively, and h_l is the altitude of the launch site, then we have approximately

$$r_l = R + h_l, \quad (13.1-1)$$

**Fig. 13.2** The launch site coordinate system

where R is the local radius of the Standard Ellipsoid, discussed in Section 2.5.1, and, according to Section 2.3.4,

$$\alpha_l = H_{G_0} + \omega_e t_l + \Lambda_l, \quad (13.1-2a)$$

$$\delta_l = \Phi_l, \quad (13.1-2b)$$

where H_{G_0} is the Greenwich hour angle of the vernal equinox at 0^h U.T. of the day of launch and ω_e is the angular velocity of the Earth. The value of H_{G_0} can be found in Reference [1].

For a description of the boost phase we introduce an *inertial launch-site coordinate system* as shown in Fig. 13.2. The origin of this system coincides with the launch site at the time of launch. The positive Z_l -axis points in outward radial direction while the X_lY_l -plane is defined as the plane normal to the local radius vector. The X_l -axis is pointing along the downrange heading, thus making an angle ψ_l (the launch azimuth or heading) with the local north direction. The Y_l -axis, finally, completes the right-handed orthogonal frame. This launch site reference system is obtained from the geocentric equatorial system by an Euler rotation about respectively the Z , the X - and the Z -axis, the Euler angles being $90^\circ + \alpha_l$, $90^\circ - \delta_l$ and $90^\circ - \psi_l$. Let \mathbf{U} be a vector with components U_x , U_y and U_z with respect to the geocentric equatorial frame, and components U_{x_l} , U_{y_l} and U_{z_l} with respect to the launch site frame, then the rotation between both sets of components is given by

$$(U_x, U_y, U_z) = (U_{x_l}, U_{y_l}, U_{z_l}) \mathbf{A}_l, \quad (13.1-3a)$$

where \mathbf{A}_l is the Euler rotation matrix:

$$\mathbf{A}_l = \begin{bmatrix} -S\alpha_l S\psi_l - C\alpha_l S \delta_l C\psi_l & C\alpha_l S\psi_l - S\alpha_l S \delta_l C\psi_l & C \delta_l C\psi_l \\ S\alpha_l C\psi_l - C\alpha_l S \delta_l S\psi_l & -C\alpha_l C\psi_l - S\alpha_l S \delta_l S\psi_l & C \delta_l S\psi_l \\ C\alpha_l C \delta_l & S\alpha_l C \delta_l & S \delta_l \end{bmatrix}, \quad (13.1-3b)$$

and $S\alpha_l = \sin \alpha_l$, $C\alpha_l = \cos \alpha_l$, etc.

As range and altitude covered during the boost phase are small as

compared to the radius of the Earth, the Earth may be considered flat during this phase. Neglecting for a moment the rotation of the Earth, the motion will be two-dimensional and the trajectory will lie in the X_lZ_l -plane of the launch site coordinate system. In Chapters 11 and 12 methods are discussed to determine two-dimensional powered flight trajectories in a homogeneous gravitational field, so we can use these theories to determine the boost phase.

Owing to the rotation of the Earth the launch site has an eastward velocity $\omega_e r_l \cos \delta_l$ with respect to inertial space. This eastward velocity can be resolved into an initial down-range velocity and an initial cross-range velocity along the X_l - and Y_l -axes respectively:

$$V_{X_l}(t_l) = \omega_e r_l \cos \delta_l \sin \psi_l, \quad (13.1-4a)$$

$$V_{Y_l}(t_l) = -\omega_e r_l \cos \delta_l \cos \psi_l. \quad (13.1-4b)$$

The initial down-range rate does not affect the two-dimensionality of the motion and therefore can easily be incorporated into the two-dimensional theories of powered flight trajectories by adjusting the initial conditions. Owing to the initial cross-range rate $V_{Y_l}(t_l)$, the trajectory cannot be planar anymore for launches neither due east nor due west. The main effect of this initial cross-range rate is a change of the effective firing azimuth. Therefore, injection azimuth, longitude and latitude will differ from the corresponding quantities as determined with the assumption that the Earth is not rotating. A simple analytic method to include the initial cross-range velocity in the analysis of the powered phase is given by Kohlhase [2]. Once the two-dimensional powered flight trajectory is determined, his method enables us to determine the necessary corrections in the shut-down conditions to account for the initial cross-range velocity. Thus, with this method it is possible to determine the shut-down or *injection state* at time t_l given by (X_l, Y_l, Z_l) and $(V_{X_l}, V_{Y_l}, V_{Z_l})$ with respect to the launch site reference system. The injection state with respect to the geocentric equatorial system may be found by applying Eq. (13.1-3a):

$$(V_{X_l}, V_{Y_l}, V_{Z_l}) = (V_{X_l}, V_{Y_l}, V_{Z_l}) \mathbf{A}_l, \quad (13.1-5a)$$

$$(X_l, Y_l, Z_l) = r_l (\cos \delta_l \cos \alpha_l, \cos \delta_l \sin \alpha_l \sin \delta_l) + (X_l, Y_l, Z_l) \mathbf{A}_l. \quad (13.1-5b)$$

As it is customary to express the injection conditions in radius, right ascension, declination, speed, azimuth and flight path angle, we will derive expressions for these quantities. Clearly the injection radius is given by

$$r_l = \sqrt{X_l^2 + Y_l^2 + Z_l^2}, \quad (13.1-6a)$$

while declination and right ascension follow from

$$\sin \delta_i = Z_i/r_i; \quad -90^\circ \leq \delta_i \leq 90^\circ, \quad (13.1-6b)$$

$$\begin{aligned} \cos \alpha_i &= X_i/(r_i \cos \delta_i); \\ \sin \alpha_i &= Y_i/(r_i \cos \delta_i); \end{aligned} \quad 0^\circ \leq \alpha_i \leq 360^\circ. \quad (13.1-6c)$$

the injection velocity is

$$V_i = \sqrt{V_{X_i}^2 + V_{Y_i}^2 + V_{Z_i}^2}. \quad (13.1-7)$$

To determine azimuth and flight path angle we introduce the vectors \mathbf{e}_{V_i} and \mathbf{e}_r in the direction of injection velocity and radius respectively:

$$\mathbf{e}_{V_i} = (V_{X_i} \mathbf{e}_X + V_{Y_i} \mathbf{e}_Y + V_{Z_i} \mathbf{e}_Z)/V_i, \quad (13.1-8a)$$

$$\mathbf{e}_r = (X_i \mathbf{e}_X + Y_i \mathbf{e}_Y + Z_i \mathbf{e}_Z)/r_i, \quad (13.1-8b)$$

where \mathbf{e}_X , \mathbf{e}_Y and \mathbf{e}_Z are the unit vectors along the X , Y and Z -axis respectively. Then the flight path angle is determined by

$$\sin \gamma_i = \mathbf{e}_{V_i} \cdot \mathbf{e}_r; \quad -90^\circ \leq \gamma_i \leq 90^\circ. \quad (13.1-9)$$

The unit vector lying in the horizontal plane at injection and pointing along the downrange heading is

$$\mathbf{e}_{VH_i} = (\mathbf{e}_{V_i} - \mathbf{e}_r \sin \gamma_i)/\cos \gamma_i, \quad (13.1-10)$$

and the injection azimuth is found from

$$\cos \psi_i = \mathbf{e}_{VH_i} \cdot \mathbf{e}_{N_i}; \quad 0^\circ \leq \psi_i \leq 360^\circ, \quad (13.1-11)$$

$$\sin \psi_i = \mathbf{e}_{VH_i} \cdot \mathbf{e}_{E_i};$$

where \mathbf{e}_{N_i} and \mathbf{e}_{E_i} are unit vectors lying in the horizontal plane at injection, pointing due north and due east respectively. From Eqs. (13.1-3) it can easily be derived that

$$\mathbf{e}_{N_i} = -\sin \delta_i \cos \alpha_i \mathbf{e}_X - \sin \delta_i \sin \alpha_i \mathbf{e}_Y + \cos \delta_i \mathbf{e}_Z, \quad (13.1-12a)$$

$$\mathbf{e}_{E_i} = -\sin \alpha_i \mathbf{e}_X + \cos \alpha_i \mathbf{e}_Y. \quad (13.1-12b)$$

We now have determined completely the shut-down conditions, which are the injection conditions for the ballistic phase which we will discuss next.

13.2 The ballistic phase

To determine the ballistic or free-fall trajectory, we will assume that the Earth is spherical and has a central inverse-square force field. Effects of the asphericity of the Earth will be discussed in Section 13.4.2. We further assume that the only force acting during the ballistic phase is the gravitational force of the Earth, neglecting attractions of Sun and Moon and aerodynamic forces.

As the motion is assumed to take place in a central inverse-square force field, the trajectory will be a Keplerian trajectory, i.e. it will lie in a single plane determined by declination, right ascension and azimuth at injection and it will be a conic section. Basic properties of Keplerian trajectories are discussed in Section 3.6, while Chapter 16 discusses their properties in more detail. We will use some results of Chapter 16 here.

13.2.1 The orientation of the trajectory plane

According to Section 16.5, the orientation of the trajectory plane is usually defined by two angles (Fig. 13.3), the *right ascension of the ascending node*, Ω , and the *inclination*, i .

In this section, we will derive expressions for Ω and i as a function of α_i , δ_i and ψ_i . As the unit vectors along velocity and radius vector at injection, \mathbf{e}_{V_i} and \mathbf{e}_r , make an angle ($90^\circ - \gamma_i$), the unit vector in the direction of the angular momentum is

$$\mathbf{e}_H = \frac{\mathbf{e}_r \times \mathbf{e}_{V_i}}{\cos \gamma_i}. \quad (13.2-1)$$

Resolving \mathbf{e}_{V_i} in outward radial direction and in two horizontal directions, one due north and one due east, we may write

$$\mathbf{e}_{V_i} = \sin \gamma_i \mathbf{e}_r + \cos \gamma_i \cos \psi_i \mathbf{e}_{N_i} + \cos \gamma_i \sin \psi_i \mathbf{e}_{E_i}, \quad (13.2-2)$$

where \mathbf{e}_{N_i} and \mathbf{e}_{E_i} are given in Eqs. (13.1-12). As \mathbf{e}_{E_i} , \mathbf{e}_{N_i} and \mathbf{e}_r form an orthogonal triad, substitution of Eq. (13.2-2) into Eq. (13.2-1) yields

$$\mathbf{e}_H = \sin \psi_i \mathbf{e}_{N_i} - \cos \psi_i \mathbf{e}_{E_i}. \quad (13.2-3)$$

Substitution of Eqs. (13.1-12) into Eq. (13.2-3) leads to

$$\begin{aligned} \mathbf{e}_H = & (\cos \psi_i \sin \alpha_i - \sin \psi_i \sin \delta_i \cos \alpha_i) \mathbf{e}_X - (\cos \psi_i \cos \alpha_i + \\ & + \sin \psi_i \sin \delta_i \sin \alpha_i) \mathbf{e}_Y + \sin \psi_i \cos \delta_i \mathbf{e}_Z. \end{aligned} \quad (13.2-4)$$

As the inclination is defined as the angle between \mathbf{e}_H and \mathbf{e}_Z (Section 16.5), we find

$$\cos i = \mathbf{e}_H \cdot \mathbf{e}_Z = \sin \psi_i \cos \delta_i; \quad 0 \leq i \leq 180^\circ. \quad (13.2-5)$$

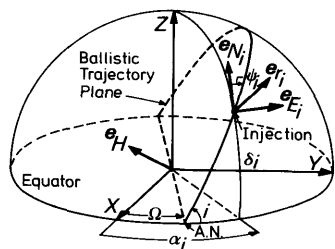


Fig. 13.3 The orientation of the trajectory plane

The unit vector from the center of the Earth to the ascending node, \mathbf{e}_{AN} , lies both in the orbital plane and in the equatorial plane and therefore is normal to \mathbf{e}_H and \mathbf{e}_Z . As the angle between \mathbf{e}_H and \mathbf{e}_Z is i , we have

$$\mathbf{e}_{AN} = \frac{\mathbf{e}_Z \times \mathbf{e}_H}{\sin i}. \quad (13.2-6)$$

Substitution of Eq. (13.2-4) into Eq. (13.2-6) yields

$$\begin{aligned} \mathbf{e}_{AN} = & \frac{\cos \psi_i \cos \alpha_i + \sin \psi_i \sin \delta_i \sin \alpha_i}{\sin i} \mathbf{e}_X + \\ & + \frac{\cos \psi_i \sin \alpha_i - \sin \psi_i \sin \delta_i \cos \alpha_i}{\sin i} \mathbf{e}_Y. \end{aligned} \quad (13.2-7)$$

As Ω is the angle between \mathbf{e}_{AN} and \mathbf{e}_X , we find

$$\cos \Omega = \mathbf{e}_{AN} \cdot \mathbf{e}_X = \frac{\cos \psi_i \cos \alpha_i + \sin \psi_i \sin \delta_i \sin \alpha_i}{\sin i}, \quad (13.2-8a)$$

$$\sin \Omega = \mathbf{e}_{AN} \cdot \mathbf{e}_Y = \frac{\cos \psi_i \sin \alpha_i - \sin \psi_i \sin \delta_i \cos \alpha_i}{\sin i}. \quad (13.2-8b)$$

These equations, together with Eq. (13.2-5), uniquely determine the right ascension of the ascending node. Somewhat simpler expressions for Ω can be obtained by multiplying Eq. (13.2-8a) by $\cos \alpha_i$ and $\sin \alpha_i$ respectively and adding the results, and by multiplying Eq. (13.2-8b) by $\sin \alpha_i$ and $\cos \alpha_i$ respectively and subtracting the results. This leads to the following expressions:

$$\cos(\alpha_i - \Omega) = \cos \psi_i / \sin i, \quad (13.2-9a)$$

$$\sin(\alpha_i - \Omega) = \sin \psi_i \sin \delta_i / \sin i. \quad (13.2-9b)$$

13.2.2 Trajectory geometry

We have seen that the orientation of the trajectory plane, specified by the angles i and Ω is determined by the components α_i , δ_i and ψ_i of the injection state. In this section, we will discuss type and shape of the trajectory and its orientation in the trajectory plane, as is shown in Fig. 13.4. It will turn out that type and shape are completely determined by the quantities r_i , V_i and γ_i , while the orientation of the trajectory in the plane will be dependent on all components of the state vector, except α_i .

From Section 3.6, we know that the polar representation of a Keplerian trajectory is given by

$$r = \frac{p}{1 + e \cos \theta}, \quad (13.2-10)$$

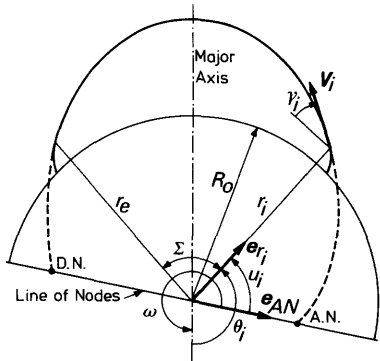


Fig. 13.4 In-plane trajectory geometry

where p and e are semi-latus rectum and eccentricity of the conic, respectively. These parameters completely determine type and shape of the trajectory. They are related to total energy and angular momentum per unit of mass, and therefore to the injection state by Eqs. (3.6-23) and (3.6-24). Introducing the *injection velocity parameter*, k_i defined as

$$k_i = \frac{V_i^2}{V_{ci}^2} = \frac{V_i^2}{\mu/r_i}, \quad (13.2-11)$$

where V_{ci} is the local circular velocity, we can write the equations for p and e as

$$p = \frac{H^2}{\mu} = r_i k_i \cos^2 \gamma_i, \quad (13.2-12a)$$

$$e = \sqrt{\frac{2\mathcal{E}H^2}{\mu^2} + 1} = \sqrt{k_i(k_i - 2)\cos^2 \gamma_i + 1}. \quad (13.2-12b)$$

Here, H and \mathcal{E} are angular momentum and total energy per unit mass (Section 3.6). The injection true anomaly, θ_i , is found by setting $r = r_i$ in Eq. (13.2-10), leading to

$$\theta_i = \arccos \left[\frac{1}{e} \left(\frac{p}{r_i} - 1 \right) \right]. \quad (13.2-13)$$

This equation yields two distinct values for θ_i . According to Eq. (16.2-5), the radial velocity is given by

$$V_r = \frac{\mu}{H} e \sin \theta, \quad (13.2-14)$$

and as at injection $V_r \geq 0$, the true anomaly at injection is given by Eq. (13.2-13) with $0 \leq \theta_i \leq 180^\circ$. Assuming re-entry to start at an altitude h_e or

radius r_e , related by

$$r_e = R_0 + h_e, \quad (13.2-15)$$

we find, by the same reasoning, for the true anomaly at re-entry

$$\theta_e = \arccos \left[\frac{1}{e} \left(\frac{p}{r_e} - 1 \right) \right]; \quad 180^\circ \leq \theta_e \leq 360^\circ. \quad (13.2-16)$$

The *ballistic angular range*, Σ , is then given by

$$\Sigma = \theta_e - \theta_i, \quad (13.2-17)$$

and the *ballistic linear range* measured along a great circle from the sub-vehicle point at injection to the sub-vehicle point at re-entry for a non-rotating Earth is

$$D_b = R_0 \Sigma. \quad (13.2-18)$$

As with the help of Eqs. (13.2-12), p and e can be expressed in the in-plane injection state, the true anomaly at injection and the true anomaly at re-entry, and thus angular and great circle linear range are only a function of V_i , γ_i , r_i and r_e . However, substitution of Eqs. (13.2-13) and (13.2-16) with Eqs. (13.2-12) into Eq. (13.2-17), yields a rather complicated expression for the angular range. A somewhat simpler expression can be obtained from the equation

$$1 + e \cos(\theta_i + \Sigma) = \frac{p}{r_e},$$

or

$$1 + e \cos \theta_i \frac{1 - \tan^2 \Sigma/2}{1 + \tan^2 \Sigma/2} - e \sin \theta_i \frac{2 \tan \Sigma/2}{1 + \tan^2 \Sigma/2} = \frac{p}{r_e}. \quad (13.2-19)$$

Solution of this equation for $\tan \Sigma/2$ and subsequent substitution of the expressions for p , $e \cos \theta_i$ and $e \sin \theta_i$, which may be obtained from Eqs. (13.2-12) to (13.2-14), yields

$$\tan \frac{\Sigma}{2} = \cos \gamma_i \frac{k_i \sin \gamma_i + \sqrt{k_i^2(1 - \rho_i^2 \cos^2 \gamma_i) - 2k_i(1 - \rho_i)}}{2 - k_i \cos^2 \gamma_i(1 + \rho_i)}, \quad (13.2-20)$$

where ρ_i stands for the ratio of injection radius and re-entry radius:

$$\rho_i = \frac{r_i}{r_e} \approx 1 + \frac{h_i - h_e}{R_0}. \quad (13.2-21)$$

The quadratic equation, Eq. (13.2-19), has two solutions. The solution given in Eq. (13.2-20) corresponds to a true anomaly, $\theta_e = \theta_i + \Sigma$, lying between 180° and 360° , which is the interval of the re-entry true anomaly as we know. In Fig. 13.5, the angular range is given as a function of ρ_i for some values of γ_i and for $k_i = 0.6$ and 0.9 . This figure shows that as γ_i increases,

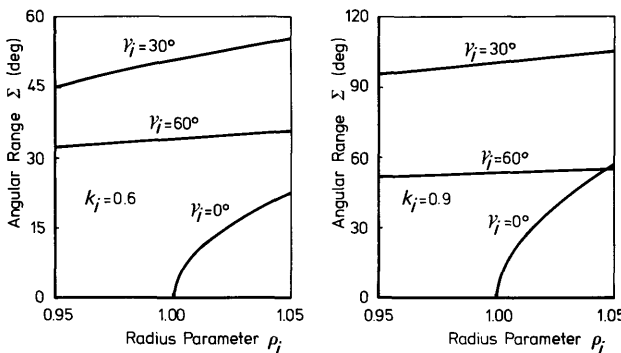


Fig. 13.5 The influence of the ratio of injection and re-entry radius, ρ_i , and flight path angle, γ_i , on the angular range

the influence of ρ_i on the angular range decreases. For injection flight path angles greater than about 30° , the angular range is an almost linear function of ρ_i .

The re-entry conditions, i.e. velocity, V_e , and flight path angle, γ_e , which are required to determine the re-entry trajectory, follow from the equations for the conservation of energy and angular momentum

$$V_e = \sqrt{V_i^2 - 2 V_{c_i}^2 \left(1 - \frac{r_i}{r_e}\right)} = V_{c_i} \sqrt{k_i - 2(1 - \rho_i)}, \quad (13.2-22a)$$

$$\cos \gamma_e = \frac{r_i}{r_e} \frac{V_i}{V_e} \cos \gamma_i = \sqrt{\frac{k_i}{k_i - 2(1 - \rho_i)}} \rho_i \cos \gamma_i \quad (13.2-22b)$$

The semi-major axis of the conic follows from

$$a = -\frac{\mu}{2\mathcal{E}} = r_i \frac{V_{c_i}^2}{2V_{c_i}^2 - V_i^2} = \frac{r_i}{2 - k_i}, \quad (13.2-23a)$$

while apogee radius and apogee altitude can be determined with

$$r_a = a(1 + e) = \frac{r_i}{2 - k_i} [1 + \sqrt{k_i(k_i - 2) \cos^2 \gamma_i + 1}], \quad (13.2-23b)$$

$$h_a = r_a - R_0. \quad (13.2-23c)$$

As, in general, the difference between injection and re-entry altitude is small as compared to the Earth's radius, a good approximation of ballistic range angle and re-entry conditions is obtained by setting $\rho_i = 1$, i.e. $r_i = r_e$. Then the expressions simplify, facilitating the analysis. From Eq. (13.2-20) we find for the range angle

$$\tan \frac{\Sigma}{2} = \frac{k_i \sin \gamma_i \cos \gamma_i}{1 - k_i \cos^2 \gamma_i}. \quad (13.2-24)$$

This relation is depicted in Fig. 13.6. This figure shows that for $k_i < 1$, i.e. injection velocity less than circular velocity, there is an optimum value of the flight path angle γ_i , yielding maximum range. For $k_i = 1$, Eq. (13.2-24) simplifies to

$$\tan \frac{\Sigma}{2} = \cot \gamma_i$$

or

$$\Sigma = \pi - 2\gamma_i \quad (13.2-25)$$

and the range decreases linearly with flight path angle, having a maximum for horizontal injection. As in this case the trajectory will be a circle, horizontal injection does not lead to a useful trajectory for a ballistic missile. For $k_i > 1$, every range angle between 0° and 360° is possible. However, for ranges larger than 180° it is of course more economic to launch in the opposite direction, at least, if we neglect the effect of the rotation of the Earth and in particular the initial eastward velocity of the launch site. If $k_i \geq 2$, the injection velocity exceeds or equals the local escape velocity and the vehicle will not return to the surface of the Earth anymore.

Given the injection conditions, k_i and γ_i , the range can be determined with Eq. (13.2-24). In general, the angular range is known, at least approximately, and the injection conditions have to be determined. Solving Eq. (13.2-24) for $\cos^2 \gamma_i$ leads to

$$\cos^2 \gamma_i = \frac{1}{2} \cos^2 \frac{\Sigma}{2} \left[1 \pm \sqrt{1 - 4 \frac{1-k_i}{k_i^2} \tan^2 \frac{\Sigma}{2}} \right] + \frac{1}{k_i} \sin^2 \frac{\Sigma}{2}. \quad (13.2-26)$$

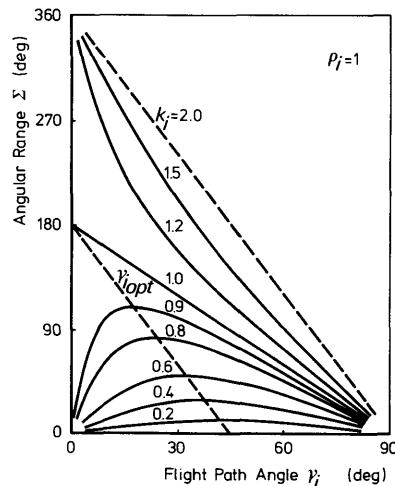


Fig. 13.6 The angular range as a function of injection flight path angle and injection velocity parameter for equal re-entry and injection radii, i.e. $\rho_i = 1$

For a known range angle and a given value of k_i , which is practically completely determined by the missile configuration used, the required injection flight path angle is found from Eq. (13.2-26). As at injection $0 \leq \gamma_i \leq 90^\circ$, this equation yields, for $k_i < 1$, at most two distinct real roots for γ_i , depending on the value of Σ . For small ranges, the discriminant in Eq. (13.2-26) will be positive and two distinct flight path angles will be found, the smaller one yielding the *low trajectory*, the larger one the *high trajectory*. Increasing the range will decrease the discriminant until it vanishes for

$$\tan \frac{\Sigma}{2} = \frac{k_i}{2\sqrt{1-k_i}}. \quad (13.2-27)$$

In that case there is just one flight path angle for the given range, or, in other words, the range is the maximum that can be covered for the given value of k_i . We will discuss these optimal trajectories in more detail in Section 13.2.4. Still further increasing the range makes the discriminant negative and no real solutions exist for γ_i .

If $k_i > 1$, Eq. (13.2-26) has two solutions: one with a plus sign before the square root yielding $k_i \cos^2 \gamma_i > 1$, and one with a minus sign, yielding $k_i \cos^2 \gamma_i < 1$. According to Eq. (13.2-24) the first solution must be used if $\Sigma > 180^\circ$, while, if $\Sigma < 180^\circ$ the second solution must be taken.

As to re-entry conditions, it is immediately clear from Eqs. (13.2-22) that if injection and re-entry altitude are equal, the re-entry velocity equals the injection velocity, while the flight path angle at re-entry is the opposite of the injection flight path angle.

13.2.3 A graphical technique

We will describe a graphical technique to determine ballistic trajectories. This technique can help to get a better insight into the problem, and as we will see in Section 13.2.4, the equations for optimal flights can be derived easily with this method.

Let P_i and P_e in Fig. 13.7 be the injection point and re-entry point respectively, and let the injection velocity be given. Using Eq. (13.2-23a), the semi-major axis of the conic through P_i and P_e can be determined. An important property of an ellipse is that the sum of the distances from any point on the ellipse to the two foci is constant and equals $2a$. As one focus is the center of the Earth, F_1 , the other focus F_2 (empty or vacant focus) must lie on a circle with P_i as center and radius $2a - r_i$, but also on a circle with P_e as center and radius $2a - r_e$. We can distinguish three possibilities concerning these two circles:

1. The two circles do not intersect, which means that their radii, and consequently the semi-major axis and the injection velocity are too small for the given range. Increasing the injection velocity will increase the semi-major

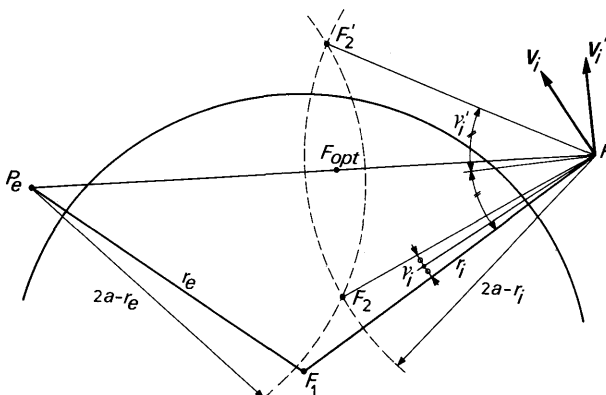


Fig. 13.7 A graphical determination of the injection velocity and flight path angle

axis and the radii of the circles, until the injection velocity is just large enough for the given range. In that case:

2. The two circles touch on the chord P_iP_e , which corresponds to the *minimum injection velocity trajectory*, to be discussed in the next section. Further enlarging the injection velocity will cause:
3. The two circles to intersect each other in two distinct points F_2 and F'_2 .

This case is depicted in Fig. 13.7. Therefore, in this case we find two possible positions for the empty focus and consequently two possible trajectories connecting P_i and P_e . Now that we have found the positions of the empty foci we can construct the required direction of the injection velocity, i.e. the flight path angle at injection, and also the flight path angle at re-entry. For this we use another important property of the ellipse, viz. that the tangent to an ellipse is normal to the bisector of the angle formed by the lines connecting the tangency point with the two foci of the ellipse. Thus, construction of the normals to the bisectors of the angles $F_1P_iF_2$ and $F_1P_iF'_2$ yields the two possible directions of the injection velocity.

As for optimal flights the empty focus lies on the chord P_iP_e , we conclude that for injection velocities greater than the minimum injection velocity we find two possible injection flight path angles, one greater than the optimum flight path angle, yielding the high trajectory and one less than the optimum flight path angle, yielding the low trajectory. As follows from Fig. 13.7, the flight path angles equal half the angles $F_1P_iF_2$ and $F_1P_iF'_2$ respectively. So the angle $F'_2P_iF_{opt}$ equals twice the difference between the flight path angle for the high trajectory and the optimum flight path angle. Likewise, the angle $F_2P_iF_{opt}$ equals twice the difference of optimal flight path angle and flight path angle for the low trajectory. As the line $F_2F'_2$ is normal to the chord P_iP_e , the two angles $F_2P_iF_{opt}$ and $F'_2P_iF_{opt}$ are equal, so we conclude

that the low and high flight path angles lie symmetrically with respect to the optimum flight path angle.

We have discussed here the determination of the flight path angle for given injection and re-entry points and given injection velocity. Likewise, it is possible to determine the re-entry point with this graphical method if injection point, injection velocity and flight path angle, and re-entry altitude are given.

13.2.4 Optimal flights

As will be clear from the foregoing discussion, and as can be seen from Figs. 13.5 and 13.6, there is an optimum injection flight path angle, such that the angular range is maximized for given V_i , r_i and r_e , or, equivalently, the injection velocity is minimized for given Σ , r_i and r_e . We will derive the conditions for these optimal flights using the graphical method discussed in the foregoing section. The geometry of an optimal flight is depicted in Fig. 13.8. We have seen that for a given range the injection velocity is a minimum if the two circles, with P_i and P_e as center and $2a - r_i$ and $2a - r_e$ as radius, touch. The point of contact, F_{opt} , will lie on the chord joining P_i and P_e . So, for optimal flights

$$a_{min} = \frac{1}{4}(c + r_i + r_e), \quad (13.2-28)$$

where c is the length of the chord P_iP_e , given by

$$c^2 = r_i^2 + r_e^2 - 2r_i r_e \cos \Sigma. \quad (13.2-29)$$

According to Eq. (13.2-23a), the semi-major axis is a function of k_i and r_i . Substitution of Eq. (13.2-23b) and Eq. (13.2-29) into Eq. (13.2-28) yields an equation for the minimum injection velocity ratio, $k_{i\min}$, the solution of which is

$$k_{i\min} = \frac{1 - \rho_i - 2 \sin^2 \Sigma/2 + \sqrt{(1 - \rho_i)^2 + 4\rho_i \sin^2 \Sigma/2}}{\cos^2 \Sigma/2}. \quad (13.2-30)$$

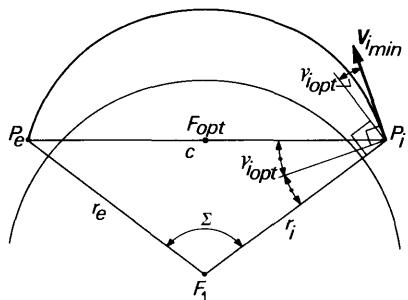


Fig. 13.8 Optimal flight geometry

This relation is depicted in Fig. 13.9a. The corresponding optimal flight path angle is found by realizing that the angle $F_{opt}P_iF_1$ equals twice the flight path angle. Using a property of plane triangles on the triangle $F_1P_iP_e$ we find

$$\tan^2 \gamma_{i_{opt}} = \frac{(r_i + r_e - c)(-r_i + r_e + c)}{(r_i + r_e + c)(r_i - r_e + c)} = \frac{r_e^2 - (r_i - c)^2}{(r_i + c)^2 - r_e^2}. \quad (13.2-31)$$

Substitution of Eq. (13.2-29) for c into Eq. (13.2-31) gives

$$\tan^2 \gamma_{i_{opt}} = \frac{1 - \rho_i - 2 \sin^2 \Sigma/2 + \sqrt{(1 - \rho_i)^2 + 4\rho_i \sin^2 \Sigma/2}}{-1 + \rho_i + 2 \sin^2 \Sigma/2 + \sqrt{(1 - \rho_i)^2 + 4\rho_i \sin^2 \Sigma/2}}. \quad (13.2-32)$$

This relation is depicted in Fig. 13.9b. Therefore, for a given range, Eqs. (13.2-30) and (13.2-32) can be used to determine the optimal injection conditions. Optimal in the sense that for a given value of injection altitude, the injection velocity is minimized. This, of course, also means that the total energy of the trajectory is minimized. Therefore, these trajectories are also called *minimum energy trajectories*. Note, however, that these trajectories are not necessarily optimal in the sense that for a given rocket vehicle the payload is maximized, because we assumed the injection altitude fixed. For the determination of a maximum payload trajectory for a particular rocket, one has to know the characteristics of the powered trajectory, in particular the relations between altitude, velocity and flight path angle. Maximum payload trajectories and minimum injection velocity trajectories will not differ much in general.

For a given injection velocity and radius, the maximum angular range is found by solving Eq. (13.2-30) for Σ . We then find the maximum range that can be reached for a given value of k_i

$$\tan^2 \frac{\Sigma_{max}}{2} = \frac{k_i}{2} \cdot \frac{k_i - 2(1 - \rho_i)}{2 - k_i(1 + \rho_i)}. \quad (13.2-33)$$

Substitution of this value of Σ into Eq. (13.2-32) yields the optimal injection flight path angle as a function of k_i

$$\tan^2 \gamma_{i_{opt}} = \frac{k_i}{2} \cdot \frac{2 - k_i(1 + \rho_i)}{k_i - 2(1 - \rho_i)}. \quad (13.2-34)$$

It follows from Eqs. (13.2-33) and (13.2-34) that for a given injection velocity

$$\tan \frac{\Sigma_{max}}{2} \tan \gamma_{i_{opt}} = \frac{k_i}{2}. \quad (13.2-35)$$

In case re-entry and injection altitudes are the same, the equations for the minimum injection velocity at given range, and maximum range for given

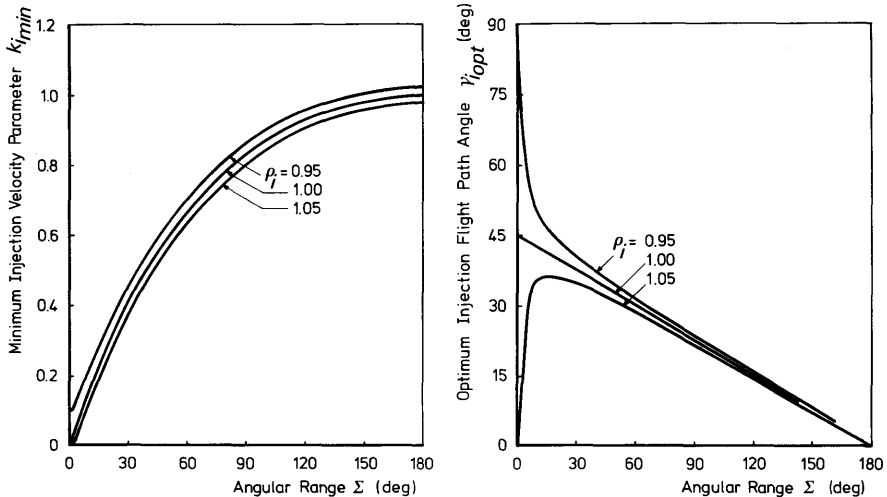


Fig. 13.9 The minimum injection velocity parameter and the optimum injection flight path angle as a function of the angular range

injection velocity and the optimal flight path angle, simplify to

$$k_{i_{min}} = \frac{2 \sin \Sigma/2}{1 + \sin \Sigma/2}, \quad (13.2-36a)$$

$$\tan \gamma_{i_{opt}} = \left[\frac{1 - \sin \Sigma/2}{1 + \sin \Sigma/2} \right]^{1/2}, \quad (13.2-36b)$$

$$\tan \frac{\Sigma_{max}}{2} = \frac{k_i}{2\sqrt{1-k_i}}, \quad (13.2-36c)$$

$$\tan \gamma_{i_{opt}} = \sqrt{1 - k_i}. \quad (13.2-36d)$$

In this case, a simpler expression for the optimum injection flight path angle can be obtained directly. As the sides P_iF_1 and P_eF_1 in the triangle $P_iF_1P_e$ are now equal, and the angle $P_eP_iF_1$ equals $2\gamma_{i_{opt}}$, we find

$$\gamma_{i_{opt}} = \frac{\pi}{4} - \frac{\Sigma}{4}. \quad (13.2-36e)$$

As the reader may verify himself, this result corresponds with Eq. (13.2-36b). We directly see that for very small ranges, i.e. $\Sigma \rightarrow 0$, the optimum injection flight path angle approaches 45° , the well-known 'flat Earth' result. By solving Eq. (13.2-36d) for k_i and substitution of the result into Eq. (13.2-12b) we find another interesting property of the optimal trajectory with equal injection and re-entry altitudes, viz.

$$e = \tan \gamma_{i_{opt}}. \quad (13.2-37)$$

13.2.5 Time of flight

To determine the time of flight of the ballistic phase we could use Eq. (16.3-11), i.e. Kepler's equation. This, however, would force us to determine the *eccentric anomalies* at injection and re-entry. For our purpose there is a more convenient expression for the time of flight along a conic arc between two points, known as *Lambert's equation* or *Lambert's theorem*. This theorem, originally discovered by Lambert and subsequently proved analytically by Lagrange, states that the time to traverse a Keplerian arc depends only upon the semi-major axis, the sum of the distances from the initial and final point of the arc to the center of force, and the length of the chord joining initial and final point. Lambert's equation also plays an important role in the analysis of interplanetary trajectories which will be discussed in Chapter 19. We will derive Lambert's equations for elliptic motion only.

Lambert's equation. Let P_1 be the initial point and P_2 be the final point of an elliptic arc and suppose that radius vector and eccentric anomaly of P_1 and P_2 are \mathbf{r}_1 and E_1 , and \mathbf{r}_2 and E_2 respectively. Then, according to Eqs. (16.3-9) to (16.3-11), the time of flight from P_1 to P_2 along the elliptic arc is given by

$$t_f = \sqrt{\frac{a^3}{\mu}} [E_2 - E_1 - e(\sin E_2 - \sin E_1)], \quad (13.2-38a)$$

or

$$t_f = \sqrt{\frac{a^3}{\mu}} [E_2 - E_1 - 2e \cos \frac{1}{2}(E_2 + E_1) \sin \frac{1}{2}(E_2 - E_1)]. \quad (13.2-38b)$$

We now introduce the variables f and g , defined by

$$\cos \frac{1}{2}(f+g) = e \cos \frac{1}{2}(E_2 + E_1); \quad 0 \leq f+g < 2\pi, \quad (13.2-39a)$$

$$f-g = E_2 - E_1; \quad 0 \leq f-g < 2\pi. \quad (13.2-39b)$$

Substitution of Eqs. (13.2-39) into Eq. (13.2-38b) leads to

$$t_f = \sqrt{\frac{a^3}{\mu}} [f - g - 2 \cos \frac{1}{2}(f+g) \sin \frac{1}{2}(f-g)],$$

or

$$t_f = \sqrt{\frac{a^3}{\mu}} [(f - \sin f) - (g - \sin g)]. \quad (13.2-40)$$

We now have to express f and g in a , c and $r_1 + r_2$. Therefore let e_P be the

unit vector pointing towards pericenter and \mathbf{e}_Q the unit vector in the plane of motion 90° ahead of \mathbf{e}_P in the direction of motion. Then

$$\mathbf{r}_1 = r_1 \cos \theta_1 \mathbf{e}_P + r_1 \sin \theta_1 \mathbf{e}_Q, \quad (13.2-41a)$$

where θ_1 is the true anomaly of P_1 . According to Eqs. (16.3-4) and (16.3-5), Eq. (13.2-41a) can also be written as

$$\mathbf{r}_1 = a(\cos E_1 - e) \mathbf{e}_P + a\sqrt{1-e^2} \sin E_1 \mathbf{e}_Q. \quad (13.2-41b)$$

A similar expression may be obtained for the position vector of P_2 :

$$\mathbf{r}_2 = a(\cos E_2 - e) \mathbf{e}_P + a\sqrt{1-e^2} \sin E_2 \mathbf{e}_Q. \quad (13.2-41c)$$

The length of the chord c joining P_1 and P_2 can be found from

$$c^2 = (\mathbf{r}_1 - \mathbf{r}_2) \cdot (\mathbf{r}_1 - \mathbf{r}_2). \quad (13.2-42)$$

Substitution of Eqs. (13.2-41b) and (13.2-41c) into Eq. (13.2-42) yields

$$c^2 = 4a^2[1 - e^2 \cos^2 \frac{1}{2}(E_2 + E_1)] \sin^2 \frac{1}{2}(E_2 - E_1),$$

or, using Eqs. (13.2-39) and the appropriate trigonometric identities,

$$c = a(\cos g - \cos f). \quad (13.2-43)$$

According to Eq. (16.3-3), we have

$$\begin{aligned} \mathbf{r}_1 + \mathbf{r}_2 &= 2a[1 - \frac{1}{2}e(\cos E_1 + \cos E_2)] = \\ &= 2a[1 - e \cos \frac{1}{2}(E_2 + E_1) \cos \frac{1}{2}(E_2 - E_1)]. \end{aligned} \quad (13.2-44)$$

Substitution of Eqs. (13.2-39) into Eq. (13.2-44) and some trigonometry leads to

$$\mathbf{r}_1 + \mathbf{r}_2 = 2a[1 - \frac{1}{2}(\cos f + \cos g)]. \quad (13.2-45)$$

Solving Eqs. (13.2-43) and (13.2-45) for $\cos f$ and $\cos g$ yields

$$\cos f = 1 - \frac{c + \mathbf{r}_1 + \mathbf{r}_2}{2a}, \quad (13.2-46a)$$

$$\cos g = 1 + \frac{c - \mathbf{r}_1 - \mathbf{r}_2}{2a}, \quad (13.2-46b)$$

or

$$\sin^2 f/2 = \frac{c + \mathbf{r}_1 + \mathbf{r}_2}{4a}, \quad (13.2-47a)$$

$$\sin^2 g/2 = \frac{\mathbf{r}_1 + \mathbf{r}_2 - c}{4a}. \quad (13.2-47b)$$

According to Eq. (13.2-28), the minimum semi-major axis of a conic

through P_1 and P_2 is

$$a_{\min} = \frac{1}{4}(c + r_1 + r_2). \quad (13.2-48a)$$

Further, define a parameter K as

$$K = 1 - \frac{c}{2a_{\min}} = \frac{r_1 + r_2 - c}{r_1 + r_2 + c}. \quad (13.2-48b)$$

Then the Eqs. (13.2-47) can be written as

$$\sin^2 f/2 = \frac{a_{\min}}{a}, \quad (13.2-49a)$$

$$\sin^2 g/2 = K \frac{a_{\min}}{a}. \quad (13.2-49b)$$

We now have derived Lambert's equation for elliptic motion, given by Eq. (13.2-40) together with Eqs. (13.2-48) and (13.2-49).

However, it is evident that Eqs. (13.2-49) do not give f and g without ambiguity. From the inequalities in Eqs. (13.2-39), we conclude that $0 \leq f < 2\pi$ and $-\pi \leq g < \pi$. Now let S be the point where the line through P_1 and P_2 cuts the major axis (Fig. 13.10). As the position vector of an arbitrary point on the line through P_1 and P_2 with respect to the center O of the ellipse, is given by

$$\mathbf{r}_c = eae_P + \lambda \mathbf{r}_1 + (1 - \lambda) \mathbf{r}_2; \quad -\infty < \lambda < \infty, \quad (13.2-50)$$

the distance s between O and S , measured positive from O in the direction of pericenter can be determined from the equation

$$\mathbf{r}_c = s \mathbf{e}_P. \quad (13.2-51)$$

Substitution of Eq. (13.2-50) with Eqs. (13.2-41b) and (13.2-41c) into

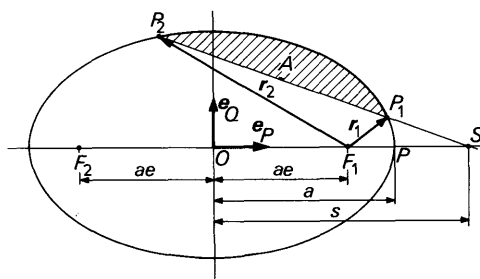


Fig. 13.10 Determination of four different cases for Lambert's equation for elliptic motion

(13.2-51), and solution of the resulting equation for λ and s yields

$$\lambda = \frac{\sin E_2}{\sin E_2 - \sin E_1}, \quad (13.2-52a)$$

$$s = a \frac{\sin(E_2 - E_1)}{\sin E_2 - \sin E_1} = a \frac{\cos \frac{1}{2}(E_2 - E_1)}{\cos \frac{1}{2}(E_2 + E_1)}. \quad (13.2-52b)$$

We then find for the distances F_1S , F_2S and PS , measured positive to the right in Fig. 13.10:

$$F_1S = s - ae = a \frac{\cos \frac{1}{2}(E_2 - E_1) - e \cos \frac{1}{2}(E_2 + E_1)}{\cos \frac{1}{2}(E_2 + E_1)}, \quad (13.2-53a)$$

$$F_2S = s + ae = a \frac{\cos \frac{1}{2}(E_2 - E_1) + e \cos \frac{1}{2}(E_2 + E_1)}{\cos \frac{1}{2}(E_2 + E_1)}, \quad (13.2-53b)$$

$$PS = s - a = a \frac{\cos \frac{1}{2}(E_2 - E_1) - \cos \frac{1}{2}(E_2 + E_1)}{\cos \frac{1}{2}(E_2 + E_1)}, \quad (13.2-53c)$$

or using Eqs. (13.2-39) and the appropriate trigonometric formulae we find from Eqs. (13.2-53)

$$\frac{F_1S}{PS} = \frac{\sin \frac{1}{2}f \sin \frac{1}{2}g}{\sin \frac{1}{2}E_1 \sin \frac{1}{2}E_2}, \quad (13.2-54a)$$

$$\frac{F_2S}{PS} = \frac{\cos \frac{1}{2}f \cos \frac{1}{2}g}{\sin \frac{1}{2}E_1 \sin \frac{1}{2}E_2}. \quad (13.2-54b)$$

Now $\sin \frac{1}{2}f$ and $\cos \frac{1}{2}g$ are always positive while, as we may take E_1 between 0 and 360° , $\sin \frac{1}{2}E_1$ is positive too. We may distinguish four cases. Let A be the area bounded by the arc P_1P_2 and the chord joining P_1 and P_2 :

- (a) If this area includes neither F_1 , nor F_2 ; $\sin \frac{1}{2}E_2 > 0$, $\frac{F_1S}{PS} > 0$ and $\frac{F_2S}{PS} > 0$, and so for this case we find

$$\sin \frac{1}{2}g > 0, \quad \cos \frac{1}{2}f > 0. \quad (13.2-55a)$$

- (b) If the area A does not include F_1 , but includes F_2 ; $\sin \frac{1}{2}E_2 > 0$, $\frac{F_1S}{PS} > 0$ and $\frac{F_2S}{PS} < 0$, and we find

$$\sin \frac{1}{2}g > 0, \quad \cos \frac{1}{2}f < 0. \quad (13.2-55b)$$

- (c) If the area A includes F_1 , but not F_2 ; $\sin \frac{1}{2}E_2 < 0$, $\frac{F_1S}{PS} > 0$ and $\frac{F_2S}{PS} < 0$,

and consequently

$$\sin \frac{1}{2}g < 0, \quad \cos \frac{1}{2}f > 0. \quad (13.2-55c)$$

(d) If the area A includes both foci; $\sin \frac{1}{2}E_2 < 0$, $\frac{F_1 S}{PS} > 0$ and $\frac{F_2 S}{PS} > 0$, and we find

$$\sin \frac{1}{2}g < 0, \quad \cos \frac{1}{2}f < 0. \quad (13.2-55d)$$

Now define the parameters α and β as

$$\alpha = 2 \arcsin \sqrt{\frac{a_{\min}}{a}}; \quad 0 \leq \alpha \leq \pi, \quad (13.2-56a)$$

$$\beta = 2 \arcsin \sqrt{K \frac{a_{\min}}{a}}; \quad 0 \leq \beta \leq \pi. \quad (13.2-56b)$$

Then, according to Eqs. (13.2-49),

$$f = \alpha \quad \text{or} \quad f = 2\pi - \alpha, \quad (13.2-57a)$$

$$g = \beta \quad \text{or} \quad g = -\beta. \quad (13.2-57b)$$

Now the time of flight for the four different cases follows from Eq. (13.2-40) together with Eqs. (13.2-55) and (13.2-57)

(a) A does not include F_1 and F_2 ,

$$t_f = \sqrt{\frac{a^3}{\mu}} [(\alpha - \sin \alpha) - (\beta - \sin \beta)]. \quad (13.2-58a)$$

(b) A does not include F_1 , but includes F_2 ,

$$t_f = \sqrt{\frac{a^3}{\mu}} [2\pi - (\alpha - \sin \alpha) - (\beta - \sin \beta)]. \quad (13.2-58b)$$

(c) A includes F_1 , but not F_2 ,

$$t_f = \sqrt{\frac{a^3}{\mu}} [(\alpha - \sin \alpha) + (\beta - \sin \beta)]. \quad (13.2-58c)$$

(d) A includes both F_1 and F_2 ,

$$t_f = \sqrt{\frac{a^3}{\mu}} [2\pi - (\alpha - \sin \alpha) + (\beta - \sin \beta)]. \quad (13.2-58d)$$

The cases a and b correspond with an angular range less than 180° , while c and d correspond with an angular range greater than 180° .

For parabolic and hyperbolic motion similar equations may be derived. For this is referred to Plummer [3] or Battin [4].

In general, for a ballistic missile the range angle is less than 180° . According to Fig. 13.7, Eq. (13.2-58a) has to be used for low trajectories, while Eq. (13.2-58b) has to be used for high trajectories.

For optimal trajectories: $a = a_{min}$, and according to Eqs. (13.2-56), $\alpha = \pi$ and $\beta = 2 \arcsin \sqrt{K}$ and substitution of these values of α and β into Eq. (13.2-58a), or equivalently into Eq. (13.2-58b), yields the flight time along an optimal trajectory

$$t_{f_{opt}} = \sqrt{\frac{a_{min}^3}{\mu}} [\pi - 2 \arcsin \sqrt{K} + 2\sqrt{K}\sqrt{1-K}]. \quad (13.2-59)$$

Using Eqs. (13.2-56), (13.2-58) and (13.2-59) we can now derive expressions for the time of flight from injection to re-entry as a function of range angle, injection radius and velocity, and re-entry radius. The chord, c , may be determined with Eq. (13.2-29) as a function of r_i , r_e and Σ ; the semi-major axis, a , is, according to Eq. (13.2-23a), a function of r_i and k_i only. Therefore, α and β are functions of r_i , r_e , Σ and k_i only and this holds for the time of flight too.

The time-of-flight expressions take a relatively simple form if injection altitude equals the re-entry altitude, which we will assume in the following. In that case

$$c = 2r_i \sin \frac{\Sigma}{2}, \quad (13.2-60a)$$

$$a_{min} = \frac{r_i}{2} \left(1 + \sin \frac{\Sigma}{2}\right), \quad (13.2-60b)$$

$$K = \frac{1 - \sin \Sigma/2}{1 + \sin \Sigma/2} = \tan^2 \left(\frac{\pi}{4} - \frac{\Sigma}{4}\right). \quad (13.2-60c)$$

Now let us first consider optimal trajectories. Substitution of Eqs. (13.2-60) into Eq. (13.2-59) yields the time of flight along a minimum velocity trajectory as a function of angular range only

$$\begin{aligned} t_{f_{opt}} &= \sqrt{\frac{r_i^3}{2\mu}} \left(1 + \sin \frac{\Sigma}{2}\right)^{3/2} \times \\ &\times \left[\frac{\pi}{2} - \arcsin \sqrt{\frac{1 - \sin \Sigma/2}{1 + \sin \Sigma/2}} + \frac{\sqrt{2} \sin \Sigma/2(1 - \sin \Sigma/2)}{1 + \sin \Sigma/2} \right] \end{aligned} \quad (13.2-61a)$$

Using Eqs. (13.2-36), relating range, velocity ratio and flight path angle, we

304 Rocket Propulsion & Spaceflight Dynamics

can express the time of flight in injection velocity or in injection flight path angle:

$$t_{f_{opt}} = \sqrt{\frac{r_i^3}{\mu}} (2 - k_i)^{-3/2} [\pi - 2 \arccos \sqrt{k_i} + 2 \sqrt{k_1(1-k_i)}], \quad (13.2-61b)$$

$$t_{f_{opt}} = \sqrt{\frac{r_i^3}{\mu}} \cos^3 \gamma_i [\pi - \arcsin (\tan \gamma_i) + 2 \tan \gamma_i \sqrt{1 - \tan^2 \gamma_i}]. \quad (13.2-61c)$$

For non-optimal trajectories, the flight time directly follows from Eqs. (13.2-56) and (13.2-58) and the expressions for a , a_{min} and K as given by Eqs. (13.2-23a) and (13.2-60) respectively

$$\alpha = 2 \arcsin \sqrt{\frac{2 - k_i}{2}} \left(1 + \sin \frac{\Sigma}{2} \right); \quad 0 \leq \alpha \leq \pi, \quad (13.2-62a)$$

$$\beta = 2 \arcsin \sqrt{\frac{2 - k_i}{2}} \left(1 - \sin \frac{\Sigma}{2} \right); \quad 0 \leq \beta \leq \pi. \quad (13.2-62b)$$

Then for low trajectories:

$$t_f = \sqrt{\frac{r_i^3}{\mu}} (2 - k_i)^{-3/2} [(\alpha - \sin \alpha) - (\beta - \sin \beta)], \quad (13.2-63a)$$

and for high trajectories:

$$t_f = \sqrt{\frac{r_i^3}{\mu}} (2 - k_i)^{-3/2} [2\pi - (\alpha - \sin \alpha) - (\beta - \sin \beta)]. \quad (13.2-63b)$$

In Fig. 13.11 these flight times, as well as the flight time along an optimal trajectory, are depicted as a function of k_i and Σ . For this figure, the injection altitude, and consequently the re-entry altitude, were taken zero ($r_i = R_0$), which corresponds to a ballistic trajectory from one point on the surface of the Earth to another point on the Earth's spherical surface, starting with an impulsive shot.

13.3 The re-entry phase

Re-entry is an extensive subject in itself and falls beyond the scope of this book. We will therefore confine ourselves to some general remarks on the re-entry phase.

The re-entry phase starts at a hypothetical '*re-entry point*'. From this point on downwards, the aerodynamic forces cannot be neglected anymore with respect to the gravitational forces. The re-entry altitude may be determined by first estimating a re-entry altitude and subsequent determination of the

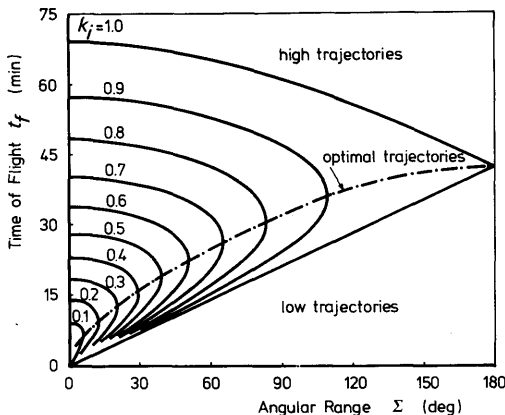


Fig. 13.11 The time of flight for high, optimal and low trajectories as a function of angular range and injection velocity parameter, for zero injection and re-entry altitude

corresponding re-entry velocity and flight path angle with Eqs. (13.2-22). Then the aerodynamic forces can be determined and compared with the gravitational forces. Should the magnitude of the total aerodynamic force be less than the set criterion, for instance 1 percent of the total gravitational force, then the re-entry altitude is estimated too large and a new lower estimate should be made. In general, re-entry altitude lies somewhere between 80 km and 150 km.

For non-maneuvering re-entry vehicles the main aerodynamic force is the drag. For maneuvering re-entry vehicles, which will not be discussed here, lift and side forces, generated for maneuvering, may influence the trajectory substantially. We thus see that for a conventional re-entry vehicle the re-entry trajectory is completely determined by the re-entry conditions, i.e. altitude, velocity and flight path angle at re-entry, and the vehicle's *weight-to-drag ratio*. A more or less exact determination of the re-entry trajectory is then possible by numerical integration of the complete re-entry equations. For preliminary analysis, however, one usually applies more rapid techniques which yield a fairly good approximation of the re-entry trajectory. Rapid analytical techniques for determining re-entry range and time of flight are developed by Moe [5] and Blum [6], for instance. Bate and Johnson [7] present a very accurate and quick method. They express the difference between the *no-drag range* and the *re-entry range* and the difference between *no-drag time of flight* and *re-entry time of flight* as a function of *range coefficients* and *time coefficients*, respectively, and entry conditions. The range and time coefficients, which are a function of the weight-to-drag ratio of the ballistic nose cone, may be obtained from graphs given in their paper. These coefficients were determined by integration of a large number

of re-entry trajectories, which covered ballistic missile ranges from about 1500 km to over 30,000 km and ballistic coefficients from 10 kPa to 70 kPa, i.e. from very blunt heat sink type to extremely sharp ablating type ballistic nose cones. Using their method, the errors for typical ICBM trajectories remain well below 2 km and 4 s, respectively, for range and flight time, so it is possible to obtain a quick and rather good approximation of re-entry range, Σ_e , and re-entry time of flight, t_{f_e} . In the next section, we will therefore assume that Σ_e and t_{f_e} are known.

13.4 The position of the impact point

Once injection conditions are known, the ballistic range and time of flight may be determined with Eqs. (13.2-20) and the formulae given in Section 13.2.5. An approximation of re-entry range and re-entry time of flight may be obtained with one of the techniques referred to in the foregoing section. The *total range angle* from injection to impact, Σ_{tot} , then equals the sum of the ballistic range angle and the re-entry range angle, while the *total time of flight* from injection to impact, $t_{f_{tot}}$, is the sum of ballistic and re-entry flight time.

In this section we will assume Σ_{tot} and $t_{f_{tot}}$ known, as well as the out-of-plane injection conditions, α_i , δ_i and ψ_i , and determine the coordinates of the impact point. We will first assume a spherical Earth, after which we will discuss the determination of the impact point using the ellipsoid model for the Earth.

13.4.1 Spherical Earth

Let \mathbf{e}_{r_i} and \mathbf{e}_{r_f} be the unit vectors from the center of the Earth in the direction of injection and impact respectively:

$$\mathbf{e}_{r_i} = \cos \alpha_i \cos \delta_i \mathbf{e}_X + \sin \alpha_i \cos \delta_i \mathbf{e}_Y + \sin \delta_i \mathbf{e}_Z, \quad (13.4-1a)$$

$$\mathbf{e}_{r_f} = \cos \alpha_f \cos \delta_f \mathbf{e}_X + \sin \alpha_f \cos \delta_f \mathbf{e}_Y + \sin \delta_f \mathbf{e}_Z. \quad (13.4-1b)$$

As the angle between these two vectors is Σ_{tot} and as both vectors are normal to the unit vector in the direction of the angular momentum, \mathbf{e}_H , we have

$$\mathbf{e}_{r_i} \cdot \mathbf{e}_{r_f} = \cos \Sigma_{tot}, \quad (13.4-2a)$$

$$\mathbf{e}_{r_i} \times \mathbf{e}_{r_f} = \mathbf{e}_H \sin \Sigma_{tot}. \quad (13.4-2b)$$

Vectorial multiplication of Eq. (13.4-2b) with \mathbf{e}_{r_i} and subsequent solution for \mathbf{e}_{r_f} leads to

$$\mathbf{e}_{r_f} = \cos \Sigma_{tot} \mathbf{e}_{r_i} - \sin \Sigma_{tot} \mathbf{e}_{r_i} \times \mathbf{e}_H. \quad (13.4-3)$$

Substitution of the expressions for \mathbf{e}_r , \mathbf{e}_r' and \mathbf{e}_H as given in Eqs. (13.4-1) and (13.2-4) into Eq. (13.4-3) leads to the following three component equations:

$$\sin \delta_f = \cos \Sigma_{tot} \sin \delta_i + \sin \Sigma_{tot} \cos \delta_i \cos \psi_i, \quad (13.4-4a)$$

$$\begin{aligned} \cos \delta_f \sin \alpha_f &= \cos \Sigma_{tot} \sin \alpha_i \cos \delta_i \\ &\quad - \sin \Sigma_{tot} (\sin \alpha_i \sin \delta_i \cos \psi_i - \cos \alpha_i \sin \psi_i), \end{aligned} \quad (13.4-4b)$$

$$\begin{aligned} \cos \delta_f \cos \alpha_f &= \cos \Sigma_{tot} \cos \alpha_i \sin \delta_i \\ &\quad - \sin \Sigma_{tot} (\cos \alpha_i \sin \delta_i \cos \psi_i + \sin \alpha_i \sin \psi_i). \end{aligned} \quad (13.4-4c)$$

As $-90^\circ \leq \delta_f \leq 90^\circ$, these equations uniquely determine declination and right ascension of the impact point. The equation for the right ascension can be simplified slightly by multiplying Eq. (13.4-4b) with $\cos \alpha_i$ and $\sin \alpha_i$ respectively, Eq. (13.4-4c) with $-\sin \alpha_i$ and $\cos \alpha_i$ respectively, and adding the results, leading to

$$\sin(\alpha_f - \alpha_i) = \frac{\sin \Sigma_{tot} \sin \psi_i}{\cos \delta_f}, \quad (13.4-5a)$$

$$\cos(\alpha_f - \alpha_i) = \frac{1}{\cos \delta_f} [\cos \Sigma_{tot} \cos \delta_i - \sin \Sigma_{tot} \sin \delta_i \cos \psi_i]. \quad (13.4-5b)$$

Once declination and right ascension are determined, the geocentric coordinates of the impact point follow from

$$\Lambda_f = \alpha_f - H_{G_0} - \omega_e(t_i + t_{f_{tot}}),$$

or with Eq. (13.1-2a)

$$\Lambda_f - \Lambda_i = \alpha_f - \alpha_i - \omega_e t_{f_{tot}}, \quad (13.4-6a)$$

and

$$\phi_f = \delta_f. \quad (13.4-6b)$$

We see that due to the rotation of the Earth during the flight of the missile, the geocentric longitude difference between injection and impact is less than the right ascension difference between injection and impact. The difference is equal to the angle that the Earth has rotated about during the time interval from injection to impact. For easterly launches this means that the effect of the Earth's rotation during the flight is a reduction of the range which can be covered, while for westerly launches the rotation of the Earth during the flight causes an increase of the range. The effects of the Earth's rotation during launch, causing an inertial eastward velocity of the launch site are just the other way round: increase of range for easterly launches and decrease of range for westerly launches. In general, we can say that for typical ICBM flights the effect of the Earth's rotation at launch dominates the effect of the rotation of the Earth during the flight, thus leading to larger ranges for easterly launches than for westerly launches.

13.4.2 Oblate Earth

In determining the trajectory and impact point of a ballistic missile we have assumed so far that the Earth is spherical and has a central inverse-square force field. The Earth, however, is flattened at the poles and bulges at the equator (Section 2.5.1). The Earth's oblateness has two effects on the trajectories of long-range ballistic missiles: a *dynamic effect* and a *geometric effect*.

The dynamic effect is the result of a non-Newtonian gravitational potential of the Earth. This potential, which can be approximated by a series of spherical harmonics (Section 18.6) creates a non-central force field, exerting torques normal to, and forces in the nominal trajectory plane. Therefore the real trajectory will deviate from the trajectory as determined with a spherical Earth model, resulting in down-range and cross-range errors. The necessary range corrections to account for this dynamic effect can be determined with perturbation procedures. We will not go into this but only mention that Wheelon [8] has derived expressions for down-range and cross-range corrections to be applied to the spherical Earth trajectory impact point, which account for the effects of the *second zonal harmonic* (J_2 -term) in the potential. The order of magnitude of these corrections is up to about 10 km. The effects of *higher-order zonal harmonics* and of the *tesseral* and *sectorial* harmonics are a few orders of magnitude less and may therefore be neglected.

The geometric effect is a result of the fact that the point where the missile's trajectory intersects the Earth's surface is dependent on the shape of the Earth. Thus assuming the Earth to be spherical will, in general, result in down-range errors. We will now determine the coordinates of the impact point on an oblate Earth, neglecting the dynamic effect, i.e. still assuming a central inverse-square gravitational field. Our analysis is a somewhat modified version of the analysis given by Ching-Seng Wu [9].

We approximate the oblate Earth by the Standard Ellipsoid. If ϕ_e is the geocentric latitude and h_e the altitude of the re-entry point, the re-entry radius may be approximated very well by

$$r_e = R_e(1 - \varepsilon \sin^2 \phi_e) + h_e, \quad (13.4-7a)$$

where ε is the flattening of the Earth defined by

$$\varepsilon = \frac{R_e - R_p}{R_e} = \frac{1}{298}, \quad (13.4-7b)$$

and R_e and R_p are equatorial and polar radius of the Earth. If Σ' is the ballistic range angle on the oblate Earth, then, according to Eq. (13.2-10), the re-entry radius is given by

$$r_e = \frac{p}{1 + e \cos(\theta_i + \Sigma')}, \quad (13.4-8)$$

where θ_i is the injection true anomaly as given by Eq. (13.2-13). According to Eqs. (13.4-4a) and (13.4-6b) the geocentric latitude of the re-entry point follows from

$$\sin \phi_e = \cos \Sigma' \sin \delta_i + \sin \Sigma' \cos \delta_i \cos \psi_i \quad (13.4-9)$$

Substitution of Eq. (13.4-9) into Eq. (13.4-7a) and setting the resulting expression for r_e equal to the expression given in Eq. (13.4-8) leads to the following equation in the ballistic range angle Σ' :

$$R_e [1 - \varepsilon (\cos \Sigma' \sin \delta_i + \sin \Sigma' \cos \delta_i \cos \psi_i)^2] + h_e = \frac{p}{1 + e \cos (\theta_i + \Sigma')} \quad (13.4-10)$$

This equation, which has to be solved numerically, yields the ballistic range angle on the oblate Earth. Once this range angle is known, the re-entry radius can be determined with Eq. (13.4-8). Then re-entry velocity and flight path angle can be computed with Eqs. (13.2-22). Subsequently, the re-entry range and flight time may be determined. Then total range angle and total time of flight from injection to impact are known and the coordinates of the impact point may be determined with Eqs. (13.4-4) to (13.4-6). A determination of the surface range from the sub-vehicle point of injection to the impact point, which for a spherical Earth is just $R_0 \Sigma_{tot}$, gives rise to a somewhat lengthy procedure which will not be discussed here. Escobal [10] has developed a technique which enables calculation of this surface range on an ellipsoid.

We will now derive an approximate expression for the down-range correction which has to be applied to the spherical Earth impact point to account for the geometric oblateness effect. Define $\Delta\Sigma$ as the difference between the ballistic range angle for an oblate Earth and the ballistic range angle for a spherical Earth,

$$\Delta\Sigma = \Sigma' - \Sigma. \quad (13.4-11)$$

Neglecting the difference between the re-entry range angles for an oblate and a spherical Earth model, as well as the time of flight differences between both models, the linear down-range correction to be applied to the range as determined with the spherical Earth model is

$$\Delta R_D = R_e \Delta\Sigma. \quad (13.4-12)$$

As $\Delta\Sigma$ is small, we may substitute Eq. (13.4-11) into Eq. (13.4-10) and linearize, resulting in an equation for $\Delta\Sigma$. Solution of this equation, and applying Eq. (13.4-12) results in the following expression for the down-range correction

$$\Delta R_D = \frac{1 + e \cos (\theta_i + \Sigma)}{e \sin (\theta_i + \Sigma)} [R_e \{1 - \varepsilon (\cos \Sigma \sin \delta_i + \sin \Sigma \cos \delta_i \cos \psi_i)^2\} - R_0] \quad (13.4-13a)$$

If the re-entry altitude is taken zero, this equation may, according to Eqs. (13.4-4a) and (13.4-6b), be written as

$$\Delta R_D = \frac{1 + e \cos(\theta_i + \Sigma)}{e \sin(\theta_i + \Sigma)} [R_e(1 - \varepsilon \sin^2 \phi_f) - R_0] \quad (13.4-13b)$$

This down-range correction is plotted in Fig. 13.12 as a function of the latitude of the impact point, ϕ_f , for $h_i = h_e = 0$. For three different range angles, curves are shown for a low, an optimum and a high trajectory. It is seen that the down-range correction increases with increasing range angle, while for a fixed range angle it decreases with increasing flight path angle at injection.

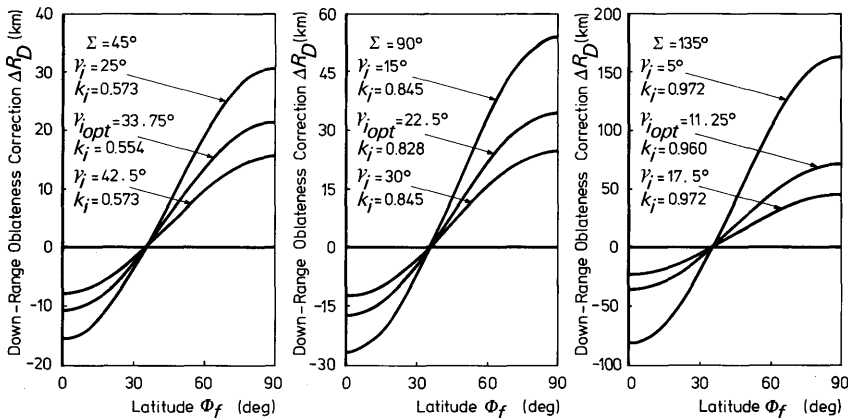


Fig. 13.12 The down-range oblateness correction as a function of the geocentric latitude of the impact point for high, optimal and low trajectories

13.4.3 Influence coefficients

For classical, non-maneuverable re-entry vehicles the position of the impact point is practically uniquely determined by position and velocity at deployment. Therefore, the guidance system of the rocket vehicle has to generate the commands necessary to ensure correct position and velocity at the time of release of the re-entry vehicle. To this end various guidance schemes are being used. The more advanced guidance laws, e.g. *Hybrid Explicit Guidance*, compute throughout the powered flight, using current position and velocity data, the position of the impact point if the re-entry vehicle were released at that time, as well as the velocity needed to go directly from the current position to the target. When the computed impact point coincides with the target a re-entry vehicle is deployed. Another widely used guidance scheme is *Delta guidance*. In this case a *reference trajectory* is stored in the onboard guidance computer of the rocket vehicle. During powered flight the current state is continuously compared with the reference

or nominal state and whenever a deviation from nominal is detected the guidance and control unit directs the missile back to its nominal flight path. To this nominal trajectory correspond nominal shut-down conditions. However, the state at shut-down of an actual missile will never exactly equal the nominal state as a result of guidance system errors. These shut-down errors, expressed in the perturbations Δr_i , $\Delta \alpha_i$, $\Delta \delta_i$, ΔV_i , $\Delta \gamma_i$ and $\Delta \psi_i$, result in impact errors, expressed by a *down-range error*, ΔR_D within the nominal trajectory plane and a *cross-range error*, ΔR_C , normal to the nominal trajectory plane. In this section, we will determine the relations between the impact errors and the shut-down errors. In general, these relations have the following form

$$\Delta R_D = \Delta R_D(\Delta r_i, \Delta \alpha_i, \Delta \delta_i, \Delta V_i, \Delta \gamma_i, \Delta \psi_i), \quad (13.4-14a)$$

$$\Delta R_C = \Delta R_C(\Delta r_i, \Delta \alpha_i, \Delta \delta_i, \Delta V_i, \Delta \gamma_i, \Delta \psi_i). \quad (13.4-14b)$$

Assuming the cut-off errors to be small, these equations may be linearized, resulting in

$$\Delta R_D = R_{D_r} \Delta r_i + R_{D_\alpha} \Delta \alpha_i + \dots + R_{D_\psi} \Delta \psi_i, \quad (13.4-15a)$$

$$\Delta R_C = R_{C_r} \Delta r_i + R_{C_\alpha} \Delta \alpha_i + \dots + R_{C_\psi} \Delta \psi_i, \quad (13.4-15b)$$

where

$$R_{D_r} = \frac{\partial \Delta R_D}{\partial \Delta r_i}, \quad R_{D_\alpha} = \frac{\partial \Delta R_D}{\partial \Delta \alpha_i}, \quad \text{etc.}$$

The coefficients R_{D_r} , R_{D_α} , ..., R_{D_ψ} are the *ballistic down-range influence coefficients*, while R_{C_r} , R_{C_α} , ..., R_{C_ψ} are the *ballistic cross-range influence coefficients*. They describe the relation between cut-off errors and impact errors, at least for small cut-off errors. For instance, R_{D_r} is the down-range error as a result of a shut-down radius error of unity.

To simplify our analysis, without affecting the results greatly, we will assume a spherical non-rotating Earth and a ballistic trajectory from launch till impact. So the boost phase is approximated by an impulsive shot, while the re-entry phase is neglected. Firstly, we observe that, with the assumptions made, the plane of the trajectory is uniquely determined by α_i , δ_i and ψ_i . This means that errors in the in-plane injection conditions r_i , γ_i and V_i do not cause any cross-range error. Secondly, a change in injection azimuth causes the trajectory plane to rotate about the injection radius vector and consequently only results in a cross-range error. Thus, we have

$$R_{C_r} = R_{C_\gamma} = R_{C_V} = R_{D_\psi} = 0,$$

and the expressions (13.4-15) simplify to

$$\Delta R_D = R_{D_r} \Delta r_i + R_{D_\alpha} \Delta \alpha_i + R_{D_\delta} \Delta \delta_i + R_{D_V} \Delta V_i + R_{D_\gamma} \Delta \gamma_i, \quad (13.4-16a)$$

$$\Delta R_C = R_{C_\alpha} \Delta \alpha_i + R_{C_\delta} \Delta \delta_i + R_{C_V} \Delta \psi_i. \quad (13.4-16b)$$

As an error in the in-plane injection state causes a down-range error,

$\Delta R_D = R_0 \Delta \Sigma$, we can write for the in-plane down-range influence coefficients

$$R_{D_r} = R_0 \frac{\partial \Sigma}{\partial r_i}, \quad R_{D_v} = R_0 \frac{\partial \Sigma}{\partial V_i}, \quad R_{D_\gamma} = R_0 \frac{\partial \Sigma}{\partial \gamma_i}. \quad (13.4-17)$$

Now, $\tan \frac{\Sigma}{2}$ is given in Eq. (13.2-20), and as

$$d\Sigma = \frac{2}{1 + \tan^2 \Sigma / 2} d\left(\tan \frac{\Sigma}{2}\right), \quad (13.4-18a)$$

we can derive the partial derivatives of range angle with respect to r_i , V_i and γ_i , noting that

$$\frac{\partial}{\partial r_i} = \frac{1}{r_i} \left[\rho_i \frac{\partial}{\partial \rho_i} + k_i \frac{\partial}{\partial k_i} \right], \quad (13.4-18b)$$

and

$$\frac{\partial}{\partial V_i} = \frac{2\sqrt{k_i}}{\sqrt{\mu/r_i}} \frac{\partial}{\partial k_i}. \quad (13.4-18c)$$

Finally, differentiation of Eq. (13.2-20), using Eqs. (13.4-17) and (13.4-18), and setting $\rho_i = 1$ and $r_i = R_0$ leads to

$$R_{D_r} = \cot \gamma_i + 2k_i \frac{\sin \gamma_i \cos \gamma_i}{\cos^2 \gamma_i (1 - k_i)^2 + \sin^2 \gamma_i}, \quad (13.4-19a)$$

$$R_{D_v} = 4 \sqrt{\frac{R_0^3}{\mu}} k_i \frac{\sin \gamma_i \cos \gamma_i}{\cos^2 \gamma_i (1 - k_i)^2 + \sin^2 \gamma_i}, \quad (13.4-19b)$$

$$R_{D_\gamma} = 2R_0 k_i \frac{\cos^2 \gamma_i (1 - k_i) - \sin^2 \gamma_i}{\cos^2 \gamma_i (1 - k_i)^2 + \sin^2 \gamma_i}. \quad (13.4-19c)$$

These relations are plotted in Fig. 13.13. The down-range error coefficients along an optimal trajectory are indicated by a dashed line. In Fig. 13.13c this dashed line coincides with the line $R_{D_\gamma} = 0$.

The error coefficients with respect to α_i , δ_i and ψ_i could be obtained by differentiating Eqs. (13.4-4), thus obtaining equations for the partial derivatives of α_f and δ_f with respect to α_i , δ_i and ψ_i . Then, using spherical geometry, the down-range and cross-range errors can be expressed in $\Delta \alpha_f$ and $\Delta \delta_f$, thus leading to the influence coefficients.

A simpler method is possible, however. Let us first consider the effect of an error $\Delta \alpha_i$ in right ascension at cut-off. In this case, the trajectory plane is rotated about the Z -axis over an angle $\Delta \alpha_i$ with respect to the nominal trajectory plane. So the declination of the impact point remains unchanged, but the right ascension and consequently the geographic longitude of the impact point increases with an amount $\Delta \alpha_i$. This means that the new impact

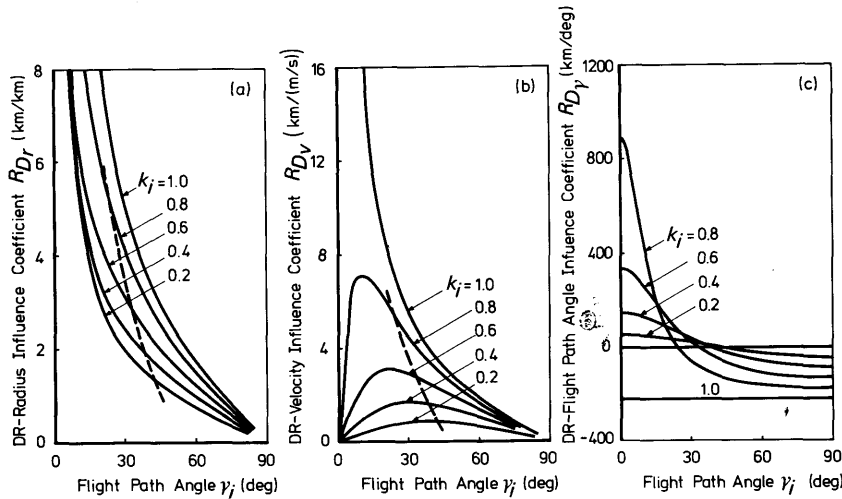


Fig. 13.13 The in-plane down-range influence coefficients as a function of injection flight path angle and velocity parameter

point is displaced due east over a distance $\Delta R = R_0 \cos \delta_f \Delta \alpha_i$. This due-east displacement can be resolved in a down-range displacement and a cross-range displacement:

$$\Delta R_D = \Delta R \sin \psi_f = R_0 \cos \delta_f \sin \psi_f \Delta \alpha_i, \quad (13.4-20a)$$

$$\Delta R_C = -\Delta R \cos \psi_f = -R_0 \cos \delta_f \cos \psi_f \Delta \alpha_i, \quad (13.4-20b)$$

where ψ_f is the azimuth at impact. Using Eq. (13.2-5), we find

$$\sin \psi_f = \sin \psi_i \frac{\cos \delta_i}{\cos \delta_f}, \quad (13.4-21a)$$

while Eq. (13.2-9a) yields

$$\cos \psi_f = \sin i \cos (\alpha_f - \Omega),$$

and using Eqs. (13.2-8) and (13.4-5), we obtain

$$\cos \psi_f = \frac{1}{\cos \delta_f} [\cos \Sigma \cos \delta_i \cos \psi_i - \sin \Sigma \sin \delta_i]. \quad (13.4-21b)$$

Substitution of Eqs. (13.4-21) into Eqs. (13.4-20) yields

$$R_{D_\alpha} = R_0 \sin \psi_i \cos \delta_i, \quad (13.4-22a)$$

$$R_{C_\alpha} = R_0 [\sin \Sigma \sin \delta_i - \cos \Sigma \cos \delta_i \cos \psi_i]. \quad (13.4-22b)$$

The error coefficient R_{C_ψ} is obtained by using the rule of cosines in the spherical triangle formed by the launch site, the nominal impact point and the impact point if an error $\Delta \psi_i$ is made at injection. The sides of this triangle are $R_0 \Sigma$, $R_0 \Sigma$ and ΔR_C , while the angle between the two equal sides

is $\Delta\psi_i$. So, we have

$$\cos \frac{\Delta R_C}{R_0} = \cos^2 \Sigma + \sin^2 \Sigma \cos \Delta\psi_i,$$

and as $\frac{\Delta R_C}{R_0}$ and $\Delta\psi_i$ are small, both cosines may be expanded in a Taylor series and terms of degree higher than the second may be neglected, leading to

$$\left(\frac{\Delta R_C}{R_0}\right)^2 = \sin^2 \Sigma (\Delta\psi_i)^2.$$

For $\Sigma < 180^\circ$, a positive $\Delta\psi_i$ yields a negative ΔR_C . So we find for the cross-range influence coefficient with respect to ψ_i

$$R_{C_\psi} = -R_0 \sin \Sigma. \quad (13.4-23)$$

The error coefficients with respect to δ_i , finally, can be obtained in the following way. Suppose that at cut-off there are only errors in α_i , δ_i and ψ_i . Then the down-range and cross-range errors are

$$\Delta R_D = R_{D_\alpha} \Delta\alpha_i + R_{D_\delta} \Delta\delta_i, \quad (13.4-24a)$$

$$\Delta R_C = R_{C_\alpha} \Delta\alpha_i + R_{C_\delta} \Delta\delta_i + R_{C_\psi} \Delta\psi_i. \quad (13.4-24b)$$

Let $\Delta\alpha_i$, $\Delta\delta_i$ and $\Delta\psi_i$ be related such that the actual injection point lies in the nominal trajectory plane and that at actual injection the azimuth equals the local nominal azimuth. In that case, the actual trajectory plane will coincide with the nominal trajectory plane and only a down-range error will result. The magnitude of this down-range error equals the distance between the sub-vehicle points of actual injection and nominal injection. As $\Delta\alpha_i$, $\Delta\delta_i$ and $\Delta\psi_i$ are small, the requirement for the injection point to lie in the trajectory plane is

$$\Delta\alpha_i = \frac{\tan \psi_i}{\cos \delta_i} \Delta\delta_i. \quad (13.4-25)$$

The local nominal azimuth, $\psi_i + \Delta\psi_i$, at position $\alpha_i + \Delta\alpha_i$, $\delta_i + \Delta\delta_i$ can be found by using Eq. (13.2-5)

$$\sin(\psi_i + \Delta\psi_i) \cos(\delta_i + \Delta\delta_i) = \sin \psi_i \cos \delta_i.$$

By linearizing this equation and solving for $\Delta\psi_i$, we obtain

$$\Delta\psi_i = \tan \delta_i \tan \psi_i \Delta\delta_i. \quad (13.4-26)$$

For arbitrary $\Delta\delta_i$, with $\Delta\alpha_i$ and $\Delta\psi_i$ as given in Eqs. (13.4-25) and (13.4-26), the down-range error is given by

$$\Delta R_D = \frac{R_0}{\cos \psi_i} \Delta\delta_i. \quad (13.4-27)$$

Substitution of Eqs. (13.4-25) to (13.4-27) into Eqs. (13.4-24), with $\Delta R_C = 0$ and solving the resulting equations for R_{D_s} and R_{C_s} yields

$$R_{D_s} = \frac{R_0}{\cos \psi_i} - R_{D_a} \frac{\tan \psi_i}{\cos \delta_i}, \quad (13.4-28a)$$

$$R_{C_s} = -R_{C_a} \frac{\tan \psi_i}{\cos \delta_i} - R_{C_b} \tan \delta_i \tan \psi_i. \quad (13.4-28b)$$

Substitution of Eqs. (13.4-22) and (13.4-23) into Eqs. (13.4-28), finally yields

$$R_{D_s} = R_0 \cos \psi_i, \quad (13.4-29a)$$

$$R_{C_s} = R_0 \cos \Sigma \sin \psi_i, \quad (13.4-29b)$$

which completes the determination of the influence coefficients. We see from Eqs. (13.4-22), (13.4-23) and (13.4-29) that the influence coefficients with respect to the out-of-plane injection state are of the same order of magnitude as R_0 , which means an error of about 6000 km/rad or about 100 km/deg. An error in cut-off flight path angle is also of the order R_0 , while it follows from Fig. 13.13 that for a range of 10,000 km errors in r_i and V_i of 1 m and 1 m/s respectively will result in impact errors of 6 m and 6 km respectively, for a nominal optimal trajectory. For a non-guided missile, the resulting errors will be too large to allow for an accurate kill. Therefore all ballistic missiles are guided, which means that during the powered flight steering commands are computed on the basis of real flight conditions.

References

- 1 Anon. (1961), *Explanatory Supplement to the American Ephemeris and Nautical Almanac*, H.M.S.O., London, p. 75.
- 2 Kohlhase, C. E. (1962), Launch-on-time analysis for space missions, *Progress in Astronautics and Rocketry*, Vol. 8, Academic Press, New York, p. 3-21.
- 3 Plummer, H. C. (1960), *An Introductory Treatise on Dynamical Astronomy*, Dover Publications, New York, p. 49-60.
- 4 Battin, R. H. (1964), *Astronautical Guidance*, McGraw-Hill, New York, p. 70-82.
- 5 Moe, M. M. (1960), An approximation to the re-entry trajectory, *A.R.S. J.*, **30**, 50-58.
- 6 Blum, R. (1962), Re-entry trajectories: flat earth approximation, *A.R.S. J.*, **32**, 616-620.
- 7 Bate, R. R. and Johnson, R. W. (1962), Empirical formulas for ballistic re-entry trajectories, *A.R.S. J.*, **32**, 1882-1887.

316 Rocket Propulsion & Spaceflight Dynamics

- 8 Wheelon,
915–926.
- 9 Ching-Sheng Wu (1960), Effect of earth's oblateness on the calculation
of the impact point of ballistic missiles, *A.R.S. J.*, **30**, 1172–1173.
- 10 Escobal, P. R. (1964), Calculation of the surface range of a ballistic
missile, *AIAA J.*, **2**, 571–573.

14 Rocket Motion in the Atmosphere

In Chapters 11 and 12 rocket motion in vacuum was considered, while in Chapter 13 the atmospheric effects were neglected for the major part of the trajectory. But the presence of the Earth's atmosphere will lead to aerodynamic forces on the vehicle and in many cases one has to account for the aerodynamic forces and moments to predict accurately the vehicle's trajectory and performances.

Because of unpredictable aerodynamic forces and moments the trajectory may deviate from the nominal trajectory. Such aerodynamic moments may be caused by steady wind, wind-gusts, atmospheric turbulence, but also by fin misalignment and production inaccuracies. The deviation of the trajectory of the rocket is known as *trajectory dispersion*. For guided vehicles, the dispersion of the impact point, for instance, is minimized by means of a special guidance system.

As an extensive discussion on aerodynamics is far beyond the scope of this book, we restrict ourselves to a short discussion to give the reader some understanding of the aerodynamic phenomena which play a role in rocketry, and we will give some engineering methods, which enable the reader to estimate the order of magnitude of the aerodynamic forces and moments.

14.1 The equations of motion

In Section 4.2.5 the dynamical equations of motion for a rigid rocket, Eqs. (4.2-58), were derived. In these equations, \mathbf{X}_a , \mathbf{Y}_a , \mathbf{Z}_a , and \mathbf{L}' , \mathbf{M}' and \mathbf{N}' stand for the aerodynamic forces and moments, respectively, which among others, depend on the velocity of the rocket with respect to the air, and the local atmospheric pressure, density and temperature. For simplicity, we will assume a quiet non-rotating atmosphere. The inertial linear velocity components are, u , v and w and the angular velocity components are p , q and r . Some important notions, frequently used in aerodynamics are the Mach number, M_a , the Reynolds number, Re , and the dynamic pressure, \hat{q} .^{*} In Section 5.1.2, the Mach number was defined already; here we will use the Mach number,

$$M_a = V_{cm}/a, \quad (14.1-1a)$$

where V_{cm} stands for the velocity of the center of mass of the vehicle. The

* Usually the notation q is used for the dynamic pressure; to avoid ambiguity with the angular velocity q , the notation \hat{q} is used here.

Reynolds number, Re , was defined in Section 8.2.4; here we use

$$Re = \rho V_{cm} L / \mu. \quad (14.1-1b)$$

The dynamic pressure is defined as

$$\hat{q} = \frac{1}{2} \rho V_{cm}^2. \quad (14.1-1c)$$

As the atmospheric quantities, p , T , μ , ρ , a , etc., are strongly variable (Section 2.6), depending on time and location, one must, for practical purposes use an estimate of their average values such as given in a *Reference Atmosphere* [1].

14.1.1 Aerodynamic forces, moments and coefficients

There is a great variety in the aerodynamic configurations of missiles and rocket vehicles. For instance, the Space Shuttle with its large wings has some aerodynamic characteristics like a plane while a launch vehicle, like the Saturn V has only four small stabilization fins. We will restrict our discussion to rocket vehicles without wings, having four stabilization fins, which lie in pairs in a plane of symmetry (cruciform configuration). Those readers who want more detailed information are referred to Nielsen [2] and Chin [3].

To simplify the treatment, we assume the vehicle's velocity vector to coincide with one of the symmetry planes through a pair of fins. We also assume that one of the symmetry planes coincides with the trajectory plane. The angle in the trajectory plane between the velocity vector and the longitudinal axis of the vehicle is the *angle of attack* or *angle of incidence*, α (Fig. 14.1).

If the velocity vector were lying in the other symmetry plane, the angle would be called the *sideslip angle*, β . These names stem from aircraft aerodynamics.

The total aerodynamic force, \mathbf{F}_a , is assumed to lie in the trajectory plane. The point where the line of force of \mathbf{F}_a intersects the rocket's center-line, is called the *center of pressure*, cp . It is evident that if there is no resultant aerodynamic moment on the vehicle, cp coincides with the center of mass, cm , which we also assume to lie on the center-line. If cp and cm do not coincide, there is an aerodynamic moment about the y -axis of the vehicle, (Section 4.1), the *pitching moment*,*

$$\mathbf{M}' = \mathbf{F}_a \times \mathbf{l}, \quad (14.1-2)$$

where

$$\mathbf{l} = \mathbf{x}_{cm} - \mathbf{x}_{cp}, \quad (14.1-3)$$

see Fig. 14.1.

The aerodynamic force \mathbf{F}_a usually is resolved either in a lift, \mathbf{L} , and a

* Usually the aerodynamic moment about the y -axis is indicated by M ; to avoid ambiguity with mass we use the notation M' here.

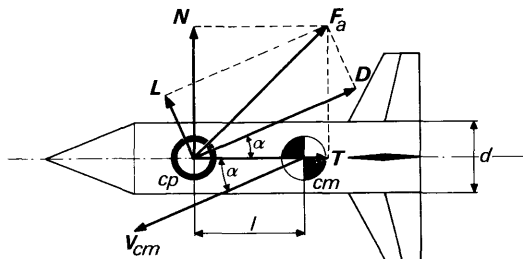


Fig. 14.1 The aerodynamic forces on a rocket, the center of pressure, cp , and the center of mass, cm

drag, D , normal and parallel to the velocity, V_{cm} , or into a normal force, N , and a tangential force, T , normal and parallel to the center-line (Fig. 14.1). Aerodynamic moments about the z - and x -axis are called the *yawing* and *rolling moment* respectively and indicated by N' and L' .

It has proved convenient in aerodynamics to use relations between dimensionless coefficients, instead of forces and/or moments. Therefore, the force (moment) is written as the product of a dimensionless coefficient, the dynamic pressure and a reference area (volume). We often take the reference area as the cross-sectional base area of the rocket, $S = (\pi/4)d^2$, the volume is Sd and d is the base diameter.

Then:

$$L = C_L \hat{q} S, \quad (14.1-4)$$

$$M' = C_m \hat{q} S d. \quad (14.1-5)$$

In this way we can define lift, drag, normal force, tangential force, pitching moment coefficients, etc. The force coefficients get a capital index while the moment coefficients get a lower case index.

From Fig. 14.1 we immediately see

$$C_N = C_L \cos \alpha + C_D \sin \alpha, \quad (14.1-6a)$$

$$C_T = -C_L \sin \alpha + C_D \cos \alpha, \quad (14.1-6b)$$

$$C_m = C_N l / d. \quad (14.1-7)$$

Note that for $C_N = 0$ and $C_m \neq 0$, $l \rightarrow \infty$.

Moreover, we find

$$C_N = -C_Z, \quad C_T = -C_X. \quad (14.1-8)$$

In the general, three-dimensional case there is a set of three independent force coefficients and three independent moment coefficients. In the two-dimensional case where the aerodynamic forces are assumed to lie in one symmetry plane, there are two independent force coefficients and there is one moment coefficient. The determination of these coefficients, which among others, for a particular vehicle, depend strongly on Mach number

and Reynolds number, belongs to the field of aerodynamics. It is possible to predict the aerodynamic coefficients with a fair degree of accuracy, but for a real accurate determination one often has to rely on experiments, such as *windtunnel tests*, or *free-flight experiments*, either with small models or with full-scale vehicles. In those experiments, it is very important that the dimensionless numbers, such as Re or M_a are the same for the vehicle and the scale-model, otherwise the results may be unreliable. For instance, it is well-known that at low Reynolds numbers, one may have *laminar boundary layers*, while at high Reynolds numbers the boundary layer usually is *turbulent*. The nature of the boundary layer not only strongly influences the magnitude of the aerodynamic forces, but also determines whether or not *flow separation* occurs. Such a separation may completely alter the nature of the flow around the rocket, and hence the information as obtained from a scale-model might be useless for application to the flight vehicle if the dimensionless scale numbers do not match.

In order to investigate the stability characteristics of flight vehicles, it is especially useful to know how the aerodynamic forces and moments vary with small changes of the independent variables. It turns out that for small motions of, and about, the center of mass, in the three-dimensional case, the components of the motions about and along the body axes hardly influence each other, so that for these small motions, the complete motion can be approximated by superposition of the respective *translational* and *rotational* motions, along and about the x -, y - and z -axis; i.e. the six Eqs. (4.2-58) can be solved independently of each other. As, in this chapter, we concern ourselves primarily with the motion in the trajectory plane, this means that we neglect small out-of-plane motions of the center of mass or the effects of *cross-winds* on the in-plane vehicle motion, etc.

As long as forces and moments remain small, we can expand any aerodynamic force, F , or moment, M' , in a Taylor series, and neglect higher-order terms:

$$F = F_o + F_\alpha \alpha + F_q q + F_{\dot{\alpha}} \dot{\alpha} + \dots$$

$$M' = M'_o + M'_\alpha \alpha + M'_q q + M'_{\dot{\alpha}} \dot{\alpha} + \dots$$

where F_o and M'_o are constants, equalling zero for a symmetric vehicle, and where F_α stands for $\partial F/\partial \alpha$, etc. These equations can also be written as

$$F = (C_{F_o} + C_{F_\alpha} \alpha) \hat{q} S + (C_{F_{\dot{\alpha}}} \dot{\alpha} + C_{F_q} q) \hat{q} S \frac{d}{2V} + \dots \quad (14.1-9a)$$

$$M' = (C_{m_o} + C_{m_\alpha} \alpha) \hat{q} S d + (C_{m_{\dot{\alpha}}} \dot{\alpha} + C_{m_q} q) \hat{q} S \frac{d^2}{2V} + \dots \quad (14.1-9b)$$

The term $d/(2V)$ arises from the use of a dimensionless time, thus

$$\dot{\alpha} = \partial \alpha / \partial (2Vt/d).$$

Terms like C_{F_α} , $C_{F_{\dot{\alpha}}}$, C_{m_q} , etc., are called *stability derivatives*. It turns out

that for a very simple, two-dimensional description of the rocket motion about the center of mass, the following stability derivatives are important: C_{N_a} , C_{m_a} , C_{m_b} and C_{m_c} . For this reason these terms were included in the series expansion above. When discussing the stability of rocket vehicles we will explain their meaning.

14.2 The magnitude of the aerodynamic coefficients

The aerodynamic coefficients for a particular vehicle depend among others on α , Re , and M_a . For low values of α , an accurate calculation of C_N , C_m and C_D has been possible for a long time for *subsonic* and *supersonic speeds*. At *transonic speeds*, $M_a \approx 1$, it is difficult to make accurate predictions. More recent methods [4] allow predictions of C_N and C_m at large values of α , while also the dynamics at these high angles of attack have been investigated. These investigations [5] showed that due to the dynamics of the pitching motion, the values of the aerodynamic coefficients, especially at high angles of attack, may deviate considerably from their static values.

We will limit our discussion to small angles of attack, and write an aerodynamic force (moment) in the form

$$F_T = F_B + F_W + F_i, \quad (14.2-1)$$

or in words: the total force (moment), F_T , is the sum of the force (moment) on the body, F_B , on the fins, F_W , and a force (moment) due to interference, F_i . We have assumed here that the vehicle only consists of a body and fins. Dividing Eq. (14.2-1) by $\hat{q}S_r$ or $\hat{q}S_r d$ yields

$$C_{F_T} = C_{F_B} + C_{F_W} + C_{F_i}, \quad (14.2-2)$$

We indicate the reference area by S_r .

For small α , the Eqs. (14.1-6) usually may be approximated by

$$C_N = C_L + C_D \alpha, \quad C_D = C_T + C_L \alpha. \quad (14.2-3)$$

So, in the following we will concern ourselves with C_N and C_D .

14.2.1 The normal force and pitching moment coefficients

For a rocket vehicle having four fins in cruciform configuration we have to consider the components C_{N_B} for the body in absence of fins, C_{N_W} for the fins alone and C_{N_p} , accounting for interference effects, to determine the complete normal force coefficient. For bodies with large *fineness*, slender-body theory [2] predicts

$$C_{N_B} = \frac{2\alpha}{S_r} \int_0^L \frac{dS}{dx} dx, \quad (14.2-4)$$

where L stands for the vehicle length considered, x for the distance from the

nose and S for the cross-sectional area. The integral in Eq. (14.2-4) for the whole vehicle immediately yields

$$C_{N_B} = 2\alpha. \quad (14.2-5)$$

Equation (14.2-4) was presented as an integral because it clearly reveals where normal forces can be expected. At the nose, where $dS/dx > 0$, we find $C_{N_n} > 0$ and at an afterbody, shaped as shown in Fig. 14.2, where $dS/dx < 0$, we find $C_{N_{ab}} < 0$. At the cylindrical part of the body slender-body theory predicts a zero normal force. Experiments show a discrepancy with the above results, due to viscosity. Allen and Perkins [6] have formulated the cross-flow theory which allows a more accurate prediction of the normal force

$$C_{N_B} = \frac{2\alpha}{S_r} \int_0^L \frac{dS}{dx} dx + \frac{\alpha^2}{S_r} \int_0^L C_{d_c} d(x) dx. \quad (14.2-6)$$

In this equation C_{d_c} represents the cross-flow drag coefficient, and for $M_a \sin \alpha < 0.4$ and $M_a \sin \alpha > 1.6$, its value usually lies somewhere between 1.2 and 1.4 [4].

The normal force coefficient C_{N_w} for a two-dimensional flow over a wing with a double-wedge airfoil (Fig. 14.3) is

$$C_{N_w} = \frac{4\alpha}{\sqrt{M_a^2 - 1}}, \quad M_a > 1. \quad (14.2-7)$$

The coefficients are based on the projected wing area. A wing with a finite span, b , will experience *tip effects* which cause losses. For a rectangular wing with a double-wedge profile and span, b :

$$C_{N_w} = \frac{4\alpha}{\sqrt{M_a^2 - 1}} \left[1 - \frac{S_w}{2b^2 \sqrt{M_a^2 - 1}} \right], \quad M_a > 1, \quad (14.2-8)$$

where S_w is the projected wing area. For wings with other planforms,

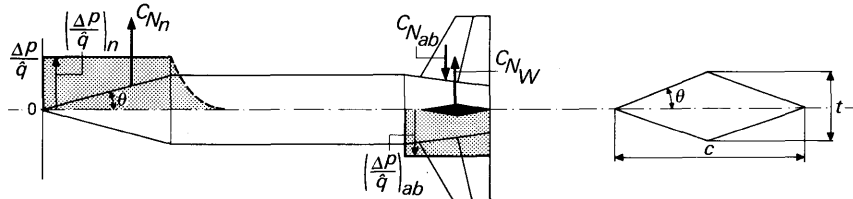


Fig. 14.2 Schematic pressure distribution on a rocket, and the normal force coefficients

Fig. 14.3 The double-wedge profile

corresponding expressions for C_N can be derived. For more detailed information the reader is referred to Pitts [7].

Interference effects make up for the difference between C_{N_T} and $C_{N_w} + C_{N_B}$. For instance, in Fig. 14.2, the pressure distribution on the body, according to slender-body theory, is shown. Some of the pressure on the nose is ‘carried over’ to the cylindrical part, as indicated by the dashed line. This is known as the *carry-over effect*. In a similar way, the pressure on the wings induces a pressure load on the body near the wing, while the presence of the body effectively increases the span and influences the pressure distribution on the wing. The interference effects, which may be fairly large, can be calculated according to Pitts [7].

The pitching moment coefficient, C_m , can be determined in the same way as C_N . For a slender-body of revolution it is found to be

$$C_{m_b} = \frac{2\alpha}{S_r} \int_0^L \frac{dS}{dx} (x_m - x) dx + \frac{\alpha^2}{dS_r} \int_0^L C_{d_e} d(x) (x_m - x) dx. \quad (14.2-9)$$

Here x_m is the coordinate of the moment axis.

For the fins we have

$$C_{m_w} = C_{N_w} \frac{x_m - x_{cp_w}}{d}. \quad (14.2-10)$$

The *cp* for a two-dimensional wing-section lies half chord. Interference and three-dimensional effects may shift this a little, but for large launch vehicles this is not of much importance. For small missiles and sounding rockets it certainly has to be accounted for, as the ratio of finchord to vehicle length usually is much larger for these vehicles than for launch vehicles.

14.2.2 The drag coefficient

The drag of a rocket vehicle can be split into the following components: *wave drag*, due to the presence of shock waves and dependent on the Mach number; *viscous drag*, due to friction; *induced drag*, due to the generation of lift; *base drag*, due to the wake behind the vehicle; *interference drag*, due to the interaction of various flow fields; and *roughness drag*, due to surface roughness such as rivets and welds.

The most comprehensive reference source on drag, certainly is Hoerner’s standard work [8], to which the reader is referred for detailed information.

The wave drag, connected with a shock wave, and hence occurring only at supersonic speeds, amounts for a conical forebody [9] to

$$C_{D_w} = \left(0.083 + \frac{0.096}{M_a^2} \right) (5.73\theta)^{1.69}, \quad M_a > 1, \quad (14.2-11)$$

where θ is the half-cone angle in radians (Fig. 14.2). The wave drag of an isolated, rectangular wing of span, b , with a double-wedge profile is [3]

$$C_{D_w} = \frac{4\theta^2}{\sqrt{M_a^2 - 1}} \left[1 - \frac{S_w}{2\sqrt{M_a^2 - 1} b^2} \right], \quad M_a > 1, \quad (14.2-12)$$

where θ is the half-wedge angle (Fig. 14.3). Both wave drag coefficients are strongly dependent on θ and decrease with increasing Mach numbers.

Viscous drag is the main drag component at subsonic speeds. It can be estimated by considering the *friction drag coefficient*, C_{D_f} , for a flat plate of equal length and equal wetted area as the rocket vehicle. For a laminar boundary layer we may estimate

$$C_{D_f} = \frac{1.328}{\sqrt{Re}}, \quad (14.2-13)$$

and for a turbulent boundary layer [8]

$$C_{D_f} = \frac{0.427}{(\log_{10} Re - 0.407)^{2.64}}. \quad (14.2-14)$$

These coefficients are based on the wetted area as a reference area. For most large rockets, one may assume the boundary layer to be turbulent. Transition from laminar to turbulent takes place around $Re = 10^6$ based on the bodylength, so that for small vehicles, still a major portion of the boundary layer may be laminar. Surface roughness may cause a transition from laminar to turbulent at lower Reynolds numbers.

Induced drag [3] is a result of the development of lift. In the subsonic case, the induced drag, based on the projected wing area, S_w , is

$$C_{D_{in}} = \frac{C_L^2 S_w}{\pi b^2 c_1}, \quad M_a < 1, \quad (14.2-15)$$

and at supersonic speeds it is well approximated by

$$C_{D_{in}} = C_N^2 / C_{Na}, \quad M_a > 1, \quad (14.2-16)$$

and c_1 is a constant.

Base drag is strongly affected by the shape of the vehicle, and the presence of a jet. The last two types of drag, base drag and roughness drag, in many cases constitute only a small amount of the total drag.

The total drag is found by addition of all components. It turns out that the total drag coefficient can well be approximated for preliminary calculations by:

$$C_D = a + bM_a^6, \quad M_a < 1, \quad (14.2-17a)$$

$$C_D = a' + \frac{b'}{M_a^2}, \quad M_a \geq 1. \quad (14.2-17b)$$

14.3 Some aspects of aerodynamic stability

An aerodynamically stable vehicle, will, after a small perturbation, return by itself to its original state. If we forego dynamic effects, we speak of *static stability*, otherwise of *dynamic stability*. We will analyse the static and dynamic longitudinal stability, and give a brief qualitative review of some important and complicated motions about the center of mass.

14.3.1 Static longitudinal stability

Consider a steady-state flight of a rocket vehicle. The total normal force applies at the center of mass (Section 14.1). A small increment in the angle of attack, $\Delta\alpha$, yields an incremental normal force, $\Delta C_N = C_{N_\alpha} \Delta\alpha$, on the rocket vehicle, and according to Section 14.2.1, we may write

$$C_{N_\alpha} = C_{N_{\alpha_B}} + C_{N_{\alpha_W}} + C_{N_{\alpha_i}} = C_{N_{\alpha_n}} + C_{N_{\alpha_{cyl}}} + C_{N_{\alpha_{ab}}} + C_{N_{\alpha_w}} + C_{N_{\alpha_i}}, \quad (14.3-1)$$

see Fig. 14.4. The increment in the normal forces, usually will not apply at the *cp*, but at the *neutral point*, *np*, which conversely is the definition of the neutral point. The (increment of the) aerodynamic moment about the *cm* is

$$\Delta C_m = C_{m_\alpha} \Delta\alpha = C_{N_\alpha} \Delta\alpha (x_{cm} - x_{np})/d, \quad (14.3-2)$$

and hence,

$$(x_{cm} - x_{np})/d = C_{m_\alpha}/C_{N_\alpha}. \quad (14.3-3)$$

The dimensionless quantity $(x_{cm} - x_{np})/d$ is called the *static stability margin*, and it is seen that for $(x_{cm} - x_{np})/d < 0$, or equivalently $C_{m_\alpha} < 0$, the vehicle is *statically stable*, while it is *neutrally stable* if the *np* and *cm* coincide. The vehicle is *statically unstable* for $x_{cm} > x_{np}$ or $C_{m_\alpha} > 0$. The position of the *np* depends, among others, on the Mach number and angle of attack. The position of the *cm* of a rocket usually shifts, due to propellant consumption. Therefore, the static stability margin varies during the flight.

Many rocket vehicles are symmetric and do not develop a normal force at $\alpha = 0$. If $N_T = 0$, the location of the *cp* is undetermined. However, at a small

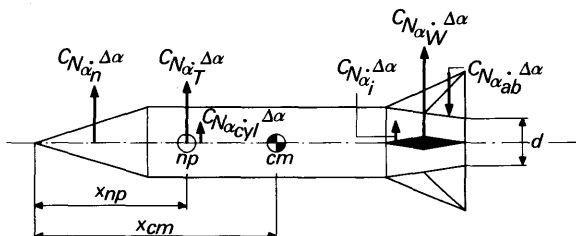


Fig. 14.4 The variation of the components of the normal force coefficient with a change in the angle of attack and the definition of the neutral point, *np*

angle of attack, $\Delta\alpha$, the total normal force, N_T , equals the increment in normal force, ΔN_T , and $x_{cp} = x_{np}$.

As is shown in Fig. 14.4, the main stabilizing forces are C_{N_w} and C_{N_i} due to fins and interference effects. This may clarify the functioning of the fins. It is also seen from Eq. (14.3-3) that a forward position of the cm helps too, in stabilizing the vehicle.

A large negative stability margin is very effective, but it also has disadvantages. It may lead to large bending moments in the structure; especially for large launch vehicles this may be unacceptable. For guided missiles, which require a quick response to a steering command, very high aerodynamic forces and moments are required if the stability margin is large negative.

Therefore, many vehicles have $C_{m_\alpha} \geq 0$ during the whole or a portion of their flight through the atmosphere. Stabilization then may be obtained by thrust vector control or by the deflection of flaps, rudders or complete fins.

Now suppose $\alpha = 0$ and the cruciform rocket vehicle is flying in a cross-wind. Then the above discussion holds if we replace the angle of attack, α , by the sideslip angle, β . It is evident that a stable rocket will try to reduce β , by turning its nose into the wind, thereby changing its flight path. For obvious reasons this is known as *weathercocking*, and C_{n_β} is called the *weathercock stability*.

14.3.2 Dynamic longitudinal stability

We return to the dynamical equations of motion, Eqs. (4.2-58), and simplify the analysis by assuming the roll and yaw rate to equal zero, like the velocity in y -direction, while the velocity in x -direction, u , is assumed constant, which implies a two-dimensional motion. This yields two coupled differential equations, Eq. (4.2-58c) and Eq. (4.2-58e). The pitch angle, θ , is the angle between the horizontal plane and the longitudinal axis, and α is the angle between the velocity vector and the longitudinal axis. Hence, $\theta = \alpha + \gamma$. Assuming the flight path angle, γ , constant, we have $q = \dot{\theta} = \dot{\alpha}$, which eliminates Eq. (4.2-58c) and we are left with

$$I_{yy}\ddot{\alpha} + [\dot{I}_{yy} + mx_e^2]\dot{\alpha} - (M_F)_y - M' = 0,$$

to describe the motion of a rocket vehicle about the y -axis, under the assumptions made. The y -component of the thrust misalignment moment, $(M_F)_y$, is

$$(M_F)_y = -x_e F_z + z_e F_x. \quad (14.3-4)$$

Substitution of Eq. (14.1-9b) and assuming $C_{m_\alpha} = 0$ yields

$$I_{yy}\ddot{\alpha} + \left[\dot{I}_{yy} + mx_e^2 - (C_{m_\alpha} + C_{m_\eta})\dot{q}S \frac{d^2}{2V} \right] \dot{\alpha} - C_{m_\alpha} d\dot{q}S\alpha - (M_F)_y = 0, \quad (14.3-5a)$$

or equivalently

$$I_{yy}\ddot{\alpha} + c_1\dot{\alpha} + c_2\alpha - (M_F)_y = 0. \quad (14.3-5b)$$

If we assume \dot{I}_{yy} negligible small, the solution is

$$\alpha - \alpha_o = A_1 e^{\lambda_1 t} + A_2 e^{\lambda_2 t}, \quad (14.3-6)$$

where α_o is the equilibrium angle of attack,

$$\alpha_o = -(M_F)_y / (C_{m_a} \hat{q} S d) \quad (14.3-7)$$

as follows from Eq. (14.3-5) and Eq. (14.3-6). The thrust misalignment, then, is balanced by an aerodynamic moment. In Eq. (14.3-6), A_1 and A_2 are integration constants while λ_1 and λ_2 stand for

$$\lambda_{1,2} = -(c_1 \pm \sqrt{c_1^2 - 4c_2 I_{yy}}) / (2I_{yy}). \quad (14.3-8)$$

In general $\lambda_{1,2}$ will be complex, and hence, the motion periodic. Only in the case that $c_1^2 - 4c_2 I_{yy} \geq 0$, $\lambda_{1,2}$ will be real, and there is an *aperiodic motion* about the y -axis. For stability, we require that a perturbation damps out, i.e. the real parts of $\lambda_{1,2}$ have to be negative. To investigate under what conditions this is the case, we consider the constant c_1 ,

$$c_1 = \dot{I}_{yy} + mx_e^2 - (C_{m_a} + C_{m_q}) \hat{q} S d^2 / (2V). \quad (14.3-9)$$

We neglect \dot{I}_{yy} , the term mx_e^2 is positive and stems from the jet damping, Section 4.2.5.

Damping in pitch is provided by the term $C_{m_a} + C_{m_q}$. The coefficient C_{m_a} stands for the pitching moment, resulting from a pure pitching motion, i.e. a motion in which α is constant and the vehicle rotates about the y -axis, Fig. 14.5a. As a result of the rotation, there is a velocity distribution, which induces normal forces on the vehicle, yielding a moment, opposing the pitching. Hence, $C_{m_a} < 0$.

To explain the meaning of C_{m_a} , consider a winged vehicle with a constant velocity, u , while accelerated in the z -direction, Fig. 14.5b. If there is no pitching but solely an increasing α , i.e. $\dot{\alpha} > 0$, the normal force on the wing is due to a transfer of momentum in z -direction from the fluid to the wing. Hence, the fluid velocity in z -direction after the wing, is less than in front of

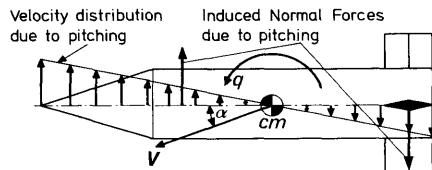


Fig. 14.5(a) Induced aerodynamic forces due to a pure pitching motion

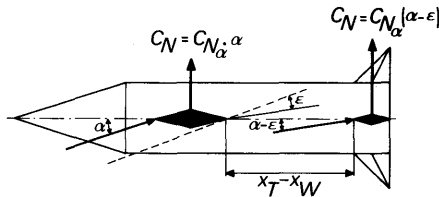


Fig. 14.5(b) Induced aerodynamic forces due to a pure α motion

the wing. This is known as *downwash*, and the *downwash angle*, ε , effectively reduces the angle of incidence at the tail, Fig. 14.5b. The normal force on the tail therefore is $C_N = C_{N_\alpha} (\alpha - \varepsilon)$. The downwash at the tail, ε_t , is related to the downwash at the wing's trailing edge, ε_w :

$$\varepsilon_t(\alpha, t) = \varepsilon_w \left(\alpha, t - \frac{x_t - x_w}{u} \right).$$

Hence, if $\dot{\alpha} > 0$, the downwash at the tail will be less than in the case $\dot{\alpha} = 0$, and the normal force on the tail will be larger than if $\dot{\alpha} = 0$. This leads to a moment opposing $\dot{\alpha}$, and it will be clear that also $C_{m_\alpha} < 0$. If there are no wings, the downwash is not so pronounced and one usually can forego C_{m_α} .

Returning to Eq. (14.3-9) we note that $c_1 > 0$, and if λ_1 and λ_2 are complex, the motion is damped as can be seen from Eq. (14.3-8). For $c_2 > 0$ and $c_1 > 0$ we always have a damped motion, and as is evident from Eqs. (14.3-5), $c_2 > 0$ means $C_{m_\alpha} < 0$ which was the condition for static longitudinal stability. If the motion is periodic, $\lambda_{1,2}$ can be expressed as $\lambda_{1,2} = -\xi \pm i\eta$, with $\xi = c_1/(2I_{yy})$, and $\eta = \sqrt{4c_2 I_{yy} - c_1^2}/(2I_{yy})$. The angle of attack follows from

$$\alpha - \alpha_o = Ae^{-\xi t} \cos(\eta t + \zeta), \quad (14.3-10)$$

where A and ζ are constants. A strong damping occurs for large ξ , i.e. small values of I_{yy} and a large value of c_1 . The constant c_1 , and so the damping, is a combination of jet damping and damping in pitch, but not of the static stability. The time it takes before the amplitude reaches half its value, $T_{\frac{1}{2}}$, follows from Eq. (4.3-10), $T_{\frac{1}{2}} = (I_{yy} \ln 4)/c_1$. The period, P , follows from Eq. (14.3-10), $P = 4\pi I_{yy}/\sqrt{4c_2 I_{yy} - c_1^2}$. In the case that there is no damping, i.e.

$$c_1 = 0: P = 2\pi\sqrt{I_{yy}/c_2}.$$

From Eq. (14.3-5b) it is clear that c_2 is equivalent to a stiffness or a spring constant. Now $c_2 = C_{m_\alpha} \hat{q} S_d$ where \hat{q} depends on the velocity and the altitude, C_{m_α} depends on M_a and α , and the product $C_{m_\alpha} \hat{q}$ is called the *aerodynamic stiffness*.

It is seen that the period of the oscillations is determined by the damping parameters and the aerodynamic stiffness. If the motor does not thrust, the

terms mx_e^2 and \dot{I}_{yy} in Eq. (14.3-9) disappear, and both period and damping will change.

14.3.3 Some aspects of non-linear instability

With the development of missiles where angles of attack up to 180° may be encountered, or for re-entry vehicles, which may also fly at very high angles of attack, the dependence of aerodynamic forces and moments on α , cannot be assumed to be linear anymore, and windtunnel investigations become of utmost importance [5]. Unstable motions associated with these high angles of attack may occur with missiles or space vehicles. Other examples of non-linear behavior that may lead to instabilities, may be associated with the *structural stiffness* and *elasticity* of the vehicle.

There are also causes of dynamic instability, which, on their onset, are not related to extreme angles of attack but are due to the generation of *unsymmetrical vortices*, or *resonance* and *coupling between modes of oscillation*. This may lead to a highly non-linear behavior. Such effects, for instance, are *roll lock-in*, *catastrophic yaw* and *Magnus instability*.

Non-linear rolling motion may occur with a spinning vehicle. To cancel out the effects of thrust misalignment and other asymmetries, one may spin the vehicle. For small rockets and missiles, the spin may originate from a fin cant, which causes a rolling moment. For small α , the roll rate is proportional to the fin cant angle, and independent of α . This is called *linear rolling* (Fig. 14.6). However, at larger angles of attack, yaw generates a damping moment that opposes the rolling moment and the spin rate decreases: *roll slow-down*. This is caused by non-linear aerodynamic effects which appear

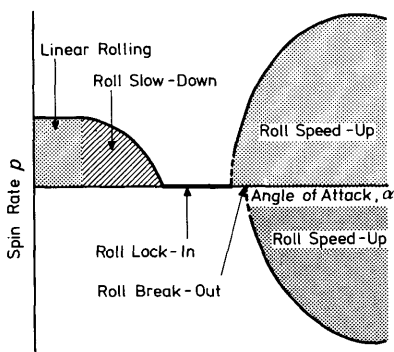


Fig. 14.6 The non-linear rolling motion

to vary periodically with the roll angle. With increasing angles of attack the damping moment, despite fin cant, reduces the spin rate to zero. This is known as *roll lock-in*. At still higher α , the vehicle starts to roll again, not necessarily according to the fin cant. This is known as *roll speed-up* and high roll rates can be achieved. It is believed that roll speed-up is caused by a highly non-linear aerodynamic phenomenon [10].

Catastrophic yaw may be the result of a second type of non-linear instability. In Fig. 14.7, the desired roll rate and the pitch rate are schematically shown for the flight of a small uncontrolled rocket or missile. Because of the decreasing mass and aerodynamic stiffness, the pitch rate decreases and, after some time, may equal the roll rate: *roll resonance*. If this roll resonance is maintained during the remainder of the flight, one again speaks of *roll lock-in*. During this roll lock-in, the resulting angular motion (*pitch-yaw*) may exhibit very large, even growing, amplitudes that finally may lead to the disintegration of the vehicle or damage of the payload (*catastrophic yaw*). On the other hand, roll lock-in not necessarily leads to catastrophic yaw. Various causes have been traced for the roll lock-in phenomenon discussed above. For instance, some normal force usually is required to make $x_{cm} = x_{cp}$. If the cm is offset with respect to the centerline, a roll moment is induced, and this moment increases with higher angles of attack. This effect is discussed by Price [11]. Nicolaides [12] showed that an asymmetric generation of vortices on the leading edges of the fins also can be traced as one of the causes of roll lock-in and catastrophic yaw. Not only on the leading edges of the wings but also on the slender, cylindrical body, asymmetric vortices are generated. It is possible to predict these asymmetric vortex effects [13] and account for them, especially for the roll and yaw moments that may be generated. These effects of roll resonance, which have been discussed above for uncontrolled rockets, in the same way play a part for re-entry vehicles. For these vehicles terms like the aerodynamic stiffness

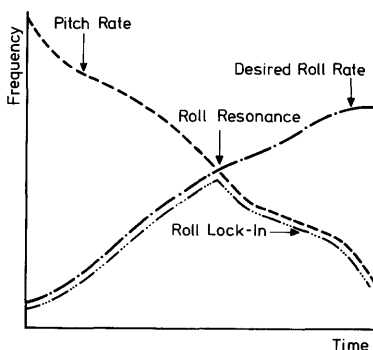


Fig. 14.7 Roll resonance and roll lock-in

increase during descent. Here too, one meets the problem of avoiding resonance followed by a lock-in. The problem has been analysed by Nayfeh [14].

Magnus instability is a third type of non-linear instability. To understand it, consider a missile flying at an angle of attack, and $\beta = 0$. Owing to the angle α , there is a cross-flow normal to the longitudinal axis. If the missile is spinning about its longitudinal axis, there will be a layer of circulating air. This *circulation* in combination with the cross-flow, creates velocity differences at the periphery of the missile, thus causing pressure differences and hence sideward forces, called *Magnus forces*. The displacement of the missile due to the Magnus forces may be small, though not negligible as dispersion is concerned. The Magnus forces usually also yield a moment about the *cm*, the *Magnus moment*. This may lead to unacceptable large yaw angles. It is seen here, that an angle of incidence, in combination with rolling, may lead to yaw. Clearly, for such motions, it is not permitted to uncouple the equations of motion, Eqs. (4.2-58).

Often one tries to avoid catastrophic yaw, due to roll resonance followed by roll lock-in, by a high enough spin rate. The pitch rate and roll rate curve, as shown in Fig. 14.7, will not intersect then, but now there is the danger of Magnus instability.

Finally we have to mention that among the dynamic instabilities, a related *spin-yaw resonance phenomenon* may occur. In this case the damping is ineffective and hence an oscillation with a growing amplitude is possible. The fact that the damping is ineffective is mainly due to the decrease in aerodynamic stiffness, $C_{m_\alpha} \hat{q}$, at great altitudes.

For controlled flight vehicles, the control system will suppress aerodynamic instabilities but a thorough knowledge of the aerodynamic forces, moments and the coupling between the various motions is necessary for a successful design of such a control mechanism.

14.4 Other atmospheric effects

We mentioned in the previous sections how aerodynamic forces are generated by a vehicle flying through the atmosphere. The effects of these forces are various: *losses and gains in performance*, *trajectory dispersion*, *aerodynamic loads* and *aerodynamic heating*, to name only a few. We cannot discuss these effects in detail, but we merely mention their most important aspects.

Performance gains as compared to vacuum performance occur mainly with winged vehicles such as cruise missiles and the Space Shuttle. The range of these vehicles and their applicability is strongly enlarged by the use of lifting surfaces. For vehicles which fly mainly vertical trajectories through the atmosphere, and where no controlled re-entry phase is required, wings are of no use.

The atmospheric drag reduces the performance of vehicles. In Section 14.2.2, we have discussed the drag coefficient. The drag, D , varies with the altitude and the velocity. The deceleration, in 'g,' of the vehicle, due to drag, or what is the same, the *drag-to-weight ratio*, is

$$D/(Mg_0) = C_D \frac{1}{2} \rho V^2 S / (Mg_0). \quad (14.4-1)$$

If one refers to the initial mass, M_0 , instead of the instantaneous mass, M , one finds

$$D/(Mg_0) = C_D \frac{1}{2} \rho V^2 S \Lambda(t) / (M_0 g_0) = C_D \frac{1}{2} \rho V^2 \Lambda(t) K. \quad (14.4-2)$$

Here S is a cross-sectional reference area, $\Lambda(t) = M_0/M(t)$, is the *instantaneous mass ratio* and $K = S/(M_0 g_0)$, is the *drag parameter*, depending on the cross-sectional area and the initial weight of the rocket vehicle. To give the reader an idea of the order of magnitude of the drag parameter, values of K for some launch vehicles and sounding rockets are listed in Table 14.1, as based on the maximum vehicle diameter. Also the initial *thrust-to-weight ratio*, $\psi_0 = F/(M_0 g_0)$ is listed.

According to Eq. (14.4-2) the quantity K is an important parameter for the influence of the drag. Low values of K mean a small deceleration due to drag, while high values of K yield large decelerations. To illustrate the influence of the drag on rocket performance, Fig. 14.8 shows for a one-stage rocket, with constant thrust, and a mass ratio $\Lambda = 3.2$, the culmination altitude for a vertical flight. The figure is based on calculations by Cornelisse [15]. It is seen that the effect of drag increases with increasing K . The vacuum performance, which is identical to $K=0$, yields the maximum altitude. Moreover, we see that for $K \neq 0$, there is an optimal value for ψ_0 .

Table 14.1 Order of magnitude of the drag parameter and the thrust-to-weight ratio for some typical launch vehicles and sounding rockets

	K (m^2/MN)	ψ_0
Launch Vehicles:		
Saturn V	0.3	1.2
Titan IID/SLV 5D	1.5	2
Delta	4	1.5
Scout D	5	2.5
L III S	6	1.2
Sounding Rockets:		
Astrobee	10	5
Black Brant 5A	13	13
Agate	18	7
Nike-Cajun	21	33
Skua I	23	32

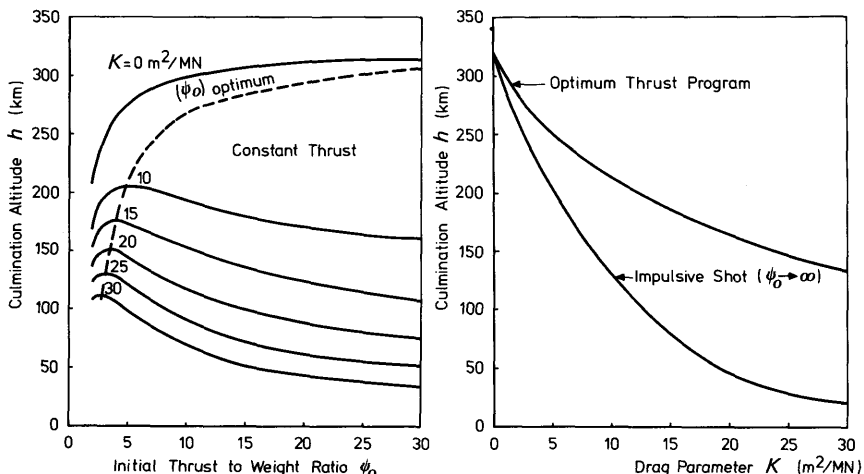


Fig. 14.8 The effect of drag on the performance of a one-stage rocket for a constant thrust, and the performance of the same vehicle for optimum thrust programming. For the case: $I_{sp} = 220$ s; $\Lambda = 3.2$; $C_D = 0.4 + 0.5 M_a^6$, $M_a \leq 1$; $C_D = 0.16 + 0.74/M_a$, $M_a \geq 1$

for a maximum culmination altitude. For a flight in vacuum, the gravity losses require an impulsive shot to get the best performance. High values of ψ_0 , however, lead to high velocities and as D is about proportional to V^2 , drag losses in the atmosphere increase steeply with ψ_0 , and will dominate. Therefore a finite value of ψ_0 will yield an optimum performance. Also plotted is the culmination altitude for the impulsive shot, $\psi_0 \rightarrow \infty$, versus K . It is seen that even for rather small values of K , drag losses become tremendous. A large performance gain is possible with an *optimum thrust program*, starting with a high thrust and followed by a low thrust [15]. It is seen from the curve for optimum thrust programming that drag losses, especially for those rockets which have a large drag parameter K , can be reduced considerably as compared to the constant thrust program. From Table 14.1 we see that this is especially important for sounding rockets, where usually $K \geq 10 \text{ m}^2/\text{MN}$. Also ψ_0 for sounding rockets is much larger than for launch vehicles. As K and ψ_0 are small for the latter vehicles, one can expect their drag losses to be small. For an initial performance estimate, it is admissible therefore to neglect drag effects for the larger launch vehicles. For launch vehicles like the Scout and the L III S drag may become of more importance. For a cursory approximation of drag losses on launch vehicles, one may use the graphs and expressions given by White [16]; however, these estimates are less suited for smaller rockets, such as missiles and sounding rockets, which, as appears from Table 14.1 and Fig. 14.8, are much more sensitive to drag.

Wind has two different effects on rockets. The first one is *structural*. As a result of wind, bending moments may be induced in the vehicle. Not only

during the flight, but also before the launch, wind loads may be considerable. Schöyer [17] has shown that, in the design of rockets, by a suitable combination of aerodynamic properties and mass distribution, windloads may be reduced. The other effect is *dispersion*. Owing to the wind velocity the vehicle is transported with the wind. On the other hand, as we saw in Section 14.3.1, a stable vehicle will turn its nose into the wind and during the powered flight of an uncontrolled vehicle this effect, which is opposite to the displacement, dominates and is one of the important causes that the trajectory deviates from the nominal trajectory.

The *wind field* itself varies with time, altitude and the location on Earth. As for other atmospheric properties, one may define mean properties of the wind field, but it is often more important to know the maximum expected wind field. Therefore one may use standard wind profiles, of which, among others, Schöyer [18] presents a compilation. Not only the wind velocity itself, but also the variation of wind velocity with altitude: *windshear*, stationary and dynamic, is very important. Stationary and dynamic windshear and gusts also cause loads on the vehicle, trajectory dispersion, and have to be accounted for if one wants to specify the requirements of the guidance and control system. An extensive discussion of wind effects on launch vehicles is given by Geissler [19].

Aerodynamic heating is the result of friction between the rapidly moving vehicle and the surrounding air. It is a well-known phenomenon for re-entry vehicles, but it may also be important for launch vehicles. For instance, the instant at which the protecting shrouds of a launch vehicle, covering a satellite may be ejected is often determined by the possibility of aerodynamic heating of the satellite or parts of it. We will not go into the subject of aerodynamic heating. In the following chapters we will mainly deal with satellite orbits and the trajectories of spacecraft. However, in Chapter 17 we will once again return to the performance of a launch vehicle.

References

- 1 Anon. (1972), *CIRA 1972 Reference Atmosphere*, Akademie Verlag, Berlin.
- 2 Nielsen, J. N. (1960), *Missile Aerodynamics*, McGraw-Hill, New York.
- 3 Chin, S. S. (1961), *Missile Configuration Design*, McGraw-Hill, New York.
- 4 Jorgensen, L. H. (1973), *Prediction of Static Aerodynamic Characteristics for Space-Shuttle-Like and Other Bodies at Angles of Attack from 0° to 180°*, NASA TN D-6996, Washington.
- 5 Smith, L. H. and Hunn, R. H. (1976), Aerodynamic characteristics of an axisymmetric body undergoing a uniform pitching motion, *J. Spacecraft*, **13**, 8–14.

Rocket Motion in the Atmosphere

- 6 Allen, H. J. and Perkins, E. W. (1951), *A Study of Effects of Viscosity on Flow over Slender Inclined Bodies of Revolution*, NACA Report 1048, Washington.
- 7 Pitts, W. C., Nielsen, J. N. and Kaatari, G. E. (1957), *Lift and Center of Pressure of Wing-Body-Tail Combinations at Subsonic, Transonic and Supersonic Speeds*, NACA Report 1307, Washington.
- 8 Hoerner, S. F. (1965), *Fluid-Dynamic Drag*, 1965 edition, published by S. F. Hoerner, Midland Park.
- 9 Bonney, B. A. (1950), *Engineering Supersonic Aerodynamics*, McGraw-Hill, New York, p. 181.
- 10 Daniels, P. (1970), A study of the nonlinear rolling motion of a four-finned missile, *J. Spacecraft*, **7**, 510–512.
- 11 Price, D. A. (1967), Sources, mechanisms and control of roll resonance phenomena for sounding rockets, *J. Spacecraft*, **4**, 1516–1525.
- 12 Nicolaides, J. D. (1966), *A Review of Some Recent Progress in Understanding Catastrophic Yaw*, AGARD Report 551, AGARD, Paris.
- 13 Fidler, J. E. and Bateman, M. C. (1975), Asymmetric vortex effects on missile configurations, *J. Spacecraft*, **12**, 674–681.
- 14 Nayfeh, A. H. and Sarie, W. S. (1971), *Nonlinear Resonances in the Motion of Reentry Bodies*, AIAA Paper 71-47, New York.
- 15 Cornelisse, J. W. (1973), *The Culmination Altitude of One-Stage Rockets for a Vertical Ascent. Constant and Optimum Thrust*, (in Dutch), Memorandum VTH-M200, Delft University of Technology, Dept. of Aerospace Eng., Delft.
- 16 White, J. F. (ed.) (1963), *Flight Performance Handbook for Powered Flight Operations*, John Wiley, New York, 2-68 to 2-92.
- 17 Schöyer, H. F. R. (1968), *Windloads on Vertically or About Vertically Ascending Rockets*, (in Dutch), Memorandum VTH-M119, Delft University of Technology, Dept. of Aerospace Eng., Delft.
- 18 Schöyer, H. F. R. (1967), *Windvelocity Profiles and Windshear up to 50 km Altitude, for Areas Between 25° North and 60° North*, (in Dutch), Memorandum VTH-M113, Delft University of Technology, Dept. of Aerospace Eng., Delft.
- 19 Geissler, E. D. (ed.) (1970), *Wind Effects on Launch Vehicles*, AGARD-Dograph no. 115, Technivision Services, Slough.

15 The Many-Body Problem

The classical problem in celestial mechanics is the determination of the motion of n bodies under their mutual gravitational attractions. These bodies are supposed to possess a spherical symmetry so that they can be regarded as point masses (Section 3.5). It is assumed that no other forces act upon these bodies. This problem has inspired many astronomers and mathematicians since Newton, but still no analytical solution for the *general n-body problem* is known. It is even very unlikely that an analytical solution will ever be found.

Only the *two-body problem* has a closed-form analytical solution. For the *three-body problem* with arbitrary masses, only two kinds of exact particular solutions have been obtained: the straight-line equilibrium solution and the equilateral-triangular equilibrium solution. In the case of two equal masses, we have the isosceles-triangular solution. Sundman [1] developed for the three-body problem a solution in the form of a series expansion. These series, however, converge so slowly that the method is of little practical value.

Because of this mathematically clear distinction between the two-body dynamics and the motion of bodies in systems with $n > 2$, we usually speak of a *many-body problem* if $n > 2$.

In classical astronomy, typical examples of n -body problems are the motion of the planets about the Sun and the motion of stars in a stellar cluster. For the motion of interplanetary spacecraft, and to a lesser extent of Earth satellites, we also deal with a many-body problem, because these motions are also governed by many gravitational fields.

15.1 The general N -body problem

Consider an inertial reference frame XYZ and a system of n bodies, each with constant mass (Fig. 15.1). The position of a body P_i ($i = 1, 2, \dots, n$), with mass m_i , relative to the inertial frame is determined by its radius vector \mathbf{R}_i . According to Newton's laws (Sections 3.2 and 3.5), the equation of motion of the body P_i relative to the inertial frame is

$$m_i \frac{d^2 \mathbf{R}_i}{dt^2} = G \sum_j^* \frac{m_i m_j}{r_{ij}^3} \mathbf{r}_{ij}, \quad (15.1-1)$$

where G is the *universal gravitational constant* and the notation \sum_j^* stands

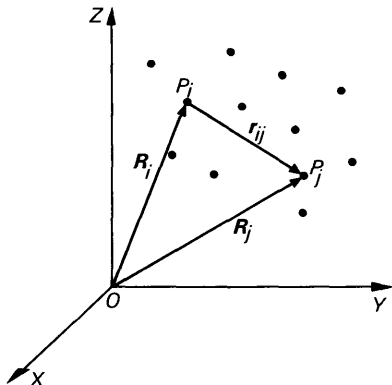


Fig. 15. The position of n bodies in the inertial reference frame XYZ

for a summation over all j , excluding $j = i$. The vector \mathbf{r}_{ij} is defined by

$$\mathbf{r}_{ij} = \mathbf{R}_j - \mathbf{R}_i. \quad (15.1-2)$$

This vector is directed from body P_i to body P_j .

For the actual determination of the motion of each body, we have to integrate numerically the equations of motion. For systems involving more than a few hundred bodies, the integration of these equations is totally impractical. To study the general evolution of such systems, we have to rely on statistical techniques [2]. Only some interesting general features of the dynamical behavior of the bodies can be obtained analytically. These are known as the *integrals of motion*.

15.1.1 Integrals of motion

In Section 3.4, the dynamics of a system of particles were discussed. Because the n bodies can be regarded as point masses, the results of that section can be applied directly to our problem. Since there are no external forces acting on the system under consideration, Eq. (3.4-7) and Eq. (3.4-13) can be written as

$$\frac{d^2 \mathbf{R}_{cm}}{dt^2} = 0, \quad (15.1-3)$$

and

$$\frac{d\mathbf{H}}{dt} = 0, \quad (15.1-4)$$

where \mathbf{R}_{cm} is the position vector of the center of mass of the system and \mathbf{H} is the angular momentum of the entire system with respect to the origin O of the inertial frame. As is customary in celestial mechanics, we will use the

symbol \mathbf{H} instead of \mathbf{B} used in Section 3.4.1 to denote the angular momentum. Integration of Eqs. (15.1-3) and (15.1-4) yields

$$\frac{d\mathbf{R}_{cm}}{dt} = \mathbf{a}, \quad (15.1-5)$$

$$\mathbf{R}_{cm} = \mathbf{a}t + \mathbf{b}, \quad (15.1-6)$$

and

$$\mathbf{H} = \mathbf{c}, \quad (15.1-7)$$

where \mathbf{a} , \mathbf{b} and \mathbf{c} are arbitrary constant vectors.

The Eqs. (15.1-5) and (15.1-6) state that the center of mass of the system, often referred to as the *barycenter*, is at rest or moves with uniform velocity relative to the inertial frame. According to the discussion in Section 3.1 on inertial frames, we may conclude that a non-rotating reference frame with its origin at the center of mass of the system is an inertial reference frame too. If we consider, for example, our solar system as a n -body system with no external forces acting upon it, Eq. (15.1-1) describes the motion of the Sun, the planets and other celestial bodies relative to an inertial frame with its origin at the center of mass of the solar system. Due to the very large solar mass compared to all other masses in the solar system (Section 2.2.1), the barycenter lies very close to the center of the Sun. Depending on the positions of the planets relative to the Sun, the distance between the center of mass of the solar system and the center of the Sun is always less than one hundredth of the distance between Earth and Sun.

Equation (15.1-7) states that the total angular momentum of the system is constant in magnitude and direction. As we consider bodies with finite dimensions, the total angular momentum of the system includes the *proper angular momentum* of the bodies due to their rotation. However, we have assumed that the mass density distribution of each body is spherically symmetrical, and so there will be no variations in the rotational velocity of each body due to the gravitational interactions between the bodies. Consequently, the *orbital angular momentum* of a system of finite bodies is constant too. The plane through the center of mass of the system normal to \mathbf{H} has a fixed orientation and is therefore called the *invariable plane (of Laplace)*. It can be used as a fundamental reference plane for the motion of the bodies. For the solar system, this plane is inclined at about $1^{\circ}39'$ to the ecliptic and lies between the orbital planes of the giant planets Jupiter and Saturn.

Returning to Eq. (15.1-1), we note that by introducing a scalar function U_i , defined as

$$U_i = -G \sum_j * \frac{m_j}{r_{ij}} + U_{i_0}, \quad (15.1-8)$$

where U_{i_0} is a constant, Eq. (15.1-1) can be written in the form

$$\frac{d^2 \mathbf{R}_i}{dt^2} = -\nabla_i U_i, \quad (15.1-9)$$

where ∇_i denotes the gradient with respect to the coordinates of body P_i . From Section 3.5 we know that U_i then is the potential of the force field governing the motion of body P_i . By convention, the value of this potential equals zero at infinity, which implies: $U_{i_0} = 0$. From inspection of Eq. (15.1-8) it will be clear that the force field represented by this potential is not central. We also note that U_i is a function of both the coordinates of P_i and the coordinates of all other bodies P_j . Even when keeping body P_i fixed relative to the frame XYZ, the potential energy of body P_i will change due to the motion of the bodies P_j . A force field with such a time-varying potential is not conservative, and the sum of kinetic and potential energy of P_i will vary with time. For the entire system of n bodies, however, an energy integral can be found as will be shown.

Scalar multiplication of Eq. (15.1-1) with $\frac{d\mathbf{R}_i}{dt}$ and summation over all i gives

$$\sum_i m_i \frac{d\mathbf{R}_i}{dt} \cdot \frac{d^2 \mathbf{R}_i}{dt^2} = G \sum_i \sum_j * \frac{m_i m_j}{r_{ij}^3} \frac{d\mathbf{R}_i}{dt} \cdot \mathbf{r}_{ij}. \quad (15.1-10)$$

Now

$$\sum_i \sum_j * \frac{m_i m_j}{r_{ij}^3} \mathbf{r}_{ij} \cdot \frac{d\mathbf{R}_i}{dt} = \sum_i \sum_j * \frac{m_i m_j}{r_{ij}^3} \mathbf{r}_{ij} \cdot \frac{d\mathbf{R}_j}{dt} - \sum_i \sum_j * \frac{m_i m_j}{r_{ij}^3} \mathbf{r}_{ij} \cdot \frac{d\mathbf{r}_{ij}}{dt}, \quad (15.1-11)$$

or

$$2 \sum_i \sum_j * \frac{m_i m_j}{r_{ij}^3} \mathbf{r}_{ij} \cdot \frac{d\mathbf{R}_i}{dt} = \sum_i \sum_j * m_i m_j \frac{d}{dt} \left(\frac{1}{r_{ij}} \right). \quad (15.1-12)$$

By substituting Eq. (15.1-12) into Eq. (15.1-10), we obtain

$$\frac{d}{dt} \left\{ \frac{1}{2} \sum_i m_i \left(\frac{d\mathbf{R}_i}{dt} \cdot \frac{d\mathbf{R}_i}{dt} \right) - \frac{1}{2} G \sum_i \sum_j * \frac{m_i m_j}{r_{ij}} \right\} = 0. \quad (15.1-13)$$

As the velocity, \mathbf{V}_i , of P_i relative to the XYZ-frame is defined by

$$\mathbf{V}_i = \frac{d\mathbf{R}_i}{dt}, \quad (15.1-14)$$

Equation (15.1-13) can be integrated to

$$\frac{1}{2} \sum_i m_i \mathbf{V}_i^2 - \frac{1}{2} G \sum_i \sum_j * \frac{m_i m_j}{r_{ij}} = \mathcal{E}, \quad (15.1-15)$$

where \mathcal{E} is a constant. The first term at the left-hand side of Eq. (15.1-15) is

the *kinetic energy*, \mathcal{E}_k , of the system. The second term (including the minus sign), which represents the internal gravitational energy of the system, is called the *potential energy*, \mathcal{E}_p , of the system. Thus, while for each individual body the sum of kinetic and potential energy is not constant, due to a continuous exchange of energy between the bodies, the *total energy*, \mathcal{E} , remains constant.

From Eq. (15.1-15) we conclude that if in a system of n bodies, two bodies approach each other very close, the velocity of at least one of the n bodies must become very large. Actual collisions should, for ‘real’ point masses always be accompanied with infinitely large velocities.

The Eqs. (15.1-5), (15.1-6), (15.1-7) and (15.1-15), which can be written as ten scalar equations, constitute the so-called *ten integrals of motion* of the n -body problem. These ten integrals are very useful for the physical insight into the dynamical behavior of a system of n bodies. In classical celestial mechanics they can also be used to check the numerical accuracy of integration procedures. For the motion of space vehicles, this last application is of no importance. Due to the very small mass of a spacecraft compared to the mass of celestial bodies, and because in numerical computations we always have a limited number of significant figures, large errors in the vehicle’s trajectory computation will hardly be noticeable in the values of the total angular momentum and the total energy of the system.

Brunns [3] and Poincaré [4] proved that the ten integrals are the only independent algebraic integrals that can be found in the n -body problem. The complete solution of the $3n$ second-order differential equations describing the motion of the n bodies requires $6n$ integration constants. With the ten integrals of motion, it is possible to reduce the order of the problem to $6n - 10$. Jacobi [5] showed that a further reduction by two is possible in the three-body problem; first, by eliminating the time and by taking one of the other variables as the independent one, and secondly by selecting a particular reference frame. The second step is known as the *elimination of the nodes*. Such a reduction may also be performed in case of the n -body problem [6]. The practical significance, however, of a reduction from $6n - 10$ to $6n - 12$ is questionable, because of the very complex analytical expressions involved.

15.1.2 The Virial theorem

The tenth integral of motion states that the total energy, \mathcal{E} , of the system is constant. Some interesting remarks can be made on the value of \mathcal{E} . Consider the motion of the n bodies with respect to an inertial reference frame XYZ with its origin at the barycenter. The polar moment of inertia, I , of this system is defined as

$$I = \sum_i m_i \mathbf{R}_i \cdot \mathbf{R}_i \quad (15.1-16)$$

Differentiating this equation with respect to time, we obtain

$$\frac{dI}{dt} = 2 \sum_i m_i \mathbf{R}_i \cdot \frac{d\mathbf{R}_i}{dt}, \quad (15.1-17a)$$

$$\frac{d^2I}{dt^2} = 2 \sum_i m_i \mathbf{V}_i \cdot \mathbf{V}_i + 2 \sum_i m_i \mathbf{R}_i \cdot \frac{d^2\mathbf{R}_i}{dt^2}. \quad (15.1-17b)$$

Substituting Eq. (15.1-1) into Eq. (15.1-17b) gives

$$\frac{d^2I}{dt^2} = 2 \sum_i m_i V_i^2 + 2G \sum_i \sum_j * \frac{m_i m_j}{r_{ij}^3} \mathbf{R}_i \cdot \mathbf{r}_{ij}. \quad (15.1-18)$$

Analogous to the derivation of Eq. (15.1-12), it can be shown easily that

$$2 \sum_i \sum_j * \frac{m_i m_j}{r_{ij}^3} \mathbf{R}_i \cdot \mathbf{r}_{ij} = - \sum_i \sum_j * \frac{m_i m_j}{r_{ij}}. \quad (15.1-19)$$

Substituting Eq. (15.1-19) into Eq. (15.1-18), and using the definitions of \mathcal{E}_k and \mathcal{E}_p , we find

$$\frac{d^2I}{dt^2} = 4\mathcal{E}_k + 2\mathcal{E}_p \quad (15.1-20a)$$

or, with Eq. (15.1-15),

$$\frac{d^2I}{dt^2} = 4\mathcal{E} - 2\mathcal{E}_p. \quad (15.1-20b)$$

The Eqs. (15.1-20) are known as the *Lagrange-Jacobi identity*. It should be remembered that \mathcal{E}_p , though a function of time, is negative definite. So, if \mathcal{E} is positive, Eq. (15.1-20b) shows that then $\frac{d^2I}{dt^2}$ is always positive, and ultimately I will increase indefinitely with time. This means that the distance from the origin of at least one body ultimately approaches infinity. We then say that such a body *escapes* from the system. Consequently, for a stable system of n bodies, i.e. a system where all bodies remain in a restricted volume around the center of mass, \mathcal{E} must be negative. Of course, this is only a necessary condition and by no means a sufficient one for the stability of the system.

The Lagrange-Jacobi identity is the basis for many qualitative methods in the many-body problem. For instance, it can be used to prove that it is impossible for all bodies to collide simultaneously after an infinite time, and that a simultaneous collision of all bodies implies that the total angular momentum of the system is zero [7]. We will discuss only one example of these interesting qualitative results.

For the relation between the average values of $\frac{d^2I}{dt^2}$, \mathcal{E}_p and \mathcal{E}_k over a

certain time interval $\Delta t = t_1 - t_0$, Eq. (15.1-20a) gives

$$\frac{1}{\Delta t} \int_{t_0}^{t_1} \frac{d^2 I}{dt^2} dt = \frac{4}{\Delta t} \int_{t_0}^{t_1} \mathcal{E}_k dt + \frac{2}{\Delta t} \int_{t_0}^{t_1} \mathcal{E}_p dt,$$

or, with Eq. (15.1-17a),

$$\frac{1}{\Delta t} \left[\sum_i m_i \mathbf{R}_i \cdot \frac{d\mathbf{R}_i}{dt} \right]_{t_0}^{t_1} = 2\bar{\mathcal{E}}_k + \bar{\mathcal{E}}_p, \quad (15.1-21)$$

where $\bar{\mathcal{E}}_k$ and $\bar{\mathcal{E}}_p$ stand for the time-averaged values of \mathcal{E}_k and \mathcal{E}_p , respectively. For a *stable* system where both the distance of a body from the center of mass and the velocity of that body are bounded, the left-hand side of Eq. (15.1-21) will tend to zero if the time interval is taken sufficiently large. We then have

$$2\bar{\mathcal{E}}_k + \bar{\mathcal{E}}_p = 0, \quad \Delta t \rightarrow \infty. \quad (15.1-22)$$

Because the total energy of the system is constant, we also have

$$\bar{\mathcal{E}}_k + \bar{\mathcal{E}}_p = \mathcal{E}. \quad (15.1-23)$$

From Eq. (15.1-22) and Eq. (15.1-23) the following relation for a stable system can be obtained:

$$\bar{\mathcal{E}}_k = -\frac{1}{2}\bar{\mathcal{E}}_p = -\mathcal{E}. \quad (15.1-24)$$

This relation, which was first found by Clausius in his studies on the kinetic theory of gases [8], is known as the *Virial theorem* or *Clausius' theorem*. It states that for a n -body system which is bounded in size and velocity, the value of the kinetic energy averaged over a large time interval equals minus half the time-averaged value of the potential energy of the entire system. The time-averaged value of the kinetic energy also equals minus the total energy. This Virial theorem is of great importance in stellar dynamics and forms a basis for statistical calculations on stellar clusters [9] and clusters of galaxies. For example, it provides the only current estimate of the mass of clusters of galaxies.

15.2 The circular restricted three-body problem

The *three-body problem* deals with the motion of three bodies under their mutual gravitational attractions, while no other forces are acting upon these bodies. In the *restricted three-body problem* [10], we assume one body to have a very small mass as compared to the masses of the other two bodies. Then the approximation can be made that the motion of the two massive bodies will not be influenced by the attraction of the third body. We will denote the two massive bodies with P_1 and P_2 , where P_1 has the largest mass.

Consider an inertial frame XYZ with its origin at the center of mass of the system (Fig. 15.2). This center of mass will, as a consequence of our

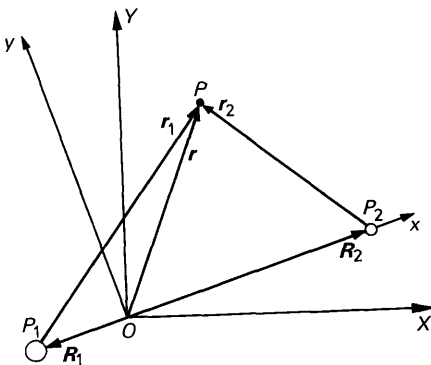


Fig. 15.2 The inertial reference frame XYZ and the rotating references frame xyz for the three-body problem

assumptions, lie on the line connecting P_1 and P_2 . For the position vectors \mathbf{R}_1 and \mathbf{R}_2 we can write

$$m_1 \mathbf{R}_1 + m_2 \mathbf{R}_2 = 0,$$

or

$$\mathbf{R}_1 = -\frac{m_2}{m_1} \mathbf{R}_2. \quad (15.2-1)$$

As the angular momentum of the system is constant, Eq. (15.1-7) can be written as

$$\mathbf{H} = m_1 \mathbf{R}_1 \times \frac{d\mathbf{R}_1}{dt} + m_2 \mathbf{R}_2 \times \frac{d\mathbf{R}_2}{dt} = \mathbf{c}. \quad (15.2-2)$$

Substituting Eq. (15.2-1) into Eq. (15.2-2), we obtain

$$\mathbf{H} = m_1 \left(1 + \frac{m_1}{m_2}\right) \mathbf{R}_1 \times \frac{d\mathbf{R}_1}{dt} = \left(1 + \frac{m_1}{m_2}\right) \mathbf{H}_1 = \mathbf{c}, \quad (15.2-3a)$$

and

$$\mathbf{H} = m_2 \left(1 + \frac{m_2}{m_1}\right) \mathbf{R}_2 \times \frac{d\mathbf{R}_2}{dt} = \left(1 + \frac{m_2}{m_1}\right) \mathbf{H}_2 = \mathbf{c}, \quad (15.2-3b)$$

where \mathbf{H}_1 and \mathbf{H}_2 stand for the angular momentum of the bodies P_1 and P_2 , respectively. By inspection of Eq. (15.2-1) and Eqs. (15.2-3), we conclude that the two massive bodies move in one plane and that the orbits of the bodies are similar. The XY -plane in Fig. 15.2 has been chosen such that it coincides with the plane of motion.

In the *circular restricted three-body problem*, we further assume the two massive bodies to move in circular orbits about the center of mass. In this circular restricted three-body problem an important partial solution can be

found. Therefore, we introduce a reference frame xyz with its origin at the center of mass of the system and with the x -axis coinciding with the line joining P_1 and P_2 ; the positive z -axis is directed along the positive Z -axis (Fig. 15.2). The xyz -frame thus rotates relative to the XYZ -frame with a constant angular velocity, Ω , about the Z -axis. The bodies P_1 and P_2 are fixed relative to the xyz -frame. If \mathbf{r} is the position vector of the third body P in the rotating frame, and the radius vectors from P_1 and P_2 to P are denoted by \mathbf{r}_1 and \mathbf{r}_2 , respectively, the equation of motion of P relative to the rotating frame is, according to Eq. (3.3-10),

$$-G \frac{m_1}{r_1^3} \mathbf{r}_1 - G \frac{m_2}{r_2^3} \mathbf{r}_2 = \frac{d\Omega}{dt} \times \mathbf{r} + \Omega \times (\Omega \times \mathbf{r}) + 2\Omega \times \frac{\delta \mathbf{r}}{\delta t} + \frac{\delta^2 \mathbf{r}}{\delta t^2}, \quad (15.2-4)$$

where $\frac{\delta}{\delta t}$ indicates the time-derivative in the rotating frame. Because Ω is a constant vector, Eq. (15.2-4) simplifies to

$$\frac{\delta^2 \mathbf{r}}{\delta t^2} = -G \left(\frac{m_1}{r_1^3} \mathbf{r}_1 + \frac{m_2}{r_2^3} \mathbf{r}_2 \right) - \Omega \times (\Omega \times \mathbf{r}) - 2\Omega \times \frac{\delta \mathbf{r}}{\delta t}. \quad (15.2-5)$$

The second and third term on the right-hand side of this equation represent the *centripetal* and *Coriolis* acceleration due to the rotation of the reference frame xyz . It can be proved that the first two terms on the right-hand side of Eq. (15.2-5) can be written as the gradient of a *potential function*, U , defined as

$$U = -G \left(\frac{m_1}{r_1} + \frac{m_2}{r_2} \right) - \frac{1}{2} \Omega_z^2 (x^2 + y^2). \quad (15.2-6)$$

This potential function not only accounts for the gravitational forces but also for the centripetal force. The introduction of this potential function is possible because \mathbf{R}_1 , \mathbf{R}_2 and Ω are constant vectors in the xyz -frame, and

$$\Omega = \Omega_z \mathbf{e}_z. \quad (15.2-7)$$

It will be evident that the Coriolis acceleration term in Eq. (15.2-5) cannot be incorporated into a potential function, because it contains the velocity of the third body.

Using the potential function, Eq. (15.2-5) can be written in the form

$$\frac{\delta^2 \mathbf{r}}{\delta t^2} = -\nabla U - 2\Omega \times \frac{\delta \mathbf{r}}{\delta t}. \quad (15.2-8)$$

15.2.1 Jacobi's integral

Scalar multiplication of Eq. (15.2-8) with $\frac{\delta \mathbf{r}}{\delta t}$ gives

$$\frac{\delta \mathbf{r}}{\delta t} \cdot \frac{\delta^2 \mathbf{r}}{\delta t^2} = -\frac{\delta \mathbf{r}}{\delta t} \cdot \nabla U - 2 \frac{\delta \mathbf{r}}{\delta t} \cdot \left(\Omega \times \frac{\delta \mathbf{r}}{\delta t} \right). \quad (15.2-9)$$

Now

$$\frac{\delta \mathbf{r}}{\delta t} \cdot \left(\boldsymbol{\Omega} \times \frac{\delta \mathbf{r}}{\delta t} \right) = \boldsymbol{\Omega} \cdot \left(\frac{\delta \mathbf{r}}{\delta t} \times \frac{\delta \mathbf{r}}{\delta t} \right) = 0,$$

and

$$\frac{\delta \mathbf{r}}{\delta t} \cdot \nabla U = \frac{\partial U}{\partial x} \frac{dx}{dt} + \frac{\partial U}{\partial y} \frac{dy}{dt} + \frac{\partial U}{\partial z} \frac{dz}{dt} = \frac{dU}{dt},$$

④

because U is only a function of the coordinates x, y, z of body P and not explicitly of the time. Substitution of these relations into Eq. (15.2-9) yields after integration

$$V^2 + 2U = -C, \quad (15.2-10)$$

where \mathbf{V} is the velocity of P relative to the rotating reference frame xyz and C is a constant of integration. For reasons that will appear later the minus sign is used. Equation (15.2-10) is known as *Jacobi's integral*.

This integral, of course, can also be expressed in terms of the coordinates and velocity components of P in the inertial frame XYZ . The velocity \mathbf{V} of P relative to the rotating frame is related to the velocity \mathbf{V}_a of P relative to the inertial frame by

$$\mathbf{V} = \mathbf{V}_a - \boldsymbol{\Omega} \times \mathbf{r}.$$

Because the origins of both reference frames coincide, we find with Eq. (15.2-7) for the magnitude of \mathbf{V}

$$V^2 = V_a^2 - 2\Omega_Z \left(X \frac{dY}{dt} - Y \frac{dX}{dt} \right) + \Omega_Z^2 (x^2 + y^2). \quad (15.2-11)$$

Substituting Eqs. (15.2-6) and (15.2-11) into Eq. (15.2-10), we obtain

$$\frac{1}{2}V_a^2 - G \left(\frac{m_1}{r_1} + \frac{m_2}{r_2} \right) - \Omega_Z \left(X \frac{dY}{dt} - Y \frac{dX}{dt} \right) = -\frac{1}{2}C. \quad (15.2-12)$$

The first two terms represent the total energy of P , per unit of mass, relative to the inertial frame. The third term on the left-hand side is the product of the constant angular velocity, Ω_Z , and the angular momentum of body P , per unit of mass, about the Z -axis. In Section 15.1, we found for the motion of n bodies relative to an inertial frame that the total energy, as well as the angular momentum of the total system, is constant. Because the bodies P_1 and P_2 move in circular orbits about the origin of the inertial frame, their total energy and angular momentum about the Z -axis are constant. We therefore may conclude that Eq. (15.2-12), and thus also Eq. (15.2-10), is nothing but a suitable combination of two general integrals of motion, which degenerates to this simple form in the circular restricted three-body problem.

15.2.2 Surfaces of zero velocity

Equation (15.2-10) shows that the velocity, V , of P relative to the rotating frame is a function of the position of P in this frame. The constant C depends on the initial position and velocity of P . The velocity of P equals zero if

$$2U = -C, \quad (15.2-13a)$$

or

$$2G\left(\frac{m_1}{r_1} + \frac{m_2}{r_2}\right) + \Omega_Z^2(x^2 + y^2) = C. \quad (15.2-13b)$$

The surfaces in three-dimensional xyz -space described by these equations are called *surfaces of zero velocity*, *surfaces of Hill*, or in astrophysics [11] *Roche equipotentials*. The surfaces are symmetrical with respect to the xy -plane.

As for every motion $V^2 \geq 0$, these surfaces form a boundary of the region where the motion of P can take place. For the region accessible to P the following relation holds:

$$2G\left(\frac{m_1}{r_1} + \frac{m_2}{r_2}\right) + \Omega_Z^2(x^2 + y^2) \geq C. \quad (15.2-14)$$

It should be realized that Eq. (15.2-14) only provides us with information on the region accessible to body P ; it does not tell us anything about the actual motion of P within this region.

Before examining the geometry of these surfaces for various values of C we will non-dimensionalize our expressions, leading to a simplification of the discussion following. We therefore select as characteristic length the distance P_1P_2 between the bodies P_1 and P_2 , and as characteristic mass the sum of the masses m_1 and m_2 . We then define

$$\mu = \frac{m_2}{m_1 + m_2}, \quad 1 - \mu = \frac{m_1}{m_1 + m_2}, \quad \hat{r}_1 = \frac{r_1}{P_1 P_2}, \quad \text{etc.} \quad (15.2-15a)$$

By requiring $\mu \leq \frac{1}{2}$, P_1 will always be the most massive body if m_1 and m_2 are different. For the distances of P_1 and P_2 from the origin, we then find

$$\hat{R}_1 = \mu, \quad \hat{R}_2 = 1 - \mu.$$

A non-dimensional time is introduced by

$$\hat{t} = t \sqrt{\frac{G(m_1 + m_2)}{(P_1 P_2)^3}}.$$

Because P_1 moves in a circular orbit about the origin of the inertial frame:

$$G \frac{m_2}{(P_1 P_2)^2} = \Omega_Z^2 R_1.$$

Using this relation, we find for the dimensionless time:

$$\hat{t} = t\Omega_Z. \quad (15.2-15b)$$

Writing our formulas in these non-dimensional quantities results in the elimination of the factors Ω_Z and G . In the remaining part of this section we will always use these dimensionless quantities. For simplicity, however, we will omit the indication \sim in the equations below.

In dimensionless form, Eq. (15.2-14) simplifies to

$$x^2 + y^2 + \frac{2(1-\mu)}{r_1} + \frac{2\mu}{r_2} \geq C, \quad (15.2-16)$$

where C now also is a dimensionless constant, and r_1 and r_2 are given by

$$\begin{aligned} r_1 &= \sqrt{[(\mu+x)^2 + y^2 + z^2]}, \\ r_2 &= \sqrt{[(1-\mu-x)^2 + y^2 + z^2]}. \end{aligned} \quad (15.2-17)$$

The determination of the actual shape of the surfaces of zero velocity for various values of C is rather tedious. We therefore will limit ourselves to analyse the geometry of these surfaces in a qualitative way and we will discuss only the intersection of the surfaces and the xy -plane.

If C is very large, this intersection will consist of three separate circles: one with a large radius (\sqrt{C}) about the origin and two small circles enclosing P_1 and P_2 . This situation is sketched in Fig. 15.3a. The region which is inaccessible to P is shaded. If body P originally is within the region about P_1 , it can never reach the region around P_2 . If P is at any time outside the outer circle, it cannot reach the close surroundings of P_1 and P_2 . For decreasing values of C , the inner circles become ovals and expand while the

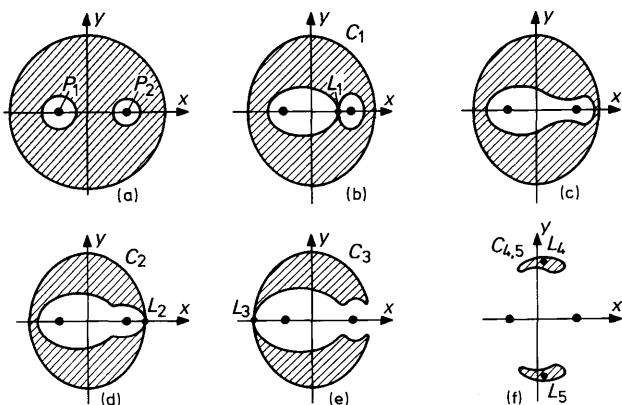


Fig. 15.3 The intersection of the zero-velocity surfaces and the xy -plane for various values of C

outer circle shrinks. When C is decreased to a value C_1 , the two inner curves meet at the point L_1 (Fig. 15.3b). A further decrease of C will cause the ovals to merge. In this situation, P can leave the region around P_1 and reach the surroundings of P_2 . A further decrease of C will let the inner contour meet the outer oval at the point L_2 (Fig. 15.3d). From now on body P can leave the regions around P_1 and P_2 and can escape from the system. For still further diminishing values of C , the shaded regions inaccessible to P shrink, until they vanish at two points L_4 and L_5 (Fig. 15.3f). As an example, Fig. 15.4 shows a more accurate illustration of the intersection of some surfaces of zero velocity and the xy -plane for the Earth-Moon system.

The fact that for certain values of C , a body which is close to P_1 never can reach an infinite distance from P_1 was first found by Hill in his studies on the motion of the Moon about the Earth [12]. Hill found that when considering the motion of Earth, Moon and Sun as a restricted three-body problem, the value of C for the lunar motion is so large that the corresponding surface of zero velocity around the Earth is closed. This surface has a maximum distance of about 110 Earth radii from the Earth's center. The Moon presently moves at about 60 Earth radii, so Hill concluded that the Moon cannot recede from the Earth beyond the limit of 110 radii. We say that the motion of the Moon is *stable according to Hill*. Hagihara [13] found that all natural satellites in the solar system, except four Jovian satellites, are stable according to Hill.

The vector ∇U is directed normal to the equipotential surfaces $U = -\frac{1}{2}C$. In the singular L -points on these surfaces we have: $\nabla U = 0$. Assume that body P is in one of these L -points with zero velocity relative to the rotating frame, then Eq. (15.2-8) yields for the motion of P : $\delta^2 \mathbf{r}/\delta t^2 = 0$. Thus, at the five points L_1 to L_5 body P will experience no acceleration relative to the rotating frame. These points thus represent *equilibrium positions* and are called *Lagrange libration points*.

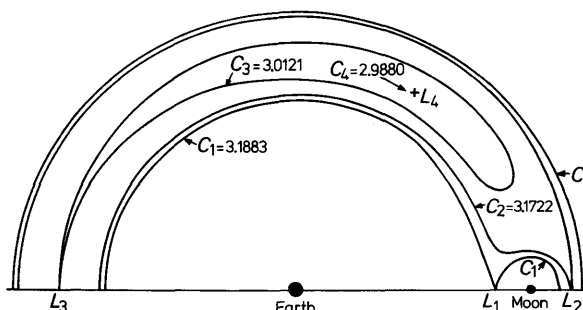


Fig. 15.4 The intersection of some zero-velocity surfaces and the xy -plane in the Earth-Moon system

The position of the libration points relative to the xyz -frame can be found by differentiating the dimensionless form of Eq. (15.2-6) with respect to x , y , z , respectively, and putting these partial derivatives equal to zero. We then obtain

$$\frac{\partial U}{\partial x} = -x + \frac{1-\mu}{r_1^3}(\mu+x) - \frac{\mu}{r_2^3}(1-\mu-x) = 0, \quad (15.2-18a)$$

$$\frac{\partial U}{\partial y} = y \left(-1 + \frac{1-\mu}{r_1^3} + \frac{\mu}{r_2^3} \right) = 0, \quad (15.2-18b)$$

$$\frac{\partial U}{\partial z} = z \left(\frac{1-\mu}{r_1^3} + \frac{\mu}{r_2^3} \right) = 0. \quad (15.2-18c)$$

Equation (15.2-18c) indicates that all libration points are in the xy -plane. Equation (15.2-18b) has the solutions

$$y = 0, \quad \text{or} \quad 1 - \frac{1-\mu}{r_1^3} - \frac{\mu}{r_2^3} = 0. \quad (15.2-19)$$

From Eqs. (15.2-17), (15.2-18) and (15.2-19), we obtain two different solutions for the positions of the libration points:

$$y = z = 0, \quad x - (1-\mu) \frac{(\mu+x)}{|\mu+x|^3} + \mu \frac{(1-\mu-x)}{|1-\mu-x|^3} = 0. \quad (15.2-20)$$

and

$$z = 0, \quad r_1 = r_2 = 1. \quad (15.2-21)$$

It can be shown that the quintic Eq. (15.2-20) has three real x -roots corresponding to the three libration points L_1 , L_2 and L_3 [14]. The distance between L_1 and body P_2 is always less than the distance between L_2 and P_2 . Both L_1 and L_2 are closer to P_2 at smaller values of μ . The distance between L_3 and body P_1 is roughly the same as the distance between the bodies P_1 and P_2 ; L_3 and P_2 , however, are on opposite sides from P_1 . In Table 15.1 the positions of the libration points L_1 , L_2 and L_3 are given for various systems.

Table 15.1 The dimensionless distances γ_1 , γ_2 and γ_3 of the libration points L_1 , L_2 and L_3

	μ	γ_1	γ_2	γ_3
Sun-Venus	2.448×10^{-6}	9.315×10^{-3}	9.373×10^{-3}	1.00000
Sun-Earth + Moon	3.040×10^{-6}	1.001×10^{-2}	1.008×10^{-2}	1.00000
Sun-Mars	3.227×10^{-7}	4.748×10^{-3}	4.763×10^{-3}	1.00000
Sun-Jupiter	9.539×10^{-4}	6.668×10^{-2}	6.978×10^{-2}	0.99944
Earth-Moon	1.215×10^{-2}	1.509×10^{-1}	1.678×10^{-1}	0.99291
Jupiter-Ganymede	8.078×10^{-5}	2.967×10^{-2}	3.027×10^{-2}	0.99995

Here γ_1 and γ_2 denote the respective dimensionless distances of L_1 and L_2 from body P_2 . The distance γ_3 is measured from body P_1 to L_3 .

According to Eq. (15.2-21), the libration points L_4 and L_5 form equilateral triangles with the bodies P_1 and P_2 . Their positions can be given by

$$x = \frac{1}{2} - \mu, \quad y = \pm \frac{1}{2}\sqrt{3}. \quad (15.2-22)$$

We found that for decreasing values of C , the surfaces of zero velocity finally vanish at L_4 and L_5 . Substituting the coordinates of L_4 and L_5 into Eq. (15.2-16), we obtain the minimum value of C for which the surfaces of Hill exist:

$$C_{\min} = 2\frac{3}{4} + (\mu - \frac{1}{2})^2.$$

Therefore, no surface of zero velocity can exist if $C < 2.75$.

15.2.3 Stability of motion near the libration points

We found that a body placed in a Lagrange libration point will not experience an acceleration relative to the rotating frame xyz . The question however remains, whether the equilibrium in these points is stable or not. In this context we say that the motion is stable if, as a result of a small, but arbitrary disturbance, the motion remains bounded in a restricted region about that Lagrange point.

For the motion of the body we obtain from Eq. (15.2-8) three scalar equations, which can be written in the dimensionless form:

$$\begin{aligned} \frac{d^2x}{dt^2} - 2 \frac{dy}{dt} &= -\frac{\partial U}{\partial x}, \\ \frac{d^2y}{dt^2} + 2 \frac{dx}{dt} &= -\frac{\partial U}{\partial y}, \\ \frac{d^2z}{dt^2} &= -\frac{\partial U}{\partial z}. \end{aligned} \quad (15.2-23)$$

A Taylor series expansion of $\frac{\partial U}{\partial x}$ in the neighborhood of a Lagrange point gives, if second-order terms are neglected,

$$\frac{\partial U}{\partial x} = (x - x_o) \left(\frac{\partial^2 U}{\partial x^2} \right)_o + (y - y_o) \left(\frac{\partial^2 U}{\partial x \partial y} \right)_o + (z - z_o) \left(\frac{\partial^2 U}{\partial x \partial z} \right)_o, \quad (15.2-24)$$

where the index o refers to the Lagrange point considered. Introducing the notation:

$$x' = x - x_o, \quad y' = y - y_o, \quad z' = z - z_o,$$

$$U_{xx} = \left(\frac{\partial^2 U}{\partial x^2} \right)_o, \quad U_{xy} = \left(\frac{\partial^2 U}{\partial x \partial y} \right)_o, \quad \text{etc.,}$$

Eq. (15.2-24) can be written as

$$\frac{\partial U}{\partial x} = x'U_{xx} + y'U_{xy} + z'U_{xz}.$$

Substituting this relation and the corresponding relations for $\frac{\partial U}{\partial y}$ and $\frac{\partial U}{\partial z}$ into Eqs. (15.2-23) we obtain the linearized equations

$$\begin{aligned}\frac{d^2x'}{dt^2} - 2 \frac{dy'}{dt} + x'U_{xx} + y'U_{xy} + z'U_{xz} &= 0, \\ \frac{d^2y'}{dt^2} + 2 \frac{dx'}{dt} + x'U_{xy} + y'U_{yy} + z'U_{yz} &= 0, \\ \frac{d^2z'}{dt^2} + x'U_{xz} + y'U_{yz} + z'U_{zz} &= 0.\end{aligned}\tag{15.2-25}$$

As all libration points lie in the xy -plane, we can simplify this system of equations. From Eq. (15.2-18), we obtain

$$U_{xz} = U_{yz} = 0, \quad U_{zz} > 0,$$

and Eqs. (15.2-25) reduce to

$$\begin{aligned}\frac{d^2x'}{dt^2} - 2 \frac{dy'}{dt} + x'U_{xx} + y'U_{xy} &= 0, \\ \frac{d^2y'}{dt^2} + 2 \frac{dx'}{dt} + x'U_{xy} + y'U_{yy} &= 0, \\ \frac{d^2z'}{dt^2} + z'U_{zz} &= 0.\end{aligned}\tag{15.2-26}$$

The third of these equations now is uncoupled from the first two, and because $U_{zz} > 0$ we conclude that body P performs an *undamped harmonic motion* in the z -direction, independent of its motion in the xy -plane. According to our definition, the motion in the z -direction of a body placed in a libration point thus is stable.

The remaining two linear differential equations with constant coefficients can easily be solved. The general solution may be written as

$$x' = \sum_{i=1}^4 A_i e^{\lambda_i t}, \quad y' = \sum_{i=1}^4 B_i e^{\lambda_i t},\tag{15.2-27}$$

where A_i , B_i and λ_i are constants. This yields the characteristic equation

$$\lambda^4 + (4 + U_{xx} + U_{yy})\lambda^2 + U_{xx}U_{yy} - U_{xy}^2 = 0.\tag{15.2-28}$$

This quartic equation in λ has four complex roots λ_i , the *eigenvalues* or *characteristic values* of the two differential equations. Equation (15.2-28) is also quadratic in λ^2 and thus has two solutions for λ^2 . Both solutions of λ^2

give two eigenvalues which are equal in magnitude but opposite in sign. In general, the motion is stable only if all λ_i are different and if the real part of all λ_i is less than or equal to zero. Because in our problem the eigenvalues have two-by-two opposite signs, the motion can only be stable if all λ_i are different and imaginary. Then the two values of λ^2 are real, unequal and negative.

We first consider the collinear Lagrange points L_1 , L_2 and L_3 . Evaluating the partial derivatives of U at these points and substituting these values into Eq. (15.2-28), we obtain

$$\lambda^4 + (2 - K)\lambda^2 + (1 + 2K)(1 - K) = 0,$$

where

$$K = \frac{1 - \mu}{r_1^3} + \frac{\mu}{r_2^3} > 0.$$

The two roots for λ^2 can only be negative if $1 - K > 0$. However, the second one of the Eqs. (15.2-20) can also be written in the form

$$1 - K = \frac{\mu(1 - \mu)}{x} \left(\frac{1}{r_1^3} - \frac{1}{r_2^3} \right).$$

By inspection of Fig. 15.3, and remembering our discussion on the location of the points L_1 , L_2 and L_3 , it will be clear that for these points the combination of x , r_1 and r_2 is such that for each point: $1 - K < 0$. Consequently, the straight line solutions represent *unstable* equilibrium positions.

Next consider the equilibrium points L_4 and L_5 . Evaluating the partial derivatives of U at these points and inserting them into Eq. (15.2-28), we obtain

$$\lambda^4 + \lambda^2 + \frac{27}{4}\mu(1 - \mu) = 0.$$

The two roots for λ^2 are different and negative if

$$1 - 27\mu(1 - \mu) > 0.$$

As by definition $0 \leq \mu \leq \frac{1}{2}$, the condition for stability is

$$\mu < \frac{1}{2} - \sqrt{\frac{23}{108}} \approx 0.0385.$$

So, for $\mu < 0.0385$ the motion of a body placed in the libration points L_4 or L_5 is *stable*. It should be realized, however, that we only have proved that this motion is infinitesimally stable, as the conclusion was reached on the basis of a linearized Taylor series expansion. A more detailed analysis [15] will therefore require the inclusion of non-linear terms in the series expansion of the derivatives of the potential function, while also the influence of the perturbing force from a fourth body could be taken into account [16].

In the general case of the restricted three-body problem, the bodies P_1 and P_2 describe elliptic orbits about the center of mass of the system. Then,

the distance between P_1 and P_2 , as well as the angular velocity of the line connecting P_1 and P_2 , varies. This implies that the potential function U depends explicitly on time, so that no Jacobi integral exists for this problem. In this *elliptical restricted three-body problem* the motion of a body in the points L_4 and L_5 can be infinitesimally stable too, depending on the values of μ and the eccentricity of the elliptic orbits [17, 18].

The Lagrange equilibrium positions in the three-body problem are not of pure academic interest, but are physical realities in our solar system. An impressive example of stable L_4 and L_5 positions is the presence of more than a dozen large asteroids, called the Trojans, oscillating about the L_4 and L_5 points with respect to Sun and Jupiter. In the Earth–Moon system, the L_4 and L_5 points also represent a stable equilibrium. These points are probably occupied by particles, which manifest themselves as a very faint nebula only visible under the best seeing conditions.

For a long time it was thought that the faint glow at the night sky, known as the *Gegenschein* or *counter glow*, was produced by sunlight reflection on material, temporarily trapped in the (unstable) L_2 position of the Sun–Earth system. Recent research [19], however, indicates that this glow is due to the reflection of sunlight by interplanetary dust at much larger distances from the Sun.

15.2.4 Applications to spaceflight

Jacobi's integral and the surfaces of zero velocity are very useful for a general discussion on the trajectory of a spacecraft within the Earth–Moon space, a so-called *lunar flight* [20]. For this, we neglect the solar gravitational attraction and assume the orbit of the Moon about the Earth to be a circle. The trajectory of the spacecraft then becomes a circular restricted three-body problem where Earth and Moon represent the massive bodies. The lunar flight starts at the Earth's surface or in a *parking orbit* about the Earth. The spacecraft is accelerated by rocket engines and is injected into its *trans-lunar trajectory*. The position and velocity of the vehicle relative to the rotating *xyz*-frame just after shut-down of the rocket motor determine the value of the constant C corresponding with the trajectory of the spacecraft. This value of C can easily be calculated from Eq. (15.2-10). In order to reach the Moon, this C -value must be less than C_1 , being the C -value for which the surface of zero velocity passes through the L_1 -point in the Earth–Moon system. This value of C thus dictates the minimum impulse delivered by the rocket engines, necessary to reach the Moon. If the C -value of the trajectory is still higher than C_2 , the spacecraft can reach the vicinity of the Moon, but still cannot escape from the Earth–Moon system. Jacobi's integral gives no information on the actual trajectory that will be flown by the spacecraft; many trajectories satisfy the same C -value. We therefore have to select the initial conditions such that a suitable lunar trajectory results. When the spacecraft arrives in the vicinity of the Moon, again rocket

thrust has to be applied in order to increase the C -value above the value of C_1 . The spacecraft will then enter an orbit about the Moon and its motion will be restricted to within a closed C -envelope around the Moon. Unless this orbit is very close to the Moon, the orbit can be perturbed considerably by the gravitational attractions of Earth and Sun [21]. This as a result of the relatively small lunar mass.

In Table 15.2 the values of C_1 to C_5 for the Earth–Moon system are given, both non-dimensional and in km^2/s^2 . It is seen that the values for the various libration points are very close. Also included in Table 15.2 is the initial velocity of the spacecraft required to fly a trajectory with these C -values. Thereby, it is assumed that at the moment of engine shut-down the spacecraft crosses the x -axis at 200 km above that side of the Earth which is directed away from the Moon. We note that to reach the Moon the velocity of the spacecraft in the rotating frame must be larger than 10.8482 km/s. A very slight velocity increase to 10.8490 km/s enables the spacecraft to escape from the Earth–Moon system. This clearly illustrates the great sensitivity of lunar trajectories to small changes in initial velocity.

A practical application of the equilibrium conditions in the libration points is the positioning of a spacecraft in these regions [22]. Because the motion at the three collinear points is unstable and at the equilateral-triangle points is unstable or neutrally stable, some form of orbit control will generally be required to keep the spacecraft in the vicinity of a libration point. A spacecraft placed in an orbit about the L_2 -point in the Earth–Moon system could be used for real-time communications between Earth and the far side of the Moon. This so-called *halo orbit* has to be selected such that the spacecraft is visible from the Earth most of the time. Breakwell [23] has shown that such halo orbits in some cases yield a purely periodic three-dimensional motion. A scientific spacecraft in the L_2 -point in the Sun–Earth system could offer a possibility of long-term measurements in the geomagnetic tail; a spacecraft in the L_1 -point of this system could function as an early-warning station for solar flares. Also for interplanetary spaceflight, rendezvous techniques in the Sun–planet system L -points could offer several attractive advantages.

Table 15.2 Critical Jacobian constants and the corresponding injection velocities for the Earth–Moon system

	L_1	L_2	L_3	L_4, L_5
$C(-)$	3.1883	3.1722	3.0121	2.9880
$C(\text{km}^2/\text{s}^2)$	3.3378	3.3208	3.1533	3.1281
$V(\text{km/s})$	10.8482	10.8490	10.8567	10.8579

15.3 Relative motion in the N -body problem

In the discussion on the general n -body problem (Section 15.1) we considered the motion of the bodies relative to an inertial reference frame. Though many interesting results appear, for practical astrodynamics we are often more interested in the motion of a body with respect to another body. For instance, when we study the motion of an artificial Earth satellite under the gravitational attraction of all celestial bodies, we are only interested in what the orbit of the satellite relative to the Earth looks like.

Let us select a reference frame xyz with origin at body P_k and which is not rotating with respect to an inertial reference frame XYZ (Fig. 15.5). Separating the attractions between the bodies P_k and P_i and between P_i and all other bodies P_j , the motion of P_i relative to the inertial frame is described by

$$\frac{d^2 \mathbf{R}_i}{dt^2} = G \frac{m_k}{r_{ik}^3} \mathbf{r}_{ik} + G \sum_j^{**} \frac{m_j}{r_{ij}^3} \mathbf{r}_{ij}, \quad (15.3-1)$$

where the notation \sum_j^{**} denotes a summation over all j , excluding $j = i$ and $j = k$. Equally, for the motion of P_k relative to the inertial frame holds

$$\frac{d^2 \mathbf{R}_k}{dt^2} = G \frac{m_i}{r_{ki}^3} \mathbf{r}_{ki} + G \sum_j^{**} \frac{m_j}{r_{kj}^3} \mathbf{r}_{kj}. \quad (15.3-2)$$

Subtracting both equations and using the relations

$$\mathbf{r}_{ki} = \mathbf{R}_i - \mathbf{R}_k, \quad \mathbf{r}_{ij} = \mathbf{r}_{kj} - \mathbf{r}_{ki}, \quad (15.3-3)$$

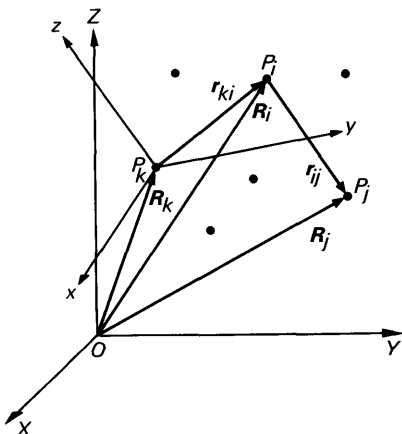


Fig. 15.5 The position of n bodies in the inertial frame XYZ and in the non-rotating frame with origin at body P_k

we obtain

$$\frac{d^2 \mathbf{r}_{ki}}{dt^2} = -G \frac{m_k + m_i}{r_{ki}^3} \mathbf{r}_{ki} + G \sum_j^{**} m_j \left(\frac{\mathbf{r}_{kj} - \mathbf{r}_{ki}}{r_{ij}^3} - \frac{\mathbf{r}_{kj}}{r_{kj}^3} \right).$$

When we measure the position of P_i and the bodies P_j relative to the non-rotating frame xyz with origin at P_k , the index k in the position vectors and distances can be omitted, and the motion of P_i relative to this frame is given by

$$\frac{d^2 \mathbf{r}_i}{dt^2} + G \frac{m_k + m_i}{r_i^3} \mathbf{r}_i = G \sum_j^{**} m_j \left(\frac{\mathbf{r}_j - \mathbf{r}_i}{r_{ij}^3} - \frac{\mathbf{r}_j}{r_j^3} \right) \quad (15.3-4)$$

We note that the influence of the bodies P_j on the motion of P_i about P_k is expressed by the right-hand side of Eq. (15.3-4). The first term in brackets represents the acceleration of P_i due to the attractions of all bodies P_j . The second term in brackets is the negative of the acceleration of P_k , the origin of our reference frame, due to the attraction by the bodies P_j . It is the difference between these two terms that counts for the influence of the bodies P_j on the motion of P_i relative to P_k .

As well for the motion of a planet about the Sun as for the motion of a satellite about the Earth, the total effect of the bodies P_j can be regarded as very small when compared to the direct two-body attraction term in Eq. (15.3-4). The reason for this is entirely different for both types of motion. Considering the motion of a planet about the Sun, we note that the ratio of the mass of a disturbing body (a planet) and that of the Sun is small. For that reason the right-hand side of Eq. (15.3-4) has only little influence. For an Earth satellite, on the other hand, the distance from the Earth is small as compared to interplanetary distances and the difference between r_{ij} and r_j takes a very small value. Consequently, in both cases mentioned the effect of the bodies P_j can, in a first approximation, be neglected. Then, Eq. (15.3-4) simplifies to the equation of motion for the two-body problem which, as we will see in Chapter 16, can be solved analytically.

Introducing a *disturbing potential*, R_i :

$$R_i = -G \sum_j^{**} m_j \left(\frac{1}{r_{ij}} - \frac{\mathbf{r}_i \cdot \mathbf{r}_j}{r_j^3} \right), \quad (15.3-5)$$

Eq. (15.3-4) can be written in the form

$$\frac{d^2 \mathbf{r}_i}{dt^2} + G \frac{m_k + m_i}{r_i^3} \mathbf{r}_i = -\nabla_i R_i, \quad (15.3-6)$$

where ∇_i denotes the gradient with respect to the coordinates of P_i in the non-inertial frame xyz . Because R_i is not only a function of the coordinates of P_i but also of the coordinates of the bodies P_j , the force field described by the potential R_i is not conservative. The treatment of this disturbing potential R_i is the major problem in the *general perturbations theory* of celestial mechanics.

15.3.1 Satellite orbit perturbations by a third body

An interesting application of Eq. (15.3-4) is the determination of Earth satellite orbit perturbations by the gravitational attraction of a third body, for instance Sun or Moon. We therefore select a non-rotating reference frame with its origin at the Earth's center of mass. The position of the satellite with mass m_s in this frame is given by \mathbf{r}_s . The position of a disturbing body with mass m_d is given by \mathbf{r}_d . The mass of the Earth is m_e . The geometry and other notations are shown in Fig. 15.6. We call the acceleration of the satellite due to the attraction between Earth and satellite the *main acceleration*, \mathbf{a}_m , of the satellite. Its magnitude is according to Eq. (15.3-4)

$$a_m = G \frac{m_e + m_s}{r_s^2}. \quad (15.3-7)$$

The *disturbing acceleration*, \mathbf{a}_d , of the satellite is due to the attraction by the disturbing body. Its magnitude is according to Eq. (15.3-4) given by

$$a_d = G m_d \sqrt{\left(\frac{\mathbf{r}_{sd}}{r_{sd}^3} - \frac{\mathbf{r}_d}{r_d^3}\right) \cdot \left(\frac{\mathbf{r}_{sd}}{r_{sd}^3} - \frac{\mathbf{r}_d}{r_d^3}\right)},$$

or

$$a_d = G m_d \sqrt{\frac{1}{r_{sd}^4} + \frac{1}{r_d^4} - \frac{2 \cos \alpha}{r_{sd}^2 r_d^2}}. \quad (15.3-8)$$

Now, according to Fig. 15.6,

$$\cos \alpha = \frac{r_d - r_s \cos \beta}{r_{sd}},$$

and

$$r_{sd}^2 = r_s^2 + r_d^2 - 2 r_s r_d \cos \beta.$$

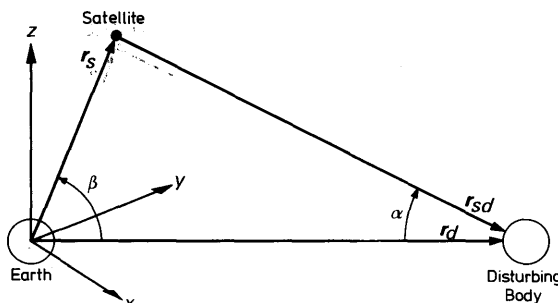


Fig. 15.6 Relative positions of Earth, satellite and disturbing body

Substituting these relations into Eq. (15.3-8), we find

$$a_d = G \frac{m_d}{r_d^2} \sqrt{1 + \frac{1}{(1 - 2\gamma \cos \beta + \gamma^2)^2}} - 2 \frac{1 - \gamma \cos \beta}{(1 - 2\gamma \cos \beta + \gamma^2)^{3/2}},$$

where $\gamma = \frac{r_s}{r_d} \ll 1$. A series expansion in terms of γ and neglecting terms of order γ with respect to 1 gives

$$a_d = G m_d \frac{r_s}{r_d^3} \sqrt{1 + 3 \cos^2 \beta}. \quad (15.3-9)$$

From Eqs. (15.3-7) and (15.3-9) we obtain for the maximum value of the ratio of disturbing and main acceleration

$$\frac{a_d}{a_m} = 2 \frac{m_d}{m_e} \left(\frac{r_s}{r_d} \right)^3, \quad (15.3-10)$$

where we have neglected the mass of the satellite relative to the mass of the Earth. The relative importance of the disturbing force thus increases with the third power of satellite distance. Table 15.3 shows values of a_d/a_m for a satellite at a distance of 42,200 km from the Earth's center. This is a so-called *geosynchronous satellite* (Section 16.2.1). The relative positions of the Earth and the disturbing body were selected such that r_d is a minimum. We may conclude from Table 15.3 that the largest third-body forces are due to the attractions of Moon and Sun, and that the effects of all other disturbing bodies are at least an order of 10^4 smaller.

Table 15.3 Disturbing acceleration of a geosynchronous satellite due to the attraction of a third body

Disturbing body	$\frac{m_d}{m_e}$	$\frac{r_d}{r_s}$	$\frac{a_d}{a_m}$
Sun	332,946	3.48×10^3	1.6×10^{-5}
Mercury	0.056	1.83×10^3	1.8×10^{-11}
Venus	0.815	9.03×10^2	2.2×10^{-9}
Moon	0.0123	9.1	3.3×10^{-5}
Mars	0.107	1.29×10^3	1.0×10^{-10}
Jupiter	317.9	1.39×10^4	2.4×10^{-10}
Saturn	95.2	2.83×10^4	8.4×10^{-12}
Uranus	14.6	6.11×10^4	1.3×10^{-13}
Neptune	17.2	1.02×10^5	3.3×10^{-14}
Pluto	0.11	1.01×10^5	2.1×10^{-16}
α Centauri A	3.6×10^5	9.68×10^8	8.0×10^{-22}

15.3.2 Sphere of influence

The motion of an interplanetary spacecraft is governed by the attracting forces of all planets and the Sun. For a first-order analysis, however, we

often assume that the trajectory can be approximated by accounting only for three gravitational fields: those of the Earth, the Sun and the target planet (Chapter 19). We then imagine the trajectory to be composed of three successive two-body trajectories; in each trajectory the spacecraft is assumed to be attracted by only one celestial body.

We will now discuss a criterion which determines the distance from the Earth, and from the target planet, where the switch between the successive two-body trajectories has to be made. It is important to realize that because of the very intense solar gravitational field, these distances will be small on the scale of interplanetary distances.

First, we consider the motion of the spacecraft with mass m_c relative to a non-rotating reference frame with its origin at the Earth's center. We assume that the only disturbing body is the Sun. The masses of Sun and Earth are denoted by m_s and m_e , respectively. From Eqs. (15.3-7) and (15.3-9) we have for the magnitudes of main acceleration, a_{m_1} , and disturbing acceleration, a_{d_1} , of the spacecraft, relative to this reference frame,

$$\begin{aligned} a_{m_1} &= G \frac{m_e}{r_{ec}^2}, \\ a_{d_1} &= G m_s \frac{r_{ec}}{r_{es}^3} \sqrt{1 + 3 \cos^2 \beta}, \end{aligned} \quad (15.3-11)$$

where \mathbf{r}_{ec} is the radius vector from the Earth to the spacecraft, and \mathbf{r}_{es} is the radius vector from the Earth to the Sun. Again, the mass of the spacecraft is neglected relative to the mass of the Earth.

If we consider the motion of the spacecraft with respect to a non-rotating reference frame with its origin at the center of mass of the Sun, and assume that the Earth is the only disturbing body, the equation of motion for the spacecraft is

$$\frac{d^2 \mathbf{r}_{sc}}{dt^2} + G \frac{m_s}{r_{sc}^3} \mathbf{r}_{sc} = G m_e \left(\frac{\mathbf{r}_{ce}}{r_{ce}^3} - \frac{\mathbf{r}_{se}}{r_{se}^3} \right),$$

where the spacecraft's mass is neglected with respect to the mass of the Sun. Relative to this frame, the magnitudes of main acceleration, a_{m_2} , and disturbing acceleration, a_{d_2} , of the spacecraft are

$$\begin{aligned} a_{m_2} &= G \frac{m_s}{r_{sc}^2}, \\ a_{d_2} &= G m_e \sqrt{\left(\frac{\mathbf{r}_{ce}}{r_{ce}^3} - \frac{\mathbf{r}_{se}}{r_{se}^3} \right) \cdot \left(\frac{\mathbf{r}_{ce}}{r_{ce}^3} - \frac{\mathbf{r}_{se}}{r_{se}^3} \right)}. \end{aligned} \quad (15.3-12)$$

A series expansion of a_{d_2} in terms of $\frac{r_{ce}}{r_{se}}$ yields, for $\frac{r_{ce}}{r_{se}} \ll 1$,

$$a_{d_2} = G \frac{m_e}{r_{ce}^2}. \quad (15.3-13)$$

When the spacecraft is on a surface around the Earth, described by

$$\frac{a_{d_1}}{a_{m_1}} = \frac{a_{d_2}}{a_{m_2}}, \quad (15.3-14)$$

we have equal right to approximate the interplanetary trajectory by a disturbed two-body orbit about the Earth or by a disturbed two-body orbit about the Sun. Substituting Eqs. (15.3-11), (15.3-12) and (15.3-13) into Eq. (15.3-14), we obtain the equation of this surface:

$$\left(\frac{r_{ec}}{r_{es}}\right)^5 = \left(\frac{m_e}{m_s}\right)^2 \frac{1}{\sqrt{1 + 3 \cos^2 \beta}}. \quad (15.3-15)$$

This surface is rotationally symmetric about the Earth-Sun line. Its shape differs little from a sphere; the ratio of the largest and smallest value of r_{ec} is about 1.15. For convenience, we therefore approximate this surface by a sphere with radius equal to the maximum value of r_{ec} . This sphere is called the *sphere of influence* or the *activity sphere* of the Earth. Equally, we can determine for each planet such a sphere of influence. If the radius of this sphere is denoted by $R_{s,i}$, and the distance between the planet and the Sun by r_{ps} , we thus find

$$R_{s,i} = r_{ps} \left(\frac{m_p}{m_s}\right)^{2/5}. \quad (15.3-16)$$

It will be evident that for a given planet the value of $R_{s,i}$ still varies with the distance of that planet from the Sun. For example, the radius of the sphere of influence of the Earth varies between 0.91×10^6 km and 0.94×10^6 km. For the other planets corresponding data will be given in Chapter 19.

The concept of a sphere of influence was introduced by Laplace [24] in his studies on the motion of comets in the immediate neighborhood of the planet Jupiter. Nowadays, it is widely used for feasibility studies in interplanetary spaceflight.

References

- 1 Sundman, K. F. (1907), Recherches sur le problème des trois corps, *Acta Societas Sci. Fennicae*, **34**, no. 6, 1–43.
- 2 Lecar, M. (ed.) (1972), *Gravitational N-Body Problem*, Reidel, Dordrecht.
- 3 Bruns, H. (1887), Über die Integrale des Vielkörper-Problemes, *Acta Math.*, **11**, 25–96.
- 4 Poincaré, H. (1890), Sur le problème des trois corps et les équations de la dynamique, *Acta Math.*, **13**, 1–270.
- 5 Jacobi, C. G. J. (1843), Sur l'élimination des noeuds dans le problème des trois corps, *Z. Reine Angew. Math.*, **26**, 115–131.

- 6 Bennett, T. L. (1905), *Messenger of Math.*, Cambridge, **34**, no. 2, 1113.
- 7 Pollard, H. (1966), Qualitative methods in the N -body problem, in: J. Barkley Rosser (ed.), *Space Mathematics*, Part 1, Amer. Math. Soc., p. 269–277.
- 8 Clausius, R. (1870), On a mechanical theorem applicable to heat, *Philos. Mag. and J. Science*, **40**, Series 4, 122–127.
- 9 Chandrasekhar, S. (1942), *Principles of Stellar Dynamics*, Univ. of Chicago Press, Chicago. Also Dover, New York, 1960, p. 200.
- 10 Szebehely, V. (1967), *Theory of Orbits, The Restricted Problem of Three Bodies*, Academic Press, New York.
- 11 Kopal, Z. (1959), *Close Binary Systems*, Chapman and Hall, London, p. 127, 505.
- 12 Hill, G. W. (1878), Researches in lunar theory, *Amer. J. Math.*, **1**, 129–147, 245–260.
- 13 Hagiwara, Y. (1952), On the stability of the satellite systems, *Proc. Japan Acad.*, **28**, 182–186.
- 14 Moulton, F. R. (1914), *An Introduction to Celestial Mechanics*, Macmillan, New York, p. 291–293.
- 15 Breakwell, J. V. and Pringle, R. (1966), Resonances affecting motion near the Earth–Moon equilateral libration points, *Progr. Astron. Aeron.*, Vol. 17, Academic Press, New York, p. 55–74.
- 16 Schechter, H. B. (1968), Three-dimensional nonlinear stability analysis of the Sun-perturbed Earth–Moon equilateral points, *AIAA J.*, **6**, no. 7, 1223–1228.
- 17 Danby, J. M. A. (1964), Stability of the triangular points in the elliptic restricted problem of three bodies, *Astron. J.*, **69**, no. 2, 165–172.
- 18 Alfriend, K. T. and Rand, R. H. (1969), Stability of the triangular points in the elliptic restricted problem of three bodies, *AIAA J.*, **7**, no. 6, 1024–1028.
- 19 Hanner, M. S. and Weinberg, J. L. (1973), Gegenschein observations from Pioneer 10, *Sky and Telescope*, **45**, no. 4, 217–218.
- 20 Ehricke, K. A. (1962), *Space Flight, Vol. 2: Dynamics*, Van Nostrand, Princeton, p. 245–282, 933–957.
- 21 Schöyer, H. F. R. (1966), *Investigation on the Stability of the Orbit of a Lunar Satellite* (in Dutch), Thesis Delft Univ. of Techn., Dept. Aerospace Eng., Delft.
- 22 Farquhar, R. W. (1970), *The Control and Use of Libration Point Satellites*, NASA TR R-346, Washington.
- 23 Breakwell, J. V. and Brown, J. V. (1976), *The Halo Family of 3-Dimensional Periodic Orbits in the Restricted 3-Body Problem*, AIAA/AAS Paper 76-825, San Diego.
- 24 Marquis de Laplace, P. S. (1845), *Traité de Mécanique Céleste, Tome 4*, Imprimerie Royale, Paris, p. 241–254.

16 The Two-Body Problem

In Section 15.3 we found that the motion of a satellite about the Earth was governed primarily by the attraction between Earth and satellite. Even for a satellite at an altitude of some ten thousands of kilometers, the effects of the gravitational attraction of Sun, Moon and planets on the satellite's orbit are very small. If, at a first approximation, we completely neglect these effects, we deal with a *two-body problem*.

This two-body approximation also holds for the motion of the planets about the Sun. In this case, the gravitational perturbations by other planets are even less important, because of the large distances involved and the relatively small masses of the planets as compared to the mass of the Sun.

Unlike the many-body problem, the two-body problem can be solved analytically, and because its solution comes very near to physical reality this solution constitutes the basic algebra of celestial mechanics. Most of the refined theories of celestial motion take the two-body model as a point of departure.

16.1 Equations of motion

Consider the motion of body P_i relative to a non-rotating reference frame with its origin at body P_k (Fig. 15.5). We assume that the bodies can be regarded as point masses and that the only force acting on body P_i is due to their mutual gravitational attraction. Then, the motion of body P_i is, according to Eq. (15.3–4), described by

$$\frac{d^2\mathbf{r}}{dt^2} = -\frac{\mu}{r^3}\mathbf{r}, \quad (16.1-1)$$

where

$$\mu = G(m_k + m_i), \quad (16.1-2)$$

and \mathbf{r} is the position vector of body P_i . The masses of the bodies P_k and P_i are denoted by m_k and m_i respectively, while G is the universal gravitational constant. Comparing Eq. (16.1-1) and Eq. (3.6-2), which describes the motion of a point mass in an inertial gravitational field (the *one-body problem*), we may conclude that both equations of motion only differ in the definition of μ . In Section 3.6, μ was defined as the product of G and the mass of the body in which gravitational field the point mass moves; here, μ is defined as the product of G and the sum of the masses of the two bodies.

Consequently, we can directly apply the relations derived for the one-body problem. However, we have to be very careful with the physical interpretation of the results. For instance, applying Eq. (3.6-8) for the two-body problem, the term $-\mu/r$ does not represent the potential energy of body P_i per unit mass, nor does the constant \mathcal{E} denote the total energy of body P_i per unit mass.

In many cases, however, such as the motion of planets about the Sun or the motion of satellites about the Earth, we deal with problems where $m_k \gg m_i$. Then, we can safely approximate μ by

$$\mu = Gm_k. \quad (16.1-3)$$

This approximation is equivalent to the statement that the reference frame with body P_k as origin is an inertial one and that the actual motion can be approximated by a one-body problem. When μ is defined according to Eq. (16.1-3), we call μ the *gravitation parameter* or the *attraction parameter* of body P_k . For the Earth it takes the value $\mu = 398601.3 \text{ km}^3/\text{s}^2$.

16.2 General characteristics of motion

From Section 3.6 we know that the motion of body P_i about body P_k takes place in a single plane through P_k , the *orbital plane*, and that the trajectory in this plane is a *conic section* with body P_k at a focus. In addition to *elliptic orbits*, in which the planets and the Earth satellites move, *parabolic* and *hyperbolic trajectories* are also physical realities. In astronomy, we observe that some comets move in these trajectories about the Sun. In spaceflight, the hyperbolic orbits are essential to interplanetary missions (Chapter 19).

In the following discussion on the motion of body P_i , we will omit those parts which were already discussed in Section 3.6. For convenience, however, some of the most important relations derived in that section will be repeated.

The trajectory of body P_i is given by

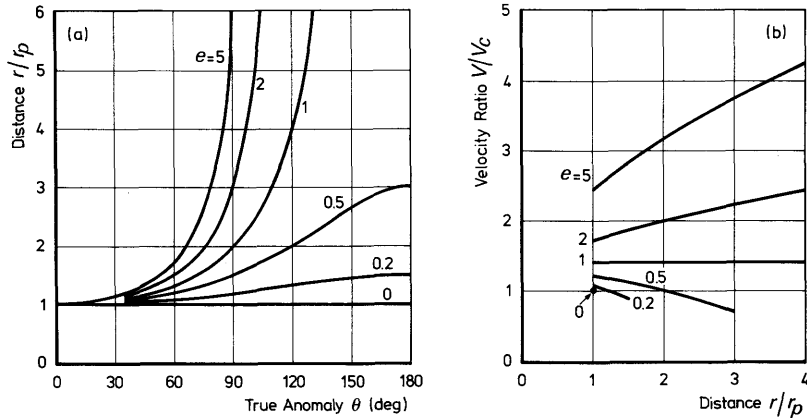
$$r = \frac{p}{1 + e \cos \theta} = \frac{H^2/\mu}{1 + e \cos \theta}, \quad (16.2-1)$$

where θ is the *true anomaly*, p is the *semi-latus rectum*, e is the (*numerical*) *eccentricity* and H is the *angular momentum per unit mass*. In Fig. 16.1a, the ratio between distance r and pericenter distance r_p is shown as a function of e for some values of e .

For the velocity, V , in a conic section, Eq. (3.6-34) gives

$$V^2 = \mu \left(\frac{2}{r} - \frac{1}{a} \right). \quad (16.2-2)$$

According to Eq. (3.6-36) and Eq. (3.6-35), the *circular* and *escape velocity*

**Fig. 16.1** Distance and velocity in some Keplerian orbits

at a distance r are given by

$$V_c = \sqrt{\frac{\mu}{r}}, \quad (16.2-3)$$

$$V_{esc} = \sqrt{\frac{2\mu}{r}} = \sqrt{2} V_c. \quad (16.2-4)$$

The ratio between velocity, V , and local circular velocity, V_c , is shown in Fig. 16.1b as a function of the distance ratio r/r_p for some values of e .

The radial velocity, V_r , can be found by differentiating Eq. (16.2-1) with respect to time and subsequently substituting Eq. (3.6-6):

$$V_r = \frac{\mu}{H} e \sin \theta. \quad (16.2-5)$$

The circumferential velocity, V_θ , follows directly from the angular momentum:

$$V_\theta = \frac{H}{r} = \frac{\mu}{H} (1 + e \cos \theta). \quad (16.2-6)$$

The *flight path angle*, γ , is given by

$$\tan \gamma = \frac{V_r}{V_\theta} = \frac{e \sin \theta}{1 + e \cos \theta}, \quad -90^\circ \leq \gamma \leq 90^\circ. \quad (16.2-7)$$

This relation is depicted in Fig. 16.2 for various values of e .

Elimination of θ from Eq. (16.2-5) and Eq. (16.2-6) leads to

$$V_r^2 + \left(V_\theta - \frac{\mu}{H} \right)^2 = \left(\frac{\mu e}{H} \right)^2.$$

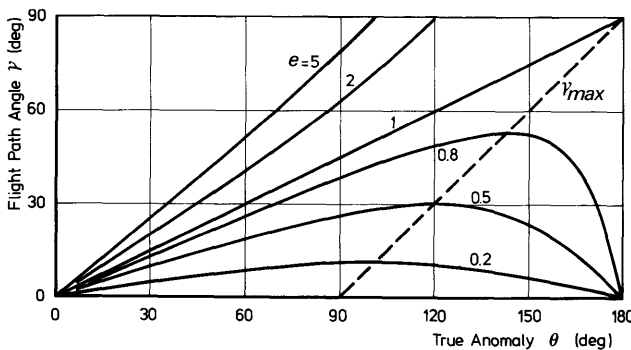


Fig. 16.2 The flight path angle as a function of the true anomaly

Thus, the *hodograph* in terms of V_r and V_θ is a circle with radius $\frac{\mu e}{H}$. Its center lies on the V_θ -axis at a distance $\frac{\mu}{H}$ from the origin. In Fig. 16.3, this hodograph is shown for an elliptic, a parabolic and a hyperbolic trajectory. As always $V_\theta \geq 0$, so that only the upper part of the hodograph for the hyperbolic motion has physical significance. In these hodographs, we can geometrically indicate the quantities θ , e and γ . The limiting value of θ in the hyperbolic motion, for which $r \rightarrow \infty$, is indicated by θ_{lim} , while the locations of pericenter, apocenter and a crossing point of the trajectory and the minor axis are denoted by p , a and b , respectively. An extensive discussion on the general hodograph theory of orbital mechanics and its many applications is given by Altman [1].

The velocity, \mathbf{V} , can also be resolved into a component \mathbf{V}_t perpendicular to the major axis and a component \mathbf{V}_n normal to the radius vector. According

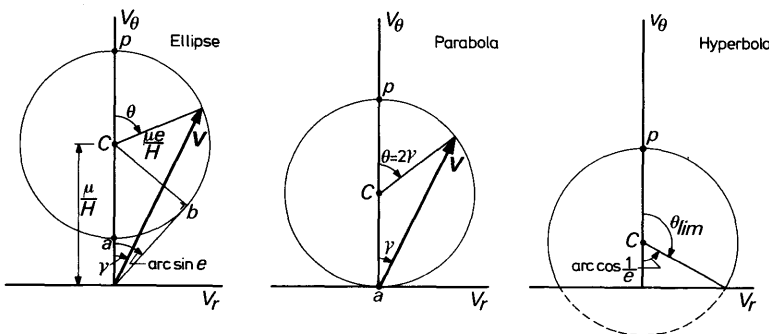


Fig. 16.3 Velocity hodographs for elliptic, parabolic and hyperbolic motion

to Fig. 16.4, we may write

$$V_l = \frac{V_r}{\sin(180 - \theta)} = \frac{V_r}{\sin \theta},$$

$$V_n = V_\theta + \frac{V_r}{\tan(180 - \theta)} = V_\theta - \frac{V_r}{\tan \theta}.$$

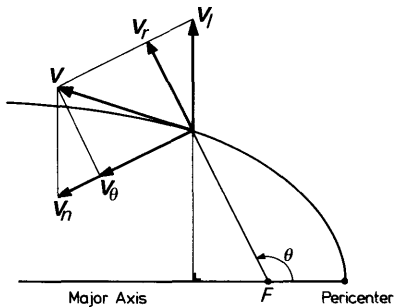


Fig. 16.4 Velocity components in a Keplerian orbit

Substitution of Eqs. (16.2-5) and (16.2-6) into these relations yields

$$V_l = \frac{\mu e}{H}, \quad V_n = \frac{\mu}{H}.$$

So, both components V_l and V_n are constant in magnitude during the motion. The component V_l is also constant in direction. The existence of these two constant velocity components is usually referred to as *Whittaker's theorem* [2].

16.2.1 The circular orbit

In Fig. 16.5a, the *circular velocity* in the gravitational field of some planets and the Moon is plotted versus the distance from the attraction center. The distance was non-dimensionalized by dividing it by the (mean) radius, R , of the celestial body considered. We note that Earth satellites in a low circular orbit have a velocity of about 7.9 km/s. A satellite in a low circular orbit about Mars or our Moon has a much lower velocity. For the giant planet Jupiter, the circular velocity at low altitudes is more than 40 km/s.

The (sidereal) period of a satellite in a circular orbit, the *circular period*, is, according to Eq. (3.6-38), given by

$$T_c = 2\pi \sqrt{\frac{r^3}{\mu}}. \quad (16.2-8)$$

In Fig. 16.5b, this period is shown as a function of the non-dimensional orbital distance for various planets and the Moon. In contrast with the

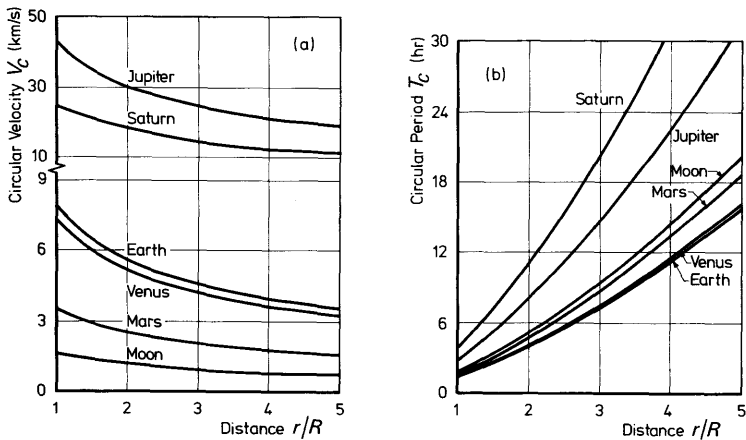


Fig. 16.5 Circular velocity and circular period as a function of distance for some planets and the Moon

circular velocities, we note that for the Earth, Mars, Venus and the Moon, the circular periods at low altitudes do not differ very much. This result is easy to explain. Suppose that body P_k has a radius R_k and a mean mass density ρ_k . For $m_i \ll m_k$, we have

$$\mu \approx Gm_k = \frac{4}{3}\pi G\rho_k R_k^3.$$

Substitution of this relation into Eq. (16.2-8) yields for $r \approx R_k$,

$$T_c \approx \sqrt{\frac{3\pi}{G}} \frac{1}{\rho_k}.$$

As the mean densities of the Moon, Mercury, Venus, Earth, Mars and Pluto do not differ very much (Tables T.2 and T.4), the periods of low-altitude circular orbits about these planets are roughly equal. The planets Jupiter, Saturn, Uranus and Neptune have a lower mean density, resulting in a greater circular period.

A special case is a satellite in a circular orbit above the Earth's equator with a period of exactly one sidereal day. If the orbital motion of this satellite is in the same direction as the Earth's rotation, the satellite will keep a *fixed position* above the equator and will not move relative to the Earth's surface. We call this a *geostationary satellite*. Such a satellite should not be confused with a *geosynchronous satellite*, where the only requirement for the orbit is that the orbital period is one sidereal day. This orbit need not be circular nor need it lie in the equatorial plane. From Eq. (16.2-8), we find for the radius of the geostationary orbit: $r = 42164 \text{ km} = 6.62 \text{ Earth radii}$. Nowadays, this type of orbit is frequently used for telecommunications satellites, because with such a satellite an uninterrupted communication link

can be established between ground stations. For certain other types of applications satellites this orbit is attractive too, since from that altitude a large part of the Earth can be monitored continuously.

16.2.2 The elliptic orbit

From Eqs. (16.2-2), (16.2-5) to (16.2-7), a number of interesting conclusions, concerning the variation of velocity with position in an elliptic orbit, can be drawn. Here we will mention only the most important ones:

1. The velocity takes a minimum value at the apocenter:

$$V_a^2 = \frac{\mu}{a} \left(\frac{1-e}{1+e} \right) = V_{c_a}^2 (1-e), \quad (16.2-9)$$

where V_{c_a} denotes the circular velocity at apocenter. The velocity at apocenter is always less than the local circular velocity (Fig. 16.1b).

2. The maximum velocity occurs at pericenter:

$$V_p^2 = \frac{\mu}{a} \left(\frac{1+e}{1-e} \right) = V_{c_p}^2 (1+e), \quad (16.2-10)$$

where V_{c_p} denotes the circular velocity at pericenter.

The velocity at pericenter is always larger than the local circular velocity (Fig. 16.1b).

3. The radial velocity is an extremum at the crossing points of the orbit and the latus rectum:

$$V_{r_{ext}} = \pm \frac{\mu e}{H} = \pm V_{c_{ext}} e, \quad (16.2-11)$$

where $V_{c_{ext}}$ denotes the circular velocity at that point of the orbit.

4. At the crossing points of the orbit and the minor axis, the flight path angle takes an extreme value (Fig. 16.3):

$$\gamma_{ext} = \arctan \left[\pm \frac{e}{\sqrt{1-e^2}} \right], \quad (16.2-12)$$

and the velocity equals in magnitude, but not in direction, the local circular velocity.

From the expression for the period in an elliptic orbit, Eq. (3.6-38), we obtain after substitution of Eq. (16.1-2),

$$\frac{a^3}{T^2} = \frac{G m_k}{4 \pi^2} \left(1 + \frac{m_i}{m_k} \right). \quad (16.2-13)$$

This equation represents an ‘improved version’ of Kepler’s third law as given in Section 3.6.3. We see that Kepler’s third law in its original version only holds for $m_i \ll m_k$.

16.2.3 The parabolic orbit

At any point of a parabolic orbit, the velocity is equal to the local escape velocity as given by Eq. (16.2-4). For parabolic orbits about the Earth, the velocity at low altitudes equals about 11.2 km/s. For Jupiter, on the other hand, the escape velocity at low altitude is more than 60 km/s. From Eq. (16.2-7) we obtain, after some trigonometric manipulations, for the flight path angle in a parabolic orbit:

$$\tan \gamma = \tan \frac{\theta}{2}.$$

As, by definition, $-90^\circ \leq \gamma \leq 90^\circ$, we find for the variation of γ with θ ,

$$\begin{aligned} 0^\circ \leq \theta \leq 180^\circ: \quad \gamma &= \frac{\theta}{2}, \\ 180^\circ < \theta < 360^\circ: \quad \gamma &= \frac{\theta}{2} - 180^\circ. \end{aligned} \tag{16.2-14}$$

The flight path angle thus increases linearly with θ from $\gamma = 0^\circ$ at pericenter to $\gamma = 90^\circ$ at $\theta = 180^\circ$ (Fig. 16.2).

16.2.4 The hyperbolic orbit

The most important conclusions from Eqs. (16.2-2), (16.2-5) to (16.2-7) for a hyperbolic orbit are:

1. The velocity is a maximum at pericenter:

$$V_p^2 = \left(\frac{\mu}{-a} \right) \left(\frac{e+1}{e-1} \right) = V_{c_p}^2 (e+1). \tag{16.2-15}$$

2. The velocity takes a minimum value for $r \rightarrow \infty$:

$$V_\infty^2 = -\frac{\mu}{a}. \tag{16.2-16}$$

This velocity at infinitely large distance from body P_k is called the *hyperbolic excess velocity*.

By substituting Eqs. (16.2-4) and (16.2-16) into Eq. (16.2-2), we obtain

$$V^2 = V_{esc}^2 + V_\infty^2. \tag{16.2-17}$$

So, at any point in a hyperbolic trajectory, the local velocity can be expressed in terms of local escape velocity and hyperbolic excess velocity. The dependence of velocity on distance in a hyperbolic orbit about the Earth is depicted in Fig. 16.6 for two values of the eccentricity. It is assumed that the perigee of both orbits is at 400 km above the Earth's surface. Also shown in this figure is a curve representing the local escape velocity. We

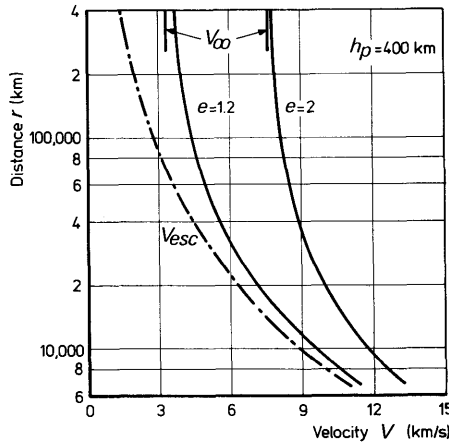


Fig. 16.6 The relation between velocity and distance for two hyperbolic trajectories about the Earth

note that a relatively small velocity increase above the escape velocity at 400 km results in rather large values of V_∞ . A second conclusion that can be drawn is that at a distance of about 400,000 km, i.e. about the distance to the Moon, the difference between the local velocity and V_∞ is small. This conclusion is of great importance in the discussion of interplanetary trajectories.

16.3 Relations between position and time

To obtain a relation between position in the orbit and time, we could start from Eq. (3.6-6) and write, with Eq. (16.2-1),

$$\frac{d\theta}{dt} = \frac{H}{r^2} = \sqrt{\frac{\mu}{p^3}} (1 + e \cos \theta)^2. \quad (16.3-1)$$

From this equation, we obtain

$$\Delta t = \sqrt{\frac{p^3}{\mu}} \int_{\theta_0}^{\theta_e} \frac{d\theta}{(1 + e \cos \theta)^2}, \quad (16.3-2)$$

where Δt is the time interval in which the body's true anomaly increases from θ_0 to θ_e . Though the integral in Eq. (16.3-2) can be evaluated for elliptic, parabolic and hyperbolic orbits, the resulting expressions are rather cumbersome if the orbit is an ellipse or a hyperbola. In these cases, we will therefore follow a different approach, yielding simpler expressions which are more convenient to solve the position-time problem.

16.3.1 The elliptic orbit

For the elliptic orbit, we introduce the concept of the *eccentric anomaly*, E , defined such that the equation of the elliptic trajectory can be written as

$$r = a(1 - e \cos E). \quad (16.3-3)$$

A simple geometrical investigation will reveal, that this angle E can be constructed by using an auxiliary circle, as is shown in Fig. 16.7. From this figure, it will be clear that we may write

$$r \cos \theta = a \cos E - ae, \quad (16.3-4)$$

$$r \sin \theta = a\sqrt{1-e^2} \sin E. \quad (16.3-5)$$

From Eqs. (16.3-3) and (16.3-4), we obtain

$$\tan \frac{\theta}{2} = \sqrt{\frac{1+e}{1-e}} \tan \frac{E}{2}. \quad (16.3-6)$$

In the derivation of this equation, the possibility of a minus sign can be rejected because $\frac{\theta}{2}$ and $\frac{E}{2}$ are always in the same quadrant.

Differentiation of Eq. (16.3-3) with respect to time yields

$$\frac{dr}{dt} = ae \sin E \frac{dE}{dt}. \quad (16.3-7)$$

Substitution of Eqs. (3.6-24), (3.6-27) and (16.2-5) into Eq. (16.3-7) gives

$$\frac{dE}{dt} = \sqrt{\frac{\mu}{a^3(1-e^2)}} \sin E.$$

With the Eqs. (16.3-3) and (16.3-5), we then obtain

$$(1 - e \cos E) \frac{dE}{dt} = \sqrt{\frac{\mu}{a^3}},$$

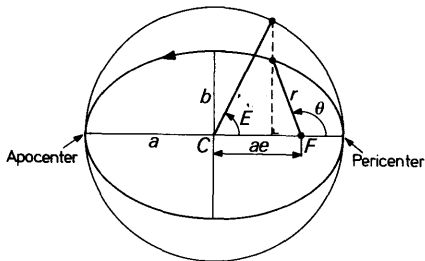


Fig. 16.7 The eccentric anomaly

which can be integrated to

$$E - e \sin E = \sqrt{\frac{\mu}{a^3}} (t - \tau), \quad (16.3-8)$$

where τ is a constant of integration. The physical meaning of τ becomes clear by substituting $E = 0$ into Eq. (16.3-8). We then find $t = \tau$; so τ is the *time of pericenter passage*. We will often use the *mean angular motion*, n , defined as

$$n = \sqrt{\frac{\mu}{a^3}}, \quad (16.3-9)$$

and the *mean anomaly*, M , defined as

$$M = n(t - \tau). \quad (16.3-10)$$

Then, Eq. (16.3-8) can be written in the form

$$E - e \sin E = M. \quad (16.3-11)$$

Equation (16.3-8) or, equivalently, Eq. (16.3-11) is known as *Kepler's equation*. It relates position, through the angle E , to time elapsed after pericenter passage. If we want to know when body P_i is at a certain angular position θ , the calculation is straightforward by using Eq. (16.3-6) and (16.3-8). More often, however, we are interested to know *where* the body is at a given time. We then have to solve Eq. (16.3-8) for E with a numerical iteration method. Figure 16.8 shows the variation of θ and the distance ratio r/r_p with M , for some values of e . In Section 16.4 we will deal with a special analytical solution of Kepler's equation, namely in the form of a series expansion in M .

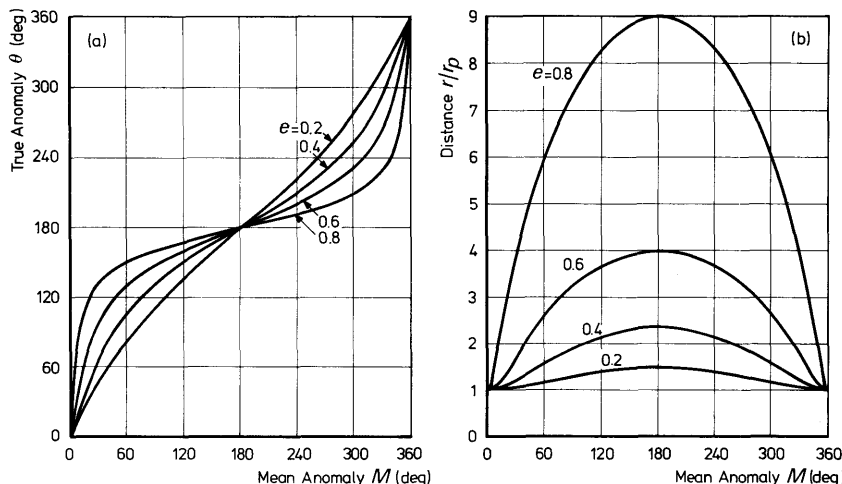


Fig. 16.8 The true anomaly and the distance versus the mean anomaly in elliptic orbits

16.3.2 The parabolic orbit

If $e = 1$, Eq. (16.3-1) can be written in the form

$$dt = \sqrt{\frac{p^3}{\mu}} \frac{d\theta}{(1 + \cos \theta)^2}, \quad (16.3-12)$$

which can be integrated to

$$\tan \frac{\theta}{2} + \frac{1}{3} \tan^3 \frac{\theta}{2} = 2 \sqrt{\frac{\mu}{p^3}} (t - \tau), \quad (16.3-13)$$

where the constant of integration τ again is the *time of pericenter passage*. Equation (16.3-13), relating true anomaly and time for parabolic orbits, is usually called *Barker's equation*. In contrast to Kepler's equation, we can solve this equation analytically to find angular position at a given time [3]. For simplicity, we will mostly use a numerical method on the computer. In Fig. 16.10, the curves for $e = 1$ show the variation of true anomaly and distance ratio r/r_p as a function of $t - \tau$. Here, the time has been non-dimensionalized by dividing it by the circular period at pericenter, T_{cp} .

The time it takes body P_i to move from $\theta = -90^\circ$ to $\theta = 90^\circ$ is, according to Eq. (16.3-13),

$$T_p = \frac{4}{3} \sqrt{\frac{p^3}{\mu}}.$$

This relation, which can also be written as

$$\frac{p^3}{T_p^2} = \frac{9}{16} \mu = \frac{9}{16} G m_k \left(1 + \frac{m_i}{m_k} \right), \quad (16.3-14)$$

can be considered as the analog of Kepler's third law for elliptic orbits.

16.3.3 The hyperbolic orbit

For the hyperbolic orbit, we use a method analogous to the one applied to the elliptic orbit. We define a *hyperbolic anomaly*, F , such that the equation of the hyperbolic trajectory can be written as

$$r = a(1 - e \cosh F). \quad (16.3-15)$$

Note that this way of introducing F is admissible as $\cosh F \geq 1$, and so r is, according to Eq. (16.3-15), allowed to vary between $a(1 - e)$ and ∞ ($a < 0$ for a hyperbola). This hyperbolic anomaly plays here the role of the eccentric anomaly for elliptic orbits, and the Eqs. (16.3-3) and (16.3-15) show a large similarity. As is shown in Fig. 16.9, both E and F can geometrically be visualized as the ratio of areas. Due to the particular properties of a circle, only E can also be interpreted as an angle.

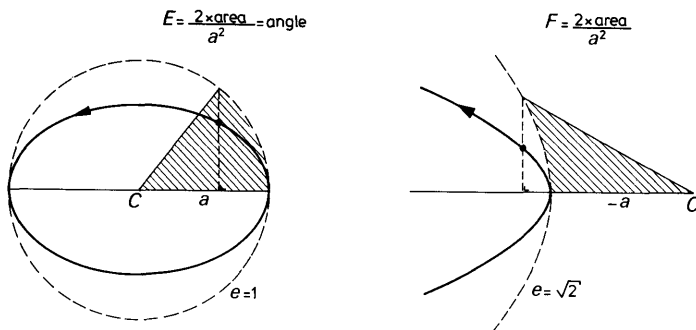


Fig. 16.9 Geometrical representation of the eccentric anomaly and the hyperbolic anomaly

Elimination of r from Eq. (16.2-1) and Eq. (16.3-15), and using Eq. (3.6-27) yields

$$\cos \theta = \frac{1}{e} \left(\frac{1-e^2}{1-e \cosh F} - 1 \right),$$

or

$$\tan \frac{\theta}{2} = \sqrt{\frac{e+1}{e-1}} \tanh \frac{F}{2}. \quad (16.3-16)$$

The choice of the plus sign in Eq. (16.3-16) implies that if $\theta < 0$, we take $F < 0$. Differentiation of Eq. (16.3-15) with respect to time leads to

$$\frac{dr}{dt} = -ae \sinh F \frac{dF}{dt}. \quad (16.3-17)$$

By substituting Eq. (16.2-5) for $\frac{dr}{dt}$, we obtain

$$\frac{dF}{dt} = \sqrt{\frac{\mu}{-a^3(e^2-1)}} \frac{\sin \theta}{\sinh F}. \quad (16.3-18)$$

With Eq. (16.3-16), we find after some algebraic manipulations

$$\frac{\sin \theta}{\sinh F} = \frac{2 \tan \frac{\theta}{2}}{\left(1 + \tan^2 \frac{\theta}{2}\right) \tanh \frac{F}{2} (\cosh F + 1)} = \frac{\sqrt{e^2 - 1}}{e \cosh F - 1}. \quad (16.3-19)$$

Substitution of Eq. (16.3-19) into Eq. (16.3-18), and subsequent integration yields

$$e \sinh F - F = \sqrt{\frac{\mu}{-a^3}} (t - \tau). \quad (16.3-20)$$

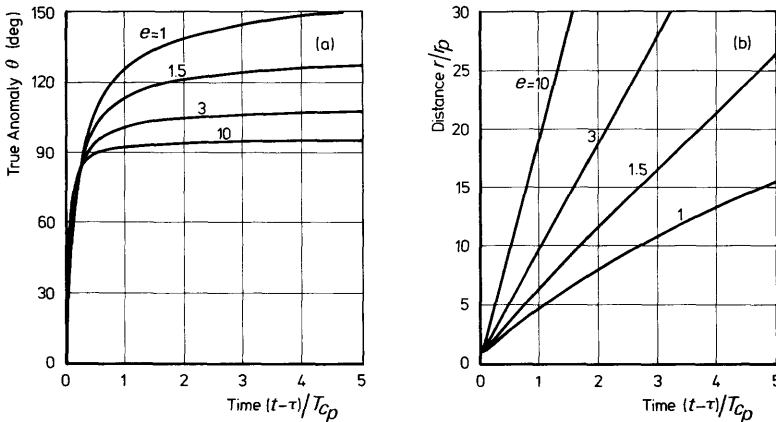


Fig. 16.10 The true anomaly and the distance versus the time after pericenter passage in parabolic and hyperbolic trajectories

Again, the integration constant τ is the *time of pericenter passage* as can be seen by substituting $F=0$ into Eq. (16.3-20). This equation, which relates position and time for a hyperbolic orbit, is analogous to Kepler's equation for the elliptic orbit. Note that the introduction of a mean anomaly is of little sense in this case, because hyperbolic motion is aperiodic. Like Kepler's equation, the equation has to be solved by numerical methods for a given time. In Fig. 16.10, the variation of θ and the distance ratio r/r_p are shown for some values of e as a function of the non-dimensional time after pericenter passage. The notation T_{c_p} stands for the circular period at pericenter.

16.4 Expansions in elliptic motion

We have found that Kepler's equation, relating time and position in an elliptic orbit, cannot be solved explicitly for position as a function of time. As, however, r , θ and E are periodic functions of M , we can expand these variables in Fourier series [4]. These series are extremely important for analytical calculations.

Writing $x = E - M$, Kepler's equation can be written in the form

$$x = e \sin(M + x). \quad (16.4-1)$$

According to Eq. (16.4-1), x is of order e . Now assume that x can be expressed as a power series in e :

$$x = \alpha_1 e + \alpha_2 e^2 + \alpha_3 e^3 + \dots \quad (16.4-2)$$

By substitution of Eq. (16.4-2) into Eq. (16.4-1), we find

$$\alpha_1 e + \alpha_2 e^2 + \dots = e \sin M \cos x + e \cos M \sin x. \quad (16.4-3)$$

A series expansion of $\sin x$ and $\cos x$ and subsequent substitution of Eq. (16.4-2) results in an equation containing only α_i , e and M . By equating the coefficients of equal powers of e , we obtain algebraic equations in α_i , with solutions:

$$\alpha_1 = \sin M, \quad \alpha_2 = \frac{1}{2} \sin 2M, \quad \alpha_3 = \frac{3}{8} \sin 3M - \frac{1}{8} \sin M, \quad \text{etc.}$$

By substituting these results, and the higher-order coefficients which can be obtained in the same way, into Eq. (16.4-2), and neglecting terms of order e^6 and higher, we finally obtain

$$\begin{aligned} E = M + e(1 - \frac{1}{8}e^2 + \frac{1}{192}e^4) \sin M + e^2(\frac{1}{2} - \frac{1}{6}e^2) \sin 2M + \\ + e^3(\frac{3}{8} - \frac{27}{128}e^2) \sin 3M + \frac{1}{3}e^4 \sin 4M + \frac{125}{384}e^5 \sin 5M. \end{aligned} \quad (16.4-4)$$

It is interesting to note that the general term of this series expansion contains the leading factor $e^k \sin kM$. Moreover, the parts in brackets are polynomials in e^2 . In celestial mechanics these properties are called the *d'Alembert characteristic* [5]. It holds for many series expansions in astrodynamics and can be used as a rule of thumb to check analytical derivations.

To obtain a series expansion of θ in terms of trigonometric functions of M , we write

$$\frac{d\theta}{dM} = \frac{d\theta}{dE} \frac{dE}{dM}. \quad (16.4-5)$$

Differentiating Eq. (16.3-6) with respect to E gives

$$\frac{d\theta}{dE} = \sqrt{\frac{1+e}{1-e}} \frac{1+\cos\theta}{1+\cos E}. \quad (16.4-6)$$

Substitution of Eq. (16.3-3) and Eq. (16.3-4) into Eq. (16.4-6) yields

$$\frac{d\theta}{dE} = \frac{\sqrt{1-e^2}}{1-e \cos E}. \quad (16.4-7)$$

Differentiating Eq. (16.3-11) with respect to M gives

$$\frac{dE}{dM} = \frac{1}{1-e \cos E}. \quad (16.4-8)$$

By substituting Eqs. (16.4-7) and (16.4-8) into Eq. (16.4-5), we obtain

$$\frac{d\theta}{dM} = \sqrt{1-e^2} \left(\frac{dE}{dM} \right)^2. \quad (16.4-9)$$

Expanding the square root, substituting for $\frac{dE}{dM}$ from Eq. (16.4-4), integrating and again neglecting terms of order e^6 and higher, finally leads to:

$$\theta = M + e(2 - \frac{1}{4}e^2 + \frac{5}{96}e^4) \sin M + e^2(\frac{5}{4} - \frac{11}{24}e^2) \sin 2M + \\ + e^3(\frac{13}{12} - \frac{43}{64}e^2) \sin 3M + \frac{103}{96}e^4 \sin 4M + \frac{1097}{960}e^5 \sin 5M. \quad (16.4-10)$$

The expression for $\theta - M$ is called the *equation of the center*.

To obtain a corresponding series expansion of r , we substitute Eq. (16.4-8) into Eq. (16.3-3) and find

$$\frac{r}{a} = \left(\frac{dE}{dM} \right)^{-1}.$$

By substituting the expression for $\frac{dE}{dM}$, which results by differentiating Eq. (16.4-4), and expanding the negative power, we obtain

$$\frac{r}{a} = 1 + \frac{1}{2}e^2 - e(1 - \frac{3}{8}e^2 + \frac{5}{192}e^4) \cos M \\ - e^2(\frac{1}{2} - \frac{1}{3}e^2) \cos 2M - e^3(\frac{3}{8} - \frac{45}{128}e^2) \cos 3M \\ - \frac{1}{3}e^4 \cos 4M - \frac{125}{384}e^5 \cos 5M. \quad (16.4-11)$$

It can be shown that the three series converge for all values of M if $e < 0.6627$ [6]. With a few exceptions, the eccentricities for the bodies in the solar system are much lower. Also for the majority of Earth satellites, the eccentricity is far below this limit and the series are very useful. It should be mentioned in this context that for hyperbolic motion it is impossible to construct series approximations which are valid over large intervals of time, because the motion is not periodic.

16.5 Orbital elements

We have found that the motion of body P_i relative to body P_k takes place in one plane: the *orbital plane*. In the non-rotating reference frame with its origin at P_k , the orientation of this orbital plane can be specified by two angles. In Section 2.3 we discussed two often used reference frames: the *non-rotating geocentric equatorial frame* and the *non-rotating heliocentric ecliptic frame*. In these reference frames the xy -plane is the *Earth's mean equatorial plane* and the *ecliptic plane*, respectively.

The intersection of the orbital plane with the xy -plane is called the *line of nodes*. This line intersects the orbit at two points. At the *ascending node* (A.N.) the z -coordinate of body P_i changes from negative to positive. The other intersection constitutes the *descending node* (D.N.). The position of

the ascending node in the xy -plane can be specified by the angle Ω (Fig. 16.11), which is called the *longitude of the ascending node* in the ecliptic frame, and the *right ascension of the ascending node* in the equatorial frame. As mentioned already in Section 2.3.4, Ω is measured positively from the point γ eastward. The angle i between the xy -plane and the orbital plane is called the *inclination*. This angle is defined between 0° and 180° . To avoid ambiguity, it is most conveniently considered as the (smallest) angle between the positive z -axis and the orbital angular momentum vector. Thus, small inclinations are associated with eastward or *direct motion*, and those near 180° with westward or *retrograde motion*. The two angles Ω and i thus define the orientation of the orbital plane and the sense of motion of body P_i in this plane.

The orbit of body P_i in this plane is a conic section with body P_k at one focus. Its shape is defined by the *eccentricity*, e , its size by the *semi-major axis*, a , or, in case of a parabola, by the *semi-latus rectum*, p . We still have to define the orientation of the conic in the orbital plane. In Section 3.6, we introduced the *argument of pericenter*, ω , which was measured from an arbitrarily chosen reference line in the orbital plane. At this stage we specify this reference line to be the line of nodes. It is interesting to mention here that the three angles i , ω , and Ω were adopted by Euler for general orientation problems. Accordingly, they are sometimes called the *classical Euler angles* and agree with one of the several conflicting modern conventions for Euler angles. To determine the position of body P_i in its orbit at a given time, we further have to know the *time of pericenter passage*, τ .

The six independent parameters a or p , e , i , ω , Ω , τ uniquely determine the motion of body P_i as a function of time. These parameters, which are all constant during the motion, are called the *classical orbital elements*. Often, τ is replaced as an orbital element by the *mean anomaly at the epoch* t_o , M_o .

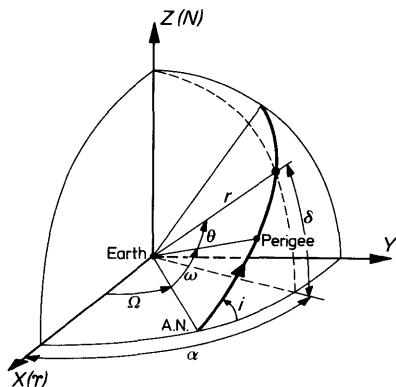


Fig. 16.11 The orientation of the orbital plane in the geocentric equatorial reference frame

defined as

$$M_o = n(t_o - \tau).$$

Then, the expression for the mean anomaly is

$$M = M_o + n(t - t_o).$$

It should be clear that there have to be six orbital elements, as the motion of body P_i is described by three scalar second-order differential equations. The solution of this set contains six integration constants. We therefore should consider the six orbital elements as a particular set of integration constants, chosen for their clear geometrical interpretation.

Apart from these classical orbital elements, other orbital elements are sometimes used as they may be more appropriate for certain problems, or because some classical elements become ill-determined when e and/or i approach zero. We will not go into detail on this subject as it is closely related to problems of orbit determination from observations. We will only mention two frequently used elements: the *longitude of pericenter*, $\bar{\omega} = \omega + \Omega$, and the *mean longitude at epoch*, $L_o = \bar{\omega} + M_o$. In the case $e=0$, the pericenter is not determined, and the position in the orbit should be measured from the ascending node. This is the reason that the circle, the simplest of all orbits, cannot be handled by many of the formulae for elliptic motion, because of the dependence upon the position of the pericenter. In the case $i=0$, the ascending node is not determined and we use e.g. the four elements a , e , $\bar{\omega}$, τ to describe the motion. In the mathematical development of refined schemes for the calculation of perturbed two-body orbits, certain other orbital elements are used which simplify the analytical treatment. This will be discussed in Section 18.4.3.

16.6 Relations between orbital elements and position and velocity

The instantaneous position and velocity of body P_i in its motion about body P_k can be described by its rectangular coordinates and velocity components:

$x, y, z, \frac{dx}{dt}, \frac{dy}{dt}, \frac{dz}{dt}$; by its spherical coordinates and velocity components: $r,$

α or λ , δ or φ , V, γ, ψ ; or by the orbital elements a or $p, e, i, \omega, \Omega, \tau$. There exist one-to-one relationships between these three sets of parameters. In one respect the last set is entirely different from the first two: the six orbital elements are *constant* during the motion. Therefore, the general scheme to compute the position of P_i at some time t is as follows. First the orbital elements are computed at t_o when the position and velocity of P_i are known. Because these elements are constant, they take the same value at time t , and by an inverse transformation the position and velocity at time t may be found.

For the transformations between the three sets of parameters mentioned above, six sets of transformation relations are needed. They can be derived easily. As an example, we will derive the transformation relations to compute rectangular coordinates and velocity components from orbital elements. Two other important transformations will be presented without derivation. The three sets of transformation relations only hold for elliptic orbits, but the derivations for parabolic and hyperbolic orbits are essentially the same. In all cases, the non-rotating geocentric equatorial frame is taken as reference frame.

16.6.1 Rectangular coordinates from orbital elements

When the orbital elements are known, the solution of Kepler's equation for a certain time t_0 provides us with the value of E at that time. From Eq. (16.3-6) we then obtain the value of θ at that time. For convenience, we now select a right-handed Cartesian reference frame $\xi\eta\zeta$ with its origin coinciding with the origin of the geocentric xyz -frame. The $\xi\eta$ -plane coincides with the orbital plane and the positive ξ -axis points towards the perigee. In this frame, the coordinates of body P_i are given by

$$\xi = r \cos \theta, \quad \eta = r \sin \theta, \quad \zeta = 0, \quad (16.6-1)$$

where r is determined by Eq. (16.2-1). The $\xi\eta\zeta$ -frame is obtained from the xyz -frame by three successive rotations. We first rotate the xyz -frame about the z -axis over the angle Ω . The frame then obtained is rotated about its x -axis by the angle i . The then resulting frame is rotated about its z -axis over the angle ω . The relation between the coordinates of a body relative to the xyz -frame and the $\xi\eta\zeta$ -frame is given by

$$(x, y, z) = (\xi, \eta, \zeta) \mathbf{A}_\omega \mathbf{A}_i \mathbf{A}_\Omega, \quad (16.6-2)$$

where the rotation matrices, \mathbf{A}_Ω , \mathbf{A}_i and \mathbf{A}_ω , are given by

$$\begin{aligned} \mathbf{A}_\Omega &= \begin{bmatrix} \cos \Omega & \sin \Omega & 0 \\ -\sin \Omega & \cos \Omega & 0 \\ 0 & 0 & 1 \end{bmatrix}, & \mathbf{A}_i &= \begin{bmatrix} 1 & 0 & 0 \\ 0 & \cos i & \sin i \\ 0 & -\sin i & \cos i \end{bmatrix}, \\ \mathbf{A}_\omega &= \begin{bmatrix} \cos \omega & \sin \omega & 0 \\ -\sin \omega & \cos \omega & 0 \\ 0 & 0 & 1 \end{bmatrix}. \end{aligned} \quad (16.6-3)$$

Evaluation of the matrix multiplication yields

$$(x, y, z) = (\xi, \eta, \zeta) \begin{bmatrix} l_1 & m_1 & n_1 \\ l_2 & m_2 & n_2 \\ l_3 & m_3 & n_3 \end{bmatrix}, \quad (16.6-4)$$

where

$$\begin{aligned}
 l_1 &= \cos \omega \cos \Omega - \sin \omega \sin \Omega \cos i, \\
 m_1 &= \cos \omega \sin \Omega + \sin \omega \cos \Omega \cos i, \\
 n_1 &= \sin \omega \sin i, \\
 l_2 &= -\sin \omega \cos \Omega - \cos \omega \sin \Omega \cos i, \\
 m_2 &= -\sin \omega \sin \Omega + \cos \omega \cos \Omega \cos i, \\
 n_2 &= \cos \omega \sin i, \\
 l_3 &= \sin \Omega \sin i, \\
 m_3 &= -\cos \Omega \sin i, \\
 n_3 &= \cos i.
 \end{aligned} \tag{16.6-5}$$

Because P_i always is in the $\xi\eta$ -plane, the orbital plane, its coordinates are given by

$$x = l_1 \xi + l_2 \eta, \quad y = m_1 \xi + m_2 \eta, \quad z = n_1 \xi + n_2 \eta. \tag{16.6-6}$$

Differentiation of Eqs. (16.6-1) and Eqs. (16.6-6) with respect to time leads to

$$\frac{dx}{dt} = l_1 \left(\cos \theta \frac{dr}{dt} - r \sin \theta \frac{d\theta}{dt} \right) + l_2 \left(\sin \theta \frac{dr}{dt} + r \cos \theta \frac{d\theta}{dt} \right), \tag{16.6-7}$$

with similar expressions for $\frac{dy}{dt}$ and $\frac{dz}{dt}$.

By substituting Eqs. (16.2-5) and (16.2-6) for $\frac{dr}{dt}$ and $r \frac{d\theta}{dt}$, we finally obtain

$$\begin{aligned}
 \frac{dx}{dt} &= \frac{\mu}{H} [-l_1 \sin \theta + l_2(e + \cos \theta)], \\
 \frac{dy}{dt} &= \frac{\mu}{H} [-m_1 \sin \theta + m_2(e + \cos \theta)], \\
 \frac{dz}{dt} &= \frac{\mu}{H} [-n_1 \sin \theta + n_2(e + \cos \theta)].
 \end{aligned} \tag{16.6-8}$$

The Eqs. (16.2-1), (16.6-1), (16.6-5), (16.6-6) and (16.6-8) allow the computation of the rectangular coordinates and velocity components at a given time if the orbital elements are known.

16.6.2 Orbital elements from rectangular coordinates

For the computation of orbital elements from the rectangular coordinates and velocity components at a given time, suitable expressions are given below in their respective order. For simplicity, time derivatives are indicated

by a dot above the variable. The derivation of these expressions is left to the reader.

$$r = \sqrt{x^2 + y^2 + z^2}, \quad (16.6-9)$$

$$V^2 = \dot{x}^2 + \dot{y}^2 + \dot{z}^2, \quad (16.6-10)$$

$$a = \frac{\mu r}{2\mu - rV^2}, \quad (16.6-11)$$

$$e \sin E = \sqrt{\frac{1}{\mu a}} (x\dot{x} + y\dot{y} + z\dot{z}), \quad (16.6-12)$$

$$e \cos E = 1 - \frac{r}{a}. \quad (16.6-13)$$

From Eqs. (16.6-12) and (16.6-13), both e and E can be determined.

$$\tau = t - \sqrt{\frac{a^3}{\mu}} (E - e \sin E), \quad (16.6-14)$$

$$\theta = 2 \arctan \left(\sqrt{\frac{1+e}{1-e}} \tan \frac{E}{2} \right), \quad (16.6-15)$$

$$H = \sqrt{\mu a (1 - e^2)}, \quad (16.6-16)$$

$$i = \arccos \left(\frac{x\dot{y} - y\dot{x}}{H} \right), \quad 0 \leq i \leq 180^\circ, \quad (16.6-17)$$

$$\sin \Omega = \frac{y\dot{z} - z\dot{y}}{H \sin i}, \quad (16.6-18)$$

$$\cos \Omega = \frac{x\dot{z} - z\dot{x}}{H \sin i}. \quad (16.6-19)$$

From Eqs. (16.6-18) and (16.6-19), Ω can be found.

$$\sin(\omega + \theta) = \frac{z}{r \sin i}, \quad (16.6-20)$$

$$\cos(\omega + \theta) = \frac{y}{r} \sin \Omega + \frac{x}{r} \cos \Omega. \quad (16.6-21)$$

From Eqs. (16.6-15), (16.6-20) and (16.6-21) the value of ω can be determined.

16.6.3 Orbital elements from spherical coordinates

To compute orbital elements from spherical coordinates, the following scheme can be applied. First, the value of a is computed from Eq. (16.6-11).

Then

$$e = \sqrt{1 - \frac{rV^2}{\mu} \left(2 - \frac{rV^2}{\mu} \right) \cos^2 \gamma}, \quad (16.6-22)$$

$$e \sin E = \frac{rV \sin \gamma}{\sqrt{\mu a}}. \quad (16.6-23)$$

From Eq. (16.6-13) and Eq. (16.6-23) the value of E can be obtained. The values of θ and τ then follow from Eqs. (16.6-15) and (16.6-14). We proceed with

$$i = \arccos(\cos \delta \sin \psi), \quad 0 \leq i \leq 180^\circ, \quad (16.6-24)$$

$$\sin(\alpha - \Omega) = \frac{\tan \delta}{\tan i}, \quad (16.6-25)$$

$$\cos(\alpha - \Omega) = \frac{\cos \psi}{\sin i}. \quad (16.6-26)$$

From Eqs. (16.6-25) and (16.6-26) Ω can be determined. Then

$$\sin(\omega + \theta) = \frac{\sin \delta}{\sin i}, \quad (16.6-27)$$

$$\cos(\omega + \theta) = \frac{\cos \delta \cos \psi}{\sin i}. \quad (16.6-28)$$

From Eqs. (16.6-15), (16.6-27) and (16.6-28), finally, ω can be found.

16.7 *f and g series*

In Section 16.6, we argued that if the position and velocity of body P_i at a time t_o are known, and we want to compute its position and velocity at some other time t , in general, we first have to determine the orbital elements. However, for small values of $t - t_o$, it is possible to avoid this and to make a direct computation, using the so-called *f and g series*.

Suppose that at a time t_o the position vector, \mathbf{r}_o , and the velocity vector, \mathbf{V}_o , are known. A Taylor series expansion of the position vector \mathbf{r} in the neighborhood of t_o gives

$$\begin{aligned} \mathbf{r} = \mathbf{r}_o &+ \left(\frac{d\mathbf{r}}{dt} \right)_o \Delta t + \frac{1}{2!} \left(\frac{d^2\mathbf{r}}{dt^2} \right)_o (\Delta t)^2 + \frac{1}{3!} \left(\frac{d^3\mathbf{r}}{dt^3} \right)_o (\Delta t)^3 + \\ &+ \frac{1}{4!} \left(\frac{d^4\mathbf{r}}{dt^4} \right)_o (\Delta t)^4 + \frac{1}{5!} \left(\frac{d^5\mathbf{r}}{dt^5} \right)_o (\Delta t)^5 + \dots, \end{aligned} \quad (16.7-1)$$

where $\Delta t = t - t_o$. Now

$$\frac{d\mathbf{r}}{dt} = \mathbf{V}, \quad (16.7-2a)$$

and, as the motion takes place in a Keplerian orbit,

$$\frac{d^2\mathbf{r}}{dt^2} = -\frac{\mu}{r^3}\mathbf{r}. \quad (16.7-2b)$$

Higher-order derivatives of \mathbf{r} are obtained by differentiation of Eq. (16.7-2b) with respect to time,

$$\frac{d^3\mathbf{r}}{dt^3} = \frac{\mu}{r^3} \left(3 \frac{\dot{r}}{r} \mathbf{r} - \mathbf{V} \right), \quad (16.7-2c)$$

$$\frac{d^4\mathbf{r}}{dt^4} = -\frac{\mu}{r^4} \left(12 \frac{\dot{r}^2}{r} - 3\ddot{r} - \frac{\mu}{r^2} \right) \mathbf{r} + 6 \frac{\mu}{r^4} \dot{r} \mathbf{V}, \quad (16.7-2d)$$

where for simplicity the notation

$$\dot{r} \equiv \frac{d\mathbf{r}}{dt}, \quad \ddot{r} \equiv \frac{d^2\mathbf{r}}{dt^2}$$

is used, and

$$\dot{r} = \frac{\mathbf{r} \cdot \mathbf{V}}{r}.$$

When evaluated at t_o , all quantities except \ddot{r} in the Eqs. (16.7-2) are directly expressible in terms of the known initial values \mathbf{r}_o and \mathbf{V}_o . To eliminate \ddot{r} , we write Eq. (3.6-11) as

$$\ddot{r} = \frac{1}{r} (\mathbf{V}^2 - \dot{r}^2) - \frac{\mu}{r^2}. \quad (16.7-3)$$

By substituting Eq. (16.7-3) into Eq. (16.7-2d), we obtain

$$\frac{d^4\mathbf{r}}{dt^4} = -\frac{\mu}{r^5} \left(15\dot{r}^2 - 3\mathbf{V}^2 + 2 \frac{\mu}{r} \right) \mathbf{r} + 6 \frac{\mu}{r^4} \dot{r} \mathbf{V}. \quad (16.7-2e)$$

Differentiation of this equation with respect to time yields

$$\frac{d^5\mathbf{r}}{dt^5} = 15 \frac{\mu \dot{r}}{r^6} \left(7\dot{r}^2 - 3\mathbf{V}^2 + 2 \frac{\mu}{r} \right) \mathbf{r} - \frac{\mu}{r^5} \left(45\dot{r}^2 - 3\mathbf{V}^2 + 8 \frac{\mu}{r} \right) \mathbf{V}, \quad (16.7-2f)$$

where Eq. (3.6-8) was used to eliminate $\dot{\mathbf{V}}$. Higher-order derivatives of \mathbf{r} can be obtained in the same way, though the analytical development becomes more and more tedious.

Substitution of the Eqs. (16.7-2) into Eq. (16.7-1) gives

$$\mathbf{r} = f\mathbf{r}_o + g\mathbf{V}_o, \quad (16.7-4)$$

with

$$\begin{aligned} f = 1 - \frac{1}{2} \frac{\mu}{r_o^3} (\Delta t)^2 + \frac{1}{2} \frac{\mu}{r_o^4} \dot{r}_o (\Delta t)^3 - \frac{1}{24} \frac{\mu^2}{r_o^6} \left\{ 2 - 3 \frac{r_o}{\mu} (V_o^2 - 5\dot{r}_o^2) \right\} (\Delta t)^4 + \\ + \frac{1}{8} \frac{\mu^2 \dot{r}_o}{r_o^7} \left\{ 2 - \frac{r_o}{\mu} (3V_o^2 - 7\dot{r}_o^2) \right\} (\Delta t)^5 + \dots, \end{aligned} \quad (16.7-5)$$

and

$$g = \Delta t - \frac{1}{6} \frac{\mu}{r_o^3} (\Delta t)^3 + \frac{1}{4} \frac{\mu}{r_o^4} \dot{r}_o (\Delta t)^4 - \frac{1}{120} \frac{\mu^2}{r_o^6} \left\{ 8 - 3 \frac{r_o}{\mu} (V_o^2 - 15 \dot{r}_o^2) \right\} (\Delta t)^5 + \dots \quad (16.7-6)$$

Because \mathbf{r}_o and \mathbf{V}_o are constant vectors, the velocity \mathbf{V} at time t is given by

$$\mathbf{V} = \frac{df}{dt} \mathbf{r}_o + \frac{dg}{dt} \mathbf{V}_o, \quad (16.7-7)$$

where one should notice that all coefficients in the power series in Δt are constant.

As in a Keplerian orbit the angular momentum, \mathbf{H} , is constant, we have

$$\mathbf{H} = \mathbf{r}_o \times \mathbf{V}_o = \mathbf{r} \times \mathbf{V}. \quad (16.7-8)$$

By substituting Eq. (16.7-4) and Eq. (16.7-7) into Eq. (16.7-8), we obtain

$$f \frac{dg}{dt} - g \frac{df}{dt} = 1. \quad (16.7-9)$$

This relation can be used to check the analytical expressions, if more terms are included in the f and g series.

The f and g series are basic to a number of procedures for orbit determination and prediction, and are also useful for solving rendezvous problems. A great advantage of the series is that they are *universal*, i.e. that the same formulae hold for all conic sections. Herrick [7] gives an extensive discussion on the use of these and other universal expressions. He also mentions that for practical purposes the usefulness of the time series end before their mathematical convergence, when the higher and more complicated terms become appreciable. As a rough criterion Herrick recommends to use the time series only if $\mu(\Delta t)^2/r_o^3 < 0.01$. Bond [8] presents a different way to determine the coefficients in the f and g series by using recursive relations.

16.8 Relativistic effects

From the *general theory of relativity* we know that Newton's law of gravitation describes only in a first approximation a real gravitational field. For a body with *spherical symmetric mass distribution*, the *geometry of space-time* is given by the so-called *Schwarzschild metric*. In case $m_i \ll m_k$, the motion of body P_i , relative to a non-rotating reference frame with origin at body P_k , is then described by [9]

$$\frac{d^2 u}{d\varphi^2} + u = \frac{\mu}{H^2} + \alpha u^2, \quad (16.8-1)$$

where

$$u = \frac{1}{r}, \quad H = r V_\varphi, \quad \alpha = 3 \frac{\mu}{c^2}, \quad \alpha u^2 = 3 \frac{\mu}{H^2} \frac{V_\varphi^2}{c^2}, \quad (16.8-2)$$

provided the orbit is *not circular*. In the equations given above, r and φ denote the angular position, c is the velocity of light and μ is the classical gravitation parameter of body P_k . Comparing Eq. (16.8-1) and Eq. (3.6-18), we note that the relativistic influence manifests itself only in the second term at the right-hand side of Eq. (16.8-1). In celestial mechanics, always $V_\varphi \ll c$, indicating the relativistic term to be very small. An approximate analytical solution of Eq. (16.8-1) can be obtained by the *method of successive approximations*. The zeroth-order solution is obtained by neglecting the relativistic term. We then find the solution for a Keplerian orbit,

$$u = \frac{\mu}{H^2} [1 + e \cos(\varphi - \omega)]. \quad (16.8-3)$$

Substitution of this expression for u into the second term on the right-hand side of Eq. (16.8-1) yields

$$\frac{d^2 u}{d\varphi^2} + u = \frac{\mu}{H^2} + \alpha \frac{\mu^2}{H^4} [1 + \frac{1}{2}e^2 + 2e \cos(\varphi - \omega) + \frac{1}{2}e^2 \cos 2(\varphi - \omega)]. \quad (16.8-4)$$

The complete solution of this differential equation is

$$u = \frac{\mu}{H^2} [1 + e \cos(\varphi - \omega)] + \alpha \frac{\mu^2}{H^4} [(1 + \frac{1}{2}e^2) + e\varphi \sin(\varphi - \omega) - \frac{1}{6}e^2 \cos 2(\varphi - \omega)]. \quad (16.8-5)$$

The first term in the relativistic part has the effect of slightly increasing u by a constant quantity; this amount will be imperceptible. Also the effect of the third term is negligible. Because of its steadily increasing amplitude, the second term creates observable effects after long enough a period. Retaining only this term for the relativistic effect, we obtain

$$u = \frac{\mu}{H^2} [1 + e \cos(\varphi - \omega) + \beta e\varphi \sin(\varphi - \omega)], \quad (16.8-6)$$

where

$$\beta = \alpha \frac{\mu}{H^2}. \quad (16.8-7)$$

Equation (16.8-6) can approximately be written as

$$r = \frac{1}{u} = \frac{H^2/\mu}{1 + e \cos(\varphi - \omega - \beta\varphi)}. \quad (16.8-8)$$

By comparing Eq. (16.8-8) and Eq. (16.2-1), we conclude that the trajectory of body P_i about body P_k can be visualized as an ellipse *with a slowly rotating major axis*. After one revolution of body P_i , the major axis is rotated by $2\beta\pi$ in the direction of motion of body P_i . Thus, due to the relativistic

effects, there is a change in the angular position of the pericenter after one revolution:

$$\Delta\omega = 2\pi\alpha \frac{\mu}{H^2} = 6\pi \frac{\mu^2}{H^2 c^2} = 24\pi^3 \frac{a^2}{T^2 c^2 (1-e^2)}, \quad (16.8-9)$$

where T is the (Keplerian) orbital period. Computing the value of $\Delta\omega$ for the planet Mercury, we find a *perihelion advance* of $43''$ per century. For the other planets, the perihelion motion is much smaller; for the Earth, we find $4''$ per century. For an Earth satellite with perigee at 500 km altitude and apogee at 1000 km altitude, the relativistic perigee motion will be about $1280''$ per century. This rather large value will, however, not be observable due to many other larger disturbing effects upon such a satellite.

Equation (16.8-9) was first found by Einstein [10], and is one of the three famous tests for the general theory of relativity. Taking into account the gravitational perturbations of the planets on the motion of Mercury when using the Newtonian attraction law, the perihelion motion of Mercury was calculated to be $532''$ per century. Observations, however, led to a figure of $574''$ per century and no reasonable explanation could be found for this difference. The predictable relativistic effect nicely fills this gap.

Because the relativistic effects are very small, the much simpler Newtonian theory can be applied to nearly all problems in celestial mechanics, especially for relatively short duration spaceflights.

References

- 1 Altman, S. P. (1965), *Orbital Hodograph Analysis*, AAS Science and Technology Series, Vol. 3, American Astronautical Society, Baltimore.
- 2 Whittaker, E. T. (1917), *A Treatise on the Analytical Dynamics of Particles and Rigid Bodies*, Cambridge University Press, London, p. 89.
- 3 Moulton, F. R. (1914), *An Introduction to Celestial Mechanics*, Macmillan, New York, p. 156.
- 4 Brouwer, D. and Clemence, G. M. (1961), *Methods of Celestial Mechanics*, Academic Press, New York, p. 60–114.
- 5 Brown, E. W. and Shook, C. A. (1933), *Planetary Theory*, Cambridge University Press, London, p. 66, 80.
- 6 Plummer, H. C. (1960), *An Introductory Treatise on Dynamical Astronomy*, Dover Publications, New York, p. 46–47.
- 7 Herrick, S. (1971), *Astrodynamic*, Vol. 1, Van Nostrand Reinhold, London, p. 197–219.
- 8 Bond, V. R. (1966), *Recursive Computation of the Coefficients of the Time-Dependent f and g Series Solution of Keplerian Motion and a Study of the Convergence Properties of the Solution*, NASA TN D-3322, Washington.

388 Rocket Propulsion & Spaceflight Dynamics

- 9 Eddington, A. (1923), *The Mathematical Theory of Relativity*, Cambridge University Press, London, p. 86.
- 10 Einstein, A. (1915), Erklärung der Perihelbewegung des Merkur aus der allgemeinen Relativitätstheorie, *Sitzungsber. Deutsche Akad. Wissens. (Math. Phys. Technik)*, Berlin, 831–839.

17 The Launching of a Satellite

Satellites are launched from the Earth's surface by means of multi-stage rockets. After ignition of the first-stage rocket engine(s), these launch vehicles first ascend vertically. A few seconds after lift-off, the rocket is tilted and it flies a curved trajectory until at cut-off the final stage and the satellite have a predetermined velocity and position. The determination of the optimum ascent trajectory of a particular launch vehicle for a prescribed satellite orbit is very complex, and is closely related to the theory of optimum spaceflight maneuvers and to the operational constraints of that launch vehicle. Because these topics are beyond the scope of this book, we will discuss only some general aspects of ascent trajectories. Launch vehicle performance data for orbital missions are presented in graphical form. A more detailed discussion will be given on the relations between the orbital parameters of a satellite and its position and velocity at the moment it enters its orbit.

17.1 Launch vehicle ascent trajectories

Two basic types of ascent trajectories can be distinguished for satellite launch vehicles (Fig. 17.1): *Direct Ascent* (D.A.) and *Hohmann Transfer Ascent* (H.T.A.).

The D.A. trajectory is selected such that its summit point lies in the required satellite orbit. When the satellite, which in most cases is still attached to the final rocket stage, approaches this summit altitude, the final-stage motor is ignited and the satellite is accelerated to the required (local) orbital velocity. In some cases, the rocket motor required for this acceleration is not the motor of the last stage, but is an integral part of the satellite itself (*apogee motor*).

In the H.T.A., the satellite and the last stage first attain a low-altitude circular *parking orbit*, just outside the densest part of the atmosphere. Usually, the altitude of this parking orbit is about 200 km. For preliminary mission and performance analyses, mostly a parking orbit is assumed at an altitude of 185 km (100 n.mi.). Either shortly after parking orbit injection (P.O.I.), or after a coasting period in this parking orbit, the vehicle is injected into an elliptic *transfer trajectory*. At perigee, this transfer ellipse is (about) tangential to the parking orbit and at apogee (about) tangential to the required satellite orbit. This type of transfer trajectory has been proposed in 1925 by W. Hohmann [1], and therefore is called a *Hohmann*

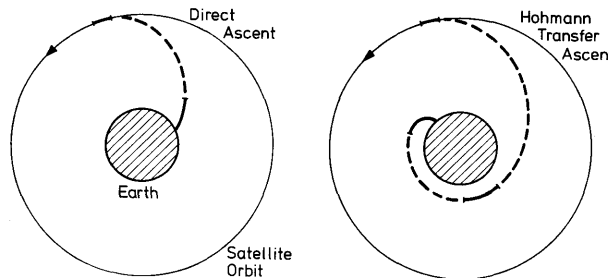


Fig. 17.1 Direct Ascent and Hohmann Transfer Ascent to a satellite orbit

transfer trajectory. We will discuss these transfer trajectories in more detail in Section 19.2.1. When the satellite is at apogee of the transfer trajectory, the last-stage rocket motor, or the satellite's apogee motor, is fired to accelerate the satellite into its final orbit.

Comparing these two types of ascent trajectories, it can be shown [2] that, generally, the H.T.A. requires less propellant for ascent into a specified orbit. The main reason for this is that the ascent trajectory for a D.A. mostly is steeper than for a H.T.A., yielding larger gravity losses. The H.T.A. would even be the absolute minimum-energy transfer trajectory if the altitude of the parking orbit were zero, and if all energy required to reach the final orbit were transferred to the satellite in the most efficient way, i.e. as a velocity increment about normal to the radius vector. Owing to the presence of the atmosphere, however, this optimum transfer cannot be realized and a low-altitude parking orbit has to be used. Only for satellite orbits below 300 km altitude, does a D.A. sometimes require less propellant.

It should be realized that apart from propellant consumption, many other operational aspects exist which must be taken into account in the selection of an ascent trajectory. Obviously, the shorter coasting periods in a D.A. may be advantageous for stages with cryogenic propellants. Problems of attitude control and other aspects of vehicle engineering are mostly reduced too when using a D.A. In addition, due to the comparatively steeper D.A., the launch vehicle can be tracked longer from the launch site. For the H.T.A., a world-wide net of tracking stations usually is a necessity. From the viewpoint of booster recovery, the shorter horizontal distance travelled by the booster during a D.A. is advantageous. Finally, it will be clear, that, in general, the H.T.A. requires at least one propulsion phase more than the D.A. Usually, this implies the application of restartable rocket engines. For launch vehicles using only solid propellants, this restart capability is difficult to provide.

17.2 The injection of a satellite

Whatever ascent trajectory is flown, the satellite, and often the last stage too, ultimately will reach a position and velocity required to follow a

prescribed orbit about the Earth. Usually, the satellite then is separated from the last stage by releasing a compressed-spring mechanism, and small rocket motors on the last stage are fired to move the stage away from the satellite. For liquid-propellant stages, usually the propellant residuals are also exhausted, without combustion, through the main engine(s), in order to increase the relative velocity between stage and satellite.

The time of separation is called the *injection epoch*; the position and velocity of the satellite at this epoch constitute the *injection parameters*. Injection epoch and injection parameters together completely determine the orbit in which the satellite will encircle the Earth.

17.2.1 General aspects of satellite injection

We will now assume that at the injection epoch, t_i , the position and velocity of the satellite relative to a non-rotating geocentric equatorial reference frame (Section 2.3.4) are known in terms of radial distance, r_i , declination, δ_i , right ascension, α_i , velocity, V_i , flight path angle, γ_i , and flight path azimuth, ψ_i . We then can determine the Keplerian elements of the orbit, and other useful orbital parameters, by using the expressions given in Section 16.6.2 and 16.6.3. From these relations, we conclude:

1. The orbital elements a and e , the time difference $t_i - \tau$ and the true anomaly at injection, θ_i , are only a function of the *in-plane injection parameters* r_i , V_i , γ_i .
2. The orbital elements i and Ω , and the argument of latitude at injection, $u_i = \omega + \theta_i$, only depend on the *out-of-plane injection parameters* α_i , δ_i , ψ_i .
3. The orbital element ω is both a function of the in-plane and the out-of-plane injection parameters.

In particular from Eq. (16.6-24), a number of important conclusions can be drawn. Because $-1 \leq \sin \psi_i \leq 1$, we may write

$$|\delta_i| \leq i \leq 180^\circ - |\delta_i|.$$

For a particular injection point, the minimum orbit inclination is reached at $\psi_i = 90^\circ$; i.e. an injection due east. The maximum inclination is reached if the satellite is injected due west. For the injection of a satellite into an equatorial orbit with $i = 0^\circ$, the conditions $\delta_i = 0^\circ$ and $\psi_i = 90^\circ$ must hold; i.e. the injection point must be located in the equatorial plane and the injection must be due east.

If the required inclination of the orbit is within one of the ranges:

$$0^\circ \leq i < |\Phi_l| \quad \text{or} \quad 180^\circ - |\Phi_l| < i \leq 180^\circ,$$

where Φ_l is the geocentric latitude of the launch site, the ascent trajectory and the final orbit cannot be coplanar. In these cases, a plane change is required during the ascent trajectory and/or at orbit injection. These so-called *dog-leg maneuvers*, which are performed at relatively large vehicle

velocities, are very expensive in terms of propellant consumption [3]. In order to launch satellites into low-inclination orbits, an *equatorial launch site* is therefore very attractive. Presently, two near-equatorial launch sites are in use: the Italian *San Marco* base (2.2°S , 40.2°E) in the Indian Ocean off the coast of Kenya, and the French/European site *Kourou* (5.2°N , 52.7°W) in Guiana. The other three Western launch sites are located in the USA, north of the equator: *Western Test Range* (*Vandenberg Air Force Base*; 34.6°N , 120.6°W) in California, *Eastern Test Range* (*Cape Canaveral*; 28.5°N , 80.6°W) in Florida and *Wallop Island* (37.8°N , 75.5°W) in Virginia.

For all launch sites, the launch azimuths which can be used are restricted by safety aspects and the availability of tracking stations. For example, for a launch from the Eastern Test Range the launch azimuth, generally, must lie within the range 45° – 115° ; for a launch from the Western Test Range a launch azimuth between 170° and 300° is generally acceptable. As a consequence, the Eastern Test Range is used primarily for launches into a more or less eastward direction, which employ the rotation of the Earth to increase effectively the inertial velocity of the vehicle, thereby improving the launch vehicle's payload capability. The Western Test Range is mainly used for near-polar orbits.

If, for a specified orbital plane, $|\Phi_l| < i < 180^{\circ} - |\Phi_l|$, the launch site will cross the orbital plane twice a day. Because of launch site constraints on launch azimuth, generally, only one of these crossings can be used to launch a satellite into its orbit by a coplanar ascent trajectory. If small plane change maneuvers are accepted, the satellite can be launched within a short period around this crossing time, constituting the so-called *daily launch window* [4].

We now meet another advantage of using a parking orbit. As the launch time is fixed and the ascent trajectory for a D.A. is prescribed by the launch vehicle capabilities, the point where the satellite enters its orbit is completely determined. Often, such as, for instance, in rendezvous missions or for applications satellites, the satellite has to enter its orbit at a specified location. Then, a coplanar launch within the launch window is mostly impossible. The best alternative to long periods of inaccessibility or expensive non-planar transfers is offered by the use of a parking orbit. By carefully selecting the orientation and altitude of the parking orbit, and the point of departure from this parking orbit, it is possible to reach any point in the final satellite orbit. A discussion on these *phasing maneuvers* for geosynchronous missions is given by Cornelisse and Wakker [5].

17.2.2 Dependence of orbital parameters on in-plane injection parameters

In this section, we will investigate how the size, shape and orientation of a satellite orbit in its orbital plane depend on the injection parameters. Therefore, we will derive expressions relating the orbital parameters a , e , p ,

r_a , r_p , θ_i and $t_i - \tau$ to the in-plane injection parameters r_i , V_i and γ_i . For an analysis of the dependence of orbit parameters on the out-of-plane injection parameters be referred to El'yasberg [6].

For the semi-major axis, a , the eccentricity, e , and the semi-latus rectum, p , we may write, according to Eqs. (13.2-23a), (13.2-12b), (13.2-12a),

$$\frac{a}{r_i} = \frac{1}{2 - k_i}, \quad (17.2-1)$$

$$e = \sqrt{1 - k_i(2 - k_i) \cos^2 \gamma_i}, \quad (17.2-2)$$

$$\frac{p}{r_i} = k_i \cos^2 \gamma_i, \quad (17.2-3)$$

where k_i is defined as

$$k_i = \frac{V_i^2}{V_{c_i}^2} \quad (17.2-4)$$

and V_{c_i} is the circular velocity at the injection point. The perigee and apogee distances, $r_{a,p}$, are given by

$$r_{a,p} = a(1 \pm e), \quad (17.2-5)$$

where the plus sign holds for the apogee and the minus sign for the perigee. Substituting Eqs. (17.2-1) and (17.2-2) into Eq. (17.2-5) yields

$$\frac{r_{a,p}}{r_i} = \frac{1}{2 - k_i} [1 \pm \sqrt{1 - k_i(2 - k_i) \cos^2 \gamma_i}]. \quad (17.2-6)$$

To obtain expressions for the true anomaly at injection, θ_i , we start from the Eqs. (16.2-5) and (16.2-6), which, after substitution of Eqs. (17.2-3) and (17.2-4), can be written as

$$e \sin \theta_i = k_i \sin \gamma_i \cos \gamma_i, \quad (17.2-7a)$$

$$e \cos \theta_i = k_i \cos^2 \gamma_i - 1. \quad (17.2-7b)$$

To determine the time difference $t_i - \tau$ as a function of r_i , V_i and γ_i , we start from Eq. (16.6-14):

$$t_i - \tau = \sqrt{\frac{a^3}{\mu}} (E_i - e \sin E_i), \quad (17.2-8)$$

where E_i is the eccentric anomaly at injection. According to Eqs. (16.6-13), (16.6-23) and (17.2-1), we may write

$$e \sin E_i = \sqrt{k_i(2 - k_i)} \sin \gamma_i, \quad (17.2-9a)$$

$$E_i = \arctan \left(\frac{\sqrt{k_i(2 - k_i)}}{k_i - 1} \sin \gamma_i \right). \quad (17.2-9b)$$

The value of E_i is uniquely determined by the condition that if $\gamma_i > 0$: $\sin E_i > 0$, and if $\gamma_i < 0$: $\sin E_i < 0$.

The dependence of e , $t_i - \tau$, θ_i , r_a and r_p on k_i and γ_i is depicted in Fig. 17.2. The perigee and apogee distances were non-dimensionalized by division by r_i ; the time difference $t_i - \tau$ by division by the orbital period, T . From this figure, we see that:

1. For specified values of r_i and V_i , e reaches a minimum at $\gamma_i = 0$.
2. For small-eccentricity orbits ($k_i \approx 1$, $\gamma_i \approx 0$), a small variation in γ_i yields large variations in e .
3. For all values of $k_i > 1$: $\theta_i = 0$ and $r_p = r_i$ at $\gamma_i = 0$. For all values of $k_i < 1$: $\theta_i = 180^\circ$ and $r_a = r_i$ at $\gamma_i = 0$. Varying k_i from 0 to 2 at $\gamma_i = 0$, yields at $k_i = 1$ a discontinuous change in the position of the perigee. For a circular orbit, $k_i = 1$ and $\gamma_i = 0$, the position of the perigee is undetermined.
4. Small variations in γ_i about $\gamma_i = 0$ yield for near-circular orbits large variations in the position of the perigee.
5. For specified values of r_i and V_i , the apogee distance is a maximum and the perigee distance a minimum at $\gamma_i = 0$.

Excluding high-altitude and highly-eccentric satellite orbits which are

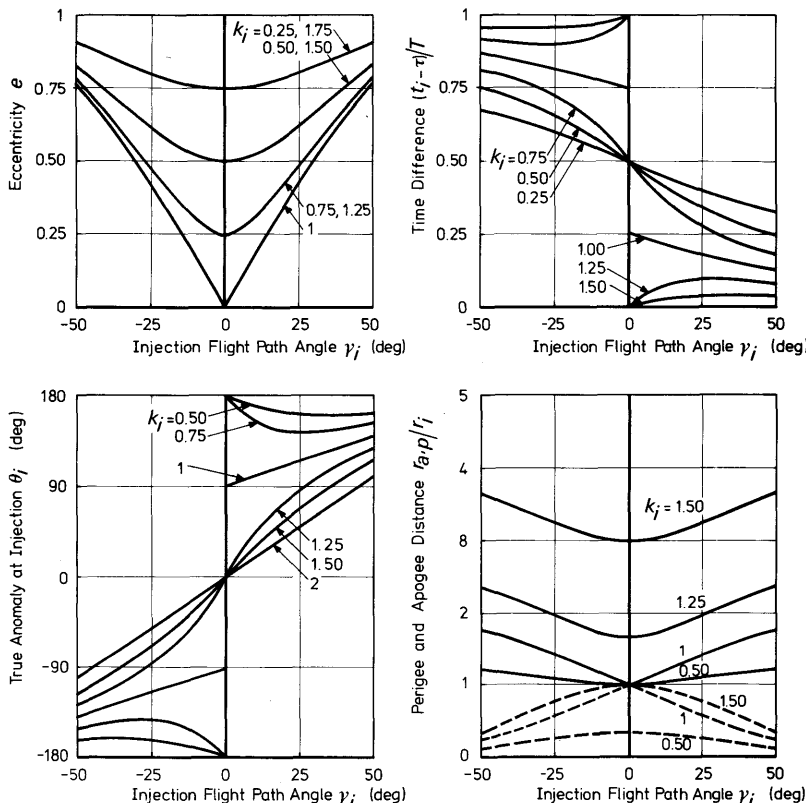


Fig. 17.2 Orbital parameters versus the in-plane injection parameters

strongly affected by luni-solar attractions [7], it is evident that the perigee altitude mainly determines the *orbital lifetime* of a satellite. For the atmospheric density increases about exponentially with decreasing altitude. The altitude of the injection point will be chosen as low as possible for maximizing the rocket payload capability. To obtain a perigee altitude as high as possible, we therefore prefer to inject a satellite at $\gamma_i = 0$.

To illustrate the *sensitivity* of the orbit altitude to the values of γ_i , V_i and r_i , consider a nominal satellite orbit with perigee and apogee altitude at 500 km and 600 km, respectively, and $\gamma_i = 0$. The nominal injection velocity then is $V_i = 7.642$ km/s. Figure 17.3 shows the allowable departures of r_i , V_i and γ_i from their nominal values in order to yield an orbit with $h_p > 425$ km and $h_a < 675$ km, and an orbit with $h_p > 350$ km and $h_a < 750$ km. We note, that even for these large altitude deviations, departures in r_i , V_i and γ_i which can be tolerated are very small. It is therefore that satellite launch vehicles have to be capable of injecting satellites with *very high precision*.

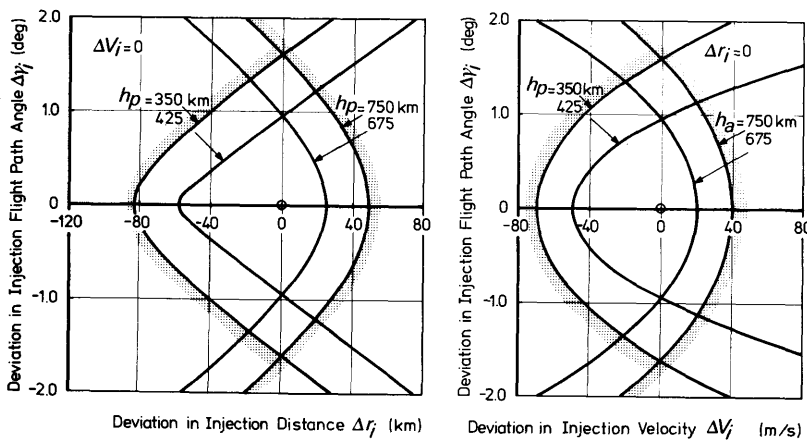


Fig. 17.3 Acceptable deviations in in-plane injection parameters for specified maximum departures in perigee and apogee altitude. Nominal orbit: $\gamma_i = 0$, $h_p = 500$ km, $h_a = 600$ km

17.3 Launch vehicle performances

For satellite mission analyses, we have to know the performances of the *available* launch vehicles. For preliminary studies, we mostly make use of performance diagrams in which the payload capability of a launch vehicle is plotted versus the so-called *launch vehicle characteristic velocity*, V_{char} (Fig. 17.5). To explain how to use these diagrams, we first recall that all existing rocket stages are high-thrust chemical systems. Once in a parking orbit, we can assume for orbit transfer maneuvers that the thrust acts for so short a

time that during motor operation only the vehicle's velocity vector is altered, but not its position vector. We thus use the concept of an *impulsive shot* (Section 11.2.3) and consider an orbit transfer maneuver as a sequence of instantaneous velocity changes. The mass of propellant required for each velocity change can be computed from *Tsiolkovsky's equation*, Eq. (11.2-4). We define a *mission characteristic velocity*, V_{char}^* , as the arithmetic sum of all velocity changes required to perform a specified mission, starting from a 185-km circular parking orbit, plus the velocity in this parking orbit relative to a non-rotating geocentric reference frame ($V_c = 7.797 \text{ km/s}$). This mission characteristic velocity thus is a measure of the energy required to fly a given mission. With the theory of orbital maneuvers, we can compute this mission characteristic velocity for each final orbit and each transfer trajectory. As this subject is not treated in this book, we will only discuss some results on the basis of Fig. 17.4. For a full treatment be referred to the standard work of Ehricke [2], and to Gobetz and Doll [8].

The dashed line in Fig. 17.4 shows the initial incremental velocity ΔV_1 , required at the parking orbit altitude to perform a *coplanar Hohmann transfer* to an apogee altitude corresponding to a desired final orbit altitude. Also indicated is the transfer time to execute this Hohmann transfer. To circularize the orbit at the apogee of the transfer trajectory, an incremental velocity ΔV_2 has to be applied. The sum of ΔV_1 and ΔV_2 is also shown in Fig. 17.4. We note that for increasing final orbit altitudes, V_{char}^* first increases, until from an altitude of about 96,000 km upwards it decreases again. One can prove that V_{char}^* for this type of transfer trajectories takes a maximum value at $r_2/r_1 = 15.58$, where r_1 is the radius of the circular parking orbit and r_2 is the radius of the final circular orbit. For $r_2/r_1 > 3.31$, we find that V_{char}^* is larger than the escape velocity in the parking orbit. For

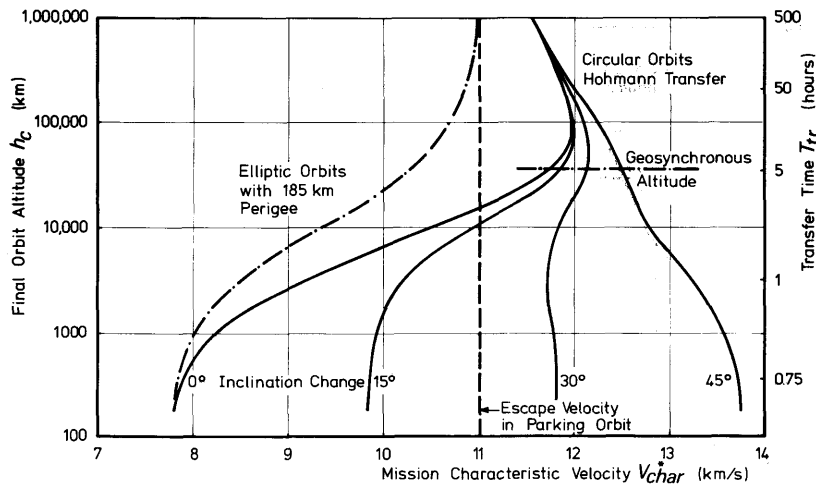


Fig. 17.4 Mission characteristic velocity for various final orbits

$r_2/r_1 > 11.94$, energy can be saved by first ascending elliptically beyond the target orbit to a greater altitude, and then returning from this high apogee elliptically into the target orbit. In such a *bi-elliptic transfer*, two velocity increments and one velocity decrement are applied. The energy savings, however, are rather small, while the transfer time becomes very large. Therefore, these bi-elliptic transfers are of little practical value.

In Fig. 17.4, the mission characteristic velocity for a *three-dimensional Hohmann transfer*, i.e. with a cotangential transfer ellipse between two inclined circular orbits, is shown too. For these missions, one has three possibilities: orbital plane change in conjunction with the perigee impulse, plane change in conjunction with the apogee impulse, or orbital plane change both at perigee and at apogee such that the sum of both changes equals the desired value. On first sight, it seems that a plane change most economically should be carried out at apogee, where the velocity of the vehicle is a minimum. It can be shown, however, that the energy minimum requires a small part of the total plane change to be accomplished at the departure from the parking orbit. The savings by carrying out such an optimum plane change maneuver are not spectacular. For example, the launch of a geostationary satellite from a 28.5°-inclination, 185-km parking orbit would require a 2.2° plane change at perigee and a 26.3° plane change at apogee, leading to a minimum characteristic velocity of 12.070 km/s [5]. If the total plane change is carried out at apogee, the mission characteristic velocity only slightly increases with about 25 m/s. In Fig. 17.4, it is assumed that when the vehicle in its 185-km parking orbit crosses the equatorial plane, it injects into a coplanar Hohmann transfer trajectory. At the apogee of this transfer trajectory, which also occurs at an equatorial crossing, the satellite is injected in such a way that the total plane change is effected and the orbit is circularized simultaneously. Curves are presented for three values of a change in orbit inclination. We note that in particular for low final orbits, the energy required for inclination changes is considerable.

The *launch vehicle characteristic velocity*, V_{char} , referred to in Fig. 17.5, is defined as the actual total velocity deliverable for a given payload after a due east launch from Cape Canaveral and use of a 185-km parking orbit. The payload indicated is considered to include all elements normally associated with the satellite that must be accelerated to the required final velocity. Only the payload adapter is not considered as part of the satellite. If the launch vehicle has sufficient coast and restart capabilities to allow this total velocity to be applied to the satellite in the same sequence of increments as assumed when determining the mission characteristic velocity, then V_{char} clearly is equivalent to V_{char}^* . For any launch that is not from Cape Canaveral and/or not in an eastward direction, the vehicle characteristic velocity is equal to the mission characteristic velocity *plus a launch site and launch azimuth velocity penalty*. This approximate velocity penalty, ΔV_{char}^* , is shown in Fig. 17.6, for launches from the Eastern Test Range and from the Western Test Range.

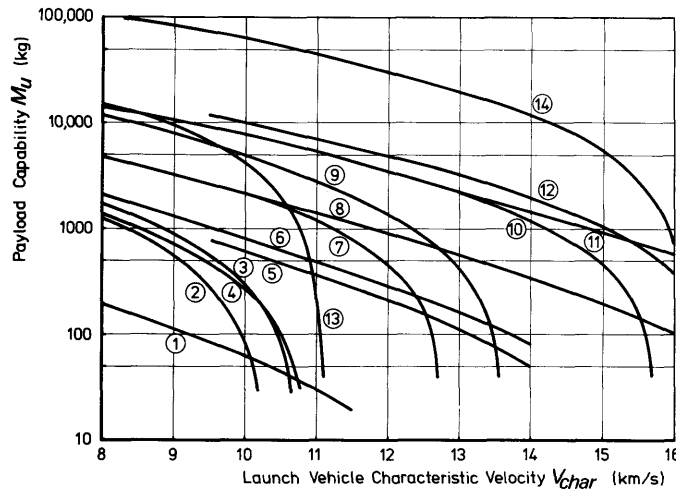


Fig. 17.5 Launch vehicle payload capability as a function of launch vehicle characteristic velocity (Reference [9]). 1: Scout D(4-stage, Algol III first stage); 2: Delta 2310 (2-stage, 3 Castor II strap-ons); 3: Delta 2910 (2-stage, 9 Castor II strap-ons); 4: TAT (3C)/Agena (2-stage, 3 Castor II strap-ons); 5: Delta 2314 (3-stage, 3 Castor II strap-ons, TE364-4 third stage); 6: Delta 2914 (3-stage, 9 Castor II strap-ons, TE364-4 third stage); 7: Atlas D/Centaur (2-stage); 8: Atlas D/Centaur/TE364-4 (3-stage); 9: Titan IIIC (3-stage, 2 five-segment 120-inch strap-ons); 10: Titan IIIE/Centaur (3-stage, 2 five-segment 120-inch strap-ons); 11: Titan IIIE/Centaur/TE364-4 (4-stage, 2 five-segment 120-inch strap-ons); 12: Titan III7/Centaur (3-stage, 2 seven-segment 120-inch strap-ons); 13: Saturn IB (2-stage); 14: Saturn V (3-stage).

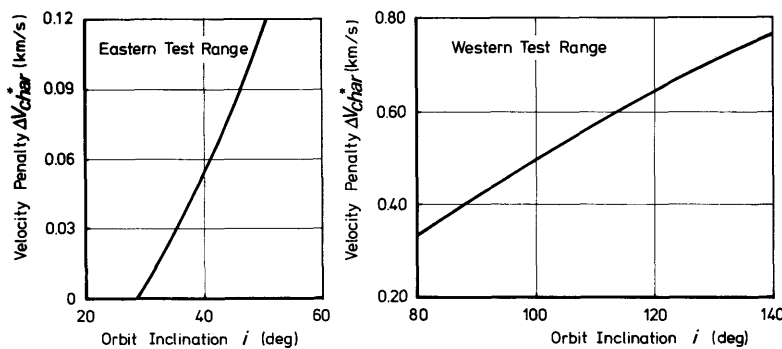


Fig. 17.6 Launch site and launch azimuth velocity penalty (Ref. [9]).

To show how to use these diagrams, we will consider the launch of a satellite by an Atlas/Centaur [10] into a 2000-km circular orbit with an inclination of 110° . If the launch takes place from the Western Test Range, a coplanar Hohmann transfer is possible. From Fig. 17.4 we read that the mission characteristic velocity is $V_{char}^* = 8.73$ km/s. The velocity penalty is, according to Fig. 17.6, $\Delta V_{char}^* = 0.57$ km/s. So, the launch vehicle characteristic velocity is $V_{char} = 9.30$ km/s. From Fig. 17.5 we find that the payload capability of the Atlas/Centaur for this mission is about $M_u = 2800$ kg.

Sometimes, constraints such as limitations on the allowable number of stage restarts, the duration of coast periods, or certain guidance system requirements, do not permit the vehicle to execute the sequence assumed in computing the mission characteristic velocity. To put it in other words: specific launch vehicle limitations may preclude a desired trajectory. For more accurate mission analyses we therefore use diagrams as shown in Fig. 17.7. Here, the payload capability of a launch vehicle is plotted versus perigee and apogee altitude for a *specific* launch site and orbit inclination. In these graphs all constraints imposed by the launch vehicle are included. The payload mass indicated includes the mass of the payload adapter. A comparison of the payload capabilities of the four-stage solid-propellant Scout D [11] for a launch due east from Wallops Island (WI) and for a launch into a polar orbit from the Western Test Range (WTR), clearly shows the payload increase, for the same orbit altitude, if the rocket is launched into an easterly direction and full benefit is taken of the rotation of the Earth. Also shown in Fig. 17.7 are the payload capabilities of some configurations of the Delta launch vehicle [12], the Atlas/Centaur and the Titan IIIC launch vehicles. For the Atlas/Centaur and the Titan IIIC, the advantage of a Hohmann Transfer (H.T.A.) over a Direct Ascent (D.A.) is clear.

Preliminary performance data for the reusable *Space Shuttle* [13] are presented in Fig. 17.8 for delivery missions from Cape Canaveral and Vandenberg. For these performance maps, it was assumed that the Orbiter always is injected into a 93 km by 185 km orbit. All subsequent maneuvers are performed by using the *orbital maneuvering system* (OMS). In addition to the Orbiter integral OMS tanks, up to three extra OMS kits, which are payload chargeable items, can be installed in the Orbiter's cargo bay for increased operational flexibility. Using these extra propellants, circular orbits up to about 1100 km altitude are possible. For missions requiring higher energies, additional propulsion stages are required. These stages are transported within the Shuttle cargo bay to a low parking orbit where they are deployed to complete the required mission. In the first period after the Shuttle becomes operational, an expendable *Interim Upper Stage* (IUS) will be used for this purpose. Ultimately, a reusable so-called *Space Tug* may be built, which after completion of its mission will return to the Shuttle. It then will be retrieved into the cargo bay of the Shuttle and returned to Earth, where maintenance can be applied to prepare it for the next flight. Preliminary performance analyses have shown [5] that with such a Shuttle-Tug

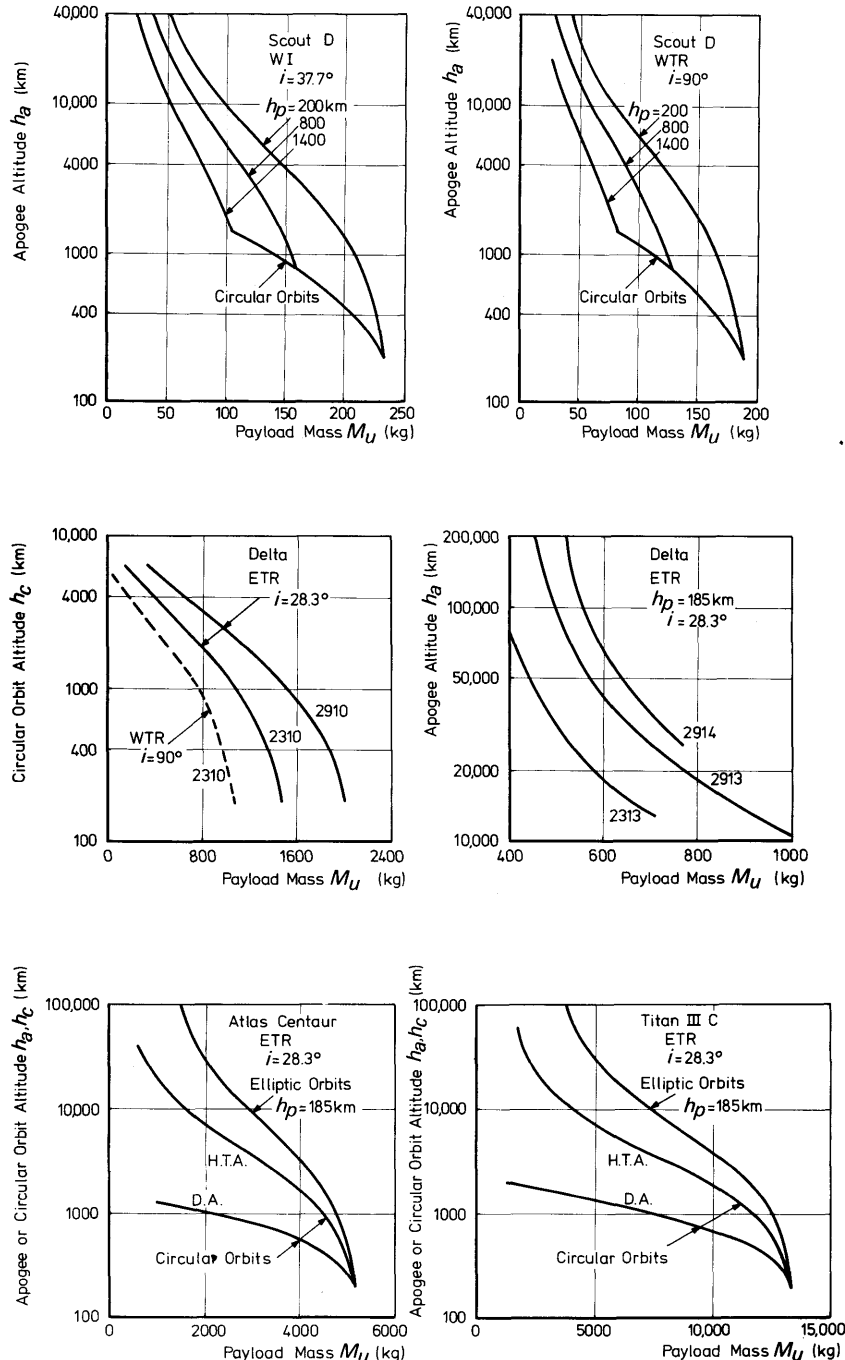


Fig. 17.7 Earth-orbital performance of satellite launch vehicles (Ref. [9]).

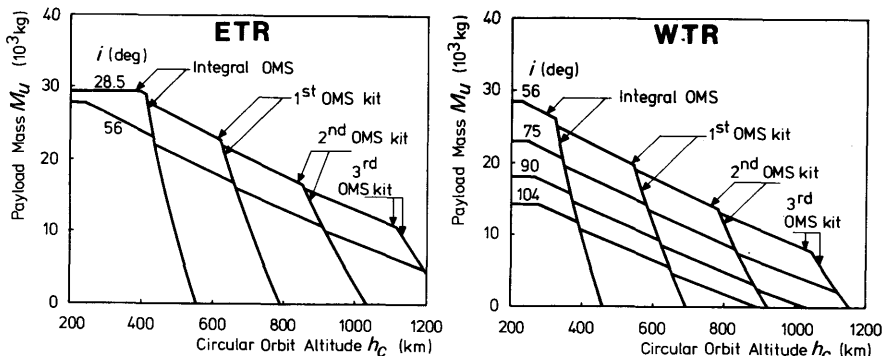


Fig. 17.8 Estimated payload capability of the Space Shuttle for delivery missions from the Eastern Test Range and the Western Test Range (Ref. [14]).

combination geosynchronous satellites up to a mass of about 2000 kg can be launched. Geosynchronous satellites with a mass up to 760 kg could also be retrieved by the Tug from their orbit down to Earth for repair.

17.4 Orbit deviations due to injection errors

As a compromise between the preferred orbit, the payload capabilities of existing launch vehicles and many operational constraints, a *nominal* orbit can be selected for a specific mission. The *actual* satellite orbit will deviate from this nominal orbit due to unavoidable *injection errors*. Deviations from the nominal launch ascent trajectory and from the final injection procedure will cause the injection parameters to differ from their nominal values. Though for modern launch vehicles these injection errors are rather small, their effect on the orbit of a satellite can be appreciable. Therefore, in selecting a nominal orbit one should always be aware of possible orbit deviations due to injection errors. In the case that the payload weighs considerably less than the launch vehicle's maximum payload for that orbit, the excess capability can be used to *shape the ascent trajectory* such that the sensitivity of the injection parameters to variations in launch vehicle and atmospheric parameters is reduced [15].

To illustrate the effects of injection errors, we will consider the launch of the Astronomical Netherlands Satellite (ANS), which was launched on August 30, 1974 by a Scout D from the Western Test Range. Nominal perigee and apogee altitudes were 510 km and 560 km, respectively [16]. The nominal values of the injection parameters and the orbital elements at injection are given in Table 17.1. The quantity Λ_i in this table denotes the geographic longitude of the injection point; all other parameters have their usual meaning. We assume that at injection all parameters but V_i and γ_i have their nominal values. With the equations given in Section 16.6.2 and

Table 17.1 Nominal injection parameters and orbital elements of ANS

$t_i = \text{August 27, 1974; } 14^{\text{h}}9^{\text{m}}41^{\text{s}} \text{ U.T.}$

$r_i = 6887.92 \text{ km}$	$a = 6913.078 \text{ km}$
$\delta_i = 13.917^\circ$	$e = 0.003640$
$\Lambda_i = -125.540^\circ$	$i = 97.801^\circ$
$V_i = 7.6211 \text{ km/s}$	$\omega = 167.329^\circ$
$\gamma_i = -0.005^\circ$	$\Omega = 241.618^\circ$
$\psi_i = 188.038^\circ$	$t_i - \tau = 94.975 \text{ min}$

Actual launch took place on August 30, 1974;
 $14^{\text{h}}7^{\text{m}}40^{\text{s}}$ U.T.

Section 16.6.3, we can compute the deviations in the orbital parameters due to errors in V_i and γ_i . For the orbital parameters e , ω , τ , h_p and h_a the results are shown in Fig. 17.9. In these graphs only errors in V_i and γ_i well within the 1σ limits for the nominal injection altitude are considered [11]. We note that even for a successful launch, rather large deviations from the nominal orbit can occur: the angular position of the perigee, for instance, can shift more than 90° with respect to its nominal location.

It should be mentioned here that in practice all injection parameters will show errors simultaneously. By statistical means, all injection accuracy data can be translated into *orbit deviation probabilities*. As an example, Fig. 17.10 shows isoprobability curves for the orbital lifetime of ANS. One curve holds for a 99 percent probability and $\frac{1}{2}$ year lifetime; the other for a 95 percent probability and 1 year lifetime. Also shown are lines representing the launch capability of the Scout D. Based on this information, and on operational requirements, a nominal 510–560 km orbit was selected for ANS. When the satellite was finally launched after a delay of three days, a malfunction occurred in the guidance system of the Scout vehicle, and the satellite actually entered an orbit with initial perigee and apogee altitudes of 266 km and 1175 km, respectively.

17.4.1 Small injection errors

If the injection errors are very small, we can obtain simple analytical expressions for the effects of these errors on the satellite orbit. In general, if β denotes any orbital parameter and x any injection parameter, we can apply a Taylor series expansion and write

$$\Delta\beta = \sum_{j=1}^6 \frac{\partial\beta}{\partial x_j} \Delta x_j + \text{higher-order terms,} \quad (17.4-1)$$

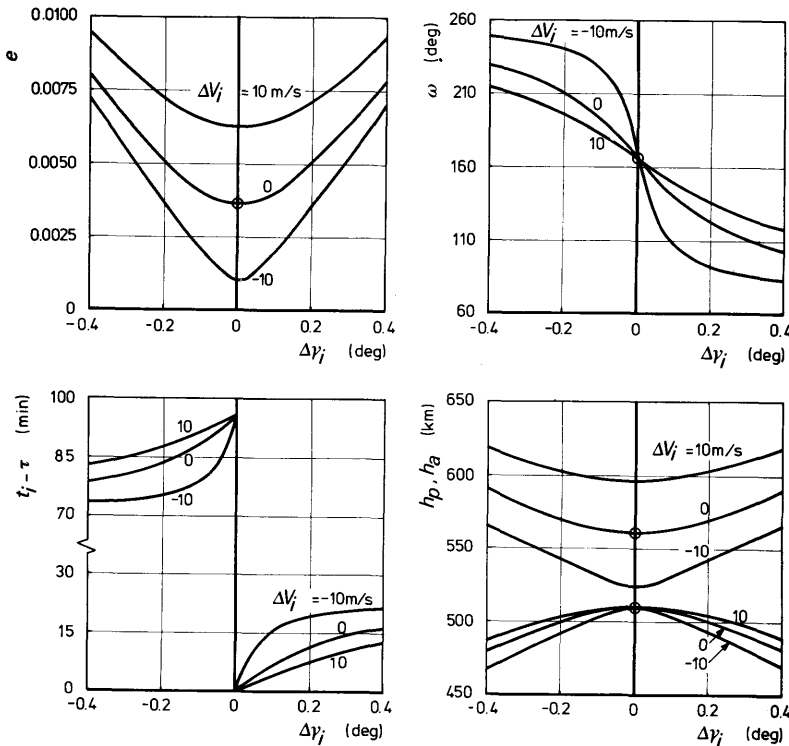


Fig. 17.9 Effects of injection errors on the orbit of ANS.

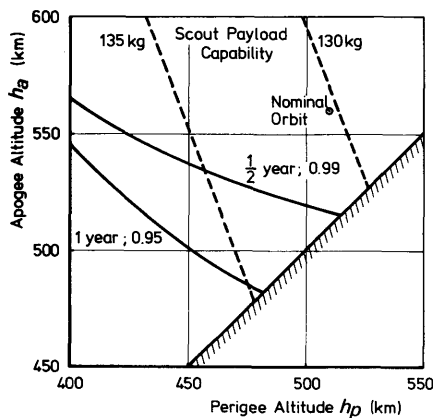


Fig. 17.10 Selection of nominal perigee and apogee altitude of ANS (Ref. [17]).

where Δ denotes a deviation of a parameter from its nominal value and the partial derivatives have to be evaluated for the nominal injection conditions. We now limit ourselves to small injection errors and assume that it is admissible to neglect the higher-order terms. It can be shown that this assumption is not valid if e becomes very small. Thus, for near-circular orbits the following analysis cannot be applied. Geyling [18] and Jenssen [19] present an alternative approach to handle these near-circular orbits.

The partial derivatives in Eq. (17.4-1) can be obtained by differentiating the relevant equations given in Section 16.6.2 and 16.6.3. For example, from Eq. (16.6-22), we obtain

$$2e \frac{\partial e}{\partial \gamma_i} = 2 \frac{r_i V_i^2}{\mu} \left(2 - \frac{r_i V_i^2}{\mu} \right) \sin \gamma_i \cos \gamma_i, \quad (17.4-2)$$

or, with Eq. (17.2-4),

$$\frac{\partial e}{\partial \gamma_i} = \frac{k_i(2 - k_i)}{2e} \sin 2\gamma_i. \quad (17.4-3)$$

Expressions for the other partial derivatives are derived by Fitzpatrick [20].

If we assume the injection to take place *at nominal perigee*, as is frequently the case, we have

$$\gamma_i = 0, \quad k_i > 1, \quad e = k_i - 1. \quad (17.4-4)$$

In this case, Eq. (17.4-3) reduces to

$$\frac{\partial e}{\partial \gamma_i} = 0. \quad (17.4-5)$$

The other partial derivatives for injection at nominal perigee can be obtained in an analogous way. Finally, this yields:

$$\begin{aligned} \frac{\partial a}{\partial r_i} &= \frac{2}{2 - k_i} \frac{a}{r_i}, & \frac{\partial a}{\partial V_i} &= \frac{2k_i}{2 - k_i} \frac{a}{V_i}, \\ \frac{\partial e}{\partial r_i} &= \frac{k_i}{r_i}, & \frac{\partial e}{\partial V_i} &= 2 \frac{k_i}{V_i}, \\ \frac{\partial i}{\partial \delta_i} &= \frac{\sin \delta_i \sin \psi_i}{\sin i}, & \frac{\partial i}{\partial \psi_i} &= -\frac{\cos \delta_i \cos \psi_i}{\sin i}, \\ \frac{\partial \omega}{\partial \delta_i} &= \frac{\cos \psi_i}{\sin^2 i}, & \frac{\partial \omega}{\partial \gamma_i} &= -\frac{k_i}{k_i - 1}, & \frac{\partial \omega}{\partial \psi_i} &= \frac{\sin 2\delta_i \sin \psi_i}{2 \sin^2 i}, \\ \frac{\partial \Omega}{\partial \delta_i} &= -\frac{\cos \delta_i \sin 2\psi_i}{2 \sin^2 i}, & \frac{\partial \Omega}{\partial \alpha_i} &= 1, & \frac{\partial \Omega}{\partial \psi_i} &= -\frac{\sin \delta_i}{\sin^2 i}, \\ \frac{\partial(t_i - \tau)}{\partial \gamma_i} &= \frac{\sqrt{k_i(2 - k_i)^3}}{2\pi(k_i - 1)} T, \end{aligned} \quad (17.4-6)$$

$$\frac{\partial r_p}{\partial r_i} = 1,$$

$$\frac{\partial r_a}{\partial r_i} = \frac{4 - k_i}{2 - k_i} \frac{r_a}{r_i}, \quad \frac{\partial r_a}{\partial V_i} = \frac{4}{2 - k_i} \frac{r_a}{V_i},$$

$$\frac{\partial T}{\partial r_i} = \frac{3}{2 - k_i} \frac{T}{r_i}, \quad \frac{\partial T}{\partial V_i} = \frac{3 k_i}{2 - k_i} \frac{T}{V_i},$$

where T is the orbital period, and

$$\sin i = \sqrt{1 - \cos^2 \delta_i \sin^2 \psi_i}.$$

The remaining 36 partial derivatives all take the value zero. Of course, the orbital parameters on the right-hand side of the expressions for the partial derivatives denote the parameters of the nominal orbit.

From Eqs. (17.4-5), a number of important conclusions can be drawn for an injection at nominal perigee:

1. The relative deviations in a and r_a due to percentage errors in r_i and V_i (i.e. $\frac{\partial a/a}{\partial r_i/r_i}$, etc.) strongly increase with increasing values of k_i . For highly-eccentric orbits ($k_i \uparrow 2$), large deviations in a and r_a may be expected.
2. The position of the perigee is only affected by errors in γ_i , δ_i and ψ_i .
3. The time difference $t_i - \tau$ is only affected by errors in γ_i .
4. The perigee distance is only a function of the injection distance.

With the theory presented in this chapter, the orbital elements at injection can be computed from the injection conditions. For a first-order analysis, we may consider these elements as characterizing the (Keplerian) orbit in which the satellite will encircle the Earth. In practice, however, the satellite will be subjected to various types of perturbing forces and its orbit will deviate from this Keplerian one. The next chapter will be devoted to the theory of perturbed satellite orbits.

References

- 1 Hohmann, W. (1925), *Die Erreichbarkeit der Himmelskörper*, Oldenbourg, Berlin, p. 63–75, Also: NASA TT F-44, Washington, 1960.
- 2 Ehricke, K. A. (1962), *Space Flight, Vol. 2: Dynamics*, Van Nostrand, Princeton, p. 90–116, 289–433.
- 3 White, J. F. (ed.) (1963), *Flight Performance Handbook for Powered Flight Operations*, Wiley, New York, p. 3–6 to 3–28.
- 4 Miner, W. E. and Silber, R. (1963), A variational launch window study, *AIAA J.*, **1**, 1125–1129.
- 5 Cornelisse, J. W. and Wakker, K. F. (1972), *Geosynchronous Space Tug Missions*, Report VTH-171, Dept. Aerospace Eng., Delft University of Technology, Delft.

- 6 El'yasberg, P. E. (1967), *Introduction to the Theory of Flight of Artificial Earth Satellites*, NASA TT F-391, Washington, p. 143–145.
- 7 Van de Graaff, R. C. (1977), *A Semi-Analytical Method for Computing Third-Body Effects on Earth's and Lunar Satellite Orbits*, Report LR 231, Dept. Aerospace Eng., Delft University of Technology, Delft.
- 8 Gobetz, F. W. and Doll, J. R. (1969), A survey of impulsive trajectories, *AIAA J.*, **7**, 801–834.
- 9 McGolrick, J. E. (1973), *Launch Vehicle Estimating Factors for Advance Mission Planning*, NHB 7100.5B, NASA, Washington.
- 10 Shramo, D. J. (1974), *Centaur—A Major Element of the Current Space Transportation System*, IAF Paper 74-075, Amsterdam.
- 11 Anon. (1976), *Scout User's Manual, Vol. 5: Performance and Flight Planning*, Vought Corp., Dallas.
- 12 Bonnett, E. W. (1971), *Delta Spacecraft Design Restraints*, DAC-61687, revision October 1971, McDonnell Douglas, Huntington Beach.
- 13 Anon. (1975), *Space Shuttle*, NASA, Houston (paper issued at 26th IAF Congress in Lisbon, 1975).
- 14 Anon. (1976), *Space Shuttle System Payload Accommodations*, JSC 07700, Vol. 14, Rev. D, Change 15, NASA.
- 15 Rosenbaum, R. (1970), *The Reduction of Launch Vehicle Injection Errors by Trajectory Shaping*, AIAA Paper 70-1078, New York.
- 16 Wakker, K. F. (1977), *Orbit Prediction for the Astronomical Netherlands Satellite*, paper presented at the B.I.S. conference on Computer Techniques for Satellite Control and Data Processing, Slough.
- 17 de Leeuw, W. H. and Pouw, A. (1974), *Mission Analysis of the Astronomical Netherlands Satellite*, IAF Paper 74-121, Amsterdam.
- 18 Geyling, F. T. and Westerman, H. R. (1971), *Introduction to Orbital Mechanics*, Addison-Wesley, Reading, p. 98–104.
- 19 Jensen, J., Townsend, G., Kork, J. and Kraft, D. (1962), *Design Guide to Orbital Flight*, McGraw-Hill, New York, p. 733–744.
- 20 Fitzpatrick, P. M. (1970), *Principles of Celestial Mechanics*, Academic Press, New York, p. 129–132.

18 Perturbed Satellite Orbits

In Chapter 16 we discussed the motion of a body P_i relative to a non-rotating reference frame with its origin at the center of mass of a body P_k . We assumed that both bodies could be regarded as point masses and that the only force acting upon P_i was due to the mutual gravitational attraction. We found that the trajectory of P_i was a conic section, a so-called *Keplerian orbit*.

In reality, where P_i represents a planet moving around the Sun, or a satellite orbiting the Earth, there will be other forces acting upon P_i . These forces, however, are relatively small as compared to the main gravitational force, and the orbits of planets and satellites can be approximated very well by conic sections. The actual trajectories of these bodies are therefore called *perturbed Keplerian orbits*. For this perturbed Keplerian motion, no closed-form analytical solution can be obtained. The approximate solution of the equations of motion of P_i under the influence of a main gravitational force and perturbing forces is one of the most developed, and most interesting, branches of celestial mechanics.

In this chapter, we will discuss only some elementary aspects of perturbed orbits; furthermore, we will limit ourselves to orbits of artificial Earth satellites.

The most important perturbing forces acting on artificial Earth satellites are due to: asphericity of the Earth, aerodynamic effects, lunar and solar attraction, solar radiation and electromagnetic effects. Baker [1] gives an extensive survey of the origin, direction and magnitude of these perturbing forces. We will discuss the nature of these forces only very superficially.

Asphericity of the Earth. Generally, this asphericity yields a very important perturbing force for satellite orbits. As the Earth's mass distribution is not perfectly spherical symmetric, gravitational force components normal to the radius vector of the satellite will be present. Because of these components, the actual orbit will deviate from a Keplerian orbit. It will be clear that the effects of the asphericity decrease with increasing distance from the Earth. For, at distances from the Earth which are large with respect to the dimensions of the Earth, we can approximate the Earth's gravitational field by that of a point mass. We will discuss these perturbing forces in more detail in Section 18.6.

Aerodynamic effects. The motion of a satellite through the upper regions of the atmosphere generates aerodynamic forces. The major force will be a

drag force, acting opposite to the satellite's velocity vector with respect to the atmosphere, but lift and side forces will occur too. The deceleration of the satellite due to airdrag can be expressed by the well-known aerodynamic relationship

$$a_D = C_D \frac{1}{2} \rho V^2 \frac{S}{M},$$

where ρ is the air density, V is the satellite's velocity relative to the atmosphere, M is the satellite's mass, S is a reference area of the satellite and C_D is a drag coefficient based on that area. For a given satellite and orbit, M and V are known, and S may be chosen. The difficulties in the analysis of the aerodynamic deceleration arise in the determination of C_D and ρ .

At satellite altitudes, the flow is of the *free-molecular type*. Then, the drag is determined by the mechanism of molecular reflection at the surfaces of the satellite. This is a very complicated process, which is as yet only partly understood. Between altitudes of 150 km and 500 km, the drag coefficient, based on projected area normal to the direction of motion, is usually about $C_D = 2.2\text{--}2.5$. At higher altitudes it may increase to $C_D = 3\text{--}5$. The atmospheric density not only varies with altitude, but also with time. It turns out that at a given altitude the density is a function of local solar time, season, disturbances of the geomagnetic field and the solar activity (Section 2.6.2). The exact relation between the density and these variables is not completely understood.

Because of the uncertainties in the drag coefficient and the air density, we can only roughly estimate the magnitude of the aerodynamic forces. The effects of the aerodynamic forces strongly diminish as the orbital altitude increases. In fact, atmospheric drag is the most important perturbing force below about 200 km altitude, and can, in most cases, completely be neglected at altitudes above 1000 km. The aerodynamic drag is the cause of the decay of Earth satellites. They dissipate their orbital energy and their orbital altitudes decrease, through which they enter denser parts of the atmosphere, where the drag becomes larger and larger. Ultimately, they burn in the low Earth's atmosphere. Sometimes, parts of satellites survive the re-entry and impact on the Earth's surface.

Lunar and solar attraction. We already discussed the effects of these attractions on the motion of an Earth satellite in Section 15.3.1. These effects increase with increasing distance from the Earth, and lunar and solar attractions become the major sources of perturbations above geostationary orbital altitudes.

Radiation pressure. A satellite about the Earth is also subjected to direct solar radiation, solar radiation reflected by the Earth (*albedo*), and radiation emitted by the Earth itself. In quantum mechanics, light is regarded as a flow of photons, which, among others, possess a momentum. If these

photons hit the satellite's surface, and are partially reflected, they impart a momentum to the satellite, which results in the so-called *radiation pressure*. As the radiation pressure in the vicinity of the Earth is extremely small, it will only have a substantial effect on the orbits of balloon-type satellites, i.e. satellites with a small mass/area ratio. In those cases, the effects of radiation pressure may be very significant, and should certainly be taken into account.

Electromagnetic effects. As the atmosphere at satellite altitudes is partly ionized, the possibility exists that a satellite acquires an electrical potential. As there is also a magnetic field, electromagnetic forces will be generated. However, generally, these effects are negligible.

In the following, we will assume the perturbing forces to be known, and we will only study some methods to compute their effects on the orbit of a satellite.

18.1 Special and general perturbations

If the motion of a satellite is described relative to a non-rotating geocentric equatorial reference frame (Fig. 2.2) and perturbing forces are taken into account, the equation of motion can be written in the form

$$\frac{d^2\mathbf{r}}{dt^2} + \frac{\mu}{r^3} \mathbf{r} = -\nabla R + \mathbf{a}, \quad (18.1-1)$$

where R , the *perturbing or disturbing potential*, includes all perturbing forces which can be expressed by a potential function, and \mathbf{a} stands for all perturbing forces which cannot be written as the gradient of a scalar function. We already met an example of a perturbing potential, describing the effects of the gravitational attraction by other bodies, in Section 15.3.

In general, Eq. (18.1-1) cannot be solved in a closed form and we have to resort to numerical techniques or to approximate analytical solutions. In the first case, we speak of *special perturbations*; in the second case, we deal with *general perturbations*.

Special perturbations methods generate just one special trajectory for a definite satellite, given its unique initial conditions. A determination of the orbit is made by means of a numerical step-by-step process. The various methods of special perturbations are usually classified according to the formulation of the equations to be integrated. The three classical methods are known as *Cowell's method*, *Encke's method* and the *method of variation of orbital elements*. These methods will be treated in subsequent sections. An important topic in special perturbations is the choice of the most suitable numerical integration technique. This highly specialized subject is beyond the scope of this book. Allione [2] and Merson [3] present surveys of modern advanced methods.

General perturbations cover the analytical methods in which the perturbing accelerations are expanded into series and integrated termwise. In

practice, only a limited number of terms of the series is taken into account. We obtain the solution of the differential equations of motion in the form of analytical expressions, describing the change of the orbit as a function of time for a particular perturbing force. These methods thus yield solutions that are generally applicable to all satellites for all initial conditions. The most important classical general perturbations method is *the method of variation of orbital elements*, which was already mentioned in connection with special perturbations. For the analytical integration, many processes are known, for example: the *method of successive approximations*, *Taylor series expansions*, *multivariable asymptotic expansions* and *averaging*. A survey of these techniques is given by Dallas [4] and Lorell [5]. The main difficulty of all general perturbations methods always was the tremendous amount of analytical labor involved, especially if higher-order approximations are required. Nowadays, most of the analysis associated with the development of higher-order theories can be performed by a computer [6].

The reader should be aware that, apart from the special and general perturbations methods mentioned, there exist numerous other specialized, and in most cases very complicated, methods. Geyling and Westerman [7] give an introduction to the application of the classical methods to perturbed satellite motion. Novel approaches to the perturbation problem are presented by Stiefel and Scheifele [8].

Comparing the special and general perturbations methods, one can make some remarks about their respective advantages and disadvantages.

Obviously, the methods of special perturbations are directly applicable to any orbit and to any perturbing force. As these are purely numerical methods, we have the problem of accumulated error and these methods are not well suited to long-term orbit predictions. Moreover, these methods require the computation of the coordinates and velocity components of the satellite at all intermediate epochs prior to the epoch of interest, leading to long integration times.

An advantage of general perturbations methods is that once the analytical expressions, describing the effects of the perturbing force, are available, the computation of a perturbed orbit for various initial conditions is much faster. Their main advantage, however, is that general perturbations methods, and in particular the method of variation of orbital elements, clearly reveal the *source* of perturbations from orbital data. Major achievements of the methods of general perturbations were the discovery of the planet Neptune in 1846, through the observed orbital perturbations of Uranus, and, more recently, the demonstration of the *Earth's pear-shape* in 1959, through the analysis of the orbital data of the Vanguard 1 satellite [9].

18.2 Cowell's method

The simplest method for the computation of perturbed satellite orbits is Cowell's method [10]. Though, originally, this method only refers to a

particular integration scheme in rectangular coordinates, the name is now used for all direct numerical integrations of the equations of motion. These equations are written in the form

$$\frac{d^2\mathbf{r}}{dt^2} = \mathbf{a}_t, \quad (18.2-1)$$

where \mathbf{a}_t represents the total acceleration,

$$\mathbf{a}_t = -\frac{\mu}{r^3} \mathbf{r} - \nabla R + \mathbf{a}. \quad (18.2-2)$$

This method thus makes no use of the fact that the actual trajectory can be approximated by a conic section, and we integrate numerically the equations of motion in their elementary form. The simplicity of the method makes it an extremely useful, flexible and attractive method for computer calculations. A disadvantage of the method is that, as the total acceleration can vary considerably over an orbital revolution, usually small integration steps are required to maintain accuracy. In addition, a large number of significant figures should be kept in the numerical integration process, in order not to lose the effects of the smaller accelerations.

18.3 Encke's method

Encke's method [11] makes use of a reference orbit, and only the deviations from that orbit are integrated numerically. For simplicity, we will assume that this reference orbit is a Keplerian one, but this restriction is by no means a necessity. The equation of motion of a satellite is written in the form

$$\frac{d^2\mathbf{r}}{dt^2} + \frac{\mu}{r^3} \mathbf{r} = -\nabla R + \mathbf{a}. \quad (18.3-1)$$

For the reference Keplerian orbit, we have

$$\frac{d^2\mathbf{p}}{dt^2} + \frac{\mu}{\rho^3} \mathbf{p} = 0, \quad (18.3-2)$$

where \mathbf{p} denotes the position vector of the satellite, if the satellite would follow the unperturbed reference orbit. We now assume that at some instant the following equalities hold:

$$t = t_o, \quad \mathbf{r} = \mathbf{p}, \quad \frac{d\mathbf{r}}{dt} = \frac{d\mathbf{p}}{dt}. \quad (18.3-3)$$

Because the reference orbit is a Keplerian one, we can solve Eq. (18.3-2) analytically to obtain position and velocity in the reference orbit at any time. For the deviation of the actual trajectory from the reference orbit at a time

t , we write

$$\Delta\mathbf{r} = \mathbf{r} - \mathbf{p}. \quad (18.3-4)$$

By differentiating Eq. (18.3-4) twice with respect to time, and subsequent substitution of Eq. (18.3-1) and Eq. (18.3-2), we obtain

$$\frac{d^2}{dt^2} \Delta\mathbf{r} = \mu \left(\frac{\mathbf{p}}{\rho^3} - \frac{\mathbf{r}}{r^3} \right) - \nabla R + \mathbf{a}. \quad (18.3-5)$$

Integration of this equation would lead to the deviations of position and velocity relative to their values in the reference orbit. The latter are computed analytically, and the actual position and velocity at a given instant t are simply obtained by adding \mathbf{p} and $\Delta\mathbf{r}$, and $\frac{d\mathbf{p}}{dt}$ and $\frac{d\Delta\mathbf{r}}{dt}$, respectively.

A practical numerical difficulty arises from the form of the first term on the right-hand side of Eq. (18.3-5). This term is the difference of two nearly equal, and small quantities, which is always undesirable in numerical computations. Therefore, Eq. (18.3-5) is mostly written in another form. First, we transform Eq. (18.3-5) into

$$\frac{d^2}{dt^2} \Delta\mathbf{r} = \frac{\mu}{\rho^3} \left[\mathbf{p} - \mathbf{r} + \mathbf{r} \left(1 - \frac{\rho^3}{r^3} \right) \right] - \nabla R + \mathbf{a}. \quad (18.3-6)$$

We then write

$$\frac{r^2}{\rho^2} = \frac{(\mathbf{p} + \Delta\mathbf{r}) \cdot (\mathbf{p} + \Delta\mathbf{r})}{\rho^2}. \quad (18.3-7)$$

Defining a quantity q as

$$q = \frac{\Delta\mathbf{r} \cdot (\mathbf{p} + \frac{1}{2}\Delta\mathbf{r})}{\rho^2}, \quad (18.3-8)$$

Eq. (18.3-7) can also be written as

$$\frac{r^2}{\rho^2} = 1 + 2q. \quad (18.3-9)$$

Using this relation, we find

$$1 - \frac{\rho^3}{r^3} = 1 - (1 + 2q)^{-3/2} = qf(q). \quad (18.3-10)$$

where f is a function of q . The form $qf(q)$ can be expanded into a binomial series, as was first done by Encke,

$$qf(q) = 3q \left(1 - \frac{5}{2}q + \frac{5.7}{2.3}q^2 - \frac{5.7.9}{2.3.4}q^3 + \dots \right), \quad (18.3-11)$$

but it can also be written as

$$qf(q) = \frac{2q}{1+2q} \left[1 + \frac{1}{1+2q+\sqrt{1+2q}} \right]. \quad (18.3-12)$$

As, according to Eq. (18.3-9), q is very small, we note that the quantity f is about 3. By substituting Eq. (18.3-4) and Eq. (18.3-10) into Eq. (18.3-6), we finally obtain

$$\frac{d^2}{dt^2} \Delta r = \frac{\mu}{\rho^3} [(\rho + \Delta r) qf(q) - \Delta r] - \nabla R + a. \quad (18.3-13)$$

This form of the equation of relative motion is mostly used when Encke's method is applied.

As in Encke's method only the perturbing accelerations are integrated numerically to obtain deviations from a reference orbit, usually the integration step can be chosen larger than in Cowell's method. However, at each integration step, Encke's method involves more computing time. Nevertheless, for small but strongly varying perturbing forces, in most cases Encke's method yields a more efficient computing process than the method of Cowell.

If the perturbations accumulate, eventually Δr can become large and the Encke formulation loses its advantage over the simpler Cowell formulation. Then, the reference orbit should be *rectified*; i.e., a new reference orbit must be selected, such that at the instant of rectification, again $\Delta r = 0$ and $\frac{d}{dt} \Delta r = 0$. As a very rough criterion for rectification, Herrick [12] gives:

$q = 0.01$. This need for rectification is a drawback of Encke's method.

An extended variant of Encke's method, especially designed for computing spacecraft trajectories, is given by Stumpff and Weiss [13].

18.4 Method of variation of orbital elements

The theory of the method of variation of orbital elements [14], also called the *method of variation of parameters* or the *method of variation of constants*, was published by Lagrange in 1808. Nowadays, it is one of the most important methods for the computation of perturbed satellite orbits.

The basic concept in this theory is the introduction of a so-called *osculating orbit*. In Section 16.6, we found that the six orbital elements $a, e, i, \omega, \Omega, \tau$ are constant for Keplerian orbits, and are uniquely determined by the position, r , and the velocity, V , of the satellite at some instant. We now generalize these results and define an imaginary conic section, such that at any time the same transformation relations hold between position and velocity in the perturbed orbit and the orbital elements of this imaginary conic section. Because the perturbed orbit is not a Keplerian one, the orbital elements obtained in this way are no longer constant, but will vary with

time. The imaginary conic section is called the *osculating orbit*; its elements are the *osculating orbital elements*. Note that the osculating orbit for time t is tangent to the actual trajectory at time t , and that the velocity at the point of osculation is the same for both the actual trajectory and the osculating orbit. To visualize such an osculating orbit, one may think of the satellite as passing continuously from one Keplerian orbit to another. At any time, this Keplerian orbit is the orbit the satellite were to follow, if all perturbations disappeared instantaneously.

The concept of an osculating Keplerian orbit is extremely useful. First, any change in the osculating elements can be ascribed directly to perturbing forces, in contrast with, for example, rectangular coordinates of the satellite which also vary in a Keplerian orbit due to the satellite's orbital motion. Secondly, the osculating elements possess a clear geometric significance and the effects of perturbing forces on the orbit can be understood physically. In our discussions, we will assume, for the sake of simplicity, that the osculating orbit is always elliptic. Moreover, we will first restrict ourselves to perturbing forces which can be derived from a disturbing potential. In Section 18.4.3, we will generalize the results to arbitrary perturbing forces.

18.4.1 Lagrange's planetary equations

In the perturbations theories of celestial mechanics, it is customary to use a *disturbing function* \tilde{R} instead of the disturbing potential R . Their relation is given by

$$\tilde{R} = -R. \quad (18.4-1)$$

Using this disturbing function, the equation of motion of the satellite can, in the case that all perturbing forces are expressible through a potential, be written in the form

$$\frac{d^2\mathbf{r}}{dt^2} + \frac{\mu}{r^3} \mathbf{r} = \nabla \tilde{R}. \quad (18.4-2)$$

From Section 16.6, we know that if there were no perturbing forces, i.e. if $\tilde{R} = 0$, the solution of Eq. (18.4-2) could be written as

$$\mathbf{r} = \mathbf{r}(\alpha_i, t), \quad i = 1, 2, \dots, 6, \quad (18.4-3)$$

where α_1 through α_6 stand for the six orbital elements. In that case, the orbit is a Keplerian one and the orbital elements are constant, so

$$\frac{d\mathbf{r}}{dt} = \frac{\partial \mathbf{r}}{\partial t}, \quad (18.4-4)$$

and the equation of motion which is satisfied by Eq. (18.4-3) can also be written as

$$\frac{\partial^2 \mathbf{r}}{\partial t^2} + \frac{\mu}{r^3} \mathbf{r} = 0. \quad (18.4-5)$$

We now use the property of the osculating orbit that the position and velocity at any point in the perturbed orbit equal the position and velocity in the instantaneous osculating orbit. Applying Eq. (18.4-3) to the true orbit, we obtain after differentiation with respect to time

$$\frac{d\mathbf{r}}{dt} = \frac{\partial \mathbf{r}}{\partial t} + \sum_i \frac{\partial \mathbf{r}}{\partial \alpha_i} \frac{d\alpha_i}{dt}. \quad (18.4-6)$$

In view of the properties of the osculating orbit, we must require

$$\sum_i \frac{\partial \mathbf{r}}{\partial \alpha_i} \frac{d\alpha_i}{dt} = 0. \quad (18.4-7)$$

Differentiating Eq. (18.4-6) again with respect to time, we obtain

$$\frac{d^2\mathbf{r}}{dt^2} = \frac{\partial^2\mathbf{r}}{\partial t^2} + \sum_i \frac{\partial^2\mathbf{r}}{\partial \alpha_i \partial t} \frac{d\alpha_i}{dt}. \quad (18.4-8)$$

We note that, in contrast to the velocities, the accelerations in the actual orbit and the osculating orbit are not identical. By substituting Eqs. (18.4-8) and (18.4-5) into Eq. (18.4-2), we obtain

$$\sum_i \frac{\partial^2\mathbf{r}}{\partial \alpha_i \partial t} \frac{d\alpha_i}{dt} = \nabla \tilde{R}. \quad (18.4-9)$$

The Eqs. (18.4-7) and (18.4-9) represent six scalar first-order differential equations in the time-derivatives of the osculating elements. It would be more convenient, however, to have differential equations written *explicitly* for the rates of change of the osculating elements. We therefore form the scalar product of Eq. (18.4-7) and Eq. (18.4-9) by $\frac{\partial^2\mathbf{r}}{\partial \alpha_j \partial t}$ and $\frac{\partial \mathbf{r}}{\partial \alpha_j}$, respectively, where α_j is any osculating element, and find

$$\sum_i \frac{\partial \mathbf{r}}{\partial \alpha_i} \cdot \frac{\partial^2\mathbf{r}}{\partial \alpha_j \partial t} \frac{d\alpha_i}{dt} = 0, \quad (18.4-10a)$$

$$\sum_i \frac{\partial \mathbf{r}}{\partial \alpha_i} \cdot \frac{\partial^2\mathbf{r}}{\partial \alpha_i \partial t} \frac{d\alpha_i}{dt} = \nabla \tilde{R} \cdot \frac{\partial \mathbf{r}}{\partial \alpha_j}. \quad (18.4-10b)$$

By subtracting Eq. (18.4-10a) from Eq. (18.4-10b), we obtain

$$\sum_i \left[\frac{\partial \mathbf{r}}{\partial \alpha_j} \cdot \frac{\partial^2\mathbf{r}}{\partial \alpha_i \partial t} - \frac{\partial^2\mathbf{r}}{\partial \alpha_i \partial t} \cdot \frac{\partial \mathbf{r}}{\partial \alpha_i} \right] \frac{d\alpha_i}{dt} = \nabla \tilde{R} \cdot \frac{\partial \mathbf{r}}{\partial \alpha_j}. \quad (18.4-11)$$

The term within brackets is written for brevity as $[\alpha_j, \alpha_i]$. It is called the *Lagrange bracket* with reference to α_j and α_i . For the right-hand side of Eq. (18.4-11) we write

$$\nabla \tilde{R} \cdot \frac{\partial \mathbf{r}}{\partial \alpha_j} = \frac{\partial \tilde{R}}{\partial x} \frac{\partial x}{\partial \alpha_j} + \frac{\partial \tilde{R}}{\partial y} \frac{\partial y}{\partial \alpha_j} + \frac{\partial \tilde{R}}{\partial z} \frac{\partial z}{\partial \alpha_j} \equiv \frac{\partial \tilde{R}}{\partial \alpha_j}. \quad (18.4-12)$$

This equation needs perhaps some clarification. For, we have $\tilde{R} = \tilde{R}(x, y, z, t)$ and we formally may write

$$\frac{\partial \tilde{R}}{\partial \alpha_j} = \nabla \tilde{R} \cdot \frac{\partial \mathbf{r}}{\partial \alpha_j} + \frac{\partial \tilde{R}}{\partial t} \frac{\partial t}{\partial \alpha_j}.$$

But we have assumed that \mathbf{r} is expressed as a function of six osculating elements, α_i , and time t (Eq. 18.4-3). Thus, when taking the partial derivatives of x , y and z with respect to an orbital element, the other elements and t should be considered as constants. Also, irrespective as to whether the disturbing function is written in the form $\tilde{R} = \tilde{R}(x, y, z, t)$ or $\tilde{R} = \tilde{R}(\alpha_j, t)$, the partial derivative with respect to an orbital element should be taken at constant t .

Now, Eq. (18.4-11) can be written as

$$\sum_i [\alpha_j, \alpha_i] \frac{d\alpha_i}{dt} = \frac{\partial \tilde{R}}{\partial \alpha_j}, \quad (18.4-13)$$

which represents a set of six equations, each containing 6 Lagrange brackets. From the definition of the Lagrange brackets, we directly obtain their properties:

$$[\alpha_j, \alpha_i] = -[\alpha_i, \alpha_j], \quad [\alpha_j, \alpha_j] = 0.$$

In view of this, we conclude that only 15 brackets need to be determined. The evaluation of these remaining Lagrange brackets is a tedious, but straightforward process. For the efficient computation of these brackets, we will use a third property of the brackets, namely that the partial derivative of a bracket with respect to time is zero.

To prove this, we differentiate a bracket with respect to time:

$$\frac{\partial}{\partial t} [\alpha_j, \alpha_i] = \frac{\partial \mathbf{r}}{\partial \alpha_j} \cdot \frac{\partial^3 \mathbf{r}}{\partial \alpha_i \partial t^2} - \frac{\partial \mathbf{r}}{\partial \alpha_i} \cdot \frac{\partial^3 \mathbf{r}}{\partial \alpha_j \partial t^2}. \quad (18.4-14)$$

Using the Newtonian two-body gravitational potential, $U = -\frac{\mu}{r}$, Eq. (18.4-5) can also be written as

$$\frac{\partial^2 \mathbf{r}}{\partial t^2} = -\nabla U. \quad (18.4-15)$$

Substitution of this equation into Eq. (18.4-14) leads to

$$\frac{\partial}{\partial t} [\alpha_j, \alpha_i] = \frac{\partial}{\partial \alpha_j} \left\{ \frac{\partial \mathbf{r}}{\partial \alpha_i} \cdot \nabla U \right\} - \frac{\partial}{\partial \alpha_i} \left\{ \frac{\partial \mathbf{r}}{\partial \alpha_j} \cdot \nabla U \right\},$$

or, as the potential U is only a function of the position coordinates,

$$\frac{\partial}{\partial t} [\alpha_j, \alpha_i] = \frac{\partial}{\partial \alpha_j} \left\{ \frac{\partial U}{\partial \alpha_i} \right\} - \frac{\partial}{\partial \alpha_i} \left\{ \frac{\partial U}{\partial \alpha_j} \right\} = 0. \quad (18.4-16)$$

So, the Lagrange brackets do not contain the time explicitly, and we may evaluate them at any point of the instantaneous osculating orbit. The perigee of the osculating orbit proves to be the best choice.

As an example, we will derive the expression for the Lagrange bracket $[a, \tau]$. For simplicity, we first split this bracket into its three parts $[a, \tau]_x$, $[a, \tau]_y$ and $[a, \tau]_z$, where

$$[a, \tau]_x = \frac{\partial x}{\partial a} \frac{\partial^2 x}{\partial \tau \partial t} - \frac{\partial^2 x}{\partial a \partial t} \frac{\partial x}{\partial \tau}, \quad \text{etc.} \quad (18.4-17)$$

The various partial derivatives can be obtained from the equations given in Section 16.6.1. It turns out to be most convenient to take the eccentric anomaly, E , as the angular variable instead of the true anomaly, θ . As can be shown easily, the Eqs. (16.6-6) and (16.6-8) then can be written as

$$x = a \{l_1(\cos E - e) + l_2 \sqrt{1-e^2} \sin E\}, \quad (18.4-18)$$

$$\frac{\partial x}{\partial t} = \sqrt{\frac{\mu}{a}} \left\{ -l_1 \frac{\sin E}{1-e \cos E} + l_2 \sqrt{1-e^2} \frac{\cos E}{1-e \cos E} \right\}, \quad (18.4-19)$$

and similar expressions can be derived for y , z , $\frac{\partial y}{\partial t}$ and $\frac{\partial z}{\partial t}$. The quantities l_1 and l_2 are only a function of the osculating elements i , ω and Ω , and are given by Eqs. (16.6-5). We further need Kepler's equation:

$$E - e \sin E = \sqrt{\frac{\mu}{a^3}} (t - \tau). \quad (18.4-20)$$

From Eq. (18.4-18), we obtain

$$\begin{aligned} \frac{\partial x}{\partial a} &= l_1(\cos E - e) - l_1 a \sin E \frac{\partial E}{\partial a} + l_2 \sqrt{1-e^2} \sin E + \\ &\quad + l_2 a \sqrt{1-e^2} \cos E \frac{\partial E}{\partial a}. \end{aligned} \quad (18.4-21)$$

From Eq. (18.4-20), we obtain

$$\frac{\partial E}{\partial a} = -\frac{3}{2} \sqrt{\frac{\mu}{a^5}} \frac{t-\tau}{1-e \cos E}. \quad (18.4-22)$$

Substitution of Eq. (18.4-22) into Eq. (18.4-21) and subsequent evaluation for $E = 0$, $t = \tau$, yields

$$\frac{\partial x}{\partial a} = l_1(1-e). \quad (18.4-23)$$

In the same way, we obtain

$$\frac{\partial x}{\partial \tau} = -l_2 \sqrt{\frac{\mu(1+e)}{a(1-e)}}. \quad (18.4-24)$$

Differentiation of Eq. (18.4-19) with respect to a , subsequent substitution of Eq. (18.4-22) and evaluation for $E = 0$, $t = \tau$, gives

$$\frac{\partial^2 x}{\partial a \partial t} = -\frac{1}{2} l_2 \sqrt{\frac{\mu(1+e)}{a^3(1-e)}}. \quad (18.4-25)$$

Following the same approach, we also find

$$\frac{\partial^2 x}{\partial \tau \partial t} = l_1 \frac{\mu}{a^2} \frac{1}{(1-e)^2} + l_2 \frac{\mu}{a^2} \frac{\sqrt{1-e^2}}{(1-e)^3}. \quad (18.4-26)$$

Substitution of Eqs. (18.4-23) through (18.4-26) into Eq. (18.4-17) finally yields

$$[a, \tau]_x = l_1^2 \frac{\mu}{a^2} \frac{1}{(1-e)} + l_1 l_2 \frac{\mu}{a^2} \sqrt{\frac{1+e}{(1-e)^3}} - \frac{1}{2} l_2^2 \frac{\mu}{a^2} \frac{(1+e)}{(1-e)}. \quad (18.4-23)$$

Similar expressions can be obtained for $[a, \tau]_y$ and $[a, \tau]_z$. Adding these relations, we obtain

$$\begin{aligned} [a, \tau] = & \frac{\mu}{a^2} \frac{1}{(1-e)} (l_1^2 + m_1^2 + n_1^2) + \frac{\mu}{a^2} \sqrt{\frac{1+e}{(1-e)^3}} (l_1 l_2 + m_1 m_2 + n_1 n_2) \\ & - \frac{1}{2} \frac{\mu}{a^2} \frac{(1+e)}{(1-e)} (l_2^2 + m_2^2 + n_2^2). \end{aligned} \quad (18.4-27)$$

From the Eqs. (16.6-5), we can easily verify that the following relations hold:

$$\begin{aligned} l_1^2 + m_1^2 + n_1^2 &= l_2^2 + m_2^2 + n_2^2 = 1, \\ l_1 l_2 + m_1 m_2 + n_1 n_2 &= 0. \end{aligned} \quad (18.4-28)$$

Using these relations, Eq. (18.4-27) simplifies to

$$[a, \tau] = \frac{\mu}{2a^2}. \quad (18.4-29)$$

In exactly the same way, we obtain for the other Lagrange brackets:

$$[a, \omega] = -\frac{1}{2} \sqrt{\frac{\mu}{a} (1-e^2)},$$

$$[a, \Omega] = -\frac{1}{2} \sqrt{\frac{\mu}{a} (1-e^2)} \cos i,$$

$$[e, \omega] = \sqrt{\frac{\mu a}{1-e^2}} e, \quad (18.4-29)$$

$$[e, \Omega] = \sqrt{\frac{\mu a}{1-e^2}} e \cos i,$$

$$[i, \Omega] = \sqrt{\mu a(1-e^2)} \sin i.$$

The nine remaining brackets are all zero. Inserting these expressions into Eqs. (18.4-13), and subsequent solution of the set of equations for the time derivatives of the osculating elements, yields:

$$\frac{da}{dt} = -2 \frac{a^2}{\mu} \frac{\partial \tilde{R}}{\partial \tau}, \quad (18.4-30a)$$

$$\frac{de}{dt} = -\frac{a(1-e^2)}{\mu e} \frac{\partial \tilde{R}}{\partial \tau} - \frac{1}{e} \sqrt{\frac{1-e^2}{\mu a}} \frac{\partial \tilde{R}}{\partial \omega}, \quad (18.4-30b)$$

$$\frac{di}{dt} = \frac{1}{\sqrt{\mu a(1-e^2)} \sin i} \left(\cos i \frac{\partial \tilde{R}}{\partial \omega} - \frac{\partial \tilde{R}}{\partial \Omega} \right), \quad (18.4-30c)$$

$$\frac{d\omega}{dt} = \sqrt{\frac{1-e^2}{\mu a}} \left(\frac{1}{e} \frac{\partial \tilde{R}}{\partial e} - \frac{\cot i}{1-e^2} \frac{\partial \tilde{R}}{\partial i} \right), \quad (18.4-30d)$$

$$\frac{d\Omega}{dt} = \frac{1}{\sqrt{\mu a(1-e^2)} \sin i} \frac{\partial \tilde{R}}{\partial i}, \quad (18.4-30e)$$

$$\frac{d\tau}{dt} = 2 \frac{a^2}{\mu} \frac{\partial \tilde{R}}{\partial a} + \frac{a(1-e^2)}{\mu e} \frac{\partial \tilde{R}}{\partial e}. \quad (18.4-30f)$$

These six simultaneous first-order differential equations, expressing the effects of a perturbing potential on the osculating orbital elements, are known as *Lagrange's planetary equations*.

In general, no exact analytical solution of these equations can be obtained, and we are committed to numerical methods, or to approximating analytical techniques. Approximate analytical solution is possible because the orbital elements are constant for a Keplerian orbit, and will only show a limited, usually rather smooth, variation for perturbed Keplerian orbits. In fact, this was the objective of transforming the original equations of motion into differential equations for the osculating elements. We will discuss such an approximate analytical technique in some detail in Section 18.5.

For special perturbations, a comparison of the methods of Lagrange and Cowell shows that, in general, Lagrange's method will allow for a larger integration step. But, as the equations are rather complicated, each integration step requires a longer computing time. It strongly depends on the type of perturbed orbit which method is preferable.

It should be mentioned, that in the mathematical derivation of the

planetary equations, we nowhere assumed the perturbing acceleration to be small relative to the central acceleration μ/r^2 . Consequently, these equations can be used whatever the magnitude of the ‘perturbing’ forces acting on the satellite may be. However, when the perturbing forces are large with respect to the central force, the osculating elements will vary over a wide range, precluding an approximate analytic solution. For numerical integrations, this method then also loses its advantage over the simpler Cowell formulation.

18.4.2 Modification of the sixth Lagrange equation

There exists a serious inconvenience in the formulation of the equation for $\frac{d\tau}{dt}$, Eq. (18.4-30f), as will be shown. In the evaluation of the partial

derivatives $\frac{\partial \tilde{R}}{\partial \alpha_i}$, we have to determine the quantities $\frac{\partial E}{\partial \alpha_i}$. These can be obtained from Kepler’s equation, Eq. (18.4-20), which shows E only to be a function of the elements a, e and τ . By taking the derivative of E with respect to e and τ , we obtain expressions where E only appears as the argument of trigonometric functions:

$$\frac{\partial E}{\partial e} = \frac{\sin E}{1 - e \cos E}, \quad \frac{\partial E}{\partial \tau} = -\sqrt{\frac{\mu}{a^3}} \frac{1}{1 - e \cos E}.$$

However, for the derivative of E with respect to a , we find

$$\frac{\partial E}{\partial a} = -\frac{3}{2} \sqrt{\frac{\mu}{a^5}} \frac{t - \tau}{1 - e \cos E} = -\frac{3}{2a} \frac{(E - e \sin E)}{(1 - e \cos E)}.$$

Because of the appearance of E outside trigonometric arguments, the evaluation of the expression for $\frac{\partial \tilde{R}}{\partial a}$ becomes rather tedious. When the planetary equations are used for general perturbations, the situation is even worse. Then integrals may result which do not have a closed-form analytical solution. From the Eqs. (18.4-30), we note that only the equation for $\frac{d\tau}{dt}$ contains the factor $\frac{\partial \tilde{R}}{\partial a}$. A classical artifice exists which circumvents the difficulties with this equation. We therefore recall our definition of the mean anomaly, M ,

$$M = n(t - \tau), \tag{18.4-31}$$

where the mean angular motion, n , is given by

$$n = \sqrt{\frac{\mu}{a^3}}, \tag{18.4-32}$$

indicating that n is only a function of a . We now consider $n(a)$ in Kepler's equation as another distinct variable and rewrite Eq. (18.4-30f) as

$$\frac{d\tau}{dt} = \frac{2a^2}{\mu} \left(\frac{\partial \tilde{R}}{\partial a} \right)_n + \frac{2a^2}{\mu} \frac{\partial \tilde{R}}{\partial n} \frac{\partial n}{\partial a} + \frac{a(1-e^2)}{\mu e} \frac{\partial \tilde{R}}{\partial e}, \quad (18.4-33)$$

where the notation $\left(\frac{\partial \tilde{R}}{\partial a} \right)_n$ signifies that the derivative has to be taken without considering the dependence of n on a , or stated in another way, at constant n or M . We may write

$$\begin{aligned}\frac{\partial \tilde{R}}{\partial \tau} &= \frac{\partial \tilde{R}}{\partial M} \frac{\partial M}{\partial \tau} = -n \frac{\partial \tilde{R}}{\partial M}, \\ \frac{\partial \tilde{R}}{\partial n} &= \frac{\partial \tilde{R}}{\partial M} \frac{\partial M}{\partial n} = (t-\tau) \frac{\partial \tilde{R}}{\partial \tau}.\end{aligned}$$

or,

$$\frac{\partial \tilde{R}}{\partial n} = -\frac{(t-\tau)}{n} \frac{\partial \tilde{R}}{\partial \tau}. \quad (18.4-34)$$

From Eq. (18.4-32), we obtain

$$\frac{\partial n}{\partial a} = -\frac{3}{2} \frac{n}{a}. \quad (18.4-35)$$

By differentiating Eq. (18.4-31) with respect to time, we obtain

$$\frac{dM}{dt} = n \left(1 - \frac{d\tau}{dt} \right) + (t-\tau) \frac{dn}{dt}, \quad (18.4-36)$$

where, according to Eq. (18.4-32),

$$\frac{dn}{dt} = -\frac{3}{2} \frac{n}{a} \frac{da}{dt}. \quad (18.4-37)$$

Substitution of Eqs. (18.4-32) through (18.4-35), Eq. (18.4-37) and Eq. (18.4-30a) into Eq. (18.4-36), finally leads to

$$\frac{dM}{dt} = n - \frac{2}{na} \left(\frac{\partial \tilde{R}}{\partial a} \right)_n - \frac{1-e^2}{na^2 e} \frac{\partial \tilde{R}}{\partial e}. \quad (18.4-38)$$

The important property of this equation is that the partial derivative of \tilde{R} with respect to a is taken at constant n . The term $\left(\frac{\partial \tilde{R}}{\partial a} \right)_n$, which must be determined in the evaluation of $\left(\frac{\partial \tilde{R}}{\partial a} \right)_n$, now becomes $\left(\frac{\partial \tilde{R}}{\partial a} \right)_n = 0$ and we avoid terms in which E does not appear in the arguments of trigonometric functions. In fact, this is one of the main reasons for using the orbital element M instead of τ in perturbations theories. It should be recognized, however, that while the orbital elements a , e , i , ω , Ω , τ are constant in

Keplerian motion, the element M varies linearly with time. When using M as an orbital element, it is appropriate to replace the factor $\frac{\partial \tilde{R}}{\partial \tau}$ in the planetary equations by $\frac{\partial \tilde{R}}{\partial M}$, their relation is given by

$$\frac{\partial \tilde{R}}{\partial M} = -\frac{1}{n} \frac{\partial \tilde{R}}{\partial \tau}. \quad (18.4-39)$$

18.4.3 Other forms of the planetary equations

In the preceding sections, we derived the planetary equations in terms of the *classical orbital elements*. As already mentioned in Section 16.5, we can describe a Keplerian orbit by any other set of six parameters, provided that the parameters form six *independent* combinations of the classical elements. One such set is:

$$\begin{aligned} \alpha_1 &= -\frac{\mu}{2a}, & \beta_1 &= -\tau, \\ \alpha_2 &= \sqrt{\mu a(1-e^2)}, & \beta_2 &= \omega, \\ \alpha_3 &= \sqrt{\mu a(1-e^2)} \cos i, & \beta_3 &= \Omega. \end{aligned} \quad (18.4-40)$$

We recognize the parameters α_1 , α_2 and α_3 as the Keplerian total energy, angular momentum and component of the angular momentum about the z -axis, all per unit mass. In terms of these elements, we find for the Lagrange brackets

$$\begin{aligned} [\alpha_1, \beta_1] &= -[\beta_1, \alpha_1] = -1, \\ [\alpha_2, \beta_2] &= -[\beta_2, \alpha_2] = -1, \\ [\alpha_3, \beta_3] &= -[\beta_3, \alpha_3] = -1, \end{aligned} \quad (18.4-41)$$

while all other brackets are zero. The planetary equations then take the extremely simple form:

$$\begin{aligned} \frac{d\alpha_1}{dt} &= \frac{\partial \tilde{R}}{\partial \beta_1}, & \frac{d\beta_1}{dt} &= -\frac{\partial \tilde{R}}{\partial \alpha_1}, \\ \frac{d\alpha_2}{dt} &= \frac{\partial \tilde{R}}{\partial \beta_2}, & \frac{d\beta_2}{dt} &= -\frac{\partial \tilde{R}}{\partial \alpha_2}, \\ \frac{d\alpha_3}{dt} &= \frac{\partial \tilde{R}}{\partial \beta_3}, & \frac{d\beta_3}{dt} &= -\frac{\partial \tilde{R}}{\partial \alpha_3}. \end{aligned} \quad (18.4-42)$$

A system of equations of this form is called *canonical*. The function \tilde{R} , in this case the disturbing function as defined by Eq. (18.4-1), is called the

perturbed Hamiltonian and the parameters β_i and α_i are said to be *canonically conjugate*. Apart from the variables given by Eq. (18.4-40), other sets of canonical variables are sometimes used in celestial mechanics. The canonical form of the planetary equations constitutes the basis of nearly all advanced higher-order theories on perturbed satellite motion. An introduction to these canonical approaches is presented by Geyling and Westerman [7].

In deriving the planetary equations, we assumed that the perturbing forces could be derived from a disturbing potential. In fact, we only made this assumption to simplify the analytical developments. A careful analysis of the derivations in Section 18.4.1 will reveal that in case the perturbing forces cannot be expressed through a potential function, we only have to replace

$$\frac{\partial \tilde{R}}{\partial \alpha_j} \quad \text{by} \quad a_x \frac{\partial x}{\partial \alpha_j} + a_y \frac{\partial y}{\partial \alpha_j} + a_z \frac{\partial z}{\partial \alpha_j},$$

where a_x , a_y , a_z are the magnitudes of the components of the perturbing acceleration along the x -, y - and z -axis, respectively. The partial derivatives $\frac{\partial x}{\partial \alpha_j}$, $\frac{\partial y}{\partial \alpha_j}$, $\frac{\partial z}{\partial \alpha_j}$ can be determined easily and, finally, we obtain planetary equations in terms of the perturbing accelerations a_x , a_y , a_z . It turns out, however, to be more convenient to write these equations in terms of other sets of orthogonal components of the perturbing acceleration. Mostly, we resolve the perturbing acceleration in the components C , S , W or T , N , W , directed as

- C in orbital plane, perpendicular to the radius vector and in the sense of motion,
- S along the radius vector,
- W normal to the orbital plane, in the direction of the orbital angular momentum vector,
- T along the velocity vector,
- N in the orbital plane perpendicular to the velocity vector and directed towards the interior of the orbit.

We will not derive these forms of the planetary equations, but simply give the results:

$$\frac{da}{dt} = 2 \frac{a^2}{\sqrt{\mu p}} \left[Se \sin \theta + C \frac{p}{r} \right], \quad (18.4-43a)$$

$$= 2 \frac{a^2 V}{\mu} T, \quad (18.4-43b)$$

$$\frac{de}{dt} = \sqrt{\frac{p}{\mu}} \left[S \sin \theta + C \frac{r}{p} (e \cos^2 \theta + 2 \cos \theta + e) \right], \quad (18.4-43c)$$

$$= \frac{1}{V} \left[2T(e + \cos \theta) - N \frac{r}{a} \sin \theta \right], \quad (18.4-43d)$$

$$\frac{di}{dt} = \frac{r}{\sqrt{\mu p}} \cos(\omega + \theta) W, \quad (18.4-43e)$$

$$\frac{d\Omega}{dt} = \frac{r}{\sqrt{\mu p} \sin i} \sin(\omega + \theta) W, \quad (18.4-43f)$$

$$\frac{d\omega}{dt} = -\frac{d\Omega}{dt} \cos i - \frac{1}{e} \sqrt{\frac{p}{\mu}} \left[S \cos \theta - C \sin \theta \left(1 + \frac{r}{p} \right) \right], \quad (18.4-43g)$$

$$= -\frac{d\Omega}{dt} \cos i + \frac{1}{eV} \left[2T \sin \theta + N \frac{r}{p} (2e + \cos \theta + e^2 \cos \theta) \right], \quad (18.4-43h)$$

$$\frac{dM}{dt} = n - \frac{2r}{\sqrt{\mu a}} S - \sqrt{1-e^2} \left[\frac{d\omega}{dt} + \frac{d\Omega}{dt} \cos i \right], \quad (18.4-43i)$$

$$= n - 2 \frac{\sqrt{1-e^2}}{V} \left[T \frac{r}{p} e \sin \theta - N \right] - \sqrt{1-e^2} \left[\frac{d\omega}{dt} + \frac{d\Omega}{dt} \cos i \right], \quad (18.4-43j)$$

where p is the semi-latus rectum, θ is the true anomaly, r is the magnitude of the local radius vector and V is the velocity. An elegant, direct derivation of these equations, without first considering the case of forces expressible through a potential, is given by Dobson [15] and Fitzpatrick [16].

Planetary equations in terms of orthogonal components of a perturbing acceleration were first obtained by Gauss in his studies on the motion of the asteroid Pallas as perturbed by Jupiter [17]. We therefore speak of the *Gauss' form of Lagrange's planetary equations*. In cases of forces which cannot be derived from a potential function, e.g. airdrag and rocket thrust, we have to use these equations instead of Eqs. (18.4-30) to calculate the effects of these forces on the satellite's orbit. But even when dealing with perturbing forces expressible through a potential function, the equations in the Gauss form are mostly preferable when the planetary equations are integrated numerically.

It should be noticed, that the Eqs. (18.4-30b), (18.4-30d), (18.4-30f), (18.4-38) and (18.4-43g) through (18.4-43j) contain terms with e in the denominator. Thus, for small eccentricities, the rates of change of the orbital elements e , ω , τ and M can become very large, unless the associated partial derivative $\frac{\partial \tilde{R}}{\partial \alpha_i}$, or perturbing acceleration component, contains a factor e in the numerator. Evaluating the partial derivatives of \tilde{R} , we find that only ω , τ

and M show these large variations. This result is closely connected with the fact that if the eccentricity tends to zero, the elements ω , τ and M become undefined. Similarly, we obtain from Eqs. (18.4-30d), (18.4-30e) and (18.4-43f) through (18.4-43h) that if the inclination becomes very small, large variations in ω and Ω will occur. Geometrically, this is because Ω and ω are undefined for zero inclination.

These large variations are undesirable, both from the viewpoint of numerical integrations and, in particular, for the general perturbations approach. It should, however, be realized that these difficulties have nothing to do with the method of Lagrange itself. It is solely a consequence of the choice of parameters to describe a Keplerian orbit. One can always select other orbital elements for which the corresponding planetary equations do not present such bad characteristics in the region of interest [18].

18.5 A simple general perturbations approach

As mentioned already in Section 18.1, there are many methods suggested to obtain approximate analytical solutions of Lagrange's planetary equations. We will only discuss here a very simple technique: the *method of successive approximations*. We note that the planetary equations for the five elements a , e , i , ω and Ω can be written in a generalized form

$$\frac{d\alpha_i}{dt} = \varepsilon f_i(\alpha_i(t), t), \quad (18.5-1)$$

where ε is a small quantity, of order of the magnitude of the perturbing acceleration. Integration of Eq. (18.5-1) yields

$$\alpha_i(t) = \alpha_{i_0} + \varepsilon \int f_i(\alpha_j(t), t) dt, \quad (18.5-2)$$

where α_{i_0} is the value of α_i at $t=0$. We assume that if the perturbing acceleration is small as compared to μ/r^2 , its effect on the orbit is also small over a considerable period of time; i.e., we expect small changes in the osculating elements during this period.

For a first-order solution of Eq. (18.5-2), it is then admissible to substitute the unperturbed values of the orbital elements into the integral, and we obtain

$$\alpha_i^{(1)}(t) = \alpha_{i_0} + \varepsilon \int f_i(\alpha_{i_0}, t) dt. \quad (18.5-3)$$

Now, the integral can be evaluated and we find an analytical expression for the first-order variation of α_i with time. Substitution of this first-order variation of the elements into the integral yields for the second-order variations:

$$\alpha_i^{(2)}(t) = \alpha_{i_0} + \varepsilon \int f_i(\alpha_j^{(1)}(t), t) dt, \quad (18.5-4)$$

and so on. Of course, we assume this process to converge. Though this method looks very simple, the analytical labor involved to obtain higher-order approximations is quite complex.

The differential equation for $\frac{dM}{dt}$ presents an additional complication. It can be written as

$$\frac{dM}{dt} = n(t) + \varepsilon f_M(\alpha_i(t), t). \quad (18.5-5)$$

Integration yields

$$M(t) = M_o + \int n(t) dt + \varepsilon \int f_M(\alpha_i(t), t) dt. \quad (18.5-6)$$

The second term on the right-hand side of this equation does not contain the small multiplicative factor ε . Therefore, to obtain a first-order solution of Eq. (18.5-6), it will suffice to substitute the unperturbed values of α_i into the integral in the third term on the right-hand side of Eq. (18.5-6), but in the second term we have to include the first-order variation of n . Thus,

$$M^{(1)}(t) = M_o + \int n^{(1)}(t) dt + \varepsilon \int f_M(\alpha_{i_0}, t) dt. \quad (18.5-7)$$

To evaluate the second term on the right-hand side of this equation, we write

$$\int n(t) dt = \int \sqrt{\frac{\mu}{\left(a_o + \int \frac{da}{dt} dt\right)^3}} dt. \quad (18.5-8)$$

For a first-order analysis, we use the approximation

$$\sqrt{\frac{\mu}{\left(a_o + \int \frac{da}{dt} dt\right)^3}} = n_o \left[1 - \frac{3}{2a_o} \int \frac{da}{dt} dt \right], \quad (18.5-9)$$

and thus obtain

$$\int n^{(1)}(t) dt = n_o \int dt - \frac{3n_o}{2a_o} \int \left\{ \int \frac{da}{dt} dt \right\} dt, \quad (18.5-10)$$

where in the expression for $\frac{da}{dt}$ the unperturbed values of the elements α_i has to be substituted. This procedure can be extended to obtain higher-order approximations of $M(t)$. We note that the penalty for replacing τ by M , as performed in Section 18.4.2, is the evaluation of a double integral.

It should be remarked, that, in reality, many perturbing forces act on the

satellite at the same time. When applying a general perturbations technique, one usually computes the effects of the various perturbing accelerations separately. Their joint effects are obtained either by adding them or by taking the square root of the sum of the individual squared perturbations. There is, however, little theoretical justification for this method, in particular when higher-order approximations are involved. The reason that this technique is still widely used is that it mostly gives satisfactory results and that one meets extreme complications when developing a theory that gives a joint treatment of all perturbing accelerations.

18.6 First-order effects of the asphericity of the Earth

As an example of how this theory can be applied, we will now derive analytical expressions for the first-order effects of the *asphericity* of the Earth on the orbit of a satellite. These effects are the predominate perturbations for orbits below some tens of thousands of kilometers altitude, where solar and lunar attractions become about equally important. Analytical expressions for all main orbit perturbations of Earth satellites are presented by Kamos [19].

The external gravitational potential of the Earth can be expanded in spherical harmonics in the following way [20]:

$$U = -\frac{\mu}{r} \left[1 - \sum_{n=2}^{\infty} J_n \left(\frac{R_e}{r} \right)^n P_n(\sin \Phi) - \sum_{n=2}^{\infty} \sum_{m=1}^n J_{n,m} \left(\frac{R_e}{r} \right)^n P_n^m(\sin \Phi) \cos m(\Lambda - \Lambda_{n,m}) \right]. \quad (18.6-1)$$

Here r , Φ and Λ are the spherical coordinates of the satellite in the geocentric rotating reference frame (Section 2.3.4): r is the geocentric radius, Φ is the geocentric latitude and Λ is the geographic longitude. The function $P_n(\sin \Phi)$ is *Legendre's polynomial* of degree n in $\sin \Phi$; $P_n^m(\sin \Phi)$ is the *associated Legendre function* of degree n and order m . The mean equatorial radius of the Earth is denoted by R_e . The quantities J_n , $J_{n,m}$ and $\Lambda_{n,m}$ are numerical coefficients. The coefficient J_2 takes the value 1.082637×10^{-3} , all other J_n and $J_{n,m}$ are of order 10^{-6} or less [21]. It should be remarked here, that terms with $n = 1$ are absent, because of the assumption that the origin of the reference frame coincides with the center of mass of the Earth. Also, as the axis of rotation of the Earth, the z -axis of our reference frame, practically coincides with a principal axis of inertia, the coefficient $J_{2,1}$ will be extremely small.

We recognize the first term on the right-hand side of Eq. (18.6-1), $-\frac{\mu}{r}$, as the classical Newtonian gravitational potential. The series in Legendre's polynomials constitutes the so-called *zonal harmonics*. The terms having $J_{n,m}$, $n \neq m$, as factors are known as the *tesseral harmonics*; those having $J_{n,m}$,

$n = m$, as the *sectorial harmonics*. The zonal harmonics describe the deviations in the north-south direction of the potential from a pure Newtonian one; the tesseral and sectorial harmonics give the deviations in an east-west direction. The term involving J_2 is closely related to the *oblateness* of the Earth. The term involving J_3 is the one referred to in describing the Earth as *pear-shaped*. The term with $J_{2,2}$ describes the *ellipticity* of the Earth's equator.

We know that it takes one day for the Earth to make one complete revolution about its axis, while the Keplerian orbit of a satellite keeps a fixed orientation in inertial space. We thus can imagine that the effects of the tesseral and sectorial harmonics are more or less 'averaged-out' over periods longer than one day. For most applications, it is therefore sufficient to account only for the effects of the zonal harmonics. We then, in fact, assume the gravitational field of the Earth to be rotational symmetric or *axial symmetric*. An important exception is formed by a geostationary satellite. Because such a satellite always keeps (nearly) the same position relative to the Earth's surface, its orbit is very sensitive to the east-west anomalies in the gravitational field, and one certainly may not neglect the tesseral and sectorial harmonics.

The disturbing function \tilde{R} for the axial symmetric field can, according to Eq. (18.6-1), be written as

$$\tilde{R} = -\frac{\mu}{r} \sum_{n=2}^{\infty} J_n \left(\frac{R_e}{r}\right)^n P_n(\sin \Phi). \quad (18.6-2)$$

For such an axial symmetric field, two exact integrals of motion can be obtained.

We note that as in this case \tilde{R} is only a function of r and Φ , and not of Λ anymore, the gravitational potential is not explicitly dependent on time. For, when keeping a fixed position in the reference frame, the potential holds a constant value although the Earth rotates. As such a force field is conservative, the sum of potential and kinetic energy of the satellite must be constant,

$$\frac{\mu}{2a} + \tilde{R} = \text{constant}. \quad (18.6-3)$$

This expression directly relates the semi-major axis of the osculating orbit to the local perturbing potential.

A second integral can be obtained as follows. If the magnitude of the component of the angular momentum about the z -axis is denoted by H_z , we may write

$$\frac{d}{dt} \left(\frac{H_z^2}{\mu} \right) = \frac{d}{dt} \{a(1-e^2) \cos^2 i\}. \quad (18.6-4)$$

By evaluating the right-hand side of Eq. (18.6-4), and substituting for $\frac{da}{dt}$,

$\frac{de}{dt}$ and $\frac{di}{dt}$ the Eqs. (18.4-30a) through (18.4-30c), we finally obtain

$$\frac{d}{dt} \left(\frac{H_z^2}{\mu} \right) = 2 \sqrt{\frac{p}{\mu}} \cos i \frac{\partial \tilde{R}}{\partial \Omega}.$$

Because the gravitational field is assumed to be axial symmetric, \tilde{R} is not a function of Ω , and we find for the second integral of motion

$$H_z = \text{constant}. \quad (18.6-5)$$

These two integrals hold for any axial symmetric field. In the next discussion, we will limit ourselves to the first-order effects of the Earth's gravitational field and will therefore only retain the J_2 -term of the zonal harmonics.

Evaluating the Legendre polynomial of the second degree and using Eq. (16.6-27), the disturbing function can be written as

$$\tilde{R} = \frac{1}{2} \mu J_2 R_e^2 \frac{1 - 3 \sin^2 i \sin^2 u}{r^3}, \quad (18.6-6)$$

where u is the argument of latitude, $u = \omega + \theta$. Suppose we want to compute the variation of the orbital element Ω due to this disturbing function. We then have, according to Eq. (18.4-30e), to find an expression for $\frac{\partial \tilde{R}}{\partial i}$. As both u and r are independent of i , we directly obtain

$$\frac{\partial \tilde{R}}{\partial i} = -3 \mu J_2 R_e^2 \frac{\sin i \cos i \sin^2 u}{r^3}.$$

By substituting this relation into Eq. (18.4-30e) and replacing the independent variable t by u , we find

$$\frac{d\Omega}{du} = -3 \mu J_2 R_e^2 \frac{\cos i \sin^2 u}{r^3 \sqrt{\mu p}} \frac{dt}{du}. \quad (18.6-7)$$

For a first-order analysis, all orbital elements on the right-hand side of Eq. (18.6-7) may be considered as constants, and we write

$$\frac{du}{dt} = \frac{d(\omega_o + \theta)}{dt} = \frac{d\theta}{dt} = \frac{\sqrt{\mu p_o}}{r_o^2}, \quad (18.6-8)$$

where the index o refers to the unperturbed conditions. Note, that in Eq. (18.6-8), θ denotes the angular position of the satellite at a given instant, if the satellite would follow an unperturbed trajectory with orbital elements equal to the initial values of the osculating elements of the perturbed orbit. This is the concept of the *unperturbed true anomaly*. The difference between perturbed and unperturbed true anomaly will be proportional to J_2 . Because

430 Rocket Propulsion & Spaceflight Dynamics

the right-hand side of Eq. (18.6-7) already contains the factor J_2 , and we are developing a first-order theory, this difference can be neglected in carrying out the integration.

Substituting Eq. (18.6-8) and

$$r = r_o = \frac{p_o}{1 + e_o \cos(u - \omega_o)}$$

into Eq. (18.6-7), and subsequent integration from $u = 0$ to u yields

$$\begin{aligned} \Omega - \Omega_o = -\frac{1}{4}J_2 \left(\frac{R_e}{p_o}\right)^2 \cos i_o [6u - 3 \sin 2u + \\ + e_o \{6 \sin(u - \omega_o) - 3 \sin(u + \omega_o) - \sin(3u - \omega_o) + 8 \sin \omega_o\}]. \end{aligned} \quad (18.6-9)$$

This equation clearly shows that the variation of Ω with u is composed of a linear variation, called the *secular perturbation*, and periodic variations with periods in the order of the orbital period. These constitute the *short-periodic perturbation*. Corresponding relations for the variations of the other orbital elements can be derived.

As an example, Fig. 18.1 shows the variation of the osculating orbital elements of the ESRO-satellite TD-1A, due to the second zonal harmonic, during its 392nd orbital revolution [22]. This satellite was launched on March 12, 1972 into a near-polar, near-circular orbit at an altitude of about 540 km.

The change in Ω after one orbital revolution, $u = 2\pi$, is according to Eq. (18.6-9)

$$\Delta_{2\pi}\Omega = -3\pi J_2 \left(\frac{R_e}{p_o}\right)^2 \cos i_o. \quad (18.6-10a)$$

For the other elements, we find:

$$\Delta_{2\pi}a = \Delta_{2\pi}e = \Delta_{2\pi}i = 0, \quad (18.6-10b)$$

$$\Delta_{2\pi}\omega = \frac{3}{2}\pi J_2 \left(\frac{R_e}{p_o}\right)^2 (5 \cos^2 i_o - 1), \quad (18.6-10c)$$

$$\Delta_{2\pi}M = n_o(t_{2\pi} - t_o) + 3\pi J_2 \left(\frac{R_e}{p_o}\right)^2 \frac{(1 + e_o \cos \omega_o)^3}{1 - e_o^2}. \quad (18.6-10d)$$

It should be realized, that when evaluating the first term on the right-hand side of the last equation, the difference between perturbed and unperturbed true anomaly cannot be neglected. Therefore, for the computation of the change in M between two successive passages through the equatorial plane, one must substitute for $t_{2\pi} - t_o$ the so-called *nodal period*, or *draconic period* [23].

The most significant perturbations are the secular effects that appear in ω and Ω . We note from Eq. (18.6-10a) that the orbital plane rotates about the Earth's polar axis; Ω increases for $i > 90^\circ$ and decreases for $i < 90^\circ$. The

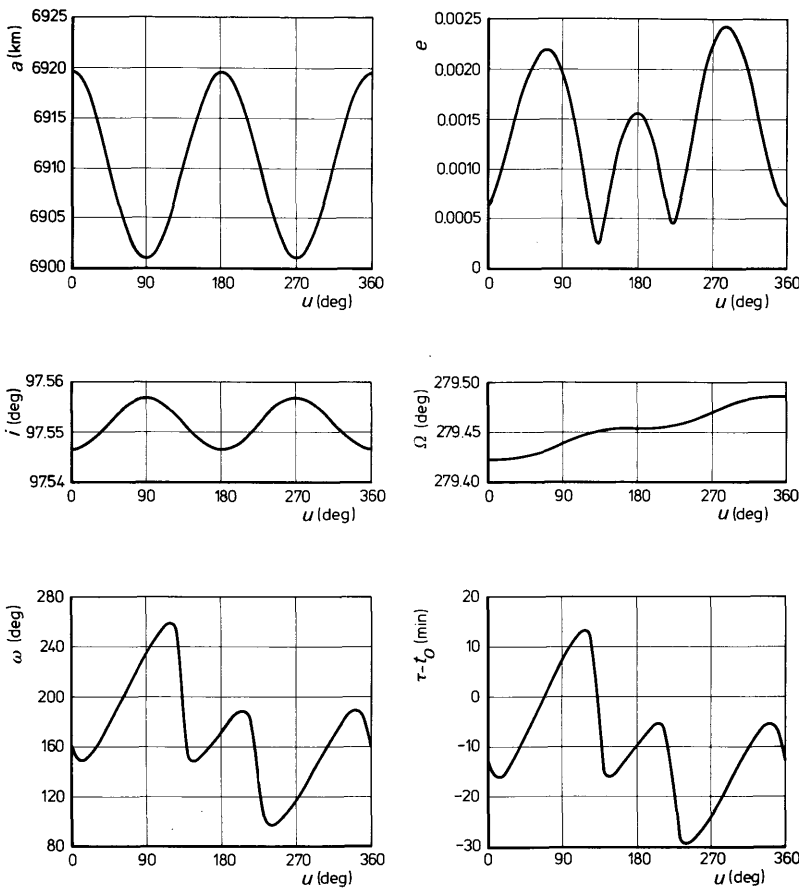


Fig. 18.1 The osculating orbital elements of the TD-1A satellite during its 392nd orbital revolution

major axis rotates, according to Eq. (18.6-10c), in the orbital plane. For low-inclination orbits it rotates in the direction of motion; for polar orbits it rotates in an opposite direction. At $i = 63.43^\circ$ and 116.57° , the *critical inclinations*, the major axis will, according to our first-order analysis, keep a fixed orientation. The values of $\Delta\omega$ and $\Delta\Omega$ per orbital revolution are shown in Fig. 18.2 as a function of p_o and i_o . Note that in Fig. 18.2 i_o only varies from 0° to 90° ; the reader himself can easily determine from Eqs. (18.6-10a) and (18.6-10c) and this figure the values of $\Delta\omega$ and $\Delta\Omega$ for $i_o > 90^\circ$.

Returning to Eq. (18.6-9), we note that the expression for the variation of Ω contains also the element ω in trigonometric arguments. As we know that ω shows a first-order secular variation, we can imagine that a second-order analysis will reveal periodic perturbations in Ω with a period in the order of the interval in which the major axis completes one revolution in the orbital

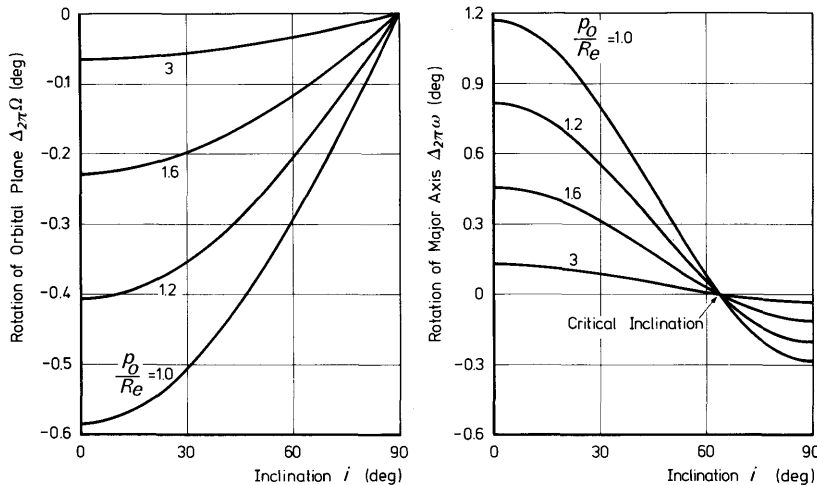


Fig. 18.2 The first-order changes of the osculating orbital elements ω and Ω after one revolution

plane. These perturbations are called *long-periodic perturbations*. As an example, Fig. 18.3 shows the predicted long-periodic perturbation of the orbital eccentricity of the TD-1A satellite due to the first seven zonal harmonics [22]. The values of the eccentricity indicated in this figure are mean values over one orbital revolution; i.e. the short-periodic variation is eliminated. Also included in Fig. 18.3 are tracking data, giving an impression of the additional effects of all other perturbing forces acting on this satellite. For a satellite in a lower orbit, aerodynamic effects can certainly not be

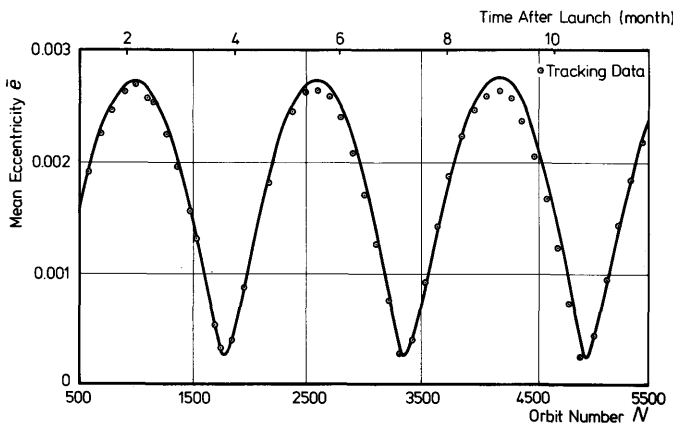


Fig. 18.3 The long-periodic perturbation of the orbital eccentricity of the TD-1A satellite

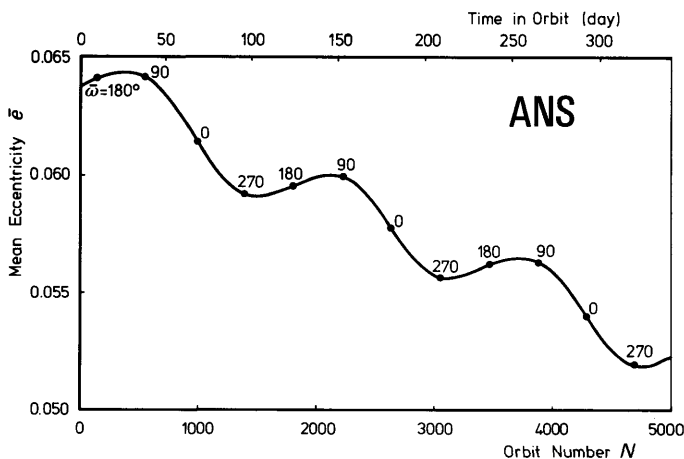


Fig. 18.4 The long-periodic perturbation of the orbital eccentricity of ANS

neglected. As an example, Fig. 18.4 shows the actual long-periodic variation in the orbital eccentricity of the ANS satellite [24]. As already mentioned in Section 17.4, this satellite was injected on August 30, 1974, into an orbit with perigee at 266 km and apogee at 1175 km altitude. The decrease in eccentricity is a result of the aerodynamic drag. The long-periodic oscillation is still clearly recognizable.

The rotation of the line of nodes has found a widespread application for satellite missions. For instance, for a circular orbit at an altitude of 600 km, we can obtain $\Delta_{2\pi}\Omega = 0.986^\circ$ per day in an easterly direction by selecting $i_o = 97.76^\circ$. Then, the rotation rate of the orbital plane equals the angular motion of the Earth about the Sun. This is called a *Sun-synchronous orbit*. From Eq. (18.6-10a) we find that circular Sun-synchronous orbits are possible for satellites below about 6000 km altitude.

Sun-synchronous orbits are very attractive for Earth observations satellites because of the constant ground lighting conditions. For example, a satellite in a Sun-synchronous orbit containing the Earth-Sun line will always cross the equator at local noon and local midnight. Sun-synchronous orbits with the Earth-Sun line perpendicular to the line of nodes are also often used. As the line of nodes will remain (about) perpendicular to the Earth-Sun line during the motion of the Earth about the Sun, and as the declination of the Sun is always within the range $-23.5^\circ < \delta < 23.5^\circ$, we can, by careful selecting the launch date, reach a situation where a satellite in a 600 km altitude orbit will remain continuously in sunlight for more than eight months. This is ideally suited for power generation by means of solar cells.

References

- 1 Baker, R. M. L. (1967), *Astrodynamic Applications and Advanced Topics*, Academic Press, New York, p. 137–220.
- 2 Allione, M. S., Blackford, A. L., Mendez, J. C. and Whittouck, M. M. (1968), *Guidance, Flight Mechanics and Trajectory Optimization, Vol. 6, The N-Body Problem and Special Perturbation Techniques*, NASA CR-1005, Washington.
- 3 Merson, R. H. (1973), *Numerical Integration of the Differential Equations of Celestial Mechanics*, ESRO CR(P)-283, Neuilly-sur-Seine.
- 4 Dallas, S. S. (1970), *Prediction of the Position and Velocity of a Satellite After Many Revolutions*, JPL TR 32-1267, Pasadena, p. 16–59.
- 5 Lorell, J., Anderson, J. D. and Lass, H. (1964), *Application of the Method of Averages to Celestial Mechanics*, JPL TR 32-482, Pasadena.
- 6 Davis, M. S. (1973), Review of non-numerical uses of computers, in: B. D. Tapley and V. Szebehely (eds.), *Recent Advances in Dynamical Astronomy*, Reidel, Dordrecht, p. 351–391.
- 7 Geyling, F. T. and Westerman, H. R. (1971), *Introduction to Orbital Mechanics*, Addison-Wesley, Reading, p. 194–310.
- 8 Stiefel, E. L. and Scheifele, G. (1971), *Linear and Regular Celestial Mechanics*, Springer, New York.
- 9 O'Keefe, J. A., Eckels, A. and Squires, R. K. (1959), The gravitational field of the Earth, *Astron. J.*, **64**, 245–253.
- 10 Cowell, P. H. and Crommelin, A. C. D. (1910), *Investigation of the Motion of Halley's Comet from 1759 to 1910*, Appendix to Greenwich Observations, 1909.
- 11 Encke, J. F. (1852), Ueber eine neue Methode der Berechnung der Planetenstörungen, *Astron. Nachr.*, **33**, no. 791, 792, 377–398; **34**, no. 814 (1853), 349–360.
- 12 Herrick, S. (1972), *Astrodynamic*, Vol. 2, Van Nostrand Reinhold, London, p. 304.
- 13 Stumpff, K. and Weiss, E. H. (1968), *A Fast Method of Orbit Computation*, NASA TN D-4470, Washington.
- 14 Lagrange, J. L. (1873), Memoire sur la théorie des variations des éléments des planètes, in: *Oeuvres de Lagrange*, Vol. 6, Gauthier-Villars, Paris, p. 713–768.
- 15 Dobson, W. F., Huff, V. N. and Zimmerman, A. V. (1962), *Elements and Parameters of the Osculating Orbit and Their Derivatives*, NASA TN D-1106, Washington.
- 16 Fitzpatrick, P. M. (1970), *Principles of Celestial Mechanics*, Academic Press, New York, p. 152–175.
- 17 Brendel, M. (1929), Über die astronomischen Arbeiten von Gauss, in: *Carl Friedrich Gauss Werke*, Vol. 11, Part 2, Springer, Berlin. Also: *Gauss' Diary*, November 1802.

- 18 Cefola, P. J. (1972), *Equinoctial Orbit Elements, Application to Artificial Satellite Orbits*, AIAA Paper 72-937, New York.
- 19 Kampos, B. (1968), *Guidance, Flight Mechanics and Trajectory Optimization*, Vol. 9, *General Perturbations Theory*, NASA CR-1008, Washington.
- 20 Wagner, C. A. (1966), *The Gravity Potential and Force Field of the Earth Through Fourth Order*, NASA TN D-3317, Washington.
- 21 Gaposchkin, E. M. (ed.) (1973), *1973 Smithsonian Standard Earth (III)*, SAO Special Report 353, p. 190, 276, 290-293.
- 22 Wakker, K. F. and Ambrosius, B. A. C. (1973), *Comparison between the Predicted and Actual Orbit of the ESRO-Satellite TD-1A*, Memorandum M-202 (in Dutch), Dept. Aerospace Eng., Delft University of Technology, Delft.
- 23 Blitzer, L. (1964), Nodal period of an Earth satellite, *AIAA J.*, **2**, no. 8, 1459.
- 24 Wakker, K. F. (1977), *Orbit Prediction for the Astronomical Netherlands Satellite*, paper presented at the B.I.S. conference on Computer Techniques for Satellite Control and Data Processing, Slough.

19 Interplanetary Missions

For interplanetary missions, a spacecraft is launched from the Earth and accelerated to a velocity larger than the local escape velocity. The spacecraft will then recede from the Earth along a hyperbolic trajectory. While its distance from the Earth increases, the solar gravitational attraction, gradually, will become more important until, ultimately, the spacecraft enters a heliocentric orbit. The trajectory is chosen such that the spacecraft will perform a specified mission. If the spacecraft has to pass a target planet at a relatively small distance, we speak of a *flyby mission*; if the spacecraft should be decelerated by a rocket engine to enter an orbit about that planet, we call it an *orbiter mission*. For a *lander mission*, the final velocity of the spacecraft relative to the planet's surface has to be reduced to a very small value by means of atmospheric braking and/or rocket engine deceleration.

In comparison with Earth satellite missions or lunar flights, interplanetary missions face higher energy requirements and much longer flight times. These flight times may range from some months to many years. A reduction in flight time can only be achieved by advanced propulsion systems [1] offering a sufficiently high thrust, and exhaust velocities as high as possible. Without succeeding in the development of such propulsion systems, the possibilities for interplanetary flight will be rather limited, in particular for manned missions.

It will be clear that for the actual detailed computation of an interplanetary trajectory, the motion of the spacecraft must be considered as a many-body problem. Apart from the gravitational attractions of the Earth, the Sun and the target planet, the attractions of the Moon and many planets also have to be taken into account. In addition, solar radiation pressure may substantially affect the trajectory. Even if one only takes into account the gravitational attractions of the Earth, the Sun and the target planet, the analysis of interplanetary trajectories is quite complex. For one has to determine the spacecraft's injection conditions such that the time of arrival at the target planet and the spacecraft's position and velocity relative to the planet closely meet their specified values. The search for the required interplanetary trajectory can only be made in an iterative way. The first step in this process is to assume that the interplanetary trajectory is part of a heliocentric conic section between the centers of the Earth and the target planet. After a range of possible trajectories is determined, the computations are extended assuming that the interplanetary trajectory can be divided into three Keplerian trajectories. Within the *sphere of influence* of

the Earth (Section 15.3.2), the trajectory is considered to be a geocentric hyperbola; within the sphere of influence of the target planet a planetocentric hyperbola. The intermediate part of the trajectory is approximated by a heliocentric conic section. This is known as the *patched conic method*. After the results from this method are obtained, the patched conic approximation can be replaced by a numerical integration analysis, which continuously takes account of the influences of the Sun, the Moon and the planets on the spacecraft's trajectory.

Throughout this chapter, we will make a number of simplifying assumptions by which an elementary analysis of interplanetary trajectories becomes feasible.

19.1 Basic concepts

Conic sections. We will assume that the interplanetary trajectory can be approximated by a succession of patched conics. In Section 15.3.2, we discussed the concept of the sphere of influence and derived an expression for its radius, $R_{s.i.}$, Eq. (15.3-16). Table 19.1 lists the radii of the spheres of influence for the nine planets. For each planet two values are given, corresponding to the minimum and maximum heliocentric distance of that planet. Also listed are $R_{s.i.}$ in units of the mean Sun–planet distance, a , and in units of the planet radius, R . We note that though $R_{s.i.}$ can be quite large, in particular for the outer planets, the radius of the sphere of influence is always small compared to the Sun–planet distance. This implies that, on interplanetary scale, we can imagine the heliocentric leg of the trajectory extending to the very centers of the Earth and the target planet.

In Section 16.2, we found that at a distance of about 400,000 km from the Earth, the local velocity in a hyperbolic trajectory nearly equals the *hyperbolic excess velocity* with respect to a non-rotating geocentric reference frame, \mathbf{V}_{∞_e} . As the radius of the Earth's sphere of influence is about one million kilometers, we certainly may approximate the spacecraft's velocity at

Table 19.1 The radii of the spheres of influence

Planet	$R_{s.i.}$ (10^6 km)	$R_{s.i.}$ ($10^{-2}a$)	$R_{s.i.}$ (10^2R)
Mercury	0.09–0.14	0.15–0.23	0.37–0.56
Venus	0.61–0.62	0.57–0.57	1.01–1.03
Earth	0.91–0.94	0.61–0.63	1.43–1.47
Mars	0.52–0.63	0.23–0.28	1.54–1.85
Jupiter	45.9–50.5	5.90–6.49	6.48–7.13
Saturn	51.6–57.7	3.61–4.04	8.59–9.61
Uranus	49.4–54.1	1.73–1.89	19.4–21.3
Neptune	85.7–87.6	1.91–1.95	34.1–34.9
Pluto	11.4–18.8	0.19–0.32	35.6–58.7

the sphere of influence by \mathbf{V}_∞ . The required magnitude and direction of \mathbf{V}_∞ follows from $\mathbf{V}_{\infty_e} = \mathbf{V}_1 - \mathbf{V}_e$, where \mathbf{V}_e is the Earth's orbital velocity and \mathbf{V}_1 is the spacecraft's heliocentric velocity at the start of the heliocentric leg; both relative to a non-rotating heliocentric reference frame. On arrival at the target planet, the planetocentric hyperbolic excess velocity, \mathbf{V}_∞ , can be obtained from $\mathbf{V}_\infty = \mathbf{V}_2 - \mathbf{V}_t$, where \mathbf{V}_2 is the spacecraft's heliocentric velocity at crossing the orbit of the target planet and \mathbf{V}_t is the target planet's orbital velocity.

Planetary orbits. In Section 19.2 we will assume that the planets move in circular orbits about the Sun and that all planetary orbits lie in the ecliptic plane. From Table T.3, we note that at first sight this seems an acceptable simplification; the errors introduced will be largest for Mercury and Pluto, the orbits of which have both a relatively large inclination and eccentricity. It turns out, however, that this assumption may yield large errors. In Section 19.3, we will discuss some effects of the inclination and eccentricity of the planetary orbits on the analysis of interplanetary trajectories.

Parking orbit and impulsive shot. We will assume that the interplanetary flight starts from a parking orbit about the Earth. For the time being, chemical propulsion systems will be used exclusively for leaving the Earth and for deceleration at the target planet. These high-thrust propulsion systems have relatively short burning-times. We therefore may apply the concept of an impulsive shot (Section 11.2.3), and assume that due to the thrust of the rocket engine, the spacecraft experiences an instantaneous velocity change, leaving the spacecraft's position unaltered. Data on the errors introduced by this simplification are presented by Willis [2]. Moreover, we assume that the departure from the parking orbit about the Earth, and the deceleration maneuver to enter an orbit about the target planet are both accomplished by only one firing of the rocket motor.

The thrusting phase in the initial parking orbit increases the orbital energy per unit mass, \mathcal{E} , of the spacecraft. This energy increase must be attained at a minimum propellant consumption. So, the question arises: how is an impulsive velocity increment $\Delta \mathbf{V}_0$ of given magnitude to be applied such that a maximum $\Delta \mathcal{E}$ will result? As the impulsive shot only changes the velocity of the spacecraft and not its position, we may write

$$\Delta \mathcal{E} = \frac{1}{2}(\mathbf{V}_0^2 - \mathbf{V}_{par_0}^2), \quad (19.1-1)$$

where \mathbf{V}_{par_0} is the spacecraft's velocity in the parking orbit just before the impulsive shot and \mathbf{V}_0 is the spacecraft's velocity just after the impulsive shot. We may rewrite Eq. (19.1-1) as

$$\Delta \mathcal{E} = \frac{1}{2}(\Delta \mathbf{V}_0)^2 + \mathbf{V}_{par_0} \cdot \Delta \mathbf{V}_0. \quad (19.1-2)$$

From this relation we note that it is most advantageous if the impulsive shot is applied *tangentially* to the parking orbit, and at a location in the parking

orbit where the orbital velocity is a maximum. In Section 17.1, however, we argued that a parking orbit altitude will be chosen as low as possible, leading to circular orbits in which the orbital velocity is constant.

For a deceleration maneuver to enter a parking orbit about the target planet, the same arguments hold. In that case too, the impulse should be applied at pericenter of the hyperbolic leg and normal to the radius vector. One should keep in mind, however, that operational constraints may force one to apply other deceleration maneuvers.

19.2 Two-dimensional interplanetary trajectories

As the impulsive shot in the circular parking orbit about the Earth, ΔV_0 , is applied tangentially to the parking orbit, we may write for the spacecraft's velocity just after the impulsive shot, V_0 ,

$$V_0 = V_{c_0} + \Delta V_0, \quad (19.2-1)$$

where V_{c_0} is the velocity in the circular parking orbit. In Section 16.2.3, we found for the relation between local velocity in a hyperbolic trajectory and hyperbolic excess velocity

$$V_0^2 = V_{esc_0}^2 + V_{\infty_e}^2, \quad (19.2-2)$$

where V_{esc_0} is the local escape velocity. Substituting Eqs. (16.2-3), (16.2-4) and (19.2-2) into Eq. (19.2-1), we obtain

$$\Delta V_0 = \sqrt{\frac{2\mu_e}{r_0} + V_{\infty_e}^2} - \sqrt{\frac{\mu_e}{r_0}}, \quad (19.2-3)$$

where r_0 is the radius of the parking orbit and the perigee distance of the hyperbolic escape trajectory. The Earth's gravitation parameter is denoted by μ_e .

For the magnitude of the impulse to decelerate the spacecraft in order to enter an orbit about the target planet, we find by the same reasoning

$$\Delta V_3 = \sqrt{\frac{2\mu_i}{r_3} + V_{\infty_i}^2} - V_{par_3}, \quad (19.2-4)$$

where μ_i is the planet's gravitation parameter, r_3 is the pericenter distance of the hyperbolic trajectory about the planet and V_{par_3} is the pericenter velocity just after deceleration. Of course, V_{par_3} should be less than the local escape velocity, or $V_{par_3} < \sqrt{2\mu_i/r_3}$. From Eq. (19.2-4), the reader can easily verify himself that if the only requirement were that of being captured by the target planet, a final orbit of high eccentricity and very low pericenter distance is most economical. For orbits with constant pericenter distance, ΔV_3 decreases with increasing values of the eccentricity. In general, there is an optimal pericenter distance if the eccentricity (or semi-major axis) is fixed.

19.2.1 Hohmann trajectories

It is interesting to investigate which two-dimensional direct interplanetary trajectory would require the least amount of propellant. In general, the total mass which can be put into the initial parking orbit about the Earth is known. For an orbiter mission, one has to determine ΔV_0 and ΔV_3 such that the useful mass in orbit about the target planet is a maximum. This requires the exhaust velocities of both rocket engines and the mass ratios of the vehicle to be known. We will simplify the problem and only determine the optimum direct interplanetary trajectory for a flyby mission. In that case ΔV_0 should take a minimum value for a specified exhaust velocity. In addition, we will only discuss a mission to an outer planet, but the same scheme can be used for flights to the inner planets.

It will be clear that an interplanetary trajectory to an outer planet must satisfy the conditions

$$r_p \leq r_e, \quad r_a \geq r_t, \quad (19.2-5)$$

where r_p and r_a are the perihelion and apohelion distances of the interplanetary trajectory, and r_e and r_t are the radii of the orbits of Earth and target planet about the Sun. Of course, for parabolic and hyperbolic heliocentric trajectories, the second condition is always met. Using the relations for Keplerian orbits, we may also write the requirements as

$$\frac{p}{r_e} \leq 1 + e, \quad \frac{p}{r_t} \geq 1 - e, \quad (19.2-6)$$

where p and e stand for the semi-latus rectum and eccentricity of the interplanetary trajectory. Following Vertregt [3], we now introduce the quantities q and n , defined as

$$q = \frac{p}{r_e}, \quad n = \frac{r_t}{r_e}, \quad (19.2-7)$$

and rewrite Eq. (19.2-6) in the form

$$q \leq 1 + e, \quad q \geq n(1 - e). \quad (19.2-8)$$

In Fig. 19.1, the region of possible interplanetary trajectories is shown in the e - q plane. The trajectory with the smallest eccentricity, being an ellipse, is indicated with the letter H . For this trajectory:

$$q_H = \frac{2n}{n+1}, \quad e_H = \frac{n-1}{n+1}. \quad (19.2-9)$$

From Fig. 19.2 we note that we can write

$$\begin{aligned} V_{\infty_e}^2 &= V_1^2 + V_e^2 - 2V_1V_e \cos \gamma_1, \\ V_{\infty_t}^2 &= V_2^2 + V_t^2 - 2V_2V_t \cos \gamma_2, \end{aligned} \quad (19.2-10)$$

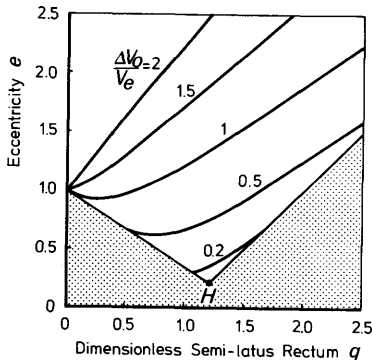


Fig. 19.1 Constant ΔV_0 contours in the e - q plane for two-dimensional trajectories to Mars. Initial parking orbit altitude: 185 km

where V_1 and V_2 are the spacecraft's heliocentric velocities at leaving the Earth's orbit and on arrival in the target planet's orbit, respectively. The respective heliocentric flight path angles are denoted by γ_1 and γ_2 . For the heliocentric velocity V_1 , we obtain from Eq. (16.2-2)

$$V_1^2 = \frac{\mu_s}{r_e} \left(2 - \frac{r_e}{a} \right), \quad (19.2-11)$$

where μ_s is the solar gravitation parameter and a is the semi-major axis of the interplanetary trajectory. Recalling that the planets were assumed to move in circular orbits and using Eq. (19.2-7), Eq. (19.2-11) can be written as

$$V_1^2 = V_e^2 \left[2 - \frac{1 - e^2}{q} \right]. \quad (19.2-12)$$

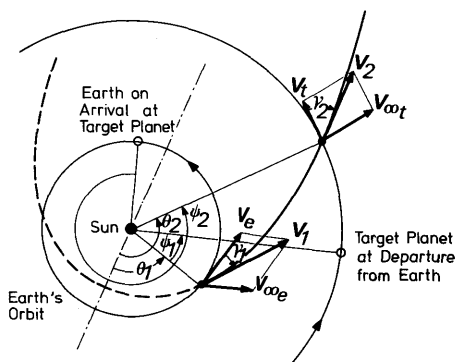


Fig. 19.2 Geometry of two-dimensional interplanetary trajectories

In exactly the same way, we find

$$V_2^2 = V_t^2 \left[2 - \frac{n}{q} (1 - e^2) \right]. \quad (19.2-13)$$

To express $\cos \gamma_1$ and $\cos \gamma_2$ in the variables n , e and q , we start from Eq. (16.2-7). By the use of standard trigonometry, we obtain

$$\cos \gamma = \frac{1 + e \cos \theta}{\sqrt{1 + 2e \cos \theta + e^2}}.$$

Using Eq. (16.2-1), we finally find

$$\cos \gamma = \frac{p/r}{\sqrt{2 \frac{p}{r} - (1 - e^2)}}.$$

Applying this relation for γ_1 and γ_2 , and using the quantities q and n , we obtain

$$\begin{aligned} \cos \gamma_1 &= \frac{q}{\sqrt{2q - (1 - e^2)}}, \\ \cos \gamma_2 &= \frac{q/n}{\sqrt{2 \frac{q}{n} - (1 - e^2)}}. \end{aligned} \quad (19.2-14)$$

For the relation between the orbital velocities of the Earth and the target planet, we have

$$\frac{V_t^2}{V_e^2} = \frac{r_e}{r_t} = \frac{1}{n}. \quad (19.2-15)$$

Substitution of Eqs. (19.2-12) through (19.2-15) into Eqs. (19.2-10), finally yields

$$\frac{V_{\infty_e}}{V_e} = \sqrt{3 - 2\sqrt{q} - \frac{1 - e^2}{q}}, \quad (19.2-16a)$$

$$\frac{V_{\infty_t}}{V_e} = \sqrt{\frac{3 - 2\sqrt{q/n}}{n} - \frac{1 - e^2}{q}}. \quad (19.2-16b)$$

To determine the optimum interplanetary trajectory, we substitute Eq. (19.2-16a) into Eq. (19.2-3), which yields

$$\frac{\Delta V_0}{V_e} = \sqrt{\frac{2\mu_e}{r_0 V_e^2} + 3 - 2\sqrt{q} - \frac{1 - e^2}{q}} - \frac{\sqrt{\mu_e/r_0}}{V_e}. \quad (19.2-17)$$

For a specified parking orbit about the Earth, ΔV_0 is only a function of q and e . We note that for a given value of q , ΔV_0 decreases with decreasing

values of e . So, for a given value of q , ΔV_0 reaches a minimum if e satisfies the boundary conditions (Fig. 19.1):

$$e = 1 - \frac{q}{n} \quad \text{or} \quad e = q - 1. \quad (19.2-18)$$

Substituting these boundary conditions into Eq. (19.2-17), it can easily be shown that for $q < q_H: \frac{\partial \Delta V_0}{\partial q} < 0$ and for $q > q_H: \frac{\partial \Delta V_0}{\partial q} > 0$. So, it will be evident that the point H indicated in Fig. 19.1 represents the *minimum-propellant trajectory*. This optimum trajectory is an ellipse, for which

$$q = n(1 - e) = 1 + e,$$

or

$$\frac{p}{r_e} = \frac{r_t}{r_e} (1 - e) = 1 + e.$$

With Eq. (3.6-27) we can write this relation as

$$r_e = a(1 - e), \quad r_t = a(1 + e),$$

which are the expressions for pericenter and apocenter distances, and we conclude that the optimum interplanetary trajectory is a heliocentric ellipse, tangential to both the Earth's orbit and to the target planet's orbit ($\gamma_1 = \gamma_2 = 0$). These minimum-propellant trajectories are called *Hohmann trajectories* [4].

In Table 19.2, some parameters of Hohmann trajectories from the Earth to the planets are given. We note that for flights to the planets beyond Jupiter the flight time, T , becomes excessive. The parameters T_{syn} , ψ_1 , ψ_2 and D given in this table are discussed in Section 19.2.2. In Table 19.3, velocity data are summarized for the Hohmann transfers. For comparison, data for a direct heliocentric escape mission are also given. One of the conclusions which can be drawn from this table is that, except for Venus and

Table 19.2 Basic data for Hohmann transfer trajectories from Earth to the planets

Target planet	n	a (AU)	e	T (year)	T_{syn} (year)	ψ_1 (deg)	ψ_2 (deg)	D (AU)
Mercury	0.387	0.6935	0.4419	0.289	0.317	108.3	76.0	0.981
Venus	0.723	0.8617	0.1605	0.400	1.599	-54.0	36.0	0.594
Mars	1.524	1.2618	0.2075	0.709	2.135	44.3	-75.1	1.594
Jupiter	5.202	3.1012	0.6775	2.731	1.092	97.2	-83.0	5.177
Saturn	9.548	5.2741	0.8104	6.056	1.035	106.1	159.8	10.492
Uranus	19.135	10.0674	0.9007	15.972	1.012	111.3	-169.7	20.120
Neptune	30.011	15.5055	0.9355	30.529	1.006	113.2	-10.1	29.027
Pluto	39.289	20.1446	0.9504	45.208	1.004	113.9	105.3	39.565

Table 19.3 Velocity data for Hohmann transfer trajectories. Departure from 185 km circular parking orbit; final parking orbit at 1.1 planet radius

Target Planet	V_e (km/s)	V_1 (km/s)	V_{∞_e} (km/s)	V_t (km/s)	V_2 (km/s)	V_{∞_t} (km/s)	ΔV_0 (km/s)	ΔV_3 (km/s)	$\Delta V_0 + \Delta V_3$ (km/s)
Mercury	29.78	22.25	-7.53	47.87	57.48	9.61	5.56	7.56	13.11
Venus	29.78	27.29	-2.49	35.02	37.73	2.71	3.51	3.26	6.76
Mars	29.78	32.73	2.94	24.13	21.48	-2.65	3.62	2.08	5.70
Jupiter	29.78	38.58	8.79	13.06	7.42	-5.64	6.31	16.98	23.29
Saturn	29.78	40.08	10.29	9.64	4.20	-5.44	7.29	10.36	17.65
Uranus	29.78	41.06	11.28	6.81	2.15	-4.66	7.98	6.51	14.48
Neptune	29.78	41.44	11.65	5.44	1.38	-4.06	8.25	6.90	15.14
Pluto	29.78	41.60	11.81	4.75	1.06	-3.69	8.36	2.68	11.04
Escape from solar system	29.78	42.12	12.34	—	0	—	8.75	0	8.75

Mars, less propellant is required for an escape flight from the solar system than for a 1.1 planet radius orbiter mission.

19.2.2 Launch opportunities

Generally, an interplanetary trajectory (and its hypothetical extension) intersects both the Earth's orbit and the orbit of the target planet twice. This implies that with one heliocentric ellipse with specified values of e and q and a specified orientation, four different missions can be flown (Fig. 19.3). Another four, which would be possible if this ellipse could be traversed in the reverse direction, are practically impossible because of the intolerably large requirements in launch energy. Thus, all interplanetary spacecraft move in the *same direction* about the Sun as the planets.

According to Eq. (16.2-1), the true anomaly, θ , of the spacecraft in its orbit is expressed by

$$\cos \theta = \frac{1}{e} \left(\frac{p}{r} - 1 \right). \quad (19.2-19)$$

Using the Eqs. (19.2-7), the true anomalies at crossing the Earth's orbit and the target planet's orbit are given by

$$\cos \theta_1 = \frac{1}{e} (q - 1), \quad \cos \theta_2 = \frac{1}{e} \left(\frac{q}{n} - 1 \right). \quad (19.2-20)$$

Up to now, we have not examined whether, when the spacecraft crosses the orbit of the target planet, the planet is actually there. This condition, however, specifies the *launch date*. From Fig. 19.2, we note that for a specified interplanetary trajectory, i.e. specified values of n , e , q , θ_1 and θ_2 , the following condition must be satisfied at the time of launch:

$$\psi_1 = \theta_2 - \theta_1 - n_t T, \quad (19.2-21)$$

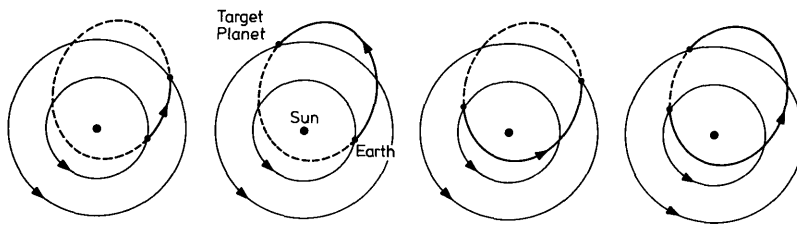


Fig. 19.3 The four types of interplanetary trajectories

where n_t is the orbital angular motion of the target planet and T is the time of flight from the Earth to the target planet. This time of flight can be found from the expressions derived in Section 16.3 for Keplerian trajectories. Thus, the required departure position angle (angular lead) of the target planet, ψ_1 , can be determined. For the arrival position angle, ψ_2 , of the target planet, we find

$$\psi_2 = \theta_2 - \theta_1 - n_e T, \quad (19.2-22)$$

where n_e is the Earth's orbital angular motion.

For a Hohmann trajectory: $\theta_1 = 0$ and $\theta_2 = 180^\circ$, and we obtain

$$\psi_{1_H} = \pi - n_t T_H, \quad \psi_{2_H} = \pi - n_e T_H. \quad (19.2-23)$$

The position angles ψ_{1_H} and ψ_{2_H} are given in Table 19.2.

The angle ψ_2 is an important parameter in the design of interplanetary trajectories. If $\psi_2 \approx 180^\circ$, the Sun will stand in between Earth and target planet when the spacecraft meets the target planet, which may be undesirable. When the spacecraft encounters the target planet, the telecommunication distance, which more or less determines the required spacecraft transmission power for a specified telemetry data rate, is found from

$$D^2 = r_t^2 + r_e^2 - 2r_t r_e \cos \psi_2,$$

or

$$\left(\frac{D}{r_e}\right)^2 = 1 + n^2 - 2n \cos \psi_2. \quad (19.2-24)$$

For a Hohmann transfer, the value of D is also listed in Table 19.2.

Suppose that at a certain epoch t_o , the departure position angle of the target planet is ψ_{1_o} . Owing to the different orbital angular velocities of Earth and target planet, the value of ψ_1 will change with time. After a certain period, the *synodic period*, T_{syn} , the departure position angle will be $\psi_1 = \psi_{1_o} \pm 360^\circ$. At that time the relative positions of Earth, Sun and target planet will be exactly the same as at t_o . As a consequence, it follows that if at t_o a target planet can be reached by a specified interplanetary trajectory, the planet can be reached by a trajectory of identical shape at $t = t_o \pm kT_{syn}$.

where k is any integer. According to Fig. 19.2, we can write

$$\psi_1(t) = \psi_{1o} - n_e(t - t_o) + n_t(t - t_o).$$

For $t - t_o = T_{syn}$, we have $|\psi_1 - \psi_{1o}| = 360^\circ$. Using the relations

$$n_e = \frac{2\pi}{T_e}, \quad n_t = \frac{2\pi}{T_t},$$

where T_e and T_t are the orbital periods of the Earth and the target planet, respectively, we find

$$\frac{1}{T_{syn}} = \left| \frac{1}{T_e} - \frac{1}{T_t} \right|. \quad (19.2-25)$$

For the planets beyond Jupiter: $T_t \gg T_e$, and $T_{syn} \approx 1$ year, which means that we can reach those planets once a year by a Hohmann trajectory. The values of T_{syn} for all planets are given in Table 19.2. We note that Mercury can be reached thrice a year by a Hohmann transfer; for Mars, on the other hand, only once every two years a Hohmann transfer is possible.

We now return to Eq. (19.2-17). For a specified parking orbit we can solve this equation analytically in the form $e = e(q, \frac{\Delta V_0}{V_e})$, and we can draw lines of constant $\Delta V_0/V_e$ in an e - q diagram. Figure 19.1 shows such curves for flyby missions to Mars. As the parameters $\theta_1, \theta_2, \psi_1, \psi_2, D$ and T all depend on e and q , we can also determine analytically the values of these parameters at specific values of q and $\Delta V_0/V_e$. As an example, Fig. 19.4 shows iso-energy contours in a diagram where the flight time, T , is plotted versus the departure position angle, ψ_1 , for a flyby mission to Mars. The parameter ψ_1 can be interpreted as a launch time within a synodic period.

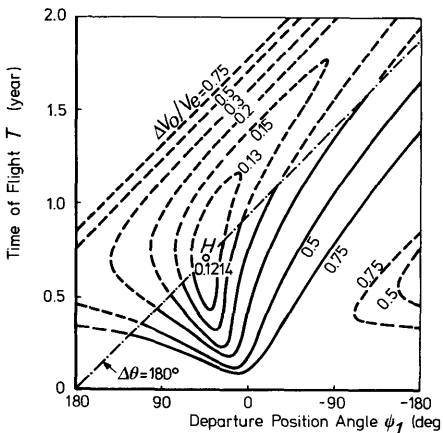


Fig. 19.4 The flight time versus the departure position angle for two-dimensional constant ΔV_0 trajectories to Mars. Initial parking orbit altitude: 185 km

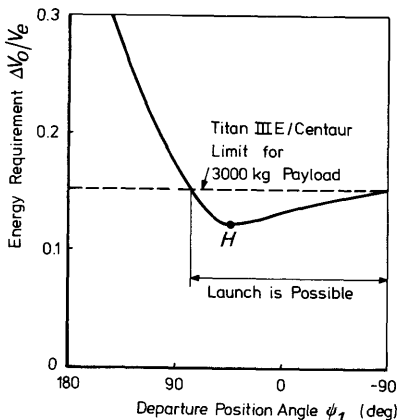


Fig. 19.5 The minimum ΔV_0 requirement versus the departure position angle for two-dimensional trajectories to Mars. Initial parking orbit altitude: 185 km

Also indicated in this figure is the line for which the transfer angle $\Delta\theta = \theta_2 - \theta_1 = 180^\circ$. Trajectories for which $\Delta\theta < 180^\circ$ are called *Type 1 trajectories*. The dashed part of the curves in Fig. 19.4, for which $\Delta\theta > 180^\circ$, represents *Type 2 transfer trajectories* [5]. From such diagrams, we can determine the minimum energy requirement if the launch takes place at a specific value of ψ_1 . This minimum energy requirement for a (hypothetical) two-dimensional Mars flyby mission is plotted in Fig. 19.5. If the spacecraft mass and the launch vehicle used are known, the maximum ΔV_0 which can be provided for by the launch vehicle is fixed. This value determines the period during which the launch vehicle can inject that spacecraft into a trajectory to the target planet. To illustrate this, in Fig. 19.5 a line is drawn representing the ΔV_0 limit for a Titan III E/Centaur launch vehicle (Fig. 17.4) and a 3000 kg spacecraft.

19.2.3 Fast interplanetary trajectories

If a spacecraft is accelerated from the initial parking orbit to a velocity larger than that required for a Hohmann transfer, the flight time may be reduced considerably. All trajectories which start tangentially to the Earth's orbit lie on the line $q = 1 + e$ in Fig. 19.1. All trajectories which intersect the Earth's orbit, but are tangential to the target planet's orbit lie on the line $q = n(1 - e)$. For all other fast interplanetary trajectories, we have $\gamma_1 \neq 0$, $\gamma_2 \neq 0$. So, we note from Fig. 19.1 that there exist hyperbolic trajectories tangential to the Earth's orbit which require less propellant than certain elliptic trajectories tangential to the target planet's orbit. A detailed analysis of many types of two-dimensional interplanetary trajectories is presented by Ehricke [6].

As a characteristic type of two-dimensional fast interplanetary trajectories,

we will discuss those trajectories for which $\gamma_1 = 0$. For these trajectories, we have

$$e = q - 1. \quad (19.2-26)$$

Substituting Eq. (19.2-26) into Eq. (19.2-12), we obtain

$$q = \frac{V_1^2}{V_e^2}. \quad (19.2-27)$$

So, q may be considered as a yardstick for departure velocity. The trajectory parameters V_{∞_e} , V_{∞_i} , γ_2 , V_2 , θ_2 can be obtained as a function of q from Eqs. (19.2-13), (19.2-14), (19.2-16), (19.2-20) by substituting Eq. (19.2-26) for e . We then obtain

$$\frac{V_2}{V_e} = \sqrt{q - 2 + \frac{2}{n}}, \quad (19.2-28)$$

$$\cos \gamma_2 = \frac{q/n}{\sqrt{q^2 - 2q(1 - 1/n)}}, \quad (19.2-29)$$

$$\frac{V_{\infty_e}}{V_e} = \sqrt{q - 1}, \quad (19.2-30)$$

$$\frac{V_{\infty_i}}{V_e} = \sqrt{q + \frac{3 - 2\sqrt{q/n}}{n} - 2}, \quad (19.2-31)$$

$$\cos \theta_2 = \frac{q/n - 1}{q - 1}. \quad (19.2-32)$$

The time of flight for an elliptic, parabolic or hyperbolic trajectory can be computed from the time-equations derived in Section 16.3.

As an example, Fig. 19.6 shows the dependence of e , θ_2 , V_3 , T , ψ_1 and D on the initial velocity increment, ΔV_0 , for such flyby trajectories to Mars and Jupiter. The parameter V_3 denotes the spacecraft's planetocentric velocity at the pericenter of the flyby trajectory. It was assumed that the flight starts from a 185-km circular Earth parking orbit, and that the pericenter of the hyperbolic encounter trajectory is at a distance of 2 planet radii. An important conclusion which can be drawn from this figure is that a relatively small increment in ΔV_0 , above the value required for a Hohmann transfer, results in a strong decrease in T and θ_2 , but in an important increase in V_3 . Thus, for orbiter missions, fast trajectories require a heavy propulsion system to decelerate the spacecraft at arrival, thereby reducing the payload capability. It is the limitations of the current space transportation vehicles that preclude really fast trajectories, in particular to the outer planets. From Fig. 17.5, we see that for a payload mass in the order of 100 to 1000 kg, a launch vehicle characteristic velocity of about 16 km/s is an upper limit for most launch vehicles. This limits ΔV_0 to about 8 km/s. From Table 19.3, we note

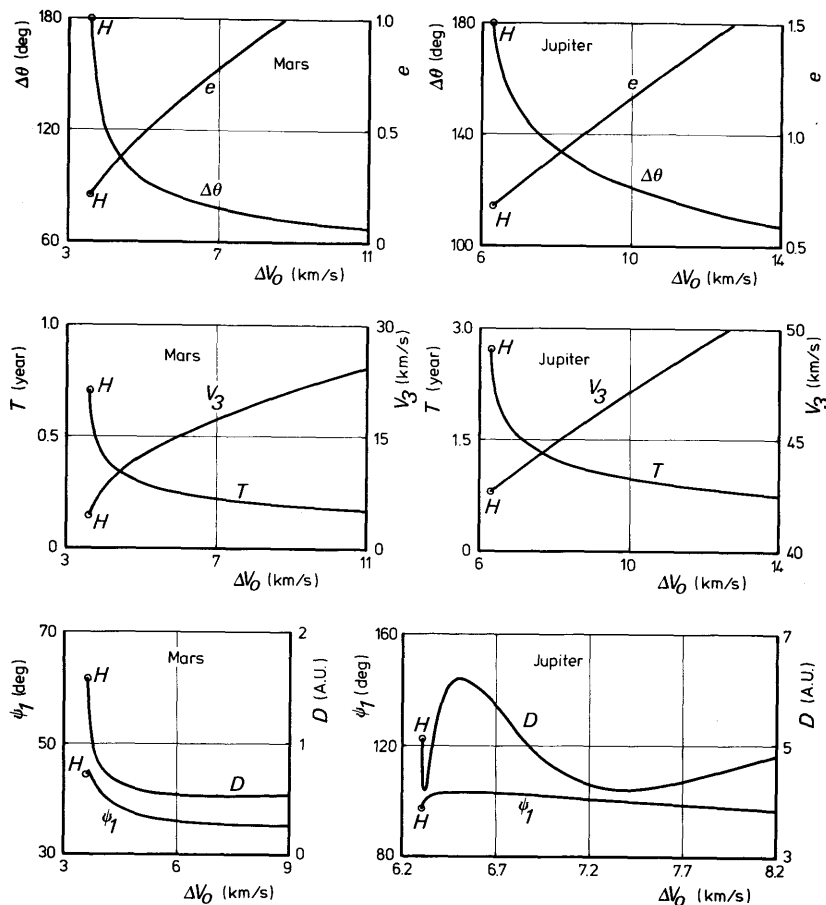


Fig. 19.6 Some parameters of two-dimensional trajectories with $\gamma_1 = 0$ to Mars and Jupiter versus ΔV_0 . Initial parking orbit altitude: 185 km. Minimum flyby distance: 2 planet radii

that even a Hohmann transfer to Saturn requires a velocity increment of 7.3 km/s, which is an indication of the limited excess available for faster missions.

19.3 Three-dimensional interplanetary trajectories

Though the eccentricity and inclination of all planetary orbits are rather small, their effects on interplanetary missions, and in particular on the energy requirements, can be considerable [7, 8]. The analysis of the *three-dimensional interplanetary trajectories* is much more elaborate than for the simplified two-dimensional case. We will only outline a basic scheme for such analysis [6, 7, 9] and discuss some results.

450 Rocket Propulsion & Spaceflight Dynamics

It is supposed that the basic variables in the computation process are the time of departure from the Earth, t_1 , and the flight time, T . Then, the time of arrival at the target planet, t_2 , is known. At t_1 , the coordinates of the Earth relative to a non-rotating heliocentric ecliptic reference frame are known too. These may, for instance, be obtained from handbooks [10], or be computed approximately by using the Earth's mean orbital elements. The heliocentric ecliptic coordinates of the target planet at t_2 can be found in the same way.

The heliocentric transfer trajectory of the spacecraft lies, excluding *mid-course plane changes*, in the plane through the Sun, the Earth at time of departure, and the target planet at time of arrival. The heliocentric transfer angle, $\Delta\theta$, covered by the spacecraft can be found from

$$\cos \Delta\theta = \frac{\mathbf{r}_e \cdot \mathbf{r}_t}{r_e r_t}, \quad (19.3-1)$$

where \mathbf{r}_e and \mathbf{r}_t are the heliocentric position vectors of the Earth at departure and the target planet on arrival. The value of $\Delta\theta$ can be determined uniquely by realizing that $\sin \Delta\theta$ must have the same sign as $(\mathbf{r}_e \times \mathbf{r}_t) \cdot \mathbf{e}_Z$, where \mathbf{e}_Z is the unit vector along the Z -axis; i.e. pointing to the ecliptic north pole. The chord, c , joining Earth at departure and target planet on arrival is found from

$$c^2 = r_t^2 + r_e^2 - 2r_t r_e \cos \Delta\theta. \quad (19.3-2)$$

Now that the lengths of the radii r_e and r_t , and the chord c are known, *Lambert's equation*, Section 13.2.5, can be solved iteratively for the specified flight time to yield the semi-major axis, a , of the trajectory. The heliocentric velocities V_1 and V_2 then can be computed from

$$V_1 = \sqrt{\mu_s \left(\frac{2}{r_e} - \frac{1}{a} \right)}, \quad V_2 = \sqrt{\mu_s \left(\frac{2}{r_t} - \frac{1}{a} \right)}. \quad (19.3-3)$$

The computation of the flight path angles, γ_1 and γ_2 , comes down to a geometrical problem. Using relations from analytical geometry, we can express these angles in terms of the known quantities r_e , r_t , c , a [7]. We now may proceed to compute the semi-latus rectum of the interplanetary trajectory

$$p = \frac{(r_e V_1 \cos \gamma_1)^2}{\mu_s}. \quad (19.3-4)$$

The eccentricity can be obtained from

$$e = \sqrt{1 - \frac{p}{a}}. \quad (19.3-5)$$

The heliocentric true anomaly at time of departure from the Earth follows

from

$$\theta_1 = \arccos \left\{ \frac{1}{e} \left(\frac{p}{r_e} - 1 \right) \right\}. \quad (19.3-6)$$

The value of θ_1 is uniquely determined as for $0 \leq \theta_1 \leq 180^\circ: \gamma_1 \geq 0$, and for $180^\circ \leq \theta \leq 360^\circ: \gamma_1 \leq 0$. The heliocentric true anomaly on arrival is found from

$$\theta_2 = \theta_1 + \Delta\theta. \quad (19.3-7)$$

The inclination of the trajectory with respect to the ecliptic is found from

$$\cos i = \mathbf{e}_W \cdot \mathbf{e}_Z, \quad (19.3-8)$$

where \mathbf{e}_W is the unit vector normal to the orbital plane:

$$\mathbf{e}_W = \frac{\mathbf{r}_e \times \mathbf{r}_t}{r_e r_t \sin \Delta\theta}. \quad (19.3-9)$$

The hyperbolic excess velocities, \mathbf{V}_{∞_e} and \mathbf{V}_{∞_t} , finally, are given by

$$\mathbf{V}_{\infty_e} = \mathbf{V}_1 - \mathbf{V}_e, \quad \mathbf{V}_{\infty_t} = \mathbf{V}_2 - \mathbf{V}_t, \quad (19.3-10)$$

where \mathbf{V}_e is the Earth's heliocentric velocity at departure and \mathbf{V}_t the target planet's heliocentric velocity on arrival.

A very instructive discussion on the effects of the eccentricity and inclination of the planetary orbits is given by Breakwell [7], from which Fig. 19.7 is taken. He considers a flyby mission to Mars and presents contours of constant departure hyperbolic excess velocity, V_{∞_e} , as a function of launch

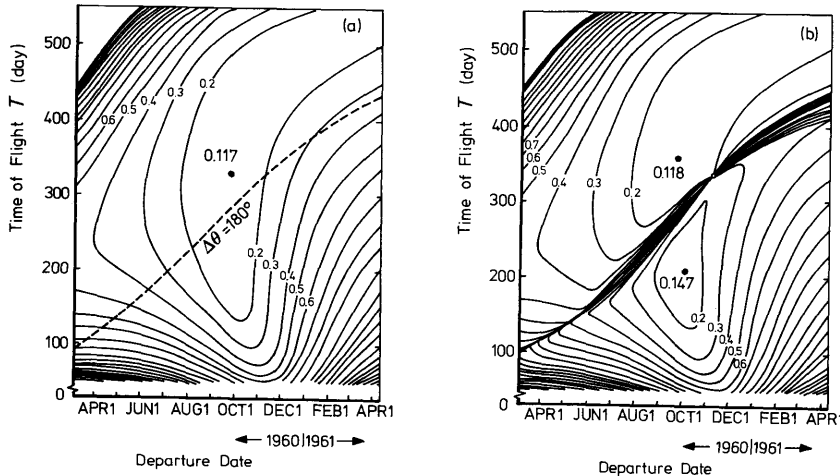


Fig. 19.7 Contours of constant departure hyperbolic excess velocity for flyby missions to Mars. (a) Co-planar, elliptical planetary orbits; (b) Mutual inclined, elliptical planetary orbits (Reference [7]). Values at the curves are for the ratio V_{∞_e}/V_e .

date and flight time. For the circular co-planar case, he obtains curves similar to Fig. 19.4, where the optimum transfer is a Hohmann transfer. Introducing the planetary orbit eccentricities, the minimum departure speed trajectory for that period now involves a transfer angle $\Delta\theta = 210^\circ$ and a longer flight time. After introducing also the planetary orbit inclinations, we see in Fig. 19.7b that the original Hohmann point has bifurcated into two local minimum trajectories with two different flight times. The two groups of closed contours represent the Type 1 and Type 2 trajectories. We also note that two trajectories usually exist for a given type, V_∞ , and launch date. Trajectories corresponding to the lower portions of each contour are designated as *Class 1 trajectories* and yield shorter flight times and smaller transfer angles; trajectories corresponding to the upper part of the contours are designated as *Class 2 trajectories* [5]. For a given launch date and V_∞ , the Type-1 Class-1 trajectory has the shortest flight time and the Type-2 Class-2 trajectory has the longest flight time.

Lee [11] gives a survey on the characteristics of Mars missions. Numerous data on various interplanetary trajectories can be found in the Space Flight Handbook [12]. In Fig. 19.8, the *mission characteristic velocity*, V_{char}^* (Section 17.3) for minimum energy trajectories to Mars and Venus within the period 1975 to 1990 is shown. For each launch opportunity, the minimum velocity requirement and the characteristic velocity for a 30-day *launch window* [14] are indicated. Also plotted are the Hohmann values as obtained from the co-planar circular planetary orbit model.

If the heliocentric transfer angle is about 180° , the plane determined by the Sun, the Earth and the target planet will, generally, be highly inclined to the ecliptic. This implies excessively high values of ΔV_0 , and for orbiter missions also a high ΔV_3 . These problems could be circumvented by applying *midcourse plane changes* [15]. Usually, these near- 180° transfer angle trajectories are avoided for a number of operational aspects, and midcourse corrections are only executed to eliminate trajectory errors and to guarantee the planetary encounter to be as accurate as possible.

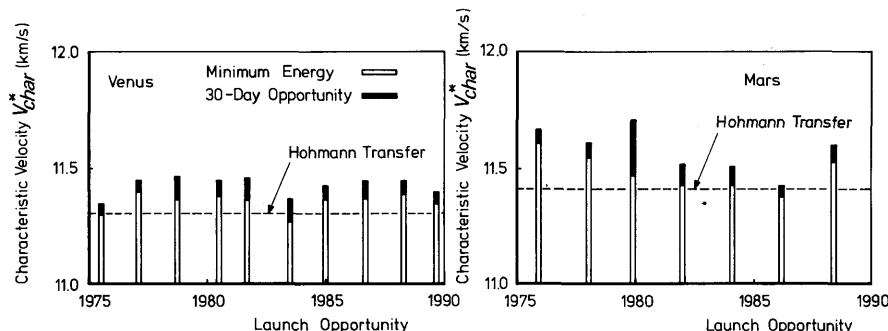


Fig. 19.8 Mission characteristic velocity requirements for flights to Venus and Mars (Reference [13])

19.4 The launch of interplanetary spacecraft

For a specified launch date and interplanetary trajectory, the departure excess velocity, \mathbf{V}_∞ , is known relative to a heliocentric reference frame. Implicit in the method outlined in Section 19.3 is that \mathbf{V}_∞ is considered to be a vector passing through the center of the Earth. By applying the usual transformation relations, we can find \mathbf{V}_∞ with respect to a non-rotating geocentric equatorial reference frame. This determines the direction of the *outgoing radial*. Because the radius of the Earth's sphere of influence is very large as compared to the radius of the Earth, for a discussion on suitable escape trajectories we may assume the *outgoing asymptote* of an escape hyperbola to coincide with the outgoing radial [11]. The required declination, δ_{as} , and right ascension, α_{as} , of this outgoing asymptote strongly influence the selection of the ascent trajectory to be flown [16].

In order to prevent excessive *dog-leg maneuvers* prior to injection, the launch vehicle ascent trajectory should lie preferably in the plane of the escape hyperbola. Then, the plane in which the motion within the sphere of influence of the Earth takes place is uniquely determined by the center of the Earth, the launch site and the outgoing asymptote. All American (and European) interplanetary missions start from Cape Canaveral. For this launch site, a launch azimuth range from 90° to 115° is most desirable [17] for interplanetary missions to take full advantage of the Earth's eastward rotational velocity and of existing tracking facilities.

According to Eq. (16.6-24), we may write

$$\cos i = \cos \delta_l \sin \psi_l = \cos \delta_{as} \sin \psi_{as}$$

or

$$\sin^2 \psi_l \leq \frac{\cos^2 \delta_{as}}{\cos^2 \delta_l}, \quad (19.4-1)$$

where ψ denotes the flight path azimuth and the index l refers to the launch conditions. From Fig. 19.9, where this inequality is plotted for a launch from Cape Canaveral ($\delta_l = 28.5^\circ$), we note that there exists a range of launch azimuths, symmetrical about due east, at which it is not possible to launch without dog-leg maneuvers. Permissible values of the asymptotic declination lie within the range -35° to 35° .

For a specific value of δ_l , we may compute from Eqs. (16.6-24) to (16.6-26) the dependence of δ_{as} and ψ_l on the difference in right ascension $\alpha_{as} - \alpha_l$. These results are depicted in Fig. 19.10 for a launch from Cape Canaveral. The shaded areas represent the range of preferable launch azimuths. During a given launch day, \mathbf{V}_∞ is, for a specified interplanetary mission, almost independent of the location of the launch site and the time of launch. Owing to the rotation of the Earth, α_l , however, varies linearly with launch time:

$$\alpha_l = H_{G_0} + \Lambda_l + \omega_e t_l, \quad (19.4-2)$$

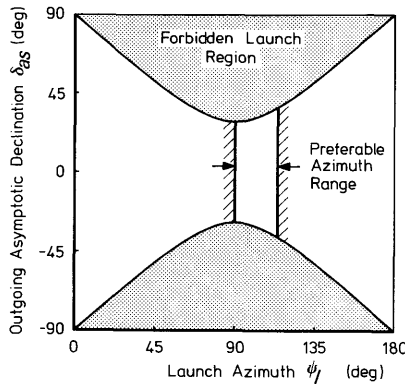


Fig. 19.9 Permissible region of the declination of the outgoing asymptote for Cape Canaveral launchings

where H_{G_0} is the Greenwich hour angle of the vernal equinox at 0 hours U.T. of the launch day, Λ_l is the geographic longitude of the launch site, ω_e is the angular velocity of the Earth and t_l is the time from midnight on the launch day (U.T.). Therefore, the time of launch is determined solely by ψ_l , δ_{as} and α_{as} . We note from Fig. 19.10 that, generally, for one specific $\mathbf{V}_{\infty e}$ and an assumed launch azimuth, two launch times may be possible each day.

Usually, a parking orbit *coast-period* is required to match the launch vehicle ascent trajectory and the hyperbolic escape trajectory. The launch vehicle ascent trajectory is chosen such that, within the constraints for that vehicle, a maximum payload can be placed in the parking orbit. This ascent trajectory determines the altitude of the parking orbit and the angular

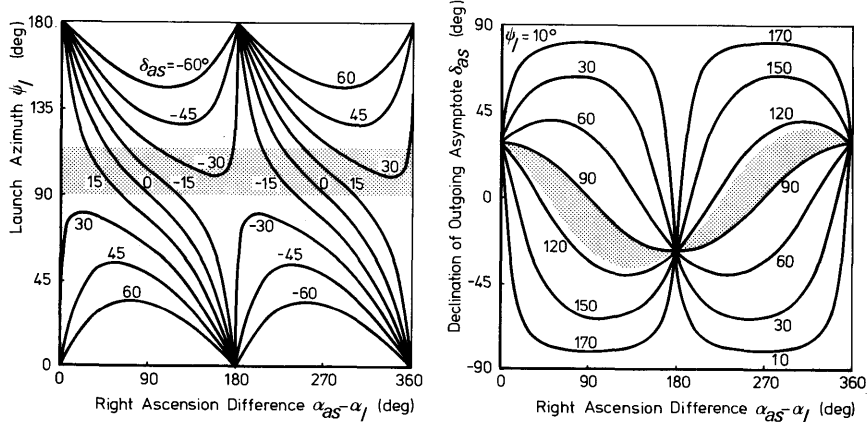


Fig. 19.10 Launch azimuth and right ascension of the launch site versus declination and right ascension of the outgoing asymptote for Cape Canaveral launchings

position where the spacecraft enters the parking orbit. To maximize the payload which can be injected into the escape trajectory, the final injection should take place near perigee of the escape hyperbola. For a fixed V_{∞} , the location in the parking orbit of this injection point is fully determined. Thus, the spacecraft coasts in its parking orbit until it reaches the point where the final burn is executed (Fig. 19.11). We found that, often, two launch times are possible each day. The required parking orbit coast-period and the location of the final injection point relative to the Earth's surface differ for these two cases. The launch time yielding the more favorable launch conditions will be selected.

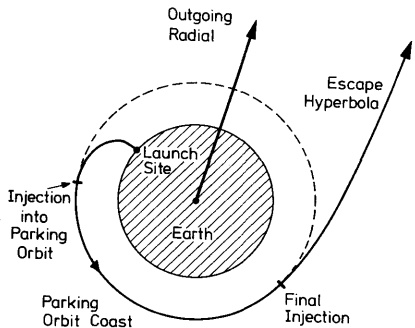


Fig. 19.11 The matching of ascent trajectory, coasting phase and escape hyperbola

From the viewpoint of launch vehicle reliability, tracking and telemetry coverage, a *direct ascent flight* of the launch vehicle is very attractive. However, such an ascent flight can only be used if at the end of the powered phase, the launch vehicle can inject the spacecraft near perigee of a hyperbola satisfying the prescribed direction of the outgoing asymptote. Generally, it is found that a combination of a northeast launch and an outward radial declination of less than -15° result in feasible direct ascent trajectories [18].

For a specified interplanetary trajectory, there will be one moment for which the launch of a spacecraft requires a minimum amount of propellant. But because of the complexity of both launch vehicle and spacecraft, a launch exactly at that optimum moment is most unlikely, and an adequate firing window must be available around the optimum instant of time: the *daily launch window*. Generally, a launch window of about 1 hour is required. As launch time is varied within this launch window, both launch azimuth and parking orbit coast-time must be altered continuously.

19.5 Trajectory about the target planet

For the trajectory of the spacecraft near the target planet, again the sphere of influence concept may be used. Having specified a launch date and a flight

time from Earth to the target planet, the spacecraft's hyperbolic excess velocity with respect to the target planet, \mathbf{V}_{∞} , is fixed. The state vector of the spacecraft on entering into the planet's sphere of influence is now completely determined if the *impact parameter*, \mathbf{B} , is specified. To define this impact parameter, we first introduce a non-rotating planetocentric coordinate system *RST* (Fig. 19.12). The *S*-axis is parallel to the incoming asymptote of the approach hyperbola; its positive direction is in the direction of \mathbf{V}_{∞} . The *T*-axis is parallel to the ecliptic plane; its positive direction is defined by

$$\mathbf{e}_T = \frac{\mathbf{e}_S \times \mathbf{e}_N}{|\mathbf{e}_S \times \mathbf{e}_N|},$$

where \mathbf{e}_S and \mathbf{e}_T are the unit vectors along the *S*- and *T*-axes, and \mathbf{e}_N is the unit vector pointing towards the ecliptic north pole. The *R*-axis completes the right-handed orthogonal coordinate frame. The vector \mathbf{B} , which specifies the *aiming point*, is a vector from the center of the planet to the point at which the incoming asymptote pierces the *RT*-plane. Usually, the aiming point is defined by the two components $\mathbf{B} \cdot \mathbf{e}_T$ and $\mathbf{B} \cdot \mathbf{e}_R$. It is spacecraft engineering requirements and scientific experiment considerations which impose numerous constraints on the selection of the aiming point. Once the aiming point is selected, it is the goal of the midcourse maneuvers to nullify any error in the trajectory such that the requirements on \mathbf{B} are satisfied. For this, an accurate *tracking* of the spacecraft during its interplanetary flight is indispensable.

The plane of the planetocentric hyperbola is determined by \mathbf{B} and \mathbf{V}_{∞} . We now consider the motion of the spacecraft in this plane. This motion is illustrated in Fig. 19.13. The velocity \mathbf{V}'_t indicated in this figure is the projection of the target planet's heliocentric velocity vector on this plane. It is important to realize that $|\mathbf{V}'_t| = |\mathbf{V}_{\infty}|$.

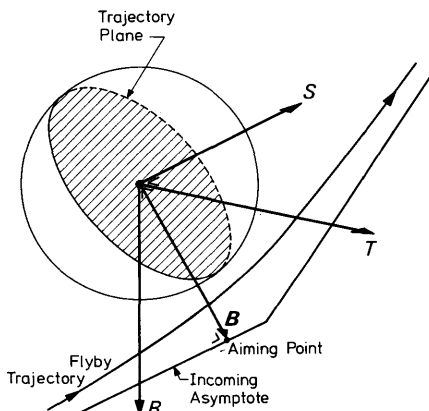


Fig. 19.12 Encounter geometry and aiming point coordinate system

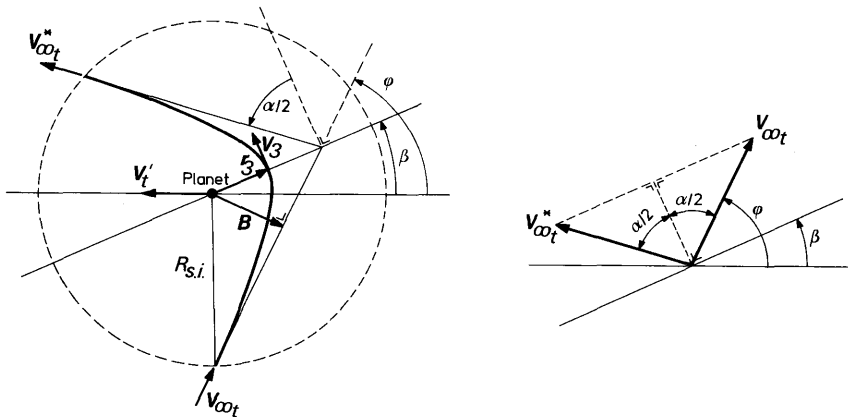


Fig. 19.13 The in-plane geometry of hyperbolic encounter trajectories

As the angular momentum per unit mass, \mathbf{H} , is a constant of motion, we have

$$BV_{\infty_i} = r_3 V_3, \quad (19.5-1)$$

where the index 3 refers to the pericenter of the trajectory. With Eq. (16.2-17), we obtain from Eq. (19.5-1) for the minimum distance, r_3 :

$$r_3 = -\frac{\mu_t}{V_{\infty_i}^2} + \sqrt{\frac{\mu_t^2}{V_{\infty_i}^4} + B^2}. \quad (19.5-2)$$

As the trajectory is a hyperbola, we can easily derive from Eq. (19.2-19):

$$\cos\left(\frac{\pi}{2} + \frac{\alpha}{2}\right) = -\frac{1}{e}. \quad (19.5-3)$$

With Eq. (16.2-16) and the geometrical relations for conic sections, we obtain from Eq. (19.5-3) for the *asymptotic deflection angle*, α :

$$\sin\frac{\alpha}{2} = \frac{1}{1 + \frac{r_3 V_{\infty_i}^2}{\mu_t}} = \frac{1}{\sqrt{1 + \frac{B^2 V_{\infty_i}^4}{\mu_t^2}}}. \quad (19.5-4)$$

The angle β , finally, follows from

$$\beta = \varphi + \frac{\alpha}{2} + \frac{\pi}{2}. \quad (19.5-5)$$

If the radius r_3 is equal to or less than the planet's radius, R , the spacecraft will *impact* on the planet's surface. According to Eq. (19.5-2), the condition

for impact is

$$\sqrt{1 + \frac{B^2 V_{\infty_i}^4}{\mu_t^2}} \leq \frac{V_{\infty_i}^2 R}{\mu_t} + 1,$$

or, with the expression for the escape velocity at the planet's surface, $V_{esc_s} = \sqrt{2\mu_t/R}$,

$$B \leq R \sqrt{1 + \frac{V_{esc_s}^2}{V_{\infty_i}^2}}. \quad (19.5-6)$$

The expression on the right-hand side of Eq. (19.5-6) determines for each value of V_{∞_i} , the so-called *capture radius*, R_{cap} . When the incoming asymptote crosses a sphere with radius R_{cap} around the planet, the spacecraft will impact somewhere on the planet. The exact impact location is, for a specific V_{∞_i} , still dependent on B . Figure 19.14 shows for an encounter with Jupiter the minimum distance, r_3 , and the deflection angle, α , as a function of B and V_{∞_i} . At any specified value of V_{∞_i} , the maximum deflection angle, α_{max} , will be reached for $r_3 = R$. The values of α_{max} for some planets are plotted in Fig. 19.15a versus V_{∞_i} . This figure clearly reveals that α_{max} is larger for planets of larger mass, and that α_{max} increases with decreasing V_{∞_i} .

From Fig. 19.13, we note that the heliocentric velocity at leaving the sphere of influence is different from the heliocentric velocity at entering this sphere. This yields the possibility to use a planet's gravitational field to increase (or decrease) the spacecraft's *total heliocentric energy*, \mathcal{E} . Such an energy increase can be applied to increase the spacecraft's heliocentric velocity such that the flight time to a more distant planet can be reduced, or to put the spacecraft into a heliocentric trajectory which was originally beyond the capabilities of the launch vehicle. If gravitational fields are intentionally used to shape interplanetary trajectories, we speak of *swingby flights* [19, 20].

As the dimensions of the sphere of influence can be neglected on interplanetary scale, the change of the spacecraft's total heliocentric energy per unit mass can be written as

$$\Delta \mathcal{E} = \frac{1}{2}(V_4^2 - V_2^2) = \frac{1}{2}(\mathbf{V}_4 + \mathbf{V}_2) \cdot (\mathbf{V}_4 - \mathbf{V}_2), \quad (19.5-7)$$

where \mathbf{V}_4 is the spacecraft's heliocentric velocity at leaving the sphere of influence. With $\mathbf{V}_2 = \mathbf{V}_t + \mathbf{V}_{\infty_i}$, $\mathbf{V}_4 = \mathbf{V}_t + \mathbf{V}_{\infty_i}^*$, Eq. (19.5-7) can be written as

$$\Delta \mathcal{E} = \mathbf{V}_t' \cdot (\mathbf{V}_{\infty_i}^* - \mathbf{V}_{\infty_i}), \quad (19.5-8)$$

or, according to the velocity diagram in Fig. 19.13,

$$\Delta \mathcal{E} = 2V_t' V_{\infty_i} \sin \frac{\alpha}{2} \cos \beta. \quad (19.5-9)$$

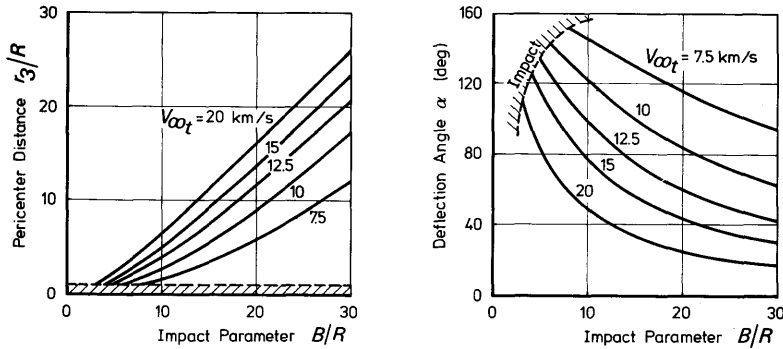


Fig. 19.14 The radius of closest approach and the asymptotic deflection angle for Jupiter flyby missions

Substituting Eq. (19.5-4) into Eq. (19.5-9), we obtain

$$\Delta \mathcal{E} = \frac{2V'_t V_{\infty t} \cos \beta}{\sqrt{1 + \frac{B^2 V_{\infty t}^4}{\mu_t^2}}} \quad (19.5-10)$$

We note that the value of $\Delta \mathcal{E}$ increases if both V'_t and μ_t increase.

For a particular planet, the value of $\Delta \mathcal{E}$ depends on the independent trajectory parameters $V_{\infty t}$, β and B . For a specified value of $V_{\infty t}$, the spacecraft will experience a maximum increase of \mathcal{E} , if $\beta = 0$ and B takes its minimum value. Substituting for this minimum value of B from Eq. (19.5-6), we finally obtain

$$\Delta \mathcal{E}_{max} = \frac{2V'_t V_{\infty t}}{1 + \frac{RV_{\infty t}^2}{\mu}} \quad (19.5-11)$$

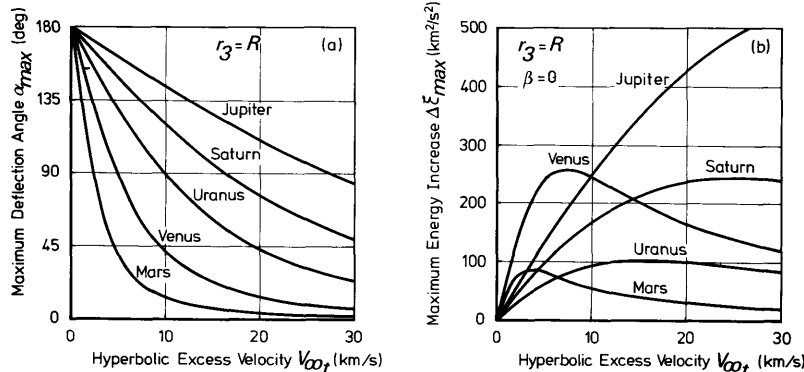


Fig. 19.15 The maximum asymptotic deflection angle (a) and the maximum heliocentric energy increase (b) for planetary flyby missions. Assumptions for (b): circular planetary orbit and $V_t = V_{\infty t}$

For some planets, this relation is plotted in Fig. 19.15b versus V_{∞} . For flights to Mercury, Venus is an attractive swingby planet; for missions to the outer planets, Mars is unattractive but Jupiter is capable of increasing \mathcal{E} considerably. For the actual computation of interplanetary swingby trajectories, the arrival conditions at the swingby planet have to be chosen such that for a given launch date the spacecraft will meet the (final) target planet after the specified flight time.

Sometimes, the configuration of a number of planets is such that it is possible to apply a *multiple swingby technique* where more gravitational fields are used to shape the spacecraft's trajectory [21]. The first spacecraft which intentionally used this swingby technique were Mariner 10 to Venus and Mercury, and Pioneer 11 to Jupiter and Saturn. Undoubtedly, this very attractive technique will be applied to many more interplanetary missions.

References

- 1 Moeckel, W. E. (1972), *Comparison of Advanced Propulsion Concepts for Deep Space Exploration*, NASA TN D-6968, Washington.
- 2 Willis, E. A. (1966), *Finite-Thrust Escape from and Capture into Circular and Elliptic Orbits*, NASA TN D-3606, Washington.
- 3 Vertregt, M. (1958), Interplanetary orbits, *J. Brit. Interplanet. Soc.*, **16**, 326–354.
- 4 Hohmann, W. (1925), *Die Erreichbarkeit der Himmelskörper*, Oldenbourg, Berlin, p. 63–75. Also: (1960), NASA TT F-44, Washington.
- 5 Clarke, V. C., Bollman, W. E., Feitis, P. H. and Roth, R. Y. (1963), *Design Parameters for Ballistic Interplanetary Trajectories*, JPL TR 32-77, Pasadena.
- 6 Ehricke, K. A. (1962), *Space Flight, Vol. 2: Dynamics*, Van Nostrand, Princeton, p. 984–1070.
- 7 Breakwell, J. V., Gillespie, R. W. and Ross, S. (1961), Researches in interplanetary transfer, *A.R.S.J.*, **31**, 201–208.
- 8 Gravier, J., Marchal, C. and Culp, R. D. (1973), Effects of inclination and eccentricity on optimal trajectories between Earth and Venus, *Astron. Acta*, **18**, 273–279.
- 9 Battin, R. H. (1959), The determination of round-trip planetary reconnaissance trajectories, *J. Aero/Space Sciences*, **26**, 545–567.
- 10 Anon., *The Astronomical Ephemeris*, H.M.S.O., London, new Volume appears every year.
- 11 Lee, V. A. and Wilson, S. W. (1967), A survey of ballistic Mars-mission profiles, *J. Spacecraft*, **4**, 129–142.
- 12 Anon., *Space Flight Handbook, Vol III: Planetary Flight Handbook*, NASA SP-35, Washington, many Parts published since 1963.
- 13 McGolrick, J. E. (1973), *Launch Vehicle Estimating Factors for Advance Mission Planning*, NHB 7100.5B, NASA, Washington.

- 14 Young, A. C. and Odom, P. R. (1967), *A Computer Simulation of the Orbital Launch Window Problem*, AIAA Paper 67-615, New York.
- 15 Fimple, W. R. (1963), Optimum midcourse plane changes for ballistic interplanetary trajectories, *AIAA J.*, **1**, 430-434.
- 16 Moeckel, W. E. (1959), *Departure Trajectories for Interplanetary Vehicles*, NASA TN D-80, Washington.
- 17 Bollman, W. E. (1963), *The Engineering Design of Interplanetary Ballistic Trajectories*, AIAA Paper 63-414, New York.
- 18 Clarke, V. C. (1963), Design of lunar and interplanetary ascent trajectories, *AIAA J.*, **1**, 1559-1567.
- 19 Flandro, G. A. (1966), Fast reconnaissance missions to the outer solar system utilizing energy derived from the gravitational field of Jupiter, *Astron. Acta*, **12**, 329-337.
- 20 Deerwester, J. M. (1969), *Jupiter Swingby Missions to Non-Specific Locations in Interplanetary Space*, NASA TN D-5271, Washington.
- 21 Bourke, R. D., Friedman, L. D., Penzo, P. A. and Stavro, W. (1971), *Design of Grand Tour Missions*, AIAA Paper 71-187, New York.

20 Low-Thrust Trajectories

All current space transportation systems use *chemical rocket engines*. In these propulsion systems, the propulsive energy source is contained in the propellant itself. A very important performance parameter of these systems is the effective exhaust velocity, c , which is even for the most energetic propellant combinations limited to about 5 to 6 km/s. There are, however, other types of propulsion systems feasible. One of them is the *electric propulsion system*, where electrically charged particles are accelerated by electric or magnetic fields. A survey of the various types of electric thrusters is given by Au [1] and Clark [2]. A number of electric thruster concepts have been developed during the last twenty years to a level where they can be applied to a variety of space missions [3]. Many thrusters have already flown successfully in space. Though, until now, electric motors have been mainly used for attitude control of satellites and orbit correction purposes, they will in the future undoubtedly be used as a primary propulsion system for spacecraft. Unlike the chemical systems, an electric propulsion system includes a separate power source and power conversion unit to impart the kinetic energy to the propellant. This power plant, which may comprise a solid-core nuclear-fission reactor or a large solar array, adds considerably to the burnout mass of the spacecraft, reducing the payload capability of the vehicle. Nevertheless, for certain space missions electric propulsion systems are superior to the chemical ones, due to the fact that the exhaust velocity of electric systems is much higher than that of chemical motors.

In this chapter, we will deal with the application of electric thrusters to the propulsion of interplanetary spacecraft. We will restrict ourselves, and mainly discuss the escape flight from the Earth's gravitational field. It should be realized, however, that the same methods can be applied to the computation of escape flights from other planets. For a detailed discussion on many aspects of low-thrust trajectories the reader is referred to Ehricke's standard work [4].

When designing an electric spacecraft for a particular interplanetary mission, a maximum payload capability is usually required for a specified flight time. We thus want to minimize the combined mass of propellant and power plant. An extensive discussion on the details of such an optimization process is given by Stuhlinger [5]. Here, we only mention that for each mission and flight time, an optimum history for the thrust and the exhaust velocity results. It then appears [5, 6] that for electric propulsion systems, the optimum values of thrust, F , per initial mass, M_0 , and effective exhaust

velocity, c , usually lie within the range:

$$\frac{F}{M_0} = 10^{-4} - 10^{-2} \text{ m/s}^2, \quad c = 50 - 150 \text{ km/s}.$$

The electrical power requirement may vary from 10 kW to 10 MW. The propellant mass flow will be in the range $m = 0.01 - 5 \text{ g/s}$. We note, that the magnitudes of specific thrust, effective exhaust velocity and mass flow are entirely different from those for the chemical propulsion systems.

As a direct consequence of the low thrust-to-mass ratio, electric propulsion cannot be used to launch a vehicle from the Earth's surface, nor will be useful if appreciable atmospheric drag is encountered. But if an electrically propelled stage is launched into a parking orbit about the Earth, even a minute thrust will force the vehicle to recede gradually from the parking orbit. Because the low thrust can be maintained for a considerable period of time, electrically propelled vehicles are capable of attaining very high velocities.

20.1 Equations of motion

Consider the motion of a spacecraft relative to a non-rotating geocentric equatorial reference frame. We approximate the gravitational field of the Earth by an inverse-square force field and assume that, apart from the gravitational attraction, the thrust, \mathbf{F} , is the only force acting on the spacecraft. If the instantaneous mass of the spacecraft is denoted by M , the equation of motion for the vehicle can be written as

$$\frac{d^2\mathbf{r}}{dt^2} + \frac{\mu}{r^3} \mathbf{r} = \frac{\mathbf{F}}{M}, \quad (20.1-1)$$

where μ is the gravitation parameter of the Earth and \mathbf{r} is the position vector of the spacecraft.

Vectorial multiplication of Eq. (20.1-1) by \mathbf{r} leads to (see Section 3.6.1)

$$\frac{d\mathbf{H}}{dt} = \mathbf{r} \times \mathbf{a}, \quad (20.1-2)$$

where \mathbf{H} is the (orbital) angular momentum per unit mass, and \mathbf{a} is the *thrust acceleration*, defined as

$$\mathbf{a} = \frac{\mathbf{F}}{M}. \quad (20.1-3)$$

Scalar multiplication of Eq. (20.1-1) by \mathbf{V} yields

$$\frac{d\mathcal{E}}{dt} = \mathbf{V} \cdot \mathbf{a}, \quad (20.1-4)$$

where \mathcal{E} is the total energy per unit mass,

$$\mathcal{E} = \frac{1}{2} V^2 - \frac{\mu}{r}. \quad (20.1-5)$$

We further assume that the thrust is acting continuously in the original plane of motion. In that case, the motion is *two-dimensional*. Using the flight path angle, γ , and the *thrust angle*, δ , as defined in Fig. 20.1, Eqs. (20.1-2) and (20.1-4) can be written as

$$\frac{dH}{dt} = ar \cos \delta, \quad (20.1-6a)$$

$$\frac{d\mathcal{E}}{dt} = aV \cos(\delta - \gamma). \quad (20.1-6b)$$

We note that the instantaneous rate of change of energy is a maximum if the thrust is acting *tangential* to the trajectory. The time-derivative of the angular momentum is a maximum if the thrust is directed *perpendicular* to the radius vector.

We now assume that the vehicle's motor starts thrusting when the vehicle is in a circular parking orbit. Then, the initial conditions are given by:

$$t = 0: \quad r = r_0, \quad \theta = 0, \quad V = V_{c_0} = \sqrt{\frac{\mu}{r_0}}, \quad \gamma = 0,$$

where θ is the polar angle, describing the angular position of the spacecraft (Fig. 20.1). When $a(t)$ and $\delta(t)$ are specified, the integration of Eq. (20.1-1) yields the trajectory flown by the spacecraft. In general, we are committed to numerical integration techniques, but in some special cases an analytical analysis of the motion is partly possible. Two of such cases will be discussed in the next sections.

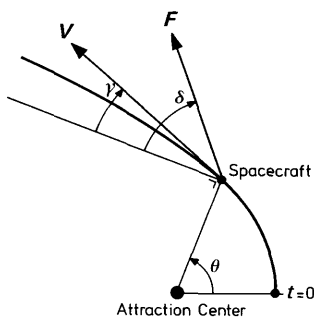


Fig. 20.1 Trajectory parameters

20.2 Constant radial thrust acceleration

The motion of a spacecraft in an inverse-square gravitational field with a thrust acting continuously in a radial direction, was first studied by Tsien [7]. If we assume that the thrust is directed *radially outwards*, Eqs. (20.1-6) simplify to

$$\frac{dH}{dt} = 0, \quad (20.2-1a)$$

$$\frac{d\mathcal{E}}{dt} = aV \sin \gamma. \quad (20.2-1b)$$

Thus, the angular momentum per unit mass is constant during the powered flight, just as it is for Keplerian trajectories. Integration of Eq. (20.2-1a) yields

$$H = r^2 \frac{d\theta}{dt} = r_0^2 \left(\frac{d\theta}{dt} \right)_0 = \sqrt{\mu r_0},$$

or

$$\frac{d\theta}{dt} = \frac{\sqrt{\mu r_0}}{r^2}. \quad (20.2-2)$$

Using Eq. (20.1-5), we can write Eq. (20.2-1b) in the form

$$\frac{d}{dt} \left\{ \left(\frac{dr}{dt} \right)^2 + r^2 \left(\frac{d\theta}{dt} \right)^2 - \frac{2\mu}{r} \right\} = 2a \frac{dr}{dt}. \quad (20.2-3)$$

Substitution of Eq. (20.2-2) into Eq. (20.2-3) yields

$$\frac{d}{dt} \left\{ \left(\frac{dr}{dt} \right)^2 + \frac{\mu r_0}{r^2} - \frac{2\mu}{r} \right\} = 2a \frac{dr}{dt}.$$

For a constant thrust-to-mass ratio, i.e. $a = a_0$, this equation can be integrated, leading to

$$\left(\frac{dr}{dt} \right)^2 = 2a_0(r - r_0) + \mu \left(\frac{2}{r} - \frac{r_0}{r^2} - \frac{1}{r_0} \right). \quad (20.2-4)$$

The radial velocity of the spacecraft equals zero, if

$$\left(\frac{r}{r_0} - 1 \right) \left\{ 2a_0 r^2 - \mu \left(\frac{r}{r_0} - 1 \right) \right\} = 0.$$

The roots of this equation are:

$$r_1 = r_0, \quad (20.2-5a)$$

$$r_{2,3} = \frac{\mu}{4a_0 r_0} \left\{ 1 \pm \sqrt{1 - 8 \frac{a_0 r_0^2}{\mu}} \right\}. \quad (20.2-5b)$$

The first root, of course, represents the initial parking orbit. Real values for r_2 and r_3 only exist, if $a_0 \leq \frac{1}{8}\mu/r_0^2$. Denoting the gravitational acceleration in the parking orbit by g_0 we may write

$$g_0 = \frac{\mu}{r_0^2}, \quad (20.2-6)$$

and the condition for real values for r_2 and r_3 becomes

$$\frac{a_0}{g_0} \leq \frac{1}{8}. \quad (20.2-7)$$

The reader should note that in this chapter g_0 stands for a reference gravitational acceleration and does not designate the standard surface gravity.

If $a_0 > \frac{1}{8}g_0$, the radial velocity will only be zero in the parking orbit and the vehicle will continuously recede from the Earth. This means, that escape from the Earth's gravitational field will be accomplished, if, at least, the thrust can be maintained long enough. If the root r_2 corresponds to the plus sign in Eq. (20.2-5b) and r_3 to the minus sign, we note that, for $a_0 < \frac{1}{8}g_0$, $r_0 < r_3 < r_2$. According to Eq. (20.2-4): $\left(\frac{dr}{dt}\right)^2 < 0$ for $r_3 < r < r_2$, which of course is physically not possible. We also find that if $r_0 < r < r_3$ or $r > r_2$: $\left(\frac{dr}{dt}\right)^2 > 0$. As we also have $\left(\frac{d^2r}{dt^2}\right)_{r_0} > 0$ and $\left(\frac{d^2r}{dt^2}\right)_{r_3} < 0$, we may conclude that if $a_0 < \frac{1}{8}g_0$, the spacecraft's distance will continuously vary between $r = r_0$ and $r = r_3$. If $a_0 = \frac{1}{8}g_0$, the distances r_2 and r_3 are equal, and $\frac{d^2r}{dt^2}$ at that distance is zero. In that case, the vehicle will asymptotically approach a circular orbit with radius

$$r = \frac{\mu}{\frac{1}{2}g_0 r_0} = 2r_0.$$

In this orbit, the thrust acceleration equals one-half the local gravitational acceleration. For the velocity of the vehicle in this limiting circular orbit, we find with Eq. (20.2-2)

$$V = \frac{1}{2} \sqrt{\frac{\mu}{r_0}} = \frac{1}{2} \sqrt{2} \sqrt{\frac{\mu}{r}}.$$

Thus, the velocity is one-half its original value in the parking orbit, and $\frac{1}{2}\sqrt{2}$ times the local circular velocity.

Some results of the numerical integration of the equations of motion are shown in Fig. 20.2. The time scale in this figure has been non-dimensionalized by dividing it by the circular period in the parking orbit, T_{c_0} ,

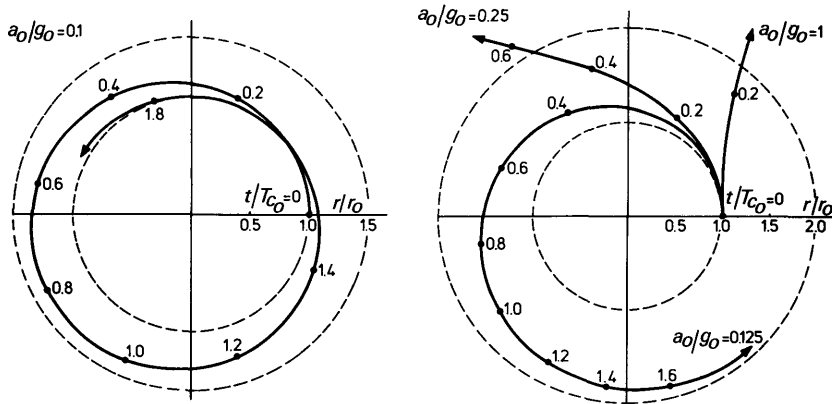


Fig. 20.2 Trajectories with constant radial thrust accelerations given by

$$T_{c_0} = 2\pi \sqrt{\frac{r_0^3}{\mu}}. \quad (20.2-8)$$

The variation of velocity with distance can be obtained as follows. First, we write

$$V^2 = \left(\frac{dr}{dt}\right)^2 + r^2 \left(\frac{d\theta}{dt}\right)^2,$$

and then substitute Eqs. (20.2-2) and (20.2-4), which yields

$$\left(\frac{V}{V_{c_0}}\right)^2 = 2 \frac{a_0}{g_0} \left(\frac{r}{r_0} - 1\right) + 2 \frac{r_0}{r} - 1. \quad (20.2-9)$$

In Fig. 20.3, this relation is depicted for some values of a_0/g_0 . Also shown

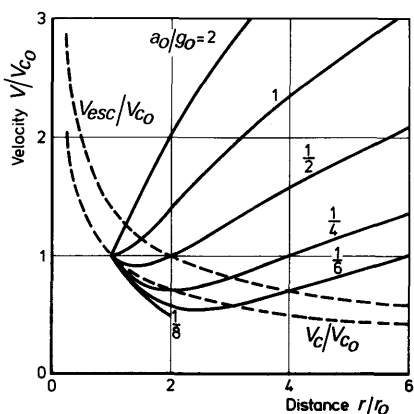


Fig. 20.3 Velocity ratio as a function of radial distance for constant radial thrust accelerations

are curves for the local circular velocity, V_c , and the local escape velocity, V_{esc} . We note that if $a_0/g_0 < 1$, the velocity first decreases to a minimum value and for $a_0/g_0 > \frac{1}{8}$ increases again at larger distances. If $a_0/g_0 > \frac{1}{8}$, the vehicle reaches the local escape velocity at a distance

$$\left(\frac{r}{r_0}\right)_{esc} = 1 + \frac{1}{2a_0/g_0}. \quad (20.2-10)$$

For an analysis of the variation of angular position, θ , with distance the reader is referred to Copeland [8].

Though radial thrust may be of some interest for certain orbital maneuvers, it will not play a significant role as the propulsion mode for interplanetary missions. The thrust level required to escape from the Earth's gravitational field with radial thrust is much higher than can be achieved with present technology.

20.3 Constant tangential thrust

The problem of programming the thrust direction of a low-thrust spacecraft to permit its escape from a low-altitude circular parking orbit with the minimum expenditure of propellant has been studied by many authors. Among the various analytical solutions available, both for constant thrust and constant thrust acceleration, in particular the publications of Lawden [9], Breakwell and Rauch [10] and Reidelhuber and Schwenzfeger [11] should be mentioned. These studies reveal that the actual *optimal* thrust direction varies with time in quite a complex way. They, however, also show that a tangential thrust is very close to the optimum thrust direction. In this section, we will consider the case of constant tangential thrust.

It should be realized that the tangential thrust steering is only near optimal if the thrust acceleration is very small relative to the local gravitational acceleration. If the vehicle moves on an interplanetary trajectory about the Sun, the situation is quite different. As at the distance of the Earth from the Sun, the gravitational acceleration of the solar field is about $5.9 \times 10^{-3} \text{ m/s}^2$, a thrust acceleration of 10^{-3} m/s^2 corresponds to about one-sixth local gravitational acceleration just outside the Earth's sphere of influence. For this relatively high value, the tangential steering not necessarily approximates the real optimum thrust program anymore. The determination of optimal interplanetary trajectories is furthermore hampered if the vehicle has to encounter another celestial body, leading to two-point boundary value problems. Melbourne [12, 13] presents examples of such optimal interplanetary trajectories.

20.3.1 Characteristics of the motion

For a tangential thrust, Eqs. (20.1-6) simplify to

$$\frac{dH}{dt} = ar \cos \gamma, \quad (20.3-1a)$$

$$\frac{d\mathcal{E}}{dt} = aV. \quad (20.3-1b)$$

If both the thrust and the effective exhaust velocity are constant, the instantaneous thrust acceleration is given by

$$a = \frac{a_0}{1 - a_0 t/c}, \quad (20.3-2)$$

and we note that the thrust acceleration slowly increases with time. Using Eq. (20.1-5), we can write Eq. (20.3-1b) in the form

$$V \frac{dV}{dt} + \frac{\mu}{r^2} \frac{dr}{dt} = aV,$$

or

$$\frac{dV}{dt} = a - \frac{\mu}{r^2} \sin \gamma. \quad (20.3-3)$$

For the variation of distance, r , and angular position, θ , with time, we may write

$$\frac{dr}{dt} = V \sin \gamma, \quad (20.3-4)$$

$$\frac{d\theta}{dt} = \frac{V}{r} \cos \gamma. \quad (20.3-5)$$

Equation (20.3-1a) can also be written as

$$\frac{d}{dt}(rV \cos \gamma) = ar \cos \gamma.$$

Substitution of Eqs. (20.3-3) and (20.3-4) into this relation, finally yields

$$\frac{d\gamma}{dt} = \frac{1}{rV} \left(V^2 - \frac{\mu}{r} \right) \cos \gamma. \quad (20.3-6)$$

The Eqs. (20.3-3) to (20.3-6) constitute a set of four first-order differential equations, describing the variation of r , θ , V and γ with time.

In Fig. 20.4, parameters representing distance, polar angle, velocity and flight path angle are plotted as a function of time for about one revolution. The notation Δ stands for the difference between the actual value of a parameter and its value at $t=0$. Because in the initial parking orbit, the polar angle, θ , increases linearly with time, for the variation of θ due to the

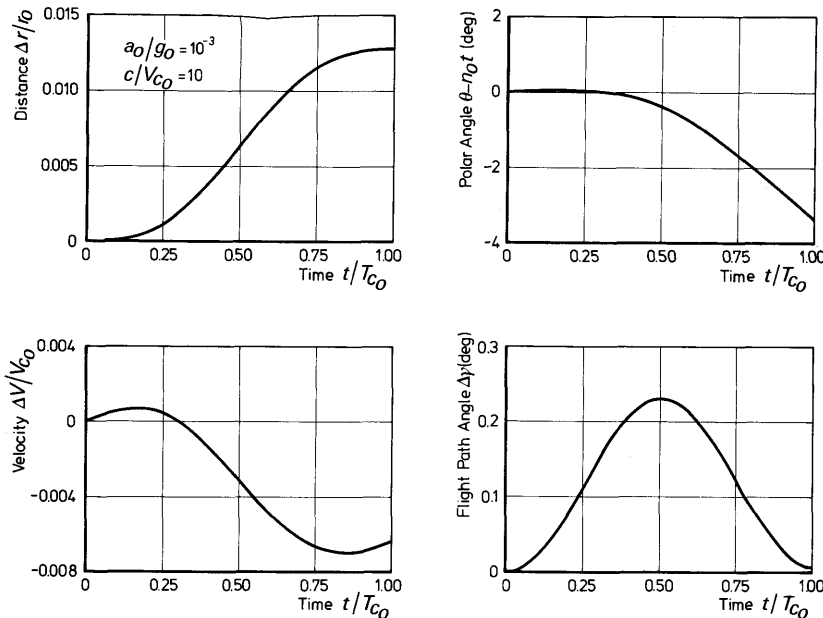


Fig. 20.4 Variation of trajectory parameters during the first revolution in an escape trajectory with constant tangential thrust

thrust only the quantity $\theta - n_0 t$ has been plotted, where n_0 is the (mean) angular motion in the parking orbit. We see that in the first part of the trajectory the velocity increases. After about one-third of a revolution, the velocity falls below the circular velocity at departure, and there is a gain of potential energy at the expense of kinetic energy. The velocity oscillates about a decreasing mean value. We thus have the apparent contradiction that a thrust acting in the direction of motion yields a decreasing velocity. It is interesting to mention in this context that for air drag on a satellite, we have the opposite situation. The drag, opposing the direction of motion, leads to a decreasing orbital altitude and an increasing velocity.

The quantity $\theta - n_0 t$ first slightly increases, but starts decreasing after about one-sixth of a revolution. The flight path angle oscillates and reaches a maximum after about half a revolution. After one complete revolution, it still has a small positive value.

The position and velocity of the spacecraft over a long period of time are shown in Fig. 20.5. Instead of the polar angle, θ , the number of revolutions, N , defined as

$$N = \frac{\theta}{2\pi}, \quad (20.3-7)$$

is plotted. Also indicated in this figure is the point where the escape velocity

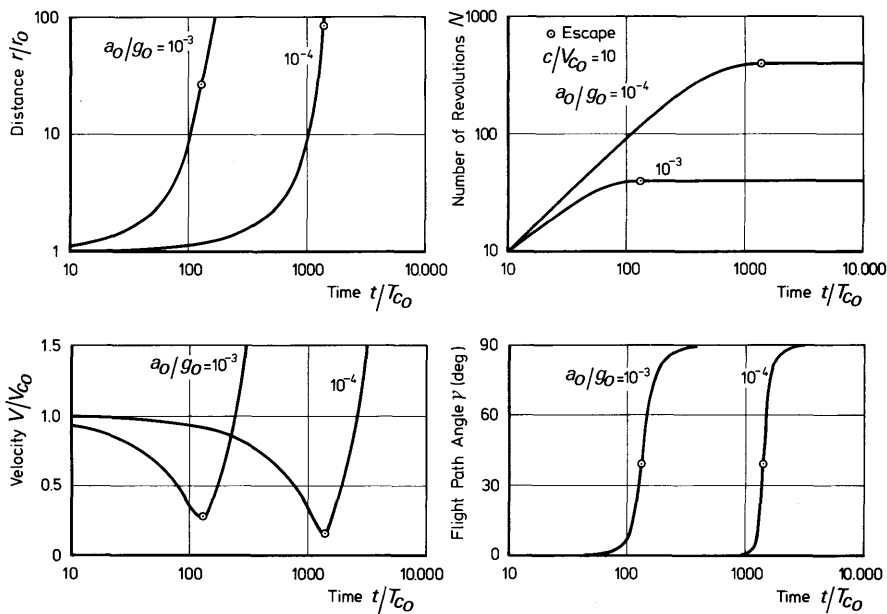


Fig. 20.5 Parameters of escape trajectories with constant tangential thrust

is reached. It should be realized that on the scale used, the oscillations shown in Fig. 20.4 are not visible. Aside from the oscillations, we note that the velocity decreases until only just before escape takes place. The escape velocity is reached at a large distance and after the spacecraft has completed many revolutions. Another important fact revealed by Fig. 20.5 is that the flight path angle remains very close to zero for a long period of time. Similar charts for many other values of thrust acceleration and exhaust velocity are presented by Moeckel [14].

In Table 20.1, the *escape time*, t_{esc} , being the time it takes to reach the

Table 20.1 Trajectory data at escape for constant tangential thrust ($c/V_{c_0} = 10$)

	a_0/g_0		
	10^{-4}	10^{-3}	10^{-2}
t_{esc}/T_{c_0}	1395.0	130.19	11.38
r_{esc}/r_0	83.9	26.65	8.51
$N_{\text{esc}}(\text{rev})$	390.18	39.12	4.02
V_{esc}/V_{c_0}	0.1542	0.2739	0.4848
$\gamma_{\text{esc}}(\text{deg})$	39.2	39.1	38.8

escape velocity, and the values of distance, number of revolutions, velocity and flight path angle at $t = t_{esc}$, are summarized for three values of the initial thrust acceleration and for $c/V_{c_0} = 10$.

The spiral trajectory flown by a spacecraft with constant tangential thrust is shown in Fig. 20.6. Because the inner windings of the spiral are very close together, only the last few revolutions are shown.

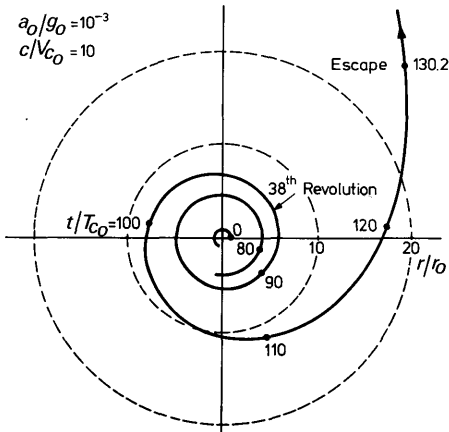


Fig. 20.6 An escape trajectory with constant tangential thrust

20.3.2 Linearization of the equations of motion

For the very first part of the escape trajectory, the deviations of distance, angular position, velocity and flight path angle from their respective values in the circular parking orbit will be very small. We then may apply the small-perturbation theory, and define

$$r' = r - r_0, \quad \theta' = \theta - n_0 t, \quad (20.3-8)$$

$$V' = V - V_{c_0}, \quad \gamma' = \gamma - \gamma_0 = \gamma.$$

Substitution of these relations into Eqs. (20.3-3) to (20.3-6), and subsequent linearization yields

$$\frac{dr'}{dt} = V_{c_0} \gamma', \quad (20.3-9a)$$

$$\frac{d\theta'}{dt} = n_0 \left(\frac{V'}{V_{c_0}} - \frac{r'}{r_0} \right), \quad (20.3-9b)$$

$$\frac{dV'}{dt} = a_0 - \frac{\mu}{r_0^2} \gamma', \quad (20.3-9c)$$

$$\frac{d\gamma'}{dt} = n_0 \left(2 \frac{V'}{V_{c_0}} + \frac{r'}{r_0} \right). \quad (20.3-9d)$$

For simplicity, we will now change from the independent variable t , to the independent variable φ , defined as

$$\varphi = \frac{V_{c_0}}{r_0} t = 2\pi \frac{t}{T_{c_0}} = n_0 t. \quad (20.3-10)$$

This angle φ thus indicates the angular position of the spacecraft at time t , if the vehicle were still to move in the initial parking orbit. So φ can be regarded as the analog of the unperturbed true anomaly, introduced in Section 18.6.

With Eqs. (20.2-6) and (20.3-10), we can write Eqs. (20.3-9) in the form

$$\frac{dr'}{d\varphi} = r_0 \gamma', \quad (20.3-11a)$$

$$\frac{d\theta'}{d\varphi} = \frac{V'}{V_{c_0}} - \frac{r'}{r_0}, \quad (20.3-11b)$$

$$\frac{dV'}{d\varphi} = V_{c_0} \left(\frac{a_0}{g_0} - \gamma' \right), \quad (20.3-11c)$$

$$\frac{d\gamma'}{d\varphi} = 2 \frac{V'}{V_{c_0}} + \frac{r'}{r_0}. \quad (20.3-11d)$$

Elimination of γ' from Eqs. (20.3-11a) and (20.3-11c) gives

$$\frac{1}{r_0} \frac{dr'}{d\varphi} + \frac{1}{V_{c_0}} \frac{dV'}{d\varphi} = \frac{a_0}{g_0},$$

which can be integrated to

$$\frac{r'}{r_0} + \frac{V'}{V_{c_0}} = \frac{a_0}{g_0} \varphi. \quad (20.3-12)$$

Differentiation of Eq. (20.3-11a) with respect to φ , and subsequent substitution of Eqs. (20.3-11d) and (20.3-12) yields

$$\frac{d^2 r'}{d\varphi^2} + r' = 2 \frac{a_0}{g_0} r_0 \varphi.$$

The general solution of this differential equation, with the initial conditions

$$\varphi = 0: r' = 0, \frac{dr'}{d\varphi} = 0,$$

is:

$$\frac{r'}{r_0} = 2 \frac{a_0}{g_0} (\varphi - \sin \varphi). \quad (20.3-13)$$

Substitution of Eq. (20.3-13) into Eq. (20.3-12) leads to

$$\frac{V'}{V_{c_0}} = - \frac{a_0}{g_0} (\varphi - 2 \sin \varphi). \quad (20.3-14)$$

Substitution of Eqs. (20.3-13) and (20.3-14) into the Eqs. (20.3-11b) and (20.3-11d), and subsequent integration yields

$$\theta' = -\frac{1}{2} \frac{a_0}{g_0} \{3\varphi^2 - 8(1 - \cos \varphi)\}, \quad (20.3-15)$$

$$\gamma' = 2 \frac{a_0}{g_0} (1 - \cos \varphi). \quad (20.3-16)$$

Remembering that φ and t are related by Eq. (20.3-10), we note by comparison with Fig. 20.4, that the approximate expressions Eqs. (20.3-13) through (20.3-16) quite accurately describe the first part of the actual trajectory.

For the general case of an *elliptic* parking orbit, basically the same method can be applied [15], though, generally, we will then apply the method of variation of orbital elements, as discussed in Section 18.4.

20.3.3 Performance analysis

In Fig. 20.7, the velocity of a spacecraft with constant tangential thrust is shown versus the distance, for some values of a_0/g_0 . Curves for the local circular velocity, V_c , and the local escape velocity, V_{esc} , are also depicted. We note that for low thrust accelerations, the velocity during the largest part of the escape trajectory is very near to the local circular velocity. Only during the last couple of revolutions before escape, the velocity rapidly deviates from the circular velocity. For an approximate performance analysis, we therefore may assume that in the escape flight the velocity is given by

$$V = V_c = \sqrt{\frac{\mu}{r}}. \quad (20.3-17)$$

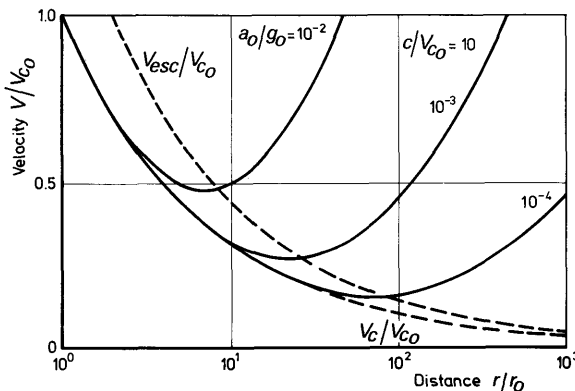


Fig. 20.7 Velocity as a function of radial distance for constant tangential thrust

This approximate relationship enables us to find approximate expressions for the dependence of radial distance on time and of angular position on radial distance, as well as for the escape time and for the propellant consumption during the escape flight.

By substitution of Eq. (20.3-17) into Eqs. (20.1-5) and (20.3-1b), we obtain

$$\mathcal{E} = -\frac{\mu}{2r}, \quad (20.3-18)$$

and

$$\frac{d\mathcal{E}}{dt} = a\sqrt{\frac{\mu}{r}}. \quad (20.3-19)$$

Elimination of \mathcal{E} from Eqs. (20.3-18) and (20.3-19) leads to

$$\frac{dr}{dt} = 2a\sqrt{\frac{r^3}{\mu}},$$

or, with Eq. (20.3-2),

$$r^{-3/2} dr = \frac{2a_0}{\sqrt{\mu}} \frac{dt}{1 - a_0 t/c}. \quad (20.3-20)$$

Integration leads with the initial conditions $t=0: r=r_0$ to

$$\frac{r}{r_0} = \left[\frac{1}{1 + c\sqrt{\frac{r_0}{\mu}} \ln(1 - a_0 t/c)} \right]^2. \quad (20.3-21)$$

This equation clearly shows that the distance will initially increase only very slowly.

An approximate relation for the escape time, t_{esc} , can be obtained from Eq. (20.3-21). Realizing that escape will take place at a finite distance, we obtain

$$t_{esc} < \frac{c}{a_0} \left\{ 1 - \exp \left(-\frac{V_{c_0}}{c} \right) \right\}.$$

For $V_{c_0}/c \ll 1$, we may linearize this relation to

$$t_{esc} < \frac{V_{c_0}}{a_0},$$

or, with Eqs. (20.2-6) and (20.2-8),

$$\frac{t_{esc}}{T_{c_0}} = \frac{\alpha}{2\pi} \frac{1}{a_0/g_0}, \quad (20.3-22)$$

where the *correction factor* α , being a function of a_0 and c , follows from a

comparison with the results of exact trajectory computations. In Fig. 20.8, α is shown for $c/V_{c_0} = 10$ and $c/V_{c_0} \rightarrow \infty$ as a function of a_0/g_0 . We see, that for the a_0/g_0 -range of interest, $a_0/g_0 = 10^{-5} - 10^{-3}$, α lies within the range 0.8 to 0.95. We thus may say that for a specific parking orbit, t_{esc} is nearly inversely proportional to the initial thrust acceleration, a_0 .

A relation between angular position θ and distance can be obtained as follows. We know from Fig. 20.5 that during the major part of the escape trajectory, the flight path angle is near to zero, and hence Eq. (20.3-5) can be approximated by

$$\frac{d\theta}{dt} = \frac{V}{r},$$

or, with Eq. (20.3-17),

$$\frac{d\theta}{dt} = \sqrt{\frac{\mu}{r^3}}. \quad (20.3-23)$$

Combination of Eq. (20.3-20) and Eq. (20.3-23) yields

$$\frac{d\theta}{dr} = \frac{\mu}{2a_0} \frac{1 - a_0 t/c}{r^3}. \quad (20.3-24)$$

From Eq. (20.3-21), we obtain

$$1 - \frac{a_0 t}{c} = \exp \left[\frac{1}{c} \left(\sqrt{\frac{\mu}{r}} - \sqrt{\frac{\mu}{r_0}} \right) \right].$$

By substitution of this relation into Eq. (20.3-24), we obtain

$$d\theta = \frac{\mu}{2a_0 \exp(V_{c_0}/c)} \frac{\exp \left(\frac{1}{c} \sqrt{\frac{\mu}{r}} \right)}{r^3} dr \quad (20.3-25)$$

To solve this differential equation, we put

$$x = \frac{\sqrt{\mu/r}}{c} = \frac{V_c}{c}. \quad (20.3-26)$$

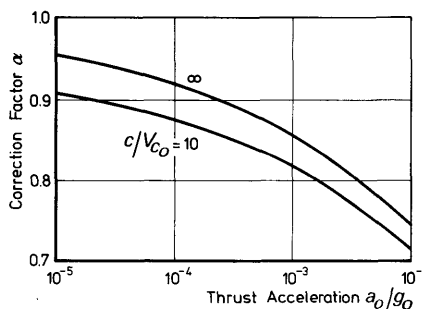


Fig. 20.8 The correction factor α for constant tangential thrust

Expressing Eq. (20.3-25) in this new variable x , leads to

$$d\theta = \frac{-c^4}{\mu a_0} e^{-x_0} x^3 e^x dx,$$

where x_0 is the value of x at $t=0$. With the initial conditions $t=0$: $\theta=0$, $x=x_0$ this equation can be integrated to

$$\theta = -\frac{c^4}{\mu a_0} e^{x-x_0} \left[x^3 - 3x^2 + 6x - 6 \right] + \frac{c^4}{\mu a_0} \left[x_0^3 - 3x_0^2 + 6x_0 - 6 \right]. \quad (20.3-27)$$

From Eqs. (20.3-26) and (20.3-27), we can, for a given parking orbit, exhaust velocity and initial thrust acceleration, determine θ as a function of r .

For electric propulsion systems, we know that both x_0 , and x at $t=t_{esc}$ are small. An approximate expression for the angular position at escape, θ_{esc} , can be obtained by a series expansion of the exponential function in Eq. (20.3-27). This finally leads to

$$\theta_{esc} = \frac{V_{c_0}^4}{4\mu a_0} \left(1 - \frac{V_{c_{esc}}^4}{V_{c_0}^4} \right). \quad (20.3-28)$$

As $V_{c_{esc}}^4/V_{c_0}^4 \ll 1$, we obtain from Eqs. (20.3-7) and (20.3-28) as an approximation for the number of revolutions before the escape velocity is reached

$$N_{esc} = \frac{1}{8\pi} \frac{V_{c_0}^4}{\mu a_0} = \frac{1}{8\pi a_0/g_0}. \quad (20.3-29)$$

This number of revolutions is, just like the escape time, for a given parking orbit inversely proportional to the initial thrust acceleration.

Because thrust and effective exhaust velocity are assumed constant, the mass of propellant consumed during the escape flight follows from

$$M_p = \frac{F}{c} t_{esc} = \frac{a_0 M_0}{c} t_{esc}. \quad (20.3-30)$$

Substitution of Eqs. (20.2-6), (20.2-8) and (20.3-22) into Eq. (20.3-30) yields

$$\left(\frac{M_p}{M_0} \right)_{esc} = \frac{\alpha}{c/V_{c_0}}. \quad (20.3-31)$$

Remembering that for a specified parking orbit, the correction factor α is, at least for small thrust accelerations, only weakly dependent on initial thrust acceleration and exhaust velocity (Fig. 20.8), we note that the propellant consumption during the escape flight is, for a given initial mass, nearly inversely proportional to the exhaust velocity. In Fig. 20.9, the propellant mass fraction required for escape, as obtained from the numerical integration of the equations of motion, is depicted as a function of the initial thrust acceleration for two values of c/V_{c_0} .

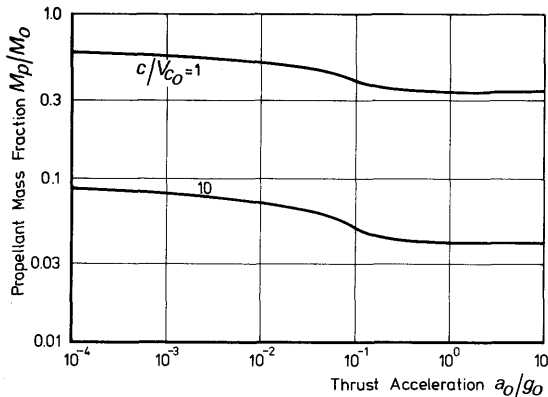


Fig. 20.9 Propellant mass fraction for an escape flight with constant tangential thrust

It is interesting to compare, from the viewpoint of propellant consumption, the escape flight of a low-thrust vehicle and that of a hypothetical high-thrust rocket with the same high exhaust velocity as the low-thrust vehicle. Of course, we also assume for the high-thrust rocket that the escape flight starts from a circular parking orbit, and that the thrust is acting tangentially to the parking orbit. Using the concept of the impulsive shot, we find for the impulsive velocity increase, ΔV , required to escape:

$$\Delta V = (\sqrt{2} - 1)V_{c_0}.$$

According to Tsiolkovsky's equation, Eq. (11.2-4), the mass of propellant involved is expressed by

$$\left(\frac{M_p}{M_0}\right)_{esc} = 1 - \exp\left[-(\sqrt{2} - 1)\frac{V_{c_0}}{c}\right].$$

If $V_{c_0}/c \ll 1$, we may approximately write

$$\left(\frac{M_p}{M_0}\right)_{esc} = \frac{\sqrt{2} - 1}{c/V_{c_0}}. \quad (20.3-32)$$

By comparison of Eqs. (20.3-31) and (20.3-32), we conclude that for the same high exhaust velocity, the escape flight with a low thrust requires about 2 to 2.2 times the mass of propellant consumed during a high-thrust escape flight. This, of course, is due to the *gravity losses* during the low-thrust flight.

At the present time, however, this comparison is not realistic. There is no choice between a high and low thrust with the same high exhaust velocity. We can only reach a high thrust by chemical or solid-core nuclear fission propulsion with their inherently relatively low exhaust velocities. Nowadays, high exhaust velocities can only be achieved by low-thrust electric propulsion systems. Hopefully, in the future, other space propulsion systems that

combine a high thrust and a high exhaust velocity will become available. Only then, short-duration interplanetary spaceflights with a relatively low propellant consumption may become feasible.

References

- 1 Au, G. F. (1968), *Elektrische Antriebe von Raumfahrzeugen*, G. Braun Verlag, Karlsruhe, p. 107–521.
- 2 Clark, K. E. (1974), *Survey of Electric Propulsion Capability*, AIAA Paper 74-1082, New York.
- 3 Hudson, W. R. and Finke, R. C. (1976), *NASA Electric Propulsion Program*, AIAA Paper 76-1068, New York.
- 4 Ehricke, K. A. (1962), *Space Flight, Vol 2: Dynamics*, Van Nostrand, Princeton, p. 611–845.
- 5 Stuhlinger, E. (1964), *Ion Propulsion for Space Flight*, McGraw-Hill, New York, p. 73–154.
- 6 Chute, F. S. (1970), Electric propulsion in space, *Canadian Aeron. Space J.*, **16**, 381–388.
- 7 Tsien, H. S. (1953), Take-off from satellite orbit, *A.R.S. J.*, **23**, 233–236.
- 8 Copeland, J. (1959), Interplanetary trajectories under low thrust radial acceleration, *A.R.S. J.*, **29**, 267–271. Also: *A.R.S. J.*, **30**, 130–131.
- 9 Lawden, D. F. (1958), Optimal escape from a circular orbit, *Astron. Acta*, **4**, 218–233.
- 10 Breakwell, J. V. and Rauch H. E. (1966), Optimum guidance for a low thrust interplanetary vehicle, *AIAA J.*, **4**, 693–704.
- 11 Reidelhuber, O. J. and Schwenzfeger, K. J. (1974), *Optimal Low Thrust Energy Increase Spiral Expansion*, IAF Paper 74-017, Amsterdam.
- 12 Melbourne, W. G. (1961), *Interplanetary Trajectories and Payload Capabilities of Advanced Propulsion Vehicles*, JPL TR 32-68, Pasadena.
- 13 Melbourne, W. G. and Sauer, C. G. (1961), *Optimum Thrust Programs for Power-Limited Propulsion Systems*, JPL TR 32-118, Pasadena.
- 14 Moeckel, W. E. (1960), *Trajectories with Constant Tangential Thrust in Central Gravitational Fields*, NASA TR R-53, Washington.
- 15 Wakker, K. F. (1967), *Ion Propulsion for Interplanetary Spaceflight* (in Dutch), Thesis Delft Univ. of Technology, Dept. Aerospace Eng., Delft, p. 108–130.

Tables

Table T.1 Physical constants

	Symbol	Value	$\sigma^{(1)}$ (ppm)	Units
Velocity of light in vacuum	c	2.9979250	0.33	10^8 m/s
Universal gravitational constant	G	6.6732	460	$10^{-11} \text{ m}^3/(\text{kg}\cdot\text{s}^2)$
Planck's constant	h	6.626196	7.6	$10^{-34} \text{ kg}\cdot\text{m}^2/\text{s}$
Boltzmann's constant	k	1.380622	43	$10^{-23} \text{ kg}\cdot\text{m}^2/(\text{s}^2\cdot\text{K})$
Avogadro's number	N_A	6.022169	6.6	$10^{26} \text{ kmol}^{-1}$
Universal gas constant	R_0	8.31434	42	$10^3 \text{ kg}\cdot\text{m}^2/(\text{s}^2\cdot\text{kmol}\cdot\text{K})$
Stefan-Boltzmann constant	σ	5.66961	170	$10^{-8} \text{ kg}/(\text{s}^3\cdot\text{K}^4)$

(1) Standard deviation, based on internal consistency in parts per million (ppm)

Table T.2 Selected astronomical constants

General

Universal gravitational constant*	$G = 6.670 \times 10^{-11} \text{ Nm}^2/\text{kg}^2$
Gaussian gravitational constant	$k = 0.01720209895 \text{ radian}$
Velocity of light	$c = 299792.5 \text{ km/s}$
Light year	$ly = 9.46054 \times 10^{12} \text{ km}$ = 499.00481 s
Light time for 1 AU	$pc = 3.08568 \times 10^{13} \text{ km} = 3.2616 ly$
Parsec	$d_E = 86400 \text{ s}$ = $(86164.09055 + 0.0015 T) \text{ s}$
Ephemeris day	= $(86400 + 0.0015 T) \text{ s}$
Sidereal day†	= $27.32166 d_E$
Mean solar day†	= $29.53059 d_E$
Sidereal month	= $365.24219 d_E$
Synodical month	= $365.25637 d_E$
Tropical year	= 365.25 days
Sidereal year	= 365.2425 days
Julian year	
Gregorian calendar year	

Galaxy

Diameter	= $90,000 ly$
Thickness	= $6500 ly$

* This value differs from that given in Table T.1, because of astronomical conventions

Table T.2 (continued)

Total mass	$= 1.4 \times 10^{11} M_{\odot}$
Sun's distance from galactic center	$= 30,000 ly$
Rotational velocity in solar neighborhood	$= 250 \text{ km/s}$
Escape velocity from near Sun	$= 360 \text{ km/s}$
<i>Sun</i>	
Mean radius	$R_{\odot} = 6.9599 \times 10^5 \text{ km}$
Mass	$M_{\odot} = 1.990 \times 10^{30} \text{ kg}$
Mean density	$= 1.409 \text{ g/cm}^3$
Gravitation parameter	$= 1.32712 \times 10^{11} \text{ km}^3/\text{s}^2$
Inclination of equator to ecliptic	$= 7^{\circ}15'$
Rotation period (latitude = 17°)	$= 25.38 \text{ days}$
Gravitational acceleration at surface	$= 273.97 \text{ m/s}^2$
Centrifugal acceleration at equator	$= 0.0057 \text{ m/s}^2$
Escape velocity at surface	$= 617.5 \text{ km/s}$
Total internal radiant energy	$= 2.8 \times 10^{40} \text{ J}$
Radiation emitted	$\mathcal{L}_{\odot} = 3.826 \times 10^{26} \text{ W}$
Solar constant	$f = 1360 \text{ W/m}^2$
Effective temperature	$T_e = 5770 \text{ K}$
<i>Planetary system</i>	
Total mass of planets	$= 447.0 M_{\oplus}$
Total mass of satellites	$= 0.12 M_{\oplus}$
Total mass of asteroids	$= 0.0003 M_{\oplus}$
Total mass of meteoric and cometary matter	$= 10^{-9} M_{\oplus}$
<i>Earth</i>	
Mass ratio Sun-Earth	$= 332945.468$
Sun-Earth distance	$= (1.4710-1.5210) \times 10^8 \text{ km}$
Astronomical unit	$AU = 1.495979 \times 10^8 \text{ km}$
Mean equatorial radius	$R_e = 6378.140 \text{ km}$
Polar radius (spheroid)	$R_p = 6356.755 \text{ km}$
Mean radius	$= 6371.00 \text{ km}$
Mass	$M_{\oplus} = 5.976 \times 10^{24} \text{ kg}$
Mean density	$= 5.517 \text{ g/cm}^3$
Gravitation parameter	$= 3.986013 \times 10^5 \text{ km}^3/\text{s}^2$
Obliquity of ecliptic [†]	$\varepsilon = 23^{\circ}27'8''.26 - 46''.86 T$
Equatorial rotational velocity	$= 0.4651 \text{ km/s}$
Gravitational acceleration at equator	$= 9.8142 \text{ m/s}^2$
Centrifugal acceleration at equator	$= 0.0339 \text{ m/s}^2$
Standard surface gravity	$g_0 = 9.80665 \text{ m/s}^2$
Escape velocity at equator	$= 11.19 \text{ km/s}$
<i>Moon</i>	
Mass ratio Earth-Moon	$= 81.3033$
Earth-Moon distance	$= 356400-406700 \text{ km}$
Mean Earth-Moon distance	$= 384401 \text{ km}$
Mean radius	$= 1738.2 \text{ km}$
Mass	$M_{\mathfrak{M}} = 7.350 \times 10^{22} \text{ kg}$
Mean density	$= 3.341 \text{ g/cm}^3$

[†] T is measured in centuries from 1900

Table T.2 (continued)

Gravitation parameter	$= 4.90265 \times 10^3 \text{ km}^3/\text{s}^2$
Mean inclination orbit to ecliptic	$= 5^\circ 8' 43''$
Mean inclination equator to ecliptic	$= 1^\circ 32' 30''$
Rotation period	$= 27.32166 d_E$
Gravitational acceleration at surface	$= 1.62 \text{ m/s}^2$
Escape velocity at surface	$= 2.38 \text{ km/s}$

Table T.3 Planetary orbital elements (Epoch 1975 July 7.0; J.D. 2442600.5)

	<i>a</i> (AU)	<i>e</i>	<i>i</i> (deg)	$\bar{\omega}$ (deg)	Ω (deg)	<i>M</i> (deg)	<i>n</i> (deg/sid.day)
Mercury	0.38710	0.20563	7.0043	77.074	48.041	290.909	4.09234
Venus	0.72333	0.00678	3.3944	131.226	76.459	120.155	1.60213
Earth	1.00000	0.01672	—	102.519	—	181.824	0.98565
Mars	1.52369	0.09338	1.8498	335.608	49.369	12.284	0.52403
Jupiter	5.20237	0.04800	1.3056	13.966	100.193	356.955	0.08310
Saturn	9.54821	0.05581	2.4885	91.879	113.470	18.171	0.03341
Uranus	19.1348	0.04507	0.7727	168.764	73.913	39.232	0.01178
Neptune	30.0111	0.01098	1.7708	41.811	131.594	209.416	0.00600
Pluto	39.2893	0.24568	17.1426	224.139	109.972	338.884	0.00400

For the inner planets the mean elements are given; for the outer planets the osculating elements. Both are referred to the mean equinox and ecliptic of date

Table T.4 Planetary orbits and physical elements

	Mercury	Venus	Earth	Mars	Jupiter	Saturn	Uranus	Neptune	Pluto
Max. distance from Sun (AU)	0.467	0.728	1.017	1.666	5.452	10.081	19.997	30.340	48.94
Min. distance from Sun (AU)	0.307	0.718	0.983	1.381	4.953	9.015	18.272	29.682	29.64
Sidereal period (trop. year)	0.2408	0.6152	1.0000	1.8809	11.861	29.50	83.70	164.41	246.28
Synodic period (day)	115.9	583.9	—	779.9	398.9	378.1	369.7	367.5	366.7
Mean orbit velocity (km/s)	47.87	35.02	29.78	24.13	13.06	9.64	6.81	5.44	4.75
Equatorial radius (km)	2432	6052	6378	3402	70850	60000	25400	25100	3200
Ellipticity	0.0	0.0	0.0034	0.010	0.061	0.109	0.03	0.021	0.0
Mass (Earth = 1)	0.0558	0.8150	1.0000	0.1074	317.891	95.179	14.629	17.222	0.111
Mean density (g/cm ³)	5.53	5.25	5.52	3.93	1.36	0.71	1.31	1.59	4.83
Equator gravitational accel. (m/s ²)	3.76	8.87	9.81	3.73	25.7	10.8	8.95	11.0	4.3
Equator centrif. accel. (m/s ²)	0.0	0.0	0.034	0.017	2.23	1.75	0.66	0.31	0.0
Equator escape velocity (km/s)	4.3	10.4	11.2	5.0	60.3	36.1	21.3	23.5	5.3
Sidereal rotation period	59 ^d	243 ^d	23 ^h 56 ^m 4.1 ^s	24 ^h 37 ^m 23 ^s	9 ^h 50 ^m	10 ^h 14 ^m	10 ^h 49 ^m	15 ^h 48 ^m	6 ^d 9 ^h
Inclination equator to orbit	0°	177°	23°27'	23°59'	3°5'	26°44'	97°55'	28°48'	
Number of satellites	0	0	1	2	14	10	5	2	0

Table T.5 Satellite orbits and physical elements

	Mean distance (10^3 km)	Inclination (deg)	Eccentricity	Sidereal period (day)	Radius (km)	Mass (planet mass)
<i>Earth</i>						
Moon	384		0.055	27.3217	1738	0.0123
<i>Mars</i>						
1. Phobos	9.4	1.0	0.021	0.3189	12	1.1×10^{-8}
2. Deimos	23.5	0.9–2.7	0.003	1.2624	6	1.4×10^{-8}
<i>Jupiter</i>						
1. Io	422	0	0.000	1.7691	1810	4.153×10^{-5}
2. Europa	671	1	0.000	3.5512	1480	2.508×10^{-5}
3. Ganymede	1070	0	0.001	7.1545	2600	8.079×10^{-5}
4. Callisto	1883	0	0.007	16.6890	2360	4.797×10^{-5}
5.	181	0.4	0.003	0.4182	80	1.8×10^{-9}
6.	11476	28	0.158	250.57	50	8.5×10^{-10}
7.	11737	26	0.207	259.65	12	3.5×10^{-11}
8.	23500	155	0.660	739	10	7.7×10^{-12}
9.	23600	156	0.275	758	9	1.5×10^{-12}
10.	11700	29	0.12	259.22	8	1.0×10^{-12}
11.	22600	163	0.207	692	9	2.0×10^{-12}
12. *	21200	147	0.169	630	8	7×10^{-13}
<i>Saturn</i>						
1. Mimas	186	2	0.020	0.9424	270	6.59×10^{-8}
2. Enceladus	238	0	0.004	1.3702	300	1.48×10^{-7}
3. Tethys	295	1	0.000	1.8878	500	1.095×10^{-6}
4. Dione	377	0	0.002	2.7369	480	2.39×10^{-6}
5. Rhea	527	0	0.001	4.4175	650	3.2×10^{-6}
6. Titan	1222	0	0.029	15.9454	2900	2.462×10^{-4}
7. Hyperion	1483	1	0.104	21.2767	220	2×10^{-7}
8. Iapetus	3560	15	0.028	79.3308	550	3.94×10^{-6}
9. Phoebe	12950	150	0.163	550.33	120	3×10^{-8}
10. Janus	159	0	0.0	0.7490	240	2×10^{-7}
<i>Uranus</i>						
1. Ariel	192	0	0.003	2.5204	350	1.5×10^{-5}
2. Umbriel	267	0	0.004	4.1442	250	6×10^{-6}
3. Titania	438	0	0.002	8.7059	500	5.0×10^{-5}
4. Oberon	586	0	0.001	13.4633	450	2.9×10^{-5}
5. Miranda	130	0	0.000	1.414	120	1×10^{-6}
<i>Neptune</i>						
1. Triton	355	160	0.00	5.8765	1900	3.3×10^{-3}
2. Nereid	5562	28	0.75	359.88	120	5×10^{-7}

* The 13th and 14th satellites of Jupiter were discovered in 1974 and 1975

Appendix 1 Gauss' Theorem

This theorem, which is also called the *divergence theorem*, relates the volume integral taken over a region, R , of the divergence (gradient, rotation) of a vector (scalar) point function to a surface integral taken over the surface, S , bounding the region R , and enclosing the volume, \mathcal{V} .

Usually Gauss' theorem is given in one of the following forms:

$$\int_S \mathbf{a} \cdot \mathbf{n} \, dS = \int_{\mathcal{V}} \nabla \cdot \mathbf{a} \, d\mathcal{V}, \quad (\text{A1-1})$$

$$\int_S \mathbf{n} \times \mathbf{a} \, dS = \int_{\mathcal{V}} \nabla \times \mathbf{a} \, d\mathcal{V}, \quad (\text{A1-2})$$

$$\int_S (\mathbf{n} \cdot \mathbf{a}) \mathbf{b} \, dS = \int_{\mathcal{V}} \{\mathbf{b}(\nabla \cdot \mathbf{a}) + (\mathbf{a} \cdot \nabla) \mathbf{b}\} \, d\mathcal{V}, \quad (\text{A1-3})$$

$$\int_S (\varphi \nabla \psi) \cdot \mathbf{n} \, dS = \int_{\mathcal{V}} \{\varphi \nabla^2 \psi + \nabla \varphi \cdot \nabla \psi\} \, d\mathcal{V}, \quad (\text{A1-4})$$

$$\int_S \mathbf{n} \varphi \, dS = \int_{\mathcal{V}} \nabla \varphi \, d\mathcal{V}, \quad (\text{A1-5})$$

$$\int_S (\varphi \nabla \psi - \psi \nabla \varphi) \cdot \mathbf{n} \, dS = \int_{\mathcal{V}} (\varphi \nabla^2 \psi - \psi \nabla^2 \varphi) \, d\mathcal{V}. \quad (\text{A1-6})$$

In these expressions, \mathbf{n} stands for the outward unit normal vector to S , the differential operator ∇ (pronounce del or nabla) stands for

$$\nabla = \mathbf{e}_x \frac{\partial}{\partial x} + \mathbf{e}_y \frac{\partial}{\partial y} + \mathbf{e}_z \frac{\partial}{\partial z}$$

$$\nabla^2 = \frac{\partial^2}{\partial x^2} + \frac{\partial^2}{\partial y^2} + \frac{\partial^2}{\partial z^2}$$

is the Laplacian, and \mathbf{a} and \mathbf{b} are vector point functions while φ and ψ are scalar point functions.

Appendix 2 Reynolds' Transport Theorem

This theorem relates the material time rate of change of a volume integral of a scalar or vector point function to the volume integral of the spatial time rate of change of that function.

Consider a material volume \mathcal{V} , i.e. a volume always containing the same particles, bounded by a closed surface S , and moving with the continuum under consideration. Let A be the function for which we want to determine $\frac{D}{Dt} \int_{\mathcal{V}} A d\mathcal{V}$. During a time interval Δt , the position and shape of the material volume will have changed, (Fig. A2.1). Now $A = A\{t, r(t)\}$, and by definition we have

$$\frac{D}{Dt} \int_{\mathcal{V}} A d\mathcal{V} = \lim_{\Delta t \rightarrow 0} \frac{1}{\Delta t} \left\{ \int_{\mathcal{V}_0 + \mathcal{V}_2} A\{t + \Delta t, r(t + \Delta t)\} d\mathcal{V} - \int_{\mathcal{V}_0 + \mathcal{V}_1} A(t, r) d\mathcal{V} \right\}.$$

The material volumes $\mathcal{V}(t)$ and $\mathcal{V}(t + \Delta t)$ have the region \mathcal{V}_0 in common, and hence, A is for that volume a function of the same coordinate r . So

$$\lim_{\Delta t \rightarrow 0} \frac{1}{\Delta t} \int_{\mathcal{V}_0} \{A(t + \Delta t, r) - A(t, r)\} d\mathcal{V} = \int_{\mathcal{V}} \frac{\partial A}{\partial t} d\mathcal{V},$$

and

$$\begin{aligned} \frac{D}{Dt} \int_{\mathcal{V}} A d\mathcal{V} &= \int_{\mathcal{V}} \frac{\partial A}{\partial t} d\mathcal{V} + \\ &+ \lim_{\Delta t \rightarrow 0} \frac{1}{\Delta t} \left\{ \int_{\mathcal{V}_2} A\{t + \Delta t, r(t + \Delta t)\} d\mathcal{V} - \int_{\mathcal{V}_1} A(t, r) d\mathcal{V} \right\}. \end{aligned} \quad (\text{A2-1})$$

To determine the integrals over \mathcal{V}_1 and \mathcal{V}_2 , recall that we deal with a material volume. These integrals represent the contribution of the value of

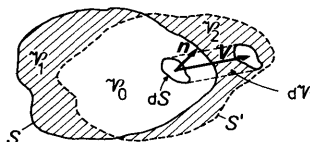


Fig. A2.1 The control surfaces and control volumes for the derivation of Reynolds' transport theorem

\mathbf{A} on the boundary S , multiplied by the volume swept by the particles during the time interval, Δt . Now $d\mathcal{V} = dS \mathbf{V} \cdot \mathbf{n} \Delta t$ (Fig. A2.1), and hence,

$$\frac{D}{Dt} \int_V A \, d\mathcal{V} = \int_V \frac{\partial A}{\partial t} \, d\mathcal{V} + \int_S A (\mathbf{V} \cdot \mathbf{n}) \, dS. \quad (\text{A2-2})$$

With the help of Gauss' theorem (Appendix 1), the right-hand side of Eq. (A2-2) can be written as a volume integral. If \mathbf{A} is a scalar point function, one finds

$$\frac{D}{Dt} \int_V A \, d\mathcal{V} = \int_V \left\{ \frac{\partial A}{\partial t} + \nabla \cdot (\mathbf{A} \mathbf{V}) \right\} d\mathcal{V}, \quad (\text{A2-3a})$$

and if \mathbf{A} is a vector point function we get

$$\frac{D}{Dt} \int_V \mathbf{A} \, d\mathcal{V} = \int_V \left\{ \frac{\partial \mathbf{A}}{\partial t} + \mathbf{A} (\nabla \cdot \mathbf{V}) + (\mathbf{V} \cdot \nabla) \mathbf{A} \right\} d\mathcal{V}. \quad (\text{A2-3b})$$

The Eqs. (A2-3) are known as *Reynolds' transport theorem* and relate the material time rate of change of a volume integral of a function, to the volume integral of the spatial time rate of change of that function.

It is convenient to derive a similar relation for the case that we deal with a volume of fixed shape. Consider a volume enclosed by a control surface S of fixed shape and moving with velocity \mathbf{V}_s through the fluid. We may apply the foregoing arguments, only the velocity of the surface element dS is now \mathbf{V}_s instead of \mathbf{V} . Thus, if we replace \mathbf{V} by \mathbf{V}_s all the foregoing equations remain valid. We now let $\mathbf{A} = \rho \mathbf{P}$, where ρ is the density and \mathbf{P} a vector function defined in the continuum, then Eq. (A2-2) becomes

$$\frac{D}{Dt} \int_V \rho \mathbf{P} \, d\mathcal{V} = \int_V \frac{\partial}{\partial t} (\rho \mathbf{P}) \, d\mathcal{V} + \int_S \rho \mathbf{P} (\mathbf{n} \cdot \mathbf{V}_s) \, dS. \quad (\text{A2-4})$$

If \mathbf{V}_{rel} is the velocity of the fluid relative to the control surface S , we have

$$\mathbf{V}_s = \mathbf{V} - \mathbf{V}_{rel}, \quad (\text{A2-5})$$

where \mathbf{V} is the absolute velocity of the fluid.

Substitution of Eq. (A2-5) into Eq. (A2-4) yields

$$\frac{D}{Dt} \int_V \rho \mathbf{P} \, d\mathcal{V} = \int_V \frac{\partial}{\partial t} (\rho \mathbf{P}) \, d\mathcal{V} + \int_S \rho \mathbf{P} (\mathbf{n} \cdot \mathbf{V}) \, dS - \int_S \rho \mathbf{P} (\mathbf{n} \cdot \mathbf{V}_{rel}) \, dS.$$

Again using Gauss' theorem, the first surface integral on the right-hand side of this equation may be written as a volume integral and we find

$$\begin{aligned} \frac{D}{Dt} \int_V \rho \mathbf{P} \, d\mathcal{V} &= \int_V \frac{\partial}{\partial t} [(\rho \mathbf{P}) + \rho \mathbf{P} (\nabla \cdot \mathbf{V}) + (\mathbf{V} \cdot \nabla) \rho \mathbf{P}] \, d\mathcal{V} \\ &\quad - \int_S \rho \mathbf{P} (\mathbf{n} \cdot \mathbf{V}_{rel}) \, dS, \end{aligned} \quad (\text{A2-6})$$

or

$$\frac{D}{Dt} \int_V \rho \mathbf{P} dV = \int_V \left[\frac{D}{Dt} (\rho \mathbf{P}) + \rho \mathbf{P} (\nabla \cdot \mathbf{V}) \right] dV - \int_S \rho \mathbf{P} (\mathbf{n} \cdot \mathbf{V}_{rel}) dS.$$

Using the continuity equation, i.e.

$$\frac{D\rho}{Dt} + \rho (\nabla \cdot \mathbf{V}) = 0,$$

we finally find

$$\frac{D}{Dt} \int_V \mathbf{P} \rho dV = \int_V \frac{D\mathbf{P}}{Dt} \rho dV - \int_S \rho \mathbf{P} (\mathbf{n} \cdot \mathbf{V}_{rel}) dS. \quad (A2-7)$$

Appendix 3 The First Law of Thermodynamics

When we speak of a thermodynamic system, we mean a well defined amount of matter contained within material or hypothetical walls, through which there is a controllable energy exchange with the surroundings. The first law of thermodynamics is nothing but the experience that energy is conserved in such a system:

$$dQ = dE + dW, \quad (\text{A3-1})$$

i.e. an infinitely small amount of heat dQ (or other forms of energy) added to the system, causes an infinitely small increment dE of the internal energy E of the system, and an infinitely small amount of work dW done by the system on the surroundings. We can also write

$$Q = E_2 - E_1 + W. \quad (\text{A3-2})$$

If we only consider expansion and compression work, the work being done by the system, is

$$dW = p dV = d(pV) - V dp, \quad (\text{A3-3})$$

where V stands for the *molar volume*. So, Eq. (A3-1) can also be written as

$$dQ = d(E + pV) - V dp. \quad (\text{A3-4})$$

The combination $E + pV$ is called the *heat function*, or *enthalpy* H :

$$H = E + pV. \quad (\text{A3-5})$$

It is customary to use C_p , C_v , H , E etc. for *molar quantities*, i.e. quantities based on the mol as basic unit and c_p , c_v , h , e , etc. as specific quantities, i.e. quantities based on the unit of mass. For gases we have

$$h = e + p/\rho, \quad (\text{A3-6})$$

and

$$dQ = dh - \frac{1}{\rho} dp. \quad (\text{A3-7})$$

By definition, the *heat capacity at constant volume* $C_v = (\partial Q / \partial T)_V$ and the *heat capacity at constant pressure* $C_p = (\partial Q / \partial T)_p$. Thus

$$C_v = \frac{\partial E}{\partial T} \quad C_p = \frac{\partial H}{\partial T}. \quad (\text{A3-8})$$

For perfect gases, where the internal energy only depends on the temperature, there follows immediately,

$$c_p = \frac{\partial}{\partial T} \left\{ e + \frac{p}{\rho} \right\}_p = \frac{\partial}{\partial T} \{e + RT\} = c_v + R. \quad (\text{A3-9})$$

Integration of the Eqs. (A3-8) yields

$$E = E_o + \int_{T_o}^T C_v dT. \quad (\text{A3-10a})$$

$$H = H_o + \int_{T_o}^T C_p dT, \quad (\text{A3-10b})$$

where T_o is a reference temperature. For small temperature intervals, C_p and C_v may, in many cases, be assumed constant. For most solids, and many liquids, the difference between C_p and C_v is negligible, leading to

$$C_p \approx C_v = C. \quad (\text{A3-11})$$

Index

- Absorptance, 153, 154
monochromatic, 154
- Absorption coefficient, spectral, 155
- Absorptivity, monochromatic, 155
- Acceleration,
absolute, 31, 36
centripetal, 32, 344
Coriolis, 32, 344
dragging, 32
relative, 32
tangential, 32
thrust, 463
- Activity, 135
sphere, 360
- Adiabatic wall, 157
- Admittance function, 205
- Aerodynamic,
-coefficient, 318–324
-drag, 319, 323, 324, 332, 408, 433, 470
-effects on satellite orbit, 407, 408, 432, 433, 470
-force, 75, 318–321, 407, 408, 433
-heating, 334
-moment, 76–78, 318–321
-pressure force, 75
-pressure moment, 76
-stability, 325–331
-stiffness, 328, 330
- Aiming point, 456
- Airfoil, double-wedge, 322
- Albedo, 408
- Aldrin, Edwin, 2
- Ammonium perchlorate (AP), 171, 174, 179
- Angle,
bank, 67, 83
downwash, 328
flight path, 14, 83, 250, 293–295, 364
- kick, 257
- nozzle, 223
-of attack or of incidence, 250, 251, 255, 318, 321, 328, 329
- pitch, 67, 83, 235, 238, 254
- sideslip, 318
- thrust, 464
- yaw, 67, 83, 331
- Angular momentum, 27, 35, 37, 45, 61, 62, 337, 338, 345, 363, 465
conservation of, 27, 61, 62
- orbital, 338
- proper, 338
- Angular motion, mean, 372, 421, 426
- Anomaly,
-at epoch, mean, 378
eccentric, 371
hyperbolic, 373
mean, 372, 420–422
true, 49, 363
unperturbed true, 429, 430, 473
- ANS, 401, 402, 433
- AP, 171, 174, 179
- Apoapsis or apocenter, 49
distance, 51
- Apollo project, 2
- Argument,
-of latitude, 391, 429
-of pericenter, 49, 378
- Aries, First Point of, 11, 13
- Armstrong, Neil, 2
- Ascending node (A.N.), 287, 377
longitude of, 378
right ascension of, 287, 378, 429, 430
- Ascent,
direct (D.A.), 389, 390, 455
hohmann transfer (H.T.A.), 389, 390
- trajectory, 247–250, 272–280,

- 389, 390, 401, 454, 455
- Asteroid**, 8, 9, 353
- Astronomical**,
 - Netherlands Satellite (ANS), 401, 402, 433
 - unit (A.U.), 8
- Asymptote**
 - incoming, 456
 - outgoing, 453
- Asymptotic deflection angle**, 457, 458
- Atmosphere**, Earth, 21–24
- Atmospheric**,
 - density, 22, 23
 - pressure, 22, 23
 - temperature, 22, 23
- Attraction**,
 - gravitational, 41–44
 - lunar or solar, 353, 354, 358, 408
 - parameter, 45, 363
- Autumnal equinox**, 11
- Avogadro's number**, 124
- Axis**,
 - major or semi-major, 51, 52, 378
 - minor or semi-minor, 51, 52
 - principle, 39
- Azimuth**
 - flight path, 14, 83, 391, 392, 453–455
 - launch, 392, 453, 455
- Baffle**, 212, 227
- Ballistic**,
 - missile, 246, 255, 282
 - missile, intercontinental (ICBM), 246, 255, 282, 283, 307
 - phase, 283, 286–305
- Bank**,
 - angle, 67, 83
 - rate, 83, 84
- Barker's equation**, 373
- Barycenter**, 338
- Beam length, equivalent**, 156
- Bipropellants**, 209
- Black-body**, 154
- Bleed-off system**, 208
- Boiling**,
 - film, 165, 166, 229
 - nucleate, 165, 166, 229
- Boltzmann**, L., 152
- constant, 152
- Boost phase**, 283–286
- Booster**, 280
- Boundary layer**, 100–104, 156, 157, 230, 320, 324
 - laminar, 320, 324
 - turbulent, 320, 324
- Brahe**, Tycho, 41
- Bray**,
 - approximation, modified, 145–148
 - freezing point, 145
- Burner**,
 - L* *-, 205
 - strand, 174
 - T* -, 205
- Burning**,
 - erosive, 194, 196, 203, 204
 - mesa-, 176
 - neutral, 196
 - perimeter, 185, 194
 - plateau-, 176
 - progressive, 196
 - regressive, 196
 - restricted, 180
 - surface, 177, 178, 194–197, 200
 - time, 239, 243, 245, 272
- Burning rate**, 174–179, 203–205
 - augmentation, acceleration-induced, 205
 - change, pressure-induced, 204, 205
 - exponent or pressure exponent, 175, 182, 184, 205
- Burnout**,
 - altitude, 248, 249, 275
 - range, 242–246
 - velocity, 248–250, 254, 255, 273–277
- Calendar**, 1, 18, 19
 - Gregorian, 18
 - Julian, 18
- Calendar year**, 18
 - civil, 18
 - Gregorian, 18
- Cape Canaveral**, 392, 453
- Capillary barrier**, 212
- Capture radius**, 458
- Carry-over effect**, 323
- Catastrophic yaw**, 329–331

- Cavitation, 212, 219–221
 Celestial,
 -equator, 11
 -latitude, 12
 -longitude, 11, 12
 -meridian, 11
 -pole, 11
 -sphere, 10, 11
 Cellulose Nitrate, 170
 Center,
 -of mass, 36, 70, 73, 107, 318
 -of mass flow, 70, 73, 107
 -of pressure, 318
 Chamber,
 combustion or thrust, 85, 86, 120,
 121, 137, 138, 208, 227, 228
 -conditions, 87–90, 100
 pre-combustion, 86, 208
 Characteristic length, 120, 121
 Characteristic velocity,
 launch vehicle, 395, 397, 448
 mission, 396, 397, 452
 rocket motor, 118–120
 Chasles' theorem, 28
 Chemical reaction, 100, 101, 124–
 130, 134, 136
 Chugging, 227
 Circular restricted three-body problem, 342–354
 Circulation, 331
 Clausius, R., 342
 theorem, 342
 Coast-time or period, 273, 390, 454,
 455
 Combustion, 85, 100, 121, 136–138,
 177–179, 196, 208, 227
 -instability, 100, 121, 196, 227
 -model, 177–179
 -oscillatory, 100, 227
 -or thrust chamber, 85, 86, 120,
 121, 137, 138, 208, 227, 228
 -products, 85, 86, 100, 101
 -staged-, 208
 -temperature, 101, 128
 -zone, 86, 100
 Comet, 8, 9
 Compound, 124
 Compression wave, 102, 103
 Condensation, 123, 135
 Condensed phase, 134–136
 Conduction, 152
 Conductivity, thermal, 152
 Conic section, 49–54
 Conservation law, 27, 54–62, 102
 Conservative field, 42, 43, 428
 Constant properties flow, 139, 140
 Consumption,
 propellant, 243, 245
 -specific, 115
 Continuity, equation of, 55, 56, 91
 Convection, 152, 156–160
 Coolant, 163–166, 229, 230
 Cooling, 100, 160, 165–168, 228–
 232
 -ablative, 231
 -active, 160, 228–231
 -dump, 229–231
 -film, 229, 230
 -heat sink, 231
 -insulation, 228–231
 -jacket, 165, 229
 -passive, 160, 228, 231, 232
 -radiation, 160, 166–168, 231
 -regenerative, 229–231
 -transpiration, 229, 230
 Coordinate system,
 -inertial launch site, 284
 -launch site, 284
 -local horizontal, 14
 -non-rotating planetocentric, 456
 Corona, 7
 Counter glow (Gegenschein), 353
 Cowell's method, 409–413, 419
 Crawford bomb, 174
 Critical,
 -inclination, 431
 -NPSE, 220
 -pressure, 165, 230
 -pressure ratio, 92, 93
 -temperature, 230
 Cross-flow theory, 322
 Cruciform configuration, 318
 Culmination,
 -altitude, 248, 249, 253, 274–277,
 332, 333
 -point, 252, 253
 -time, 248, 251, 276
 D'Alembert characteristic, 376
 Dalton's law, 132

- Dark zone, 178
 Date line, international, 17
 Day, 15
 civil, 17
 mean solar, 17
 sidereal, 16
 solar, 16, 17
 De Saint Venant's equation, 93
 De Vieille's or St. Robert's law, 175
 Declination, 12
 Density,
 atmospheric, 22, 23
 mass flow, 203, 204
 optical, 155
 Descending node (D.N.), 377
 Diffuser, 214, 215
 Diffusivity, thermal, 152
 Discharge coefficient, 226
 Dispersion, trajectory, 234, 317, 334
 Dissociation, 123, 129, 130
 Disturbing,
 -function, 414, 416, 422, 428, 429
 -potential, 356, 409, 428
 Diurnal motion, 11
 Divergence theorem, 485
 Downwash, 328
 -angle, 328
 Drag,
 aerodynamic, 319, 323, 324, 332, 408, 433, 470
 base, 323, 324
 -coefficient, 319, 322–324, 408
 -coefficient, friction, 324
 induced, 323, 324
 interference, 323
 -parameter, 332
 roughness, 323, 324
 viscous, 323, 324
 wave, 323
 -to weight ratio, 305, 332
 Earth, 7, 8, 19–24
 -asphericity or oblateness, 20, 21, 308–310, 407, 427
 -atmosphere, 21–24
 -climate, 22
 -equator, 9, 20, 21, 377, 427, 428
 -equator, ellipticity of the, 21, 428
 -(mean) equatorial plane, 9, 20, 377
 -(mean) equatorial radius, 20, 427
 -pear-shape, 20, 410, 428
 -polar radius, 20, 21
 -(mean) radius, 19
 Eastern Test Range (E.T.R.), 392
 Eccentricity, 49–51, 363, 378
 Ecliptic, 11
 axis of the, 11
 obliquity of the, 11, 13
 plane, 11, 13
 pole, 11
 Einstein, A., 387
 theory of relativity, 27, 385, 387
 Element, orbital, 377–379, 422
 Ellipsoid, standard, 20, 21
 Emissivity, monochromatic, 155
 Emittance, 153, 154
 Encke's method, 409, 411–413
 Energy
 chemical, 85
 conservation of, 47, 58–61, 150, 151, 187, 188, 489
 free, 133
 internal, 58, 125, 489
 kinetic, 47, 59, 339–342, 470
 potential, 43, 47, 339–342, 470
 total, 340, 342, 345, 458
 Enthalpy, 59, 125, 128, 130, 140, 489
 absolute, 128
 free, 130
 sensible, 128
 Entropy, 130, 140
 Ephemeris time (E.T.), 18
 Equation
 Barker's, 373
 de Saint Venant's, 93
 Euler's, 58
 Kepler's, 372, 375
 Kirchoff's, 127
 Lambert's, 298–305
 Navier-Stokes, 150
 Oberth's, 238
 -of continuity, 55, 56, 91
 -of motion, Euler's, 40

- of motion of rocket, 63–84, 234–238, 246, 247
- of motion of rocket, dynamical, 69–79
- of motion of rocket, kinematical, 79–81
- of rotational motion, 35, 37, 39, 237
- of the center, 377
- planetary, 419–425
- reaction, 124
- Sieder-Tate, 166
- Stefan-Boltzmann, 153
- Tsiolkovsky's, 2, 3, 238, 239
- Equator,**
 - celestial, 11
 - Earth's, 9, 20, 21, 377, 427, 428
 - ellipticity of Earth's, 21, 428
- Equilibrium**
 - chemical, 124, 130–136, 144, 148
 - constant, 133, 138
 - flow, 139, 144, 145
- Equinox**
 - autumnal, 11
 - vernal, 11, 13, 14
 - line, 11
- Erosion function, 204
- Error,
 - cross-range, 308, 311
 - cut-off, 311
 - down-range, 308, 311
 - impact, 311
- Escape,
 - time, 471, 475
 - trajectory or flight, 354, 439, 453–455, 463–479
 - velocity, 53, 363, 369, 470–472
- Euler, L., 378
 - angles, 66, 67, 378
 - equation, 58
 - equations of motion, 40
- Eulerian description, 54
- Excess velocity, hyperbolic, 369, 437–439, 451
- Exhaust velocity, 3, 71, 87–90, 120, 140
 - effective, 120
- Exit,
 - cone, extendable, 111
- flexible, 110
- pressure, 90, 93–96
- surface, 87, 94–98, 107, 108
- Exosphere, 23, 24**
- Expansion,**
 - ratio, 94, 104, 140, 143
 - wave, 102, 103
- Extinguishment, DP/DT, 205**
- f and g series, 383–385**
- Feed System, propellant, 100, 213–226**
- Field strength, 42**
- Fineness, 321**
- Fizz zone, 178**
- Flame,**
 - diffusion, 179
 - monopropellant, 179
 - premixed, 178
 - temperature, adiabatic, 128, 137–141
 - zone, 178
- Flight, optimal (ballistic missile), 295–297**
- Flight path,**
 - angle, 14, 83, 250, 293–295, 364
 - azimuth, 14, 83, 391, 392, 453–455
- Flow,**
 - constant properties, 139, 140
 - equilibrium, 139, 144, 145
 - free molecular, 408
 - frozen, 139–143
 - rate, volumetric, 218
 - sonic, 90, 92
 - subsonic, 92
 - supersonic, 90, 92, 194
 - two-phase, 100
- Fluid injection, 109**
- Fluorine, 209, 211**
- Flyby mission, 436, 440, 446–448, 451**
- Foam region, 178**
- Force,**
 - aerodynamic, 75, 318–321, 407, 408, 433
 - aerodynamic pressure, 75
 - apparent, 41, 69–71
 - coefficient, normal, 319–323

- Coriolis, 32, 40, 41, 70, 71, 78
dragging, 32
external, 33, 41, 69, 74–76
frictional, 74, 75
gravitational, 19, 41, 74
internal, 33
Magnus, 331
normal, 319
perturbing, 407–409
pressure, 74, 75
relative, 40, 41, 71
tangential, 319
- Fourier, J., 152
–law, 152
- Friction, 86, 219
- Frozen flow, 139–143
- Fuel, 85, 86
- Fugacity, 134, 135
- Galaxy, 6, 342
- Galilean transformation, 26, 27
- Galileo's principle of relativity, 26
- Gas
–constant, 89
–constant, universal, 89
–law, perfect or ideal, 60, 126, 188, 490
–generator, 86, 208
- Gauss, C. F., 424
–theorem, 485
- Gegenschein (counter glow), 353
- Geocentric latitude, 10, 12, 20, 427
- Geographic
–latitude, 20
–longitude, 10, 12, 66, 82, 427
- Geoid, geophysical, 20, 21
- Geopotential, 19, 427
- Geostationary
–orbit, 367, 408
–satellite, 367, 397, 428
- Geosynchronous satellite, 358, 367, 392
- Gibb's free energy, 130
- Glyceroltrinitrate, 170
- Goddard, R. H., 2
- Grain (propellant), 86, 180, 185–203
- Granular diffusion flame model (GDF), 178
- Graphite, pyrolytic, 231
- Gravitation, 27, 41–45, 75, 362, 387
Newton's law of, 27, 41, 42, 387
parameter, 45, 75, 362
- Gravitational,
–attraction, 41–44
–constant, universal, 42, 336
–field, 42–44, 385, 427, 428
–force, 19, 41, 74
–mass, 27
–moment, 76
- Gravity,
standard surface, 114, 237, 246
–loss or gravitational loss, 248, 250, 260, 273, 280, 333, 390, 478
–turn, 255–261
- Greenwich,
–mean solar time, 17
–sidereal time, 16
- Growth factor, 264
- Guidance, 255, 282, 283, 310, 326
delta, 310
hybrid explicit, 310
- Hamiltonian, perturbed, 423
- Harmonic,
sectorial, 308, 428
spherical, 427
tesseral, 308, 427, 428
zonal, 308, 427–429
- Heading, down-range, 284
- Heat,
–capacity, 489
–function, 489
–of formation, standard, 127–130
–of reaction, 125–128
–of transition, 129
–sink, 160, 163
–transfer, 86, 100, 101, 150–168, 225
–transfer coefficient, convective, 157, 161
- Heating, aerodynamic, 334
- Heliocentric,
–latitude, 13
–longitude, 13
- Herschel, F. W., 7
- Hess' law, 127
- Hill, G. W., 348

- surface of, 346–350
- Hodograph, 254, 365
- Hohmann, W., 2, 389
 - transfer ascent (H.T.A.), 389, 390
 - transfer trajectory, 396, 397, 440–446
- Horizontal plane, local, 14
- Hour, 15
 - angle, 15, 65, 284, 354
 - circle, 11
- Hydrazine, 86, 209
- Hydrogen, 90, 209, 230
 - fluoride, 85
 - peroxide, 85, 209
- Ignition,
 - auto-, 195
 - device, 180
- Impact,
 - parameter, 456
 - point, 4, 253, 254, 306–315, 457, 458
 - time of, 253
- Impeller, 214, 215, 218
 - shroud, 214, 215
- Impulse,
 - specific, 114–116, 147, 211, 243, 245
 - thrust, 77, 98, 99
 - total, 114, 115
- Impulsive shot, 243, 244, 249, 254, 333, 396, 438, 439, 478
- Inclination, 287, 378, 431
 - critical, 431
- Incoming asymptote, 456
- Inertia,
 - moment of, 38, 39
 - product of, 38
 - tensor, 38, 73
- Influence, sphere of, 358–360, 437, 456
- Influence coefficient, 310–315
 - ballistic cross-range, 311, 314
 - ballistic down-range, 311, 312
- Inhibitor, 180
- Injection,
 - error, 401–405
 - main tank (MTI), 213
 - of satellite, 390–395
 - parameter, in-plane, 391–395
- parameter, out-of-plane, 391, 393
- parking orbit (P.O.I.), 389
- state or condition, 285, 286, 292, 391–395
- velocity parameter, 289, 293–297, 393, 394
- Injector, 224–226
- Instability,
 - combustion, 100, 121, 196, 225, 227
 - magnus, 329, 331
 - non-linear, 329–331
- Interference, aerodynamic, 323
- Interplanetary,
 - spacecraft, 202, 336, 340, 358, 436–462
 - trajectory, 436–460, 468
- Invariable plane of Laplace, 338
- Ionization, 123
- Ionosphere, 23
- Jacobi, C. G. J., 340
 - integral, 344, 345, 353
- Jet,
 - assisted take-off (JATO), 116
 - damping, 327, 328
 - vanes, 109
- Jetavator, 109
- Julian Date (J.D.), 19
 - modified (M.J.D.), 19
- Jupiter, 7, 8
- Kennedy, J. F., 2
- Kepler, J., 41
 - equation, 372, 375
 - laws, 41, 46, 50, 53, 54, 368, 373
- Keplerian orbit or trajectory, 4, 5, 47–54, 362–385
- Kerosine, 230
- Kinetic energy, 47, 59, 339–342, 470
- Kirchhoff's,
 - equation, 127
 - law, 154
- Klemmung, 182
- Kourou, 392
- Lagrange, J. L., 298, 413
 - bracket, 415–419, 422

- Jacobi identity, 341
- libration point, 348–354
- Lagrangian description, 54
- Lambert's equation or theorem, 298–305
- Laplace, P. S. Marquis de, 360
 - invariable plane of, 338
- Laplacian, 485
- Latitude,
 - celestial, 12
 - geocentric, 10, 12, 20, 427
 - geographic or geodetic, 20
 - heliocentric, 13
- Latus rectum, 50, 363, 378
- Launch,
 - azimuth, 392, 453, 455
 - opportunity, 444–447, 452
 - site, 392, 453
 - vehicle, 333, 390, 398–401, 448, 455
 - vehicle characteristic velocity, 395, 397, 448
 - vehicle performance, 396–401
 - window, 452
 - window, daily, 392, 455
- Law,
 - conservation, 27, 54–62, 102
 - Dalton's, 132
 - de Vieleille's or St. Robert's, 175
 - Fourier's, 152
 - Hess', 127
 - Kepler's, 41, 46, 50, 53, 54, 368, 373
 - Kirchhoff's, 154
 - Newton's, 25–32
 - Newton's gravitation, 27, 41, 42, 387
 - of thermodynamics, first, 58, 125, 489, 490
 - of thermodynamics, second, 130
 - perfect or ideal gas, 60, 126, 188, 490
 - Piobert's, 194
 - Wien's, 153
- Libration point, Lagrange, 348–354
- Lifetime, orbital, 395
- Lift, 318, 319, 323, 324
- Light year, 6
- Linear momentum, 25, 27, 56–58
- conservation of, 56–58
- Liner, 231
- Loading fraction, volumetric, 197–202
- Longitude,
 - at epoch, mean, 379
 - celestial, 11, 12
 - geographic, 10, 12, 66, 82, 427
 - heliocentric, 13
 - of ascending node, 378
 - of pericenter, 379
- Loss
 - divergence, 98, 100, 106
 - gravity or gravitational, 248, 250, 260, 273, 280, 333, 390, 478
- Lunar
 - attraction, 353, 354, 358, 408
 - trajectory or flight, 353, 354
- Mach number, 90, 92, 317
- Magnetosphere, 23
- Maneuver
 - dog-leg, 391, 453
 - midcourse, 450, 452, 456
 - phasing, 392
- Many-body problem, 336–360
- Mars, 7, 8
- Mass
 - center of, 36, 70, 73, 107, 318
 - conservation of, 54–56, 185, 186
 - gravitational, 27
 - inertial, 27
 - payload, 240, 263, 398, 399
 - propellant, 240, 263, 477, 478
 - ratio, 3, 4, 239–241, 264, 332
 - structural, 240, 242, 263
- Mass flow, 70, 73, 87, 93–96, 101, 107, 113, 203, 204, 245
 - center of, 70, 73, 107
 - density, 203, 204
 - factor, 120
 - parameter, 217
- Material volume, 56
- Mercury, 7, 8
 - perihelion advance of, 387
- Meridian, 9
 - celestial, 11
- Mesosphere, 23
- Metals, refractory, 232

- Meteor, 9
 Meteorite, 9
 Meteroid, 8, 9
 Midcourse maneuver, 450, 452, 456
 Milky Way, 6
 Minute, 15
 Missile, 255, 282, 283, 307, 323, 326, 333
 Mission
 flyby, 436, 440, 446–448, 451
 lander, 436
 orbital or orbiter, 436, 440, 448
 -characteristic velocity, 396, 397, 452
 Molar quantity, 123, 124, 489
 Molecular weight, 89, 124, 139
 Moment
 aerodynamic, 76–78, 318–321
 aerodynamic pressure, 76
 apparent, 41, 69, 72, 73
 coefficient, pitching, 319–323
 Coriolis, 40, 41, 72, 73, 78
 external, 41, 69, 76, 77
 frictional, 77
 gravitational, 76
 inertial, 74
 jet damping, 78
 Magnus, 331
 pitching, 318, 327
 pressure, 76
 relative, 41, 73
 rolling, 319
 thrust misalignment, 77, 78
 yawing, 319
 Momentum,
 angular, 27, 35, 37, 45, 61, 62, 337, 338, 345, 363, 465
 linear, 25, 27, 56–58
 Monopropellant, 85, 209
 Moon, 2, 8, 348, 353
 Moons, 8
 Motion,
 constants of, 45–47
 direct, 378
 diurnal, 11
 integral of, 337–340, 345
 retrograde, 378
 rotational, 28, 35, 37, 39–41
 translational, 28, 34–37, 40, 41
 Multiple flames model (MF), 179
 N-body problem, 336–342, 355, 356
 Navier-Stokes equation, 150
 Neptune, 7, 8, 410
 discovery of, 7, 410
 Net positive suction energy (NPSE), 219
 critical, 220
 Neutral point, 325
 Newton, I., 157
 -laws, 25–32
 -law of gravitation, 27, 41, 42, 387
 Nitrocellulose, 170
 Nitroglycerine, 170
 Node,
 ascending (A.N.), 287, 377
 descending (D.N.), 377
 Nodes,
 elimination of the, 340
 line of, 377, 378
 Nozzle, 85, 90–93, 98–111, 221
 -angle, 223
 ball and socket, 109, 110
 bell-shaped, 91, 106
 contour, 91, 98, 106
 -deflection, 109
 de Laval, 91, 106
 -efficiency, 117
 -entrance, 86
 expansion-deflection, 106
 flexible-seal, 110
 fluid-bearing, 110
 pintle, 110, 111
 plug, 106
 rotating, 110
 translating inlet, 110
 truncated plug, 106
 Nusselt number, 158
 Nutation, 13, 14
 Oberth, H., 2
 equation of, 238
 Obliquity of the ecliptic, 11, 13
 One-body problem, 45, 362
 Orbit,
 circular, 8, 53, 366–368

- determination, 385
- elliptic, 368, 371, 372, 375–377, 380–383
- geostationary, 367, 408
- halo, 354
- hyperbolic, 363, 369, 370, 373–375
- keplerian, 4, 5, 47–54, 362–385
- osculating, 413–433
- parabolic, 363, 369, 373
- parking, 389, 392, 438, 439, 454, 455, 463
- perturbation, 5, 407–433
- perturbed, 308, 354, 357, 358, 386, 387, 407–433
- planetary, 41, 438
- prediction, 385, 410, 432
- sun-synchronous, 433
- Orbital,**
 - element, 377–379, 422
 - element, classical, 378, 379
 - element, osculating, 413–433
 - elements, variation of, 409, 410, 413–425
 - lifetime, 395
 - mission, 436, 440, 448
 - parameters, 379, 392–395
 - plane, 8, 377
- Outgoing,**
 - asymptote, 453
 - radial, 453
- Over-expansion, 102–106**
- Oxidizer, 85, 86**
- Oxygen, liquid (LOX), 209**
- Ozone, 22, 23, 85**

- Patched conic method, 437**
- Payload, 240, 263, 397, 399**
 - mass, 240, 263, 398, 399
 - ratio, 240–242, 264, 266
 - ratio, total, 264, 268–271
- Performance diagram, 398–401**
- Periapsis or pericenter, 49**
 - distance, 51
- Period, 53, 54, 366, 367, 430, 445**
 - circular, 366, 367
 - nodal or draconic, 430
- sidereal, 366**
- synodic, 445**
- Perturbations,**
 - general, 356, 409, 410, 425–430
 - long-periodic, 432
 - secular, 430
 - short-periodic, 430
 - special, 409, 410
 - theory, 356, 407–433
- Photosphere, 7**
- Piobert's law, 194**
- Pitch,**
 - angle, 67, 83, 235, 238, 254
 - damping in, 327, 328
 - program, 237, 238
 - rate, 83, 84, 236, 330
- Planck, M., 152**
 - constant, 152
- Planet, 7, 8**
- Planetary orbit, 41, 438**
- Planetary equations, 419–425**
 - canonical form of, 422, 423
 - Gauss' form of, 423, 424
 - Lagrange's, 419–425
- Pluto, 7, 8**
- Pogo, 100, 213, 219**
- Poisson relations, 60, 88, 91–93**
- Pole,**
 - celestial, 11
 - ecliptic, 11
 - north, 9, 11
 - south, 9
- Port area, 185**
- Potential, 42, 43, 339, 344, 353, 356, 409, 427, 428**
 - disturbing or perturbing, 356, 409, 428
 - energy, 43, 47, 339–342, 470
- Prandtl, L., 156**
 - number, 157, 160
- Precession, 13**
- Pre-combustion, 86**
 - chamber, 86, 208
- Preparation zone, 178**
- Prepolymers, 174**
- Pressure,**
 - atmospheric, 22, 23
 - center of, 318

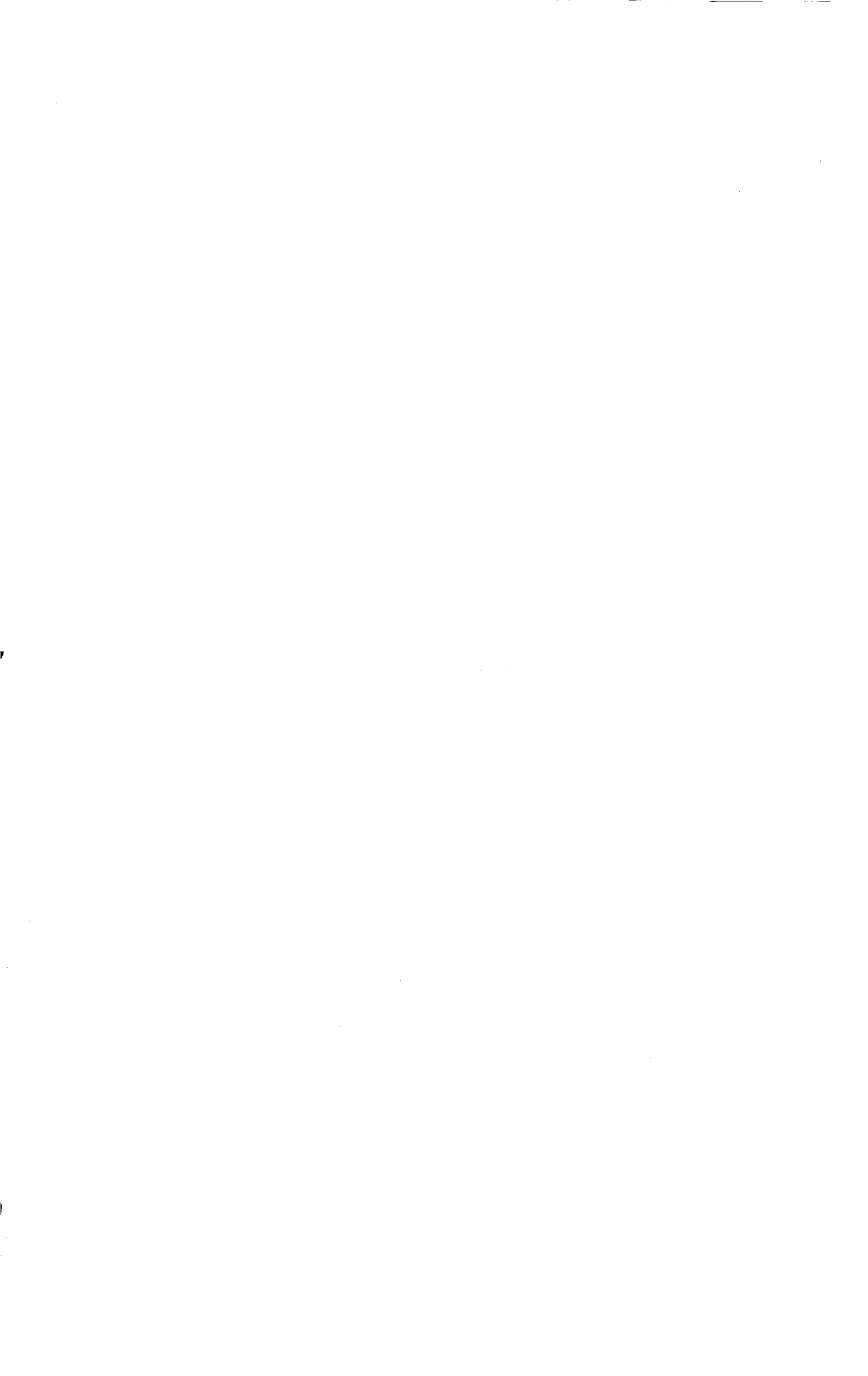
- critical, 165, 230
 dynamic, 317, 318
 equilibrium, 180–185
 exit, 90, 93–96
 partial, 131
 radiation, 5, 408, 409, 436
 supercritical, 229
 exponent or burning rate exponent, 175, 182, 184, 205
 –parameter, 217
 –ratio, 88–94
 –ratio, critical, 92, 93
 –thrust, 75, 77, 98, 99
Primeval Fireball, 6
Principle,
 –axis, 39
 of equivalence, 27
Problem,
 many-body, 336–360
 N-body, 336–342, 355, 356
 one-body, 45, 362
 three-body, 336, 340, 342–354
 two-body, 336, 362–387
Product, 124
Propellant, 3, 85
 colloidal, 170
 composite, 86, 170–174, 178, 179
 composite modified double-base (CMDB), 170, 174
 cryogenic, 209, 390
 double-base (DB), 86, 170, 171, 178
 –feed system, 100, 213–226
 homogeneous, 170, 171
 hybrid, 85, 115
 hypergolic, 209
 liquid, 85, 115, 116, 209–211, 391
 –mass, 240, 263, 477, 478
 –mass, useful, 240
 –ratio, 240, 242, 264
 –ratio, total, 264, 270
 –tank, 86, 211–213
 solid, 85, 115, 116, 170–179, 390
 storables, 209
Pump, 86, 213–221
 centrifugal, 214, 215
 –specific speed, 218, 219
 turbo-, 86, 213, 218, 219
Pumphead, 214
Radiation, 152–156
 solar, 21, 408, 436
Radiator, ideal, 153
Range, 242–246, 253, 254, 290–293, 305, 306, 309
 ballistic angular, 290–293, 309
 ballistic linear, 253, 254, 290
 burnout, 242–246
 –function, 243, 244
 no-drag, 305
 re-entry, 305
 total angular, 306
Reactant, 124
Reaction,
 chemical, 100, 101, 124–130, 134, 136
 endothermal, 126
 –equation, 124
 exothermal, 126, 134
 extent of, 125
 heat of, 125–128
 –time, 136
Recombination, 100, 101, 123, 130
Recovery,
 –factor, 159, 192
 –temperature, 158
Re-entry,
 –phase, 283, 305, 306
 –point, 305
 –state or condition, 291, 305
 –vehicle, 282, 305, 306, 310
Reference frame, 9–14, 25–31, 64–69, 234, 235, 338
 geocentric, 12
 geocentric mean equinox of date, 14
 heliocentric, 13
 inertial, 25–27, 31, 64, 234, 338
 non-inertial, 28–31
 non-rotating geocentric equatorial, 12, 64–67
 non-rotating heliocentric ecliptic, 13
 rotating geocentric, 12, 64–66
 vehicle, 65–67, 235

- vehicle-centred horizontal, 65, 66
- Reference state, standard, 128
- Reflectance, 153
- Relativity,
 - Einstein's theory of, 27, 385, 387
 - Galileo's principle of, 26
- Rendezvous, 385
- Residence time, 120–123, 139
- Resonance,
 - roll, 330, 331
 - spin-yaw, 331
- Response function, 205
- Reynolds,
 - number, 158, 317, 318
 - transport theorem, 486–488
- Right ascension, 12
- Rigid,
 - body, 37–40
 - rocket, 63, 64
- Roche equipotential, 346
- Rocket,
 - dynamical equation of motion of, 69–79
 - equation of motion of, 63–84, 234–238, 246, 247
 - kinematical equation of motion of, 79–81
 - multi-stage, 240, 262–281, 389, 397–401
 - parameter, 239–242, 262–265
 - rigid, 63, 64
 - single-stage, 234–251, 277, 279
 - sounding, 246, 323, 333
 - stage, 262, 263, 391, 398
 - step, 262
 - sub-, 262, 263
 - testing, 113, 114
 - two-stage, 276–280
 - Vernier, 212
- Rocket motor or engine,
 - characteristic velocity, 118–120
 - chemical, 3, 4, 85–121, 169–232, 478
 - electric, 3, 4, 462, 463, 477–479
 - hybrid, 3, 4, 85, 86
 - liquid, 3, 4, 85, 100, 106, 113, 208–232
 - nuclear, 3, 4, 85, 478
 - pressure-fed, 208, 213
 - pump-fed, 213
 - solid, 3, 4, 85, 86, 107, 113, 169–205
- Roll,
 - lock-in, 329–331
 - rate, 330
 - resonance, 330, 331
 - slow-down, 329
 - speed-up, 330
- Rolling, linear and non-linear, 329, 330
- Rotation, 28–30
- Rotational motion, equation of, 35, 37, 39, 237
- Rotor, 221, 222
- Roughness, surface, 104, 323, 324
- San Marco, 392
- Satellite,
 - geostationary, 367, 397, 428
 - geosynchronous, 358, 367, 392
 - launching of, 389–405
- Saturn, 7, 8
- Schwarzschild metric, 385
- Screaming, 227
- Second, 15, 18
 - atomic, 18
 - ephemeris, 18
- Semi-latus rectum, 50, 363, 378
- Semi-major axis, 51, 52, 378
- Semi-minor axis, 51, 52
- Separation,
 - flow, 104, 105, 320
 - stage, 262, 280, 281, 391
- Shock, 86, 102–105
 - oblique, 103–105
- Sidereal time, 15–17
- Siedler-Tate equation, 166
- Slender-body theory, 321–323
- Sliver, 195, 200
- Solar,
 - attraction, 353, 354, 358, 408
 - flare, 7, 354
 - system, 6–9
 - time, 15–17
 - time, apparent, 16, 17
 - time, Greenwich mean, 17
 - time, mean, 17
 - wind, 7, 9

- Solidification principle, 40, 41
 Space Shuttle, 2, 318, 399
 -main engine (SSME), 111, 220, 230
 Space Tug, 399, 401
 Spacecraft, interplanetary, 202, 336, 340, 358, 436–462
 Specific,
 -impulse, 114–116, 147, 211, 243, 245
 -impulse, volumetric, 115, 116
 -quantity, 489
 -speed, pump, 218, 219
 -thrust, 114, 242, 245, 246, 260
 Speed,
 -subsonic, 92, 321, 324
 -suction specific, 220
 -supersonic, 90, 92, 321–324
 Sphere of influence, 358–360, 437, 456
 Spin-yaw resonance, 331
 Splash plate, 224
 St. Robert's or de Vieille's law, 175
 Stability,
 -aerodynamic, 325–331
 -derivative, 320, 321
 -dynamic longitudinal, 325–329
 -margin, 325, 326
 -neutral, 325
 -static longitudinal, 325, 326
 -weathercock, 326
 Stages,
 -identical, 269, 270
 -rocket, 262, 263, 391, 398
 -separation of, 262, 280, 281, 391
 Staging,
 -parallel, 280, 281
 -tandem, 280
 Standard time, 17
 Stanton number, 157
 Stator, 221
 Steering program, 254, 468
 Stefan, A. J., 152
 --Boltzmann constant, 153
 --Boltzmann equation, 153
 Step, rocket, 262
 Stiffness,
 -aerodynamic, 328, 330
 -structural, 329
 Stoichiometric,
 -coefficient, 125
 -mixture, 125
 Stratosphere, 22, 23
 Streamline, 86, 87
 Structural,
 -efficiency, 240–242, 264, 270
 -efficiency, total, 264, 270
 -mass, 240, 242, 263
 Structure,
 -factor, 272
 -ratio, 270
 Sub-rocket, 262, 263
 Successive approximations, method of, 386, 425–427
 Summerfield criterion, 104
 Sun, 6, 7, 16, 17
 -mean, 17
 Sunspot, 7
 Surface,
 -gravity, standard, 114, 237, 246
 -of constant properties, 86, 87, 97, 101
 -of Hill or of zero velocity, 346–350
 Swingby flight, 458–460
 Tap-off system, 208
 TD-1A satellite, 430–432
 Temperature,
 -adiabatic flame, 128, 137–141
 -atmospheric, 22, 23
 -auto-ignition, 176
 -combustion, 101, 128
 -critical, 230
 -exospheric, 23
 -film, 158
 -recovery, 158
 -sensitivity coefficient, 182
 Test,
 -static, 77, 113, 114
 -windtunnel, 320
 Teststand, 113
 Theorem,
 -Chasles', 28
 -Clausius', 342
 -Gauss' or divergence, 485
 -Reynolds' transport, 486–488
 -Virial, 340–342

- Whittaker's, 36
 Thermochemistry, 123–148
 Thermodynamics,
 chemical, 123–136
 first law of, 58, 125, 489, 490
 second law of, 130
 Thermosphere, 23
 Thoma parameter, 220
 Three-body problem, 336, 340,
 342–354
 circular restricted, 342–354
 (elliptical) restricted, 342, 352,
 353
 Throat, 91, 100, 142–144, 162
 Thrust, 75, 77, 87, 97–99, 116, 246
 -angle, 464
 -coefficient, 116–118
 -coefficient, characteristic, 117
 effective, 246
 -history, 86, 100, 180, 468
 impulse, 77, 98, 99
 -magnitude control (TMC), 110,
 111, 203
 -misalignment, 77, 107, 108, 114
 -modulation, 110, 111, 226
 pressure, 75, 77, 98, 99
 -program, 333, 468
 -specific, 114, 242, 245, 246, 260
 --to-mass ratio, 463, 465
 --to-weight ratio, 242, 249, 250,
 272, 332
 -vector control (TVC), 77, 108–
 111, 114, 326
 Time, 15–18
 apparent solar, 16, 17
 atomic (A.T.), 15, 18
 burning-, 239, 243, 245, 272
 ephemeris (E.T.), 18
 greenwich mean solar, 17
 greenwich sidereal, 16
 mean solar, 17
 -of flight, 298–306, 447, 448,
 452, 475
 -of flight, no-drag, 305
 -of flight, re-entry, 305
 -of pericenter passage, 372–375,
 378
 reaction, 136
 residence, 120–123, 139
 sidereal, 15–17
 solar, 15–17
 standard, 17
 universal (U.T.), 17, 18
 vertical rise, 257
 zone, (Z.T.), 17
 Topping cycle, 208
 Total or stagnation conditions, 87,
 88
 Trajectory,
 ascent, 247–250, 272–280, 389,
 390, 401, 454, 455
 ballistic or free-fall, 4, 282, 286–
 305
 ballistic missile, 282–315
 class 1, 452
 class 2, 452
 dispersion, 234, 317, 334
 escape, 354, 439, 453–455, 463–
 479
 interplanetary, 436–460, 468
 Keplerian, 4, 5, 47–54, 362–385
 low-thrust, 462–479
 lunar, 353, 354
 minimum energy or minimum
 propellant, 296, 390, 438–444,
 452, 468
 reference, 310, 411–413
 transfer, 396, 397, 440–452, 468
 type 1, 447, 452
 type 2, 447, 452
 zero-lift, 255
 Transfer trajectory, 396, 397, 440–
 452, 468
 bi-elliptic, 397
 Hohmann, 396, 397, 440–446
 Transmittance, 153
 Trojans, 353
 Troposphere, 22
 Tsiolkovsky, K. E., 2
 -equation, 2, 3, 238, 239
 Turbine, 86, 221–224
 impulse, 221, 222
 pressure compound impulse, 222,
 224
 reaction, 221
 velocity compound impulse, 221,
 224
 Turbopump, 86, 213, 218, 219

- Two-body problem, 336, 362–387
- UDMH, 209
- Ullage volume, 212
- Under-expansion, 102, 106
- Universal time (U.T.), 17, 18
- Universe, 6
- Uranus, 7, 8, 410
discovery of, 7
- Van 't Hoff, J. H., 134
—reaction isobar, 134
- Vandenberg Airforce Base (V.A.F.B.), 392
- Vandenkerckhove function, 94
- Vanes, impeller, 216–218
- Vapor pull through, 212
- Variation of constants, 413–425
- Vehicle,
 launch, 333, 390, 398–401, 448, 455
 re-entry, 282, 305, 306, 310
- Velocity,
 absolute, 30
 angular, 28, 73
 areal, 46
 burnout, 248–250, 254, 255, 273–277
 circular, 53, 363, 366
 effective exhaust, 120
 escape, 53, 363, 369, 470–472
 exhaust, 3, 71, 87–90, 120, 140
 hyperbolic excess, 369, 437–439, 451
 ideal, 239, 241, 265–272
 launch vehicle characteristic, 395, 397, 448
 mission characteristic, 396, 397, 452
 relative, 31
 rocket motor characteristic, 118–120
 —parameter, injection, 289, 293–297, 393, 394
 —penalty, launch site and launch azimuth, 397
 —ratio, ideal, 268
- Venus, 7, 8
- Vernal equinox, 11, 13, 14
- Verne, Jules, 1
- Vernier rocket, 212
- Vertical,
 —flight or ascent, 247–250, 272–280
 —rise time, 257
- Vertregt, M., 266, 440
- Virial theorem, 340–342
- Viscous effects, 101, 150, 219, 322
- Vis-viva integral, 52
- Vortex, 329, 330
- Wake, 104, 105
- Wallops Island, 392
- Weathercocking, 326
- Web,
 —fraction, 196
 —thickness, 196
- Western Test Range (W.T.R.), 392
- Whittaker's theorem, 366
- Wien's law, 153
- Wind, 334
- Windtunnel test, 320
- Yaw
 —angle, 67, 83, 331
 —rate, 83, 84
- Year, 17–19
 civil calendar, 18
 Gregorian calendar, 18
 Julian, 18
 leap, 18
 tropical, 17, 18
- Zenith, 11
- Zone time (Z.T.), 17



THE AUTHORS

Jacobus W Cornelisse is a Staff Member at the European Space Research and Technology Centre (ESTEC), Noordwijk.

Herman F R Schöyer is a Senior Faculty Member of the Department of Aerospace Engineering at Delft University of Technology, and a Consultant for the Technological Laboratory of TNO.

Karel F Wakker is a Senior Faculty Member of the Department of Aerospace Engineering at Delft University of Technology.

ROCKET PROPULSION AND SPACEFLIGHT DYNAMICS

CORNELISSE
SCHÖYER
WAKKER

Other titles available

Aircraft Electrical Systems

E H J Pallett, UK Civil Aviation Authority
1977, 167 pages, illustrated, ISBN 0 273 36159 7

Catastrophe Theory and its Applications

Tim Poston, Battelle, Geneva and Ian Stewart, University of Warwick
1978, 509 pages, illustrated ISBN 0 273 01029 8

Mathematical Modelling Techniques (Research Note in Mathematics)

R Aris, University of Minnesota
1978, 203 pages, illustrated, ISBN 0 273 08413 5

Introduction to Microprocessors

Edited by A Aspinall and E L Dagless, University College of Swansea
1977, 170 pages, illustrated, ISBN UK 0 273 01060 3, USA 0 12 064550 5

Nonlinear Analysis and Mechanics: Heriot-Watt Symposium Volumes I and II

(Research Notes in Mathematics)
Edited by R J Knops, Heriot-Watt University
Volume I, 1977, 249 pages, illustrated, ISBN 0 273 01128 6
Volume II, 1978, 320 pages, illustrated, ISBN 0 273 08420 8

Ore Deposits of the USSR

Edited by V I Smirnov, Moscow State University
1977, illustrated
Volume I, 260 pages, ISBN 0 273 01034 4
Volume II, 432 pages, ISBN 0 273 01037 9
Volume III, 500 pages, ISBN 0 273 01039 5
Collective ISBN 0 273 01073 5

Technical Literature Search and the Written Report

D J Maltha, Wageningen Agricultural University
1976, 183 pages, illustrated, ISBN 0 273 00399 2



PITMAN
LONDON · SAN FRANCISCO · MELBOURNE



PITMAN